VNIVERSITAT DE VALÈNCIA

Functional molecular materials: supramolecular networks and coordination polymers with optical and/or magnetic properties

Verónica Jornet Mollá

Memòria per a l'obtenció del títol de Doctor en Nanociència i Nanotecnologia per la Universitat de València

Octubre, 2020

Treball dirigit per:

Prof. Francisco Manuel Romero Martínez

Prof. Francisco Lloret Pastor

En **FRANCISCO LLORET PASTOR**, Catedràtic del Departament de Química Inorgànica de la Universitat de València, i En **FRANCISCO MANUEL ROMERO MARTÍNEZ**, Professor Titular del Departament de Química Inorgànica de la Universitat de València,

CERTIFIQUEN:

Que la memòria presentada per Na VERÓNICA JORNET MOLLÁ amb títol "**Functional molecular materials: supramolecular networks and coordination polymers with optical and/or magnetic properties**" correspon a la seua tesi doctoral, que ha sigut realitzada sota la seua direcció en l'Institut de Ciència Molecular de la Universitat de València i autoritzen la seua presentació per a ser avaluada pel tribunal corresponent.

En Paterna, a 6 d'octubre de 2020

Prof. Francisco Lloret Pastor Prof. Francisco Manuel Romero Martínez

Agraïments

M'agradaria agrair a tota la gent i institucions que han fet possible la realització d'aquesta Tesi Doctoral:

En primer lloc, al meu director, Francisco M. Romero. Aquest ha sigut un camí llarg i ple d'esdeveniments inesperats, però sense cap dubte ell sempre ha sabut trobar una explicació coherent per als incessants contratemps. És una persona increïblement intel·ligent, sempre té alguna cosa interessant a dir independentment del tema de conversa. Moltes gràcies per tot el que m'has ensenyat i pel teu valuós guiatge tant a nivell científic com personal, ja que sense la teua espenta no hauria desenvolupat cap de les dos estades d'investigació que han sigut realment enriquidores per a mi.

A Paco Lloret, com a codirector, per acceptar-me com la seua estudiant amb tot el que això ha suposat per a mi. Moltes gràcies per tota la teua col·laboració i ajuda que m'has brindat sempre que les he necessitat.

A Eugenio Coronado, com a director del grup d'investigació de Materials Moleculars (UIMM) i de l'Institut de Ciència Molecular (ICMol), i a Carlos Gómez, com a director del grup de Materials Moleculars Multifuncionals Modulables (M4), per donar-me l'oportunitat de desenvolupar aquest treball en els seus grups d'investigació.

A Carlos Giménez, per tota l'ajuda prestada a l'hora de resoldre estructures cristal·lines mitjançant difracció de Raigs-X de monocristall i per la seua paciència en les nombroses sessions de dubtes.

A Yan Duan, per ensenyar-me a mesurar estructures cristal·lines mitjançant la tècnica de difracció de Raigs-X de monocristall.

A Samia Benmansour, per ensenyar-me a mesurar difracció de Raigs-X en pols.

A totes aquelles persones amb les que he col·laborat durant el desenvolupament d'aquesta Tesi:

A João C. Waerenborgh, per les mesures de Mössbauer realitzades.

A Ren-Gen Xiong i a tots els membres del seu grup amb els que vaig treballar (Wei-Qiang Liao, Wan-Ying Zhang, Yuan-Yuan Tang, Peng-Fei Li), per les mesures de ferroelectricitat, per acollir-me en el seu grup d'investigació en la

Southeast University (Nanjing, China) i per brindar-me allotjament i companyia durant la meua estada.

A Judith A. K. Howard i a Dmitry Yufit, per les mesures de difracció de Raigs-X sota irradiació a molt baixes temperatures i per acollir-me en el grup de cristal·lografia de Raigs-X de la Universitat de Durham durant la meua estada.

A Laura Cañadillas, per les mesures de difracció de neutrons a diferents temperatures desenvolupades en el ILL (Grenoble, França).

Al Ministeri d'Educació, Cultura i Deport per la dotació econòmica de la beca FPU concedida que ha permès la realització d'aquest treball.

A tots els membres de la part tècnica del grup que han ajudat al desenvolupament del meu treball. Particularment a Chema i a Glòria per totes les mesures magnètiques, de DSC i de TG, així com pels innumerables favors als quals gratament han accedit al llarg de tots estos anys. A Alejandra, per estar sempre disponible a ajudar-me i per les mesures de difracció en pols a temperatura variable. A Jose, per totes les comandes dutes a terme. A Ángel i a Cristian per estar sempre disposats a ajudar en qualsevol cosa. A Manuel per les incidències informàtiques que m'ha resolt. A Paco per la seua ajuda en els tràmits burocràtics del màster i del doctorat, i a Ruth i a Estrella pel seu recolzament administratiu.

A tots els companys del laboratori, per l'ajuda prestada dia a dia i per la seua companyia que han fet més agradable el meu treball diari: als companys de despatx originals (Néstor, Yan, Patricia), als temporals (Marc, Garin) i als actuals (Ramón, Roger, Katia, Chandan, Isaac, Iván). Moltes gràcies a Yan, pel seu indescriptible suport durant la meua etapa d'iniciació a la investigació. A Samuel, per mostrar-me com funciona el món de la investigació durant els meus primers anys al laboratori i per la seua amable predisposició. A Marc, per compartir amb mi dies inacabables de treball al laboratori, innumerables consells i la seua gran saviesa. A Garin, per la seua amistat, ajuda i companyia diària. A Ramón, Javi López i Javi Castells per totes les experiències viscudes durant el màster i per la seua ajuda durant tot aquest temps. A Eugenia, per totes les vegades que ha sabut animar-me, pels cafés amb converses que m'han distret durant dies pesats de treball i pel seu genial humor.

A Natalia, Safaa, Prakash, Garin, Isabel, Marc i Yan per tots els sopars, eixides al cine o passejos per València que m'han deixat records increïbles. Realment moltes d'aquestes experiències han sigut *úniques i irrepetibles*.

A Neus i Hèctor per tots els soparets i totes les vesprades de *carxiscaris* que hem viscut junts, pel seu suport i amistat. A Isabel, per haver estat sempre present des dels inicis de la nostra vida universitària, per la seua incondicional ajuda en qualsevol situació. Moltes gràcies per haver compartit amb mi aquest camí ple d'aventures, *mi persona*.

Als meus pares, per tots els esforços i les il·lusions que han depositat en mi. Moltes gràcies a ma mare per infondre'm ànims diaris i per recordar-me que *la paciència és la mare de la ciència*. Sense ella aquest camí no hauria sigut possible. Moltes gràcies als meus germans, Kike i Raquel, per estar sempre al meu costat quan els he necessitat. I a Didi pel seu reconfortant afecte caní.

I molt especialment a Marcos, per creure en mi i per mostrar-me la part positiva de les coses. Gràcies per traure'm un somriure sempre que ho he necessitat i per animar-me a seguir endavant. En definitiva, per fer-me sentir completa i per ser la millor companyia possible durant aquesta etapa.

[*I, a vegades, ens en sortim*].

Table of contents

Background, motivation and objectives

Background and motivation

"In the initial phase of the process (…), the scientist works through the imagination, as does the artist. Only afterwards, when critical testing and experimentation come into play, does science diverge from art …"

François Jacob (1920-2013)

The field of *molecular materials* attracts the interest of many scientists due to the huge potential of molecular chemistry in materials design and fine tuning of materials properties. The two different projects addressed in this thesis represent two topics that stand out in this area, *spin crossover* (SCO) compounds and *metal organic frameworks* (MOFs), due to their significant progress and rapid development in the last years.

Regarding the first topic, SCO compounds are remarkable **molecular switches** that can be reversed between two different electronic configurations as a function of different chemical and physical stimuli in a detectable way. The possibility of choice of the external stimulus leads to other appealing applications of SCO materials, including sensors, display devices, building blocks for spintronics and molecular electronics, mechanical actuators, luminescent and plasmonic devices, high-density memory units and intelligent contrast agents for magnetic resonance imaging (MRI).[1,2] A line of research in our group has been focused on combining SCO with other physical or chemical properties, such as magnetic ordering[3,4] and high electrical conductivity.[5] In these materials the structural changes associated to the spin crossover phenomenon are cooperatively transmitted through elastic interactions that depend on the intermolecular interactions between SCO centres. These modifications can be subtle or, in the case of *abrupt* spin conversions, result in *structural phase transitions* (SPTs) that play a major role in *defining the properties of the multifunctional switchable materials*.[6,7]

Concerning the second project, although great progress has been achieved in the expansion of porous materials, novel structures with voids and stable networks still need to be designed due to the potential applications of these materials in several fields.[8,9] Specifically, early **molecular recognition** of

nitroaromatic compounds (NACs) and Fe^{3+} ions is a pressing issue, since they are being accumulated in water as pollutants. In addition, NACs exhibit a high degree of toxicity and explosivity, causing harmful effects in human health. In this context, *lanthanide* ions are excellent candidates to solve issues such as industrial waste discharge and water pollution due to their striking luminescence properties.[10] Another field that deserves special attention concerns the oxidation of alkanes C–H bonds. In particular, the *selective oxidation of cyclohexane* produces a mixture of cyclohexanol and cyclohexanone that is an intermediate in the petroleum industrial chemistry, in which current conversions need to be enhanced and additional catalyst separation steps must be avoided by the development of novel and efficient heterogeneous catalysts. In these materials, the metal ions and the linkers are connected through coordination bonds, thus, by increasing the stability of the building blocks (for instance through the use of *chelating anionic ligands*[11]), it is possible to obtain porous materials with stable structures. In this context, ethynyl-bridged **picolinate** ligands are promising *chelating* anionic linkers for the construction of robust coordination polymers with potential applications in the sensing field in aqueous medium and for the development of novel catalysts.

References

[1] M. M. Khusniyarov, *Chem*. *Eur*. *J*. **2016**, 22, 15178-15191
[2] K. S. Kumar, M. Ruben, *Coord*. *Chem*. *Rev*. **2017**, 346, 176-205
[3] E. Coronado, M. C. Giménez-López, C. Giménez-Saiz, J.M. Martínez-Agudo, F.M. Romero, *Polyhedron*. **2003**, 22, 2375-2380
[4] E. Coronado, J. R. Galán Mascarós, M. C. Giménez-López, M. Almeida, J.C. Waerenborgh, *Polyhedron*. **2007**, 26, 1838-1844
[5] E. Coronado, J. C. Dias, M. C. Giménez-López, C. Giménez-Saiz, C. J. Gómez-García, *J*. *Mol*. *Struct*. **2008**, 890, 215-220
[6] M. Shatruk, H. Phan, B. A. Chrisostomo, A. Suleimenova, *Coord*. *Chem*. *Rev*. **2015**, 62-73
[7] H. Zheng, Y.-S. Meng, G.-Li. Zhou, C.-Y. Duan, O. Sato, S. Hayami, Y. Luo, T. Liu, *Angew*. *Chem*. *Int*. *Ed*. **2018**, 57, 8468-8472
[8] a) Z. Ma, B. Moulton, *Coord. Chem. Rev*. **2011**, 255, 1623-1641. b) H. Li, Y. Wang, Y. He, Z. Xu, X. Zhao, Y. Han, *New. J. Chem*. **2017**, 41, 1046- 1056. c) T. Sherstobitova, K. Maryunina, S. Tolstikov, G. Letyagin, G. Romanenko, S. Nishihara, K. Inoue, *ACS Omega*. **2019**, 4, 17160-17170. d) A. Geersing, N. Ségaud, M. G. P. van der Wijst, M. G. Rots, G. Roelfes, *Inorg. Chem*. **2018**, 57, 7748-7756. e) Y.-P. Zhao, Y. Li, C.-Y. Cui, Y. Xiao, R. Li, S.-H. Wang, F.-K. Zheng, G.-C. Guo, *Inorg. Chem*. **2016**, 55, 7335-7340. f) J. S. Seo, D. Whang, H. Lee, S. I. Jun, J. Oh, Y. J. Jeon,

K. Kim, *Nature*. **2000**, 404, 982-986. g) S. Hasegawa, S. Horike, R. Matsuda, S. Furukawa, K. Mochizuki, Y. Kinoshita, S. Kitagawa, *J. Am. Chem. Soc*. **2007**, 129, 2607-2614
[9] Z.-H. Zhu, H.-L. Wang, H.-H. Zou, F.-P. Liang, *Dalton Trans*. **2020**, 49, 10708-10723
[10] a) J.-J. Ma, W.-s. Liu, *Dalton Trans*. **2019**, 48, 12287-12295. b) Y. Pu, Z. Yu, F. Wang, Y. Fu, *Sensor Rev*. **2019**, 39, 149-161
[11] a) M. T. Kapelewski, S. J. Geier, M. R. Hudson, D. Stück, J. A. Mason, J. N. Nelson, D. J. Xiao, Z. Hulvey, E. Gilmour, S. A. FitzGerald, M. Head-Gordon, C. M. Brown, J. R. Long, *J. Am. Chem. Soc*. **2014**, 136, 12119-12129. b) M. Hmadeh, Z. Lu, Z. Liu, F. Gándara, H. Furukawa, S. Wan, V. Augustyn, R. Chang, L. Liao, F. Zhou, E. Perre, V. Ozolins, K. Suenaga, X. Duan, B. Dunn, Y. Yamamto, O. Terasaki, O. M. Yaghi, *Chem. Mater*. **2012**, 24, 3511-3513

Objectives

The objectives proposed for the development of this doctoral thesis are the following:

- Preparation of **new Fe(II) supramolecular networks** in which the **spin crossover is combined with a second physical functionality or with an additional structural feature of interest** *through the appropriate selection of the anionic sublattice*. First, $[Fe(bpp)_2]^{2+}$ salts with different dicarboxylate and pyridinecarboxylate anions will be synthesised in order to determine the effect of the degree of hydration and the nature of the contraanion (flexibility/rigidity, monoanion/dianion) employed in the SCO properties. In addition, special attention will be devoted to highlight the relevance of thermal conditions used in the dehydration process of these materials. Then, the structural rearrangements encompassing the thermal- and light-induced spin transitions will be studied in detail. These analyses will show the *coexistence* of SCO and *ferroelectric* properties, and the interplay between SCO and *hydrogen bond isomerisation* or *proton migration* in these novel systems. Moreover, the *vital influence of hydrogen bonding* on defining the iron(II) spin state will be shown.

- Synthesis of a new family of **ethynyl-bridged picolinate polytopic ligands** and study of its coordination chemistry. The presence of ethynyl bridges provides rigidity to the system and facilitates the prediction of the topology in the final assembly. Besides, the chelating picolinate functional group presumably endows the system with *higher stability towards basic or acid extreme conditions*. This will be verified by analysing the stability of all the complexes synthesised in water solution at different pH values. In particular, Eu(III) and Zn(II) coordination polymers based on this family of ligands will be synthesised and their *luminescent properties* tested for the *sensing* of organic molecules (NACs) and cation recognition (Fe^{3+}). On the other hand, an Fe(II) complex will be prepared and its catalytic performance in cyclohexane oxidation evaluated.

Organisation

This doctoral thesis is divided in *two main parts*. The first part (Chapters 1-3) is based on the use of hydrogen bond in the design of novel iron(II) supramolecular networks exhibiting the spin crossover phenomenon. In some of these complexes, the spin transition takes place in association with a second property or structural rearrangement such as ferroelectricity, proton displacement or H bond isomerisation. The second part (Chapters 4-7) relies on the synthesis and characterisation of coordination polymers based on a novel family of ethynyl-bridged polytopic ligands that, in some cases, combine the picolinate subunit with a second non-chelating functional group.

- **Chapter 1** is an introduction to the spin crossover phenomenon from the perspective of Fe(II) complexes based on the bpp ligand (2,6-bis(pyrazol-3-yl)pyridine). First, a brief summary of known $[Fe(bpp)_2]^{2+}$ systems is conducted, with a short description of their (photo)magnetic properties and technological interest. Then, different structural arrangements that occur at the same time that the spin state transition are surveyed, with special emphasis in magnetoelectric coupling.

- **Chapter 2** shows the results of the structural, (photo)magnetic and thermal properties of new salts combining the $[Fe(bpp)_2]^{2+}$ cation with two different dicarboxylate anions as hydrogen bond acceptors: the flexible adipate ($C_6H_4O_4^{2-}$) and the rigid terephthalate ($C_8H_6O_4^{2-}$). The comparison of the magnetic properties of both compounds ($[Fe(bpp)_2](C_6H_8O_4)\cdot 4H_2O$ (**1**$\cdot 4H_2O$) and $[Fe(bpp)_2](C_8H_4O_4)\cdot 5H_2O$ (**2**$\cdot 5H_2O$)) will reveal the influence of the flexibility of the linkers in the cooperativity of the spin transition and in the crystallinity of the material towards the dehydration process. Moreover, the vital role of thermal conditions during the desolvation of these compounds will be highlighted through the structural study of the anhydrous adipate derivative ($[Fe(bpp)_2](C_6H_8O_4)$ (**1**)).

- **Chapter 3** relies on the incorporation of acentric mononegative anions in $[Fe(bpp)_2]^{2+}$ hydrogen-bonded networks and study of their structural, (photo)magnetic and thermal properties. First, isonicotinate and nicotinate anions were selected as hydrogen bond acceptors, crystallising the resulting salts (anhydrous $[Fe(bpp)_2](isonic)_2$ (**3**) and $[Fe(bpp)_2](nic)_2\cdot 4H_2O$ (**4**$\cdot 4H_2O$)) in polar space groups. Therefore, their

ferroelectric nature was investigated. In addition, the comparative study of these salts will allow to extract some conclusions about the influence of the N-atom of the anion in the spin crossover properties of both Fe(II) salts. Secondly, the isonicotinate N-oxide anion was combined with the same cationic sublattice and the compound $[Fe(bpp)_2](isonicNO)_2 \cdot 2.4H_2O$ (**5**$\cdot 2.4H_2O$) was obtained. Crystallographic analyses of this material at different temperatures will show a hydrogen bond isomerisation that takes place in synergy with the SCO process. Finally, a co-crystal composed by the isonicotinic N-oxide acid both in its deprotonated and free forms was effectively combined with $[Fe(bpp)_2]^{2+}$ cations yielding a new compound ($[Fe(bpp)_2](isonicNO)_2 \cdot HisonicNO \cdot 5H_2O$ (**6**$\cdot 5H_2O$)). In this latter case, neutron crystallography studies will unambiguously show that a proton migration occurs between the anion and its conjugate base in association with the SCO process. Likewise, the dehydration-rehydration processes were studied in all the materials obtained, with detail of the structural transformations in those cases in which the crystallinity of the sample is not lost in the anhydrous phase.

- **Chapter 4** is an introduction to the second part of this thesis. A brief summary about coordination polymers, synthetic approaches, current limitations and relevant applications is firstly presented. Also, a general overview of ethynyl-bridged picolinate systems is carried out. Finally, a more detailed description of luminescent lanthanide coordination complexes and d^{10} transition metal compounds towards Fe^{3+} and NACs detection is included.

- **Chapter 5** describes the synthesis and characterisation of a novel family of rigid ethynyl-bridged polytopic picolinate ligands in which homopolytopic (**H_2L1**-**H_2L5**) and heteroditopic (**HL6**-**H_2L8**) ligands can be distinguished. First, the molecular structure and preparation of each ligand is presented, together with the reaction mechanism. Then, the ligand characterisation by ^{1}H- and ^{13}C-NMR (nuclear magnetic resonance), IR (infrared spectroscopy), EA (elemental analysis) and ESI-TOF (electrospray ionisation time-of-flight) mass spectra will be shown.

- **Chapter 6** explores the coordination chemistry of these ethynyl-bridged picolinate ligands with divalent metal transition ions. Five

crystalline compounds were isolated: $[Cu_2(\mathbf{L7})_4]$ (**7**), $[Cu_3(\mathbf{MeL8})_6]$ (**8**), $[Fe(H_2O)_2(\mathbf{L2})]$ (**9**), $[Zn(\mathbf{L7})_2]$ (**10**) and $[Zn(H_2O)_2(\mathbf{L8})]$ (**11**). Their synthesis, structural and thermal characterisation will be described, as well as their magnetic, luminescent properties in the context of metal sensing and detection of small organic molecules and catalytic application towards cyclohexane oxidation.

- **Chapter 7** gathers the progress achieved on the preparation of lanthanide coordination complexes based on these ethynyl-bridged picolinate ligands. Eleven crystalline materials were prepared from ligands **H_2L8** ($[NH_2(CH_3)_2][Ln(H_2O)_2(\mathbf{L8})_2]$, Ln = Eu(**12**), Gd(**13**), Tb(**14**), Dy(**15**), Ho(**16**) and Er(**17**)) and **H_2L2** ($[NH_2(CH_3)_2][Ln(\mathbf{L2})_2]\cdot 1H_2O\cdot 1HAc$, Ln = Eu(**18**), Gd(**19**), Tb(**20**), Dy(**21**) and Ho(**22**)). The synthetic methodology, thermal, structural, magnetic and luminescent characterisation will be described for both series of coordination complexes. Furthermore, the solvatochromic behaviour and sensing of metal ions for the europium derivatives will be shown.

- **Chapter 8** compiles the general conclusions of the present dissertation. Apart from specific conclusions that have been included at the end of each chapter, the most relevant findings are summarised in this part of the thesis.

A summary of the thesis in Valencian, an appendix section with specific information about the characterisation techniques, a list of publications and a drop-down list of compounds are given at the end of this manuscript.

Part I. Hydrogen-bonded networks of $[Fe(bpp)_2]^{2+}$ complexes and (pyridine)carboxylate anions

Chapter 1: Introduction to spin crossover

Spin transitions have been reported since the 1930s when Cambi and co-workers studied the magnetic properties of a series of dithiocarbamato complexes of iron(III).[1] Thereafter, many more complexes have been synthesised exhibiting this phenomenon and thoroughly investigated. The earlier developments in iron(II) systems were reviewed by König in 1968, Goodwin in 1976 and Gütlich in 1981.[2-4] On the other hand, it has to be noted that spin transitions are also found in natural systems, exhibiting a fundamental role in controlling biological functions[5] such as the efficient oxygen transport,[6] or in certain minerals.[7] In general, coordination compounds of transition metal ions may present a switching phenomenon between two labile electronic configurations as a consequence of a given external perturbation such as light irradiation, temperature, application of pressure or a magnetic field or the insertion of a guest molecule into the system.[8] This phenomenon is known as spin crossover (SCO) or spin transition and it has been observed in iron(II), iron(III), cobalt(II) and, to less extent, in cobalt(III), chromium(II), manganese(II) and manganese(III).[8a,9] This thesis has been focused on Fe(II) systems since the most studied SCO centres are based on this ion.

The crystal field theory describes the nature of the metal–ligand bond in transition metal coordination compounds and it is based on an electrostatic model of the bonding that considers the ligand lone pair (L:) as a negative charge and the central metal ion as a positive charge. In an octahedral environment,[10] the *d* orbitals of Fe^{2+} cations are split into two subsets of t_{2g} (d_{xy}, d_{yz}, d_{zx}) and e_g (d_{z^2} and $d_{x^2-y^2}$) orbitals, being the ligand field splitting Δ the difference in energy between them (Figure 1.1a). This is due to different interactions of the electrons in the *d* orbitals of the metal with the ligands. In d_{z^2} and $d_{x^2-y^2}$ orbitals, the electrons are concentrated close to the ligands along the axis and they are strongly repelled. Instead, the electrons of the d_{xy}, d_{yz} and d_{zx} orbitals are concentrated in regions that lie between the ligands, being the repulsion lower and accounting for the dissimilarity in the energy destabilisation and stabilisation of these orbitals. The Fe^{2+} ions can change their spin state between the $^1A_1$ diamagnetic low-spin (LS; $S = 0$; $(t_{2g})^6$) and $^5T_2$ paramagnetic high-spin (HS; $S = 2$; $(t_{2g})^4(e_g)^2$) states depending on the magnitude of Δ relative to the spin-pairing energy (P) of the electrons. When $\Delta > P$, the LS state that corresponds to the maximum possible spin-pairing (resulting from a strong ligand field) will be populated. Instead, when $\Delta < P$ (favoured by weaker ligand fields), the electrons will fill the orbitals according to Hund's rule, maximising the spin multiplicity

and giving rise to the HS configuration. In the case in which the difference between P and Δ is very small, an intra-ionic electron transfer between the e_g and t_{2g} orbitals may take place leading to SCO behaviour. This situation implies that the splitting Δ induced by a given ligand set lies close to the discontinuity observed in the corresponding Tanabe-Sugano diagram (Δ_c) for the metal ion (Figure 1.1.b).[11]

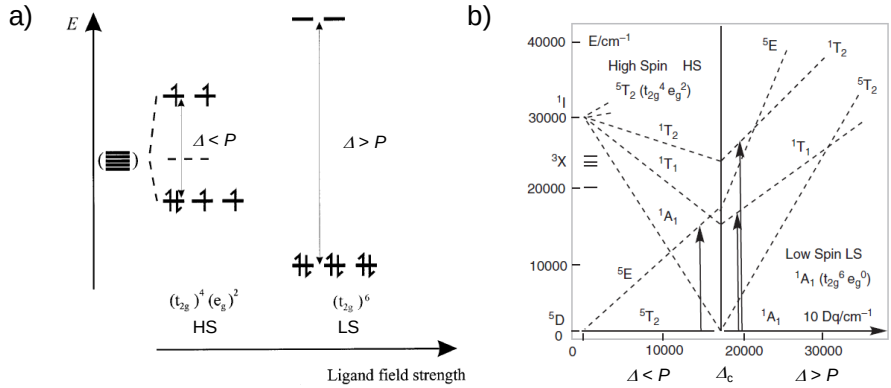

Figure 1.1. a) Diagram that shows the electronic configuration of the two possible spin states of a d^6 iron(II) ion in an octahedral environment (LS and HS states). It also represents the equilibrium between these two states as a function of the ligand field parameter (Δ) and the spin-pairing energy (P). Adapted from reference [10]. b) Simplified Tanabe-Sugano diagram for an octahedral Fe(II), d^6 complex. The arrows show the spin-allowed electronic transitions ($^5T \longrightarrow {}^5E$) in the HS regime and ($^1A_1 \longrightarrow {}^1T_1$ and $^1A_1 \longrightarrow {}^1T_2$) in the LS regime. Adapted from reference [11].

The plot of the potential energy of the SCO centre *vs* the average metal-to-ligand bond length is represented in Figure 1.2. Since the e_g subset has an antibonding character, its population occurs with an increase in the metal-to-ligand bond distances. Thus, the potential energy diagram for the HS state is shifted towards greater Fe–N distances, being the typical change in Fe–N bond lengths (Δr_{HL}) about 0.2 Å between both spin states.[10,12] The vertical displacement of the potential wells depends on the nature of the donor ligand and indicates that for an isolated SCO molecule the LS state is stabilised in comparison to the HS state by an energy $\Delta E°_{HL}$. When this energy difference between the lowest vibrational energy levels of the potential wells of the two states ($\Delta E°_{HL} = E°_{HS} - E°_{LS}$) is equal to $k_B T$ (order of thermal energy), a thermally induced SCO may occur. At low temperatures, the LS state will be predominantly populated. As the temperature increases, the SCO centre transforms the thermal energy into vibrational energy, thus, populating the excited vibrational levels until reaching a point in which the enthalpy energy cost between the HS and LS states is compensated by the

entropy difference between both states (being larger in the HS case as a consequence of the higher number of vibrational levels per unit of energy).[13] Then, the population of the HS state is favoured at high temperatures. The spin transition is not only associated to a change of the electronic structure of the central ion, it affects the complex molecule as a whole. This significantly affects the physical and chemical properties of the material, being the most striking changes those involving magnetic behaviour and colour.[9a]

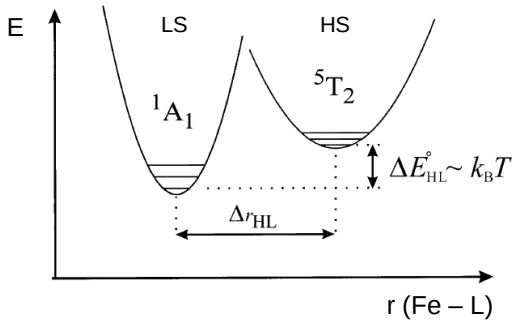

Figure 1.2. Representation of the potential wells for the HS and LS states of an iron(II) SCO system. The x coordinate is the metal-donor atom distance. Adapted from reference [10].

1.1. Cooperativity of SCO transitions

The cooperativity of the system can be defined as the extent to which the effects of the spin change (electronic and structural due to the change in metal–ligand bond length) are propagated through the crystal lattice. Although the origin of the spin transition is purely molecular, elastic interactions between SCO molecules organised into a crystalline network can propagate these changes, leading to long-range interactions. Such elastic interactions can be ferroelastic or antiferroelastic-like. In the first case, the population of the same spin state is favoured, while the second scenario is responsible for alternating HS/LS states.[14] A strong degree of cooperativity gives rise to abrupt interconversion between the two spin states and a thermal hysteresis can appear, providing bistability and thus a memory effect to the system. In an abrupt transition the SCO process takes place in a narrow range of temperature and the term bistability refers to the ability of a system to be observed in two different electronic states in a certain range of some external perturbation (normally temperature).[10] This is the most desirable situation that can find several applications in different fields such as smart sensing, information storage and display devices.[15] And even more if the transition takes place near room temperature.[16]

On the contrary, if the cooperativity of the system is weak, a gradual transition appears without thermal hysteresis. In this case, the spin transition occurs over a wide temperature range. The limiting case of this behaviour is the spin transition in solution, in which the curve can be best described in agreement with a simple thermal equilibrium involving a Boltzmann distribution over the two spin states.[9f] These different behaviours can be analysed by representing (Figure 1.3) the fraction of high spin centres (γ_{HS}) as a function of temperature. The shape of each representation clearly indicates the type of SCO process. There are also other types of transitions: incomplete (Figure 1.3.e) transformations where the spin transition does not occur for all the metal centres, or stepped transitions in which the system populates intermediate phases between the LS and HS states. Figure 1.3.d shows a two-step transition in which the iron centres exhibit different transition temperatures, with the population of a mixed HS/LS phase as an intermediate. This state can arise from structurally inequivalent Fe^{2+} centres or by symmetry breaking.[9f,17-18]

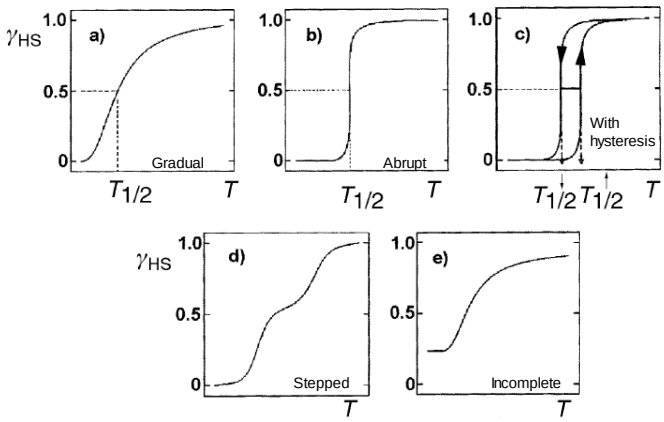

Figure 1.3. Representation of the main types of spin transition curves. $T_{1/2}$ is the transition temperature defined as the temperature at which the fractions of HS and LS centres are equal. The width of the hysteresis loop is described by two transition temperatures ($T_{1/2}^{\uparrow}$ and $T_{1/2}^{\downarrow}$). Adapted from reference [10].

In general, multi-step SCO behaviour arises from the existence of elastic frustration resulting from the competition between ferroelastic and antiferroelastic-type interactions in the materials.[19-20] The synthesis of multi-step SCO materials is appealing due to their potential applications in high-data order storage and multi-switches, however, its design is still challenging.

In order to increase the cooperativity of the system, three different strategies[9a] have been developed: i) linking the metal centres through covalent bonds, ii) favour the formation of strong hydrogen bonds from the choice of appropriate ligands and hydrogen-bonding acceptors, iii) induce the establishment of π-π stacking interactions between the aromatic rings (Figure 1.4). For instance, the study of $[Fe(L)_2(NCS)_2]$ complexes where L is a variable bidentate α-diimine ligand, such as 2,2'-bipyridine (bpy), 1,10-phenanthroline (phen), dipyrido [3,2-*a*:2',3'-*c*]phenazine (dpp) or 2,2'-bithiazoline (btz), confirms that the degree of cooperativity can be modulated by modifying the intermolecular contacts (Figure 1.5).[21-22] The btz derivative exhibits a smooth transition without cooperative effects due to the limited intermolecular interactions. Instead, for bpy and phen ligands that can establish π-π contacts, the transitions are abrupt. Finally, π-π interactions are stronger for the dpp derivative thanks to its extended aromatic character that result in the observation of thermal hysteresis. In this thesis, the last two strategies concerning the increase of intermolecular interactions between the iron centres have been successfully applied for the synthesis of novel spin crossover complexes.

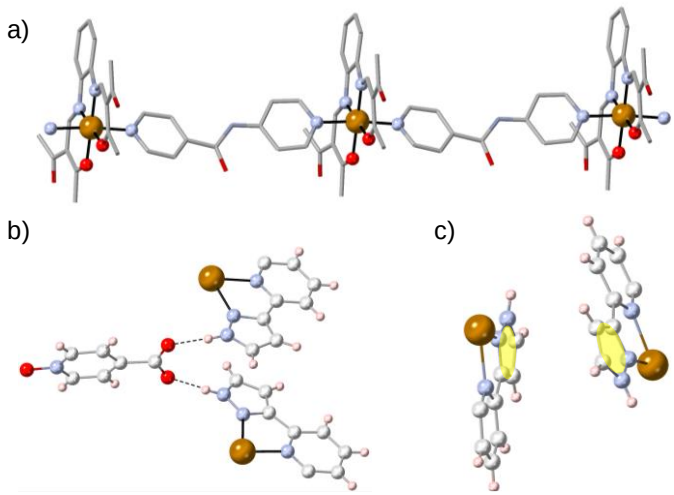

Figure 1.4. Strategies used in order to obtain systems with high cooperativity between the SCO centres in the solid state: a) connecting iron(II) centres via bridging ligands (extracted from reference [23]); b) presence of strong hydrogen-bonds; c) increasing the amount of π-π stacking interactions. Dashed lines refer to hydrogen bonds and yellow spheres to π-π interactions.

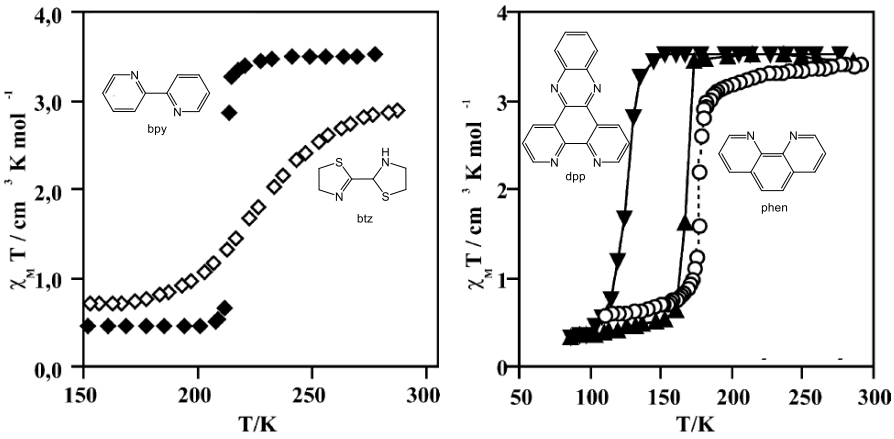

Figure 1.5. Magnetic properties of $[FeL_2(NCS)_2]$ and molecular structure of the corresponding ligands. Left: L = bpy and btz (black and white rhombuses, respectively). Right: L = phen and dpp (circles and black triangles, respectively). Adapted from reference [21].

1.2. SCO in $[FeN_6]^{2+}$ complexes

Most of the iron(II) SCO complexes known exhibit an FeN_6 coordination sphere. However, there are other donor atom sets known for switchable six-coordinate iron(II) systems including N_4O_2,[24] N_4S_2,[25] P_4Cl_2 and P_4Br_2.[26] Even there are a few examples in which a seven coordinate iron centre displays SCO with an $N_3O_2C_2$ donor atom set.[27] Among FeN_6 coordination complexes, ligands of variable denticity have been employed, for instance, bidentate diimine ligands (phen and bipy),[28-29] tridentate N-donor ligands (as in bis[hydro-tris(pyrazolyl-borato)]iron(II)),[30-31] hexadentate systems (as in tetrakis(2-pyridylmethyl)ethylenediamine)[32] and even six monodentate N-donating ligand molecules (as in $[Fe(N\text{-alkyl-tetrazole})_6]X_2$).[33] In general, the systems exhibiting $[FeN_6]$ coordination environments can be classified in two main subsets:

- Neutral entities that present the following general formula $[FeL_iX_2]$ (being X a coordinative anion and L a ligand that can be mono-, bi- or tetradentate with i values of 4, 2 and 1, respectively).
- Cationic systems that are represented by a general formula $[FeL_i]^{2+}$ (where i is 6, 3 or 2 depending if the ligand is mono-, bi- or tridentate). In this case, neutrality is achieved by means of non-coordinative anions.

In the latter case, tridentates of the terimine type, of which the terpyridine (terpy) is the parent system, are among the most studied ligands. $[Fe(terpy)_2]^{2+}$

is LS (S = 0) and it does not exhibit SCO behaviour but several [FeN_6] complexes have been synthesised using tridentate ligands of this type in which the terminal pyridine rings have been substituted by five-membered heterocycles so that the field strength can be brought directly into the electronic crossover range for iron(II). In particular, imidazole, triazole and pyrazole rings have been employed due to the fact that they are less σ-donating agents than the pyridine ring (Figure 1.6). The tridentate 2,6-bis(pyrazol-3-yl)pyridine (bpp) ligand, used in the development of this thesis, belongs to this subset.

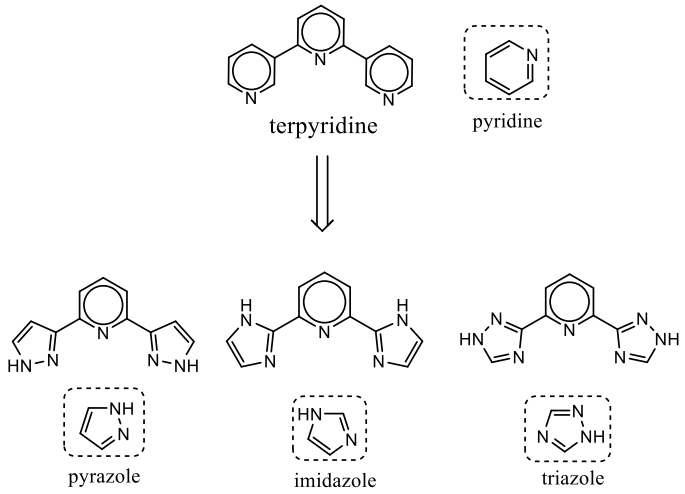

Figure 1.6. top) Terpyridine ligand; bottom) Active SCO ligands formed by replacing the pyridine ring by different heterocycles of five members.

1.3. Iron(II) complexes containing the bpp ligand

The bpp ligand is formed replacing a pyridine group by a pyrazole fragment in the positions 2 and 6 (Figure 1.7). Metal complexes of the type [$Fe(bpp)_2$]X_2·nsolv are typically obtained by using this ligand, in which two tridentate molecules coordinate in a chelating fashion around one Fe(II) centre. Imine N atoms in the bpp ligand allow coordination to the iron cation whereas the non-coordinative amine -NH groups enable the formation of strong hydrogen bonds with solvent molecules and/or counteranions. In addition, in these systems offset face-to-face (OFF, $\pi\cdots\pi$) and edge to-face (EF, C-H $\cdots$ π) π-type interactions are established between the aromatic rings (Figure 1.8).

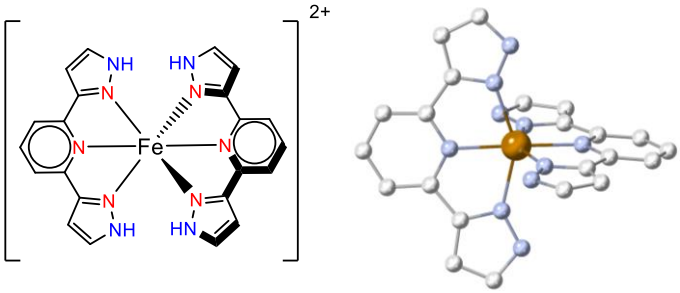

Figure 1.7. left) Scheme of the $[Fe(bpp)_2]^{2+}$ complex, showing in red N atoms that coordinate to the iron cation and in blue -NH groups that allow interaction through hydrogen bonding; right) 3D representation of the $[Fe(bpp)_2]^{2+}$ cation. Hydrogen atoms have been omitted for clarity.

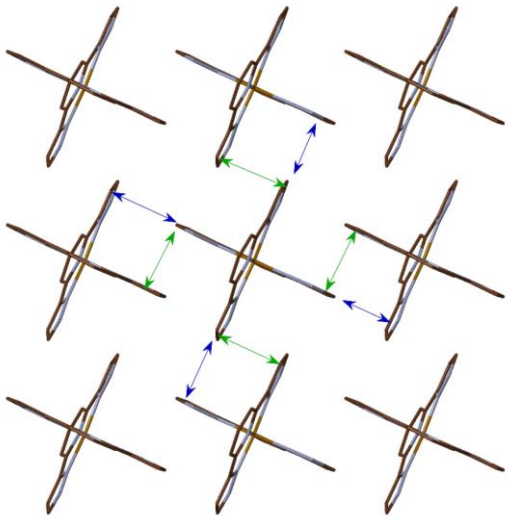

Figure 1.8. Illustration of the *terpyridine embrace* (each iron centre interacts with four adjacent moieties) motif present in $[Fe(bpp)_2]Cl_2{\cdot}6.5H_2O$, adapted from reference [34]. Green arrows indicate $\pi\cdots\pi$ stacking interactions whereas blue arrows represent C-H$\cdots\pi$ contacts. Hydrogen atoms have been omitted for clarity.

Thanks to the establishment of these interactions, $[Fe(bpp)_2]^{2+}$ systems usually present abrupt transitions with thermal hysteresis and it is well-known that their magnetic properties depend on the second iron coordination sphere (solvent molecules and/or counteranions establishing hydrogen bonds with the iron centres). H. A. Goodwin and K. H. Sugiyarto have synthesised and characterised the systems based on the following anions: Cl^-,[34] BF_4^-, NO_3^-, PF_6^-, Br^-, I^-,[35] $CF_3SO_3^-$,[36] NCS^-, $NCSe^-$[37] and $[Fe(CN)_5NO]^{2-}$.[38] These authors demonstrated that a wide variety of magnetic behaviours could be obtained

using $[Fe(bpp)_2]^{2+}$ complexes depending on the solvent molecules and the nature of the counteranions present in the crystal lattice (Figure 1.9). Later, G. Aromí and co-workers prepared and characterised structurally the perchlorate derivative. [39]

The chloride derivative is diamagnetic in both hydrated and anhydrous forms. In a similar way, $[Fe(bpp)_2](NO_3)_2 \cdot 2H_2O$ is predominantly low-spin and only a slightly increase in the magnetic signal is observed while increasing the temperature (Figure 1.9.a). For the hexafluorophosphate salt, a dihydrate, a monohydrate, as well as the anhydrous species were obtained. For these three compounds, gradual and incomplete spin transitions are observed (with the occurrence of a two-step transition for the hydrated hexafluorophosphate salts, Figure 1.9.b). Instead, the thiocyanate, selenocyanate and nitroprusside derivatives are high-spin at room temperature and they undergo abrupt and complete transitions to the LS state on cooling down the samples (that for the thiocyanate occurring in two steps, Figure 1.9.c-d). As-synthesised bromide and iodide derivatives are low-spin at room temperature and an increase in the magnetic signal is registered while heating the samples. This occurs in the temperature range in which dehydration of the compounds takes place, which results in a conversion to the high-spin state. The hydrated salt of the perchlorate anion is predominantly low-spin at room temperature whereas the hydrated salt of the fluoroborate anion presents a gradual SCO with a high temperature transition. However, the anhydrous salts of bromide, perchlorate, iodide and fluoroborate anions were found to be completely paramagnetic at room temperature, undergoing complete transitions to the low-spin state upon decreasing the temperature (Figure 1.9.a, e-f). In particular, the anhydrous fluoroborate salt shows a thermal hysteresis loop of 10 K width (with $T_{1/2}^{\downarrow}$ = 173 K and $T_{1/2}^{\uparrow}$ = 183 K, Figure 1.9.e).

Probably, the most remarkable magnetic behaviour of these simple salts concerns the triflate derivative, that depends strongly on the extent of hydration. $[Fe(bpp)_2](CF_3SO_3)_2 \cdot 3H_2O$ is low-spin, whereas its anhydrous form is high-spin in the whole temperature range studied. Instead, its monohydrate $[Fe(bpp)_2](CF_3SO_3)_2 \cdot H_2O$ is high-spin at room temperature but undergoes an extremely abrupt transition with two steps in the heating mode (Figure 1.10). It also displays a very broad thermal hysteresis of 140 K at its widest point, being the largest observed for any molecular spin crossover system.[40]

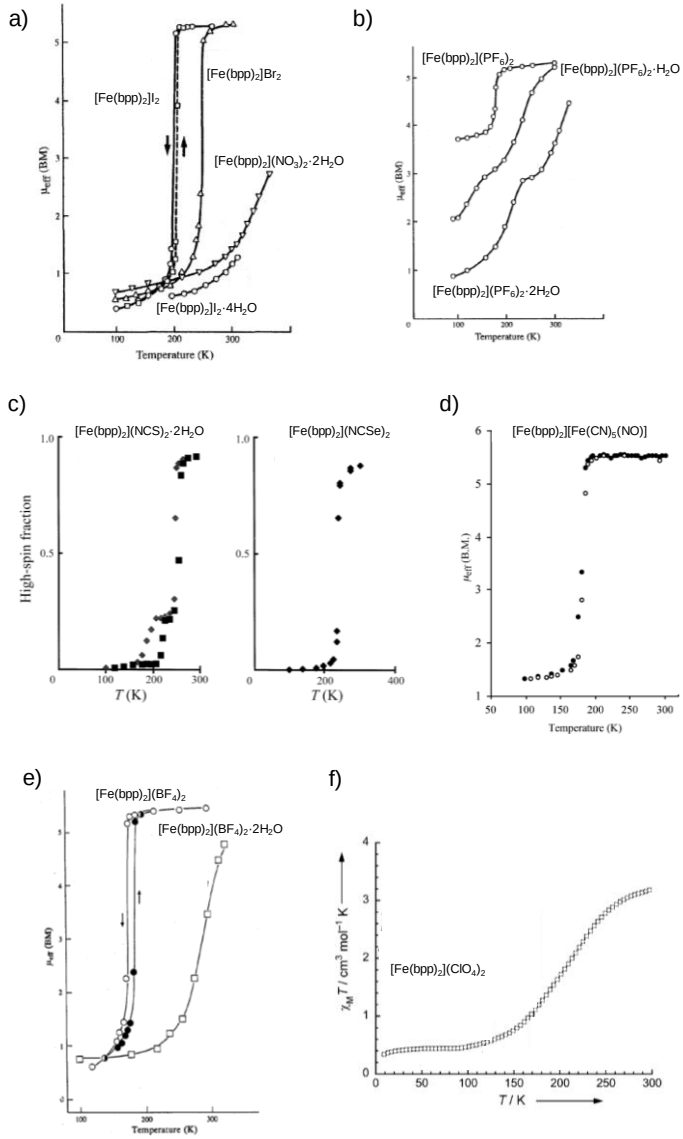

Figure 1.9. a) Temperature dependence of the magnetic moment of $[Fe(bpp)_2]I_2$ (continuous line decreasing *T*; broken line increasing *T*), $[Fe(bpp)_2]Br_2$, $[Fe(bpp)_2](NO_3)_2{\cdot}2H_2O$ and $[Fe(bpp)_2]I_2{\cdot}4H_2O$. b) Temperature dependence of the magnetic moment of $[Fe(bpp)_2](PF_6)_2$, $[Fe(bpp)_2](PF_6)_2{\cdot}H_2O$ and $[Fe(bpp)_2](PF_6)_2{\cdot}2H_2O$. c) Spin transition curve for $[Fe(bpp)_2](NCS)_2{\cdot}2H_2O$ (diamonds decreasing *T*; squares increasing *T*) and $[Fe(bpp)_2](NCSe)_2$. d) Temperature dependence of the magnetic moment of $[Fe(bpp)_2][Fe(CN)_5(NO)]$ (filled circles decreasing *T*; open circles increasing *T*). e) Temperature dependence of the magnetic moment of $[Fe(bpp)_2](BF_4)_2$ and $[Fe(bpp)_2](BF_4)_2{\cdot}2H_2O$. f) Plot of χT versus *T* for $[Fe(bpp)_2](ClO_4)_2$. Adapted from references [35-39].

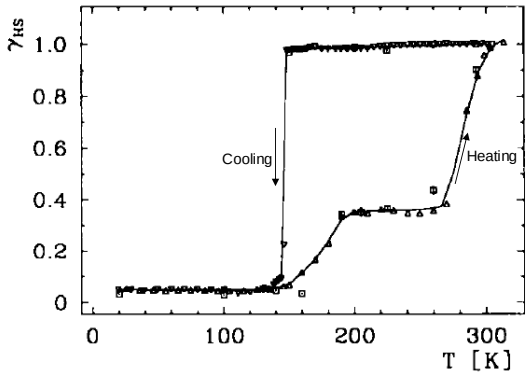

Figure 1.10. Thermal dependence of the fraction of HS centres (γ_{HS}) in $[Fe(bpp)_2](CF_3SO_3)_2 \cdot H_2O$. The squares are obtained from Mössbauer measurements and the triangles are derived from magnetic susceptibility experiments. Adapted from reference [40].

In this context, Barrett and co-workers have studied in solution the effect of hydrogen bonding on the magnetic properties of the fluoroborate derivative, concluding that the temperature of spin crossover shifts to 60-70 K higher in water compared to organic solvents.[41] However, in a few cases, it has also been observed the stabilisation of the HS phase in solvated materials.[42-43] A proper reason that explains this difference still remains unknown.

Apart from simple anions, other kind of anionic linkers have been employed in order to build multifunctional spin crossover complexes. Previously in our group, salts that combine the bpp cations with different paramagnetic anions have been synthesised: $[Cr(L)(ox)_2]^-$ (L = 2,2'-bipyridine (bpy), 1,10-phenanthroline (phen)), $[Cr(ox)_3]^{3-}$, $[Cr(CN)_6]^{3-}$ and $[MnCr(ox)_3]^-$.[42,44-46] Furthermore, with the aim of achieving a compound exhibiting high electrical conductivity and SCO properties, a copper diselonate complex has been used as anion to compensate the positive charge of the $[Fe(bpp)_2]^{2+}$ moieties.[47] More recently, M. A. Halcrow and co-workers have synthesised new solvated salts of $[Fe(bpp)_2]^{2+}$ systems with the following anions: $[Au(SCN)_2]^-$, $[Au(CN)_2]^-$, $[Ag(CN)_2]^-$ and $[BPh_4]^-$.[48] In principle, the three first compounds were prepared in order to tune the fluorescence properties of the resulting salts by switching the spin state of the iron centres, although powder samples of these four compounds exhibit very gradual spin transitions (Figure 1.11.a). On the other hand, it has been shown by G. Chastanet and co-workers[49] that in spite of the incomplete and gradual conversion showed by the hydrated dicyanoaurate salt, the anhydrous material (crystallised as a desolvated phase) presents a two-step transition with an associated thermal hysteresis of 45 K (Figure 1.11.b). This is

another example of solvatomorphism, in which solvatomorphs exhibit markedly different spin crossover properties.

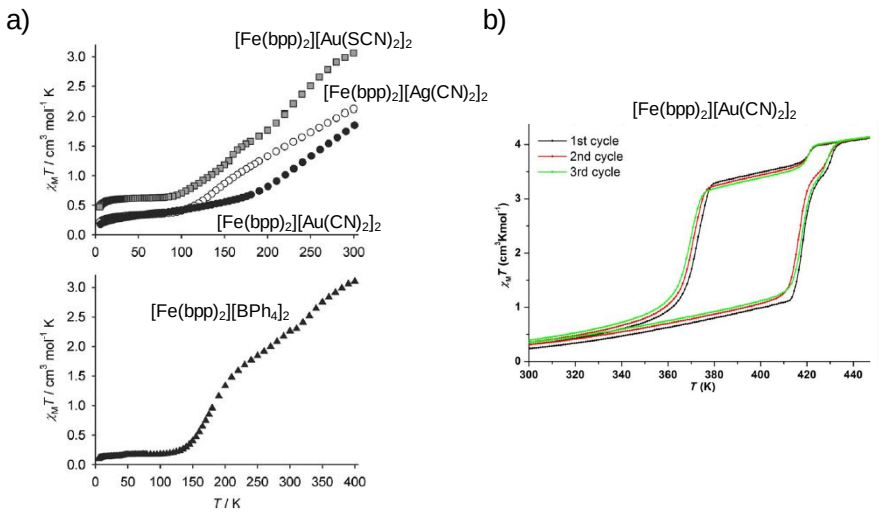

Figure 1.11. a) Variable temperature magnetic susceptibility data of dried powder samples of $[Fe(bpp)_2][Au(CN)_2]_2{\cdot}H_2O$, $[Fe(bpp)_2][Ag(CN)_2]_2{\cdot}H_2O$, $[Fe(bpp)_2][Au(SCN)_2]_2{\cdot}CF_3CH_2OH$ and $[Fe(bpp)_2][BPh_4]_2{\cdot}2CH_3NO_2{\cdot}(C_2H_5)_2O$. b) Thermal dependence of the χT product of $[Fe(bpp)_2][Au(CN)_2]_2$, obtained as a desolvated phase. Adapted from references [48] and [49].

This field has been expanded through the modification of the bpp ligand by the incorporation of other functional groups with the aim of increasing the cooperativity of the system. With this idea in mind, a wide variety of functionalised-bpp type ligands have been synthesised and employed in their own or as mixed ligands, covered mostly by M. A. Halcrow and G. Aromí (Figure 1.12).[50-58] When ligands with bulky substituents are used, the resulting iron(II) complexes usually show HS behaviour during the whole interval of temperature.[50a, 52, 59] Specifically, alkylation of the four pyrazolyl N1 sites in $[Fe(bpp)_2]^{2+}$ removes the thermal spin transition, regardless of the steric properties of the new substituents (Figure 1.13.a). Worth mentioning are a few examples involving stepped transitions, as observed for the compound $[Fe(L1)_2](ClO_4)_2{\cdot}2H_2O$ (Figure 1.13.b),[57] and recent examples of systems that undergo abrupt SCO with thermal hysteresis but well below room temperature ($[Fe(L3)_2](ClO_4)_2{\cdot}H_2O{\cdot}2(CH_3)_2CO$[50c,60,61] and $[Fe(L1)_2](BF_4)_2{\cdot}2H_2O$[55]). Indeed, it is surprising that two salts of the same $[FeL1]^{2+}$ cation that are isostructural at room temperature (BF_4^- and ClO_4^- derivatives) present remarkable differences in their magnetic properties (Figure 1.13.b).[57]

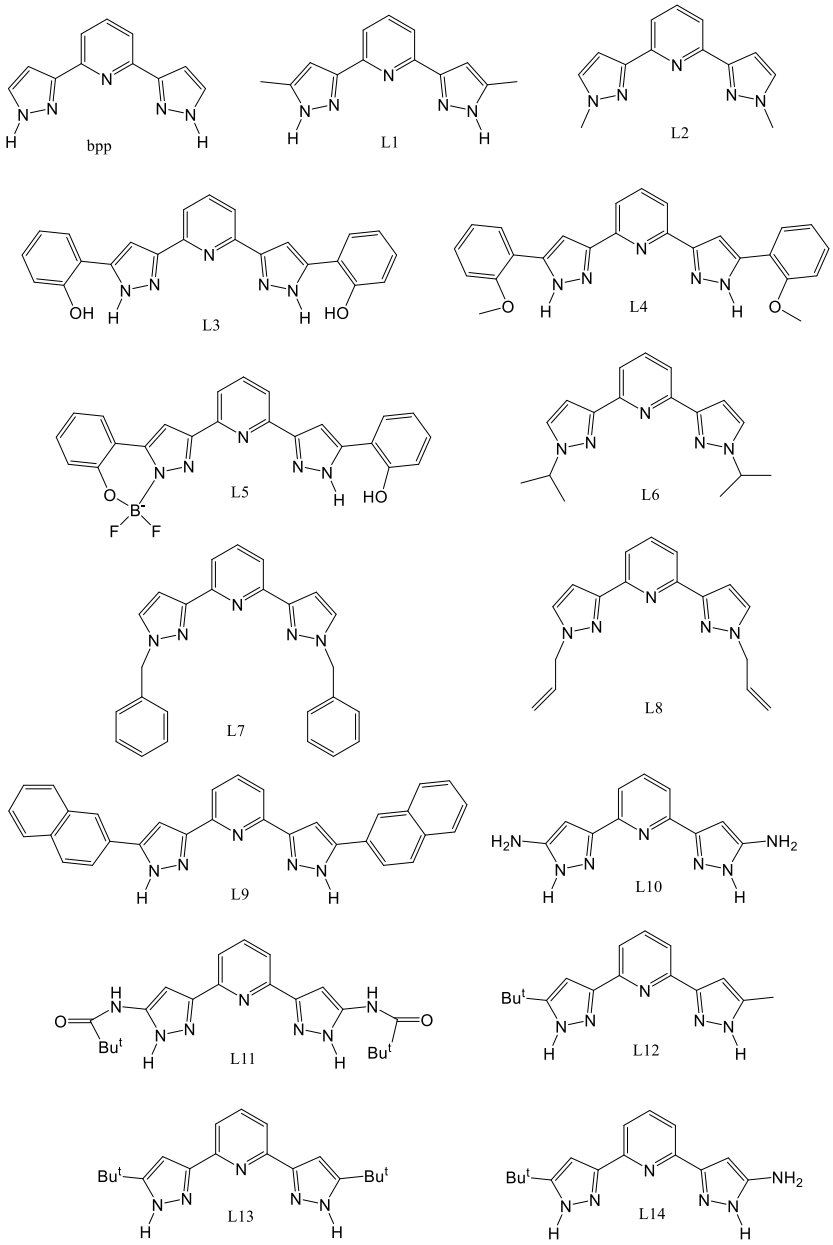

Figure 1.12. Ligand bpp and the derivatives that have been employed in SCO field (L1-L14).

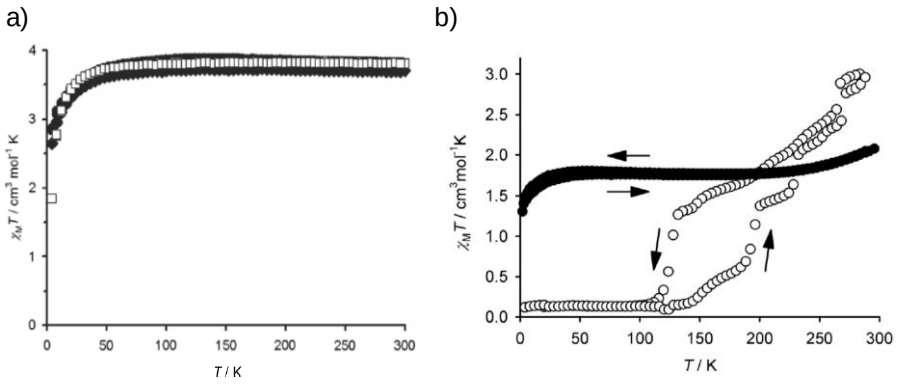

Figure 1.13. a) Thermal dependence of magnetic susceptibility data for $[Fe(L2)_2](BF_4)_2$ (filled squares) and $[Fe(L2)_2](PF_6)_2$ (empty squares). Variable temperature susceptibility measurements for $[Fe(L2)_2](ClO_4)_2$, $[Fe(L6)_2](PF_6)_2$, $[Fe(L6)_2](BF_4)_2{\cdot}H_2O$, $[Fe(L7)_2](BF_4)_2$ and $[Fe(L8)_2](BF_4)_2$ are essentially identical to these data. b) Magnetic susceptibility behaviour of $[Fe(L1)_2](BF_4)_2{\cdot}2H_2O$ (filled circles) and $[Fe(L1)_2](ClO_4)_2{\cdot}2H_2O$ (empty circles). $[Fe(L1)_2](BF_4)_2{\cdot}2H_2O$ presents an almost invariant 50% HS and 50% LS population between 5-300 K. $[Fe(L1)_2](ClO_4)_2{\cdot}2H_2O$ is 85% HS at room temperature and exhibits a two-step crossover when cooling down the sample until the 100% LS state. Heating up the sample reveals a thermal hysteresis that spans 65 K at its widest point. Extracted from references [59] and [57].

To sum up, salts based on the bpp ligand offer a wide variety of spin crossover behaviours. In general, the solvated materials are diamagnetic at room temperature and a conversion from the LS state to the HS state at higher temperatures is observed. In most of the cases, these transitions are interrupted by desolvation processes that result in a fast change to the paramagnetic state. These anhydrous systems usually show very abrupt transitions with thermal hysteresis thanks to the formation of several intermolecular interactions (strategies ii and iii mentioned in section 1.1) between the -NH fragments of the bpp ligands and the anions present in the crystal lattice. Moreover, dehydration is accompanied by a change of colour, generally, from red-brown to orange-yellow, as a consequence of the change in the electronic ground state of iron(II).

1.4. Excited-state trapping

The verification that the spin state of some highly cooperative compounds could be switched by light irradiation was first observed in solution by McGarvey and Lawthers in 1982[62] and achieved by Decurtins and co-workers in the solid state in 1984.[63-64] They irradiated the compound $[Fe(ptz)_6](BF_4)_2$ (ptz = 1-propyltetrazole) at cryogenic temperatures and the relaxation back to the LS state was slow enough to enable trapping of the sample in a metastable HS state. This phenomenon is known as LIESST (*Light Induced Excited Spin State*

Trapping) effect and its mechanism is illustrated in Figure 1.14. Irradiation of the sample in the LS state induces the spin allowed $^1A_1 \longrightarrow {}^1T_1$ absorption. Then, the excited molecule relaxes non-radiatively to the $^5T_2$ HS state *via* double intersystem crossing through the triplet states. At low temperatures, the lifetime of this state is very long because the relaxation back to the LS state is forbidden. Thus, the sample becomes trapped in a photoinduced high-spin (PIHS) state. Likewise, it is possible to pump the system back to the LS state by selective irradiation into the spin allowed $^5T_2 \longrightarrow {}^5E$ absorption band of the HS state, which is called *reverse-LIESST*. This state decays fast by double intersystem crossing via $^3T_{1,2}$ to the $^1A_1$ LS state.

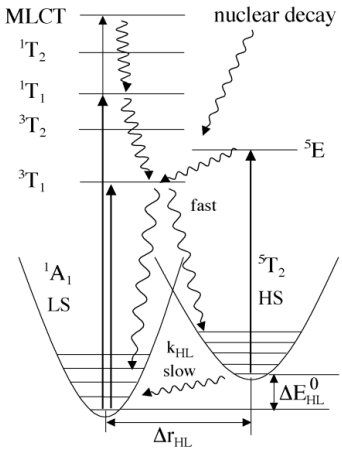

Figure 1.14. Schematic representation of the electronic structure of Fe(II) SCO complexes showing the mechanisms of LIESST and reverse-LIESST effects. Adapted from reference [65].

In order to characterise the LIESST effect, two main parameters are considered: the efficiency of the conversion from the LS state to the PIHS state and the T(LIESST) value which is calculated as the minimum of the $\delta(\chi T)/\delta T$ *vs* T plot of the data obtained during warming at 0.3 K·min^{-1}. The T(LIESST) value indicates the thermal limit of the metastable HS state, whereas the first parameter can be defined as the number of iron(II) LS centres converted to the HS state after absorption of light, which is rather difficult to calculate since several experimental parameters need to be controlled accurately. Qualitatively, the LIESST effect is quite efficient and a value of 0.8 might be considered as typical. Nevertheless, the light–induced HS $\longrightarrow$ LS conversion is only partially accomplished as a consequence of the possible spectral overlap between the $^5T_2 \longrightarrow {}^5E$ transition band of the HS state and the $^1A_1$ to ^3T transition bands of the LS state.[65]

In this regard, $[Fe(bpp)_2]X_2 \cdot nH_2O$ complexes are particularly attractive due to the fact that the desolvated material usually exhibits very abrupt transitions and presents LIESST effect, with long-lived lifetimes of the PIHS metastable phases, [40, 42c, 66] higher than the lifetimes observed for similar compounds.[67] This opens interesting perspectives in the design of devices with optical switches or/and magnetooptical storage properties. Unfortunately, above 50 K the HS ⟶ LS relaxation rate constant exhibits a fast increase for these systems and magnetic information is lost. Therefore, efforts are being made with the aim of obtaining systems with long-lived metastable HS states within the temperature range of real applications. Table 1.1 shows the T(LIESST) values for the different $[Fe(bpp)_2]X_2 \cdot nH_2O$ salts that exhibit this phenomenon. The anhydrous fluoroborate salt presents the higher T(LIESST) obtained for the $[Fe(bpp)_2]X_2$ family with a value of 110 K. Although T(LIESST) values larger than this have been reported, for instance in the case of $[FeL(CN)_2] \cdot H_2O$ (L = is a Schiff-base macrocyclic ligand derived from the condensation of 2,6-diacetylpyridine with 3,6-dioxaoctane-1,8-diamine) with a T(LIESST) = 130 K,[68] these are still too low to achieve real applications.

Table 1.1. T(LIESST), $T_{1/2}^{\uparrow}$ and $T_{1/2}^{\downarrow}$ values (in K) obtained for the different $[Fe(bpp)_2]X_2 \cdot nH_2O$ salts. Extracted from reference [66].

Compound	$\mathbf{T_{1/2}^{\uparrow}}$	$\mathbf{T_{1/2}^{\downarrow}}$	T(LIESST)
$[Fe(bpp)_2](BF_4)_2$	168	184	110
$[Fe(bpp)_2](PF_6)_2$	170	172	82
$[Fe(bpp)_2]Br_2$	250	254	77
$[Fe(bpp)_2]I_2 \cdot 2H_2O$	256	256	77
$[Fe(bpp)_2](NCSe)_2$	230	232	75
$[Fe(bpp)_2](NCS)_2 \cdot 2H_2O$	227	227	74
$[Fe(bpp)_2](BF_4)_2 \cdot 3H_2O$	288	288	70
$[Fe(bpp)_2]Br_2 \cdot 5H_2O$	340	340	40

Correlations between the relaxation rate and the thermal transition temperature ($T_{1/2}$) show that higher values of $T_{1/2}$ lead to a faster relaxation process. Moreover, J.-F. Létard and co-workers compared the T(LIESST) with corresponding $T_{1/2}$ values for more than sixty iron (II) SCO materials with nitrogen-donor ligands and they could establish empirical correlations between both parameters. Based on these data, it has been shown that the following linear expression:[69-70]

$$T(\text{LIESST}) = T_0 - 0.3T_{1/2} \quad \text{(Eq.1.1)}$$

governs the photomagnetic properties of most of these compounds, where T_0 is an empirical parameter that depends mainly on the distortion of the octahedral coordination sphere (denticity and rigidity of the ligand). Four parallel lines have been obtained, as illustrated in Figure 1.15, with values of 100 K, 120 K, 150 K and 200 K. The remarkable point is that the line with a T_0 value of 150 K that corresponds to $[Fe(bpp)_2]^{2+}$ complexes shows some complexes with a $T_{1/2}$ value near room temperature and a measurable T(LIESST) value.

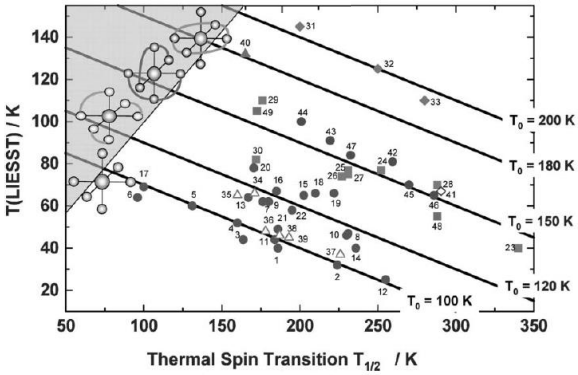

Figure 1.15. Correlation between T(LIESST) and $T_{1/2}$ extracted and adapted from reference [69]. The grey region represents the impossible overlap of the two values.

According to this equation, it is impossible to obtain Fe(II) complexes that combine spin transitions near room temperature with T(LIESST) values higher than 100 K. Thus, it is not surprising the lack of compounds exhibiting the aforementioned properties. Nevertheless, there are important deviations from this law and it has to be highlighted a recent report that describes a complex $[Fe(bpCOOH_2p)_2](ClO_4)_2{\cdot}3.5Me_2CO$ ($bpCOOH_2p$ is a 2,6-bis(pyrazol-1-yl)pyridine derivative functionalised with carboxylic acid groups in the 4-positions of the two pyrazolyl groups of the ligand) exhibiting an abrupt SCO around room temperature with a T(LIESST) value of 120 K.[71] This compound exhibits a strongly distorted HS geometry, and this probably explains the stabilisation of the PIHS state and increase in T(LIESST).[72] Thus, photoinduced structural changes are suggested to be at the origin of this unexpected behaviour. In fact, a similar compound ($[Fe(L)_2](BF_4)_2{\cdot}MeNO_2$, being L = 4-(isopropylsulfanyl)-2,6-di(pyrazol-1-yl)pyridine) presents a T(LIESST) lower than that predicted from Eq.1.1, this dissimilarity being ascribed to a crystallographic phase transition induced by light irradiation.[73] The complete understanding of the photoinduced structural changes induced by light might be

a step towards finding an operative molecular light-induced complex at room temperature.

An interesting situation is found when the T(LIESST) value is close to the $T_{1/2}$ value. In this case, the equation described above (Eq.1.1) gives physically impossible values, due to the fact that the HS phase becomes trapped and the kinetically slow thermal HS ⟶ LS transition is not complete (Figure 1.16). For instance, in $[Fe(dpms)_2(NCSe)_2]$ (dpms = 4,4'-dipyridylmethyl sulphide), the $T_{1/2}$ is high enough with respect to T(LIESST) ($T_{1/2}$ = 135 K, T(LIESST) = 50 K) and this complex displays a complete HS ⟶ LS conversion. However, for $[Fe(dpms)_2(NCS)_2]$, both values are very similar ($T_{1/2}$ = 75 K, T(LIESST) = 58 K) and a conversion of only 30% is achieved in the thermal HS to LS transition.[74] Application of pressure in the latter system results in a shifting of the $T_{1/2}$ value from 75 K at 1 bar to 280 K at 10.6 Kbar and a complete transformation to the fully LS state is reached. Therefore, this verifies that kinetic trapping effects are behind the hindered complete SCO transition at ambient pressure.[75]

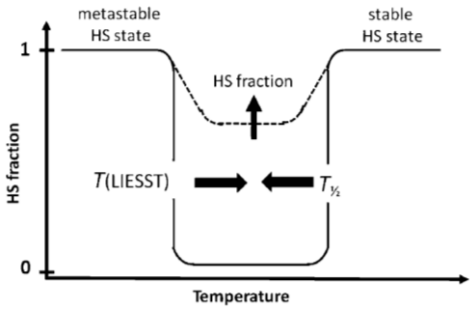

Figure 1.16. Scheme showing the repercussion in the fraction of HS centres when T(LIESST) approaches $T_{1/2}$ value. Extracted from reference [74].

When the initial spin state is a mixed spin state, it is possible to obtain a bi-directional LIESST effect, with population of the fully LS or HS states using different irradiation wavelengths, providing tristability to the system (Figure 1.17.a).[76-77] Very recently, an additional annealing process at liquid nitrogen temperature after a light or temperature application has resulted in a pair of two-step novel pathways in a 2D Hofmann-type polymer ($[Fe(isoq)_2[Au(CN)_2]_2]$, isoq = isoquinoline).[78] These are named *Light-* and *Temperature-Assisted Spin State Annealing* (LASSA and TASSA, Figure 1.17.b and c) and provide access to hidden phases which are undetectable under usual conditions. Thus, in this compound multistability is achieved by means of an elegant interaction between kinetic and thermodynamic effects.

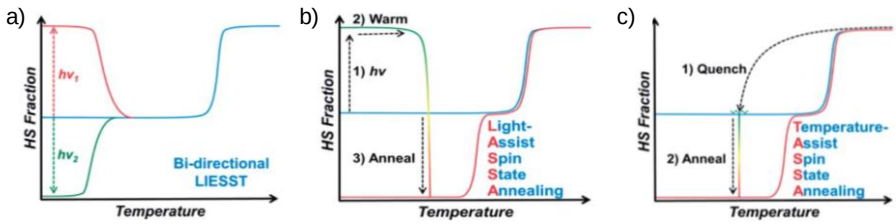

Figure 1.17. Schematic representations of a) a bi-directional LIESST system, b) LASSA and c) TASSA processes. Adapted from reference [78].

Another way of trapping a metastable HS state and exploiting the switching between the two states of Fe^{II} is through thermal quenching (by fast cooling of the sample from a temperature where HS is the stable state).[79] This is known as TIESST (*Thermally Induced Excited Spin State Trapping*) effect. There are examples in which the structure of the metastable phase is practically the same regardless the way in which it was achieved, for instance in *cis*-$[Fe(picen)(NCS)_2]$ (picen = N,N'-bis(2-pyridylmethyl)1,2-ethanediamine), showing only subtle differences regarding relaxation kinetics.[80] For other systems, dissimilarities are noticed between the relaxation processes from the photoexcited phase and from the thermally trapped phase.[40,50c] Indeed, it has been possible to elucidate the single crystal X-ray structures corresponding to both metastable phases in a few cases. For the compound $[Fe(L3)_2](ClO_4)_2{\cdot}2(CH_3COCH_3){\cdot}H_2O$ (L3 ligand is shown in Figure 1.12),[61] the metastable HS phase obtained by thermal trapping shows disorder in half of the perchlorate anions and all the acetone molecules, whereas the LS phase lacks of disorder. Thus, the thermal switch from HS to LS in this compound is associated to a disorder/order transition. On the other hand, the crystal structure of the PIHS state is free of disorder in the perchlorate anions and the structural disorder observed in acetone solvent molecules is significantly reduced (Figure 1.18). Therefore, it was proposed that in the TIESST relaxation the phase would undergo an order-disorder transition prior to the relaxation of the iron centres from the HS to the LS state. Meanwhile, in the LIESST relaxation the iron centres would relax directly from the HS to the LS state. These suppositions were confirmed by kinetic measurements, being the first example in which crystallographic data have allowed the prediction of such relaxation mechanisms.

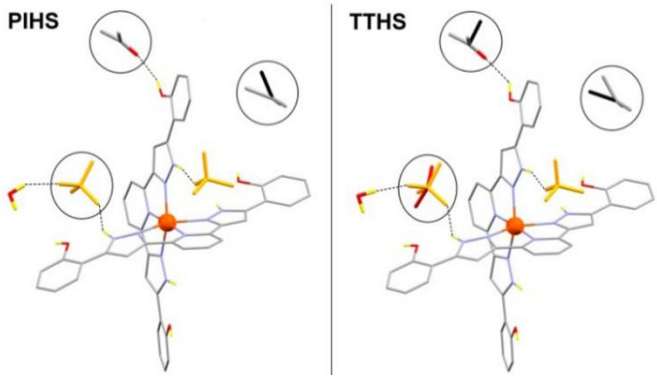

Figure 1.18. Illustration of the asymmetric unit of the photoinduced HS (PIHS) and thermally trapped HS (TTHS) states of $[Fe(L3)_2](ClO_4)_2{\cdot}2(CH_3COCH_3){\cdot}H_2O$, showing the difference in the disorder of two molecules of acetone and one perchlorate anion. C atoms are shown in gray (or black); solvent O atoms in red; ClO_4^- anions in orange, N atoms in blue, H atoms (only shown those on heteroatoms) in yellow and Fe ions in dark-orange. Hydrogen bonds are represented by dashed lines. Extracted from reference [61].

1.5. Interplay of Spin Conversion and Structural rearrangements

As cooperativity increases, the transition becomes more abrupt (often called discontinuous) and a first-order structural phase transition (SPT) is expected to take place, conferring bistability and a memory function to the material. Thus, structure-property correlations in SCO systems can reveal the origin of cooperative behaviour during spin state switching. Within this context, there is a wide variety of structural reorganisations that are linked to thermally-induced spin crossover transitions, such as rotation of coordinated ligands,[81-83] reorientation of coordinated anions[84-86] and alterations involving ligand substituents.[87] For instance, in the complex $[FeL(CN)_2]{\cdot}H_2O$ (L = 2,13-dimethyl-6,9-dioxa-3,12,18-triazabicyclo[12.3.1]octadeca-1(18),2,12,14,16-pentaene), the abrupt spin transition drives a surprising structural rearrangement from a hepta-coordinated iron(II) in the HS state to a hexa-coordinated iron(II) centre in the LS state with the formation of an additional hydrogen bond in the latter case. The structural distortion due to the SCO is propagated through ligand torsion and inversion of the O-CH_2-CH_2-O ethylene ring conformation to the whole crystal lattice in a reversible way (Figure 1.19.a).[88] A second example involves $[Fe(pyrazine)][Pt(CN)_4]$,[82] a complex based on classical Hofmann clathrate compounds that display fascinating cooperative thermal- and light-induced SCO properties. In this salt, the pyrazine ligands exhibit rotation about the coordinating nitrogen axis in the HS state, this motion being stopped in the LS phase (Figure 1.19.b). Correlation between motion and spin transition has

been clearly demonstrated by quasielastic neutron scattering and solid-state ^{2}H-NMR spectroscopy. Furthermore, perturbations concerning non-coordinated anions or non-coordinated solvent molecules have shown to have a direct impact into the iron(II) spin state as a consequence of the high degree of connectivity between all the components of the crystal lattice through elastic intermolecular interactions.[50c,9k,89] Most of these structural changes are based on the existence of multiple orientations that leads to order-disorder behaviour of non-coordinated molecules.[90]

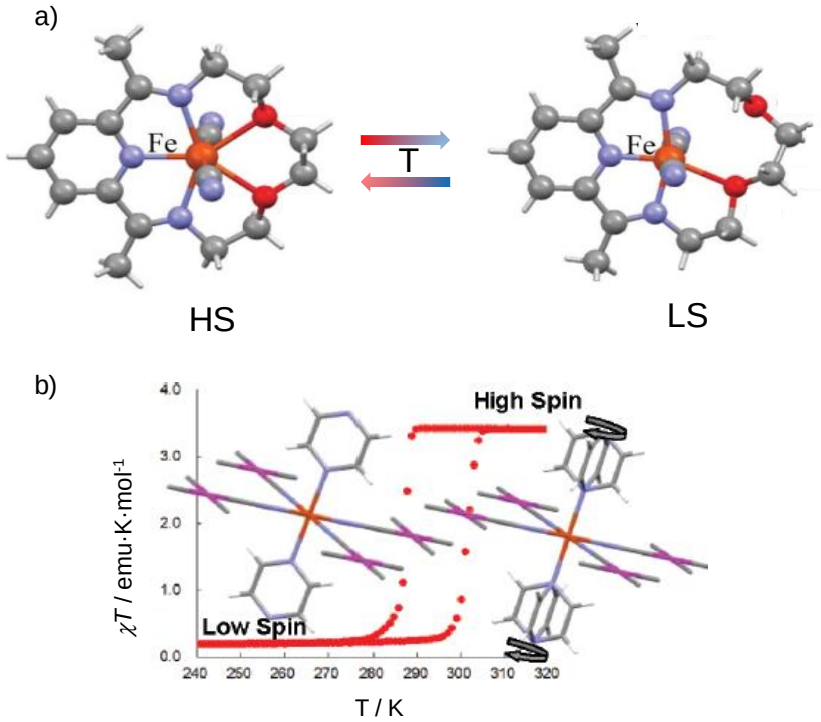

Figure 1.19. a) X-ray diffraction structures of $[FeL(CN)_2]\cdot H_2O$ in the HS and LS states showing the change in the coordination number of the iron site from 7 to 6, respectively. Adapted from reference [88]. b) Thermal dependence of the χT product of $[Fe(pyrazine)][Pt(CN)_4]$ showing that the change of Fe(II) spin state takes place in association with the switching of the rotation of the pyrazine ligand. Adapted from reference [82].

These transformations can be classified depending on the origin of the structural rearrangements.[91] The first situation concerns SPTs that arise as a consequence of concerted displacive motion of the SCO molecules triggered by the significant distortion of the octahedral cation environment. In a second place, there are structural modifications caused by a stepwise transition that leads to the

appearance of crystallographically inequivalent iron centres in the asymmetric unit. The HS/LS intermediate phase might exhibit a lower symmetry or might be characterised by the formation of a superstructure with respect to the HS or LS phases. In these situations, reentrant structural transitions are usually observed with a restoration of the symmetry after completion of the SCO process. Finally, the SPTs can take place without exhibiting a synergy with the SCO transition, which mainly occurs due to ordering of disordered solvent molecules, counterions or, more rarely, substituents on the coordinating ligands at low temperatures. In these cases, the SCO might be gradual and take place at a temperature different from that of the SPT. It seems that symmetry breaking does not need to be associated to a change of space group type, although in some cases it occurs and, eventually, also a change in crystal system is observed.

For instance, the nitroprusside salt of the $[Fe(bpp)_2]^{2+}$ family exhibits a cooperative transition with thermal hysteresis accompanied by a tilting of the $[Fe(CN)_5(NO)]^{2-}$ octahedra in order to maintain the hydrogen-bonded network (Figure 1.20). In this case, a breaking of the tetragonal symmetry from *P*4/*ncc* in the HS state to *Pnca* in the LS state takes place.[38] On the other hand, a thiophene-functionalised $[Fe(phen)_2(SCN)_2]$ complex that shows an abrupt transition with 10 K hysteresis width remains in the *Aba*2 orthorhombic space group in both spin states. In this case, the high degree of cooperativity is ascribed to the presence of weak C–H···S and N–H···S intermolecular contacts only in the LS phase (Figure 1.21).[92]

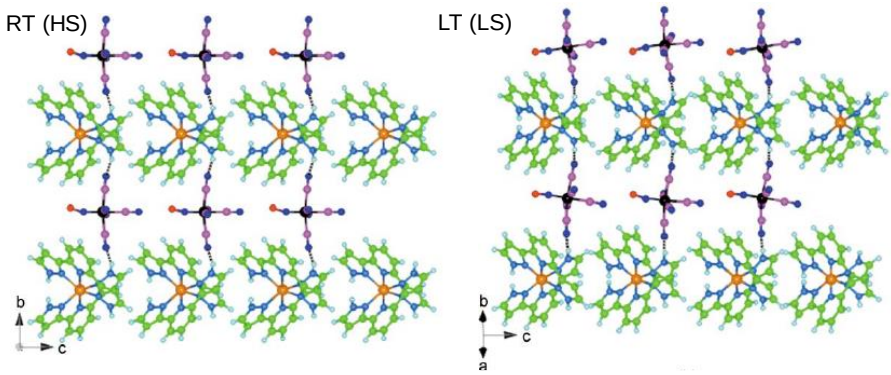

Figure 1.20. View of the crystal structure of $[Fe(bpp)_2][Fe(CN)_5(NO)]$ in the room-temperature (RT) tetragonal and low-temperature (LT) orthorhombic structures. Note the difference between the anionic lattice at the two temperatures, whereas the cationic subnetwork remains unaltered. Adapted from reference [38].

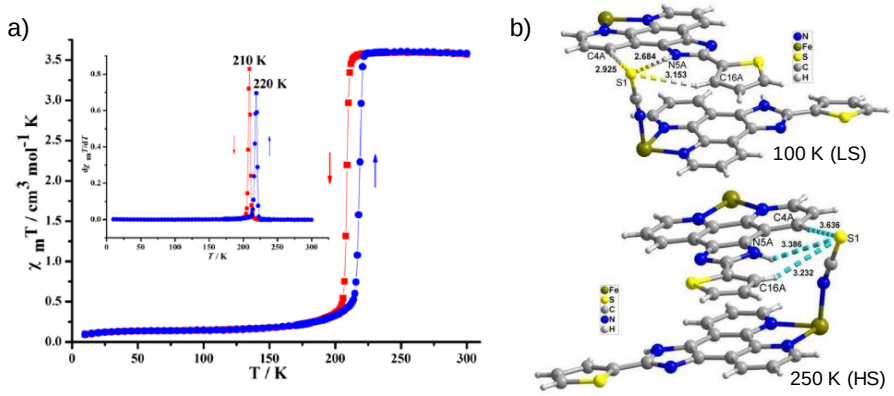

Figure 1.21. a) Thermal dependence of the χT product of a thiophene-functionalised $[Fe(phen)_2(SCN)_2]$ complex. The inset shows the $\delta(\chi T)/\delta T$ curve. b) View of the hydrogen-bonding interactions in the LS and HS phases, highlighting the presence of C4A-H···S1 and N5A-H···S1 hydrogen bond interactions only in the LS structure. Adapted from reference [92].

Among the different factors that affect SCO, probably the anion is one of the most interesting because it can lead to important changes in the crystal lattice with the subsequent variation in the magnetic properties of the compound. In this context, order-disorder transitions of anions are quite frequent and some of them result in cooperative SCO. For instance, in $[Fe(DAPP)(abpt)](ClO_4)_2$ (DAPP = bis(3-aminopropyl)(2-pyridyl-methyl)amine, abpt = 4-amino-3,5-bis(pyridine-2-yl)-1,2,4-triazole)[89a] where the occurrence of two order-disorder transitions in the DAPP ligand and in the perchlorate anions is encompassing the SCO process (Figure 1.22). $[Fe(L3)_2][ClO_4]_2{\cdot}H_2O{\cdot}2(CH_3)_2CO$ (ligand L3 is shown in Figure 1.12), displays different structural transformations with the presence of disorder for one ClO_4^- and two acetone molecules in the HS states, whereas the LS phases show a complete ordering.[50c] Also, in stepped transitions such as that exhibited by $[Fe(picpzpz)_2](BF_4)_2{\cdot}MeOH$ (picpzpz = 3-(2-pyrazinyl)-1-([(2-pyridyl)methyl]pyrazole), where the abrupt step is associated to anion and solvent order-disorder transformations (Figure 1.23).[89c] $[Fe(hbtz)_2(CH_3CN)_2](BF_4)_2$ (hbtz = 1,6-di(tetrazol-2-yl)hexane) complex is an example that deserves special attention, in which reorganisation of the anionic network results in a significant displacement of cationic Fe-based layers. This structural transformation occurs on cooling, at $T_{SPT} << T_{SCO}$ (Figure 1.24). If temperature is maintained above T_{SPT}, SCO in heating mode is identical to that observed upon cooling. Instead, if the temperature is further lowered and the phase transition occurs, stabilisation of the LS phase is observed with a shift of the LS ⟶ HS transition towards higher temperatures.[93]

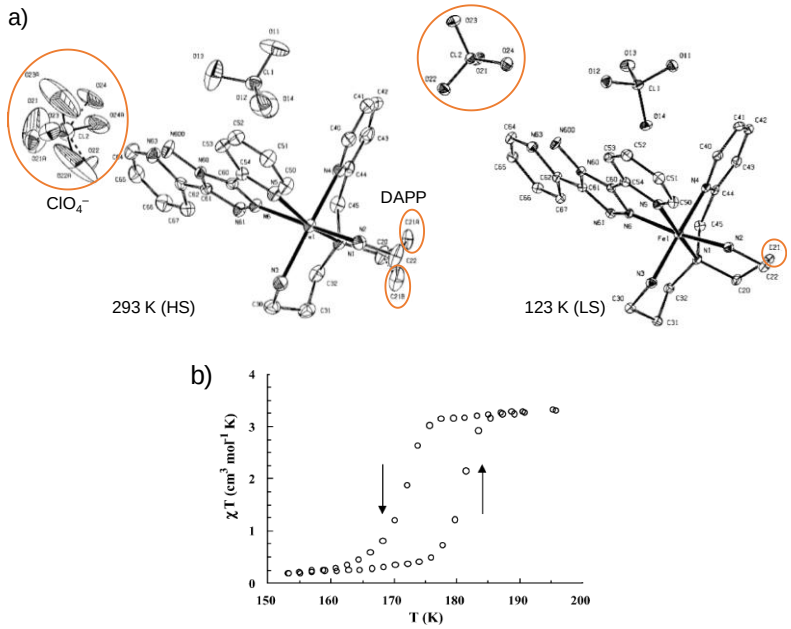

Figure 1.22. a) View of the crystal structure of $[Fe(DAPP)(abpt)](ClO_4)_2$ at 293 K and 123 K showing the two different types of order-disorder transitions between both temperatures. b) Thermal variation of the χT product of $[Fe(DAPP)(abpt)](ClO_4)_2$. Adapted from reference [89a].

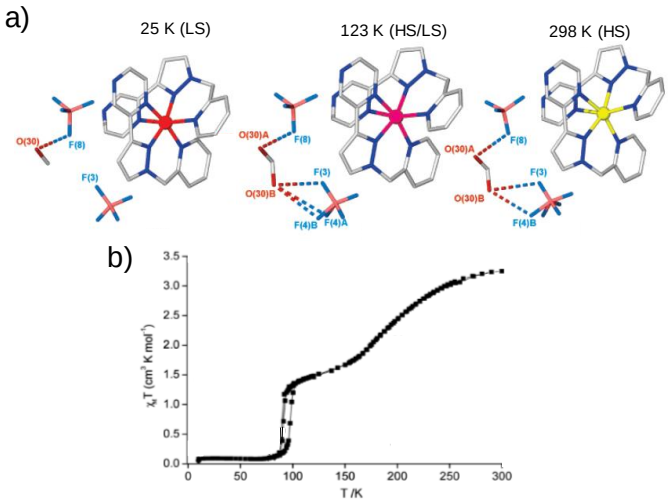

Figure 1.23. a) View of the crystal structure of $[Fe(picpzpz)_2](BF_4)_2 \cdot MeOH$ showing the hydrogen-bonding interactions between the methanol and BF_4^- anion at 25 K, 123 K and 298 K. The methanol molecule and BF_4^- anion are disordered at 123 K and 298 K. b) Thermal variation of the χT product of $[Fe(picpzpz)_2](BF_4)_2 \cdot MeOH$. Adapted from reference [89c].

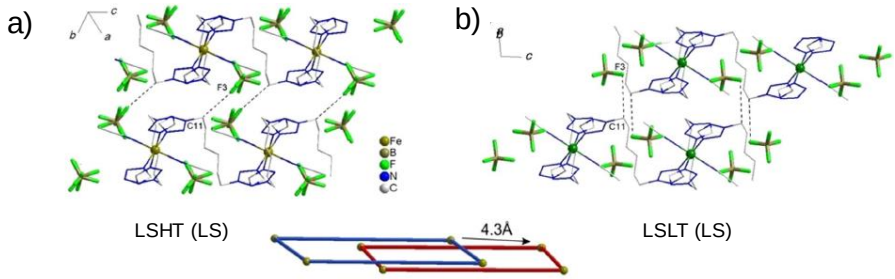

Figure 1.24. Crystal packing of $[Fe(hbtz)_2(CH_3CN)_2](BF_4)_2$ in a) the high- (a) and low- (b) temperature crystal structures of the low-spin form (LSHT and LSLT, respectively). The superposition of polymeric skeletons built from Fe^{2+} ions in the LSHT (blue) and LSLT (red) structures shows their relative shift by about 4 Å. Adapted from reference [93].

In addition, an abrupt SCO near room temperature with a thermal hysteresis of 34 K has been described for the complex $[Fe(qsal\text{-}I)_2]NTf_2$ (being qsal-I = (N-8-quinolyl)-5-iodo-salicylaldiminate and NTf = triflimide anion), in which a twisting of the qsal-I ligands in the HS state and significant changes in the anion conformation are at the origin of the high cooperativity exhibited by this system. It has to be noted that in this case, the anion is ordered in both spin states, changing its conformation from *syn* in the HS phase to an intermediate conformation in the LS state (Figure 1.25).[94]

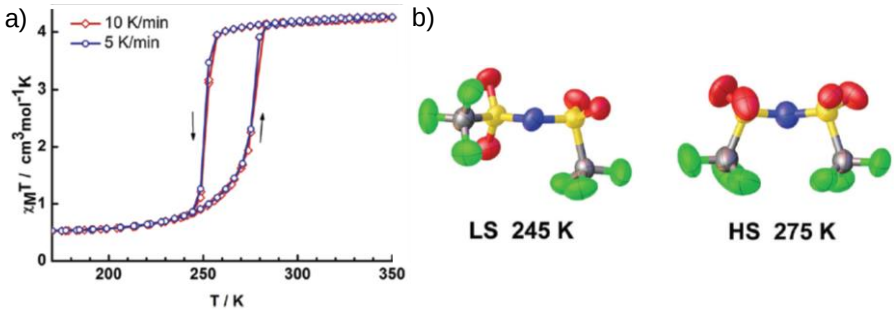

Figure 1.25. a) Thermal dependence of the magnetic susceptibility of $[Fe(qsal\text{-}I)_2]NTf_2$. b) View of the change in the conformation of the triflimide anions between the HS and LS phases. Adapted from reference [94].

Another recent report involves a complex molecular alloy system, that displays two thermally-induced cooperative SCO processes depending on its composition. In particular, two reversible structural phase transitions are displayed which have been shown to be related to different conformation of ligand-appended butyl groups and PF_6^- anions.[95] Thus, this Fe^{II} complex shows

that the decoupling of SCO and intrinsic SPTs can be realised by selecting the suitable isomorphous substitution to discriminate between two separated spin transitions.

On the other hand, several compounds exhibiting LIESST effect have been reported. However, complete structural characterisation of the phases involved in the LS ⟶ PIHS transformation are still scarce. Among the limited number of available SPTs, there are some examples in which only subtle modifications of the unit cell parameters and iron coordination sphere are found between the PIHS state and the high-temperature stable HS state.[61,96] The opposite situation involving drastic rearrangements between both HS phases is also observed. For $[Fe^{II}H_2L^{2\text{-}Me}][AsF_6]_2$ and $[Fe^{II}H_2L^{2\text{-}Me}][PF_6]_2$ (being $H_2L^{2\text{-}Me}$ = bis([(2-methylimidazol-4-ylmethylidene]-3-aminopropyl)ethylenediamine), a triplicate cell parameter is present in the photogenerated state and the origin of the symmetry breaking with respect to the HS phase relies on molecular distortion/rotation/displacements of the ions or layers, respectively (Figures 1.26-1.27).[97] In another example (*trans*-$[Fe(abpt)_2(NCS)_2]$, being abpt = 4-amino-3,5-bis(pyridine-2-yl)-1,2,4-triazole), also a triplicate cell parameter is reached after laser irradiation, but this time a modulated structure is obtained with the existence of two additional iron centres slightly reoriented in comparison with those present in the non-modulated structure.[98]

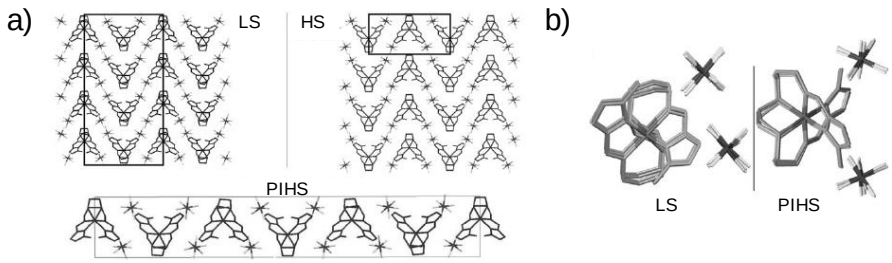

Figure 1.26. a) Crystal structure of $[Fe^{II}H_2L^{2\text{-}Me}][AsF_6]_2$ in the LS phase (4*a*, *b*, *c* cell), PIHS state (*a*, *b*, 3*c* cell) and HS phase (*a*, *b*, *c* cell). Unit cells are illustrated by rectangles. b) Projections of the structures in the LS and PIHS phases showing the motions of the ions. Adapted from reference [97a].

In a recent report, competition between spin transition and structural ligand ordering leads to the generation of six different phases in a rigid 2D coordination polymer formulated as $[Fe(Hg(SCN)_3)_2\mu\text{-}(4,4'\text{-bpy})_2]$ (4,4'-bpy = 4,4'-bipyridine).[99] Specifically, the internal dihedral angle of the bipyridine ligands plays a pivotal role in the multistep behaviour of this compound (Figure 1.28). A HS phase of low symmetry is reached after photoirradiation (phase 6), with a

doubled unit cell with respect to the HS phase achieved at thermal equilibrium (phase 1).

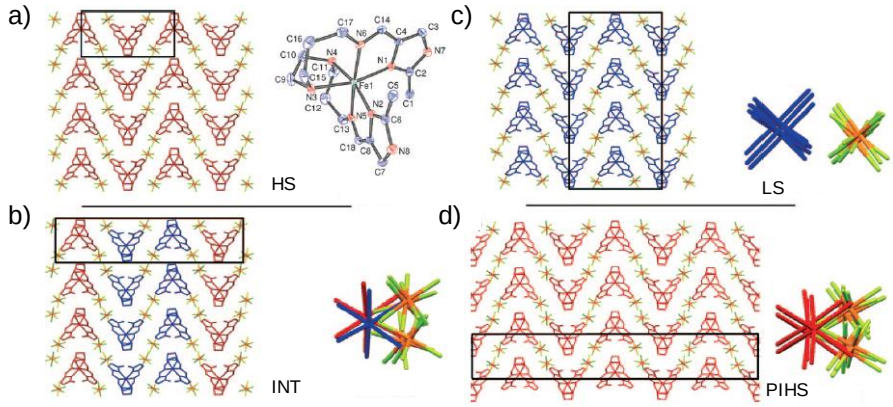

Figure 1.27. Crystal structure of $[Fe^{II}H_2L^{2\text{-}Me}][PF_6]_2$ in the a) HS phase (*a*, *b*, *c* cell), b) intermediate (INT) phase (*a*, *b*, 2*c* cell), c) LS phase (4*a*, *b*, *c* cell) and d) PIHS phase (*a*, *b*, 3*c* cell). Unit cells are illustrated by rectangles. Additional projections along the multiplied crystal axes on the right show the ions motion. Adapted from reference [97b].

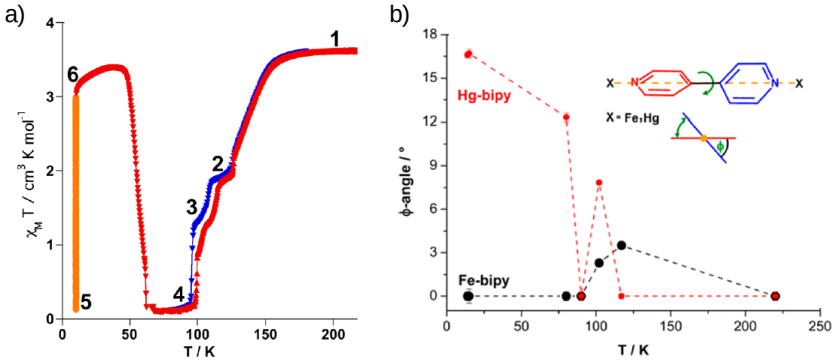

Figure 1.28. a) (Photo)magnetic properties of $[Fe(Hg(SCN)_3)_2\mu\text{-}(4,4'\text{-bpy})_2]$ revealing 1-6 crystallographic phases (blue and red triangles indicate cooling and heating modes, respectively. Orange data correspond to irradiation of the sample at 10 K). b) Variation of the angle between the pyridine rings of the 4,4'-bpy ligands during thermal spin transition and under light excitation. Adapted from reference [99].

Despite the large number of related examples, there is a lack of reports in which the connectivity of the mononuclear Fe(II)centres and the anionic sublattice is affected by a significant structural rearrangement of the crystal network.

1.6. Multifunctionality in SCO materials. Magnetoelectric coupling

Materials exhibiting magnetic ordering, electrical conductivity, fluorescence, porous properties or chemical sensing simultaneously with the spin crossover have been synthesised. In some cases, SCO modulates, inhibits or enhances the second property. Instead, in other complexes, both functions coexist in the same temperature range but without any interplay between them. For instance, the system $[Fe^{III}(qsal)_2][Pd(dmit)_2]_5$·acetone (qsalH = N-(8-quinolyl)-salicylaldimine, dmit = 4,5-dithiolato-1,3-dithiole-2-thione) exhibiting interplay between SCO and electrical conductivity is built up from Fe(III) cationic centres that show a cooperative SCO transition and anionic radical conducting salts that allow the electronic transport (Figure 1.29.a).[100]

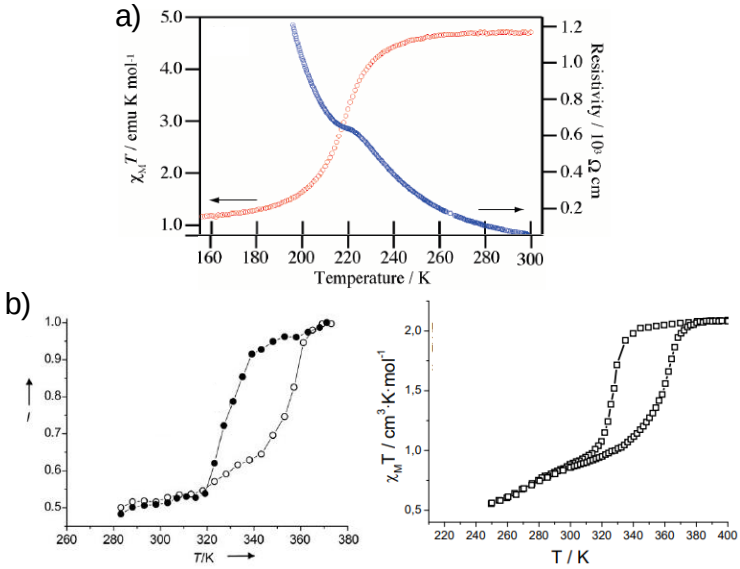

Figure 1.29. a) Temperature dependence of the χT product and resistivity of $[Fe^{III}(qnal)_2][Pd(dmit)_2]_5$·acetone. The χT value at 300 K indicates that the Fe(III) ion is in the HS state and one spin on five $Pd(dmit)_2$ survives. This compound is a semiconductor at room temperature and the anomaly of resistivity is observed at 220 K, exactly as the transition to the LS state. b) Thermal variation of the fluorescence intensity (I) at 495 nm in the heating (open circles) and cooling (filled circles) modes for 3-dansyl ($[Fe_{0,5}Zn_{0,5}(HTrz)_2(Trz)](BF_4)]_n$ functionalised with 3-(dansylamido)propyltrimethoxysilane), and plot of χT *vs* T for the same sample. Adapted from references [100] and [101].

Moreover, different SCO complexes in which the fluorescence is higher in the HS state and it decreases as the iron centres undergo thermal transition to the LS

state have been synthesised, as observed in nanoparticles of $[Fe(trz)(Htrz)_2](BF_4)$ (Htrz = 1,2,4-triazole; trz = 1,2,4-triazolate) coated by various fluorophores (Figure 1.29.b).[101] Porous SCO polymers such as $[Fe(pz)M(CN)_4]$ (M(II) = Ni, Pd and Pt and pz = pyrazine) are able to absorb different molecules and change their spin state with the concomitant variation in colour. This allows an easy sensing of a wide variety of analytes.[102] SCO complexes able to recognise different anions in solution have been obtained. For instance, $[Fe(H_2bip)_3](BPh_4)_2$[103] (bip = 2,2'-bi-1,4,5,6-tetrahydropyrimidine) exhibits colour changes based on hydrogen-bonding interactions with the anions. Coupling between magnetic ordering and SCO behaviour has been observed in discrete polynuclear and polymeric complexes.[104] In these systems, the HS sites switch to the LS state upon cooling down the sample or increasing pressure which results in a cancellation of the magnetic exchange. In addition, the magnetic ordering can be restored by light irradiation at low temperatures through the LIESST effect (Figure 1.30).

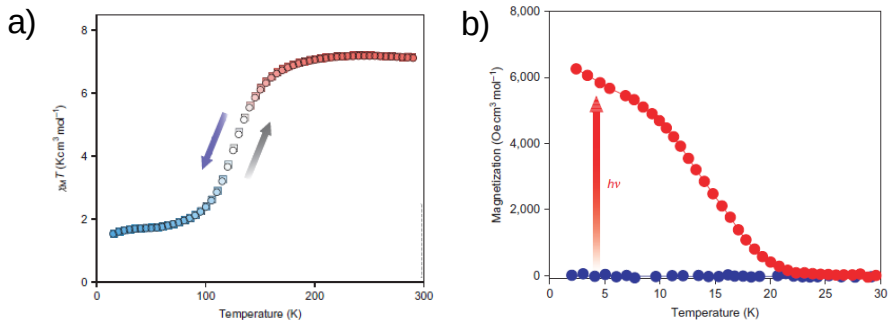

Figure 1.30. a) Temperature dependence of the χT product of properties of $Fe_2[Nb(CN)_8]\cdot(4\text{-pyridinealdoxime})_8\cdot 2H_2O$. b) Magnetisation versus temperature curves at 100 Oe for the same compound. Light-induced SCO triggers a spontaneous magnetisation. Adapted from reference [104a].

The coexistence of dielectric and magnetic transformations in switchable molecular materials is a highly desirable situation due to the fact that simultaneous modifications in dielectric and magnetic properties allow for a purely electronic readout of the magnetic state by means of an easy capacitive measurement, which is relevant to new information processing technologies.[105] As described in the previous point, there are many examples in which SCO leads to SPTs involving a breaking of symmetry or displacive movement of the molecules that might induce changes in the local electric dipoles between the HS and LS states. Since dielectric properties depend on the distribution of positive and negative charges, the SCO process might result in a dielectric anomaly and

even in ferroelectric behaviour. Thus, SCO materials are suitable candidates for this synergic purpose. There are previous works that show a synergy between both functions, however, the changes in dielectric constant between HS and LS states are usually very small (0.07-0.3).[106] This is ascribed to the fact that only the local structural rearrangements involving the SCO centres are contributing to the dielectric variations.[107] Therefore, it is necessary to enhance the dielectric response in order to enable the sensitive detection of the magnetic state *via* capacitive measurement.

In order to obtain drastic variations in both properties, the SCO induced structural changes affecting the electric dipoles have to be propagated to the whole structure. This has been done recently in a rational way by coupling positively charged SCO subunits and negatively charged paramagnetic components. Specifically, positively charged Fe^{II} ions have been linked by negatively charged $[(Tp)Fe^{III}(CN)_3]^-$ (Tp = hydrotris(pyrazolyl)borate, Figure 1.31.a) magnetic subunits and 4,4'-azopyridine (azp) ligands to form a layered compound.[107] This material exhibits an abrupt temperature-induced SCO and its spin state can also be reversed by light irradiation and application of pressure (changing $T_{1/2}$ from 171 K to 303 K). More importantly, the interconversion between paramagnetic and diamagnetic Fe^{II} centres leads to a rotation of the negative building blocks (Figure 1.31.b), with the subsequent variation in relative distribution of positive and negative charges but without change in the monoclinic $P2_1/n$ space group.

Dielectric measurements show the appearance of steps in the temperature range in which SCO takes place, revealing the synergic nature of both properties. In this case, there is a significant change of the dielectric tensor ε' from 3.4 to 5.3 with an associated thermal hysteresis of 25 K. Thus, significant and synchronised changes in magnetic and dielectric properties were achieved (Figure 1.32).

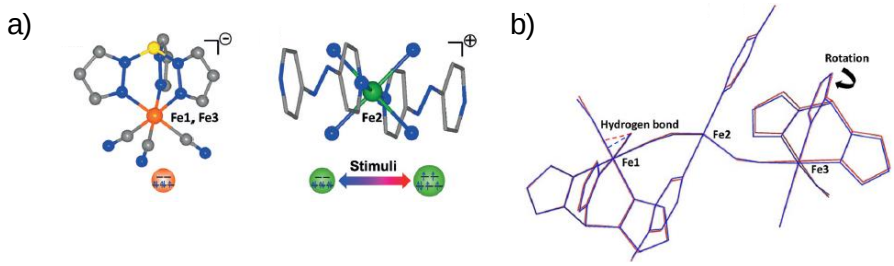

Figure 1.31. a) Structure of $[(Tp)Fe^{III}(CN)_3]^-$ and Fe^{II} SCO building blocks. b) Structural modification of the asymmetric $Fe^{III}_2Fe^{II}$ unit at 10 K (blue) and 250 K (red). Dashed lines refer to hydrogen bonds. Adapted from reference [107].

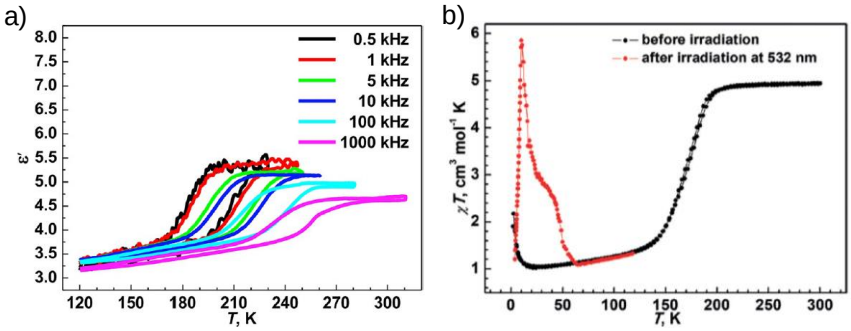

Figure 1.32. a) Thermal dependence of the real part of the dielectric constant at different frequencies for $[(Tp)Fe^{III}(CN)_3]_2Fe^{II}(azp)\cdot 4H_2O$. b) Temperature dependence of the χT product of $[(Tp)Fe^{III}(CN)_3]_2Fe^{II}(azp)\cdot 4H_2O$ before and after irradiation with a laser source. Extracted from reference [107].

Ferroelectric compounds are a special subclass of dielectrics that are characterised by spontaneous electric polarisation that arises from the collective alignment of dipole moments inside a compound, whose direction can be reversed by electric field. All ferroelectrics exhibit pyroelectricity, piezoelectricity and second harmonic generation (SHG) properties (Figure 1.33.a).[108]

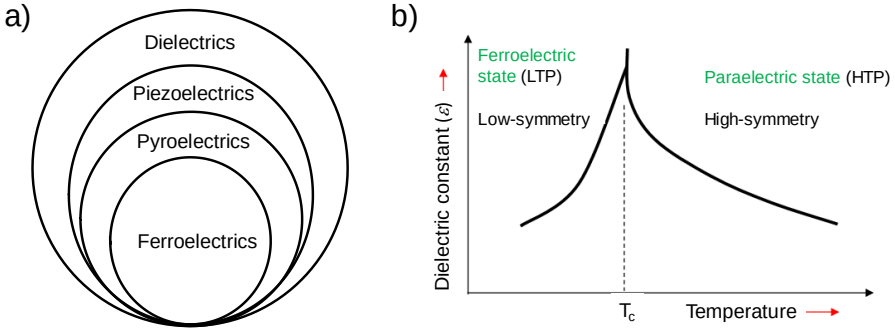

Figure 1.33. a) Inter-relationships of ferroelectrics, pyroelectrics, piezoelectrics and dielectrics. b) Schematic representation of the characteristic ferroelectric transition involving symmetry breaking from a paraelectric high-temperature phase (HTP) to a ferroelectric low-temperature phase (LTP).

Due to these properties, their use for a variety of technical applications such as ferroelectric field-effect transistors, infrared detectors, nonlinear optical devices, capacitors and ferroelectric random access memory (FeRAM) has been extensively investigated.[108] The nature of ferroelectric compounds is directly related to the appearance of electric polarisation in the structure, being the

characteristic transition from a paraelectric (high-temperature, high-symmetry, centrosymmetric) to a ferroelectric (low-temperature, low-symmetry, noncentrosymmetric) phase (Figure 1.33.b). This transformation implies that some symmetry elements are lost upon cooling (symmetry breaking) and it is usually accompanied by significant anomalies in physical properties and changes in crystal network below and above the transition temperature (T_c).[109] For instance, the dielectric constant varies from tens to even 10^6 in the vicinity of the T_c. In the paraelectric phase, the crystal can belong to any point group, while in the ferroelectric phase, the crystal should adopt one of the ten polar point groups (Figure 1.34.a). In addition, the space group of the ferroelectric phase should be a subgroup of the paraelectric one. Thus, a change in the SHG signal can be found when a transformation from a centrosymmetric paraelectric phase to a noncentrosymmetric ferroelectric one occurs (Figure 1.34.b).[109]

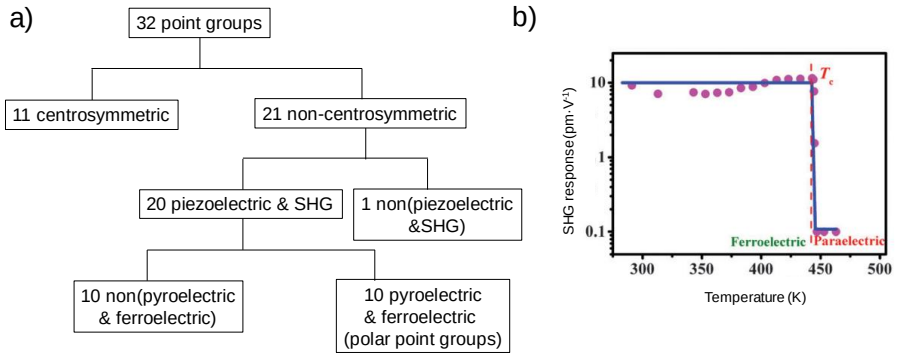

Figure 1.34. a) Classification of the 32 point groups. b) Temperature dependence of the SHG signal of $[(Me_2CH)_2NH_2]Cl$, showing an abrupt increase from zero above T_c to a saturation value below T_c that reveals symmetry breaking from a centrosymmetric paraelectric phase to a noncentrosymmetric ferroelectric phase. Adapted from reference [109c].

These materials can be classified in two general subsets depending on the origin of the structural modification taking place at T_c (Figure 1.35). In *displacive* type transitions, relative displacement of the ions generates spontaneous polarisation. Instead, reorientation of the ions creates ferroelectricity in *order-disorder* type transformations, being the dipole moments ordered without cancelling each other in the ferroelectric state and disordered in the paraelectric state. $BaTiO_3$ belongs to the first case, whereas $NaNO_2$ is an example of the second subgroup. It has to be noted that in actual ferroelectric compounds both mechanisms can be observed.

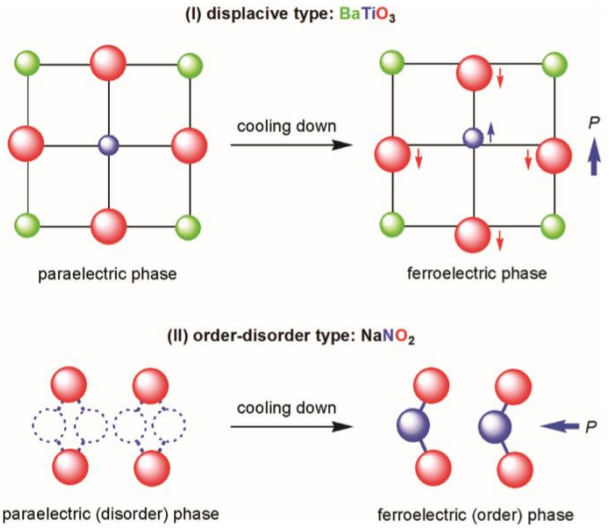

Figure 1.35. Schematic representation for the *displacive*-type and *order-disorder* type ferroelectrics. Extracted from reference [108].

Apart from traditional pure inorganic ferroelectrics, a wide variety of hybrid systems including one-, two- or three-dimensional structures and zero-dimensional coordination complexes have been reported. It is worth mentioning that dynamics of proton transfer between ditopic hydrogen bond acceptors can drive ferroelectric phase transitions (so-called *hydrogen bond ferroelectrics*) in hydrogen-bonded ionic compounds.[110] Indeed, Rochelle salt ($[KNa(C_4H_4O_6)]\cdot 4H_2O$, $C_4H_4O_6^{2-}$ = tartrate anions), the first ferroelectric compound discovered in 1920, relies on hydrogen bonding.[111] This salt exhibits two critical temperatures at 255 K and 297 K (Figure 1.36.a). At T > 297 K and T < 255 K, it crystallises in the orthorhombic $P2_12_12$ (paraelectric phases), whereas at 255 < T < 297 K it adopts the monoclinic $P2_1$ (ferroelectric phase). In the crystal structure, there are rows of tartrate ions parallel to the *a* axis, connected along the *b* axis by rows of alternating K^+ and Na^+ ions (Figure 1.36.b). Single-crystal structural measurements reveal that, in the ferroelectric phase, there are two different polarised chains, one similar to those observed in the high-temperature paraelectric phase (T > 297 K) and the other one very close to those present in the low-temperature paraelectric phase (T < 255 K). The principal difference between the ferroelectric and the two paraelectric phases is the orientation of the tartrate anions with respect to the crystallographic axes, giving rise to a different polarisation vector parallel to the *a* axis. Thus, the source of ferroelectricity in this case is not related to proton transfer. Analyses with a deuterated sample showed a little variation in the ferroelectric properties,

suggesting an order-disorder type transition. The two paraelectric phases can be considered as mixtures of the two chains (disordered structures), being the total polarisation zero by the crystal symmetry.

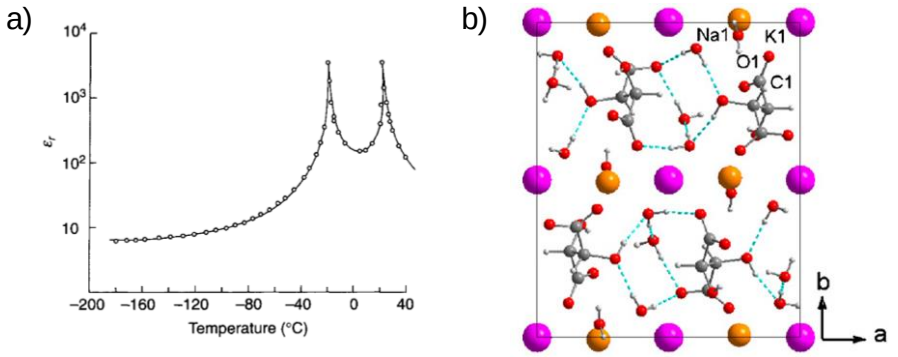

Figure 1.36. a) Thermal variation of the dielectric constant of Rochelle salt. b) View of the unit cell content of Rochelle salt (paraelectric phase). Adapted from references [111b] and [111c].

A typical example of inorganic ferroelectric material in this context is KH_2PO_4 (KDP), with extensive hydrogen bonds in its structure that forms a diamondoid network (Figure 1.37.a). In this compound, transfer of protons in the O–H···O bonds triggers the spontaneous polarisation (Figure 1.37.b).[110] In the case of hydrogen-bonded organic systems, a prototype has been found in diazabicyclo[2.2.2]octane (dabco) salts with inorganic tetrahedral anions.[112] $Hdabco^+$ cations are connected by $N–H^+···N$ hydrogen bonds between the basic nitrogen and its conjugate acid form. This connectivity leads to a linear chain that can undergo a proton-transfer process (Figure 1.37.c) with polarisation reversal and occurrence of ferroelectricity. The proton transfer mechanism has also been applied in systems with two or more organic components. For instance, in systems that combine the 2,5-dihalo-3,6-dihydroxy-*p*-benzoquinones (or anilic acid) as the acidic component that acts as proton donor with various bipyridine bases as hydrogen bond acceptors.[113] The vital role of acidic protons in generating ferroelectricity has been unambiguously confirmed in the phenazine derivative by a detailed neutron diffraction study. A thermally induced migration of the hydrogen near the centre of the strong hydrogen bond occurs, being this asymmetry the origin of the dipole moment.[114] The similar proton affinity between the hydrogen bond donor and acceptor species reduces the potential barrier for H to move towards the base and, consequently, enables the proton displacement. In addition, deuterium substitution experiments show an increase in T_c by more than 50 K for the same derivative, confirming the *proton transfer* mechanism.

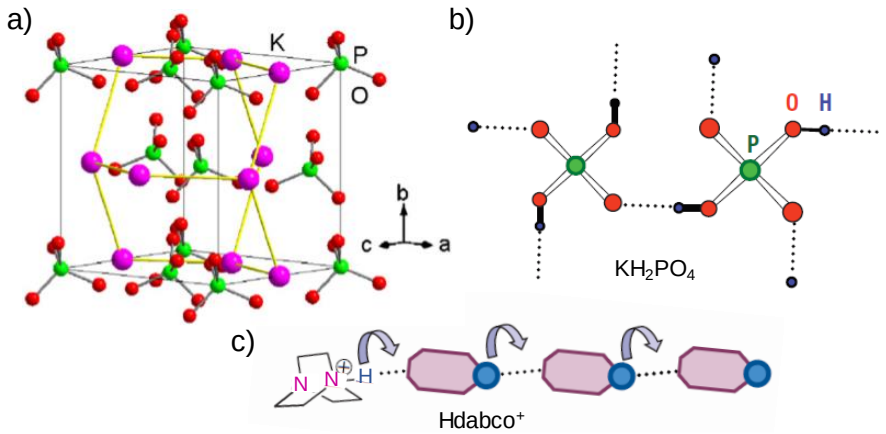

Figure 1.37. a) View of the unit cell content of KDP (paraelectric phase). Typical ferroelectric materials showing the H^+ transfer processes that are at the origin of the ferroelectricity: b) inorganic and c) organic assemblies. Adapted from references [111b] and [110].

In these situations in which proton displacement is observed, usually short strong hydrogen bonds (SSHBs) of quasi-covalent nature are involved (limit distance between heteroatoms of 2.45 Å for O–H···O and 2.55 Å for N–H···O systems). The H atom generally occupies a centred position in symmetric interactions at high temperatures and temperature dependent proton migration is revealed upon cooling. Typically, the potential energy surface of this proton exhibits a broad single-well potential or a double potential well with a low barrier to proton motion across the SSHB that can occur under different external stimulus apart from change in temperature, including the application of an electric field or variation in pressure.[115] In $(Hdabco^+)_2(TCNQ)_3$ (TCNQ = 7,7,8,8-tetracyano-*p*-quinodimethane), two hydrogen-bonding protonic sites are found at 100 K, which merge at 373 K into one site at the midpoint between the two nitrogen atoms. The localisation of the protonic lattice at 100 K results in the dipole structure, whereas the thermally fluctuating proton between the two nitrogen sites removes the dipole structure within the chain. This order/disorder transition of the hydrogen-bonding protons is schematised in Figure 1.38, together with the possible double-well potential curves of the protons.

The study of systems combining SCO and proton transfer, or ferroelectricity in general, can provide interesting multifunctional materials. Very recently, Sato and co-workers have reported the first compounds that couple spin crossover with proton transfer.[116] In these compounds, the SCO process drives an

intramolecular proton transfer from a coordinated hydrazine unit to an appended pyridine moiety (Figure 1.39).

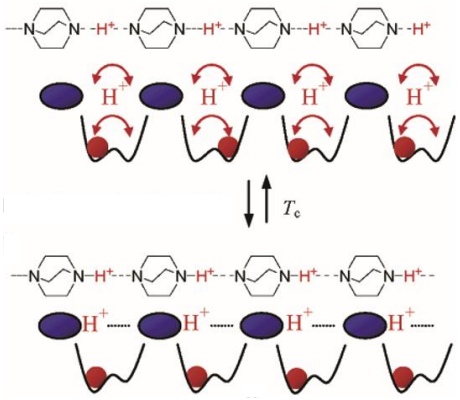

Figure 1.38. Schematic representation of double-well proton coordinates along the 1D hydrogen-bonding chain of $(Hdabco^{+})_2(TCNQ)_3$ in the high-temperature and low-temperature phases. Adapted from reference [115b].

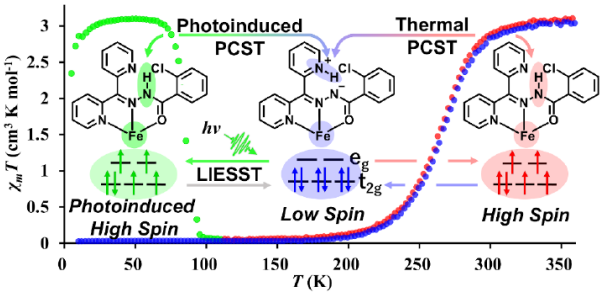

Figure 1.39. Thermal dependence of the χT product in $[Fe(HL\text{-}Cl)_2](AsF_6)_2$ (HL-Cl = N'-(di(pyridin-2-yl)methylene)-2-chlorobenzohydrazide) and scheme of molecular structures showing the proton transfer coupled spin transition. Extracted from reference [116a]. PCST refers to Proton Transfer Coupled Spin Transition.

Reports concerning the interception between SCO and ferroelectricity are limited up to now. Recently, ferroelectric iron(II)metallomesogens exhibiting an associated SCO behaviour have been obtained,[117] and ferroelectric polarisation of the substrate has proven to present a strong influence on the SCO efficiency of thin films of an iron(II) SCO compound.[118] In addition, the spin state of a thin film of a SCO complex has been driven by the polarisation of a ferroelectric organic substrate through the change of the electric field at the interface between both layers (Figure 1.40.a).[119] Figure 1.40.b shows the magnetic properties of the bulk SCO material at 300 K (in the HS state) and at 100 K (in

the LS state). When the film was polarised "up", the behaviour corresponding to the HS state was obtained down to 100 K. Instead, when the film was polarised "down", the diamagnetic behaviour was measured up to room temperature (Figure 1.40.c).

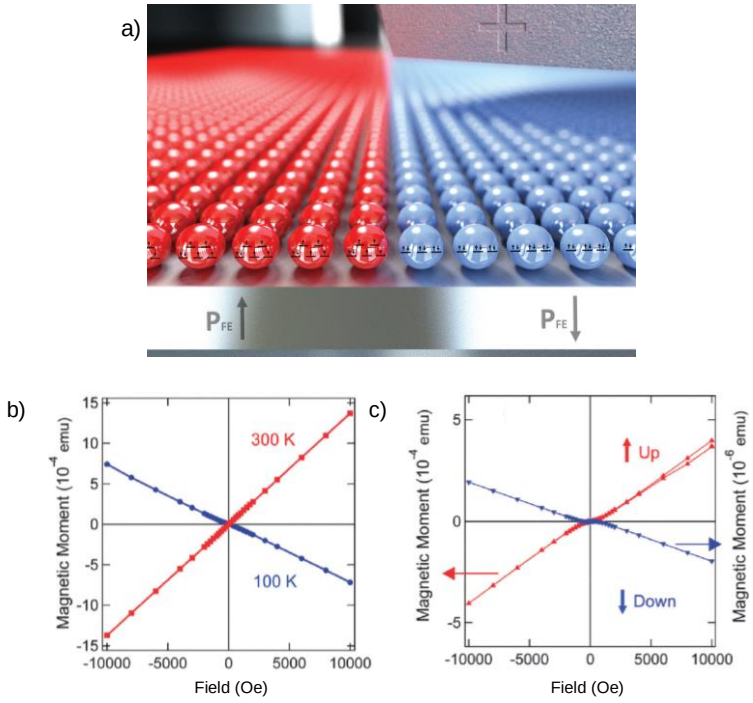

Figure 1.40. a) Scheme illustrating the spin state transition encompassing the change in the polarisation of the substrate. b) Magnetic properties of $[Fe(H_2B(pz)_2)_2(bipy)]$ ($H_2B(pz)_2$ = bis(hydrido)bis(1H-pyrazol-1-yl)borate, bipy = 2,2'-bipyridine) powder at 100 K (LS, blue) and 300 K (HS, red). c) Magnetic properties of thin films of $[Fe(H_2B(pz)_2)_2(bipy)]$ on a ferroelectric substrate for different polarisations ("up" in red and "down" in blue). Extracted from reference [119].

The implementation of ferroelectricity is tricky probably because the possible space groups in which the ferroelectric phase can crystallise are reduced and only a few structural transformations meet the crystallographic requirements for a ferroelectric transition, despite the fact that many SCO transitions occur in association with SPTs.

1.7. References

[1] a) L. Cambi, A. Cagnasso, *Atti. R. Accad. Naz. Lincei*. **1931**,13, 809-813. b) L. Cambi, L. Szegö, *Ber. Dtsch. Chem. Ges. B*. **1931**, 64, 2591-2598. c) L. Cambi, L. Szegö, A. Cagnasso, *Atti. R. Accad. Naz. Lincei*. **1932**, 15, 266-271. d) L. Cambi, L. Szegö, A. Cagnasso, *Atti. R. Accad. Naz. Lincei*. **1932**, 15, 329-335. e) L. Cambi, L. Szegö, *Ber. Dtsch. Chem. Ges. B*. **1933**, 66, 656–661. f) L. Cambi, L. Malatesta, *Ber. Dtsch. Chem. Ges. B*. **1937**, 70, 2067-2078

[2] E. König, *Coord. Chem. Rev*. **1968**, 3, 471-495

[3] H. A. Goodwin, *Coord. Chem. Rev*. **1976**, 18, 293-325

[4] P. Gütlich, *Struct. Bonding*. **1981**, 44, 83-195

[5] W. R. Scheidt, C. A. Reed, *Chem. Rev*. **1981**, 81, 543-555

[6] M. F. Perutz, G. Fermi, B. Luisi, B. Shaanan, R. C. Liddington, *Acc. Chem. Res*. **1987**, 20, 309-321

[7] M. Womes, J. C. Jumas, J. Olivier-Fourcade, F. Aubertin, U. Gonser, *Chem. Phys. Lett*. **1993**, 201, 555-558

[8] a) P. Gütlich, H. A. Goodwin, *Top. Curr. Chem*. **2004**, 233, 1-47. b) O. Kahn, *Curr. Opin. Solid State Mater. Sci*. **1996**, 1, 547-554. c) X. Bao, H. J. Shepherd, L. Salmon, G. Molnár, M.-L. Tong, A. Bousseksou, *Angew. Chem. Int. Ed*. **2013**, 52, 1198-1202. d) C. Bartual-Murgui, L. Salmon, A. Akou, N. A. Ortega-Villar, H. J. Shepherd, M. C. Muñoz, G. Molnár, J. A. Real, A. Bousseksou, *Chem. Eur. J*. **2012**, 18, 507-516. e) K. A. Zenere, S. G. Duyker, E. Trzop, E. Collet, B. Chan, P. W. Doheny, C. J. Kepert, S. M. Neville, *Chem. Sci*. **2018**, 9, 5623-5629

[9] a) P. Gütlich, A. B. Gaspar, Y. Garcia, *Beilstein J. Org. Chem*. **2013**, 9, 342-391. b) K. S. Murray, *Eur. J. Inorg. Chem*. **2008**, 20, 3101-3121. c) S. V. Larionov, *Russ. J. Coord. Chem*. **2008**, 34, 237-250. d) H.-J. Krüger, *Coord. Chem. Rev*. **2009**, 253, 2450-2459. e) B. Weber, E.-G. Jäger, *Eur. J. Inorg. Chem*. **2009**, 465-477. f) M. A. Halcrow, *Spin-crossover materials: properties and applications*. **2013**, John Wiley&Sons. g) H. A. Goodwin, *Top. Curr. Chem*. **2004**, 234, 23-47. h) S. Hayami, Y. Komatsu, T. Shimizu, H. Kamihata, Y. H. Lee, *Coord. Chem. Rev*. **2011**, 255, 1981-1990. i) Y. Garcia, P. Gütlich, *Top. Curr. Chem*. **2004**, 234, 49-62. j) G. G. Morgan, K. D. Murnaghan, H. Müller-Bunz, V. Mckee, C. J. Harding, *Angew. Chem. Int. Ed*. **2006**, 45, 7192-7195. k) P. N. Martinho, B. Gildea, M. M. Harris, T. Lemma, A. D. Naik, H. Müller-Bunz, T. E. Keyes, Y. Garcia, G. G. Morgan, *Angew. Chem. Int. Ed*. **2012**, 51, 12597-12601. l) A. J. Fitzpatrick, E. Trzop, H. Müller-Bunz, M. M. Dïrtu, Y. Garcia, E. Collet, G. G. Morgan, *Chem. Commun*. **2015**, 51, 17540-17543. m) K. Pandurangan, B. Gildea, C. Murray, C. J. Harding, H. Müller-Bunz, G. G. Morgan, *Chem. Eur. J*. **2012**, 18, 2021-2029

[10] P. Gütlich, Y. Garcia, H. A. Goodwin, *Chem*. *Soc*. *Rev*. **2000**, 29, 419-427

[11] J.-P. Launay, M. Verdaguer, *Electrons in Molecules*. **2014**, Oxford University Press

[12] A. Hauser, *Top*. *Curr*. *Chem*. **2004**, 233, 49-58

[13] a) J. P. Tuchages, A. Bousseksou, G. Molnár, J. J. McGarvey, F. Varret, *Top*. *Curr*. *Chem*. **2004**, 235, 85-103. b) J. A. Wolny, R. Diller, V. Schünemann, *Eur*. *J*. *Inorg*. *Chem*. **2012**, 2635-2648

[14] G. Chastanet, N. F. Sciortino, S. M. Neville, C. J. Kepert, *Eur*. *J*. *Inorg*. *Chem*. **2018**, 314-319

[15] a) J.-F. Létard, P. Guionneau, L. Goux-Capes, *Top*. *Curr*. *Chem*. **2004**, 235, 221-249. b) K. Szacilowski, *Chem*. *Rev*. **2008**, 108, 3481-3548. c) M. S. Alam, M. Stocker, K. Gieb, P. Müller, M. Haryono, K. Student, A. Grohmann, *Angew*. *Chem*. *Int*. *Ed*. **2010**, 49, 1159- 1163. d) J. Dugay, M. Giménez-Marqués, T. Kozlova, H. W. Zandbergen, E. Coronado, H. S. J. van der Zant, *Adv*. *Mater*. **2015**, 27, 1288-1293. e) M. D. Manrique-Juárez, S. Rat, L. Salmon, G. Molnár, C. M. Quintero, L. Nicu, H. J. Shepherd, A. Bousseksou, *Coord*. *Chem*. *Rev*. **2016**, 308, 395-408. f) K. S. Kumar, M. Ruben. *Coord*. *Chem*. *Rev*. **2017**, 346, 176-205

[16] M. M. Khusniyarov. *Chem*. *Eur*. *J*. **2016**, 22, 15178-15191

[17] G. S. Matouzenko, J.-F. Létard, S. Lecocq, A. Bousseksou, L. Capes, L. Salmon, M. Perrin, O. Kahn, A. Collet, *Eur*. *J*. *Inorg*. *Chem*. **2001**, 2935-2945

[18] H. Köppen, E. W. Müller, C. P. Kohler, H. Spiering, E. Meissner, P. Gütlich, *Chem*. *Phys*. *Lett*. **1982**, 91, 348-352

[19] a) M. Paez-Espejo, M. Sy, K. Boukheddaden, *J*. *Am*. *Chem*. *Soc*. **2016**, 138, 3202-3210. b) E. Trzop, D. Zhang, L. Piñeiro-López, F. J. Valverde-Muñoz, M. C. Muñoz, L. Palatinus, L. Guerin, H. Cailleau, J. A. Real, E. Collet, *Angew*. *Chem*. *Int*. *Ed*. **2016**, 55, 8675-8679

[20] a) C.-J. Zhang, K.-T. Lian, G.-Z. Huang, S. Bala, Z.-P. Ni, M.-L. Tong, *Chem*. *Commun*. **2019**, 55, 11033-11036. b) C.-J. Zhang, K.-T. Lian, S.-G. Wu, Y. Liu, G.-Z. Huang, Z.-P. Ni, M.-L. Tong, *Inorg*. *Chem*. *Front*. **2020**, 7, 911-917

[21] J. A. Real, A. B. Gaspar, V. Niel, M. C. Muñoz, *Coord*. *Chem*. *Rev*. **2003**, 236, 121-141

[22] J. A. Real, A. B. Gaspar, M. C. Muñoz, *Dalton Trans*. **2005**, 12, 2062-2079

[23] C. Lochenie, W. Bauer, A. P. Railliet, S. Schlamp, Y. Garcia, B. Weber, *Inorg*. *Chem*. **2014**, 53, 11563-11572

[24] a) D. Boinnard, A. Bousseksou, A. Dworkin, J. M. Savariault, F. Varret, J. P. Tuchagues, *Inorg*. *Chem*. **1994**, 33, 271-281. b) E. König, R. Schnakig, G. Ritter, W. Irler, B. Kanellakopulos, B. Powietzka, *Inorg*. *Chim*. *Acta*, **1979**, 35, 239-248

[25] V. A. Grillo, L. R. Gahan, G. R. Hanson, R. Stranger, T. W. Hambley, K. S. Murray, B. Moubaraki, J. D. Cashion, *J*. *Chem*. *Soc*. *Dalton Trans*. **1998**, 2341-2348

[26] a) E. König, G. Ritter, S. K. Kulshreshtha, J. Waigel, L. Sacconi, *Inorg*. *Chem*. **1984**, 23, 1241-1246. b) C. C. Wu, J. Jung, P. K. Gantzel, P. Gütlich, D. N. Hendrickson, *Inorg*. *Chem*. **1997**, 36, 5339-5347

[27] S. M. Nelson, P. D. A. Mcllroy, C. S. Stevenson, E. König, G. Ritter, J. Waigel, *J*. *Chem*. *Soc*. *Dalton Trans*. **1986**, 991-995

[28] K. Madeja, E. König, *J*. *Inorg*. *Nucl*. *Chem*. **1963**, 25, 377-385

[29] W. A. Jr. Baker, H. M. Bobonich, *Inorg*. *Chem*. **1964**, 3, 1184-1188

[30] J. P. Jesson, S. Trofimenko, D. R. Eaton, *J*. *Am*. *Chem*. *Soc*. **1967**, 89, 3158-3164

[31] C. Hannay, M.-J. Hubin-Franskin, F. Grandjean, V. Briois, J.-P. Itié, A. Polian, S. Trofimenko, G. J. Long, *Inorg*. *Chem*. **1997**, 36, 5580-5588

[32] H.-R. Chang, J. K. McCusker, H. Toftlund, S. R. Wilson, A. X. Trautwein, H. Winkler, D. N. Hendrickson, *J*. *Am*. *Chem*. *Soc*. **1990**, 112, 6814-6827

[33] L. Wiehl. *Acta Cryst.* **1993**, B49, 289-303

[34] M. L. Scudder, D. C. Craig, H. A. Goodwin, *CrystEngComm*. **2005**, 7, 642-649

[35] a) K. H. Sugiyarto, H. A. Goodwin, *Aust*. *J*. *Chem*. **1988**, 41, 1645-1663. b) K. H. Sugiyarto, D. C. Craig, A. D. Rae, H. A. Goodwin, *Aust*. *J*. *Chem*. **1994**, 47, 869-890

[36] K. H. Sugiyarto, K. Weitzner, D. C. Craig, H. A. Goodwin, *Aust*. *J*. *Chem*. **1997**, 50, 869-873

[37] K. H. Sugiyarto, M. L. Scudder, D. C. Craig, H. A. Goodwin, *Aust*. *J*. *Chem*. **2000**, 53, 755-765

[38] K. H. Sugiyarto, W.-A. McHale, D. C. Craig, A. D. Rae, M. L. Scudder, H. A. Goodwin, *Dalton Trans*. **2003**, 2443-2448

[39] G. A. Craig, J. S. Costa, O. Roubeau, S. J. Teat, G. Aromí, *Chem*. *Eur*. *J*. **2012**, 18, 11703-11715

[40] T. Buchen, P. Gütlich, K. H. Sugiyarto, H. A. Goodwin, *Chem*. *Eur*. *J*. **1996**, 2, 1134-1138

[41] S. A. Barrett, C. A. Kilner, M. A. Halcrow, *Dalton Trans*. **2011**, 40, 12021-12024

[42] a) M. Clemente-León, E. Coronado, M. C. Giménez-López, F. M. Romero, *Inorg*. *Chem*. **2007**, 46, 11266-11276. b) M. C. Giménez-López, M. Clemente-León, E. Coronado, F. M. Romero, S. Shova, J.-P. Tuchagues, *Eur*. *J*. *Inorg*. *Chem*. **2005**, 14, 2783-2787. c) M. Clemente-León, E. Coronado, M. C. Giménez-López, F. M. Romero, S. Asthana, C. Desplanches, J.-F. Létard, *Dalton Trans*. **2009**, 38, 8087-8095

[43] E. Coronado, M. C. Giménez-López, C. Giménez-Saiz, F. M. Romero, *CrystEngComm*. **2009**, 11, 2198-2203

[44] E. Coronado, M. C. Giménez-Lopez, C. Giménez-Saiz, J. M. Martínez-Agudo, F. M. Romero, *Polyhedron*, **2003**, 22, 2375-2380

[45] E. Coronado, J. R. G. Mascarós, M. C. Giménez-López, M. Almeida, J. C. Waerenborgh, *Polyhedron*, **2007**, 26, 1838-1844

[46] M. C. Giménez-López, M. Clemente-León, C. Giménez-Saiz, *Dalton Trans*. **2018**, 47, 10453-10462

[47] E. Coronado, J. C. Dias, M. C. Giménez-Lopez, C. Giménez-Saiz, C. Gómez-García, *J*. *Mol*. *Struct*. **2008**, 890, 215-220

[48] P. King, J. J. Henkelis, C. A. Kilner, M. A. Halcrow, *Polyhedron*, **2013**, 52, 1449-1456

[49] A. Djemel, O. Stefanczyk, M. Marchivie, E. Trzop, E. Collet, C. Desplanches, R. Delimi, G. Chastanet, *Chem*. *Eur*. *J*. **2018**, 24, 14760-14767

[50] a) G. A. Craig, J. S. Costa, O. Roubeau, S. J. Teat, G. Aromí, *Chem*. *Eur*. *J*. **2012**, 18, 11703-11715. b) G. A. Craig, J. S. Costa, O. Roubeau, S. J. Teat, G. Aromí, *Eur*. *J*. *Inorg*. *Chem*. **2013**, 745-752. c) G. A. Craig, J. S. Costa, O. Roubeau, S. J. Teat, G. Aromí, *Chem*. *Eur*. *J*. **2011**, 17, 3120-3127

[51] M. A. Halcrow, *New J*. *Chem*. **2014**, 38, 1868-1882

[52] L. A. Barrios, E. Peyrecave-Lleixà, G. A. Craig, O. Roubeau, S. J. Teat, G. Aromí, *Eur*. *J*. *Inorg*. *Chem*. **2014**, 6013-6021

[53] T. D. Roberts, M. A. Little, L. J. K. Cook, M. A. Halcrow, *Dalton Trans*. **2014**, 43, 7577-7588

[54] L. A. Barrios, C. Bartual-Murgui, E. Peyrecave-Lleixà, B. L. Guennic, S. J. Teat, O. Roubeau, G. Aromí, *Inorg*. *Chem*. **2016**, 55, 4110-4116

[55] T. D. Roberts, F. Tuna, T. L. Malkin, C. A. Kilner, M. A. Halcrow, *Chem*. *Sci*. **2012**, 3, 349-354

[56] J. S. Costa, S. Rodriguez-Jimenez, G. A. Craig, B. Barth, C. M. Beavers, S. J. Teat, G. Aromí, *J*. *Am*. *Chem*. *Soc*. **2014**, 136, 3869-3874

[57] T. D. Roberts, M. A. Little, F. Tuna, C. A. Kilner, M. A. Halcrow, *ChemComm*. **2013**, 49, 6280-6282

[58] C. Bartual-Murgui, R. Diego, S. Vela, S. J. Teat, O. Roubeau, G. Aromí, *Inorg*. *Chem*. **2018**, 57, 11019-11026

[59] T. D. Roberts, M. A. Little, L. J. K. Cook, S. A. Barrett, F. Tuna, M. A. Halcrow, *Polyhedron*. **2013**, 64, 4-12

[60] G. A. Craig, J. S. Costa, O. Roubeau, S. J. Teat, H. J. Shepherd, M. Lopes, G. Molnar, A. Bousseksou, G. Aromí, *Dalton Trans*. **2014**, 43, 729-737

[61] G. A. Craig, J. S. Costa, S. J. Teat, O. Roubeau, D. S. Yufit, J. A. K. Howard, G. Aromí. *Inorg*. *Chem*. **2013**, 52, 7203-7209

[62] J. J. McGarvey, I. Lawthers, *J*. *Chem*. *Soc*. *Chem*. *Commun*. **1982**, 906-907

[63] S. Decurtins, P. Gütlich, C. P. Kohler, H. Spiering, A. Hauser, *Chem*. *Phys*. *Lett*. **1984**, 105, 1-4

[64] S. Decurtins, P. Gütlich, K. M. Hasselbach, A. Hauser, H. Spiering, *Inorg*. *Chem*. **1985**, 24, 2174-2178

[65] A. Hauser, *Top*. *Curr*. *Chem*. **2004**, 234, 155-198

[66] S. Marcén, L. Lecren, L. Capes, H. A. Goodwin, J.-F. Létard, *Chem*. *Phys*. *Lett*. **2002**, 358, 87-95

[67] J.-F. Létard, L. Capes, G. Chastanet, N. Moliner, S. Létard, J. A. Real, O. Kahn, *Chem*. *Phys*. *Lett*. **1999**, 313, 115-120

[68] S. Hayami, Z-z Gu, Y. Einaga, Y. Kobayasi, Y. Ishikawa, Y. Yamada, A. Fujishima, O. Sato, *Inorg*. *Chem*. **2001**, 40, 3240-3242

[69] J.-F. Létard, *J*. *Mater*. *Chem*. **2006**, 16, 2550-2559

[70] J.-F. Létard, P. Guionneau, O. Nguyen, J. S. Costa, S. Marcén, G. Chastanet, M. Marchivie, L. Goux-Capes, *Chem*. *Eur*. *J*. **2005**, 11, 4582-4589

[71] V. García-López, M. Palacios-Corella, S. Cardona-Serra, M. Clemente-León, E. Coronado, *Chem*. *Commun*. **2019**, 55, 12227-12230

[72] L. J. K. Cook, F. L. Thorp-Greenwood, T. P. Comyn, O. Cespedes, G. Chastanet, M. A. Halcrow, *Inorg*. *Chem*. **2015**, 54, 6319-6330

[73] R. Kulmaczewski, E. Trzop, L. J. K. Cook, E. Collet, G. Chastanet, M. A. Halcrow, *Chem*. *Commun*. **2017**, 53, 13268-13271

[74] N. F. Sciortino, S. M. Neville, C. Desplanches, J.-F. Létard, V. Martinez, J. A. Real, B. Moubaraki, K. S. Murray, C. J. Kepert, *Chem*. *Eur*. *J*. **2014**, 20, 7448-7457

[75] J.-F. Létard, C. Carbonera, J. A. Real, S. Kawata, S. Kaizaki, *Chem*. *Eur*. *J*. **2009**, 15, 4146 –4155

[76] E. Milin, V. Patinec, S. Triki, E.-E. Bendeif, S. Pillet, M. Marchivie, G. Chastanet, K. Boukheddaden, *Inorg*. *Chem*. **2016**, 55, 11652-11661

[77] T. Boonprab, S. J. Lee, S. G. Telfer, K. S. Murray, W. Phonsri, G. Chastanet, E. Collet, E. Trzop, G. N. L. Jameson, P. Harding, D. J. Harding, *Angew*. *Chem*. *Int*. *Ed*. **2019**, 58, 11811-11815

[78] Y.-C. Chen, Y. Meng, Y.-J. Dong, X.-W. Song, G.-Z. Huang, C.-L. Zhang, Z.-P. Ni, J. Navarík, O. Malina, R. Zboril, M.-L. Tong, *Chem*. *Sci*. **2020**, 11, 3281-3289

[79] M. Marchiviea, P. Guionneaua, J. F. Létard, D. Chasseau, J. A. K. Howard, *J*. *Phys*. *Chem*. *Solids*. **2004**, 65, 17-23

[80] J.-F. Létard, S. Asthana, H. J. Shepherd, P. Guionneau, A. E. Goeta, N. Suemura, R. Ishikawa, S. Kaizaki, *Chem*. *Eur*. *J*. **2012**, 18, 5924-5934

[81] Y. Garcia, O. Kahn. L. Rabardel, B. Chansou, L. Salmon, J. P. Tuchagues, *Inorg*. *Chem*. **1999**, 38, 4663-4670

[82] J. A. Rodríguez-Velamazán, M. A. González, J. A. Real, M. Castro, M. C. Muñoz, A. B. Gaspar, R. Ohtani, M. Ohba, K. Yoneda, Y. Hijikata, N. Yanai, M. Mizuno, H. Ando, S. Kitagawa, *J*. *Am*. *Chem*. *Soc*. **2012**, 134, 5083-5089

[83] A. Bialonska, R. Bronisz, K. Darowska, K. Drabent, J. Kusz, M. Siczek, M. Weselski, M. Zubko, A. Ozarowski, *Inorg*. *Chem*. **2010**, 49, 11267-11269

[84] J. J. M. Amoore, C. J. Kepert, J. D. Cashion, B. Moubaraki, S. M. Neville, K. S. Murray, *Chem*. *Eur*. *J*. **2006**, 12, 8220-8227

[85] N. Bréfuel, S. Shova, J. Lipkowski, J.-P. Tuchagues, *Chem*. *Mater*. **2006**, 18, 5467-5479

[86] S. M. Neville, B. A. Leita, D. A. Offermann, M. B. Duriska, B. Moubaraki, K. W. Chapman, G. J. Halder, K. S. Murray, *Eur*. *J*. *Inorg*. *Chem*. **2007**, 1073-1085

[87] M. Seredyuk, M. C. Muñoz, M. Castro, T. Romero-Morcillo, A. B. Gaspar, J. A. Real, *Chem*. *Eur*. *J*. **2013**, 19, 6591-6596

[88] P. Guionneau, F. L. Gac, A. Kaiba, J. S. Costa, D. Chasseau, J.-F. Létard, *Chem*. *Commun*. **2007**, 3723-3725

[89] a) G. S. Matouzenko, A. Bousseksou, S. A. Borshch, M. Perrin, S. Zein, L. Salmon, G. Molnar, S. Lecocq, *Inorg*. *Chem*. **2004**, 43, 227-236. b) T. Fujinami, K. Nishi, D. Hamada, K. Murakami, N. Matsumoto, S. Iijima, M. Kojima, Y. Sunatsuki, *Inorg*. *Chem*. **2015**, 54, 7291-7300. c) B. A. Leita, S. M. Neville, G. J. Halder, B. Moubaraki, C. J. Kepert, J.-F. Letard, K. S. Murray, *Inorg*. *Chem*. **2007**, 46, 8784-8795

[90] a) M. Hostettler, K. W. Törnroos, D. Chernyshov, B. Vangdal, H.-B. Bürgi, *Angew*. *Chem*. *Int*. *Ed*. **2004**, 43, 4589-4594. b) K. W. Törnroos, M. Hostettler, D. Chernyshov, B. Vangdal, H.-B. Bürgi, *Chem*. *Eur*. *J*. **2006**, 12, 6207-6215

[91] M. Shatruk, H. Phan, B. A. Chrisostomo, A. Suleimenova, *Coord*. *Chem*. *Rev*. **2015**, 62-73

[92] Q. Yang, C. Gao, Y.-X. Wang, B.-W. Wang, Z.-M. Wang, S. Gao, *Inorg*. *Chem*. **2016**, 55, 7805-7807

[93] M. Ksiazek, M. Weselski, M. Ilczyszyn, J. Kusz, R. Bronisz, *Chem*. *Eur*. *J*. **2019**, 25, 2250-2261

[94] N. Phukkaphan, D. L. Cruickshank, K. S. Murray, W. Phonsri, P. Harding, D. Harding, *Chem*. *Commun*. **2017**, 53, 9801-9804

[95] F. J. Valverde-Muñoz, M. Seredyuk, M. Meneses-Sánchez, M. C. Muñoz, C. Bartual-Murgui, J. A. Real, *Chem*. *Sci*. **2019**, 10, 3807-3816

[96] a) E. J. MacLean, C. M. McGrath, C. J. O'Connor, C. Sangregorio, J. M. W. Seddon, E. Sinn, F. E. Sowrey, S. J. Teat, A. E. Terry, G. B. M. Vaughan, N. A. Young, *Chem*. *Eur*. *J*. **2003**, 921, 5314-5322. b) V. A. Money, I. R. Evans, M. A. Halcrow, A. E. Goeta, J. A. K. Howard, *Chem*. *Commun*. **2003**, 158-159. c) H. E. Mason, M. L. Hamilton, J. A. K. Howard, H. A. Sparkes, *New*. *J*. *Chem*. **2018**, 42, 18028-18037. d) M. M. Ndiaye, S. Pillet, E-E. Bendeif, M. Marchivie, G. Chastanet, K. Boukheddaden, S. Triki, *Eur*. *J*. *Inorg*. *Chem*. **2018**, 305-313. e) M. Weselski, M. Skiazek, J. Kusz, A. Bialonska, D. Paliwoda, M. Hanfland, M. F. Rudolf, Z. Ciunik, R. Bronisz, *Eur*. *J*. *Inorg*. *Chem*. **2017**, 1171-1179

[97] a) N. Bréfuel, E. Collet, H. Watanabe, M. Kojima, N. Matsumoto, L. Toupet, K. Tanaka, J.-P. Tuchagues, *Chem. Eur. J.* **2010**, 16, 14060-14068. b) N. Bréfuel, H. Watanabe, L. Toupet, J. Come, N. Matsumoto, E. Collet, K. Tanaka, J.-P. Tuchagues, *Angew. Chem. Int. Ed.* **2009**, 48, 9304-9307

[98] C.-H. Shih, C.-F. Sheu, K. Kato, K. Sugimoto, J. Kim, Y. Wang, M. Takata, *Dalton Trans.* **2010**, 39, 9794-9800

[99] D. Zhang, E. Trzop, F. J. Valverde-Muñoz, L. Piñeiro-López, M. C. Muñoz, E. Collet, J. A. Real, *Cryst. Growth Des.* **2017**, 17, 2736-2745

[100] K. Takahashi, H.-B. Cui, Y. Okano, H. Kobayashi, H. Mori, H. Tajima, Y. Einaga, O. Sato, *J. Am. Chem. Soc.* **2008**, 130, 6688-6689

[101] S. Titos-Padilla, J. M. Herrera, X.-W. Chen, J. J. Delgado, E. Colacio, *Angew. Chem. Int. Ed.* **2011**, 50, 3290-3293

[102] F. J. M. Lara, A. B. Gaspar, D. Aravena, E. Ruiz, M. C. Muñoz, M. Ohba, R. Ohtani, S. Kitagawa, J. A. Real, *Chem. Commun.* **2012**, 48, 4686-4688

[103] Z. Ni, M. P. Shores, *J. Am. Chem. Soc.* **2009**, 131, 32-33

[104] a) S.-i. Ohkoshi, K. Imoto, Y. Tsunobuchi, S. Takano, H. Tokoro, *Nat. Chem.* **2011**, 3, 564-569. b) A. B. Gaspar, M. C. Muñoz, J. A. Real, *J. Mater. Chem.* **2006**, 16, 2522-2533

[105] a) T. Mahfoud, G. Molnár, S .Bonhommeau, S. Cobo, L. Salmon, P. Demont, H. Tokoro, S. Ohkoshi, K. Boukheddaden, A. Bousseksou, *J. Am. Chem. Soc.* **2009**, 131, 15049-15054. b) S. Ohkoshi, H. Tokoro, T. Matsuda, H. Takahashi, H. Irie, K. Hashimoto, *Angew. Chem. Int. Ed.* **2007**, 46, 3238-3241. c) O. Sato, T. Kawakami, M. Kimura, S. Hishiya, S. Kubo, Y. Einaga, *J. Am. Chem. Soc.* **2004**, 126, 13176-13177

[106] a) A. Bousseksou, G. Molnár, P. Demont, J. Menegotto, *J. Mater. Chem.* **2003**, 13, 2069-2071. b) S. Bonhommeau, T. Guillon, L. M. L. Daku, P. Demont, J. S. Costa, J.-F. Létard, G. Molnár, A. Bousseksou, *Angew. Chem. Int. Ed.* **2006**, 45, 1625-1629. c) J.-L. Wang, Q. Liu, Y.-S. Meng, H. Zheng, H.-L. Zhu, Q. Shi, T. Liu, *Inorg. Chem.* **2017**, 56, 10674-10680

[107] H. Zheng, Y.-S. Meng, G.-L. Zhou, C.-Y. Duan, O. Sato, S. Hayami, Y. Luo, T. Liu, *Angew. Chem. Int. Ed.* **2018**, 57, 8468-8472

[108] W. Zhang, R.-G. Xiong, *Chem. Rev.* **2012**, 112, 1163-1195

[109] a) M. E. Lines, A. M. Glass, *Principles and Applications of Ferroelectrics and Related Materials*. **1977**, Clarendon Press: Oxford, U.K. b) J. Grindlay, *An Introduction to the Phenomenological Theory of Ferroelectricity*. **1970**, Pergamon Press: Oxford, U.K. c) P.-P. Shi, Y.-Y. Tang, P.-F. Li, W.-Q. Liao, Z.-X. Wang, Q. Ye, R.-G. Xiong, *Chem*. *Soc*. *Rev*. **2016**, 45, 3811-3827

[110] S. Horiuchi, Y. Tokura, *Nat*. *Mater*. **2008**, 7, 357-366

[111] a) J. Valasek, *Phys*. *Rev*. **1921**, 17, 475-481. b)W. Zhang, H.-Y. Ye, R.-G. Xiong, *Coord*. *Chem*. *Rev*. **2009**, 253, 2980-2997. c) V. L. Hablutzel, J. Helv, *Phys*. *Acta*. **1939**, 12, 489. d) X. Solans, C. Gonzalez-Silgo, C. Ruiz-Pérez, *J*. *Solid State Chem*. **1997**, 131, 350-357

[112] M. Szafranski, A. Katrusiak, G. J. McIntyre, *Phys*. *Rev*. *Lett*. **2002**, 89, 215507

[113] a) S. Horiuchi, F. Ishii, R. Kumai, Y. Okimoto, H. Tachibana, N. Nagaosa, Y. Tokura, *Nat*. *Mater*. **2005**, 4, 163-166. b) R. Kumai, S. Horiuchi, Y. Okimoto, Y. Tokura, *J*. *Chem*. *Phys*. **2006**, 125, 084715. c) S. Horiuchi, R. Kumai, Y. Tokura, *Angew*. *Chem*. *Int*. *Ed*. **2007**, 46, 3497-3501

[114] R. Kumai, S. Horiuchi, H. Sagayama, T. Arima, M. Watanabe, Y. Noda, Y. Tokura, *J*. *Am*. *Chem*. *Soc*. **2007**, 129, 12920-12921

[115] a) L. K. Saunders, H. Nowell, L. E. Hatcher, H. J. Shepherd, S. J. Teat, D. R. Allan, P. R. Raithby, C. C. Wilson, *CrystEngComm*. **2019**, 21, 5249-5260. b) T. Akutagawa, S. Takeda, T. Hasegawa, T. Nakamura, *J*. *Am*. *Chem*. *Soc*. **2004**, 126, 291-294

[116] a) T. Nakanishi, Y. Hori, H. Sato, S.-Q. Wu, A. Okazawa, N. Kojima, T. Yamamoto, Y. Einaga, S. Hayami, Y. Horie, H. Okajima, A. Sakamoto, Y. Shiota, K. Yoshizawa, O. Sato, *J*. *Am*. *Chem*. *Soc*. **2019**, 141, 14384-14393. b) T. Nakanishi, Y. Hori, S. Wu, H Sato, A. Okazawa, N. Kojima, Y. Horie, H. Okajima, A. Sakamoto, Y. Shiota, K. Yoshizawa, O. Sato, *Angew*. *Chem*. *Int*. *Ed*. **2020**, 59, 14781-14787

[117] R. Akiyoshi, Y. Hirota, D. Kosumi, M. Tsutsumi, M. Nakamura, L. F. Lindoy, S. Hayami, *Chem*. *Sci*. **2019**, 10, 5843-5848

[118] C. Wäckerlin, F. Donati, A. Singha, R. Baltic, S. Decurtins, S.-X. Liu, S. Rusponi, J. Dreiser, *J*. *Phys*. *Chem*. *C*. **2018**, 122, 8202-8208

[119] X. Zhang, T. Palamarciuc, J.-F. Létard, P. Rosa, E. Vega Lozada, F. Torres, L. G. Rosa, B. Doudin, P. A. Dowbe, *Chem*. *Commun*. **2014**, 50, 2255-2257

Chapter 2: Hydrogen-bonded networks of $[Fe(bpp)_2]^{2+}$ spin crossover complexes and dicarboxylate anions

This chapter describes the syntheses, crystal structures, thermal and (photo)magnetic properties of novel spin crossover salts of formula $[Fe(bpp)_2](C_6H_8O_4)\cdot 4H_2O$ (**1**·4H$_2$O), $[Fe(bpp)_2](C_8H_4O_4)\cdot 2MeOH\cdot H_2O$ (**2**·2MeOH·H$_2$O) and $[Fe(bpp)_2](C_8H_4O_4)\cdot 5H_2O$ (**2**·5H$_2$O), being bpp = 2,6-bis(pyrazol-3-yl)pyridine, $C_6H_8O_4^{2-}$ = adipate dianion and $C_8H_4O_4^{2-}$ = terephthalate dianion. We have analysed the magnetic properties of both hydrated and dehydrated phases and, in addition, the rearrangement of the hydrogen-bonded network in the terephthalate compound after inclusion of methanol molecules. Furthermore, it was possible to dehydrate **1**·4H$_2$O in a single-crystal-to-single-crystal transformation; thus, the structural and photomagnetic characterisation of anhydrous **1** was also conducted. Similar experiments with **2**·5H$_2$O did not result in single crystals of enough X-ray quality.

2.1. Introduction to pyrazolyl systems

The pyrazolyl (HPz) ligand has been widely used in coordination chemistry, being one of the easiest and most flexible N-donor heterocycle to be involved in larger polydentate ligand structures.[1] Simple pyrazoles usually bind metal ions through the Lewis basic imine N-donor N2 (Scheme 2.1), leaving the Lewis acid pyrrolic N–H group at N1 free to interact with anions or solvent molecules as hydrogen bond acceptors. In this context, several supramolecular architectures have been synthesised for anions with extensive hydrogen-bonded networks.[2] The deprotonated pyrazolido anion has been associated to twenty different coordination modes and can bind up to four metal ions. Together with the possibility of coordinating both N–donor atoms, the relatively straightforward functionalisation of the pyrazolyl ring[3] has led to the synthesis of a wide variety of compounds that are of interest in several fields such as molecular magnetism[4,5], luminescence[6] and catalysis,[7] among others.

Nonetheless, our interest is focused on the neutral Hpz ring where the presence of the amino group ensures the formation of strong hydrogen bonds. In this way, we are favouring the establishment of intermolecular interactions either through the formation of hydrogen bonds or in the form of π-π stacking interactions between the ligand and the anion or solvent molecules. As

mentioned in the previous chapter, these are two of the possible strategies used in order to increase the cooperativity of the SCO systems, which is a key aspect in the development of molecular sensors, devices for switching and information storage applications.[8]

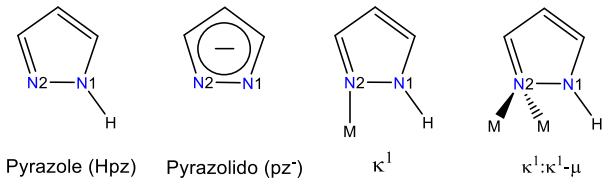

Scheme 2.1. Molecular structure of pyrazole and pyrazolido anion. Known coordination modes of Hpz are also included.

In particular, this part of the thesis has been focused on the 2,6-bis(pyrazol-3-yl) pyridine (bpp, Scheme 2.2) ligand because it allows the formation of strong H-bonds and an important part of SCO systems exhibiting LIESST effect has been constructed based on it (Sections 1.3-1.4, Chapter 1). On the other hand, polycarboxylate anions have been widely used in the construction of coordination complexes and hydrogen-bonded frameworks.[9] Therefore, symmetric dicarboxylate anions (adipate and terephthalate, Scheme 2.2) have been chosen as hydrogen-bond acceptors, in which those presenting aromatic rings are also able to establish π-π stacking interactions either with the cationic network or between them. In this way, the number of intermolecular interactions that contribute to the enhancement of the cooperativity of the system may increase considerably in comparison with $[Fe(bpp)_2]^{2+}$ complexes bearing simple anions (for instance, Cl^-, NO_3^- or ClO_4^-).

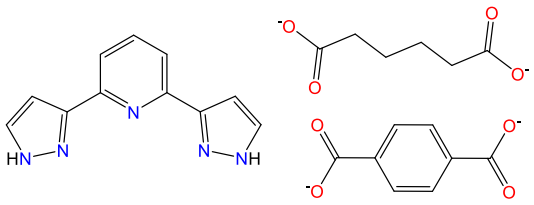

Scheme 2.2. Structures of bpp, adipate dianion and terephthalate dianion.

2.2. Organisation and objectives

This work is intended to exploit the high directionality of hydrogen bonds in the design of novel supramolecular Fe(II) SCO frameworks.[10] On the one hand, the aim of this work is to compare the (photo)magnetic properties of the

anhydrous spin crossover salt $[Fe(bpp)_2](C_6H_8O_4)$ (**1**) with those of the as-synthesised compound (**1**·$4H_2O$). This study highlights the relevance of the thermal conditions used in the desolvation process, which have a direct impact into both crystallinity and magnetic behaviour.

On the other hand, a comparison between two $[Fe(bpp)_2]L{\cdot}nH_2O$ salts, the first one containing adipate ($L = C_6H_8O_4^{2-}$) dianions and the second one built up from terephthalate ($L = C_6H_4O_4^{2-}$) dianions, is presented. Despite the fact that both anions exhibit an analogous connectivity (linear ditopic topology) and charge, there is a relevant difference between both building blocks. The flexibility of the adipate dianion allows the existence of multiple conformations in the crystal structure, whereas this situation is not possible for the rigid terephthalate dianion. The present study has addressed the influence of these variations on the ground spin state of the resulting iron(II) complexes *via* hydrogen bonding.

In this chapter, the work is divided in two main parts:

- Influence of thermal treatment during the dehydration process in $[Fe(bpp)_2]^{2+}$ salts containing adipate dianions (Section 2.4).

- Comparison of $[Fe(bpp)_2]^{2+}$ salts with adipate and terephthalate dianions (Section 2.5).

2.3. Synthesis

Metathesis reactions of $[Fe(bpp)_2]SO_4$ with the corresponding barium carboxylates (BaL) were successfully employed for the preparation of complexes **1**·$4H_2O$ and **2**·$5H_2O$ (Scheme 2.3). In these reactions, insoluble barium sulphate is formed which is eliminated by filtration. Therefore, this synthetic method allows the removal of other hydrogen-bond acceptors that might be in competition with the dicarboxylate anions, being in solution only the components of interest that crystallise after slow evaporation of the solvent. This strategy has been previously shown to be efficient for obtaining the desired hydrogen-bonded networks.[11] Two different phases are isolated for the terephthalate derivative. Red plates of **2**·$5H_2O$ and some red needles of **2**·$2MeOH{\cdot}H_2O$. The plates appeared after few days and some needles only crystallised in one case, together with the plates. Thus, the plates were generally the only product or the major product obtained in the worst scenario. Since the needles lose easily methanol, they were only characterised by single crystal X-ray diffraction. For the interpretation of the bulk properties, the formula of

2·5H_2O was considered due to the fact that powder X-ray diffraction of the bulk material is in agreement with the crystal structure of this solvate (Section 2.5.1.B, *vide infra*). For the adipate salt, red prisms of **1**·4H_2O crystallised together with some white needles of free bpp ligand. The red crystals were hand-picked in order to isolate this compound for its further characterisation.

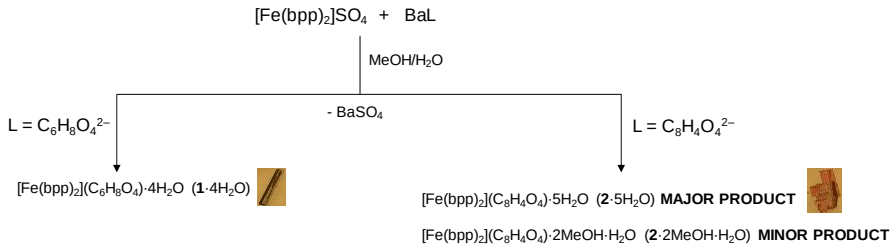

Scheme 2.3. Schematic illustration for the synthesis of **1**·4H_2O and **2**·5H_2O.

On the other hand, thermal treatment of the adipate derivative **1**·4H_2O resulted in the formation of anhydrous single crystals of enough quality for X-ray crystal structure determination. Dehydration of **1**·4H_2O was carried out by placing the sample in a glass tube inside an oil bath at 453 K under vacuum for 2 h. Then, a drop of water was added in order to facilitate the rehydration of the compound. A change of colour from yellow to red was observed. Finally, the sample was dehydrated again following the same procedure but this time at 400 K. One of these crystals was used for single crystal X-ray experiments. Furthermore, instead of performing two dehydration cycles, a sample with poorer crystallinity can be obtained from direct heating of the original compound at 400 K under vacuum. Nonetheless, an essentially amorphous material is obtained when only one heating process at 453 K is applied.

2.4. $[Fe(bpp)_2](C_6H_8O_4)·4H_2O$ (**1**·4H_2O) and $[Fe(bpp)_2](C_6H_8O_4)$ (**1**)

2.4.1. Structural characterisation of 1·4H_2O

A. Single crystal X-ray diffraction

1·4H_2O crystallises in the monoclinic space group $P2_1/c$ (Table 2.1). Its crystal structure is built up from isolated $[Fe(bpp)_2]^{2+}$ cations, adipate dianions and water molecules. In the asymmetric unit, there is only one inequivalent

adipate dianion, four water molecules and one crystallographically independent Fe(II) centre, with Fe–N bond distances characteristic of a LS state (1.913(11)–1.979(4) Å). As can be seen in Figure 2.1, the two tridentate bpp ligands are occupying the meridional positions of the distorted octahedral Fe^{2+} environment. In fact, the coordination to the iron site takes place in an almost perpendicular way (the dihedral angle between the planes that contain each bpp ligand is 91.06°), resulting in a pseudo C_{2v} symmetry.

Table 2.1. Crystallographic data and structural refinement for $[Fe(bpp)_2](C_6H_8O_4)\cdot 4H_2O$ (**1**·$4H_2O$).

1·$4H_2O$	
Empirical formula	$C_{28}H_{34}FeN_{10}O_8$
Formula weight	694.50
Crystallographic system	Monoclinic
Space group	$P2_1/c$ (no. 14)
a/ Å	8.07580(10)
b/ Å	25.2815(3)
c/ Å	16.1326(3)
α/ °	90
β/ °	112.381(18)
γ/ °	90
V/ Å^3	3045.65(8)
Z	4
R(int)	0.0554
ρ_{calc}/ g·cm^{-3}	1.515
μ/ mm^{-1}	0.563
Crystal dimensions/ mm	0.25 x 0.15 x 0.08
T/ K	150(2)
λ/ Å	0.71073
2θ range/ °	3.18< 2θ <55.02
Index ranges for h, k , l	-10/10, -32/32, -20/20
Completeness to θ = 25.242° (%)	99.9
Refinement method	Full-matrix least-squares on F^2
Collected reflections	13393
Unique reflections	6963
Data/Restraints/Parameters	6963 / 14/ 457
Goodness-of-fit on F^2	1.076
R1, wR2 [I > 2sigma(l)][a]	R1 = 0.0543, wR2 = 0.1397
R1, wR2 (all data)[a]	R1 = 0.1031, wR2 = 0.1890
$\Delta\rho_{max}$ and $\Delta\rho_{min}$ (e·Å^{-3})	0.81, -1.06

[a] $R1 = \Sigma(||F_o| - |F_c||)/\Sigma|F_o|$; $wR2 = \{\Sigma[w(F_o^2 - F_c^2)^2]/\Sigma[w(F_o^2)^2]\}^{1/2}$

Octahedral distortion parameters, φ and Σ, are also typical of LS species (φ = 178.22° and Σ = 89.99°, shown in Figure 2.1). The first parameter (φ) corresponds to the *trans* N–Fe–N angle formed by the coordination of the central pyridine fragments to the iron cation, being its ideal value 180°. The second parameter is the sum of the deviation away from 90° of the twelve possible cis-

N–Fe–N bite angles (α_i). Thus, a value of 0 is expected for an ideal octahedron and increases with the deformation. It is calculated as follows:

$$\Sigma = \sum_{i=1}^{12} |90 - \alpha_i| \text{ (Eq. 2.1)}$$

Previous reports have shown that complexes in the HS state exhibit higher degrees of distortion than LS systems.[12] Many salts of this type containing the bpp ligand or its derivatives are observed to be LS as a consequence of their degree of hydration, with a concomitant population of the HS state upon heating the system to release the lattice water molecules.[13] Thus, **1**·4H$_2$O exhibits the usual stable spin state for a hydrated [Fe(bpp)$_2$]$^{2+}$ salt.

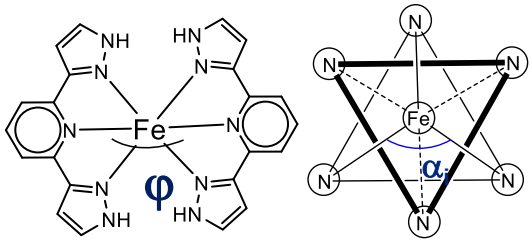

Figure 2.1. Left: An illustration of the coordination of two bpp ligands to an Fe centre with the parameter φ indicated. Right: A view of the bite angles α_i that are used to calculate the parameter Σ.

One bpp ligand is hydrogen-bonded to two adipate anions (N1···O4: 2.612(18) Å, N5···O2: 2.768(12) Å), giving rise to the formation of centrosymmetric Fe(II) cyclic dimers (Figure 2.2). The other bpp ligand is establishing H bonds with one adipate anion (N6···O3: 2.673(2) Å) and one water molecule (N10···O1W: 2.700(9) Å). Therefore, the second coordination sphere of the Fe(II) centre is occupied by three adipate anions and one water molecule. A related HS compound in which [Fe(bpp)$_2$]$^{2+}$ complexes are combined with monoprotonated cyclohexanetricarboxylate dianions has been published.[10] In this case, the number of carboxylate anions that are acting as H-bond acceptors towards the cationic fragments is two, whereas in **1**·4H$_2$O it is increased to three. This increases the electron density in the pyrazolyl rings, resulting in stronger Fe–N(imine) bonds and correspondingly shorter Fe–N distances, characteristic of LS centres due to higher electrostatic attraction to the negative charges of the dianions. Therefore, the different spin state found in both salts despite the fact of exhibiting similar crystal structures might be explained simply by charge density considerations.

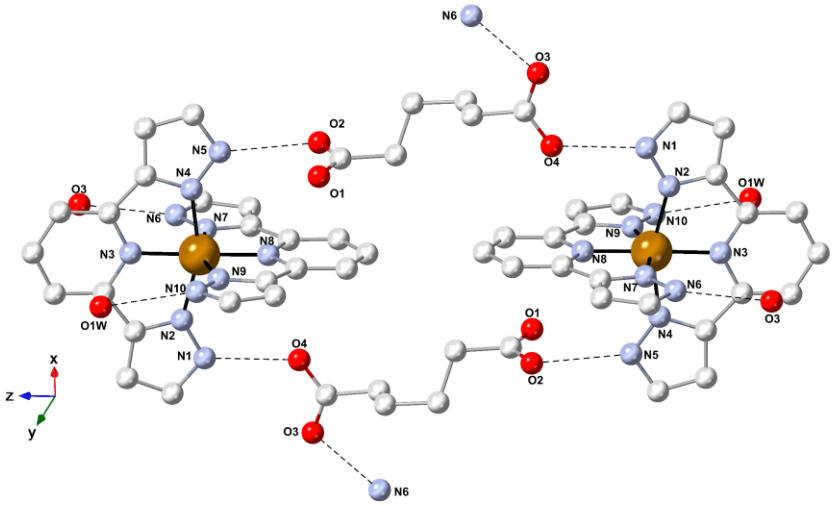

Figure 2.2. Crystal structure of **1**·4H_2O showing a cyclic hydrogen-bonded Fe(II)centrosymmetric dimer. Dashed lines represent hydrogen bonds.

On the other hand, the adipate anions exhibit an *anti*, *gauche*, *anti* conformation and are interacting as H-bond acceptors with three $[Fe(bpp)_2]^{2+}$ moieties and one water molecule (O1···O3W: 2.727(2) Å). The cyclic dimers are bridged by a carboxylate fragment (O3–C–O4) that displays a bidentate *syn*, *anti* hydrogen-bond connectivity, forming a corrugated layer (Figure 2.3). The second carboxylate moiety only contributes to the formation of the cyclic dimers and points outside the layers through water molecule O1W. As a result, the latter carboxylate fragment presents a less symmetric distribution of the electron density (C23–O1: 1.239(10) Å, C23–O2: 1.265(8) Å) in comparison with the bridging carboxylate (C28–O3: 1.256(5) Å, C28–O4: 1.246(15) Å). As can be seen in Figure 2.3, each dimer is establishing H-bonds with four identical dimeric subunits, with an alternation of cyclic dimers and cyclic tetramers along the *y* and [201] directions. This hydrogen-bonded assembly presents channels that are filled by crystallisation water molecules, which are engaged in several H bond interactions (Table 2.2). It is worth mentioning that O1W exhibits H-bond distances lower than the remaining water molecules, indicating that it is bonded stronger than the others to the crystal lattice. This is consistent with the fact that O1W is the only water molecule located in the second iron coordination sphere.

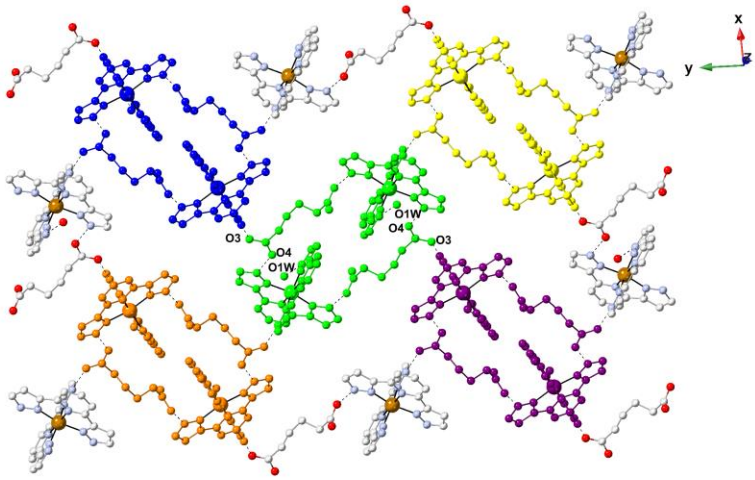

Figure 2.3. View of the crystal structure of **1**·4H_2O showing the H-bonded network in the *xy* plane. A central centrosymmetric dimer (shown in green) is interacting with four equivalent dimers (single-coloured) to afford a layered structure. H atoms have been omitted for clarity and only one water molecule is represented (O1W). Hydrogen bonds are shown as dashed lines.

Table 2.2. Intermolecular hydrogen bonds present in **1**·4H_2O between donors and acceptors (D-H···A).

D···A	$d_{D\cdots A}$ / Å
N1···O4#1	2.612(18)
N5···O2#2	2.768(12)
N6···O3	2.673(2)
N10···O1W	2.700(9)
O1···O3W	2.727(2)
O2···O2W	2.844(15)
O2···O4W#3	2.790(2)
O3···O1W#4	2.745(7)
O1W···O4W#5	2.717(7)
O2W···O2W#6	2.861(4)
O2W···O3W#3	2.842(19)
O3W···O4W	2.756(13)

Symmetry transformations used to generate equivalent atoms: #1 x – 1, – y + 1/2, z – 1/2; #2 –x, y – 1/2, – z + 3/2; #3 x – 1, y, z; #4 x + 1, y, z; #5 x – 1, – y + 1/2, z + 1/2, #6 – x, – y + 1, – z + 2

A view along the *a* axis shows that the $[Fe(bpp)_2]^{2+}$ cationic moieties are connected by π-π stacking interactions between their pyrazolyl fragments. Each $[Fe(bpp)_2]^{2+}$ complex interacts with only three neighbours, giving rise to the formation of double chains running parallel to the *a* axis (Figure 2.4). In addition, two different π-π stacking interactions can be distinguished. First, stronger interactions with a distance between adjacent pyrazolyl mean planes of 3.23(8) Å are observed for equivalent bpp ligands related by a translation along the *x*

direction. Secondly, the other independent bpp ligand is involved in π-π interactions with equivalent ligands related by a centre of symmetry, exhibiting longer interplane distances equal to 3.354(3) Å.

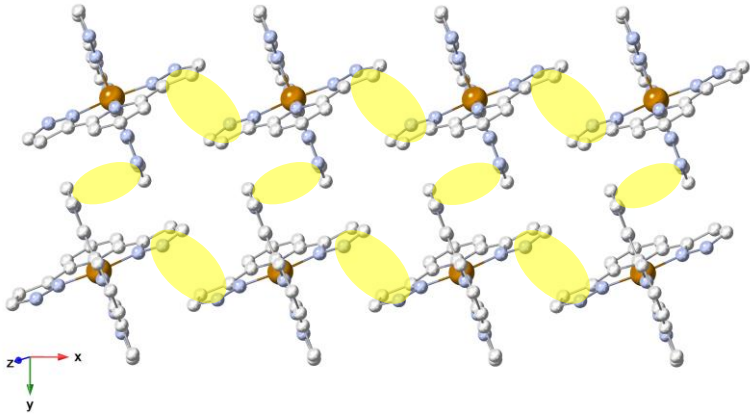

Figure 2.4. Crystal structure of **1**·4H_2O showing the π-π stacked $[Fe(bpp)_2]^{2+}$ double chains running along the *a* axis. H atoms have been omitted for clarity and π-π interactions are represented by yellow spheres.

B. Thermal properties

A thermogravimetric (TG) analysis of **1**·4H_2O was performed under nitrogen atmosphere in order to get insights into the stability of the sample and determine which is the best temperature range for solvatomagnetic measurements (Figure 2.5.a). The loss of water molecules occurs in two different steps. The first one takes place between 300-377 K and is associated to the release of three water molecules (observed: 6.6%; calcd: 7.7%). The second weight loss is ascribed to one water molecule (observed: 2.4%; calculated: 2.8%) and takes place in the 380-435 K range. The existence of two separate processes for solvent loss suggests that the water molecule that is released at higher temperatures is bound more tightly than the others. This observation is in agreement with the crystal structure described for **1**·4H_2O which shows the presence of O1W in the second iron coordination sphere. In addition, the remaining water molecules located in the voids of the hydrogen-bonded structure are lost easily, as expected from the X-ray crystal structure determination. Above 458 K, decomposition of the compound takes place. These results indicate that the desolvation of the sample requires heating above 400 K, which is the maximum temperature available in our SQUID equipment.

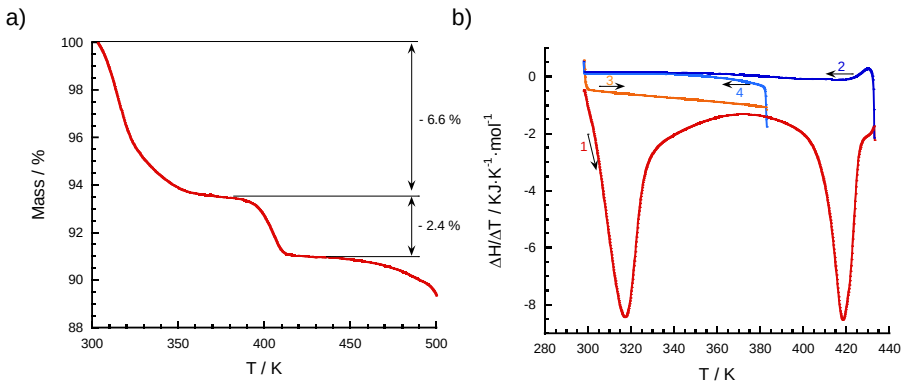

Figure 2.5. a) Thermogravimetric analysis of **1**·4H$_2$O. b) Differential scanning calorimetry curve of **1**·4H$_2$O. Curves 1 and 2: First heating and cooling processes, respectively. Curves 3 and 4: second temperature cycle.

The differential scanning calorimetry (DSC) measurement of **1**·4H$_2$O is shown in Figure 2.5.b. In the first heating process (curve 1), two sharp endothermic peaks are registered, which are associated to the first (317 K) and the second (418 K) dehydration steps observed in the TG curve. The peak centred at 317 K presents a high-temperature tail, in accordance with the gradual character of the first dehydration process observed in TG data. Upon cooling to room temperature (curve 2), a featureless plot is obtained, as well as in a subsequent temperature cycle (curves 3 and 4). The lack of peaks in the DSC measurement of the anhydrous phase indicates that the compound does not exhibit abrupt transitions induced by temperature, at least in the temperature range of study (300-380 K). The presence of a featureless calorimetric curve indicating the absence of a thermally induced transition has been also obtained for other $[Fe(bpp)_2]^{2+}$ salts.[14]

C. Powder X-ray diffraction

Powder X-ray diffraction experiments have been performed in order to confirm the phase purity of the bulk material and study the reversibility of the dehydration-rehydration process. Figure 2.6 shows the X-ray diffractograms at room temperature of **1**·4H$_2$O as-synthesised, desolvated at 453 K for 2 h and rehydrated after addition of one drop of water and subsequent exposure to ambient conditions. Moreover, the simulated diffractogram for the original compound obtained from the single crystal X-ray data at 150 K is included. There is a perfect agreement between the simulated and the experimental patterns of

1·4H_2O, discarding the presence of impurities and any phase transition between room temperature and 150 K.

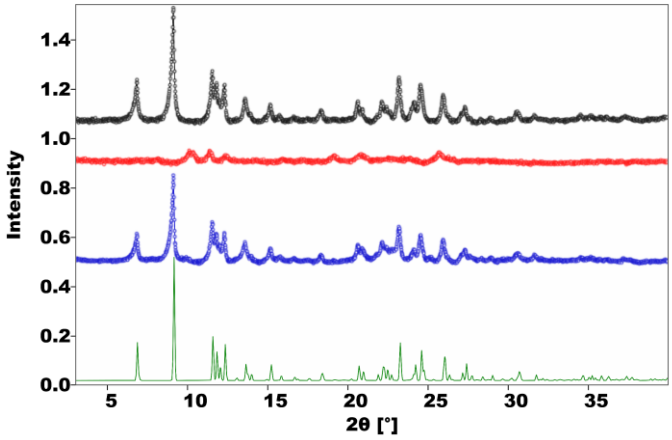

Figure 2.6. Powder X-ray diffractograms at room temperature of **1**·4H_2O as-synthesised (black dots), dehydrated at 453 K for 2 h (red dots), rehydrated in water (blue dots) and simulated from single crystal X-ray data for **1**·4H_2O using *CrystalDiffract* software (green pattern).

Dehydration of the sample at 453 K results in a loss of crystallinity, being the anhydrous phase **1** practically an amorphous material. Nonetheless, after contact with water, surprisingly the crystallinity is recovered and a diffraction pattern identical to that displayed for the original compound is registered. This indicates that the rehydrated material is isostructural to the original solvate **1**·4H_2O. Indeed, the indexation of the unit cell for the rehydrated sample from PXRD data at RT leads to the following monoclinic unit cell with parameters very close to those of the original unit cell for **1**·4H_2O: a = 8.1043 Å, b = 25.4337 Å, c = 16.2643 Å, α = γ = 90°, β = 112.494° and V = 3097.3977 Å^3. In a similar hydrogen-bonded network, original and rehydrated samples present the same structure, showing that the dehydration-rehydration process occurs through a different crystal structure in the desolvated phase, which preserves crystallinity.[15] In our case, the surprising fact is that the crystallinity is lost upon dehydration and after it is restored in the resolvated material. This might be explained taking into consideration the flexibility of the adipate dianions that allow them to adopt several conformations in the desolvated material, resulting in a loss of crystalline order that is recovered after rehydration with the original conformation.

2.4.2. Magnetic characterisation

Magnetic susceptibility (χ) measurements were carried out under a 1000 Oe magnetic field on **1**·4H$_2$O as-synthesised (Figure 2.7.a). The temperature dependence of the χT product is typical of a diamagnetic LS Fe(II) complex in the heating mode from 2 K up to 315 K. At higher temperatures, dehydration of the sample starts and an increase of the magnetic signal is observed upon heating. Nonetheless, saturation of the signal is not reached even after 2h at 400 K (maximum temperature at which our SQUID equipment can work). This is consistent with the fact that complete dehydration of the sample takes place at higher temperatures (above 430 K), as indicated by thermal analyses.

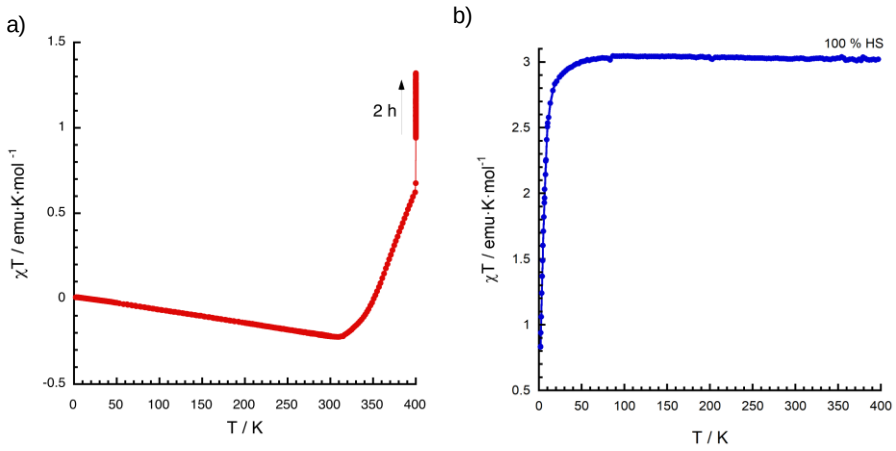

Figure 2.7. a) Thermal variation of the χT product of **1**·4H$_2$O as-synthesised. b) Temperature dependence of the χT value of **1** dehydrated at 453 K under vacuum. No diamagnetic corrections were applied.

Therefore, the original sample was dehydrated prior to its introduction in the SQUID equipment to achieve complete desolvation of the material. For this purpose, the original hydrate was inserted in a glass tube, heated at 453 K for 2h in an oil bath under vacuum and sealed (Figure 2.7.b). At 400 K, the anhydrous material exhibits a χT product of 2.9 emu·K·mol^{-1}, which is close to the spin-only value of 3.0 emu·K·mol^{-1} expected for one high-spin Fe^{2+} per formula unit. On lowering the temperature, the Fe^{2+} centres do not undergo spin crossover and remain in the high-spin state between 400 and 50 K. Below this temperature, the χT value starts to decrease steadily as a consequence of the zero-field splitting of the high-spin Fe^{2+} ground state and reaches a value of 0.79 emu·K·mol^{-1} at 2 K. Subsequent heating of the sample results in an analogous behaviour to that

described for the cooling process (not shown). The thermal dependence of the magnetic signal is in agreement with a high-spin Fe^{2+} complex in the whole temperature domain of study and is consistent with the DSC measurements which do not exhibit any sign of transitions in the temperature regime of investigation.

Next, the same anhydrous sample measured above was rehydrated and its magnetic susceptibility response registered again. The rehydrated sample was *in situ* desolvated in the SQUID equipment at 400 K (Figure 2.8). As expected, at room temperature the χT product has a value of 0.07 emu·K·mol^{-1}, which indicates that the rehydrated sample is essentially in the low-spin state. During the heating process (curve 1), the χT product increases abruptly from 370 to 400 K and, surprisingly, reaches saturation after being 2h at this temperature. These observations indicate that despite being isostructural the rehydrated material, its desolvation process is easier and takes place completely in the SQUID equipment at 400 K, in contrast with the behaviour observed for the original sample. It seems that the rehydrated phase presents a smaller size of the crystallites and/or a different arrangement of crystal facets that facilitate the loss of water molecules.

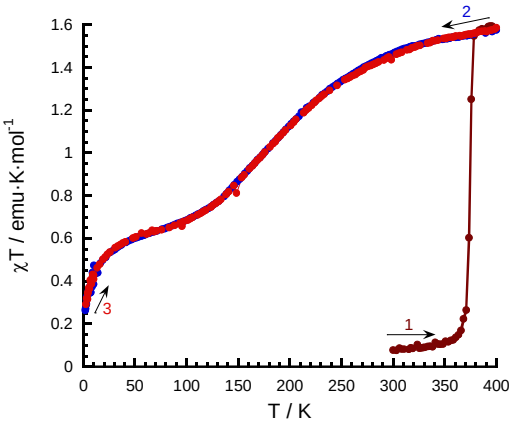

Figure 2.8. Temperature dependence of the χT product of **1** after *in situ* dehydration of **1**·4H_2O (rehydrated) for 2h at 400 K.

The value of the magnetic signal at saturation is 1.51 emu·K·mol^{-1}, which may suggest that 50% of the Fe^{2+} centres are in the high-spin state as a consequence of an incomplete spin crossover or even the presence of two different iron sites (one LS and the other one HS). On cooling (curve 2), this value decreases gradually and reaches a small plateau at 70 K with $\chi T \approx 0.60$ emu·K·mol^{-1}. Below

70 K, the χT product exhibits an additional decrease until reaching a value of 0.25 emu·K·mol^{-1} at 2 K. This is due to the significant residual fraction of high-spin centres at 70 K, that undergoes zero-field splitting (ZFS) on further cooling. The second heating process (curve 3) reveals a very gradual transition without thermal hysteresis.

These observations are in contrast with the sample obtained by dehydration of **1**·4H_2O under vacuum at 453 K, indicating that both anhydrous phases are different and highlighting the vital point of thermal treatment in defining the magnetic properties of **1**. An essentially amorphous high-spin material is obtained when desolvating the sample at 453 K under vacuum for 2 h. This compound undergoes rehydration and recovers the crystallinity to yield the original hydrate **1**·4H_2O. By decreasing the temperature of the second thermal treatment down to 400 K, it is possible to obtain an anhydrous phase of **1** exhibiting spin-crossover from the rehydrated sample. The following point will show that this new phase of **1** preserves crystallinity and, in addition, that it can be directly accessed by dehydration from the pristine tetrahydrate at 400 K under vacuum (Scheme 2.4). However, when the original sample is heated at 400 K without vacuum (conditions used in the first SQUID measurement, Fig. 2.7.a) a complete dehydration of the sample is not achieved. A polycrystalline sample of **1** is stable in ambient conditions, thus, its further characterisation could be performed.

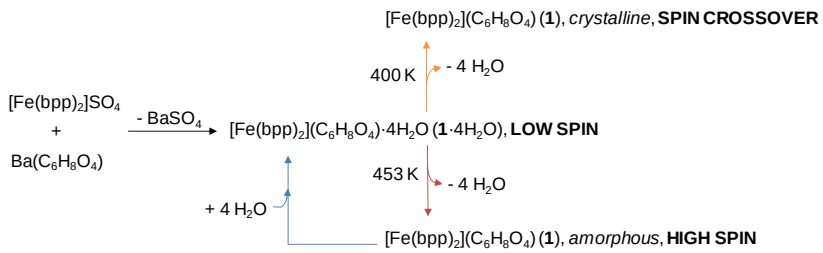

Scheme 2.4. Schematic illustration of the synthesis and spin changes upon reversible dehydration of **1**·4H_2O. Both heating processes were performed under vacuum. A detail of the crystalline state of the anhydrous phases is also included.

2.4.3. Structural characterisation of 1

A. Single crystal X-ray diffraction

The anhydrous salt **1** crystallises in the monoclinic space group $C2/c$ at 298 K (Table 2.3). Now, the asymmetric unit contains two crystallographically

inequivalent iron centres located in special positions (both sitting on a two-fold axis), Fe1 and Fe2, and one adipate dianion that is disordered in two positions, denoted as A and B, with occupancy factors of 0.55 and 0.45, respectively (Figure 2.9). The conformations of both adipate anions are different between them and also differ from that present in the original tetrahydrate, being *gauche*, *anti*, *gauche* for adipate A and *gauche*, *anti*, *anti* for adipate B (Figure 2.10).

Table 2.3. Crystallographic data and structural refinement for $[Fe(bpp)_2](C_6H_8O_4)$ (**1**).

	1 at 298 K	**1** at 120 K
Empirical formula	$C_{28}H_{26}FeN_{10}O_4$	$C_{28}H_{26}FeN_{10}O_4$
Formula weight	622.44	622.44
Crystallographic system	Monoclinic	Monoclinic
Space group	$C2/c$ (No. 15)	$C2/c$ (No. 15)
a/ Å	18.4520(2)	18.3091(5)
b/ Å	20.1395(3)	20.1160(4)
c/ Å	15.0697(2)	14.9144(3)
α/ °	90	90
β/ °	94.2540(10)	93.730(2)
γ/ °	90	90
V/ Å^3	5584.68(13)	5481.4(2)
Z	8	8
R(int)	0. 0449	0. 0739
ρ_{calc}/ g·cm^{-3}	1.481	1.508
μ/ mm^{-1}	0.595	0.606
Crystal dimensions/ mm	0.406x0.178x0.073	0.194x0.065x0.059
T/ K	298.00(10)	119.9(2)
λ/ Å	0. 71073	0. 71073
2θ range/ °	4.87< 2θ <59.98	6.024 < 2θ <59.58
Index ranges for h, k , l	-25/25, -28/28, -20/21	-25/25, -26/27, -20/20
Completeness to θ = 28.50°(%)	99.8	99.5
Refinement method	Full-matrix least-squares on F^2	Full-matrix least-squares on F^2
Collected reflections	68072	65272
Unique reflections	7758	7476
Data/Restraints/Parameters	7758/174/ 498	7476/294/ 498
Goodness-of-fit on F^2	1.039	1.116
R1, wR2 [I > 2sigma(l)][a]	0.0393/ 0.0888	0.0541/ 0.1014
R1, wR2 (all data)[a]	0.0650/ 0.1029	0.0747/ 0.1093
$\Delta\rho_{max}$ and $\Delta\rho_{min}$ (e·Å^{-3})	0.276/ – 0.345	0.501/ – 0.579

[a] $R1 = \Sigma(||F_o| - |F_c||)/\Sigma|F_o|$; $wR2 = \{\Sigma[w(F_o^2 - F_c^2)^2]/\Sigma[w(F_o^2)^2]\}^{1/2}$

Just as observed in **1**·4H_2O, both iron centres are coordinated by two bpp ligands in meridional positions with distorted octahedral geometries (the dihedral angle between the planes that contain each bpp ligand are 92.34° and 92.10° for Fe1 and Fe2 centres, respectively).

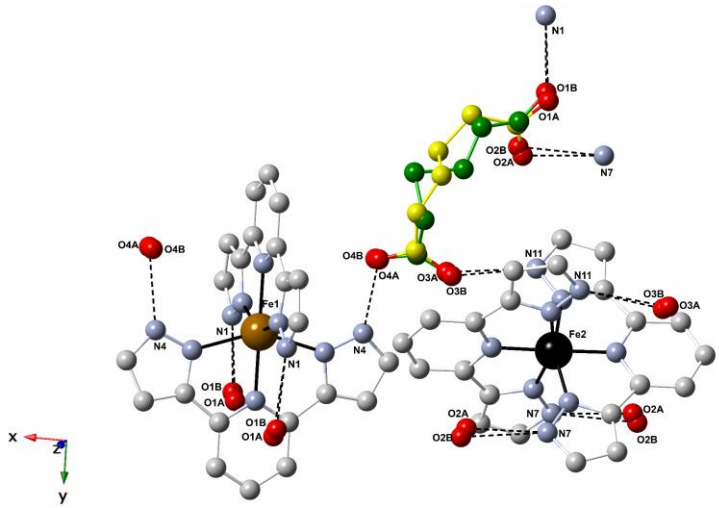

Figure 2.9. View of the crystal structure of **1** at 298 K showing the two inequivalent $[Fe(bpp)_2]^{2+}$ cations and the disordered adipate anion. Yellow and green colours illustrate adipates A and B, respectively. Dashed lines refer to hydrogen bonds.

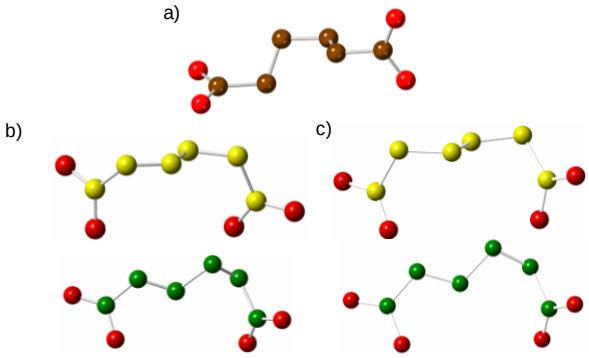

Figure 2.10. View of the adipate dianions found in the crystal structures of a) **1**·$4H_2O$, b) **1** at 298 K and c) **1** at 120 K. Yellow and green colours illustrate adipates A and B in the anhydrous phases, respectively.

Fe1 presents Fe1–N bond distances characteristic of a high-spin state, within the 2.11-2.19 Å range (Table 2.4), whereas the Fe2 site exhibits Fe2–N bond lengths typical of a low-spin configuration (between 1.91 and 1.97 Å). Accordingly, the Fe2 centre displays a more regular octahedral environment than the Fe1 site, as evidenced by the value of the distortion parameter Σ. For the Fe2 centre, the Σ parameter has a value of 90.49° which is very similar to that calculated for **1**·$4H_2O$ (89.99°). Instead, this parameter for the Fe1 site has a considerably

higher value of 141.29°. In both cases the calculated values compare well with those reported for LS and HS systems, respectively.[12] On the other hand, the φ parameter (the *trans* N(py)–Fe–N(py) angle) has a value of 180° and 178.77° for Fe1 and Fe2 sites, respectively. However, in this case its use as an indicator of the degree of distortion is not appropriate because Fe1 is located on a special position that implies a strict N(py)–Fe–N(py) linearity (the C_2 axis contains the Fe–N(py) bond).

Table 2.4. Fe–N bond distances of Fe1 and Fe2 centres of **1** at 298 K and 120 K.

	1 (298 K)	**1** (120 K)
Fe1–N2	2.1772(15)	2.058(2)
Fe1–N3	2.111(2)	2.002(3)
Fe1–N5	2.1849(15)	2.069(2)
Fe1–N6	2.117(2)	2.006(3)
Fe2–N8	1.9638(14)	1.9663(18)
Fe2–N9	1.9154(13)	1.9161(19)
Fe2–N10	1.9671(14)	1.9613(18)

Regarding the second iron coordination sphere, both $[Fe(bpp)_2]^{2+}$ complexes are hydrogen-bonded through their NH fragments to four adipate anions in a pseudotetrahedral arrangement. Likewise, each adipate dianion is acting as a hydrogen bond acceptor towards four cationic entities, two iron Fe1 centres and two Fe2 sites *via syn*, *anti* carboxylate moieties. The connectivity involving HS Fe1 centres gives rise to the formation of a two-dimensional (4,4) hydrogen-bonded rhombic layer in the *xy* plane, with Fe1 complexes located in the corners and adipate anions sitting on the sides of the rhombuses (Figure 2.11). The Fe1–Fe1 distance along the rhombic lattice is 13.6572(5) Å.

Consecutive layers are disposed in an alternative way along the *z* direction, resulting in an ABAB layer stacking pattern (Figure 2.12). In this arrangement, adjacent $[Fe1(bpp)_2]^{2+}$ complexes are defining zigzag chains by π-π interactions along the *c* axis with a distance between the centroids defined by adjacent pyrazolyl rings of 3.55(9) Å and a Fe1–Fe1 distance of 8.3633(3) Å (Figure 2.13.a). The voids present within the Fe1 lattice are occupied by low-spin Fe2 complexes (Figure 2.14) that are doubly H-bonded to adipate dianions defining zigzag chains (Figure 2.15). Simultaneously, π-π stacking interactions are connecting the Fe2 centres along the *c* axis (distance between centroids: 3.40(7) Å) with a shorter Fe2–Fe2 distance of 8.1502(2) Å (Figure 2.13.b).

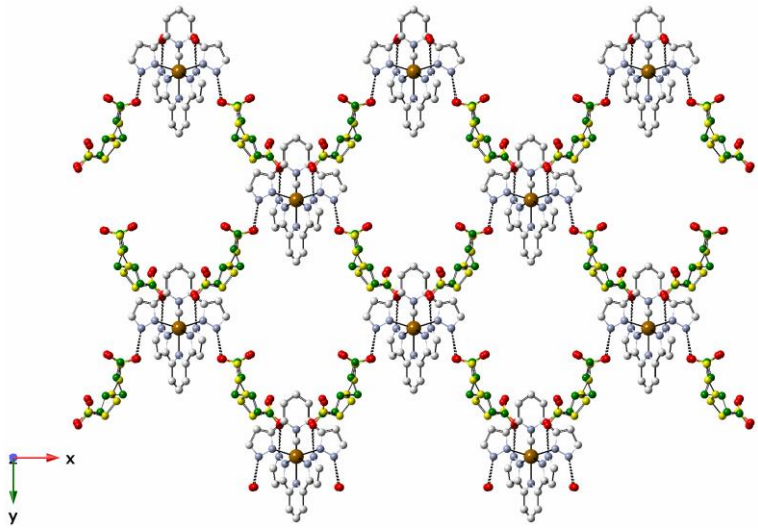

Figure 2.11. Crystal structure of **1** at 298 K showing a rhombic 2D lattice of high-spin Fe1 centres linked by disordered adipate anions. Yellow and green colours illustrate adipates A and B, respectively. Dashed lines refer to hydrogen bonds.

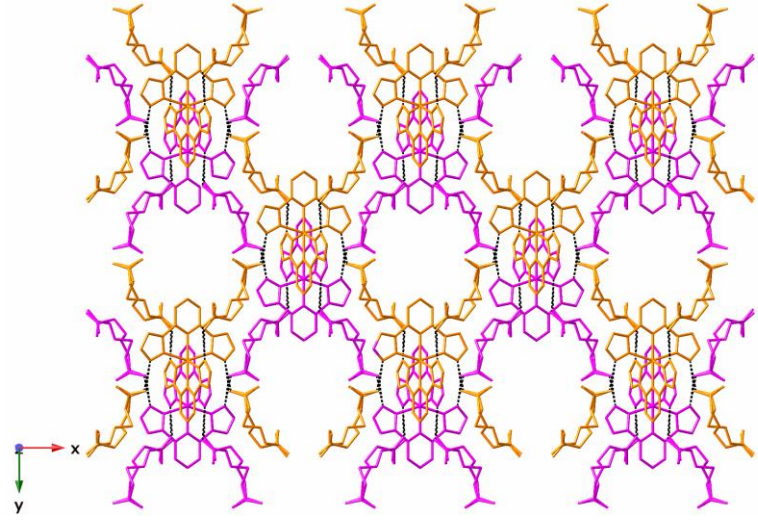

Figure 2.12. Stick view of the crystal structure of **1** at 298 K showing the packing of the rhombic 2D layers of high-spin Fe1 centres connected by disordered adipate anions in an ABAB fashion. Each H-bonded layer is shown in a different colour. Dashed lines refer to hydrogen bonds.

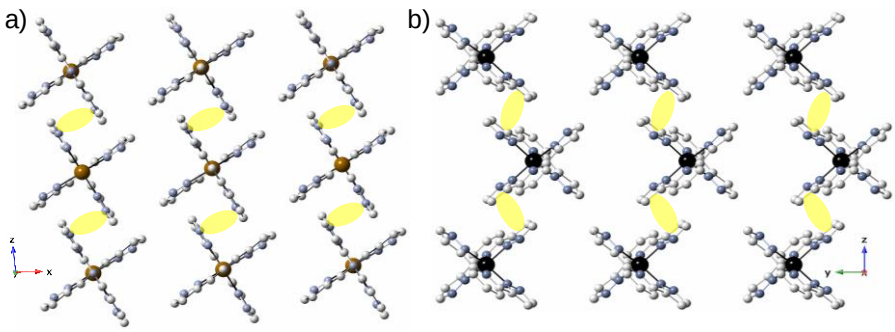

Figure 2.13. View of the π-π stacked zigzag chains running along the *c* axis of **1** at 298 K for a) $[Fe1(bpp)_2]^{2+}$ and b) $[Fe2(bpp)_2]^{2+}$. In yellow are represented π-π stacking interactions.

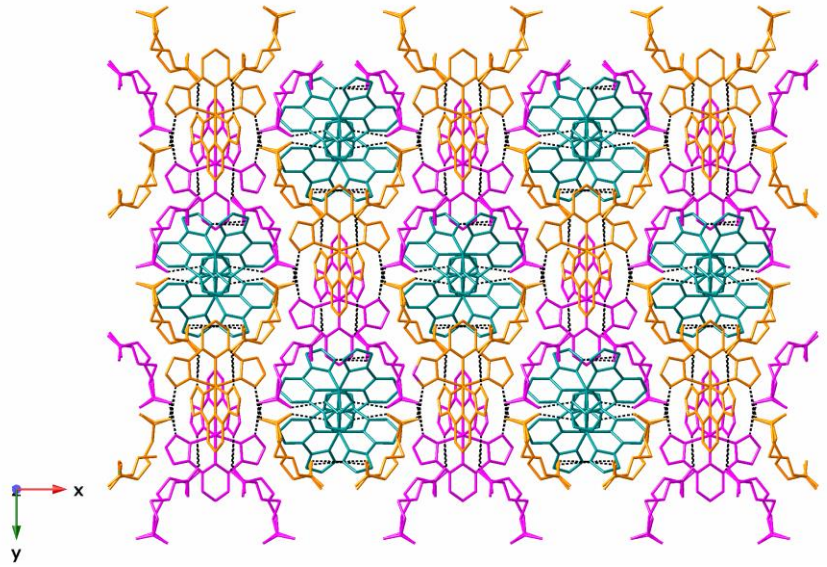

Figure 2.14. Stick view of the crystal structure of **1** at 298 K showing two consecutive HS Fe1 hydrogen-bonded layers linked by adipate dianions (depicted in orange and magenta). The free space within these layers is filled by LS Fe2 networks (light blue coloured). Dashed lines refer to hydrogen bonds.

As mentioned above, Fe1 layers and Fe2 chains are connected to each other by bidentate carboxylate fragments of the adipate dianions in a *syn*, *anti* bridging mode, giving rise to the formation of a 3D hydrogen-bonded structure. The well-known *terpyridine embrace* motif commonly found in $[Fe(bpp)_2]^{2+}$ complexes[13] is not observed for **1** due to the fact that adipate dianions occupy the space between the stacks (Figure 2.16). In **1**·$4H_2O$, the establishment of this motif is

also prevented, as a consequence of the presence of water molecules and anions that lead to mutual displacement of the cations. In this case, some hydrogen bond distances are unrealistically short for O···N distances (< 2.5 Å, Table 2.5), as a consequence of static disorder in the positions of the adipate anions. Therefore, any exhaustive analysis of the H-bond interactions is precluded.

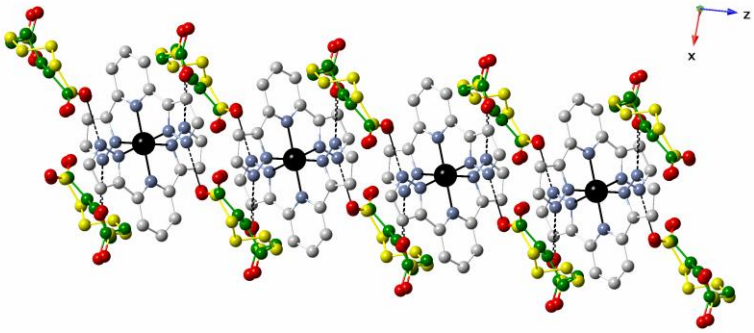

Figure 2.15. Crystal structure of **1** at 298 K showing the stacks of low-spin Fe2 centres linked by double adipate bridges and π- π interactions. Yellow and green colours depict adipates A and B, respectively. Dashed lines refer to hydrogen bonds.

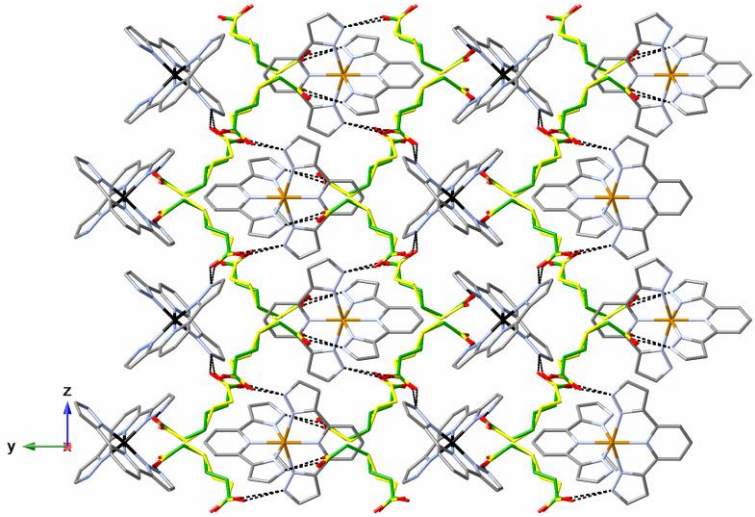

Figure 2.16. Stick view of a fragment of the crystal structure of **1** at 298 K showing the two inequivalent iron centres forming independent stacks along the *c* axis (Fe1 and Fe2 are shown in orange and black, respectively). Adipate anions (depicted in yellow and green) are occupying the space between the stacks. Dashed lines refer to hydrogen bonds.

Table 2.5. Intermolecular hydrogen bonds present in **1** at 298 and 120 K (D-H···A).

D···A	$d(298\ K)_{D\cdots A}$ / Å	$d(120\ K)_{D\cdots A}$ / Å
N1···O1A#1	2.723(16)	2.750(7)
N1···O1B#1	2.529(18)	2.440(8)
N4···O4A	2.603(19)	2.656(10)
N4···O4B	2.49(3)	2.343(14)
N7···O2A#2	2.537(17)	2.724(16)
N7···O2B#2	2.70(2)	2.54(2)
N11···O3A#3	2.760(16)	2.749(15)
N11···O3B#3	2.60(2)	2.62(2)

Symmetry transformations used to generate equivalent atoms: #1 – x + 1/2, y + 1/2, – z + 3/2; #2 – x + 1, – y, – z + 2; #3 – x + 1, y, – z + 3/2

At 120 K, the compound is isostructural with the high-temperature phase described at 298 K (Table 2.3), with slightly lower values of unit cell parameters. In particular, the cell volume has decreased by 1.8% in comparison with the value obtained at room temperature. Concerning the iron centres, the coordination geometry of Fe2 sites has experienced an almost insignificant change (Figure 2.17). Fe2–N bond distances (1.92-1.97 Å) and octahedral distortion parameters (Σ = 89.51°; φ = 178.51°) are typical of LS species. Instead, the Fe1 sites present shorter Fe1–N bond lengths (2.00-2.07 Å, Table 2.4) and lower Σ parameter (115.65°) with respect to those found at 298 K (Figure 2.17). These values are intermediate between those characteristic for LS and HS centres, pointing towards an incomplete spin crossover.

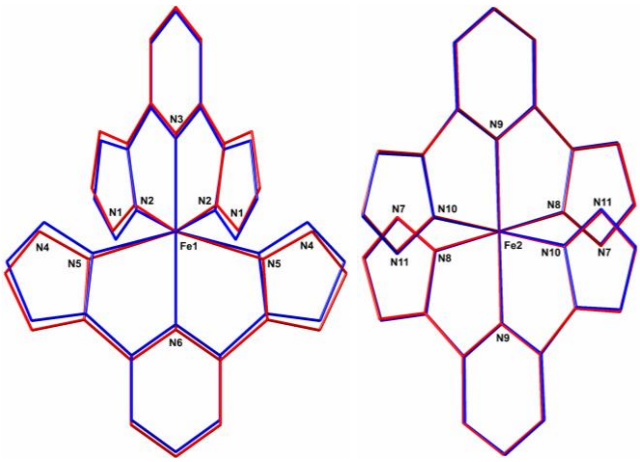

Figure 2.17. Superposition of the stick view of **1** at 298 K (red) and 120 K (blue), showing the coordination environment of Fe1 (left) and Fe2 (right) centres.

As expected, the Fe1–Fe1 distance between corners of the rhombuses (defined in the *ab* plane) decreases upon cooling (13.6003(6) Å, Δd = 0.0569 Å), due to

both thermal contraction and spin crossover of some Fe1 sites. However, the intermetallic distance Fe2–Fe2 inside the chains of LS complexes running along the *c* axis decreases approximately the double (8.0483(3) Å, Δd = 0.1019 Å), in spite of not exhibiting SCO. In addition, the Fe1–Fe1 distance along the parallel Fe1 stacks is also considerably decreased (8.2513(3) Å, Δd = 0.112 Å). This suggests that the contraction of the structure is stronger outside the *ab* plane, as a result of the constraints generated by hydrogen bonding.

On the other hand, the adipate anions still present disorder; in fact, the two conformations A and B are identical to those observed at 298 K (*gauche*, *anti*, *gauche* and *gauche*, *anti*, *anti* for adipates A and B, respectively, Figure 2.10), with very similar occupancy factors (0.56 and 0.44 respectively for A and B). This indicates that the disorder is not related to thermal vibration, which verifies its static nature. Nevertheless, there are significant variations regarding torsion angles (more than 20° in some cases), suggesting that the adipate anions are capable of accommodating a great deal of the internal pressure coming from SCO. In particular, the fraction of volume occupied by the adipate anions is 29.6% in the HS phase (1651.8 $Å^3$) and 31.7% (1740.1 $Å^3$) in the LS phase, calculated by the SQUEEZE option of PLATON.[16] At 298 K, some Fe1 sites undergo SCO to the HS state with the subsequent increase in Fe1–N bond distances that leads to higher volume occupied by the Fe1 centres. Thanks to the flexibility of the adipate anions, they are able to accommodate this variation by contracting their structure, as observed from the SQUEEZE calculation results.

B. Powder X-ray diffraction

The simulated diffractogram of **1** from single crystal X-ray data at 298 K is compared with the polycrystalline sample obtained by dehydration of the original tetrahydrate at 400 K under vacuum. There is a perfect match between both patterns, discarding the presence of impurities and verifying that the transformation affects the whole bulk material. Moreover, this anhydrous phase is stable in ambient conditions, as evidenced by powder X-ray diffraction measurements after 6 h of exposure to ambient moisture (Figure 2.18). This contrasts with the amorphous HS sample obtained by dehydration at 453 K, which rehydrates almost immediately upon exposure to ambient humidity.

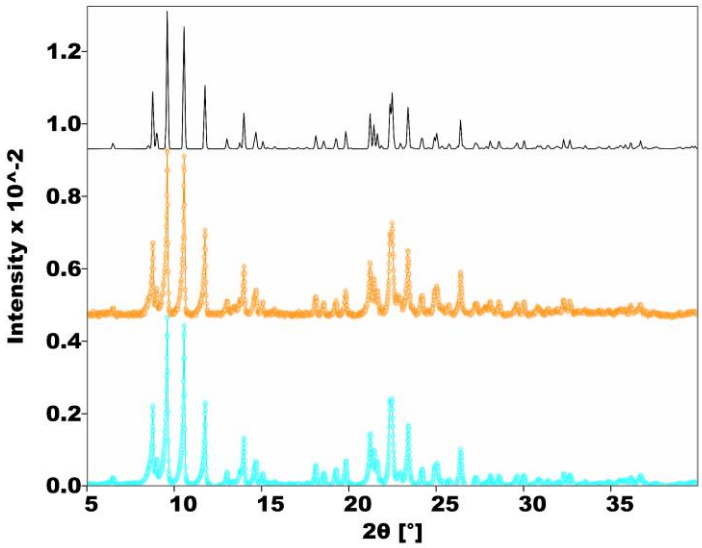

Figure 2.18. Comparison of room temperature powder X-ray patterns of **1** just after dehydration (orange) and after exposure to the open air during 6 h (blue). The simulated diffractogram from single crystal X-ray data at 298 K is shown in black.

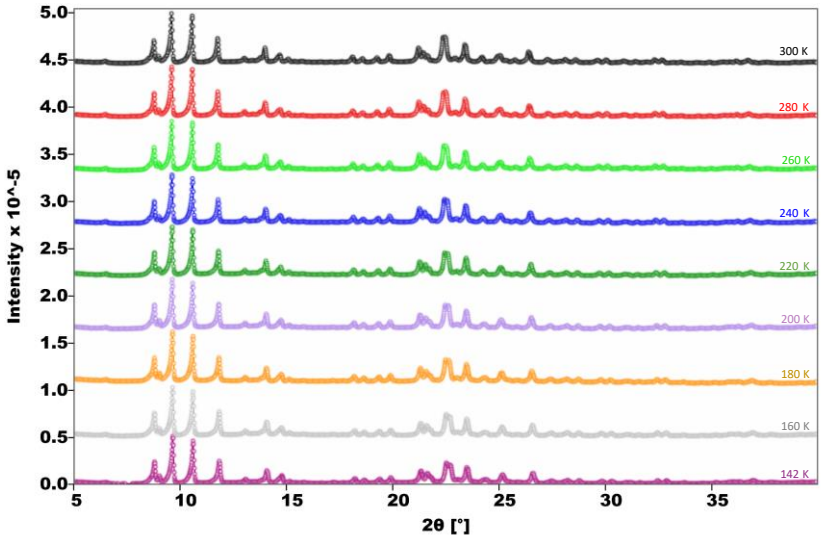

Figure 2.19. Powder X-ray patterns of **1** at different temperatures between 300 K and 142 K.

Temperature dependent PXRD measurements were carried out between 300 K and 142 K (Figure 2.19). It can be seen that the same pattern is obtained in all cases, being the only difference that some peaks shift gradually to higher 2θ values upon cooling as a consequence of thermal contraction. This indicates a lack of a phase transition in the temperature range of study.

C. Temperature dependence of the lattice cell parameters

Unit cell parameters of **1** were measured on the same single crystal between 298 K and 120 K. On cooling, the thermal variation of the unit cell volume follows a linear decrease (Figure 2.20) that has been fitted to the expression $V(\text{Å}^3) = 5401.5 + 0.66T(K)$. The calculated volumetric thermal expansion coefficient is α = 118·10^{-6} K^{-1}, which is a small value consistent with the fact that thermal contraction is the major contribution to the volume change.[17]

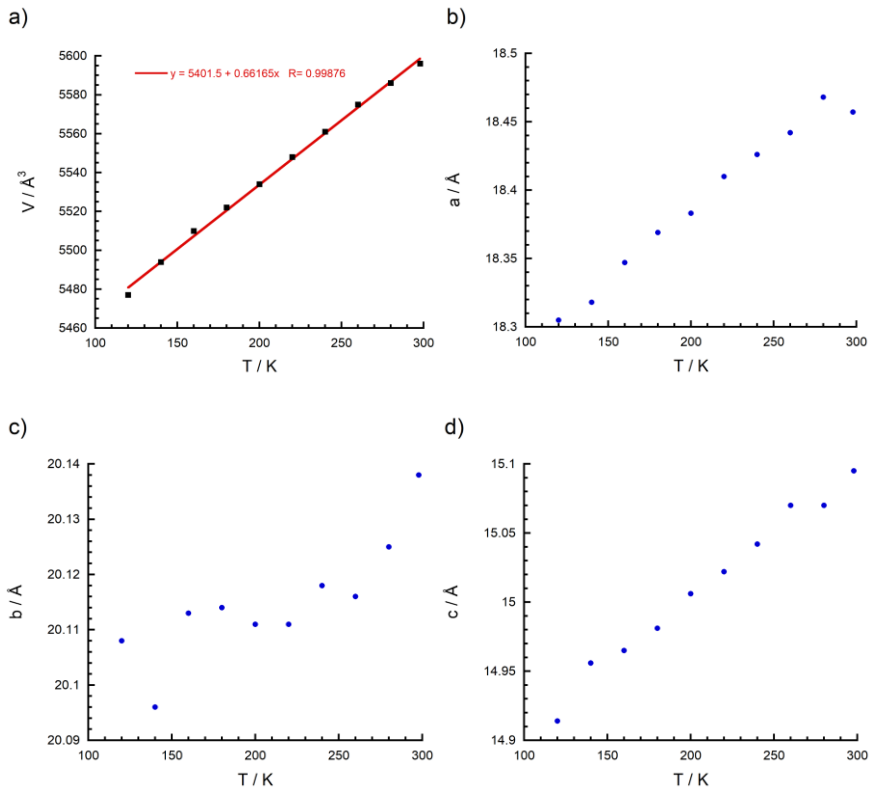

Figure 2.20. Thermal dependence of unit cell parameters of **1** between 298 K and 120 K.

The thermal variation of the unit cell parameters *a* and *c* also reveals a linear decrease upon cooling, whereas the *b* parameter is essentially constant during the thermal treatment. The absence of critical points suggests the lack of a crystallographic phase transition in the 298-120 K temperature range, which is in agreement with the temperature dependent PXRD measurements.

2.4.4. Magnetic characterisation of 1

A. Magnetic properties

Figure 2.8 showed the thermal variation of the χT product of **1**. Upon heating at 400 K, the value of χT at saturation of 1.51 emu·K·mol^{-1} is in accordance with the structural data described for the anhydrous material at 298 K, showing one iron centre in the LS state (Fe2) and one Fe site in the HS state (Fe1). The plateau reached on cooling, where χT = 0.60 emu·K·mol^{-1}, corresponds to a fraction of HS centres γ_{HS} = 0.2. This indicates that 60% of Fe1 centres undergo SCO on cooling down with a residual fraction of HS Fe1 sites of 40% still present at low temperatures. The fraction of HS Fe1 centres that undergo SCO to the LS state follows a Boltzmann distribution (Figure 2.21), which indicates that the transition is gradual and that cooperative interactions are relatively weak.

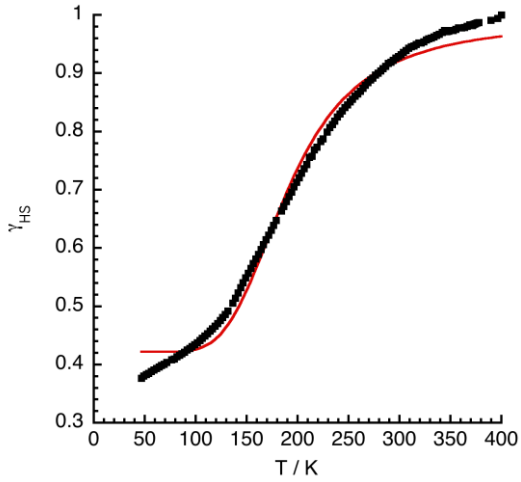

Figure 2.21. Thermal dependence of the fraction of high-spin centres corresponding to the Fe1 site of compound **1.** The line represents the best fit to a Boltzmann distribution. The residual fraction of Fe1 HS centres at low temperatures is γ_{res} = 0.42.

Associated thermodynamic parameters are ΔH = 8.4 ± 0.2 kJ·mol^{-1} and ΔS = 30 ± 1 J·mol^{-1}·K^{-1}. Typical values associated with the LS → HS conversion are 50-80 J·mol^{-1}·K^{-1} and 10-20 kJ·mol^{-1} for entropy and enthalpy changes, respectively.[18] Thus, the values calculated for **1** are small with respect to other $[Fe(bpp)_2]^{2+}$ complexes, mainly ascribed to the partial character of the crossover and the slight structural distortions encompassing SCO in this system.

B. Mössbauer spectroscopy

In order to verify the observations extracted from magnetic susceptibility analyses and obtain additional information about the spin state of Fe(II), Mössbauer spectroscopy measurements were conducted. This technique provides two well resolved quadrupole doublets, as long as the spin isomers have lifetimes larger than 10^{-7} s. One of these doublets is associated with low-spin centres and the other one with high-spin molecules. HS iron(II) shows relatively high quadrupole splitting (QS ≈ 2-3 mm·s^{-1}) and isomer shift (IS ≈ 1 mm·s^{-1}). Instead, these parameters for LS iron(II) are smaller (QS ≤ 1 mm·s^{-1} and IS ≤ 0.5 mm·s^{-1}).[19] The Mössbauer spectrum of **1**·4H_2O recorded at 295 K (Figure 2.22) shows a single quadrupole doublet with estimated IS and QS of 0.29 mm·s^{-1} and 0.67 mm·s^{-1}, respectively (Table 2.6). These values are similar to those reported for low-spin $[Fe(bpp)_2]^{2+}$ complexes.[20]

Table 2.6. Estimated parameters from the Mössbauer spectra of **1**·4H_2O and **1** recorded at different temperatures.

Compound	T / K	IS / mm·s^{-1}	QS / mm·s^{-1}	Γ / mm·s^{-1}	I / %	Spin state
1·4H_2O	295	0.29	0.67	0.27	100	LS
1	295	0.30	0.67	0.29	61	LS
		1.01	2.43	0.73	39	HS
1	220	0.34	0.67	0.30	64	LS
		1.02	2.63	0.72	32	HS
1	55	0.39	0.67	0.34	75	LS
		1.09	2.96	0.51	25	HS
1	4	0.39	0.66	0.33	75	LS
		1.11	2.96	0.50	25	HS

IS: Isomer shift relative to metallic α-Fe at 295 K; *QS*: Quadrupole splitting, Γ: Full width at half height; *I*: Relative areas. Estimated errors are ≤ 0.02 mm·s^{-1} for *IS*, *QS* and Γ, and ≤ 2% for *I*.

Anhydrous compound **1** was obtained by heating the tetrahydrate at 400 K under vacuum for 2 h and its spectrum reveals the appearance of an additional doublet with *IS* and *QS* values indicative of HS Fe^{II} species.[20a]

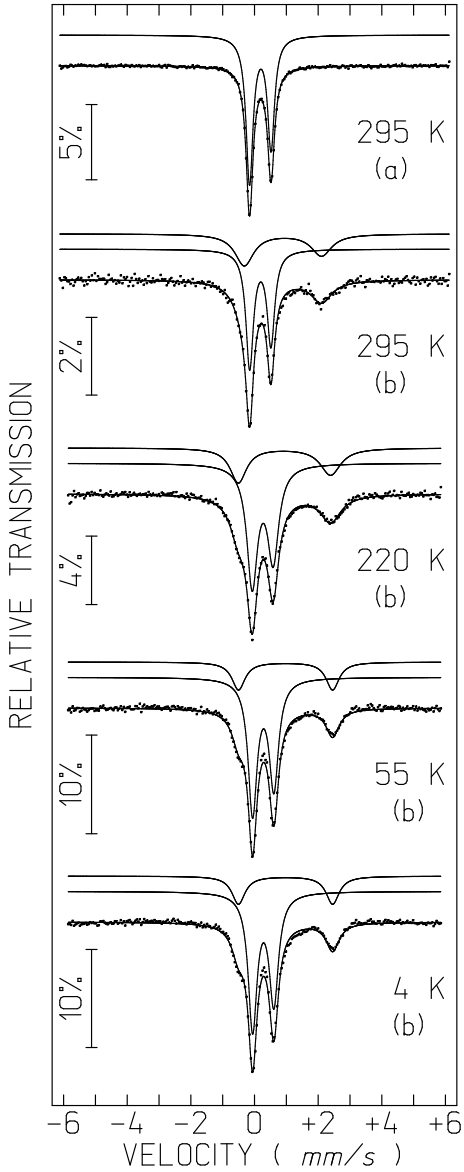

Figure 2.22. Mössbauer spectra of a) **1**·4H_2O and b) **1** at different temperatures. The curves over the experimental points correspond to a) a single quadrupole doublet (LS Fe^{II}) or b) the sum of two quadrupole doublets (HS and LS Fe^{II}). Corresponding parameters are gathered in Table 2.6.

The estimated relative area of the HS signal (I_{HS}) is 39% at 295 K and decreases on lowering the temperature until reaching a value of 25% at 55 K and at 4 K. At 4 K, the recoil-free fractions of HS and LS Fe^{II} atoms are similar, therefore, the

corresponding relative areas (I) may be used as a good approximation of the fraction of iron centres that are in each spin state. Magnetic susceptibility data (Figure 2.8) suggests the coexistence of 80% LS Fe^{II} and 20% HS Fe^{II} centres at 70 K, which is approximately equal to the results obtained from Mössbauer spectroscopy at 55 K and 4 K (75% LS and 25% HS). However, as the temperature increases, the recoil-free fraction of LS Fe^{II} molecules becomes higher than that of HS Fe^{II}. This is a consequence of the shorter Fe–N bond lengths in the LS Fe^{II} state. Thus, the real fraction of HS Fe^{II} molecules at room temperature is expected to be slightly higher than I_{HS}.[21] The increase of I_{HS} while heating is in agreement with the temperature dependence of χT. Indeed, the value of 39% obtained for I_{HS} at 295 K is fully consistent with the fact described above, justifying that it has a lower value than the expected at room temperature from the magnetic susceptibility data (50%). Moreover, the existence of an intermediate spin state or the presence of Fe^{3+} impurities can be excluded.

C. Photomagnetic properties

The LS–HS photoconversion of **1** was investigated in bulk conditions. First, **1**·4H_2O was dehydrated *in situ* as described above. Then, the compound was cooled down to 10 K (Figure 2.23). The gradual spin crossover involving Fe1 centres was reproduced, obtaining $\chi T \approx 0.5$ emu·K·mol^{-1} at 10 K ($\gamma_{HS} = 0.16$, residual fraction of HS Fe1 sites of 33%). The material was irradiated at this temperature with a green laser ($\lambda = 532$ nm), observing an abrupt increase of the magnetic signal. After 280 min of irradiation, saturation of the signal was reached. The laser was switched off and the magnetic signal recorded while heating at 0.3 K·min^{-1} (standard conditions for a T(LIESST) experiment). After a small increase of the χT product due to a zero-field splitting of the $S = 2$ ground state, the χT product is 1.55 emu·K·mol^{-1}. This value indicates that only Fe1 sites are photoinduced to the HS state, remaining the Fe2 centres in the LS state even under light irradiation. While heating, the magnetic signal decreases smoothly and reaches a minimum value of 0.5 emu·K·mol^{-1} at 76 K, indicative of the HS Fe1 residual fraction of 33% registered before irradiation. The inset of Figure 2.23 shows the first derivative of the χT product versus temperature, which presents a minimum value at 61 K. This gives the T(LIESST) value, which is in agreement with that reported for similar$[Fe(bpp)_2]^{2+}$ compounds.[22]

As described in the introduction, there is a linear correlation between the thermal spin crossover temperature ($T_{1/2}$) and T(LIESST).[23] In particular, the following expression has been found to be suitable for $[Fe(bpp)_2]^{2+}$ compounds: $T(\text{LIESST}) = T_0 - 0.3 \cdot T_{1/2}$, being $T_0 = 150$ K. Considering $T_{1/2} = 184$ K, the equation

yields a calculated *T*(LIESST) value of 94.8 K. This value differs significantly from the experimental one (61 K) and this can be due to the partial and gradual character of the transition.

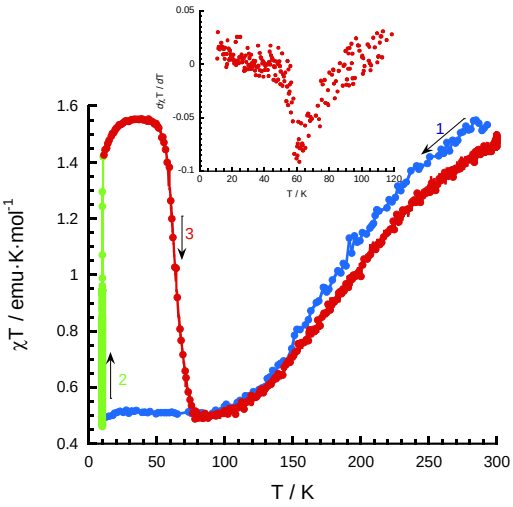

Figure 2.23. Photomagnetic properties of **1**. Blue circles: cooling mode without irradiation; green circles: data recorded while irradiation at 10 K; red circles: heating mode without irradiation at a rate of 0.3 K·min^{-1} (*T*(LIESST) measurement). The inset shows the first derivative of the *T*(LIESST) plot.

2.4.5. Conclusions and perspectives

Hydrogen-bonded assemblies of $[Fe(bpp)_2]^{2+}$ cations and adipate anions in both hydrated (**1**·4H_2O) and anhydrous (**1**) forms have been obtained and fully characterised. After desolvation, the crystal structure of **1**·4H_2O suffers a complete reorganisation that precludes any comparative analysis between both crystal networks. The tetrahydrate is low-spin at room temperature, being necessary its dehydration in order to observe spin crossover. This is the general situation found for $[Fe(bpp)_2]^{2+}$ hydrated salts, in which the conversion to the high-spin state is induced by heating the system to drive off the lattice water molecules.[13] Within this context, the thermal treatment used in the desolvation process is extremely relevant. The present work provides a fascinating example in which by modifying the temperature of the dehydration process completely different behaviours are observed: an amorphous HS material lacking of SCO properties (453 K, under vacuum) and a crystalline mixed phase showing a gradual SCO phenomenon (400 K, under vacuum).

Usually, $[Fe(bpp)_2]X_2$ systems show very abrupt transitions upon solvent removal. In the current case, the lack of a phase transition, together with the small value of the thermal expansion coefficient and a featureless DSC plot, are in agreement with the rather smooth SCO registered for the anhydrous phase **1**. The continuous character of the SCO is a consequence of the low cooperativity of the system, which has been already stated for similar compounds and demonstrated by the lack of the *terpyridine embrace* motif.[24-25] Thus, the less efficient packing observed in **1** limits the direct contact between the cations through $\pi\cdots\pi$ interactions, resulting in a low level of connectivity (weak cooperativity) between the spin-active building blocks of the network. This is presumably attributed to the presence of the flexible adipate anions, which are able to adjust their conformation in order to accommodate the structural arrangements accompanying SCO. This anion exhibits different conformations in the hydrated and in the anhydrous phases due to the energetically easy rotation of central carbon chains. Up to ten different adipate conformations have been found previously[26] and the *gauche*, *anti*, *gauche* conformation seems to be the lowest energy conformation and the most widely observed.[27] At least six low-energy conformers are predicted to have relative energies differing by less than 10 kJ/mol,[28] thus, it is not surprising to find disorder involving adipate dianions.[29] Therefore, the crucial issue of cooperativity would be related to the rigidity of the building blocks. For verifying this hypothesis unambiguously, a comparison of this salt with another $[Fe(bpp)_2]^{2+}$ complex bearing a rigid dianion should be carried out. In this regard, the rigid terephthalate dianion was selected as a good candidate because it presents double connectivity, charge -2 and is symmetrical, in analogy to the adipate dianion. This is the aim of the following section.

2.5. $[Fe(bpp)_2]L$ (L = $C_6H_8O_4^{2-}$ for **1**·4H_2O, L = $C_6H_4O_4^{2-}$ for **2**·5H_2O and **2**·2MeOH·H_2O)

2.5.1. Structural characterisation of **2**·5H_2O and **2**·2MeOH·H_2O

A. Single crystal X-ray diffraction

As explained in the synthesis section, the reaction between $[Fe(bpp)_2]^{2+}$ cations and terephthalate dianions yields two different types of crystals, being **2**·5H_2O the major product (Scheme 2.5). Thus, a comparative analysis of both crystal structures will be performed.

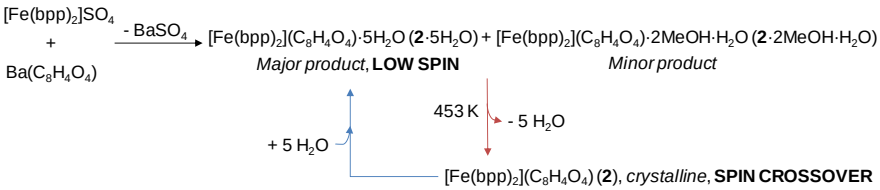

Scheme 2.5. Schematic illustration of the synthesis and spin changes upon reversible dehydration of **2**·5H_2O.

2·2MeOH·H_2O crystallises at 128 K in the triclinic space group *P*–1 (Table 2.7) and its crystal structure comprises isolated $[Fe(bpp)_2]^{2+}$ complexes, terephthalate dianions and solvent molecules (water and methanol). The asymmetric unit contains two inequivalent iron sites, Fe1 and Fe2, with Fe–N bond distances ranging from 1.909(4)-1.985(5) Å, indicating a low-spin state in both cases. Again, the two bpp ligands occupy meridional positions of a distorted octahedron (dihedral angle between planes that contain each bpp ligand of 88.86° and 88.88° for Fe1 and Fe2, respectively). The distortion parameter Σ and the *trans* N(py)–Fe–N(py) angle (φ) have the following values for Fe1 and Fe2 centres, respectively: Σ = 97.09° and 93.86°; φ = 175.09° and 177.55°. Both parameters show slightly higher deviations from the ideal octahedral geometry than those observed for the low-spin iron centres found in the hydrated and anhydrous phases of the adipate salts. Nevertheless are still indicative of a low-spin state.[12] In this structure, the two iron centres exhibit differences in the composition of the second iron coordination sphere. Fe1 is hydrogen-bonded to four terephthalate dianions (N1···O3: 2.649(6) Å, N5···O4: 2.641(6) Å, N6···O6: 2.679(7) Å, N10···O8: 2.592(6) Å), whereas Fe2 is only interacting with two

terephthalate dianions (N11···O1: 2.591(6) Å, N15···O2: 2.704(7) Å), being the remaining hydrogen bonds satisfied with one methanol (N16···O3S: 2.638(6) Å) and one water (N20···O1W: 2.635(6) Å) molecules (Figure 2.24).

Table 2.7. Crystallographic data and structural refinement for **2**·2MeOH·H_2O and **2**·5H_2O

	2·2MeOH·H_2O	**2**·5H_2O
Empirical formula	$C_{32}H_{32}FeN_{10}O_7$	$C_{30}H_{32}FeN_{10}O_9$
Formula weight	724.53	732.51
Crystallographic system	Triclinic	Triclinic
Space group	*P*–1 (No. 2)	*P*–1 (No. 2)
a/ Å	8.0628(4)	8.1799(4)
b/ Å	16.4572(7)	8.0776(4)
c/ Å	24.6825(11)	25.9260(12)
α/ °	98.352(4)	90.532(4)
β/ °	90.601(4)	93.150(4)
γ/ °	93.125(4)	89.370(4)
V/ Å^3	3235.0(2)	1710.28(14)
Z	4	2
R(int)	0. 0938	0.0866
ρ_{calc}/ g·cm^{-3}	1.488	1.422
μ/ mm^{-1}	0. 532	0.508
Crystal dimensions/ mm	0.2004x0. 0706x0. 0501	0. 1197x0. 0807x0. 0256
T/ K	128(10)	120(10)
λ/ Å	0. 71073	0. 71073
2θ range/ °	5.02< 2θ <57.34	6.68 < 2θ <60.02
Index ranges for h, k , l	-10/10, -21/22, -32/32	-11/11, -11/11, -36/35
Refinement method	Full-matrix least-squares on F^2	Full-matrix least-squares on F^2
Collected reflections	29084	22391
Unique reflections	14486	8562
Data/Restraints/Parameters	14486/20/ 953	8562/161/ 533
Goodness-of-fit on F^2	1.013	1.086
R1, wR2 [I > 2sigma(l)][a]	0.0789/ 0.1143	0.1275/ 0.3066
R1, wR2 (all data)[a]	0.1801/ 0.1528	0.1966/ 0.3580
$\Delta\rho_{max}$ and $\Delta\rho_{min}$ (e·Å^{-3})	0.75/ – 0.71	2.08/ – 0.72

[a] $R1 = \Sigma(||F_o| - |F_c||)/\Sigma|F_o|$; $wR2 = \{\Sigma[w(F_o^2 - F_c^2)^2]/\Sigma[w(F_o^2)^2]\}^{1/2}$

In this case, each cationic entity interacts with four neighbouring iron complexes via π-π stacking interactions, giving rise to the formation of the pseudotetragonal *terpyridine embrace* motif (Figure 2.25). Along the *a* axis, independent Fe1 and Fe2 sites form stacks individually with distances between adjacent pyrazolyl mean planes equal to 3.24(16) Å (for the Fe1 stacks) and 3.12(11) Å (for the Fe2 stacks). Along the *b* axis, an alternation of both types of stacks is observed, establishing between them weaker π-π contacts with interplane distances of 3.36(6) Å and 3.25(4) Å. In this way, a 2D packing is formed, in which the pseudobinary axes of the Fe2 centres are almost collinear with the *c* axis, whereas those associated with the Fe1 centres are slightly tilted. The packing of

adjacent layers shows that they are shifted with respect to each other along the *y* direction, leading to an AA'AA' arrangement type.

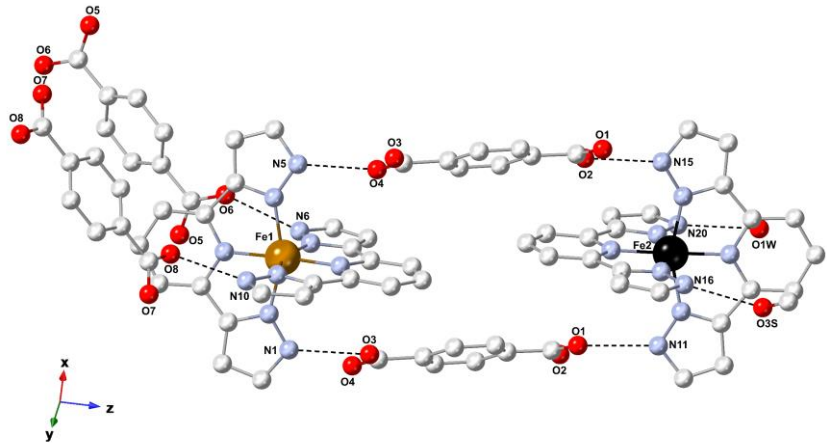

Figure 2.24. View of the crystal structure of **2**·2MeOH·H_2O showing the two independent $[Fe(bpp)_2]^{2+}$ cations, the three inequivalent terephthalate dianions and the two solvent molecules present in the second iron coordination sphere of the Fe2 site. Dashed lines indicate H bonds.

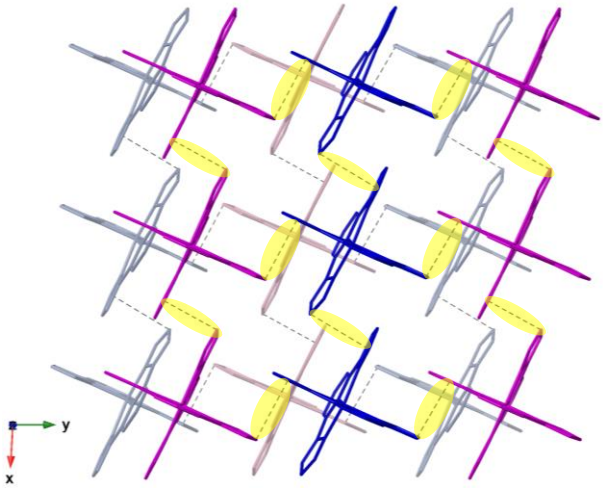

Figure 2.25. Stick view of the crystal structure of **2**·2MeOH·H_2O in the *xy* plane showing two consecutive $[Fe(bpp)_2]^{2+}$ cationic layers (terephthalate anions and solvent molecules are omitted). The independent Fe1 and Fe2 centres are shown, respectively, in blue and magenta colour. Dashed lines represent π-π interactions. In yellow are highlighted π-π interactions involving the first cationic layer.

The crystal packing is, thus, composed of layers of $[Fe(bpp)_2]^{2+}$ cations and terephthalate dianions and solvent molecules are located within the space between the sheets. Cations and anions alternate along the *c* axis, as can be seen in a view parallel to the layers (Figure 2.26). In this perspective, the three crystallographically inequivalent terephthalate dianions present in the structure can be distinguished. The first anion (shown in orange in Figure 2.26) is hydrogen-bonded to four $[Fe(bpp)_2]^{2+}$ cations, acting as a pillar between two consecutive iron layers. In particular, one carboxylate fragment (O1O2) bridges two consecutive Fe2 centres of the same stack (shown in magenta in Figure 2.25), whereas the second carboxylate moiety (O3O4) connects adjacent Fe1 sites within the stack that is just above in an upper iron layer. Both carboxylate anions exhibit a *syn*, *syn* bidentate hydrogen-bonding coordination mode with a quite symmetric distribution of the electron density over the $-CO_2$ fragments (C52–O3 = 1.268 Å and C52–O4 = 1.260 Å; C51–O1 = 1.255 Å and C51–O2 = 1.263 Å).

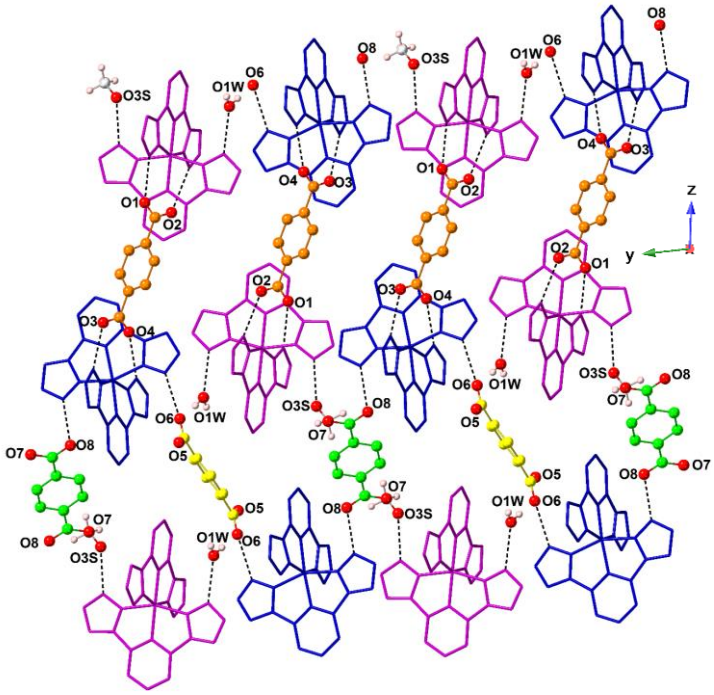

Figure 2.26. View of the crystal structure of **2**·2MeOH·H_2O in the *yz* plane showing the presence of terephthalate dianions at both sides of the two $[Fe(bpp)_2]^{2+}$ cationic layers shown in Figure 2.25 (only solvent molecules present in the second iron coordination sphere are shown. The remaining solvent molecules are located in the voids and are omitted). Non-equivalent anions are illustrated in orange, yellow and green colour. Dashed lines indicate hydrogen bonds.

The other two terephthalate dianions (depicted in green and yellow in Figure 2.26) are located on a centre of symmetry and are disposed in an alternative way across the *y* direction. In addition, only one type of oxygen atom is acting as H-bond acceptor towards Fe1 centres in both anions, resulting in a less symmetric distribution of the electron density over the $-CO_2$ fragments (C56–O5 = 1.271 Å and C56–O6 = 1.252 Å; C60–O7 = 1.259 Å and C60–O8 = 1.245 Å). These anions are bridging stacks (shown in blue in Figure 2.25) of different layers and acting also as pillars of the iron layers, yielding a total structure of the ABA'B' type (A = cationic layer; B = anionic layer). The difference between the connectivity provided by both anions is that one of them (O5O6, illustrated in yellow) links two iron centres along the *y* direction, while the second terephthalate dianion (O7O8, shown in green) connects two iron sites across the *x* and *y* directions. Another common feature is that the second type of oxygen atom in both anions is establishing hydrogen bonds with solvent molecules. As observed in **1**·$4H_2O$, the hydrogen-bonded lattice presents channels along the *a* axis that are filled by methanol and water solvent molecules, which are engaged in several hydrogen bonds. Table 2.8 contains relevant hydrogen-bonding information.

Table 2.8. Intermolecular hydrogen bonds present in **2**·2MeOH·H_2O (D-H···A).

D···A	$d_{D\cdots A}$ / Å
N1···O3#1	2.649(6)
N5···O4#2	2.641(6)
N6···O6	2.679(7)
N10···O8	2.592(6)
N11···O1	2.591(6)
N15···O2#3	2.704(7)
N16···O3S	2.638(6)
N20···O1W#4	2.635(6)
O2···O4S#5	2.731(9)
O3···O1S#1	2.784(8)
O5···O2S#3	2.702(6)
O5···O2W#3	2.811(8)
O6···O1W	2.793(7)
O7···O3S	2.591(7)
O1W···O2W	2.780(8)
O2W···O2S#6	2.806(8)

Symmetry transformations used to generate equivalent atoms: #1 – x, – y + 1, – z + 2; #2 – x + 1, – y + 1, – z + 2; #3 x – 1, y, z; #4 x, y + 1, z; #5 x + 1, y, z; #6 – x + 1, – y, – z + 1

2·$5H_2O$ crystallises in the same triclinic space group (*P*–1) than the previous solvate (Table 2.7). In fact, the unit cell parameters are very similar, with the exception that *b* is approximately halved with respect to that obtained for **2**·2MeOH·H_2O. In this new structure, there is only one crystallographically inequivalent iron centre in the asymmetric unit (Figure 2.27), and the number of formula units per unit cell (*Z* parameter) is decreased from 4 to 2. Considering

the volume per formula unit, it is 5.7% higher in **2**·5H_2O (V = 1710.28 Å^3, Z = 2) with respect to that obtained for the methanol solvate in which four iron complexes were found in the unit cell (V = 3235.0 Å^3, Z = 4). This expansion does not have a great impact on the FeN_6 first coordination sphere, since the Fe–N bond lengths are even shorter for the present solvate (1.914(5)-1.973(7) Å). These values are still in agreement with a low-spin state, which is further verified by the distortion parameters φ and Σ (φ = 178.30° and Σ = 95.16°) that present similar values to those calculated for **2**·2MeOH·H_2O. Therefore, the change in the unit cell parameters might be related to the volume occupied by the solvent molecules. With respect to the terephthalate anions, this crystal structure shows the existence of two independent anions, one of them being disordered.

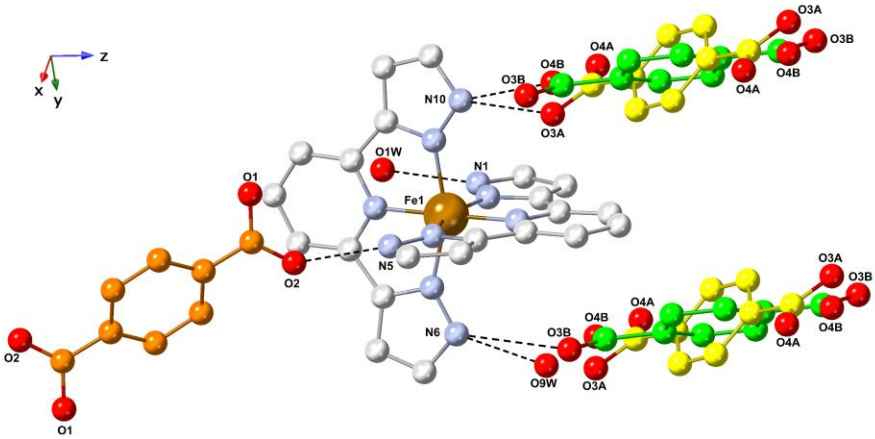

Figure 2.27. Crystal structure of **2**·5H_2O showing the second iron coordination sphere of the only one inequivalent Fe1 site. Each terephthalate anion is shown in a different colour. There are two anions disordered into two positions, A (yellow) and B (green). Dashed lines refer to hydrogen bonds.

One bpp ligand is hydrogen-bonded to one water molecule (N1···O1W: 2.651(9) Å) and one terephthalate anion (N5···O2: 2.584(11) Å) that is depicted in orange. The second bpp ligand is forming hydrogen bonds with two terephthalate dianions that are disordered into two positions: A (yellow) and B (green). In position B, each carboxylate moiety exhibits a *syn*, *syn* arrangement and interacts as hydrogen bond acceptor with two $[Fe(bpp)_2]^{2+}$ entities (N6···O3B: 2.885(15) Å and N10···O4B: 2.567(13) Å). Instead, in position A only one carboxylate oxygen atom is involved in hydrogen bonding (N10···O3A: 2.705(13) Å) and a second water molecule is found in the second iron coordination sphere (N6···O9W: 2.520(11) Å).

The crystal packing exhibits a strong resemblance to that described for **2**·2MeOH·H_2O, with an equivalent alternation of cationic and anionic layers along the *c* axis exhibiting an ABA'B' pattern. However, in **2**·5H_2O, adjacent cationic layers A and A' shift in comparison with the previous solvate and the resulting arrangement is almost eclipsed (Figure 2.28). Thus, the *terpyridine embrace* motif is closer to be tetragonal with distances between consecutive pyrazolyl mean planes of 3.26(10) Å (inside the stacks) and 3.27(8) Å (between the stacks). In addition, the pseudobinary axes of the iron centres are subtly tilted (9.14°) with respect to the *c* axis.

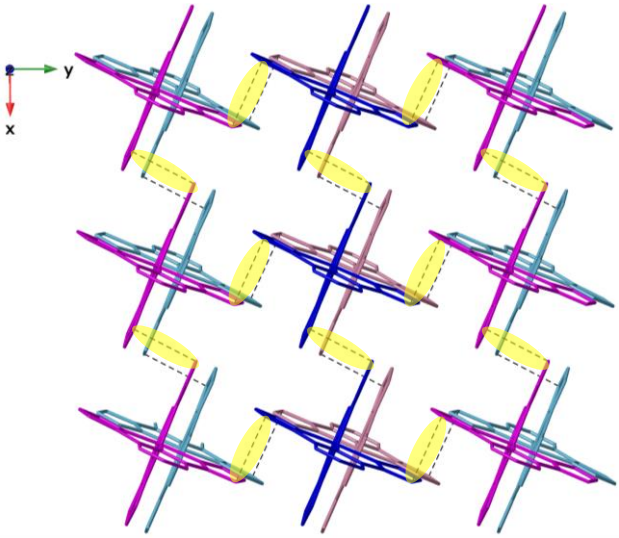

Figure 2.28. A view of **2**·5H_2O in the *xy* plane showing two consecutive $[Fe(bpp)_2]^{2+}$ cationic sheets (terephthalate anions and solvent molecules are omitted). Blue and magenta colours allow comparison with the independent Fe1 and Fe2 centres described in Fig. 2.25. Dashed lines refer to π-π interactions. In yellow are highlighted π-π interactions involving the first cationic layer.

A comparative view parallel to the sheets reveals the differences between the two crystal networks (Figure 2.29 and 2.26). Firstly, when the MeOH molecule located in the second iron coordination sphere of Fe2 is lost, the vacant position is occupied by the closest terephthalate anion, which is the one depicted in green. Thus, this anion acts as a *syn*, *syn* hydrogen bond acceptor involving both carboxylate oxygen atoms (O3B, O4B) in **2**·5H_2O. Secondly, the terephthalate dianion illustrated in orange, which was at the beginning hydrogen-bonded to four $[Fe(bpp)_2]^{2+}$ cations, loses two of these interactions and only connects two iron complexes through O2 carboxylate oxygen atom. The remaining oxygen atom of this carboxylate moiety is engaged in a hydrogen bond with a water

molecule in **2**·5H_2O. Finally, the third anion (illustrated in yellow) remains in the same position, linking two iron centres along the *y* direction through O3A.

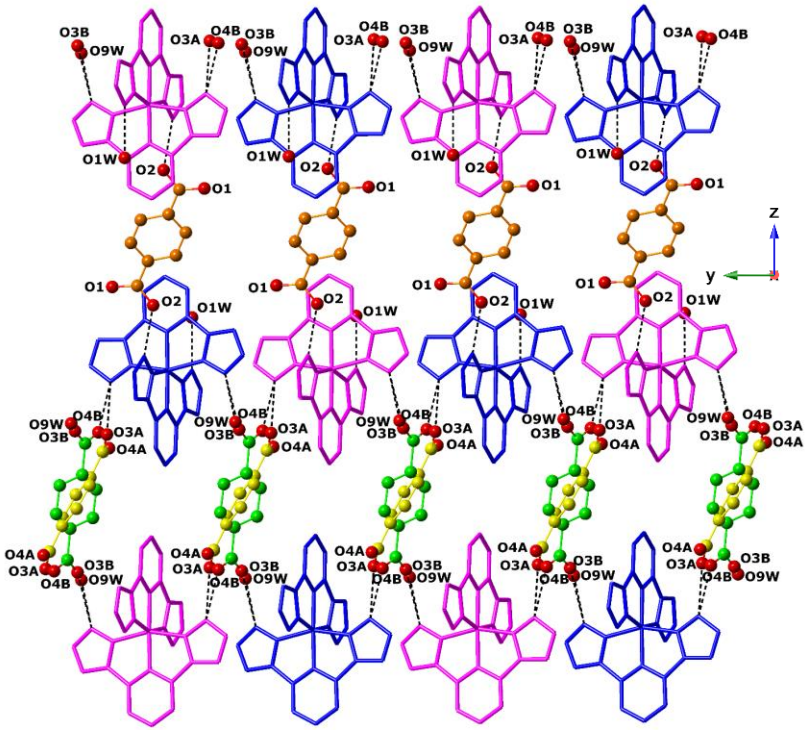

Figure 2.29. A view of the crystal structure of **2**·5H_2O parallel to the *a* axis. Blue and magenta colours allow comparison with the non-equivalent Fe1 and Fe2 centres shown in Fig. 2.26. The independent anions are shown in orange, green and yellow colours. Dashed lines refer to hydrogen bonds.

The two independent Fe^{2+} centres present in **2**·2MeOH·H_2O become equivalent as a consequence of the structural rearrangement associated to the solvent exchange process. This leads to the reduction observed in the unit cell volume (approximately the half) and introduces the disorder in some terephthalate dianions (yellow and green), which is translated to some water molecules that exhibit occupancy factors less than unity. The hydrogen-bonded lattice forms channels along the *a* axis, as observed in the methanol solvate, but in this case are filled only by water molecules. Relevant hydrogen-bonding parameters are included in Table 2.9.

Table 2.9. Intermolecular hydrogen bonds present in **2**·5H_2O (D-H···A).

D···A	$d_{D\cdots A}$ / Å
N1···O1W#1	2.651(9)
N5···O2#2	2.584(11)
N6···O3B#1	2.885(15)
N6···O9W#1	2.520(11)
N10···O3A#3	2.705(13)
N10···O4B#3	2.567(13)
O1···O3W	2.924(11)
O2···O1W#4	2.739(11)
O3B···O8W#5	2.849(15)
O4A···O10W	2.572(13)
O4A···O8W	2.883(15)
O1W···O2W	2.724(8)
O3W···O3W#6	2.811(6)
O4W···O6W	2.702(8)
O5W···O6W#7	2.960(8)
O7W···O8W#7	2.910(8)
O7W···O10W	2.499(8)
O8W···O9W#1	2.458(7)

Symmetry transformations used to generate equivalent atoms: #1 x – 1, y, z; #2 x, y – 1, z; #3 x – 1, y 1, z; #4 x, y + 1, z; #5 x + 1, y, z; #6 – x , – y + 1, – z – 1; #7 – x + 1, – y + 1, – z

B. Powder X-ray diffraction

At the light of the comparative analysis of the two crystal structures, it seems feasible that **2**·5H_2O could be obtained by desolvation and subsequent rehydration of **2**·2MeOH·H_2O. Nevertheless, this fact could not be demonstrated unambiguously because the methanol solvate is a rather elusive minor product and it exhibits a fast desolvation. Thus, this raises doubts about the nature of a polycrystalline sample of the terephthalate salt. In order to elucidate if it is **2**·2MeOH·H_2O, **2**·5H_2O or a mixture of both phases, powder X-ray diffraction experiments were carried out. Figure 2.30 (top) shows the diffractograms measured at room temperature of the sample as-synthesised, desolvated for 2 h at 453 K and after rehydration. The sample was desolvated at this temperature because TG and DSC measurements (*vide infra*, thermal properties) show that at this temperature the compound has completely lost the solvent molecules.

It can be seen that the sample after desolvation preserves crystallinity and that its pattern is quite similar to that obtained for the original sample. This indicates that the loss of solvent molecules does not imply a big reorganisation of the crystal structure, suggesting that the transformation from **2**·2MeOH·H_2O to **2**·5H_2O is possible. However, some peaks become broader and the unit cell slightly shrinks (shift of main peak to higher angles). The first observation indicates that the sample becomes less crystalline, in agreement with the fact that single crystal diffraction experiments of the anhydrous material were not

successful. And the second suggests that spin crossover to the high-spin state takes place after desolvation.

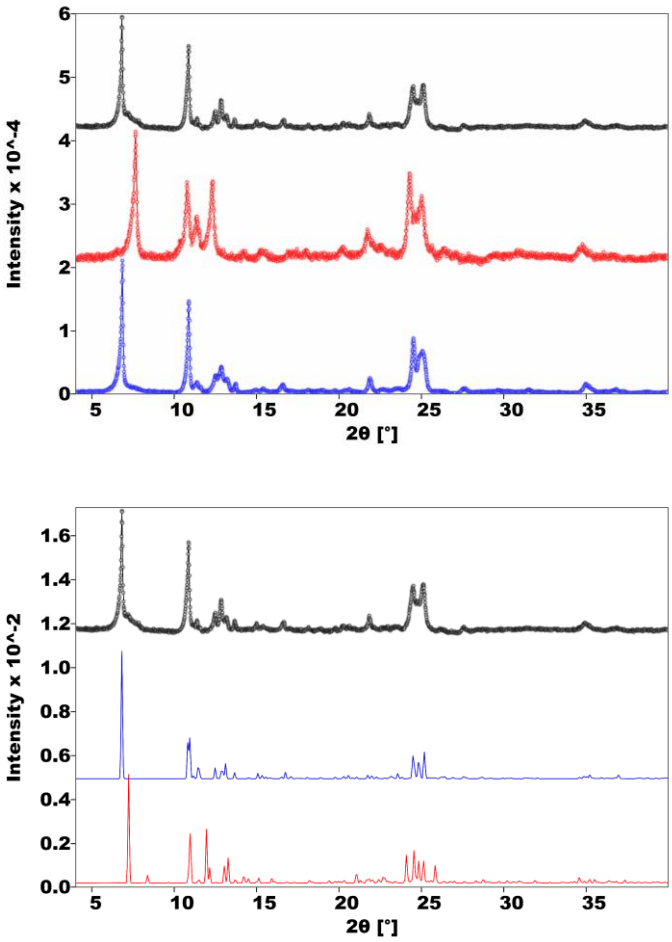

Figure 2.30. Top: Room temperature powder X-ray diffractograms of **2**·5H$_2$O as-synthesised (black dots), dehydrated at 453 K during 2 h (red dots) and rehydrated in water (blue dots). Bottom: Comparison of the experimental powder diffractogram of a polycrystalline sample of **2**·5H$_2$O (black dots) with the simulations obtained from single crystal data of **2**·5H$_2$O and **2**·2MeOH·H$_2$O (blue and red lines, respectively).

On the other hand, it is clear the agreement between the diffractogram of the rehydrated sample and that obtained for the as-synthesised material. This verifies two relevant points. First, that the dehydration is reversible and, secondly, that the composition of the original sample is **2**·5H$_2$O. Moreover, the presence of impurities of **2**·2MeOH·H$_2$O in the starting material can be excluded

by comparing the simulation of the powder diffractograms of both solvates from the single crystal data with the experimental measurement for the as-synthesised material (Figure 2.30, bottom). The simulation of **2**·5H₂O matches perfectly with the experimental data, whereas evident mismatches can be detected for **2**·2MeOH·H₂O.

C. Thermal properties

The TG plot of **2**·5H₂O recorded under nitrogen atmosphere (Figure 2.31.a) shows that the loss of water molecules takes place readily in a single step between room temperature and 400 K. It is associated to the release of five water molecules (observed: 12.6%; calcd: 12.3%), in accordance with the crystal structure described for this compound that shows the presence of most of these water molecules in the voids of the hydrogen-bonded structure. Decomposition of the polycarboxylate anion is observed above 550 K.

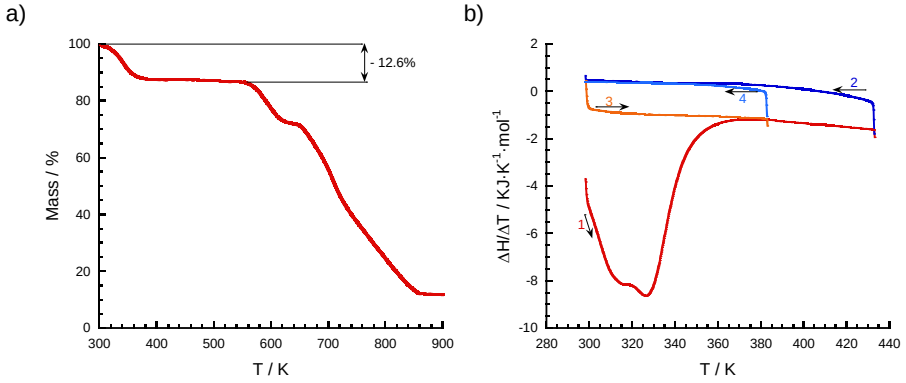

Figure 2.31. a) Thermogravimetric analysis of **2**·5H₂O. b) Differential scanning calorimetry curve of **2**·5H₂O. Curves 1 and 2: First heating and cooling processes, respectively. Curves 3 and 4: second temperature cycle.

The DSC measurement of **2**·5H₂O (Figure 2.31.b) presents only one slightly split endothermic peak around 320 K in the first heating process (curve 1). This is consistent with the presence of a single weight loss step observed in the TG data. As in **1**·4H₂O, the anhydrous material exhibits a featureless plot on cooling back to room temperature (curve 2), and in a subsequent temperature cycle (curves 3 and 4). This indicates a lack of an abrupt thermally-induced transition in the temperature range of study (300-380 K).

2.5.2. Magnetic characterisation of 2·5H$_2$O

A. Magnetic properties

The thermal variation of the χT product of **2**·5H$_2$O is shown in Figure 2.32. At low temperatures, the compound is mainly diamagnetic. Above 300 K, the magnetic signal starts to increase abruptly and reaches a value of 3.78 emu·K·mol^{-1} at 400 K (curve 1. The sample was held at 400 K for 133 min in order to ensure complete dehydration). This value is higher than the "spin-only" value (χT = 3.0 emu·K·mol^{-1}) expected for one high-spin Fe^{2+} cation per formula unit. In this temperature range (300-400 K), desolvation of the sample occurs. Thus, concomitant to the dehydration, population of the high-spin state is observed. Cooling down the sample to 2 K, reveals a spin crossover in two steps (curve 2), which may be attributed to the presence of two different iron sites in the anhydrous material (A and B). The first transition involves 50% of the spins (iron sites A) and occurs over a wide temperature range, suggesting a non-cooperative behaviour. It is centred around T_1 = 240 K and its gradual nature is verified by the fact that the fraction of high-spin centres ($(\gamma_{HS})_A$) follows a Boltzmann distribution.

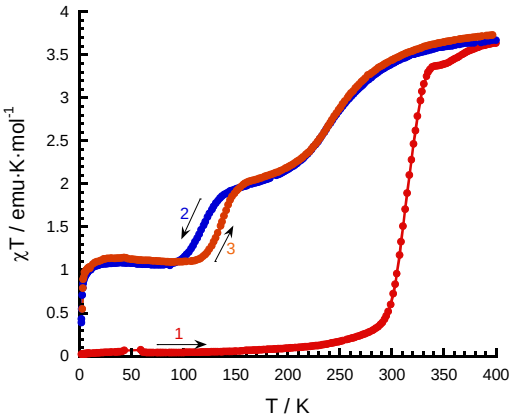

Figure 2.32. Temperature dependence of the χT product of **2**·5H$_2$O. Curve 1: first heating process. Curves 2 and 3: first temperature cycle.

Figure 2.33 shows the best fit with thermodynamic parameters ΔH = 17.2 ± 0.3 kJ·mol^{-1} and ΔS = 57.8 ± 1.2 J·K^{-1}·mol^{-1}. These values are similar to those previously reported for compounds exhibiting two-step transitions.[30] In comparison with anhydrous **1**, both values are approximately the double, in agreement with the fact that in the present case essentially 100% of iron sites A

are involved in the transition whereas in **1** the percentage of Fe1 centres involved was reduced to 60%.

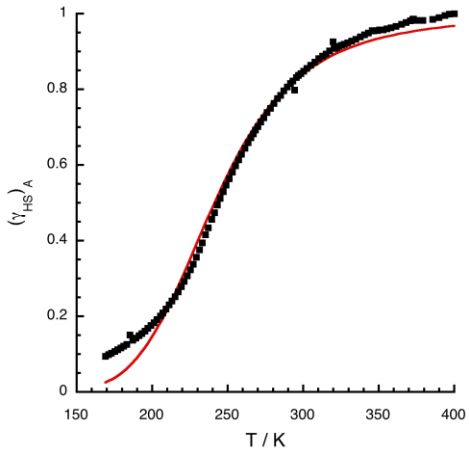

Figure 2.33. Temperature dependence of the fraction of high-spin centres corresponding to the Fe site A of compound **2**·5H_2O. The red line shows the best fit to a Boltzmann distribution.

The second transition involves 25% of Fe^{2+} cations (the half of iron centres B) and takes place more abruptly around $T_2 \downarrow$ = 119 K until reaching a plateau of 1.12 emu·K·mol^{-1}. Further cooling of the sample (below 10 K) leads to a drop in the χT product due to the zero-field splitting of the remaining 25% of Fe^{2+} centres in the high-spin state. The second heating process (curve 3) shows that this second transition is associated with a thermal hysteresis of 20 K, being now located at $T_2 \uparrow$ = 139 K. A second thermal cycle (curves 4 and 5) shows the same thermal variation of χT (not included in Figure 2.32).

B. Mössbauer spectroscopy

First, the room temperature spectrum of **2**·5H_2O was registered (Figure 2.34.a). It shows a single quadrupole doublet with an *IS* (relative to metallic α-Fe at 300 K) and *QS* values of 0.32 and 0.66 mm^{-1}, respectively (Table 2.10), which are in agreement with a low-spin state for Fe(II). Indeed, these values are similar to those reported for other $[Fe(bpp)_2]^{2+}$ salts.[20]

Next, anhydrous **2** was obtained by heating the pentahydrate at 400 K during 4 h. Then, the sample was cooled under nitrogen and spectra recorded at different temperatures (Figure 2.34.b-f). In addition to the low-spin signal, a second doublet appears with higher *IS* and *QS* values, characteristic of high-spin Fe(II) complexes.[20a]

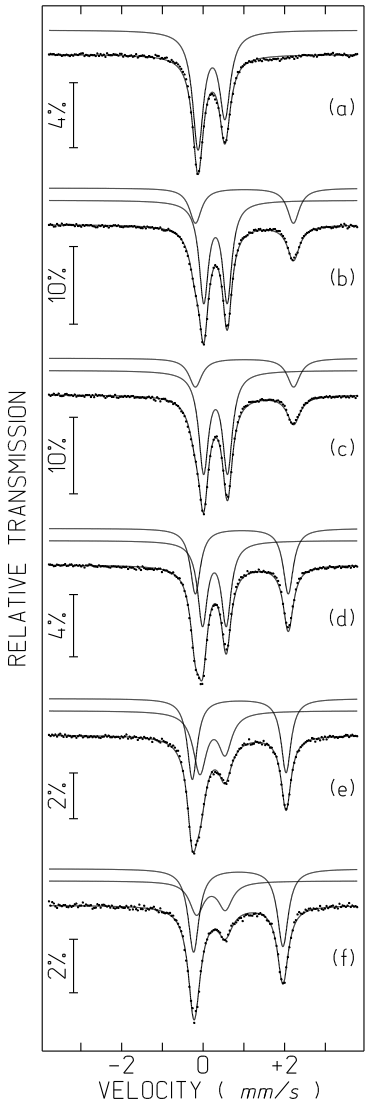

Figure 2.34. Mössbauer spectra of a) **2**·5H_2O at 300 K, and desolvated **2** at b) 4 K, c) 100 K, d) 170 K, e) 250 K and f) 300 K. The line over the experimental points corresponds to one doublet in the case of **2**·5H_2O (a) and to the sum of two doublets in the case of desolvated **2**, shown slightly shifted for clarity.

At 4 K, the relative area of high-spin Fe(II) (I_{HS}) is practically 25%, as expected from magnetic susceptibility measurements (Figure 2.32). At 100 K, I_{HS} presents almost the same value, whereas at 170 K it increases until reaching a value close

to 50%, in agreement with the second SCO observed in the magnetic properties around 139 K. At T = 250 K and 300 K, the value of I_{HS} further increases, consistent with the thermal behavior of χT. The final value at 300 K of I_{HS} is 67%, lower than the expected value from the first and complete SCO registered at 240 K. This can be explained taking into consideration that the recoil-free fraction of LS Fe(II) becomes greater than that of HS Fe(II) at this temperature. Therefore, the real fraction of HS Fe(II) molecules at high temperatures is expected to be higher than I_{HS}[21]. In addition, the fit of the experimental data suggests that only one type of HS and LS iron environments are present in **2** for the whole temperature range of study.

Table 2.10. Estimated parameters from the Mössbauer spectra of **2**·5H$_2$O and **2** measured at different temperatures.

Compound	T / K	IS / mm·s^{-1}	QS / mm·s^{-1}	Γ / mm·s^{-1}	I / %	Spin state
2·5H$_2$O	300	0.32	0.66	0.31	100	LS
2	4	0.42	0.59	0.29	74	LS
		1.11	2.44	0.35	26	HS
2	100	0.41	0.59	0.30	77	LS
		1.11	2.46	0.34	23	HS
2	170	0.39	0.58	0.28	55	LS
		1.06	2.29	0.28	45	HS
2	250	0.35	0.61	0.45	44	LS
		1.01	2.30	0.32	56	HS
2	300	0.31	0.70	0.42	33	LS
		0.98	2.19	0.32	67	HS

IS: Isomer shift relative to metallic α-Fe at 300 K; *QS*: Quadrupole splitting, Γ: Full width at half height; *I*: Relative areas. Estimated errors are ≤ 0.02 mm·s^{-1} for *IS*, *QS* and Γ, and ≤ 3 % for *I*.

C. Photomagnetic properties

In order to determine if complex **2** presents LIESST effect, first, **2**·5H$_2$O was dehydrated *in situ* at 400 K. The value of χT at saturation was 3.3 emu·K·mol^{-1}, a value lower than that observed previously due probably to crystal reorientation effects. After this, the cooling mode of the anhydrous material was recorded until reaching a temperature of 10 K (Figure 2.35, curve 1). The spin crossover in two steps was reproduced, being the first transition gradual and involving 50% of the iron centres whereas the second one is more abrupt and involves 25% of the spins. Then, the sample was irradiated with green light (λ = 532 nm) and a drastic increase in the magnetic signal was observed (curve 2). After 300 min of irradiation, saturation was reached with a χT value of 4.2 emu·K·mol^{-1}. This extremely high value is obtained as a

consequence of orientation effects,[31] and indicates that both spin transitions are reversed under light irradiation. Next, the T(LIESST) curve was recorded (curve 3) in the dark at 0.3 K·min^{-1}. A small increase in the magnetic signal as a result of the zero-field splitting of HS Fe^{2+} centres is observed before complete relaxation of the χT product that occurs above 85 K.

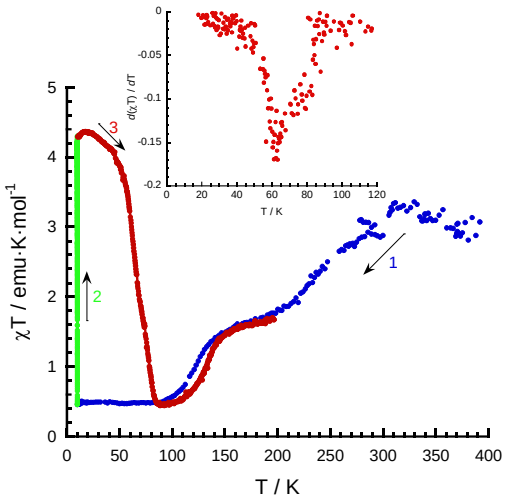

Figure 2.35. Photomagnetic properties of **2**. Blue circles: cooling mode without irradiation; green circles: data recorded while irradiation at 10 K; red circles: heating mode without irradiation at a rate of 0.3 K·min^{-1} (T(LIESST) measurement). The inset shows the first derivative of the T(LIESST) plot.

The T(LIESST) value associated to this curve is calculated to be 63 K, very similar to the value obtained for **1** (61 K). As mentioned previously, it has been shown that the thermal spin crossover temperature and T(LIESST) values are related by the following expression for $[Fe(bpp)_2]^{2+}$ complexes: $T(\text{LIESST}) = T_0 - 0.3 \cdot T_{1/2}$, being T_0 = 150 K.[23] Considering $T_{1/2}$ = 129 K (the average value between $T_2 \downarrow$ and $T_2 \uparrow$), the equation yields a T(LIESST) value of 111 K. Again, the application of this expression provides an irrealistic value. In this case, the decay of the magnetic signal is accelerated by a first relaxation step corresponding to the first spin crossover observed at 240 K. Clearly, both SCO events contribute to the relaxation process which cannot be predicted by an equation based on a single relaxation process.

2.5.3. Discussion 1·4H_2O and 2·5H_2O

1·4H_2O and **2**·5H_2O show a hydrogen-bonded assembly of $[Fe(bpp)_2]^{2+}$ cations and polycarboxylate anions that presents channels, which are filled by solvent molecules. Magnetic measurements and Mössbauer spectroscopy, together with thermogravimetric and calorimetric analyses of $[Fe(bpp)_2](C_6H_8O_4)\cdot 4H_2O$ and $[Fe(bpp)_2](C_8H_4O_4)\cdot 5H_2O$ are in agreement and indicate that the removal of water molecules induces a change in the spin state of the complexes (LS → HS). Powder X-ray diffraction measurements show that structural rearrangements are associated with the desolvation process and, in both cases, rehydration allows to regenerate the original 100% LS material exhibiting the same structure that the starting hydrated compound.

The flexible adipate salt losses its crystallinity upon heating at 453 K, whereas the terephthalate salt preserves it. In addition, in these conditions, the anhydrous adipate salt does not exhibit spin crossover, due to the fact that this anion can present several conformations in the high-spin anhydrous material. This parallels the increase of volume experimented by the iron(II) centres, favouring the match between the charge densities of anionic and cationic sublattices and stabilising the HS phase. On the contrary, the rigid terephthalate salt does not present this possibility and undergoes a transition in two steps with relatively high cooperativity (hysteretic behaviour). Even though we were not able to obtain the crystal structure of the anhydrous terephthalate salt, the powder diffraction measurements show that the main structural integrity of the material remains upon dehydration. Consequently, the *terpyridine embrace* present in the pristine pentahydrate is supposed to be also present in **2**. This fact is in agreement with the enhanced properties exhibited by this salt. Therefore, the advantage of using rigid hydrogen bond acceptors in obtaining materials with interesting SCO properties is clearly demonstrated.

2.5.4. Conclusions and perspectives

The comparative analysis of the magnetic properties of the adipate and terephthalate salts demonstrates that the rigidity of the building blocks has a key role in defining the characteristics of the magnetic transition. Therefore, it is expected that by increasing the rigidity of the building blocks (for instance, increasing the number of aromatic rings), so does the cooperativity of the resulting systems. This is one of our current lines of research. Furthermore, another strategy to enhance the cooperativity of the SCO process is based on the optimisation of the hydrogen-bonding connectivity. In the best case, each

$[Fe(bpp)_2]^{2+}$ cation would be surrounded by four anions, which implies that each dianion would also be linked to four cations. This situation is difficult for a rigid dianion, however, it improves if mononegative anions are used instead of dicarboxylates. In the latter scenario, the hydrogen-bonding connectivity would be optimised being only one anion interacting with two $[Fe(bpp)_2]^{2+}$ cations, which is more feasible. For this reason, the next chapter is focused on the combination of $[Fe(bpp)_2]^{2+}$ cations with mononegative pyridinecarboxylate anions.

On the other hand, it has been well documented that $[Fe(bpp)_2]^{2+}$ systems exhibit solvent sensing SCO properties.[11,22b] In the present case, taking advantage of the high directionality of hydrogen bonds, porous structures have been designed. The possibility of encapsulating different solvent molecules without losing the crystallinity in these novel architectures is being explored, with the aim of determining its influence over the spin crossover properties.

2.6. Experimental Section

2.6.1. Synthesis of precursors

Synthesis of ligand bpp

Ligand bpp (2,6-bis(pyrazol-3-yl) pyridine) was prepared in two steps by the previously published procedure by Lin and Lang.[32] First, the formation of an α,β-unsaturated carboxylic intermediate (1,1'-(2,6-pyridinediyl)-bis-3-(dimethylamino)-2-propen-1-one) by the Claisen-Schmidt reaction takes place (Figure 2.36).

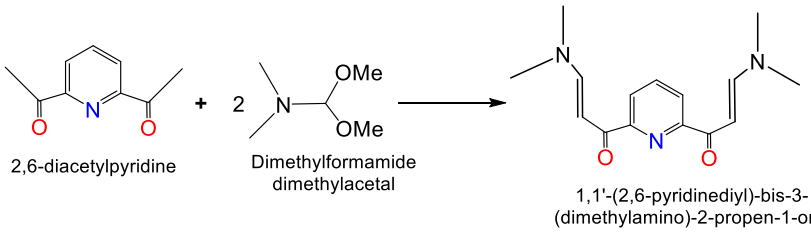

Figure 2.36. Scheme for the synthesis of the intermediate 1,1'-(2,6-pyridinediyl)-bis-3-(dimethylamino)-2-propen-1-one.

Secondly, this intermediate experiments two consecutive reactions. First, it reacts with hydrazine hydrate at room temperature in ethanol to give the corresponding hydrazone, by nucleophilic attack of the nitrogen at the ketone group of the 3-(dimethylamino)-2-propen-1-one. In a second step, the pyrazol

ring is formed by nucleophilic attack of the second nitrogen to the double bond, followed by a loss of dimethylamine and subsequent cyclisation (Figure 2.37).

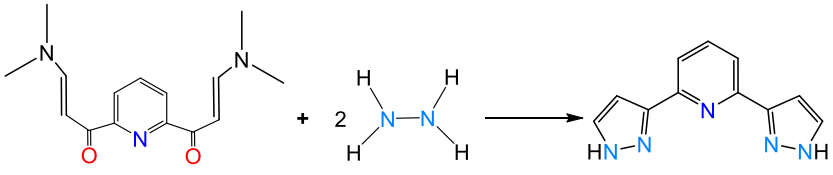

Figure 2.37. Scheme for the synthesis of the ligand bpp from the intermediate 1,1'-(2,6-pyridinediyl)-bis-3-(dimethylamino)-2-propen-1-one.

a) Synthesis of 1,1'-(2,6-pyridinediyl)-bis-3-(dimethylamino)-2-propen-1-one

A suspension of 2,6-diacetylpyridine (12.5 g, 76.5 mmol) in dimethylformamide dimethylacetal (25 ml) was refluxed (105°C) for 10 h. After cooling, the solvent in excess was evaporated in a rotary evaporator. The isolated orange product was recrystallised from dichloromethane/hexane to give yellow crystals that were filtrated and washed with hexane. Yield: 75%, 15.7 g. Anal. Calcd for $C_{15}H_{19}N_3O_2$: C, 65.91; H, 7.01; N, 15.37 %. Found: C, 65.54; H, 7.08; N, 15.41 %. ^{1}H-NMR ($CDCl_3$): δ = 2.95 (s, 16H, -CH_3), 3.25 (s, 6H, -CH_3), 6.55 (d, 2H, -CO-CH), 7.86 (m, 3H, -CH_{Ar}), 8.05 (d, 2H, -CH-N) ppm. Selected IR (KBr, cm^{-1}): 3438.6, 3129.0, 3024.8, 2916.1, 2808.5, 1654.3, 1652.1, 1592.3, 1729.5, 1496.2, 1438.7, 1408.0, 1397.2, 1367.2, 1265.2, 1129.9, 1067.8, 898.5, 787.9, 642.3. The corresponding infrared spectrum is shown in Figure 2.38.a.

b) Synthesis of 2,6-bis(pyrazol-3-yl) pyridine

A suspension of 1,1'-(2,6-pyridinediyl)-bis-3-(dimethylamino)-2-propen-1-one (15.7 g, 57 mmol) in 80 ml of ethanol and 16 ml of hydrazine hydrate was stirred at room temperature for 3 h 30 min. The original suspension is completely solubilised after approximately 1 h of reaction, giving rise to a colourless solution. After this, a white solid is formed during the progress of the reaction. Once the reaction is finished, 25 ml of water were added and the product was isolated by filtration. After washing the solid with water, it was recrystallised from methanol/hexane to give white needles. Yield: 64%, 7.76 g. Anal. Calcd for $C_{11}H_9N_5$: C, 62.55; H, 4.29; N, 33.16 %. Found: C, 62.65; H, 4.40; N, 33.10 %. ^{1}H-NMR (DMSO): δ = 6.90 (d, 2H, -CH), 7.60 (d, 2H, -CH), 7.80 (m, 3H, -CH_{Ar}), 13.0 (s, 1H, -NH), 13.50 (s, 1H, -NH) ppm. Selected IR (KBr, cm^{-1}): 3444.1, 3208.5, 1601.0,

1576.3, 1473.6, 1301.3, 1099.2, 960.2, 929.3, 827.9, 813.0. The infrared spectrum of bpp is shown in Figure 2.38.b.

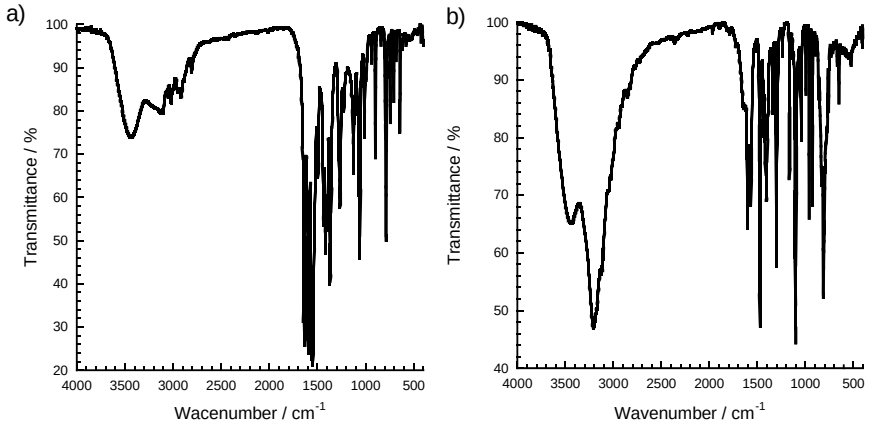

Figure 2.38. a) Infrared spectrum of 1,1'-(2,6-pyridinediyl)-bis-3-(dimethylamino)-2-propen-1-one in a KBr pellet. b) Infrared spectrum of the bpp ligand in a KBr pellet.

Synthesis of $Ba(C_6H_8O_4)\cdot 0.1C_6H_{10}O_4$

A suspension of adipic acid (1.46 g, 10 mmol) was prepared in 5 ml of water. Then, an aqueous solution of KOH (5 ml, 4 M) was added and a complete solubilisation was observed. The resulting solution was slowly added to a solution of $BaCl_2\cdot 2H_2O$ (2.44 g, 10 mmol) in 10 ml H_2O. Next, the total volume of the mixture was reduced to 5 ml in a rotary evaporator and a white microcrystalline solid appeared. A first crop of product was filtered. Further evaporation of the mother liquor provided a second batch of the titled material. Yield: 61%, 1.20 g. Anal. Calcd for $C_{6.6}H_9BaO_{4.4}$: C, 26.78; H, 3.06 %. Found: C, 26.78; H, 2.95 %. Selected IR (KBr, cm^{-1}): 3441, 2943, 2925, 1523, 1460, 1443, 1423, 1411, 1326, 1293, 1208, 1141, 1040, 930, 908, 734, 716, 604, 499. Thermogravimetric analysis (Figure 2.39.a) is consistent with the loss of the adipic acid content. Solvent molecules of crystallisation are not present in this salt. The infrared spectrum of $Ba(C_6H_8O_4)\cdot 0.1C_6H_{10}O_4$ is shown in Figure 2.39.b.

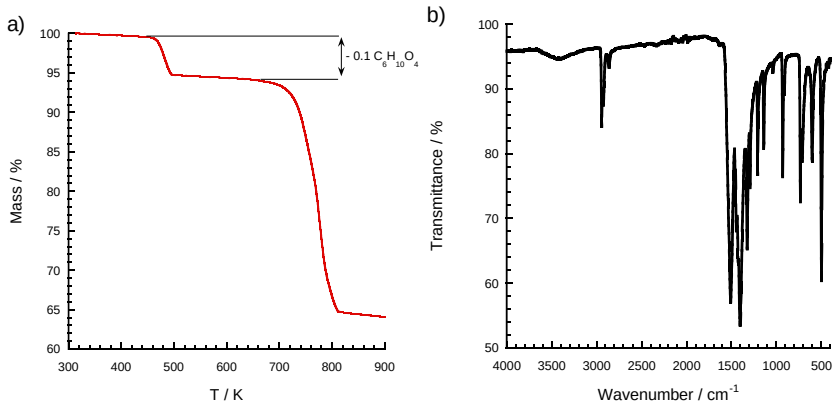

Figure 2.39. a) Thermogravimetric analysis of $Ba(C_6H_8O_4)\cdot 0.1C_6H_{10}O_4$. The plot confirms the anhydrous character of this salt. b) Infrared spectrum of $Ba(C_6H_8O_4)\cdot 0.1C_6H_{10}O_4$ in a KBr pellet.

Synthesis of $Ba(C_8H_4O_4)$

A suspension of terephthalic acid (0.84 g, 4 mmol) in 5 ml H_2O was solubilised in 5 ml of an aqueous solution of KOH (2.4 M). The resulting solution was combined with a solution of $BaCl_2\cdot 2H_2O$ (2.44 g, 10 mmol) in 10 ml H_2O. An immediate precipitation of a white solid was observed. This product was collected by filtration and washed with MeOH, yielding 1.17 g (97 %) of the desired salt. Anal. Calcd for $C_{6.6}H_9BaO_{4.4}$: C, 31.88; H, 1.34 %. Found: C, 31.79; H, 1.26 %. Selected IR (KBr, cm^{-1}): 3443, 2924, 1591, 1544, 1522, 1456, 1406, 1381, 1312, 1283, 1149, 1111, 1095, 1016, 995, 898, 855, 814, 756, 563, 501, 443. The TG plot is in agreement with the anhydrous character of this salt (Figure 2.40.a). The infrared spectrum of $Ba(C_8H_4O_4)$ is shown in Figure 2.40.b.

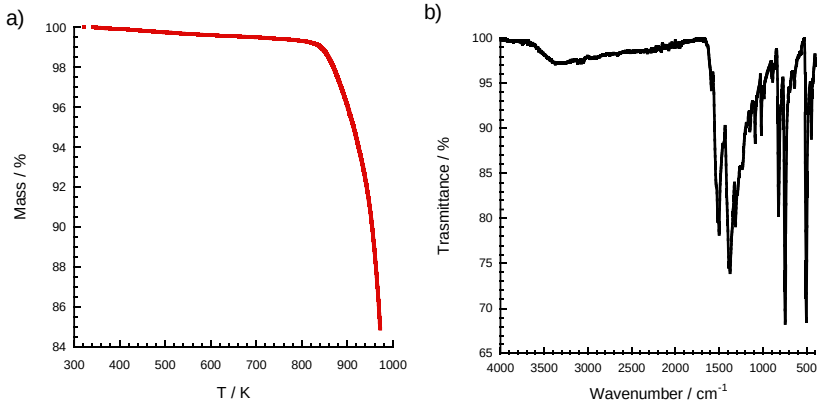

Figure 2.40. a) Thermogravimetric analysis of $Ba(C_8H_4O_4)$. The plot confirms the anhydrous character of this salt. b) Infrared spectrum of $Ba(C_8H_4O_4)$ in a KBr pellet.

2.6.2. Synthesis of complexes

Synthesis of $[Fe(bpp)_2](C_6H_8O_4)\cdot 4\ H_2O$ ($1\cdot 4H_2O$)

$FeSO_4\cdot 7H_2O$ (0.070 g, 0.25 mmol) was added as a solid to a solution of ligand bpp (0.106 g, 0.5 mmol) in 10 ml MeOH under an argon atmosphere. A deep red colour appears after solubilisation of the iron salt. Then, a solution of $Ba(C_6H_8O_4)\cdot 0.1C_6H_{10}O_4$ (71 mg, 0.25 mmol) in 10 ml H_2O was added. An immediate turbidity was formed and the reaction mixture was stirred during 2 h in order to ensure complete precipitation of $BaSO_4$. This precipitate was eliminated by filtration and washed with methanol to dissolve the iron complex retained jointly with the $BaSO_4$. By slow evaporation of the combined filtrate and washings, red prisms were formed. Unfortunately, this compound crystallised together with some white needles of free ligand. The red crystals were hand-picked to yield 81.5 mg (47%). Anal. Calcd for $C_{28}H_{34}FeN_{10}O_8$: C, 48.43; H, 4.93; N, 20.17 %. Found: C, 48.45; H, 4.56; N, 19.92 %. Selected IR (KBr, cm^{-1}): 3422, 3145, 2930, 1617, 1560, 1536, 1500, 40 1440, 1408, 1353, 1337, 1279, 1213, 1145, 1112, 1069, 891, 809, 764, 617, 492. The infrared spectrum of **1**·$4H_2O$ is shown in Figure 2.41.

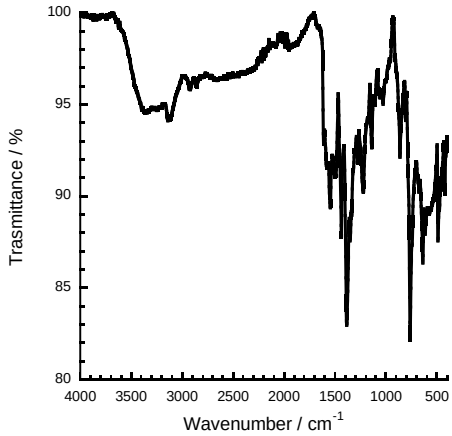

Figure 2.41. Infrared spectrum of **1**·$4H_2O$ in a KBr pellet.

Synthesis of $[Fe(bpp)_2](C_6H_8O_4)$ (1)

Dehydration of **1**·$4H_2O$ was carried out by placing a glass tube with the sample in an oil bath and heating at 453 K under vacuum during 2 h. A drop of water was added to the anhydrous sample to facilitate its rehydration. Then, the crystals were heated again but this time at 400 K using the same procedure. Instead, a

sample with poorer crystallinity can be directly prepared from the original tetrahydrated sample by a single thermal treatment at 400 K. Anal. Calcd for $C_{28}H_{26}FeN_{10}O_4$: C, 53.11; H, 4.33; N, 22.12 %. Found: C, 53.28; H, 4.23; N, 21.98 %.

Synthesis of $[Fe(bpp)_2](C_8H_4O_4)\cdot 2MeOH\cdot H_2O$ (2·2MeOH·H2O) and $[Fe(bpp)_2](C_8H_4O_4)\cdot 5H_2O$ (2·5H2O)

$FeSO_4\cdot 7H_2O$ (0.070 g, 0.25 mmol) was added as a solid to a solution of ligand bpp (0.106 g, 0.5 mmol) in 10 ml MeOH under an argon atmosphere. A deep red colour appears after solubilisation of the iron reagent. A suspension of $Ba(C_8H_6O_4)$ (76 mg, 0.25 mmol) in 10 ml H_2O was added and the resulting mixture kept under stirring for 2 h. A precipitate corresponding to $BaSO_4$ is formed during the reaction, which was filtered and washed with hot MeOH in order to dissolve the retained iron complex. The combined filtrate and washing were left undisturbed. Red plates of **2**·5H2O appeared after a few days. Only in one case, some needles of **2**·2MeOH·H2O also crystallised. Yield: 59 mg (32%). Anal. Calcd for $C_{30}H_{22}FeN_{10}O_4\cdot 1.7H_2O$: C, 53.54; H, 3.80; N, 20.81 %. Found: C, 53.12; H, 3.35; N, 20.83 %. Selected IR (KBr, cm^{-1}): 3405, 3147, 2884, 1616, 1560, 1518, 1437, 1372, 1354, 1282, 1147, 1102, 1085, 1059, 1020, 995, 959, 888, 765, 745, 618, 514. The infrared spectrum of **2**·5H2O is shown in Figure 2.42.

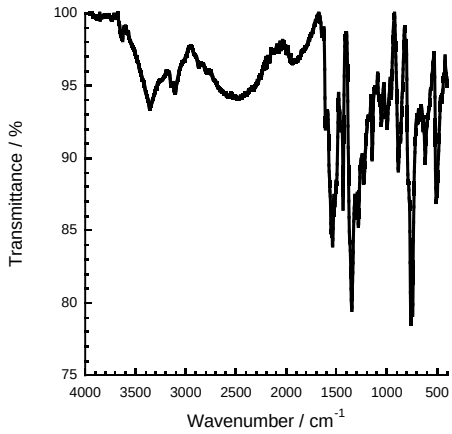

Figure 2.42. Infrared spectrum of **2**·5H2O in a KBr pellet.

2.7. References

[1] M. A. Halcrow, *Dalton Trans*. **2009**, 2059-2073

[2] J. Pérez, L. Riera, *Chem*. *Commun*. **2008**, 533-543

[3] M. Viciano-Chumillas, S. Tanase, L. J. d. Jongh, J. Reedijk, *Eur*. *J*. *Inorg*. *Chem*. **2010**, 3403-3418

[4] M. Viciano-Chumillas, G. d. Ruiter, S. Tanase, J. M. M. Smits, R. d. Gelder, I. Mutikainen, U. Turpeinen, J. J. d. Jongh, J. Reedijk, *Dalton*. *Trans*. **2010**, 39. 4991-4998

[5] J. Y. Shi, P. Y. Chen, M. Z. Wu, L. Tian, Z. Y. Liu, *Dalton Trans*. **2019**, 48, 9187-9193

[6] W.-N. Liu, W.-Q. Tong, L.-L. Ma, Y. Wang, J.-M. Wang, L. Hou, Y.-Y. Wang, *Dalton Trans*. **2019**, 48, 7786-7793

[7] J. García-Antón, R. Bofill, L. Escriche, A. Llobet, X. Sala, *Eur*. *J*. *Inorg*. *Chem*. **2012**, 4775-4789

[8] K. A. Zenere, S. G. Duyker, E. Trzop, E. Collet, B. Chan, P. W. Doheny, C. J. Kepert, S. M. Neville, *Chem*. *Sci*. **2018**, 9, 5623-5629

[9] a) B. R. Bhogala, S. Basavoju, A. Nangia, *CrystEngComm*. **2005**, 7, 551-562. b) Z. Ni, A. Yassar, T. Antoun, O. M. Yaghi, *J*. *Am*. *Chem*. *Soc*. **2005**, 127, 12752-12753

[10] E. Coronado, M. C. Giménez-López, C. Giménez-Saiz, F. M. Romero, *CrystEngComm*. **2009**, 11, 2198-2203

[11] a) M. Clemente-León, E. Coronado, M. C. Giménez-López, F. M. Romero, *Inorg*. *Chem*. **2007**, 46, 11266-11276. b) M. C. Giménez-López, M. Clemente-León, E. Coronado, F. M. Romero, S. Shova, J.-P. Tuchagues, *Eur*. *J*. *Inorg*. *Chem*. **2005**, 2783-2787

[12] P. Guionneau, M. Marchivie, G. Bravic, J.-F. Létard, D. Chasseau, *Top*. *Curr*. *Chem*. **2004**, 234, 97-128

[13] G. A. Craig, O. Roubeau, G. Aromí, *Coord*. *Chem*. *Rev*. **2014**, 269, 13-31

[14] M. C. Giménez-López, M. Clemente-León, C. Giménez-Saiz, *Dalton*. *Trans*. **2018**, 47, 10453-10462

[15] a) E. Coronado, M. C. Giménez-López, C. Giménez-Saiz, J. M. Martínez-Agudo, F. M. Romero, *Polyhedron*. **2003**, 22, 2375-2380. b) Giménez-López, M. C. (**2006**). *Materiales Multifuncionales de Interés en Magnetismo Molecular: Sistemas*

Biestables y Materiales Híbridos Basados en la Química de Coordinación [Doctoral dissertation, University of Valencia]

[16] In order to calculate these values, first, the 'SQUEEZE' [A. L. Spek, *Acta*. *Cryst*. **2015**, C71, 9-18] option of PLATON [A. L. Spek, *Acta Cryst*. **2009**, D65, 148-155] was used to check that the crystal structure at both temperatures does not contain any residual solvent accessible void. Next, the coordinates of the adipate anion were removed from the .ins file and an additional refinement step was conducted, generating new files that were inputted into the PLATON software. Then, the 'SQUEEZE' option yielded a total potential solvent area volume of 1651.8 $Å^3$ (per unit cell volume 5584.7 $Å^3$, 29.6%) and 1740.1 $Å^3$ (per unit cell volume 5481.4 $Å^3$, 31.7%) for **1** at 298 K and 120 K, respectively.

[17] P. Guionneau, M. Marchivie, G. Bravic, J.-F. Létard, D. Chasseau, *J. Mater*. *Chem*. **2002**, 12, 2546-2551

[18] P. Gütlich, H. A. Goodwin, *Top*. *Curr*. *Chem*. **2004**, 233, 1-47

[19] P. Gütlich, Y. Garcia, H. A. Goodwin, *Chem*. *Soc*. *Rev*. **2000**, 29, 419-427

[20] a) T. Buchen, P. Gütlich, K. H. Sugiyarto and H. A. Goodwin, *Chem*. *Eur*. *J*. **1996**, 2, 1134. b) A. Bhattacharjee, J. Kusz, V. Ksenofontov, K. H. Sugiyarto, H. A. Goodwin, P. Gütlich, *Chem*. *Phys*. *Lett*. **2006**, 431, 72.

[21] M. Clemente-León, E. Coronado, M. López-Jordà, G. Mínguez Espallargas, A. Soriano-Portillo, J. C. Waerenborgh, *Chem*. *Eur*. *J*. **2010**, 16, 2207-2219
[22] a) S. Marcén, L. Lecren, L. Capes, H. A. Goodwin, J.-F. Létard, *Chem*. *Phys*. *Lett*. **2002**, 358, 87-95. b) M. Clemente-León, E. Coronado, M. C. Giménez-López, F. M. Romero, S. Asthana, C. Desplanches, J.-F. Létard, *Dalton Trans*. **2009**, 8087-8095
[23] J.-F. Létard, P. Guionneau, O. Nguyen, J. S. Costa, S. Marcén, G. Chastanet, M. Marchivie, L. Goux-Capes, *Chem*. *Eur*. *J*. **2005**, 11, 4582-4589
[24] a) R. Pritchard, C. A. Kilner, M. A. Halcrow, *ChemComm*. **2007**, 577-579. b) T. D. Roberts, F. Tuna, T. L. Malkin, C. A. Kilner, M. A. Halcrow, *Chem*. *Sci*. **2012**, 3, 349-354
[25] P. King, J. J. Henkelis, C. A. Kilner, M. A. Halcrow, *Polyhedron*. **2013**, 52, 1449-1456
[26] T. K. Kim, K. J. Lee, M. Choi, N. Park, D. Moon, H. R. Moon, *New J*. *Chem*. **2013**, 37, 4130-4139
[27] A. Banisafar, D. P. Martin, J. S. Lucas, R. L. LaDuca, *Cryst*. *Growth Des*. **2011**, 11, 1651-1661
[28] T. H. Nguyen, D. E. Hibbs, S. T. Howard, *J*. *Comput*. *Chem*. **2005**, 26, 1233-1241
[29] a) C. L. White, R. L. LaDuca, *CrystEngComm*. **2016**, 18, 6789-6797. b) D. Cechová, I. Svoboda, K. Jomová, Z. Ruzicková, M. Valko, J. Moncol, *Transition Met Chem*. **2015**, 40, 857-868

[30] J.-A. Real, H. Bolvin, A. Bousseksou, A. Dworkin, O. Kahn, F. Varret, J. Zarembowitch, *J*. *Am*. *Chem*. *Soc*. **1992**, 114, 4650-4658
[31] S. Decurtins, P. Gütlich, K. M. Hasselbach, A. Hauser, H. Spiering, *Inorg*. *Chem*. **1985**, 24, 2174-2178
[32] Y. Lin, S. A. Lang, *J*. *Heterocycl*. *Chem*. **1977**, 14, 345-347

Chapter 3: Interplay between spin crossover and structural rearrangements in Hydrogen-bonded assemblies of $[Fe(bpp)_2]^{2+}$ cations and pyridinecarboxylate anions

This chapter describes the syntheses, crystal structures, thermal and (photo)magnetic properties of four spin crossover complexes, containing dissymmetric H-bond acceptors, of formula $[Fe(bpp)_2](isonic)_2 \cdot 2H_2O$ (**3**$\cdot 2H_2O$), $[Fe(bpp)_2](nic)_2 \cdot 4H_2O$ (**4**$\cdot 4H_2O$), $[Fe(bpp)_2](isonicNO)_2 \cdot 2.4H_2O$ (**5**$\cdot 2.4H_2O$) and $[Fe(bpp)_2](isonicNO)_2 \cdot HisonicNO \cdot 5H_2O$ (**6**$\cdot 5H_2O$), being bpp = 2,6-bis(pyrazol-3-yl)pyridine, isonic = isonicotinate anion, nic = nicotinate anion, isonicNO = isonicotinate N-oxide anion and HisonicNO = isonicotinic acid N-oxide. Both, hydrated and dehydrated phases, were analysed by magnetic susceptibility measurements and, in two cases, these results could be correlated with the crystal structure of the desolvated materials (compounds **3** and **5**). Remarkably, some of these novel SCO materials exhibit fascinating properties, such as the presence of ferroelectricity, the existence of a hydrogen-bond isomerisation or a proton migration triggered by the spin transition.

3.1. Introduction

The employment of transition metal coordination complexes in the field of ferroelectrics has emerged as a potential tool for coupling electrical and magnetic properties (magnetoelectric (ME) materials) within the same compound,[1] because of their properties distinctive from those of pure inorganic ferroelectric compounds.[2] These materials exhibit ferroelectricity and ferromagnetism simultaneously and, more importantly, allow the manipulation of magnetic moments by an external electric field, or electric polarisation by a magnetic field.[3] Since the discovery of two milestones, which are the magnetic-field-controllable ferroelectric polarisation in the manganite perovskite $TbMnO_3$ and the giant ferroelectric polarisation in $BiFeO_3$, the interest in the multiferroicity field has increased significantly.[4] Multiferroic ME materials such as $BiFeO_3$ and rare-earth manganates have been widely investigated, in addition to some other Bi-containing systems.[5] Also, ferroelectric behaviour has been associated with a Dy^{III} cluster that exhibits single-molecule magnet and white-light emitting properties, together with several single-molecule magnets.[6] In parallel, intrinsic and induced ferroelectricity in MOFs is being investigated with special emphasis in the influence of guest molecules.[7] Ferroelectricity has been recently combined with a second property, for instance, thermochromism or

photoluminescence, which offers great potential for the fabrication of novel multifunctional devices.[8]

In spite of the richness of this emerging field, the coexistence of spin crossover and ferroelectricity is almost unexplored for a molecular material. There are only a couple of recent works involving both properties, as mentioned in the introduction.[9-11] This lack of reports is surprisingly curious, due to the fact that many HS ↔ LS transitions take place in association with structural transformations that imply a considerable reorganisation of the crystal structure. In some cases, a breaking of symmetry might be observed along the SCO process, with a displacive movement of the SCO centres that might result in the dipole moments necessary for inducing ferroelectricity.[12] The explanation for this lies in the fact that only some structural rearrangements fulfil the requirements for a ferroelectric transition to take place, namely, a phase transition from a high-temperature phase (HTP) that is paraelectric to a low-temperature phase (LTP) that is ferroelectric. According to the definition, the low-symmetry phase (ferroelectric compound, below Curie temperature T_c) must crystallise in one of the ten polar point groups (Figure 1.33, Chapter 1).[1]

In order to obtain dual-function materials exhibiting ferroelectricity and spin crossover, we decided to introduce a rational design. It is based on the synthesis of acentric MOFs developed by Lin and co-workers, which consists in linking tetrahedral metal nodes with acentric linkers to afford a diamond-like noncentrosymmetric structure for second-order nonlinear optics (NLO).[13] It takes advantage of the well-defined geometry of metal centres and highly directional metal-ligand coordination bonds. Instead, in our case, coordination bonds are replaced by hydrogen bonds. The diamond crystal itself crystallises in a centrosymmetric space group, thus, being necessary to break the centre of symmetry to achieve NLO properties. There are two approaches for this: connect the tetrahedral nodes by acentric bridging ligands or the employment of different adjacent linking nodes (Figure 3.1).

With this idea in mind, we have chosen the well-known $[Fe(bpp)_2]^{2+}$ complex as a tetrahedral metal node, that acts as a pseudotetrahedral (4-fold) hydrogen bond donor through its N–H moieties. Following the first approach mentioned above, necessarily unsymmetric linkers as hydrogen bond acceptors are required for obtaining an acentric packing. In this regard, nicotinate and isonicotinate anions have been selected, thanks to their bidentate character, linear geometry (2-fold) and simplicity (Scheme 3.1).

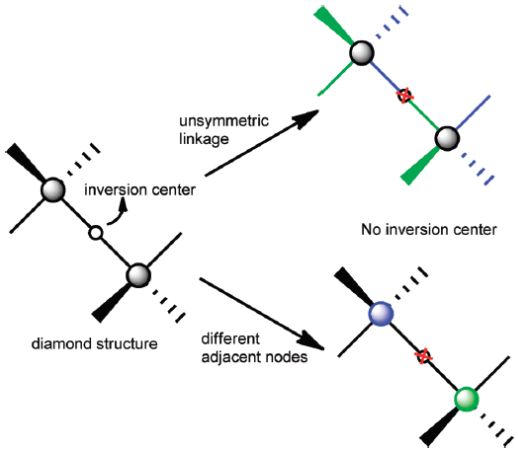

Figure 3.1. Schematic representation of two different ways to remove inversion centres in diamond-like structures. Extracted from reference [13].

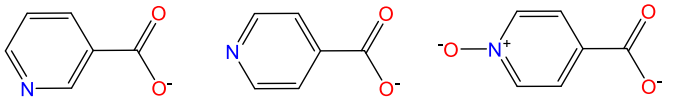

Scheme 3.1. Structures of the pyridinecarboxylate anions employed in this part of the thesis.

3.2. Organisation and objectives

This work is intended to exploit the high directionality of hydrogen bonds in the design of novel materials in which ferroelectricity and spin crossover coexist in the same temperature range, following the synthetic strategy described above. First, the assembly of $[Fe(bpp)_2]^{2+}$ complexes with isonicotinate anions was conducted ($[Fe(bpp)_2](isonic)_2 \cdot 2H_2O$ (**3**·$2H_2O$)). Then, this linker was replaced by the nicotinate anion in order to study the effect of the position of the nitrogen atom on the properties of the resulting material ($[Fe(bpp)_2](nic)_2 \cdot 4H_2O$ (**4**·$4H_2O$)). This comparison allows the correlation of the strength of the hydrogen bonds with the connectivity of the resulting material that, in turn, defines the symmetry of the system. Moreover, the ability of the $[Fe(bpp)_2]^{2+}$ system to generate noncentrosymmetric structures with diamond-like topology by tuning the length of the *p*-pyridinecarboxylate linker was investigated. Specifically, the isonicotinate anion was replaced by the isonicotinate N-oxide anion, which incorporates an additional oxygen atom (Scheme 3.1). Unfortunately, the adventitious presence of solvent molecules

engaged in hydrogen bonding and the weaker N-donor character of the nicotinate and isonicotinate N-oxide anions with respect to the isonicotinate[14] result in the deviation from the predicted diamondoid structure and centrosymmetric networks are generated. However, in the latter case, two different systems have been obtained ($[Fe(bpp)_2](isonicNO)_2 \cdot 2.4H_2O$ (**5**$\cdot 2.4H_2O$) and $[Fe(bpp)_2](isonicNO)_2 \cdot HisonicNO \cdot 5H_2O$ (**6**$\cdot 5H_2O$)), which present striking properties.

On the one hand, **5**$\cdot 2.4H_2O$ exhibits a phase transition associated to an extremely abrupt spin crossover near room temperature that drives a supramolecular hydrogen bond isomerisation. Despite the fact that there is a wide variety of examples in which subtle structural changes occur in association with the SCO process,[15] there is a lack of reports regarding drastic rearrangements of the crystal network. In the present compound, the H-bond isomerisation affects the connectivity between the cationic subunits and the anionic sublattice, in a reversible way.

On the other hand, **6**$\cdot 5H_2O$ is a co-crystal containing isonicotinic acid N-oxide both in its free and deprotonated form. Proton displacement between hydrogen bond acceptors is a well-known dynamic process that may originate a ferroelectric phase transition[16] and it usually occurs along short strong hydrogen bonds (SSHBs).[17] In this context, **6**$\cdot 5H_2O$ displays SCO encompassing proton migration and hydrogen bond formation in two steps, with breaking of symmetry and generation of a metastable high-spin/low-spin (HS/LS) pair.

In this chapter, the work is divided in three main sections:

- Description of a water-responsive ferroelectric assembly of iron(II) SCO complexes and isonicotinate linkers. Comparison of $[Fe(bpp)_2]^{2+}$ salts comprising isonicotinate and nicotinate anions (Section 3.3).

- Study of a $[Fe(bpp)_2]^{2+}$ salt built up from isonicotinate N-oxide anions that exhibits a reversible H bond isomerisation triggered by an abrupt SCO near RT (Section 3.4).

- Combination of a stepped-SCO and proton migration inside a SSHB between two isonicotinate N-oxide anions in an iron(II) material (Section 3.5).

3.3. $[Fe(bpp)_2](isonic)_2{\cdot}2H_2O$ (**3**$\cdot 2H_2O$) and $[Fe(bpp)_2](nic)_2{\cdot}4H_2O$ (**4**$\cdot 4H_2O$)

3.3.1. Synthesis

First, the synthesis of silver salts exempts of counterions was conducted from silver carbonate and the corresponding pyridinecarboxylic acid. Then, metathesis reactions of $[Fe(bpp)_2]Cl_2$ with the corresponding silver salt (Ag(nic) or Ag(isonic)) afforded compounds **3**$\cdot 2H_2O$ and **4**$\cdot 4H_2O$ as pure phases (Scheme 3.2).

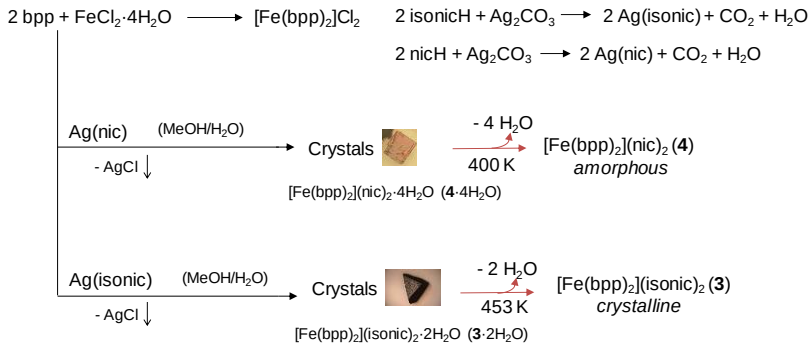

Scheme 3.2. Scheme of the synthetic pathways for the synthesis of **3**$\cdot 2H_2O$ and **4**$\cdot 4H_2O$.

3.3.2. Structural characterisation of 3·2H₂O

A. Single crystal X-ray diffraction

As expected, **3**$\cdot 2H_2O$ crystallises in a noncentrosymmetric space group (tetragonal *I*–4) (Table 3.1). Its crystal structure comprises isolated $[Fe(bpp)_2]^{2+}$ cations, isonicotinate anions and water molecules. All the anions are equivalent, acting as acceptors of hydrogen bonds through the pyridine N7 (N7···N1: 2.778(3) Å) and the carboxylate O2 (O2···N4: 2.847(3) Å) atoms and connecting unsymmetrically the $[Fe(bpp)_2]^{2+}$ cationic entities in a 3D diamond-like structure. As a result, necessarily two crystallographically independent iron centres, Fe1 and Fe2, are present in the asymmetric unit. The two Fe^{2+} cations are located in special (four-fold) positions and are coordinated by two perpendicular bpp ligands in a distorted octahedral geometry, with Fe–N bond distances characteristic of a LS state in both cases (average Fe–N distances of 1.96(4) Å and 1.95(3) Å respectively for Fe1 and Fe2 centres) (Figure 3.2). In addition, the values of the octahedral distortion parameters Σ compare well with

those reported for LS species (Σ = 92.51° and 88.13° for Fe1 and Fe2, respectively).[18] In this case, the *trans* N–Fe–N angle is strictly 180° because both iron centres sit on a special position with the four-fold improper axis of rotation containing the Fe–N(py) bond.

Table 3.1. Crystallographic data and structural refinement for $[Fe(bpp)_2](isonic)_2 \cdot 2H_2O$ (**3**·$2H_2O$).

	3·$2H_2O$
Empirical formula	$C_{34}H_{30}FeN_{12}O_6$
Formula weight	758.55
Crystallographic system	Tetragonal
Space group	$I\bar{4}$ (no. 82)
a/ Å	15.58570(18)
b/ Å	15.58570(18)
c/ Å	13.5724(3)
α/ °	90
β/ °	90
γ/ °	90
V/ Å^3	3296.93(10)
Z	4
R(int)	0.0674
ρ_{calc}/ g·cm^{-3}	1.528
μ/ mm^{-1}	0.525
Crystal dimensions/ mm	0.1718 x 0.1121 x 0.0939
T/ K	120.05(10)
λ/ Å	0.71073
2θ range/ °	6.572< 2θ <74.948
Index ranges for h, k , l	-26/26, -26/26, -23/23
Completeness to θ = 25.242° (%)	99.7
Refinement method	Full-matrix least-squares on F^2
Collected reflections	25747
Unique reflections	8038
Data/Restraints/Parameters	8038 / 0 / 301
Goodness-of-fit on F^2	1.039
R1, wR2 [I > 2sigma(l)][a]	R1 = 0.0493, wR2 = 0.0990
R1, wR2 (all data)[a]	R1 = 0.0690, wR2 = 0.1135
Absolute structure parameter	-0.020(10)
$\Delta\rho_{max}$ and $\Delta\rho_{min}$ (e·Å^{-3})	0.711, −1.039

[a] $R1 = \Sigma(||F_o| - |F_c||)/\Sigma|F_o|$; $wR2 = \{\Sigma[w(F_o^2 - F_c^2)^2]/\Sigma[w(F_o^2)^2]\}^{1/2}$

As can be seen in Figure 3.2, both independent Fe(II) centres are hydrogen-bonded to four isonicotinate anions but the difference between them lies in the configuration of their second coordination spheres: Fe1 centre is linked to the isonicotinate anions *via* the pyridine ring (N7), whereas Fe2 is connected through the carboxylate anion (O2). As mentioned in the previous chapter, **3**·$2H_2O$ exhibits the usual spin state for a hydrated $[Fe(bpp)_2]^{2+}$ salt.[18] In the present case, the number of carboxylate anions that establish hydrogen bonds with the cationic entities is maximised to four, increasing the electronic density in the pyrazolyl rings and favouring the low spin state. The packing of tetrahedra

($[Fe(bpp)_2]^{2+}$ units) connected through lineal bridges (isonicotinate anions) by hydrogen bonds is shown in Figure 3.3.

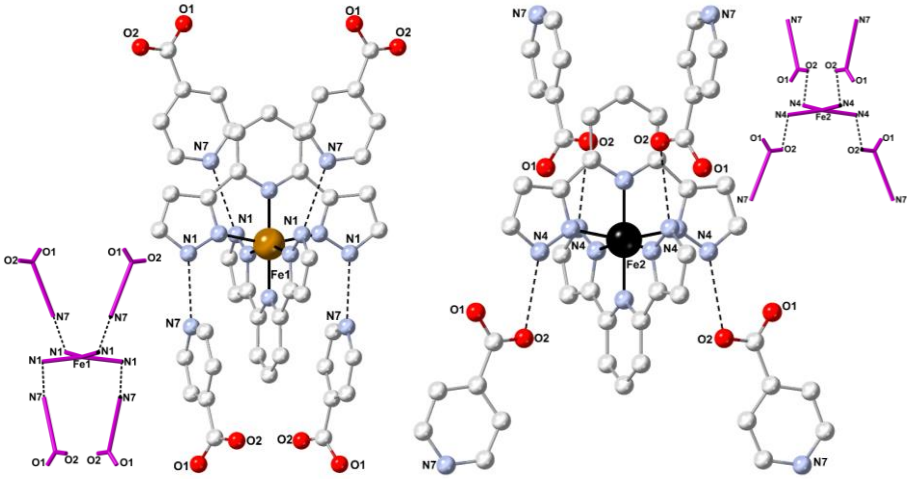

Figure 3.2. Crystal structure of **3**·$2H_2O$ showing the two inequivalent $[Fe(bpp)_2]^{2+}$ complexes. A schematic view of the hydrogen-bonded connectivity is shown as magenta sticks. H-bonds are represented by dashed lines.

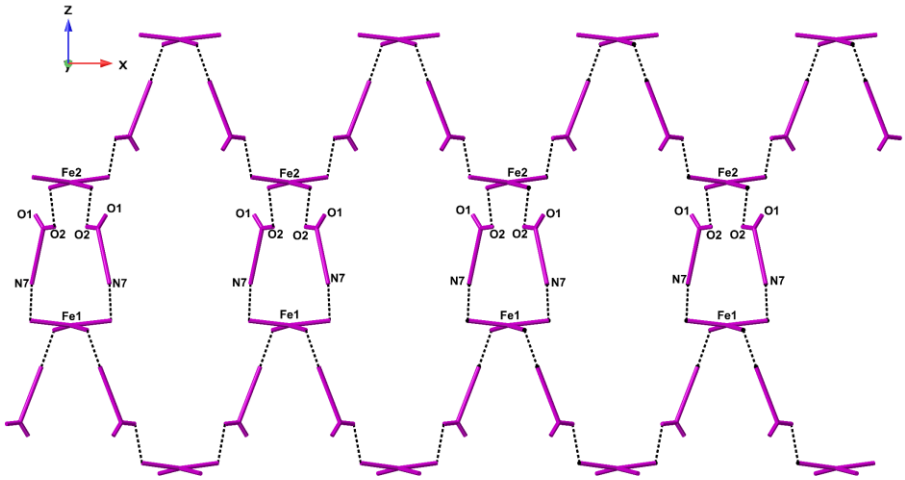

Figure 3.3. Schematic representation of the crystal structure of **3**·$2H_2O$ in the *xz* plane showing one tetragonal hydrogen-bonded network (diamondoid network). Each cationic entity is represented as a FeN_4 tetrahedron. Only the carboxylate fragment and the pyridine nitrogen atom of the isonicotinate anions are shown. Dashed lines refer to hydrogen bonds.

There is an alternation of Fe1 and Fe2 centres along the *c* axis, giving rise to the formation of a 3D structure. The large cavities within the 3D network are filled by lattices of the same type, yielding a triply interpenetrated structure (Figure 3.4). The acentric nature of the overall packing is ensured by the odd-number-fold degree of interpenetration.

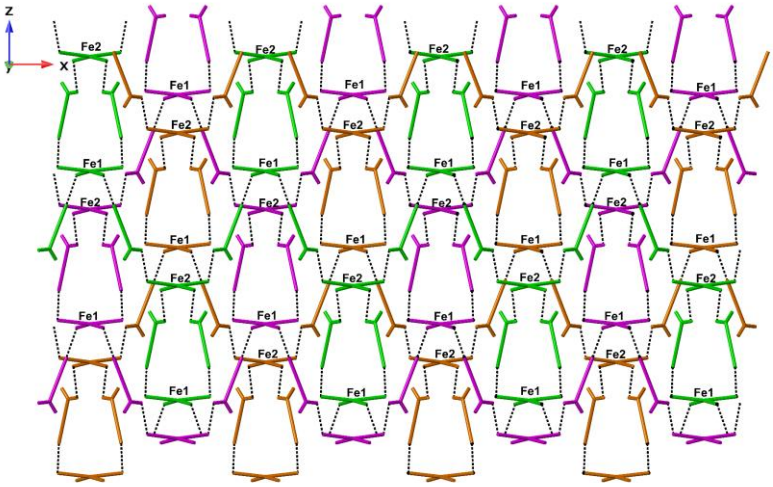

Figure 3.4. Schematic representation of the crystal structure of **3**·2H_2O in the *xz* plane showing the triply interpenetrated hydrogen-bonded network (each network is shown in a different colour). Each cationic entity is represented as a FeN_4 tetrahedron. Only the carboxylate fragment and the pyridine nitrogen atom of the isonicotinate anions are shown. Dashed lines refer to hydrogen bonds.

The other oxygen atom of the isonicotinate anion is engaged in hydrogen bonds with crystallisation water molecules (O1W···O1: 2.733(4) Å). Thus, these solvent molecules are tightly bound and lie buried inside the interpenetrated nets. Table 3.2 contains hydrogen bonding information.

Table 3.2. Intermolecular hydrogen bonds present in **3**·2H_2O between donors and acceptors (D-H···A).

D···A	$d_{D\cdots A}$ / Å
N1···N7#1	2.778(3)
N4···O2#2	2.847(3)
O1W···O1	2.733(4)
O1W···O2#5	3.098(4)

Symmetry transformations used to generate equivalent atoms: #1 – y + 1, x, – z + 1; #2– y + 1, x, – z + 2; #5 y, – x + 1, – z + 2

A view along the *a* axis shows that the $[Fe(bpp)_2]^{2+}$ cationic moieties are not connected by strong π-π stacking interactions, since the distance between the centroid coordinates of adjacent Fe1 and Fe2 pyrazolyl fragments is equal to

4.81(5) Å (Figure 3.5). This anticipates a low degree of cooperativity for this system, which is associated to gradual spin transitions.[19]

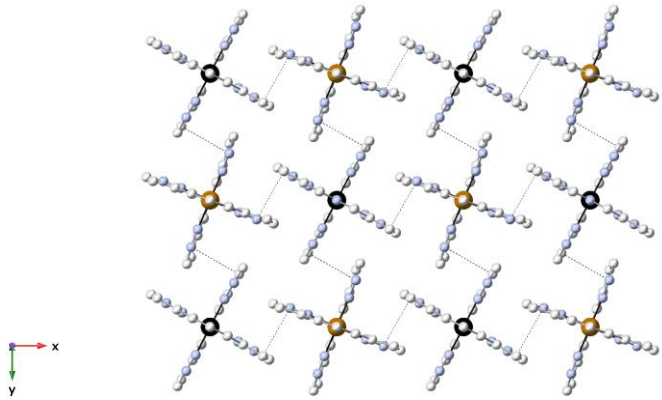

Figure 3.5. View of the crystal structure of **3**·$2H_2O$ showing the $[Fe(bpp)_2]^{2+}$ subunits along the *a* axis. Typical π-π stacking interactions are not observed. H atoms have been omitted for clarity.

B. Thermal properties

TG measurements of **3**·$2H_2O$ under nitrogen were performed in order to characterise the presence of solvent in the structure and the thermal stability of the salt (Figure 3.6.a). The first weight decrease takes place in a single step at approximately 423 K and corresponds to the loss of two water molecules per iron centre. This is in agreement with the formulation deduced from the single crystal X-ray analysis. Indeed, the temperature needed for dehydration is relatively high and consistent with the fact that the water molecules are strongly bound to the crystal network. Above 495 K, decomposition of the sample starts. On other hand, these results indicate that it is necessary to heat above 400 K (the maximum temperature available in our SQUID equipment) for achieving complete desolvation of the compound.

Figure 3.6.b shows the DSC properties of **3**·$2H_2O$. First, the low-temperature region (150-300 K) was investigated for the as-synthesised material, but it is featureless (not shown in the plot). In the first heating process (curve 1), a very intense endothermic peak is observed, which fits in the temperature range of dehydration determined from TG measurements (T = 422 K). Therefore, it is ascribed to the desolvation of the sample. Upon cooling to room temperature (curve 2), a sharp and exothermic peak is detected at 321 K, indicating a phase transition. The second heating process (curve 3) exhibits a sharp endothermic peak at 325 K, revealing that the thermally induced transition is reversible. A

second additional cycle exhibits the same behaviour (curves 4 and 5, not shown). Table 3.3 contains the values of enthalpy and entropy changes associated to these processes, being the calculated values from curve 1 much higher than the others, due to the fact that it includes the dehydration enthalpy/entropy.[20]

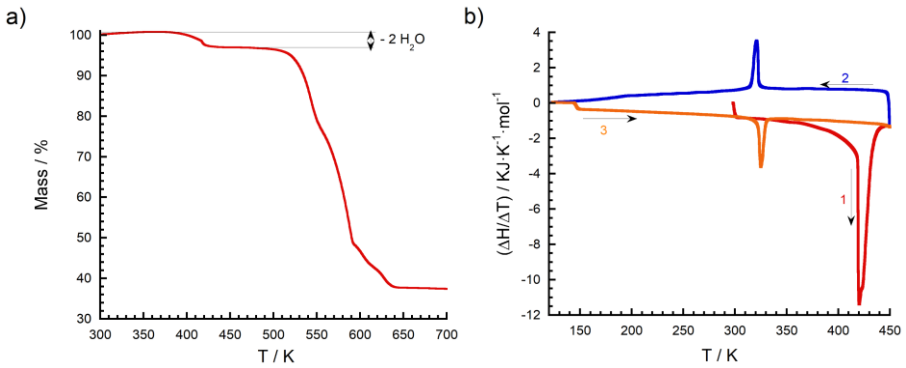

Figure 3.6. a) Thermogravimetric analysis of **3**·2H_2O. b) Differential scanning calorimetry curve of **3**·2H_2O. Curves 1 and 2: First heating and cooling processes, respectively. Curve 3: second heating process.

Table 3.3. Enthalpy and entropy changes observed for DSC measurements of **3**·2H_2O.

Curve	T_{peak}/ K	ΔH / kJ·mol^{-1}	ΔS / J·mol^{-1}·K^{-1}
1	422	133	325
2	321	-18	-54
3	325	17	54

C. Powder X-ray diffraction

The powder X-ray diffractogram of **3**·2H_2O measured at room temperature is shown in Figure 3.7, together with the simulated pattern obtained from single crystal X-ray diffraction data at 120 K. The good agreement between both patterns discards the existence of impurities and the occurrence of a phase transition between 120 K and room temperature.

Furthermore, the reversibility of the dehydration-rehydration process was investigated. Figure 3.8 shows the X-ray patterns at room temperature of **3**·2H_2O as-synthesised, desolvated and rehydrated at ambient conditions. Despite the high temperatures, dehydration took place without loss of crystallinity by heating the pristine dihydrate at 453 K for 2 h under vacuum. Moreover, the process is completely reversible, observing an extremely fast restoration of the

hydrated diffractogram upon exposure of the anhydrous material **3** to ambient humidity.

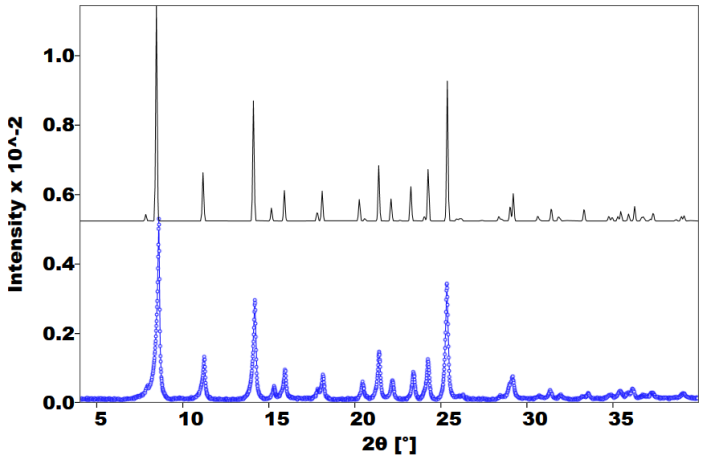

Figure 3.7. Powder X-ray simulation of **3**·2H_2O from single crystal X-ray data at 120 K (black lines). The experimental pattern at room temperature is also included for comparison (in blue).

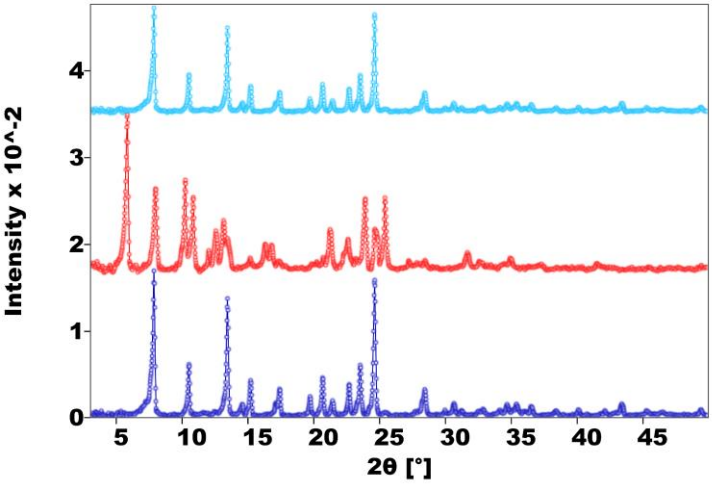

Figure 3.8. Powder X-ray diffractograms at room temperature of **3**·2H_2O as-synthesised (dark blue), dehydrated at 453 K for 2 h (red) and after rehydration at ambient conditions during 12 h (light blue).

3.3.3. Structural characterisation of 3

A. Single crystal X-ray diffraction

Powder X-ray diffraction measurements revealed that it is possible to dehydrate **3**·2H_2O without losing its crystallinity. Thus, this sample was placed inside a glass tube and heated in an oil bath under vacuum at 453 K for 2 h to afford anhydrous **3** in a single-crystal to single-crystal (SCSC) transformation. Lattice cell parameters were measured on a single crystal of **3** at different temperatures between 338 K and 303 K. The thermal variation (Figure 3.9) exhibits a discontinuity between 323 K and 328 K, which is in accordance with the existence of a crystallographic phase transition exactly in the temperature range where the DSC peaks were observed.

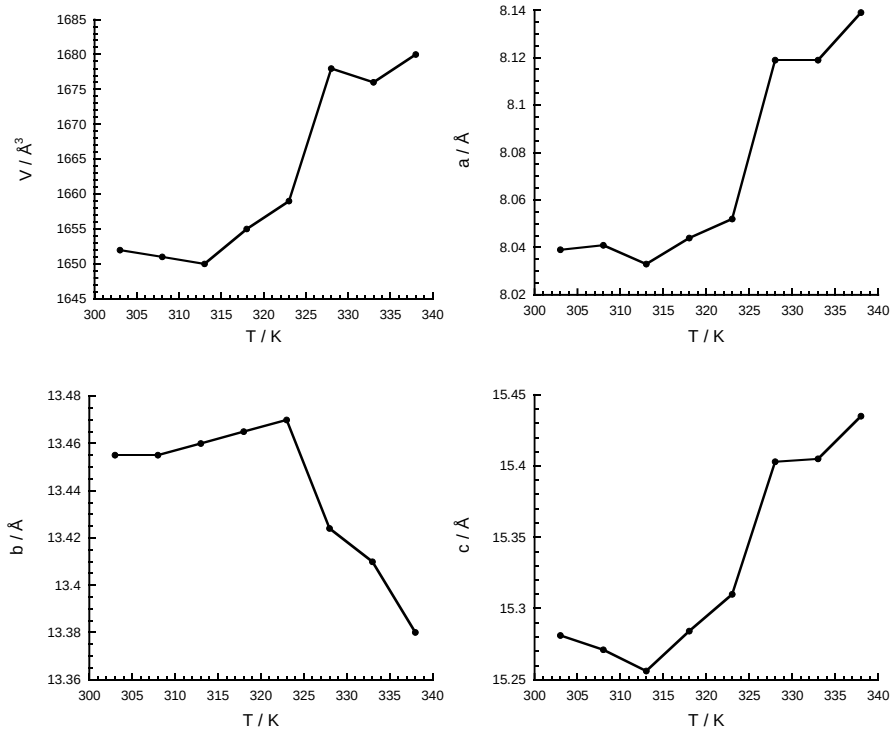

Figure 3.9. Thermal dependence of unit cell parameters of **3**.

The crystal structure of **3** was solved above (in the high-temperature phase, HTP, *T* = 338 K) and below (in the low-temperature phase, LTP, *T* = 120 K) the phase transition deduced from DSC measurements. At 120 K, the anhydrous salt

crystallises in the *polar* monoclinic space group *Pc* (Table 3.4). The asymmetric unit contains two inequivalent isonicotinate anions and only one independent Fe^{2+} cation, with an average Fe1–N bond distance of 1.95(5) Å that is typical of low-spin species. The octahedral distortion parameters (Σ = 93.21°, φ = 178.94°) are also consistent with this spin state.

Table 3.4. Crystallographic data and structural refinement for anhydrous $[Fe(bpp)_2](isonic)_2$ (**3**).

	3 at 338 K	**3** at 120 K
Empirical formula	$C_{34}H_{26}FeN_{12}O_4$	$C_{34}H_{26}FeN_{12}O_4$
Formula weight	722.52	722.52
Crystallographic system	Monoclinic	Monoclinic
Space group	*Pc* (no. 7)	*Pc* (no. 7)
a/ Å	8.14735(10)	8.0022(3)
b/ Å	13.40094(18)	13.3391(4)
c/ Å	15.4298(3)	15.2067(5)
α/ °	90	90
β/ °	92.1604(14)	91.863(3)
γ/ °	90	90
V/ Å^3	1683.46(4)	1622.33(9)
Z	2	2
R(int)	0.0665	0.0491
ρ_{calc}/ g·cm^{-3}	1.425	1.479
μ/ mm^{-1}	0.506	0.525
Crystal dimensions/ mm	0.2180 x 0.1045 x 0.0739	0.15 x 0.09 x 0.08
T/ K	338.00(10)	120.00(10)
λ/ Å	0.71073	0.71073
2θ range/ °	6.50< 2θ <55.41	5.94 < 2θ <59.93
Index ranges for h, k , l	-10/10, -17/17, -20/20	-11/11, -18/18, -21/21
Completeness to θ = 25.242° (%)	99.6	99.9
Refinement method	Full-matrix least-squares on F^2	Full-matrix least-squares on F^2
Collected reflections	86182	24070
Unique reflections	7356	8350
Data/Restraints/Parameters	7356 / 23 / 473	8350 / 6 / 473
Goodness-of-fit on F^2	1.075	1.035
R1, wR2 [I > 2sigma(I)][a]	R1 = 0.0486, wR2 = 0.1060	R1 = 0.0485, wR2 = 0.1077
R1, wR2 (all data)[a]	R1 = 0.0848, wR2 = 0.1199	R1 = 0.0646, wR2 = 0.1183
Absolute structure parameter	0.40(3)	0.51(2)
$\Delta\rho_{max}$ and $\Delta\rho_{min}$ (e·Å^{-3})	0.278, –0.225	0.574, -0.378

[a] $R1 = \Sigma(||F_o| - |F_c||)/\Sigma|F_o|$; $wR2 = \{\Sigma[w(F_o^2 - F_c^2)^2]/\Sigma[w(F_o^2)^2]\}^{1/2}$

The connectivity of the hydrogen-bonded lattice is different to that observed for the hydrated compound. Each $[Fe(bpp)_2]^{2+}$ unit is again connected to four

isonicotinate anions (Figure 3.10.a), but now three positions of the second iron coordination sphere are occupied by carboxylate fragments (mean N···O distance = 2.63(3) Å, Table 3.5), while the remaining one is filled by one pyridine unit (N1···N11 = 2.783(6) Å). On the other hand, two inequivalent isonicotinate anions are present in the structure (Figure 3.10.b). One of them exhibits the same connectivity as in the hydrated material: links two iron centres via the pyridine N11 and carboxylate O1 atoms, while the second acts as a *syn*,*syn*-bridging carboxylate unit (O3O4). The dramatic change in the propagation of hydrogen bonds results in a disentanglement of the triply interpenetrated structure, which can be best described in **3** as an assembly of 2D corrugated layers (Figure 3.11).

Table 3.5. Intermolecular hydrogen bonds present in **3** between donors and acceptors (D-H···A) at 338 K and at 120 K.

D···A	$d_{D\cdots A}$ / Å (338 K)	$d_{D\cdots A}$ / Å (120 K)
N10···O4	2.705(9)	2.697(5)
N6···O3#1	2.678(11)	2.631(5)
N1···N11#2	2.848(11)	2.783(6)
N5···O1	2.607(9)	2.572(5)

Symmetry transformations used to generate equivalent atoms: #1 x – 1, y, z; #2 x, – y, z – ½

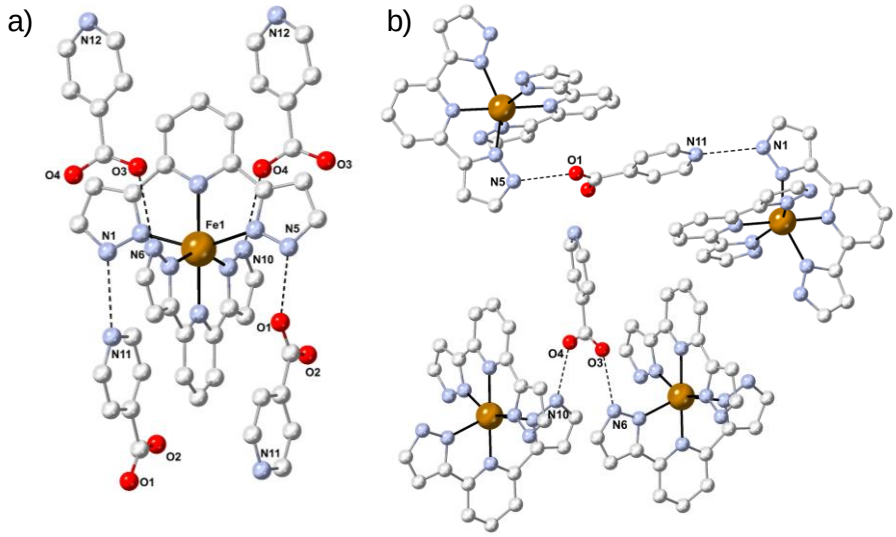

Figure 3.10. View of the crystal structure of **3** at 120 K showing a) the second iron coordination sphere and b) the binding modes of the two inequivalent isonicotinate anions. Dashed lines refer to hydrogen bonds.

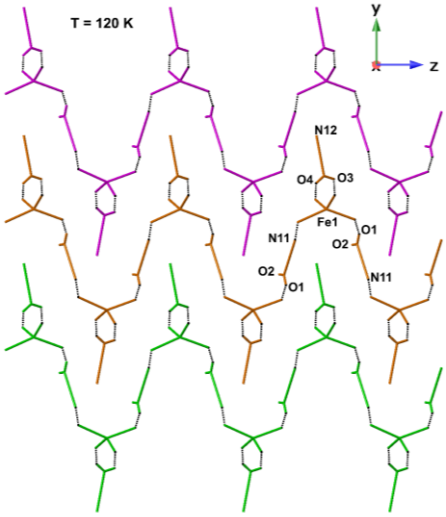

Figure 3.11. Schematic view of the 2D crystal packing of **3** in the *yz* plane showing each corrugated layer in a different colour at 120 K. $[Fe(bpp)_2]^{2+}$ cations are illustrated as FeH_4 tetrahedra. Only the carboxylate fragment and the pyridine nitrogen atom of the isonicotinate anions are shown. Dashed lines refer to hydrogen bonds.

The mechanism of the SCSC transformation can be visualised as follows: upon loss of water molecules, half of the isonicotinate anions lose their H-bond through the pyridine unit and bind to two neighbouring Fe(II) complexes using a bridging carboxylate fragment in a *syn*,*syn*-bidentate mode. This brings the adjacent $[Fe(bpp)_2]^{2+}$ complexes into short contact (Fe1–Fe1 distance of 8.002(1) Å), giving rise to chains of $[Fe(bpp)_2]^{2+}$ subunits running along the *a* axis where π-π stacking interactions can be satisfied with a distance between centroids of 3.45(4) Å. Simultaneously, along the *c* axis the iron centres are also linked by weaker π-π interactions (distance between centroids: 3.45(3) Å, Fe1–Fe1 distance of 8.114(1) Å). Therefore, the driving force for this transformation is the establishment of the *terpyridine embrace* motif (Figure 3.12). Another effect induced by this transformation is that the iron(II) cations become equivalent, thereby halving the volume of the unit cell (V = 3296.93 Å^3 for **3**·2H_2O and V = 1683.46 Å^3 for **3**).

At 338 K, **3** crystallises in the same space group that at 120 K (Table 3.4), with slightly higher values of cell parameters. The cell volume increase from the value obtained at 120 K is about 3.63%. The Fe1–N bond lengths (Table 3.6) and the Σ value (138.04°) increase considerably in comparison with the values observed in the low-temperature phase (Figure 3.13), and the *trans* N–Fe1–N angle

decreases considerably (φ = 177.31°). Fe1–N bond distances exhibit an average value of 2.14(4) Å, which is intermediate between the high-spin and low-spin states. Indeed, the octahedral distorsion parameters are in the range where the cations can be considered as "mixed spin". In this case, both LS and HS cations occupy the same site within the lattice in a random distribution, preventing the observation of two crystallographically independent iron centres.[18] This indicates that at 120 K all the iron cations are in the LS state, whereas at 338 K these values are intermediate between those described for HS and LS species, suggesting that a partial SCO takes place between both temperatures.

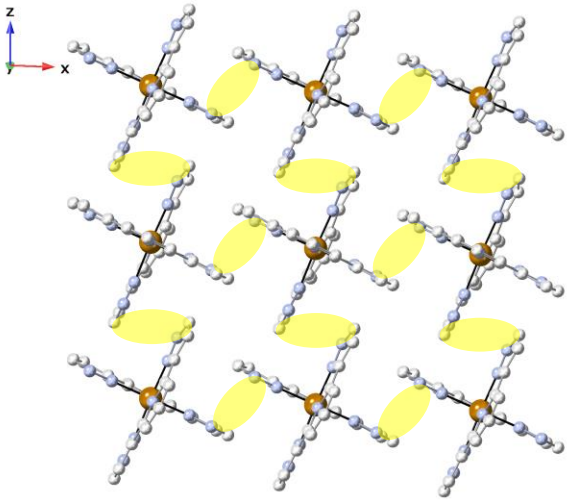

Figure 3.12. View of the crystal structure of **3** at 120 K showing the terpyridine embrace motif where each $[Fe(bpp)_2]^{2+}$ complex is connected to four adjacent equivalent units via $\pi\cdots\pi$ stacking interactions (indicated in yellow).

Table 3.6. Fe1–N bond distances of **3** at 338 K and 120 K.

	3 (338 K)	**3** (120 K)
Fe1–N2	2.176(6)	1.970(4)
Fe1–N3	2.099(4)	1.920(3)
Fe1–N4	2.149(6)	1.981(4)
Fe1–N7	2.153(6)	1.966(4)
Fe1–N8	2.107(4)	1.918(3)
Fe1–N9	2.184(5)	1.973(4)

The Fe1–Fe1 distance between adjacent stacks along the *a* axis increases from 8.002 Å at 120 K to 8.147 Å at 338 K. Similarly, the interplanar metallic distance along the *b* axis increases as the crystal is warmed (from 8.114 Å to 8.443 Å).

This can be explained as a consequence of both thermal expansion and SCO of some Fe1 sites, being more pronounced the expansion of the structure between the corrugated layers. However, the Fe1–Fe1 intralayer distance along the *c* axis decreases as warming up the sample from 12.969 Å to 12.608 Å. In addition, the *terpyridine embrace* motif is still observed at 338 K but with higher distances between centroids of adjacent pyrazolyl fragments of $[Fe(bpp)_2]^{2+}$ stacks along the *a* and *c* axis (3.49(2) Å and 3.62(7) Å, respectively).

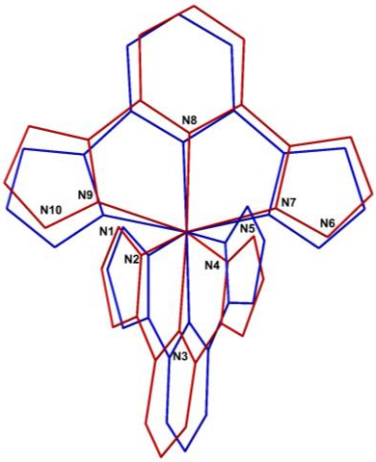

Figure 3.13. Superposition of the stick view of **3** at 338 K (red) and 120 K (blue), showing the coordination environment of Fe1.

A comparative view of the corrugated layers in the *xy* plane at both temperatures highlights other differences concerning the bidentate anions (Figure 3.14). In the high temperature phase, the interplanar distances between O3–O3 and O4–O4 oxygen atoms are shorter and the distance between N12–N12 nitrogen atoms is bigger (Table 3.7). These observations can be explained considering a displacive movement of the bidentate anions (indicated in Figure 3.14 by black arrows). In order to decrease the distance between O3 and O4 atoms, half of the bidentate anions rise upward whereas the other half deviate downward when heating the sample. As a consequence of this relative displacement, the distance between adjacent iron centres within the same layer is decreased, whereas the distance between the pyridine fragments of different layers increases.

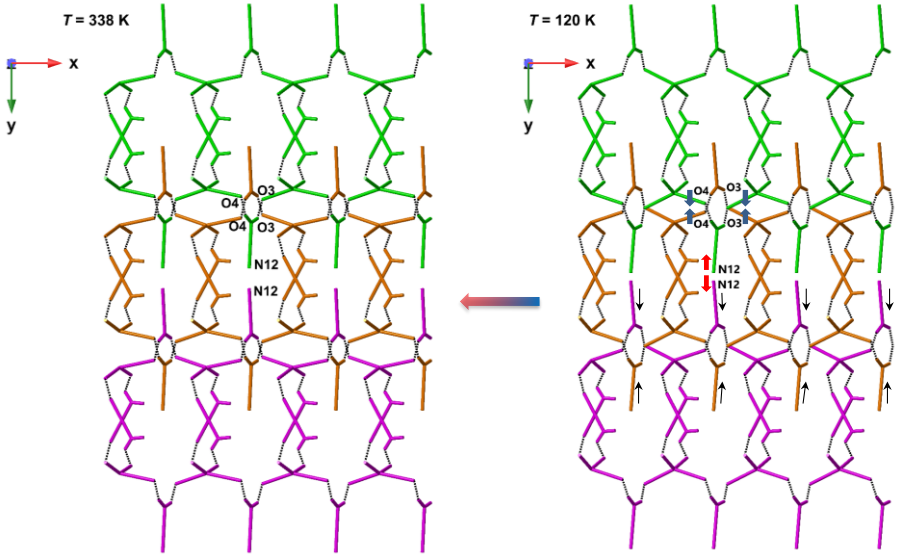

Figure 3.14. Projection of the crystal structure of **3** along the *c* axis showing a schematic representation of the crystal packing at 338 K (left) and 120 K (right). Black arrows represent the displacive movement of the bidentate anions.

Table 3.7. Changes observed in distances between the structures of **3** at 338 K and 120 K.

Distance / Å	**3** at 338 K	**3** at 120 K
d(O3–O3)	8.002(9)	8.346(5)
d(O4–O4)	7.865(9)	8.025(4)
d(N12–N12)	7.95(3)	7.643(9)
d(Fe1–Fe1) (*a* axis)	8.147(1)	8.002(1)
d(Fe1–Fe1) (*b* axis)	8.443(1)	8.114(1)
d(Fe1–Fe1) (*c* axis)	12.608(1)	12.969(1)

The examination of the hydrogen bonds between the four NH pyrazole functions and the four H-bond acceptors (second iron coordination sphere), reveals that they are stronger in the low-spin phase (mean distance N···Acceptor: 2.669 Å, measured at 120 K) as compared to the structure in which the iron centres are in a mixed state (mean distance N···Acceptor: 2.708 Å, measured at 338 K, Table 3.5). The increase in H-bond strength as the Fe(II) centre undergoes crossover to the LS phase can be simply explained based on an electrostatic model: the LS state presents a lower volume, thus, higher charge density and higher electrostatic attraction to the negative charges of the anions. Therefore, this results in shorter hydrogen bond distances. There is only one reported hydrogen-bonded $[Fe(bpp)_2]^{2+}$ complex in which the HS and LS phases exhibit

an equivalent environment. It is the perchlorate salt with formula $[Fe(bpp)_2](ClO_4)_2 \cdot 1.75CH_3COCH_3 \cdot 1.5Et_2O$, which displays a gradual and incomplete SCO around 205 K between two isostructural phases.[21] Hydrogen bonds are shorter for the LS phase (at 90 K, mean distance N···O: 2.834 Å) with respect to the HS structure (at 250 K, mean distance N···O: 2.871 Å), following the same trend as that observed for compound **3**.

B. Powder X-ray diffraction

Powder X-ray diffraction measurements were performed and Figure 3.15. shows the simulated pattern of **3** from the single crystal X-ray data at 120 K. This diffractogram is in agreement with that obtained experimentally, discarding the presence of impurities and the existence of a phase transition between 120 K and room temperature.

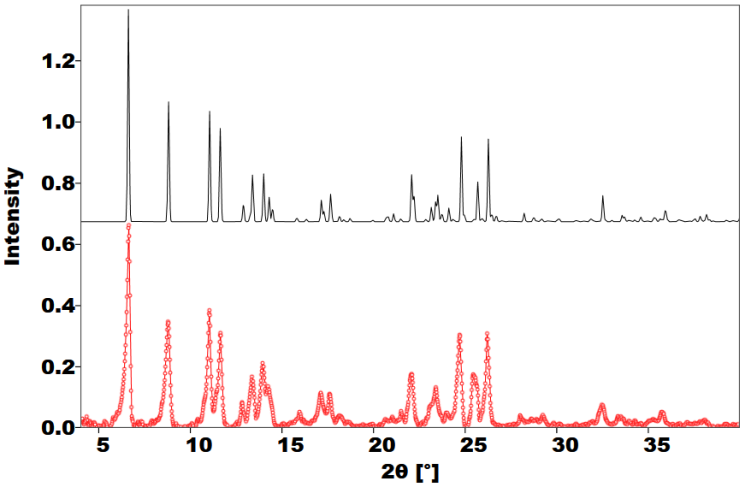

Figure 3.15. Powder X-ray simulation of **3** from single crystal X-ray data at 120 K (black lines). The experimental pattern at room temperature is also included for comparison (in red).

Furthermore, temperature dependent powder X-ray diffraction measurements of anhydrous **3** confirmed the presence of a crystallographic phase transition (Figure 3.16). The diffractograms above (HTP) and below (LTP) the phase transition deduced from DSC measurements (321-324 K) are in agreement with the corresponding simulations from the single crystal data at 338 K and 120 K, respectively. At the same time, both patterns are very similar, suggesting that the HTP and LTP are isostructural with only small differences that are reproduced in the experimental diffractograms.

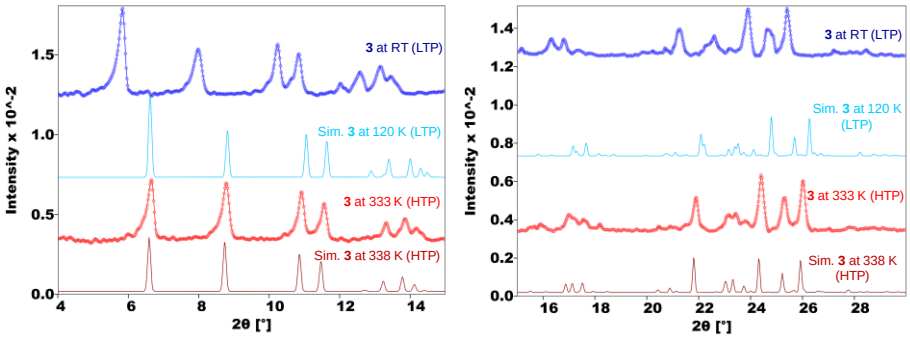

Figure 3.16. Powder X-ray simulations of **3** at 120 K and 338 K from single crystal X-ray data. Experimental patterns at RT and at 333 K are also included for comparison.

3.3.4. Magnetic characterisation of 3

The DSC plot of the as-synthesised material showed a lack of transitions associated to the hydrated material in both cooling and heating modes. Thus, the magnetic properties of **3** were studied after thermal dehydration in a sealed tube at 453 K under vacuum. The temperature dependence of the χT product is typical of a diamagnetic LS Fe(II) complex at low temperatures (Figure 3.17).

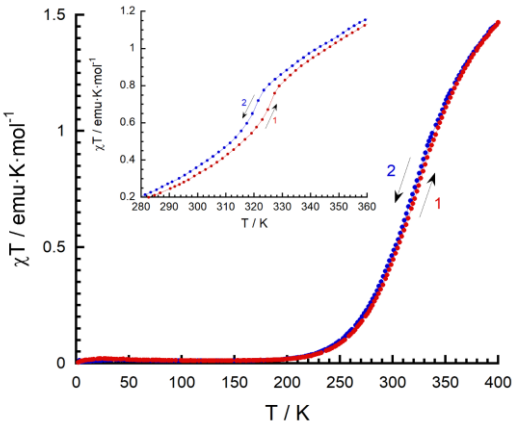

Figure 3.17. Thermal variation of the χT product for **3**. The inset shows a zoom in the spin crossover temperature range.

Above 200 K, χT increases continuously (curve 1) in the heating mode up to 400 K. At this point, χT has a value of 1.46 emu·K·mol^{-1}, lower than that expected for a high-spin Fe^{2+} cation per formula (3.0 emu·K·mol^{-1}). This indicates that the spin crossover is not complete at this temperature (saturation of the signal is not reached at the maximum temperature of 400 K). A critical point is observed at

324 K (inset Figure 3.17), which is attributed to the crystallographic phase transition detected by DSC and XRD measurements. The cooling plot (curve 2) shows the reversibility of the process with a small hysteresis around this critical point. These results show a very gradual SCO between 200 K and 400 K that is overlaid with the crystallographic phase transition. As can be clearly seen, the impact of the phase transition in the magnetic properties of the material is very small, which is in agreement with the previous structural analyses.

3.3.5. Dielectric properties and SHG effect of 3

Compound **3** is expected to display dielectric response triggered by temperature as a consequence of the structural changes accompanying the spin transition.[22] **3**·2H_2O was dehydrated *in situ* at 453 K and the temperature dependence of the real part (ε') of the dielectric constant and the dielectric loss taken at 10 KHz in the cooling mode (Figure 3.18). A very weak dielectric anomaly at approximately 323 K (50 °C) upon cooling is observed in both cases, which is consistent with the DSC feature and the critical point observed in the magnetic properties. However, the dielectric hysteresis was not obtained, probably because of the relatively weak cooperativity of the system and small thermal hysteresis loop.[23]

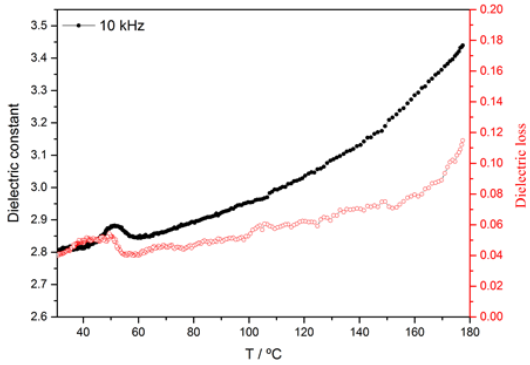

Figure 3.18. Temperature dependence of the real part of the dielectric constant and dielectric loss at 10 KHz for compound **3**.

The magnitude of the dielectric variation is related to the characteristics of the transition itself. In the present case, the phase transition occurs with a small relative displacement of the anions and without change of the polar *Pc* space group, being the weak dielectric anomalies found for **3** in agreement with the described behaviour. This excludes the existence of a ferroelectric transition that

would require a change from a centrosymmetric structure above T_c to a noncentrosymmetric one below T_c.

In addition, the second harmonic generation (SHG) was studied on a powder sample of **3**·2H$_2$O (Figure 3.19). It is only allowed in crystals without inversion symmetry, thus, being a powerful method of testing if crystalline materials exhibit centre of symmetry or not.[24] The original sample is SHG-active, as well as the anhydrous material at 453 K, 348 K and 311 K. These results confirm that both HTP and LTP are noncentrosymmetric, further verifying the absence of a ferroelectric transition.

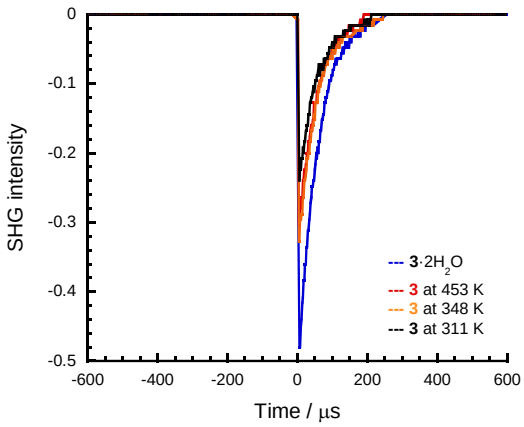

Figure 3.19. Second harmonic generation (SHG) signal of polycrystalline **3**·2H$_2$O at RT and **3** at different temperatures.

3.3.6. Domain structures and polarisation reversal of 3

In agreement with the polar character of its crystal structure, **3** displays ferroelectric behaviour. In this context, piezoresponse force microscopy (PFM) is an extremely useful method, since it offers a visualisation of the micro-scale domain structure.[25] The vertical PFM amplitude and phase images allow examination of the magnitude of the piezoelectric response and the orientation of the polarisation, respectively. First, a film of **3**·2H$_2$O was prepared and its piezoresponse registered, which is relatively low (Figure 3.20.a). Its phase image exhibits uniform contrast, indicating an absence of any ferroelectric domain structure (Figure 3.21.a). This means that the hydrated material is piezoelectric but not ferroelectric, which is consistent with the assigned $I\bar{4}$ space group.

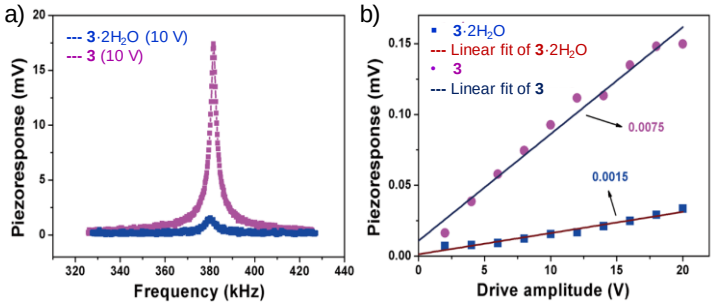

Figure 3.20. Comparison of a) PFM resonance peaks and b) effective piezoelectric coefficient of films of **3** and **3**·2H_2O.

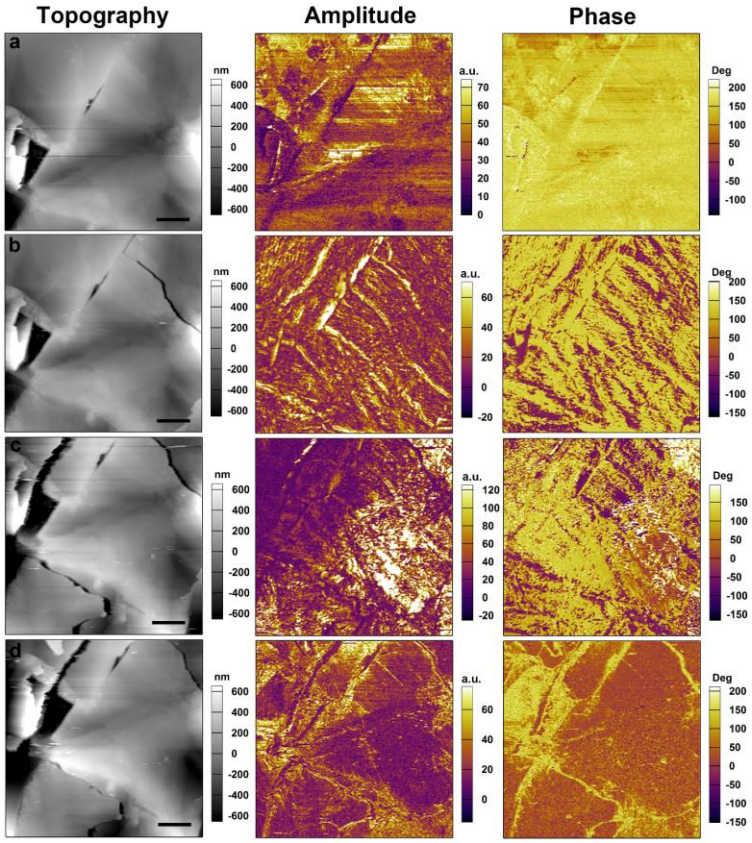

Figure 3.21. Temperature dependence of the domain structure of the thin film: topography (left), vertical PFM amplitude (middle), vertical PFM phase (right). a) Images for the as-grown state (in **3**·2H_2O). Images obtained after heating to 453 K and cooling back to b) 385 K (in the HTP of **3**) and c) 298 K (in the LTP of **3**). d) Images recorded at 298 K after staying in ambient condition for 12 hours (returning to **3**·2H_2O). Scale bar: 10 μm.

Secondly, after thermal treatment, anhydrous **3** exhibits an enhanced piezoelectric signal at 385 K (in the HTP, Figure 3.20.a). The film was driven across resonance using PFM and the resonance curve fitted properly to the damped harmonic oscillator model. Then, the intrinsic piezoresponse was plotted with respect to the driving voltage and a good linearity was obtained for both compounds (Figure 3.20.b). This confirms that the response is piezoelectric. Comparing the response of the two compounds, the slope of **3** is five times higher than that of **3**·2H_2O, presenting the anhydrous material an increased effective piezoelectric coefficient. Furthermore, an evident dipolar domain structure appears, as revealed in the phase image of Figure 3.21.b.

In order to study the ferroelectricity of **3**, the vertical (out-of-plane) and lateral (in-plane) PFM images for the film at 385 K have been acquired, being the image of the domain patterns exactly the same in the two configurations (Figure 3.22).

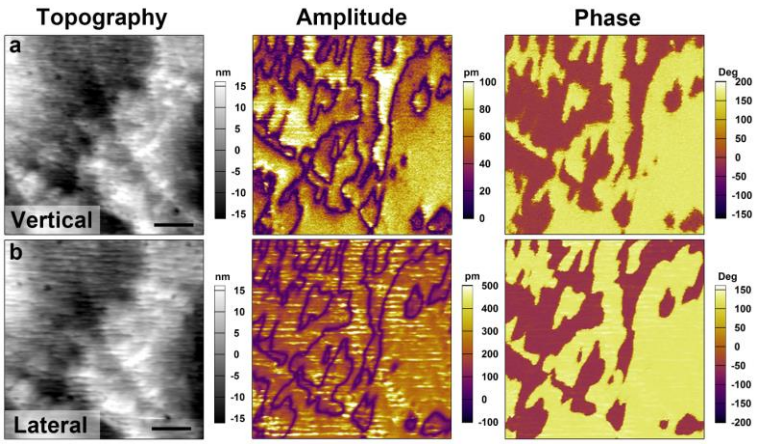

Figure 3.22. a) Vertical and b) lateral PFM phase and amplitude images in the thin film of **3** at 385 K. The images have been acquired over an area of 5 μm × 5 μm. Scale bar: 1 μm.

In the phase images, the 180° phase contrast indicates that the polarisation in two adjacent domains are antiparallel, whereas dark features in the amplitude contrast reveal the existence of domain walls. Note that there is no difference for the signals in the two consecutive domains on both sides of the domain walls. On the other hand, the vertical PFM phase and amplitude mappings have been overlaid on 3D topography to demonstrate that the piezoresponse has no obvious correlation with the topology of the sample surface (Figure 3.23). Therefore, the presence of ferroelectric domains in the HTP of **3** can be unambiguously stated.

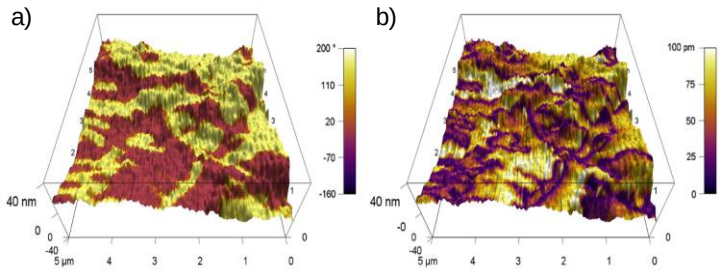

Figure 3.23. a) Vertical PFM phase and b) amplitude mappings overlaid on the 3D topography in the film of **3** at 385 K.

Indeed, bipolar piezoelectric hysteresis loops triggered by the applied voltage could be obtained for this compound (Figure 3.24.b and c), which is typical of the polarisation reversal of ferroelectric domains.

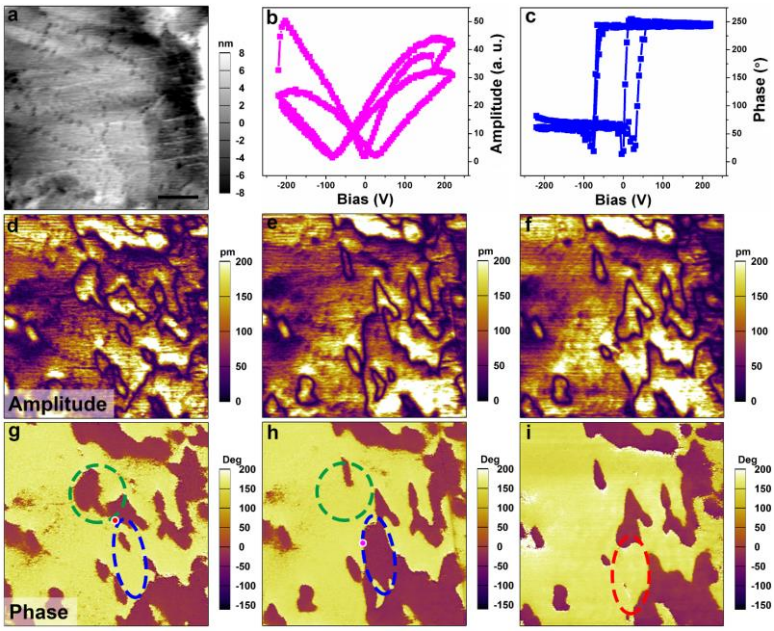

Figure 3.24. Polarization reversal of **3** measured from the film at 385 K. The panels in each row are arranged as the following sequence: a) topographic image and b), c) single-point PFM hysteresis loops (top), then vertical PFM amplitude (middle) and last phase (bottom) images of the film surface. d), g) Initial state. e), h) After the first switching with positive bias at +200 V for 2 s. Bias was applied at the position marked with a red dot in Figure 2g. f), i) After the succeeding switching with negative bias at −200 V for 2 s. Bias was applied at the position marked with a pink dot in Figure 3.24.h. Yellow and purple regions in phase images indicate the regions with polarisation oriented upward and downward, respectively. Scale bar: 1 µm.

Furthermore, local manipulation experiments on the film surface were conducted in order to visualise the domain switching process. A tip bias of +200 V was applied and the polarisation directions of the regions illustrated by blue and green dashed ellipses in Figures 3.24 (g and h) were switched, as evidenced by the change in the colour contrast observed in the phase images (from yellow to dark red and from dark red to yellow, respectively). At the same time, this process can be also observed from the domain wall motions shown in the amplitude images (Figures 3.24.d and e). Upon subsequent application of a negative bias of -200 V at the position marked with a red dot (Figure 3.24.i), the polarisation direction of the region defined by a red dashed ellipse could also be reversed. This means that the polarisation in some domains can be switched forth and back in a reversible way. After cooling down to 298 K quickly, the LTP of **3** still exhibits electrically switchable spontaneous polarisation, as evidenced by the typical hysteresis and butterfly loops obtained from local PFM spectroscopic measurements (Figure 3.25). Accordingly, the dipolar domain structure is still preserved (Figure 3.21.c). Therefore, the LTP of **3** is also ferroelectric and the phase transition is a ferroelectric-to-ferroelectric one. However, the amplitude becomes weaker in some areas, which may indicate that the film starts to undergo rehydration. In fact, after being 12 h under ambient conditions, the phase and amplitude signals both lack of any ferroelectric domain structure and there is a clear correlation with the local topology of the sample surface (Figure 3.21.d). This suggests that the film has been completely rehydrated, recovering the original *I*–4 space group that is only piezoelectric.

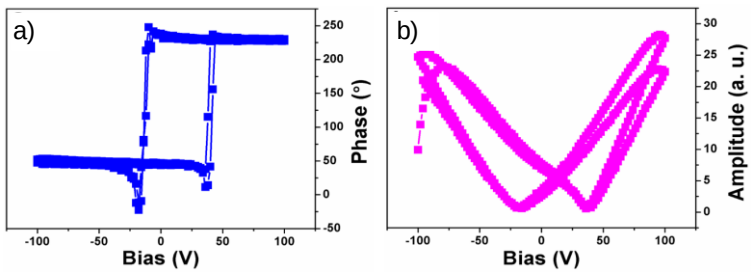

Figure 3.25. Vertical a) phase and b) amplitude signals as functions of the tip voltage for a selected point, showing the local PFM hysteresis loops for the LTP of **3** at 298 K.

3.3.7. Discussion 3·2H$_2$O and 3

The original compound (**3**·2H$_2$O) is low-spin in the whole thermal range of study. It undergoes a reversible single-crystal-to-single-crystal transformation upon dehydration, which can be rationalised through the loss

and gain of hydrogen bonds, being the driving force for the dehydration process the formation of the *terpyridine embrace* motif. This anhydrous phase is low-spin at 120 K and its thermal treatment resulted in the appearance of a gradual population of high-spin centres increasing up to γ_{HS} = 0.5 between 200 K and 400 K. At 325K, a small hysteresis loop opens, which is ascribed to the crystallographic phase transition revealed by XRD measurements. The structural origin of this transition is a displacive movement of the isonicotinate anions and accounts for the sharp and intense features observed in DSC measurements. However, this transition is decoupled with the Fe(II) spin state, having a small impact on the magnetic properties of the material. At 338 K, a "mixed spin" phase is obtained with a random distribution of HS and LS centres. While the original hydrated material is noncentrosymmetric (*I*–4 space group), the anhydrous phases are polar (*Pc* space group) in both HTP and LTP. Accordingly, the hydrated material exhibits piezoelectricity and the anhydrous phases display ferroelectric behaviour, although the effect of the phase transition on the ferroelectric properties has not been clearly elucidated (Scheme 3.3).

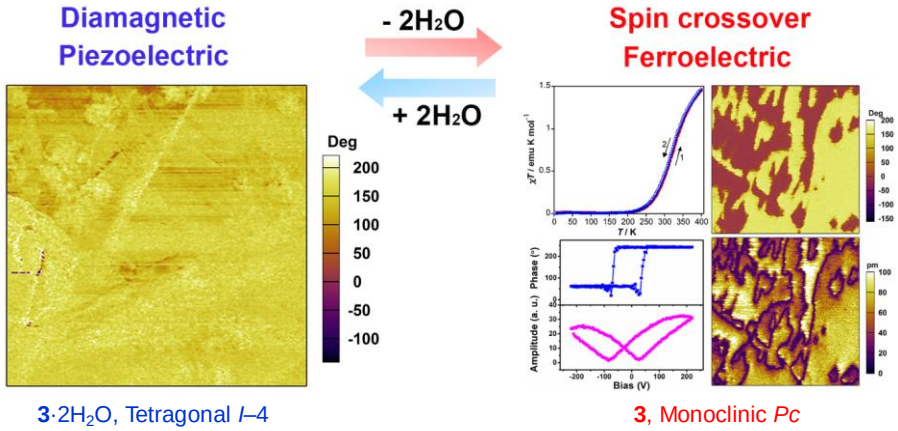

Scheme 3.3. Schematic representation of the dehydration/rehydration process in **3**·2H₂O, detailing the changes observed between both compounds.

The transition between the two ferroelectric anhydrous phases takes place in the same temperature range than the spin crossover, being this the first dual-function material combining ferroelectricity and spin crossover.

3.3.8. Structural characterisation of 4·4H$_2$O

A. Single crystal X-ray diffraction

4·4H$_2$O crystallises in the noncentrosymmetric and polar *Pc* monoclinic space group (Table 3.8). The crystal structure comprises isolated [Fe(bpp)$_2$]$^{2+}$ cations, nicotinate anions and water molecules. In the asymmetric unit there is only one inequivalent Fe(II) centre, Fe1, two independent nicotinate anions and four water molecules. The Fe^{2+} cation is located in a general position and its coordination environment is very similar to that described for **3**·2H$_2$O (octahedral FeN$_6$, bound to two bpp tridentate ligands in mutual perpendicular orientations, being the dihedral angle between planes that contain each bpp ligand of 89.35°).

Table 3.8. Crystallographic data and structural refinement for **4**·4H$_2$O

	4·4H$_2$O
Empirical formula	$C_{34}H_{34}FeN_{12}O_8$
Formula weight	794.58
Crystallographic system	Monoclinic
Space group	*Pc* (No. 7)
a/ Å	8.17633(10)
b/ Å	8.15854(9)
c/ Å	26.9671(3)
α/ °	90
β/ °	92.0138(10)
γ/ °	90
V/ Å^3	1797.78(4)
Z	2
R(int)	0.0635
ρ_{calc}/ g·cm^{-3}	1.468
μ/ mm^{-1}	0.490
Crystal dimensions/ mm	0.2006 x 0. 1469 x 0. 1130
T/ K	119.95(10)
λ/ Å	0. 71073
2θ range/ °	5.74< 2θ <59.93
Index ranges for h, k , l	-11/11, -11/11, -37/37
Refinement method	Full-matrix least-squares on F^2
Collected reflections	84313
Unique reflections	9867
Data/Restraints/Parameters	9867/18 / 532
Goodness-of-fit on F^2	1.055
R1, wR2 [I > 2sigma(l)][a]	0.0324/0.0664
R1, wR2 (all data)[a]	0.0398/0.0711
$\Delta\rho_{max}$ and $\Delta\rho_{min}$ (e·Å^{-3})	0.265/ -0.395
Absolute structure parameter	-0.016(5)

[a] $R1 = \Sigma(||F_o| - |F_c||)/\Sigma|F_o|$; $wR2 = \{\Sigma[w(F_o^2 - F_c^2)^2]/\Sigma[w(F_o^2)^2]\}^{1/2}$

Fe1–N bond distances range from 1.925(3) Å to 1.971(2) Å, indicating a low-spin ground state for the Fe^{2+} cation as expected for a hydrated $[Fe(bpp)_2]^{2+}$ complex. This spin state has been verified by the values obtained for the distortion parameters Σ and φ (Σ = 93.87°, φ = 177.95°), which are very similar to those obtained for **3**·$2H_2O$ and typical for low-spin configurations.

Regarding the second iron coordination sphere (Figure 3.26), it is markedly different in comparison with **3**·$2H_2O$. Each cationic subunit is hydrogen-bonded to only two (instead of four) nicotinate anions (N5···O1: 2.662(3) Å, N10···O4: 2.635(3) Å) and the remaining positions are occupied by two water molecules (N1···O3W: 2.633(3) Å, N6···O4W: 2.671(3) Å). The nitrogen atom of the nicotinate anions is not interacting with the $[Fe(bpp)_2]^{2+}$ complexes, instead is engaged in hydrogen bonds with water molecules (O1W···N11: 2.987(4) Å, O2W···N12: 2.900(4) Å). Therefore, in this case the diamond-like structure has not been formed as a consequence of the unpredictable establishment of hydrogen bonds with water molecules.

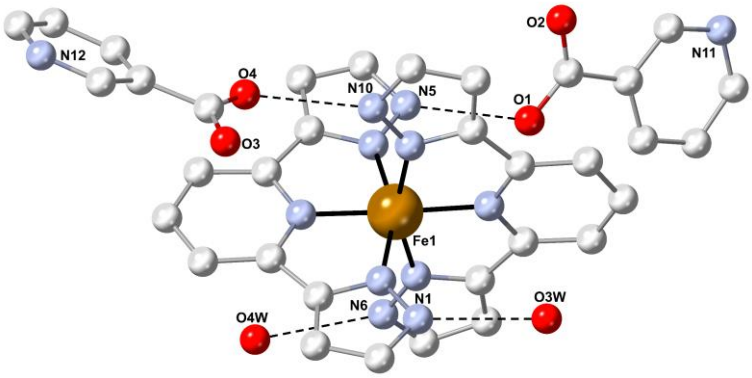

Figure 3.26. Crystal structure of **4**·$4H_2O$ showing the $[Fe(bpp)_2]^{2+}$ complex, the two crystallographically inequivalent anions and the two water molecules present in the second iron coordination sphere. Dashed lines refer to hydrogen bonds.

The crystal structure can be described as a packing of cationic and anionic layers that alternate along the *c* axis (Figure 3.27). These layers are held together by the presence of hydrogen bonds, either directly or involving water molecules of crystallisation. Table 3.9 contains relevant hydrogen-bonding parameters.

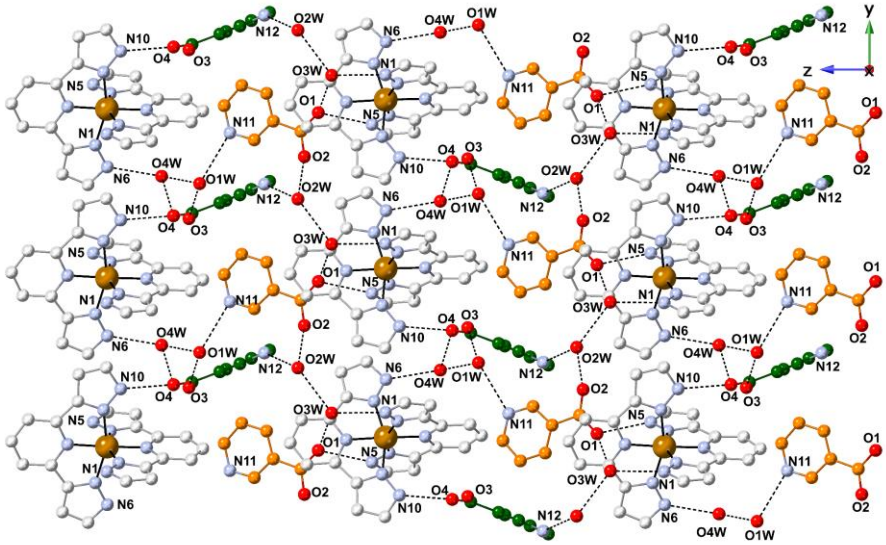

Figure 3.27. A view of the crystal structure of **4**·4H_2O along the *a* axis, showing the alternation of $[Fe(bpp)_2]^{2+}$ cationic layers and nicotinate anionic layers. The two inequivalent nicotinate anions are illustrated in orange and green. Dashed lines refer to hydrogen bonds.

Table 3.9. Intermolecular hydrogen bonds present in **4**·4H_2O (D-H···A).

D···A	$d_{D\cdots A}$ / Å
N1···O3W	2.633(3)
N5···O1#1	2.662(3)
N6···O4W#2	2.671(3)
N10···O4	2.635(3)
O1W···O3#3	2.757(3)
O1W···N11	2.987(4)
O2W···O2#4	2.745(3)
O2W···N12#5	2.900(4)
O3W···O2W	2.722(3)
O3W···O1	2.749(3)
O4W···O1W	2.778(3)
O4W···O4#6	2.764(3)

Symmetry transformations used to generate equivalent atoms: #1 x – 1, y, z; #2 x – 1, – y + 1, z – 1/2; #3 x, – y, z + 1/2; #4 x, y + 1, z; #5 x, – y + 1, z + 1/2; #6 x + 1, – y, z + 1/2

A view perpendicular to the sheets shows that the cationic layers exhibit the typical *terpyridine embrace* motif, interacting each $[Fe(bpp)_2]^{2+}$ complex with four neighbouring iron subunits *via* π-π stacking interactions (Figure 3.28). Equivalent bpp ligands form stacks along the *a* and *b* axes with a distance between the centroid coordinates defined by each pyrazolyl ring of 3.710(8) Å and 3.686(7) Å, respectively. Across the third direction, the iron complexes of

adjacent layers are twisted with respect to each other and shifted along the *b* axis, leading to an alternated packing of the AA'AA' type.

The connectivity of the two independent nicotinate anions can be seen in Figure 3.27. The first one (illustrated in orange) is hydrogen-bonded to three water molecules (O1W, O2W and O3W) and one $[Fe(bpp)_2]^{2+}$ complex (N5). In a similar way, the second nicotinate anion (depicted in green) is also hydrogen-bonded to three water molecules (O1W, O2W and O4W) and one $[Fe(bpp)_2]^{2+}$ cation (N10). Thus, the common feature is that they are only interacting with one Fe^{2+} centre through a carboxylate oxygen atom that is simultaneously hydrogen-bonded to one water molecule. The other oxygen atom and the nitrogen of the pyridine unit are engaged in hydrogen bonding with additional water molecules. Both anions occupy the space between the cationic layers and alternate along the *y* direction.

A view of the crystal structure in the *xy* plane shows the presence of two different types of water molecules (Figure 3.29): those forming the layers through direct hydrogen bonds with the bpp ligands (O3W and O4W), and those filling the voids within the layers (O1W and O2W).

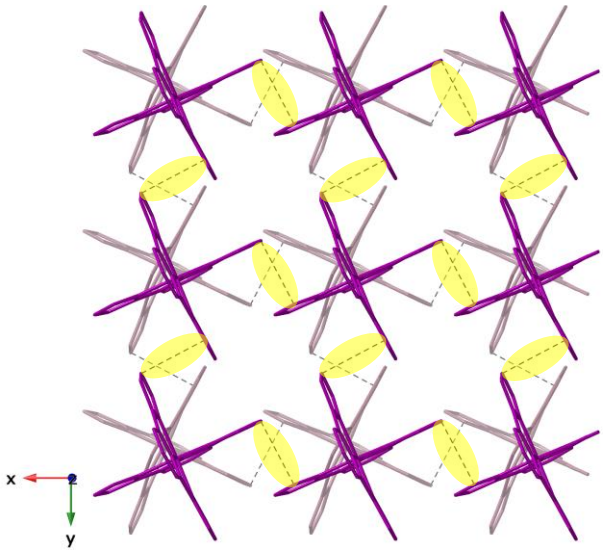

Figure 3.28. Stick view of the crystal structure of **4**·4H_2O in the *xy* plane showing two consecutive $[Fe(bpp)_2]^{2+}$ cationic layers (nicotinate anions and water molecules are omitted). Dashed lines represent π-π interactions. In yellow are highlighted π-π interactions involving the first cationic layer (dark-coloured).

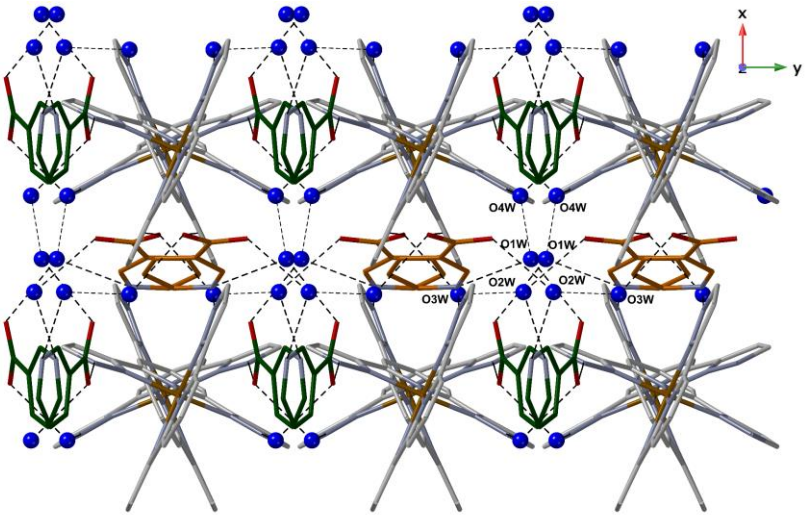

Figure 3.29. Stick view of the 2D packing of **4**·4H_2O in the *xy* plane showing the two different types of water molecules that are represented by blue balls. The two inequivalent nicotinate anions are illustrated in orange and green. Dashed lines represent hydrogen bonds.

On the account of the polar character of its crystal structure, piezoresponse force microscopy (PFM) was used to study its ferroelectric behaviour. Nevertheless, its phase image exhibits uniform contrast, indicating a lack of any ferroelectric domain structure. Probably, the crystal structure of the material is not preserved in the thin films used for PFM measurements.

B. Thermal properties

TG analysis of **4**·4H_2O was performed under nitrogen atmosphere (Figure 3.30.a) in order to determine the temperature range of stability of the compound and the most suitable thermal conditions for magnetic experiments. The first weight loss occurs at 327 K with a decrease of 6.30%, which is attributed to the loss of approximately three water molecules per iron cation (calculated: 6.80%). The fourth water molecule comes off at higher temperatures (observed: 2.20%, calculated: 2.43%), in the 443-493 K temperature range which is near the thermal decomposition of the sample. In total, four water molecules per iron cation, in agreement with the formula obtained from the X-ray crystal structure experiment. In addition, these results suggest the presence of different types of water molecules in the crystal structure.

DSC measurements were also conducted (Figure 3.30.b). The as-synthesised material does not present any feature during the cooling mode down to 133 K

(black line). In the first heating process (curve 1), an intense endothermic peak is observed at 334 K. According to TG data, desolvation of the material takes place in this temperature range, then, this endothermic peak is ascribed to the dehydration of the sample. In the subsequent cooling process (curve 2), a broad feature between 373 K and 323 K is registered, in addition to three very weak exothermic peaks at 282 K, 262 K and 218 K. The intensities exhibited by these peaks are very low, indicating either the existence of a partial spin crossover or the signature of a phase transition. The second heating process (curve 3) shows three endothermic peaks at 229 K, 264 K and 289 K, meaning that these transformations are reversible and proceed with thermal hysteresis. Corresponding values of enthalpy and entropy are gathered in Table 3.10. Calculated values for curve 1 are much higher than the others, in agreement with the fact that it includes the dehydration enthalpy/entropy, being both values similar to those obtained for **3**·2H_2O. For curves 2 and 3, considering the sum of the contributions of the three peaks, a total enthalpy and entropy values of 4.8 kJ·mol^{-1} and 20.6 J·K^{-1}·mol^{-1} were obtained, respectively (calculated as average values from the cooling and warming curves). These parameters are low but lie within the range expected for a spin crossover process.[20]

Table 3.10. Enthalpy and entropy changes observed for DSC measurements of **4**·4H_2O.

Curve	T_{peak}/ K	ΔH / kJ·mol^{-1}	ΔS / J·mol^{-1}·K^{-1}
1	334	147	450
2	218/262/282	0.54/1.53/2.2	5.50/6.30/8.33
3	229/264/289	1.0/1.28/3.1	5.50/5.24/10.4

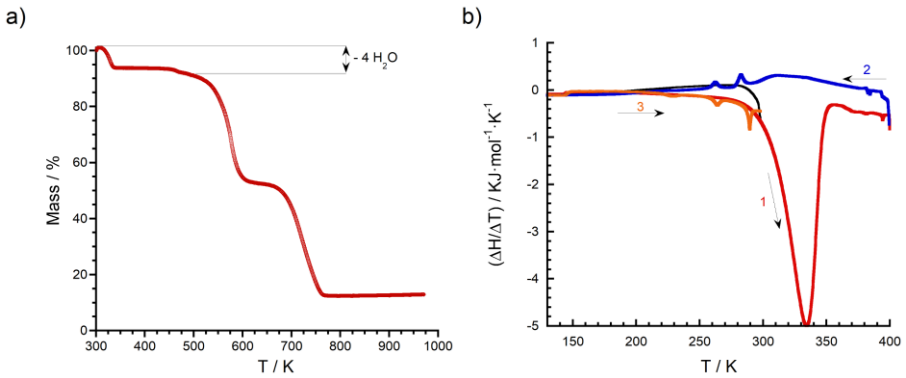

Figure 3.30. a) Thermogravimetric analysis of **4**·4H_2O. b) Differential scanning calorimetry curve of **4**·4H_2O. Black line: cooling down to 133 K. Curves 1 and 2: First heating and cooling processes, respectively. Curve 3: second heating process.

C. Powder X-ray diffraction

The comparison between the X-ray pattern measured at room temperature of **4**·4H_2O and the simulation from the single crystal data recorded at 120 K (Figure 3.31) indicates that the bulk sample is pure and excludes the existence of a phase transition within this temperature range (RT-120 K).

Furthermore, in order to check if it was possible to dehydrate **4**·4H_2O without resulting in an amorphisation of the sample, powder X-ray diffraction measurements were conducted at different temperatures. Figure 3.32 shows that the material exhibits the same pattern upon heating from 298 K to 353 K. At this point, according to TG data, three water molecules have been removed. Instead, heating at 400 K results in a complete loss of the crystallinity (Figure 3.32.a), which has to be a consequence of complete dehydration (loss of the fourth water molecule). However, TG measurements showed that the fourth water molecule is lost at higher temperatures (443-493 K). This discrepancy arises because TG measurements are carried out at a high-temperature sweeping rate, whereas PXRD is performed under static conditions.

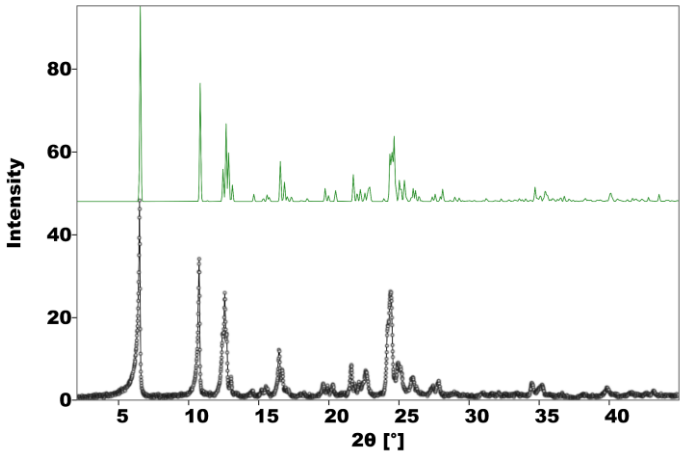

Figure 3.31. Comparison of the experimental powder diffractogram of **4**·4H_2O (black dots) with the simulation obtained from single crystal data (green lines).

On the other hand, the reversibility of the dehydration-rehydration process was also studied. After thermal dehydration at 400 K for 2 h, the anhydrous material was allowed to rehydrate at ambient conditions. The diffractogram of the rehydrated sample is identical to that obtained for the original compound (Figure 3.32.b), confirming both the integrity of the sample and the reversibility

of the process. A second dehydration-rehydration cycle was performed, revealing the same behaviour.

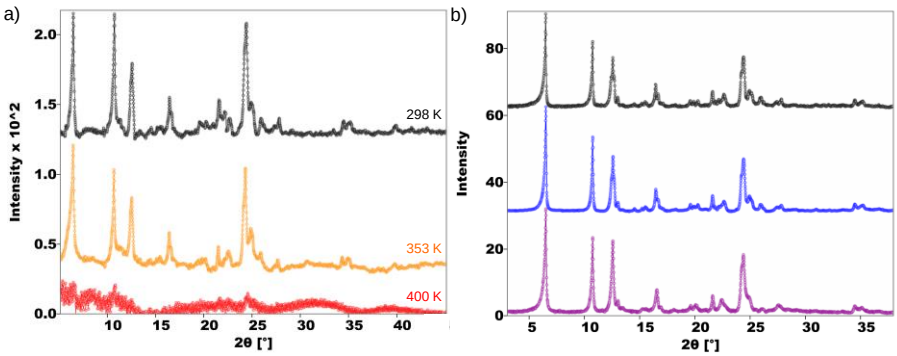

Figure 3.32. a) Powder X-ray diffractograms of **4**·4H$_2$O at different temperatures. b) Room temperature powder X-ray diffractogram of **4**·4H$_2$O as-synthesised (black dots), after dehydration under vacuum at 400 K for 2 h and subsequent rehydration (blue dots) and after a second dehydration-rehydration cycle (purple dots).

3.3.9. Magnetic characterisation of 4·4H$_2$O

A. Magnetic properties

The temperature dependence of the χT product of **4**·4H$_2$O is shown in Figure 3.33. At low temperatures, the sample is diamagnetic, in agreement with the low-spin ground state determined for this Fe(II) complex from XRD at 120 K. Above 300 K, the magnetic signal starts to increase continuously and reaches a value of 3.21 emu·K·mol^{-1} at 400 K (curve 1, the sample was held at 400 K for 1 h). This value indicates a complete spin crossover to the high-spin state triggered by the dehydration of the sample. During the cooling process (curve 2), the magnetic signal decreases smoothly and a critical point at 283 K is observed (exactly at the same temperature at which the first feature is observed in DSC, cooling mode). At this point, χT has a value of 2.21 emu·K·mol^{-1}, corresponding to a fraction of high-spin centres (γ_{HS}) of approximately 2/3. Then, it decreases more abruptly until T = 273 K and continuously again until reaching a plateau below 83 K where χT is equal to 0.41 emu·K·mol^{-1} ($\gamma_{HS} \approx 1/8$). Below 15 K, a sharp decrease is observed as a consequence of the zero-field splitting of the remaining 12.5% of Fe^{2+} centres in the high-spin state.

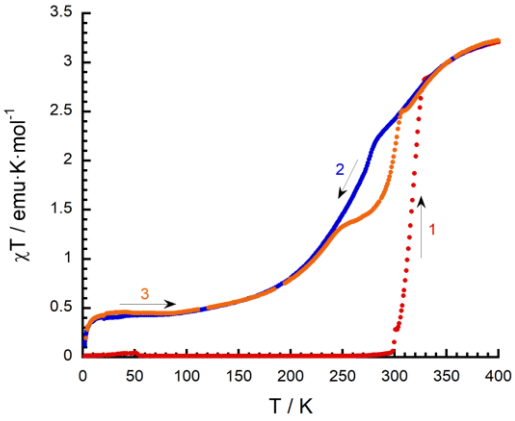

Figure 3.33. Thermal variation of the χT product of **4**·4H$_2$O. Curve 1: first heating process. Curves 2 and 3: first cooling and second heating processes, respectively.

The second heating process (curve 3) matches the cooling curve until 245 K, above this temperature a hysteresis loops opens (ΔT = 30 K). At 307 K the cooling and heating curves merge and practically saturation of the signal is reached, yielding a χT value corresponding to 100% of the iron centres in the high-spin state.

B. Photomagnetic properties

The sample was dehydrated in situ in the SQUID magnetometer at 400 K for 1 h prior to its irradiation at 10 K (Figure 3.34). Initially, almost all the iron centres were in the LS state at this temperature. Upon irradiation with a green laser light (λ = 532 nm), an abrupt increase in the magnetic signal was registered and saturation was reached after 3 h. A limiting value of ca. 2 emu·K·mol^{-1} was obtained, indicating that approximately 2/3 of the iron centres undergo crossover to the high-spin state. The fraction of iron centres that does not exhibit photoexcitation (≈ 1/3) corresponds to the fraction of Fe^{2+} centres that undergo SCO above room temperature. Then, the light was switched off and the magnetic response recorded in the dark at a heating rate of 0.3 K·min^{-1}.[26] A T(LIESST) value of 56 K was obtained from the first derivative plot (inset Figure 3.34), which is close to those obtained for compounds **1** and **2** in the previous chapter (61 K and 63 K, respectively). Complete relaxation of the photoinduced high-spin state is observed at higher temperatures, with a χT value of 0.5 emu·K·mol^{-1}. This value is similar to the residual fraction of high-spin centres measured before irradiation (1/8).

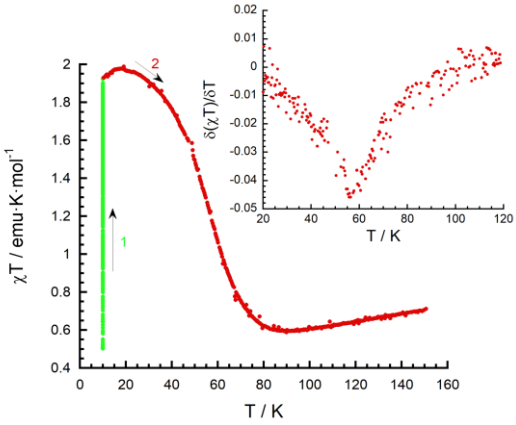

Figure 3.34. Photomagnetic properties of **4**. Curve 1 (green circles): data recorded while irradiation at 10 K with a green laser (no photomagnetic response was observed under red light). Curve 2 (red circles): heating mode without irradiation at a rate of 0.3 K·min^{-1} (T(LIESST) measurement). The inset shows the first derivative of the T(LIESST) plot.

As previously mentioned, the following linear expression governs the photomagnetic properties of most iron(II) spin crossover materials with nitrogen-donor ligands: $T(\text{LIESST}) = T_0 - 0.3 \cdot T_{1/2}$ (Eq. 3.1), being T_0 = 150 K for $[Fe(bpp)_2]^{2+}$ complexes. Considering that $T_{1/2}$ = 281 K (average value between $T_{1/2}^{\uparrow}$ and $T_{1/2}^{\downarrow}$), a value of T(LIESST) equal to 66 K is calculated with this equation, which is in rough agreement with the experimental result.

3.3.10. Discussion 3·2H$_2$O and 4·4H$_2$O

3·2H$_2$O and **4**·4H$_2$O are constructed from isonicotinate and nicotinate anions, respectively. In the first compound, the linearity of the isonicotinate anion allows the establishment of strong hydrogen bonds between the bpp ligands and the isonicotinate anions. Thus, the second iron coordination sphere is occupied by four anions, providing a strong directionality that enables the prediction of the connectivity of the resulting network. However, in the second complex, the angular character of the nicotinate anion hinders the formation of these interactions and water molecules are found in the second iron coordination sphere. The adventitious presence of solvent molecules leads to the formation of unpredictable crystal structures. Another contribution to the different behaviour observed for these similar salts could be the slightly different basicities of the nicotinate (pK_b = 4.77) and isonicotinate (pK_b = 4.90) anions,[14] being the isonicotinate linker a stronger N-donor. With respect to the crystal packing, a relevant difference between both compounds is the existence

of the *terpyridine embrace* motif, which is only present in **4**·4H_2O, where π-π stacking interactions are predominant. Another consequence of the incorporation of water molecules directly interacting with the bpp ligands is that upon solvent removal, **4**·4H_2O loses its crystallinity whereas **3**·2H_2O preserves it.

3.3.11. Conclusions and perspectives

Following a basic principle of crystal engineering, we have applied a novel strategy for the synthesis of $[Fe(bpp)_2]^{2+}$ spin crossover complexes exhibiting acentric diamond-like crystal structures. It has been successful only when using isonicotinate anions, being the position of the nitrogen atom in the nicotinate anion a hindrance for the establishment of strong hydrogen bonds with the bpp ligands. In any case, the resulting anhydrous material **4** presents spin crossover with relatively high cooperativity and thermal hysteresis. In addition, it can be partially photoswitched to the metastable high-spin state using green light at 10 K with a *T*(LIESST) value of 56 K. Unfortunately, this compound amorphises after removal of solvent molecules, which precludes the establishment of any structure-property correlation. On the contrary, **3**·2H_2O exhibits a hydrogen-bonded diamondoid network. It is a piezoelectric low-spin Fe(II) assembly that undergoes a SCSC transformation upon removal of solvent molecules, yielding a ferroelectric material that, in addition, changes reversibly its spin state for the first time. This enables the switching of the electric polarisation and the magnetic moment of the material in the same temperature range, opening the way towards the fabrication of electric and magnetic bistable devices for data storage.

On the other hand, the main drawback of compound **3** is the high stability of the polar phase. The relative displacement of positive and negative charges required for the switching of electric polarisation is hampered by the strength of hydrogen bonds. Thus, this prevents the detection of a ferroelectric phase transition even at high temperatures (DSC measurements were performed until 493 K without the existence of an additional feature that may indicate a transition above 325 K). In order to solve this situation, we turned our attention towards proton migration as one of the processes that originates ferroelectric phase transitions,[27-28] which usually takes place along short strong hydrogen bonds. The progress achieved in this context will be shown in section 3.5.

Furthermore, with the idea of tuning the SCO properties while keeping the same crystal structure, we have chosen the isonicotinate N-oxide anion as a good

candidate for replacing the isonicotinate linkers. It increases in one atom the length of the linear bridge, therefore, the compound might exhibit a stronger tendency to undergo crossover to the high-spin state and a complete transition might be obtained. The results involving this anion will be described in the following section (3.4).

3.4. $[Fe(bpp)_2](isonicNO)_2 \cdot 2.4H_2O$ (**5**$\cdot 2.4H_2O$)

3.4.1. Synthesis

In order to isolate **5**$\cdot 2.4H_2O$ as a pure phase (orange rhombuses, Scheme 3.4), a metathesis reaction between the barium isonicotinate N-oxide salt and $[Fe(bpp)_2]SO_4$ was carried out at room temperature in MeOH/H_2O 1:1. The barium salt was prepared from the corresponding acid and barium hydroxide octahydrate. A considerable excess of this salt (stoichiometric ratio of 4:1) was added in order to avoid inclusion of the sulphate anions in the final material. After filtering the $BaSO_4$ precipitate, the solution was left undisturbed to slowly evaporate in a thermostatic bath at 25^0C. A deuterated sample was also prepared following the same procedure as described for **5**$\cdot 2.4H_2O$, but using deuterated solvents (D_2O and CD_3OD) instead of H_2O and CH_3OH. IR spectrum shows a considerable fraction of non-deuterated compound. The fraction of H_2O molecules was calculated as the ratio of absorbances corresponding to the O–H stretching vibration in the normal and deuterated samples for different batches (old and freshly prepared samples). A consistent result reveals that 75% of water molecules are not deuterated, leading to an approximate composition of the deuterated sample of **5**$\cdot 1.8H_2O \cdot 0.6D_2O$.

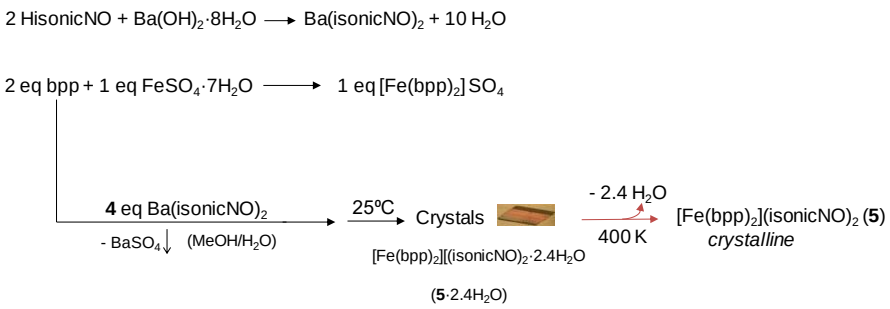

Scheme 3.4. Scheme for the synthesis of **5**$\cdot 2.4H_2O$.

Moreover, it was possible to dehydrate this compound in a single-crystal-to-single-crystal transformation (SCSC) by heating at 400 K for 2 h under vacuum.

3.4.2. Magnetic characterisation

A. Magnetic properties

The χT product for **5**·2.4H_2O has a value of 3.51 emu·K·mol^{-1} at 280 K, indicating that 100% of the iron centres are in the high-spin state (Figure 3.35.a, black dots). Upon cooling below 275 K (curve 1) in SET mode (average scan rate in the 280-265 K temperature range: 0.06 K·min^{-1}), a first decrease in the magnetic signal is observed, which reaches a χT value of 2.84 emu·K·mol^{-1} at 274.6 K ($T_1^{\downarrow}$) and accounts for 20% of the iron centres undergoing crossover to the LS state. Further cooling shows a second step in which an extremely abrupt decrease in the χT product is observed, which vanishes completely at 273 K ($T_2^{\downarrow}$ = 273.8 K). Thus, the transition HS → LS is complete and the sample remains in the diamagnetic state while cooling further to 2 K. The heating process (curve 2) shows that the compound remains in the low-spin state until 273 K, where the magnetic response increases sharply in one step ($T_{1/2}^{\uparrow}$ = 274.9 K) and reaches saturation of the signal at 276 K with a χT value corresponding to the paramagnetic limit (complete LS → HS transformation). This SCO behaviour suggests that an associated first-order phase transition takes place.

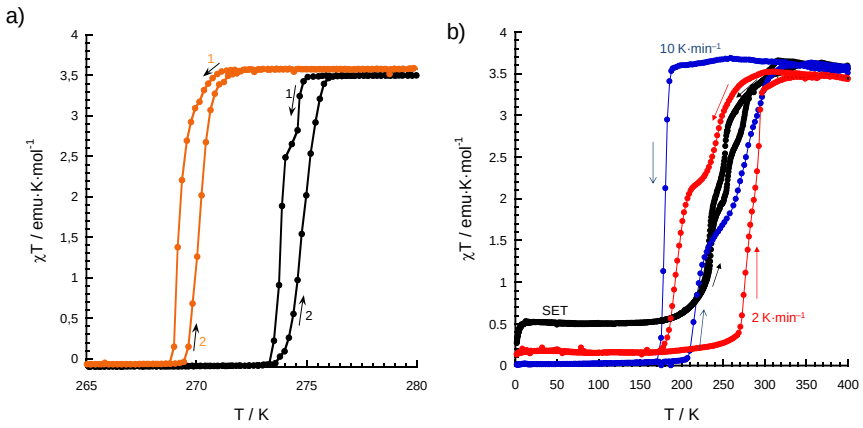

Figure 3.35. a) Thermal dependence of the χT product for **5**·2.4H_2O (black dots) and **5**·1.8H_2O·0.6D_2O (orange dots) in SET mode. b) Temperature dependence of the χT product for **5** after heating 2 h at 400 K under different conditions: settle mode (average scan rate: 0.19K·min^{-1}, black dots) and sweep mode (2 K·min^{-1}, red dots; 10 K·min^{-1}; blue dots). A second cycle in SET mode shows that the processes are reversible. SET means that at each *T* the device will wait until the *T* has stabilised to within a chosen % before taking the measurement (in our case, 5% of tolerance).

In addition, the magnetic properties of the deuterated sample (**5**·1.8H_2O·0.6D_2O) were investigated also in SET mode. Figure 3.35.a (orange dots) reveals a similar behaviour to that obtained for the original compound, being the only difference the $T_{1/2}$ shift to lower temperatures ($\Delta T \sim 5$ K), which evidences the vital importance of hydrogen-bonding in defining the SCO properties. In this case, only one step is observed during the cooling process, probably due to the partial deuterium exchange.

On the other hand, **5**·2.4H_2O was dehydrated *in situ* at 400 K for 2 h and its magnetic properties measured (Figure 3.35.b). A huge dependence on the temperature scan rate can be seen. The χT product measured at 10 K·min^{-1} has a constant value of 3.6 emu·K·mol^{-1} on cooling from 400 K down to 190 K. At 169 K ($T_{1/2}^{\downarrow}$), the signal decreases abruptly and reaches the low-spin state. On heating up the sample, it remains in the diamagnetic state up to 207 K. Further heating shows a spin transition in two abrupt steps at around $T_{1/2}^{\uparrow}$ = 257 K. Changing the sweeping rate to 2 K·min^{-1} yields a similar behaviour, with a step around 225 K in cooling mode and a shift of $T_{1/2}^{\uparrow}$ towards higher temperatures (293 K). In this conditions, a residual fraction of high-spin molecules of ~ 5% is present at low temperatures. The measurement in SET mode (average scan rate: 0.19 K·min^{-1}) upon cooling reveals a stepped crossover with $T_{1/2}^{\downarrow}$ = 242 K and a higher residual fraction of high-spin centres (13%). At 400 K, the χT product has a value of 3.56 emu·K·mol^{-1}. Then, it decreases in two steps, being the first gradual until a χT value of 2.18 emu·K·mol^{-1} at 243 K ($\gamma_{HS} \approx 2/3$), and the second one more abrupt and reaching a value of 0.56 emu·K·mol^{-1} at 201 K. This indicates that a residual HS fraction of ~ 13% is present at low temperatures and below 12 K an additional decrease of the magnetic signal is observed due to zero-field splitting effects of the quintet state. Heating now the sample reveals the same residual fraction of HS centres up to 240 K, when a transition in three steps takes place and a hysteresis loop opens ($\Delta T \approx 24$ K in its widest point, $T_{1/2}^{\uparrow}$ = 257 K). The hysteretic behaviour disappears at 283 K, where the heating and cooling curves merge and the initial χT value corresponding to the 100% HS material is reached. Under these quasistatic conditions, the second cooling/heating cycle is practically identical to the first one (not shown), with a slightly narrower hysteresis loop.

These results are indicative of kinetic effects.[29] In the 300-180 K range of the cooling mode, the HS phase of **5** is metastable. At 10 K·min^{-1}, internal pressure increases until a complete spin transition with a high cooperativity takes place. In SETTLE conditions, the transition proceeds more gradually (internal pressure

cannot be completely released) and it is partial. Likewise, the heating mode shows also that he LS phase of **5** is metastable between 200 K and 270 K.

B. Photomagnetism and excited spin-state trapping

Photomagnetic experiments of both the as-synthesised and the anhydrous samples were carried out in a SQUID magnetometer. First, **5**·2.4H_2O was cooled down to 10 K (curve 1, Figure 3.36.a) and irradiated at this temperature with a red laser light (λ = 630 nm). The magnetic signal with an initial χT value of 0.010 emu·K·mol^{-1}, started to increase and reached saturation after 8 h of irradiation (unusually long irradiation time) when χT was equal to 5.03 emu·K·mol^{-1}. This means that all the iron centres have been efficiently trapped in the photoinduced high-spin state, although this value is much higher than that observed at RT (3.92 emu·K·mol^{-1}), what is ascribed to crystal reorientation effects. The laser was switched off and the magnetic signal recorded while heating the sample (at 0.3 K·min^{-1}).[26] An initial increase was observed due to the zero-field splitting of the quintet ground state. Then, above 40 K, χT decreases sharply and its value vanishes completely at 66 K. The first derivative plot (inset Figure 3.36.a) gives a T(LIESST) = 63 K. For $T_{1/2}$ = ½ ($T_{1/2}^{\downarrow}$ + $T_{1/2}^{\uparrow}$) = 274.4 K, applying the expression that correlates the SCO temperature ($T_{1/2}$) and T(LIESST) (Eq. 3.1), a value of T(LIESST) = 68 K is obtained. The prediction is close to the experimental value.

Secondly, **5**·2.4H_2O was dehydrated *in situ* at 400 K for 2 h and cooled down to 10 K. Then, the anhydrous sample was irradiated (curve 1, Figure 3.36.b) at this temperature with a red laser source and the magnetic signal increased until reaching saturation at a χT value of 3.55 emu·K·mol^{-1} (after almost 4 h of irradiation). This value indicates an efficient trapping of the iron centres in the photoinduced high-spin (PIHS) state. Irradiation was stopped and the temperature dependence of the susceptibility was measured by heating in the dark at 0.3 K·min^{-1} (curve 2). Again, an initial increase of the magnetic signal due to zero-field splitting effects is registered. Then, χT decreases smoothly with an inflection point at 47 K (χT = 2.15 emu·K·mol^{-1}, corresponding to $\gamma_{HS} \approx 2/3$). On further heating a plateau at 72 K is reached, where χT is equal to 0.72 emu·K·mol^{-1} ($\gamma_{HS} \approx 1/6$). Finally, at 98 K the χT product restores the initial value before irradiation (0.25 emu·K·mol^{-1}). The first derivative plot (inset Figure 3.36.b) shows more than one minimum, in accordance with the fact that the PIHS phase of **5** exhibits a relaxation in three steps (T(LIESST) = 44 K, 60 K and ≈ 82 K, being the last value quite high in comparison to those usually obtained for

$[Fe(bpp)_2]^{2+}$ systems). For $T_{1/2}$ = ½ ($T_{1/2}^{\downarrow}$+ $T_{1/2}^{\uparrow}$) = 247 K (at 2K·min^{-1}), equation 3.1 gives a T(LIESST) of 76 K, which lies within the range observed for the multi-step relaxation.

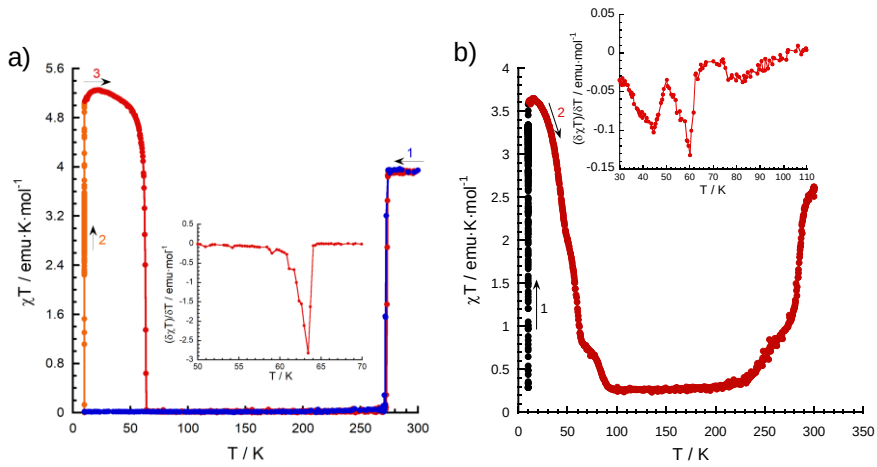

Figure 3.36. a) Temperature dependence of the χT product for **5**·2.4H$_2$O on cooling before irradiation (blue), under irradiation at 10 K (orange) and subsequent heating in the dark (red). The inset shows the first derivative of the LIESST plot. b) Temperature dependence of the χT product for **5** (dehydrated *in situ*) under irradiation at 10 K (black) and subsequent heating in the dark (red). The inset shows the first derivative of the LIESST plot.

In another experiment, **5**·2.4H$_2$O was cooled down to 10 K, irradiated with red light until saturation of the signal and its magnetic response registered while irradiating both in warming and cooling modes (between 10 and 110 K, Figure 3.37.a). An associated hysteresis of 32 K is observed, which is known as light induced thermal hysteresis (LITH) phenomenon.[30] The existence of a LITH effect suggests a strong degree of intermolecular cooperativity in the relaxation of the PIHS state in this compound, in accordance with the relaxation measurements that will be shown next.

The metastable high-spin state can also often be accessed by rapid thermal quenching of the compound (so-called thermally induced excited spin-state trapping, TIESST).[31] Nevertheless, cooling the sample of **5**·2.4H$_2$O from room temperature to 10 K over a period of seconds did not trap the compound in its HS form (a χT value near to 0 emu·K·mol^{-1} was obtained). Instead, quenching the sample of anhydrous **5** at 10 K afforded a partial TIESST effect (Figure 3.37.b), with a fraction of trapped high-spin centres of 0.34 and a T(TIESST) value of 100

K. This value is higher than T(LIESST), indicating that different high-spin metastable phases are reached after photoirradiation and thermal quenching.

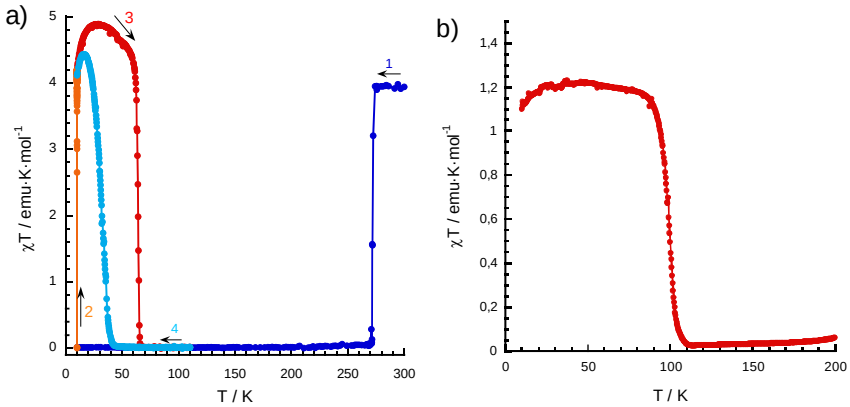

Figure 3.37. a) Temperature dependence of the χT product for **5**·2.4H$_2$O on cooling before irradiation (dark blue), under irradiation at 10 K (orange) and subsequent heating and cooling while irradiating the sample (red and light blue). b) TIESST measurement for anhydrous **5** recorded on heating at 0.3 K·min^{-1}.

C. Relaxation measurements

Relaxation measurements were carried out for **5**·2.4H$_2$O at different temperatures in the thermally activated regime below 60 K. First, **5**·2.4H$_2$O was irradiated at 10 K until saturation of the signal and, then, it was heated until the selected temperature. At this point, the light was switched off and the time dependence of γ_{HS} was recorded in the dark (Figure 3.38.a).

An initial decrease of approximately 20% of the magnetic signal is observed at 54 K and 55 K (the lowest temperatures). The shape of all the relaxation curves is clearly sigmoidal, which is indicative of a strongly cooperative process. Thus, the rate constant ($k^*(T)$) depends on the remaining fraction of high-spin centres (γ_{HS}) through a self-acceleration factor ($\alpha(T)$). In addition, a residual high-spin fraction (γ_{HS}^{res}) has to be considered for all the cases. This behaviour is represented by the following equations:

$$\gamma_{HS} = \gamma_{HS}^{res} + 0.2e^{-k_3 t} + (0.8 - \gamma_{HS}^{res})e^{-k^*(T)t} \quad \text{(Eq.3.2)}$$

$$k^*(T) = k(T)e^{\alpha(T)(1-\gamma_{HS})} \quad \text{(Eq.3.3)}$$

$$k(T) = k(\infty)e^{-E_a/kT} \quad \text{(Eq.3.4)}$$

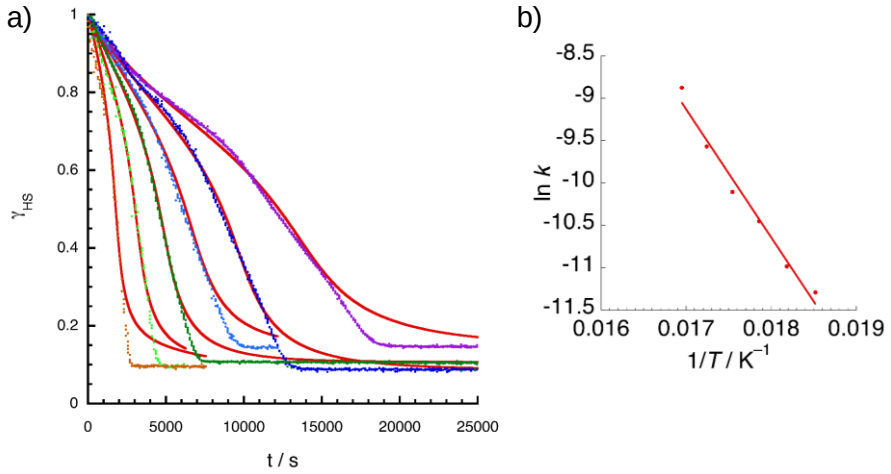

Figure 3.38. a) Time dependence of the γ_{HS} of Fe^{2+} cations in **5**·2.4H_2O at 54 K (purple), 55 K (dark blue), 56 K (light blue), 57 K (dark green), 58 K (light green) and 59 K (brown). Red lines represent the best fit to equation 3.2. b) Arrhenius plot corresponding to the thermal variation of the relaxation rate constants at the different temperatures, as well as with the best-fit to the Arrhenius equation (red line).

The values of k and α at different temperatures have been extracted from fitting the relaxation data to equations 3.2-3.3 (Table 3.11). The non-cooperative rate constant ($k(T)$) follows the Arrhenius equation (Eq.3.4, Figure 3.38.b), from which the apparent activation energy (E_a) and the preexponential factor ($k(\infty)$) have been calculated: E_a = 1052 cm^{-1} (compares well with values reported for similar systems[32]) and $k(\infty) = 1.606 \cdot 10^7$ s^{-1}. Remarkably, the self-acceleration factor ($\alpha(T)$) presents very high values (> 2.5), indicating that the process exhibits an exceptional cooperativity.

Table 3.11. Kinetic parameters extracted from fitting the relaxation measurements at different temperatures (k_3 = 2.7·10^{-4} s^{-1} was kept constant in the whole temperature range to avoid overparametrisation. It is associated to the faster process).

T / K	γ_{HS}^{res}	k / s^{-1}	α
54	0.147	1.25·10^{-5}	2.85
55	0.088	1.7·10^{-5}	2.80
56	0.144	2.9·10^{-5}	2.75
57	0.107	4.1·10^{-5}	2.70
58	0.095	7.0·10^{-5}	2.65
59	0.096	1.4·10^{-4}	2.60

Usually, the self-accelerated relaxation model overestimates the relaxation rate at low γ_{HS} values. This is a result of the presence of defects that decreases the

relaxation rate. However, in our case the relaxation is faster and much more abrupt than that predicted with self-acceleration. This may indicate that below a certain value of γ_{HS}, a crystallographic phase transition takes place with a concomitant increase in the abruptness of the relaxation process.

3.4.3. Structural characterisation

A. Thermal properties

DSC and TG measurements of **5**·2.4H_2O have been performed under nitrogen atmosphere. The TG curve (Figure 3.39.a) shows a first step at 370 K that is associated to a weight loss of 5.37%, corresponding to 2.40 water molecules per iron cation (calculated value: 5.42%). This matches well with the formula deduced for this compound (from X-ray crystal structure experiments and elemental analysis). Above 500 K, decomposition of the material takes place.

The DSC plot of **5**·2.4H_2O confirms the existence of a first-order phase transition taking place in the 270-275 K temperature range (Figure 3.39.b). Upon cooling, a sharp exothermic feature located at 270.7 K is observed. This value is lower than $T_1^{\downarrow}$ and $T_2^{\downarrow}$ obtained from magnetic measurements in SET mode, due to the different temperature sweeping rates used in the two experiments (10K·min^{-1} in DSC, ~ 0.06 K·min^{-1} in magnetic data). As expected, consistent results between DSC and magnetic measurements have been obtained by increasing the sweeping rate in the thermal variation of the magnetic susceptibility to 0.5 K·min^{-1} ($T_{1/2}^{\downarrow}$ = 270.7 K, Figure 3.39.c). On heating the sample back to 300 K, a sharp endothermic peak appears at 274.8 K. This corresponds to $T_{1/2}^{\uparrow}$, with the same value to that observed from magnetic measurements. Enthalpy and entropy changes associated to these processes are summarised in Table 3.12. These values are in agreement with those reported for other similar complexes exhibiting also abrupt transitions with a high degree of cooperativity.[33] Therefore, DSC and magnetic measurements are in accordance and mirror the behaviour of an extremely abrupt SCO.

Table 3.12. Thermodynamic parameters ΔH and ΔS extracted from DSC measurements of **5**·2.4H_2O and **5**·1.8H_2O·0.6D_2O.

Compound	Curve	T_{peak}/ K	ΔH / kJ·mol^{-1}	ΔS / J·mol^{-1}·K^{-1}
5·2.4H_2O	1	270.7	-14.3	-52.8
	2	274.8	14.7	53.6
5·1.8H_2O·0.6D_2O	1	266.6	-16.2	-60.7
	2	271.7	16.3	60.0

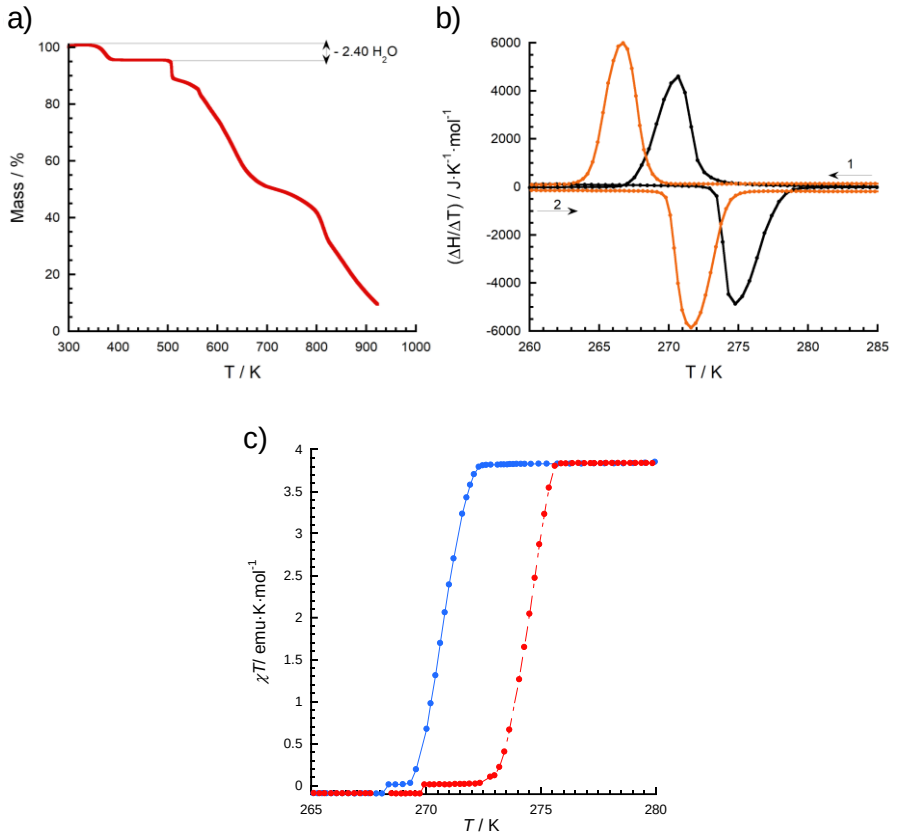

Figure 3.39. a) Thermogravimetric analysis of **5**·2.4H_2O. b) Differential scanning calorimetry curve of **5**·2.4H_2O (black) and **5**·1.8H_2O·0.6D_2O (orange). Curves 1 and 2: First cooling and heating processes, respectively. A second thermal cycle reveals the same behavior (not shown). c) Thermal variation of χT for **5**·2.4H_2O in sweep mode (0.5 K·min^{-1}).

Moreover, DSC measurements of the deuterated sample (**5**·1.8H_2O·0.6D_2O, Figure 3.39.b) parallel the magnetic behaviour, with peak maxima shifted to lower temperatures. The exothermic peak is located at 266.6 K, whereas on heating the endothermic feature appears at 271.7 K. Indeed, thermal hysteresis of **5**·2.4H_2O (ΔT = 4.1 K) and **5**·1.8H_2O·0.6D_2O (ΔT = 5.1 K) are similar. The enthalpy and entropy changes associated to the SCO process increase slightly with respect to the non-deuterated compound (Table 3.12).

On the other hand, DSC measurements of the anhydrous sample were also performed. First, the pristine hydrate was desolvated by heating at 400 K for 2 h (Figure 3.40, curve 1). A very broad endothermic feature located at 369.7 K is observed, which fits in the temperature range where dehydration of the material

takes place. The cooling process (curve 2) shows an exothermic peak centred at $T_{anh}^{\downarrow}$ = 165 K (near $T_{1/2}^{\downarrow}$ = 169 K from magnetic measurements performed at 10 K·min^{-1}, the same scan rate than in DSC data), together with some irreversible and minor features at higher temperatures. The heating mode (curve 3) reveals that this process is reversible with the appearance of a similar endothermic peak at $T_{anh}^{\uparrow}$ = 209 K (near 207 K in magnetic data recorded at 10 K·min^{-1}, temperature above which the diamagnetic behaviour was lost) and an associated thermal hysteresis of 44 K. A second cooling/heating cycle shows that the phase transition is reversible (with a small displacement of the peak maxima towards higher temperatures). Thermodynamic parameters associated to these processes are shown in Table 3.13. The values corresponding to the first curve are much higher than the others, in agreement with the dehydration process. Curves 2 and 3 present values lower than those obtained for the hydrated material, but are still characteristic of SCO processes.[33]

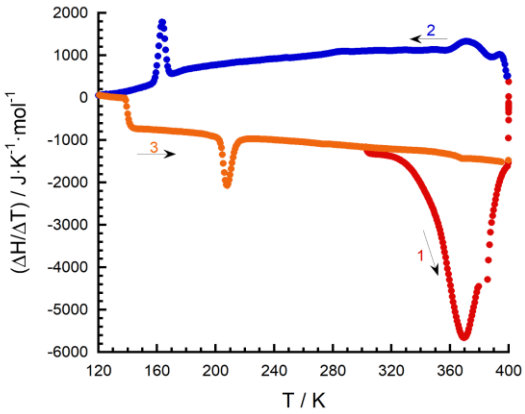

Figure 3.40. DSC curve of **5**·2.4H_2O. Curve 1: First heating process (dehydration of the material). Curves 2 and 3: First cooling and second heating processes, respectively.

Table 3.13. Thermodynamic parameters ΔH and ΔS extracted from DSC measurements of **5**.

Compound	Curve	T_{peak}/ K	ΔH / kJ·mol^{-1}	ΔS / J·mol^{-1}·K^{-1}
5	1	369.7	126	350
	2-3 (mean values)	207.8	8	43.3

B. Temperature dependence of unit cell parameters

Single crystal X-ray diffraction measurements of the unit cell parameters of **5**·2.4H_2O were carried out in the 120-300 K temperature range (Figure 3.41).

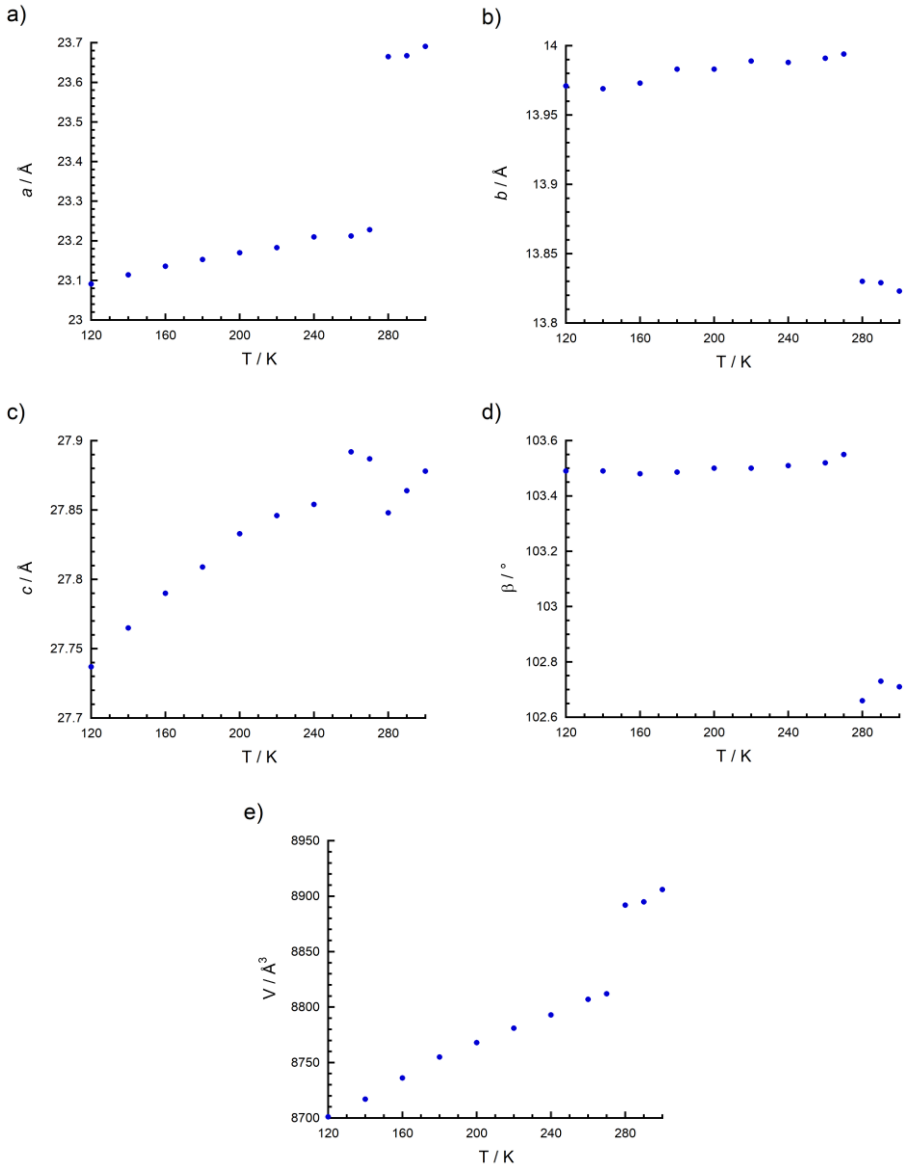

Figure 3.41. Temperature dependence of unit cell parameters of **5**·2.4H_2O.

The expected crystallographic phase transition between 270 K and 280 K was detected by sharp discontinuities for the three parameters *a*, *b*, *c* and the β angle. The unit cell volume also exhibits a significant discontinuity between 270 K and 280 K as a signature of the phase transition. The magnitude of the variation is moderate (with very small variation of the *b* parameter) but anisotropic with Δa = + 0.437 Å (1.9 %), Δb = – 0,164 Å (– 1.2 %) and Δc = – 0,039 Å (– 0.14 %), being positive the thermal expansion of the three parameters below the phase transition. The temperature dependence of the unit cell volume can be fitted to the linear expression $V(Å^3)$ = 8616.6 + 0.74*T*, yielding a volumetric thermal expansion coefficient for the LS phase of $84 \cdot 10^{-6}$ K^{-1}. Unit cell parameters of anhydrous **5** were also measured from single crystal X-ray data in the 400-220 K temperature range in both heating and cooling modes (Figure 3.42).

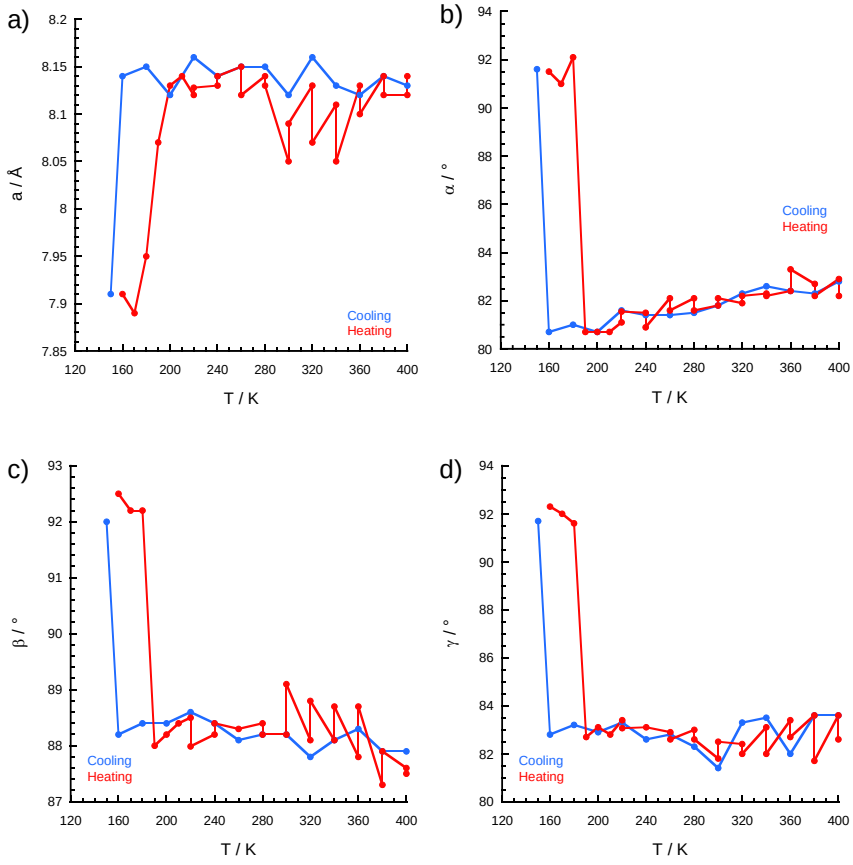

Figure 3.42. Temperature dependence of unit cell parameters of **5**.

Notable discontinuities for the a parameter and angles α, β and γ indicate a crystallographic phase transition between 160 K and 150 K on cooling, and between 180 K and 190 K on heating. These values are in rough agreement with the expected transition temperatures extracted from DSC measurements, probably due to the different cooling and heating rates.

C. Single crystal X-ray diffraction

5·2.4H_2O crystallises in the monoclinic $P2/c$ space group (Table 3.14).

Table 3.14. Single crystal X-ray diffraction data collection and refinement details for **5**·2.4H_2O at different temperatures.

T / K	296	270	260	250	200	120	30[b]	80[c]
Empirical formula	$C_{34}H_{30.8}FeN_{12}O_{8.4}$							
Formula weight	797.75							
Crystallographic system	Monoclinic							
Space group	$P2/c$							
a/ Å	27.820 (4)	27.818(6)	27.884(7)	27.807(7)	27.7875 (2)	27.71871(18)	27.176 (10)	27.609(7)
b/ Å	13.803 (2)	13.953(3)	13.983(3)	13.971(3)	13.96103(9)	13.95482(8)	13.766 (5)	13.906(4)
c/ Å	23.626 (4)	23.121(7)	23.189(6)	23.094(6)	23.0980 (18)	23.03852(15)	23.385 (8)	22.889(6)
α/ °	90	90	90	90	90	90	90	90
β/ °	102.820(5)	103.566 (11)	103.567 (9)	103.527 (10)	103.5634 (8)	103.5834(7)	101.991(11)	103.685(9)
γ/ °	90	90	90	90	90	90	90	90
V/ Å^3	8846 (2)	8724 (4)	8789 (4)	8723 (3)	8710.82 (12)	8662.25 (10)	8557(5)	8539 (4)
Z	10							
R(int)	0.0807	0.0759	0.0577	0.0706	0.0922	0.0705	0.0940	0.0866
T / K	296(2)	270(2)	260(2)	250(2)	199.95(10)	120.00(10)	30(2)	80(2)
δ_{calc}/ g·cm^{-3}	1.497	1.518	1.507	1.519	1.521	1.529	1.548	1.551
μ/ mm^{-1}	0.498	0.505	0.502	0.505	0.506	0.509	0.515	0.516
Crystal dimensions/ mm	0.669 × 0.216 × 0.078	0.388 x 0.167 x 0.083	0.388 x 0.167 x 0.083	0.388 x 0.167 x 0.083	0.213 x 0.172 x 0.134	0.241 x 0.155 x 0.089	0.599 × 0.220 × 0.124	0.599 × 0.220 × 0.124
λ/ Å	0.71073	0.71073	0.71073	0.71073	0.71073	0.71073	0.71073	0.71073
θ range/ °	2.252-29.610	1.506-26.623	2.254-36.996	1.506-25.143	2.069-27.699	2.101-27.768	2.094-25.668	2.084-26.245
Index ranges for h, k , l	–38/38, –19/19, –32/32	-33/ 35, –17/ 17, –27/29	–47/47, –23/23, –39/39	–33/33, –16/16, –26/27	–35/35, –18/18, –30/30	–36/35, –18/18, –29/30	-32/33, -16/16, -28/28	–34/33, –17/17, –28/20
Refinement method	Full-matrix least-squares on F^2							
Collected reflections	128967	99349	241413	88295	359250	295805	92971	65239
Unique reflections	24804	18278	44545	15589	19538	19593	16160	17127
Data/Restraints/ Parameters	24804 / 32 / 1320	18278 / 706 / 1500	44545 / 460 / 1500	15589 / 746 / 1500	19538 / 709 / 1506	19593 / 697 / 1506	16160/ 25/ 1326	17127 / 719 / 1506
Goodness-of-fit on F^2	1.024	1.013	0.821	1.037	1.027	1.035	1.017	1.024
R1, wR2 [I > 2sigma(I)][a]	0.0587, 0.1390	0.0492,0.105	0.0501,0.106	0.0465,0.104	0.0462, 0.0981	0.0418, 0.0893	0.0450, 0.0954	0.0511,0.106
R1, wR2 (all data)[a]	0.1018, 0.1613	0.0830,0.121	0.0908,0.133	0.0729,0.117	0.0904, 0.1180	0.0706, 0.1046	0.0860, 0.1095	0.1066,0.123
$\Delta\rho_{max}$ and $\Delta\rho_{min}$ /e·Å^{-3}	0.620, –0.759	0.416, –0.449	0.684, –0.584	0.395, –0.436	0.498, –0.646	0.526, –0.672	0.572, –0.690	0.520, –0.749

[a]$R1 = \Sigma(||F_o| - |F_c||)/\Sigma|F_o|$; $wR2 = \{\Sigma[w(F_o^2 - F_c^2)^2]/\Sigma[w(F_o^2)^2]\}^{1/2}$. [b]Photoindued high-spin phase (PIHS). [c]Structure obtained after full relaxation of the PIHS phase.

It does not exhibit the expected diamond-like structure and is found in a centrosymmetric space group, preventing the existence of ferroelectric properties. Nevertheless, this compound deserves special attention by several reasons (including its magnetic behaviour) that will be exposed hereafter. The compound belongs to the same space group in the low- (120 K) and high-temperature (296 K) phases (LTP and HTP, respectively). The unit cell parameters are very similar, being the biggest differences found in the *c* parameter and β angle. The crystal structure comprises three inequivalent Fe^{2+} cations (Fe1, Fe2 and Fe3), each one coordinated to two bpp ligands that occupy meridional positions of their distorted octahedral FeN_6 coordination spheres. Fe1 and Fe2 are found in general positions, whereas Fe3 is located on a twofold rotation axis. Each $[Fe(bpp)_2]^{2+}$ subunit interacts with four adjacent complexes *via* π-π stacking ineractions, giving rise to a two-dimensional pattern similar to the well-known *terpyridine embrace* (Figure 3.43.a). However, in this case the layers are corrugated: the cationic stacks alternate along the [–101] direction across the average plane of the layer (Figure 3.43.b), being adjacent layers all equivalent (AA packing).

Regarding the second iron coordination sphere, Fe1 and Fe3 sites are hydrogen-bonded to four anions (either using the carboxylate fragment or the oxygen atom of the N-oxide function). Instead, Fe2 is hydrogen-bonded to three anions and one water molecule. A view parallel to the cationic sheets (Figure 3.44) shows that the crystal structure of **5**·2.4H_2O can be described as an alternation of cationic $[Fe(bpp)_2]^{2+}$ and anionic isonicNO layers along the *b* axis.

There are five inequivalent isonicNO anions, denoted by the label of the corresponding N-oxide oxygen atom. IsonicNO(3) (orange) and isonicNO(15) (purple) connect two adjacent Fe centres within the same layer through hydrogen bonds involving *syn*, *syn*-carboxylate bridges and form stacks along the [–101] direction. IsonicNO(3) (orange) bridges Fe1 and Fe3 centres, giving rise to the formation of Fe1Fe3Fe1 trimers. Instead, isonicNO(15) (purple) connects Fe1 and Fe2 sites, forming dimers. Therefore, symmetric pentamers along the stacks are obtained as a result of both H-bond interactions (Figure 3.45, represented by a green oval in Figure 3.43.a). Anions isonicNO(6) (magenta) and isonicNO(9) (brown) are hydrogen-bonded to two $[Fe(bpp)_2]^{2+}$ complexes of different layers, involving both monodentate carboxylate and N-oxide functional groups. Whereas isonicNO(9) (brown) connects Fe1 and Fe3 sites, isonicNO(6) (magenta) links Fe1 and Fe2 centres. Finally, isonicNO(12) (light gray) is only hydrogen-bonded to the Fe2 site through the N-oxide function, being the carboxylate fragment engaged in hydrogen bonds with H_2O molecules. In

addition, there are six crystallographically inequivalent water molecules per asymmetric unit that fill the interlayer space.

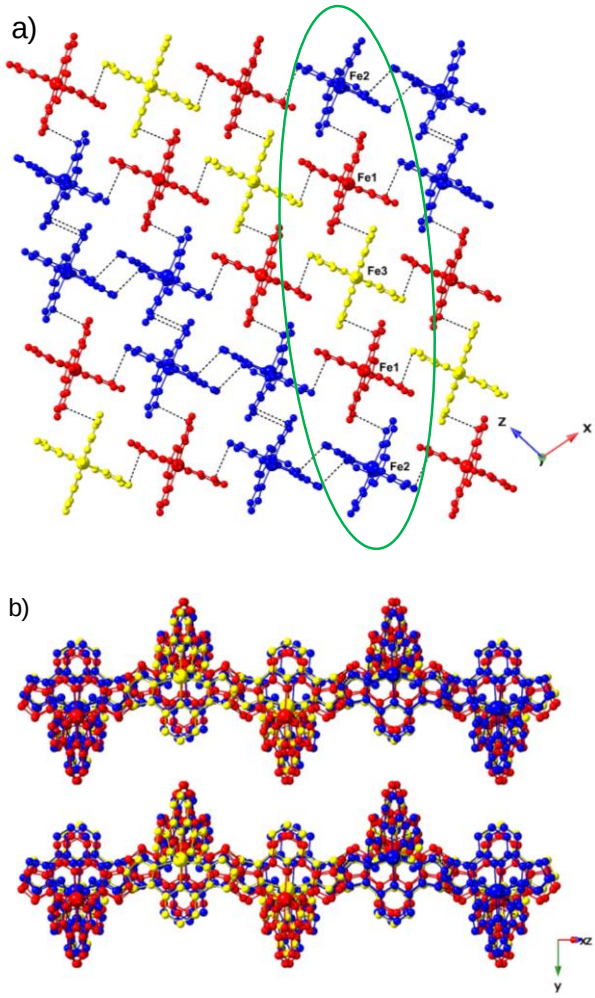

Figure 3.43. a) View of the X-ray crystal structure (T = 296 K, HS phase) of **5**·2.4H_2O along the *b* axis showing the 2D *terpyridine-embrace* motif of $[Fe(bpp)_2]^{2+}$ cations. The green oval highlights the presence of pentamers stacked along the [–101] direction. b) X-ray crystal structure of **5**·2.4H_2O along the [–101] direction, showing two corrugated $[Fe(bpp)_2]_{2+}$ layers. Water molecules and ionicNO anions are omitted. The three independent Fe(II) complexes are depicted in different colours: Fe1 (red), Fe2 (blue), Fe3 (yellow). Dashed lines refer to π-π stacking interactions.

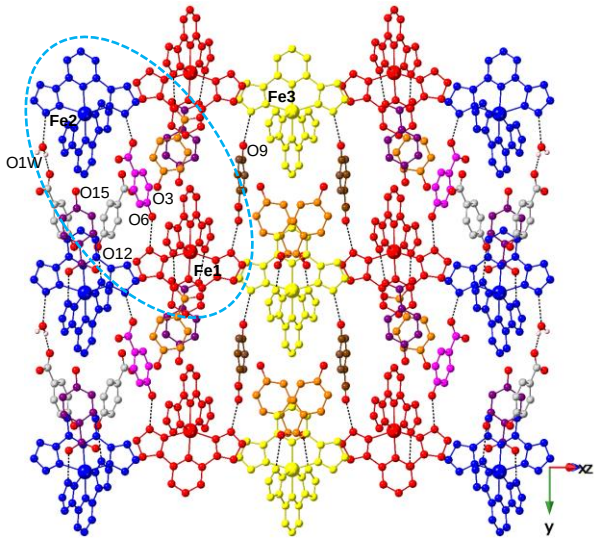

Figure 3.44. View of the X-ray crystal structure (T = 296 K, HS phase) of **5**·2.4H_2O showing the alternation of cationic and anionic layers. The blue dashed oval emphasises the presence of isonicNO(6) (magenta) and isonicNO(3) (orange) that are involved in the isomerisation process. The remaining anions are shown in brown (isonicNO(9)), light gray (isonicNO(12)) and purple (isonicNO(15)). Also, the three independent Fe(II) complexes are depicted in different colours: Fe1 (red), Fe2 (blue), Fe3 (yellow). Only water molecule O1W is shown. Dashed lines refer to hydrogen bonds.

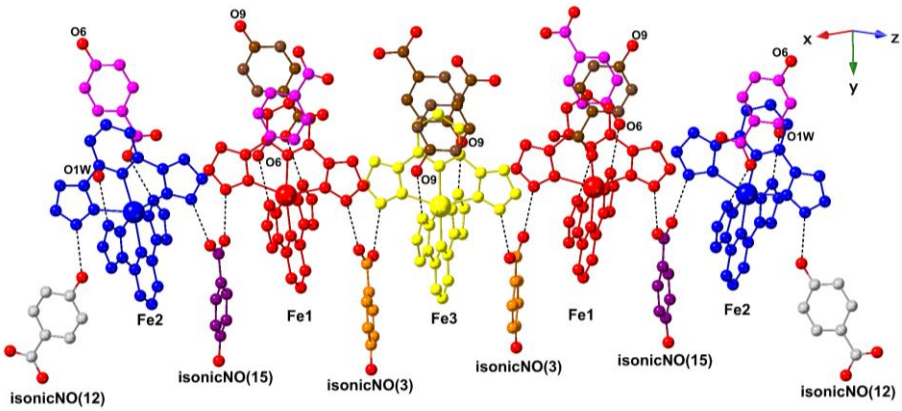

Figure 3.45. View of the X-ray crystal structure (T = 296 K, HS phase) of **5**·2.4H_2O showing the formation of C_2-symmetric Fe2Fe1Fe3Fe1Fe2 pentamers defined by hydrogen bonds through *syn*, *syn*-carboxylate bridges.

At 296 K, Fe–N bond distances (mean distances of 2.160 Å, 2.167 Å and 2.162 Å for Fe1, Fe2 and Fe3, respectively) lie in the expected range for a high-spin

ground state, in agreement with magnetic measurements. Accordingly, octahedral distortion parameters for the three iron sites are characteristic of high-spin complexes (Table 3.15).[18] Below the SCO temperature, the coordination sphere decreases in volume and becomes less distorted, as expected. At 120 K, all Fe–N bond lengths are lower than 2.0 Å (mean distances of 1.956 Å, 1.959 Å and 1.954 Å for Fe1, Fe2 and Fe3, respectively), indicating that the transition proceeds fully to a low-spin material (in accordance with SQUID data). In addition, the trans N–Fe–N angle approaches 180° and Σ presents a considerably lower value in comparison to the HTP. The variations are less pronounced for Fe3, which is located in a special position. Thus, its octahedral geometry is less distorted than those exhibited by Fe1 and Fe2 centres, being easier its transformation to the low-spin state. On the other hand, it represents 20% of the total amount of iron. Consequently, it might be the responsible for the faster relaxation process observed in the LIESST experiment (Figure 3.38.a) and the first transition registered around 274.7 K in the χT *vs* T plot in SET mode (Figure 3.35.a).

Table 3.15. Octahedral distortion parameters of the Fe^{2+} cations in **5**·$2.4H_2O$ at different temperatures.

T / K		296 (**HS**)	270 (LS)	260 (LS)	250 (LS)	200 (LS)	120 (LS)	30 (**HS**)[a]	80 (LS)[b]
φ / °	Fe1	**170.80**	177.81	177.90	177.88	177.81	177.99	**171.10**	178.15
	Fe2	**173.60**	178.76	178.85	178.77	178.66	178.70	**173.36**	178.89
	Fe3	**180.00**	180.00	180.00	180.00	180.00	180.00	**180.00**	180.00
Σ / °	Fe1	**145.35**	96.06	95.39	96.05	95.55	95.41	**148.97**	95.17
	Fe2	**142.70**	94.83	94.36	94.34	94.29	94.40	**142.93**	94.34
	Fe3	**139.75**	93.29	93.14	93.90	93.80	93.43	**141.06**	92.63

[a] Photoinduced high-spin (PIHS) phase; [b] Structure obtained after full relaxation of the PIHS phase.

The strong cooperativity of the system relies on the combination of the efficient hydrogen-bonded network that connects the iron sites and strong π-π stacking interactions. In fact, stacking is reinforced in the LS phase, keeping the 2D embrace motif but with lower dihedral angles between the neighbouring pyrazolyl mean planes (Table 3.16). Similarly, it can be seen that hydrogen bonds are shorter for the LS phase in most cases (Table 3.17). This is in agreement with the results described previously for compounds **1** and **3**.

Table 3.16. Dihedral angles (θ) and distances (d) between pyrazolyl rings involved in π-π stacking interactions in the crystal structure of **5**·2.4H_2O at different temperatures.

T / K	Pyrazolyl ring [a]	296 (HS)	270 (LS)	260 (LS)	250 (LS)	200 (LS)	120 (LS)	30 (HS)[b]	80 (LS)[c]
θ / °[d]	N1N2^ N14N15	20.74	12.65	12.52	12.28	11.92	11.59	20.77	11.54
	N4N5^ N21N22	8.91	4.07	4.14	4.13	4.14	4.11	9.57	4.14
	N6N7^ N19N20	15.18	12.12	12.29	12.11	12.27	12.24	14.94	12.07
	N9N10^ N24N25	9.44	8.02	8.12	8.22	8.39	8.76	10.95	8.99
	N11N12^ N11N12	0.00	0.00	0.00	0.00	0.00	0.00	0.00	0.00
	N16N17^ N16N17	1.90	1.35	1.30	1.54	1.23	1.21	3.18	1.45
d/Å[e]	N1N2^ N14N15	3.8567 (17)	3.7713 (17)	3.7837 (14)	3.7581 (15)	3.75486(11)	3.73040(11)	3.749 (4)	3.6945 (16)
	N4N5^ N21N22	3.5273(23)	3.561(3)	3.569(3)	3.553(3)	3.5448 (3)	3.52019(22)	3.463 (5)	3.492(3)
	N6N7^ N19N20	3.684 (3)	3.649(6)	3.656(5)	3.641(6)	3.6358 (5)	3.6151 (4)	3.545 (8)	3.591(5)
	N9N10^ N24N25	3.399(4)	3.401(7)	3.410(6)	3.398(7)	3.4017 (5)	3.3916 (5)	3.341(10)	3.375(6)
	N11N12^ N11N12	3.3458 (18)	3.443(3)	3.454(3)	3.437(3)	3.43065(23)	3.41234(22)	3.292 (5)	3.386(3)
	N16N17^ N16N17	3.454(4)	3.443(7)	3.447(5)	3.431(6)	3.4208 (5)	3.3958 (4)	3.364 (8)	3.375(5)

[a] Pyrazolyl rings are denoted by the corresponding N atoms. [b] Photoinduced high-spin (PIHS) phase. [c] Structure obtained after full relaxation of the PIHS phase. [d] Angle between pyrazolyl mean planes. [e] Distance between pyrazolyl ring centroids.

As a consequence of the abruptness of the phase transition, a strong rearrangement of the anionic lattice takes place. The most noticeable variation concerns the isonicNO(6) anion (magenta), which undergoes a hydrogen bond isomerisation. At 296 K (Figure 3.46.a), its N-oxide moiety is hydrogen-bonded to a bpp ligand of the Fe1 site (N1···O6: 2.661(3) Å), whereas the carboxylate function is interacting with the Fe2 site (N15···O4: 2.664(3) Å) in a monodentate mode, being the other carboxylate oxygen atom hydrogen-bonded to a disordered water molecule (O5···O3WA: 2.836(10) Å). The carboxylate unit exhibits different C–O distances due to the different strength of these interactions (C63–O5: 1.231(4) Å; C63–O4: 1.258(4) Å), revealing a polarisation of the electron density towards the oxygen atom engaged in the shorter hydrogen bond (O4). At 120 K, isonicNO(6) rotates approximately 10° with respect to the cationic network (Figure 3.46.b). The hydrogen bond between the N-oxide function and the pyrazolyl fragment of the Fe1 site is preserved (N1···O6A: 2.603(4) Å); nevertheless, there is a considerable increase in the N1···O6 –N28 bonding angle (from 132.8(4)° to 139.8(3)°) upon cooling. On the other hand, the N15···O4 hydrogen bond is broken and the rotational movement of isonicNO(6) brings O5 into a more appropriate position to act as a H-bond acceptor (N15···O5A: 2.724(3) Å). The interaction with the water molecule is not

lost and now it takes place in a bifurcated way (O5A···O3WA: 2.797(3) Å).

Table 3.17. Hydrogen bond distances (Å) in the crystal structure of **5**·2.4H_2O at different temperatures.

H-bond D···A	296 K (**HS**)	270 K (LS)	260 K (LS)	250 K (LS)	200 K (LS)	120 K (LS)	30 K (**HS**)[a]	80 K (LS)[b]
N1···O6#1	2.661(3)						2.653(3)	
N1···O6A#1		2.615(9)	2.611(6)	2.623(8)	2.621(6)	2.603(4)		2.610(5)
N1···O6B#1		2.61(3)	2.64(2)	2.61(3)	2.62(5)	2.80(5)		2.68(3)
N5···O7#2	2.681(3)	2.633(3)	2.645(2)	2.634(3)	2.649(3)	2.645(3)	2.668(3)	2.635(4)
N5 O8C69O7#2	3.788(4)	3.791(4)	3.813(3)	3.795(4)	3.814(3)	3.812(3)	3.801(3)	3.793(4)
N6···O14#2	2.653(3)	2.608(3)	2.612(2)	2.609(3)	2.609(3)	2.609(2)	2.646(3)	2.604(3)
N6 O13C86O14#2	3.647(3)	3.582(3)	3.585(2)	3.579(3)	3.565(3)	3.545(2)	3.583(3)	3.530(3)
N10···O1	2.697(3)						2.689(3)	
N10 O2C57O1	4.161(3)						4.181(3)	
N10···O1A		2.662(8)	2.671(5)	2.672(8)	2.667(5)	2.672(4)		2.672(6)
N10···O1B		2.71(3)	2.68(2)	2.69(3)	2.70(4)	2.71(4)		2.63(4)
N10 O2AC57AO1A		4.103(10)	4.107(4)	4.094(10)	4.100(5)	4.112(3)		4.111(4)
N10 O2BC57BO1B		3.92(3)	3.940(19)	3.97(4)	3.93(4)	3.90(3)		3.91(3)
N11···O1W#3	2.703(3)	2.656(3)	2.6566(19)	2.659(3)	2.658(3)	2.656(2)	2.692(3)	2.645(3)
N15···O4	2.664(3)						2.648(4)	
N15 O5C63O4	3.567(3)						3.589(3)	
N15 O4AC63AO5A		3.114(5)	3.112(3)	3.120(5)	3.113(3)	3.115(3)		3.104(4)
N15···O4B		2.627(15)	2.653(8)	2.637(16)	2.64(2)	2.63(2)		2.67(2)
N15···O5A		2.768(4)	2.759(2)	2.760(4)	2.740(3)	2.724(3)		2.706(4)
N15 O5BC63BO5B		3.191(13)	3.205(9)	3.176(14)	3.143(18)	3.133(18)		3.177(17)
N16···O12	2.763(4)	2.724(3)	2.727(2)	2.727(3)	2.728(3)	2.724(2)	2.761(3)	2.717(3)
N20···O13	2.657(3)	2.659(3)	2.6690(19)	2.661(3)	2.669(3)	2.669(2)	2.669(4)	2.665(3)
N20 O14C86O13	3.829(4)	3.940(3)	3.957(2)	3.947(3)	3.966(3)	3.984(2)	3.843(3)	3.978(3)
N21···O9#1	2.709(4)	2.642(4)	2.648(2)	2.642(4)	2.642(3)	2.639(3)	2.745(4)	2.627(4)
N24···O2	2.732(4)						2.746(3)	
N24 O1C57O2	3.319(3)						3.250(3)	
N24···O2A		2.763(9)	2.758(4)	2.779(9)	2.751(5)	2.747(3)		2.755(4)
N24···O2B		2.50(3)	2.51(2)	2.44(4)	2.46(4)	2.41(3)		2.40(3)
N24 O1AC57AO2A		3.400(10)	3.417(6)	3.440(11)	3.399(6)	3.381(4)		3.378(7)
N24 O1BC57BO2B		3.52(4)	3.45(3)	3.39(4)	3.47(5)	3.43(5)		3.33(5)
O1W···O2W	2.817(4)	2.838(4)	2.846(3)	2.837(4)	2.833(3)	2.823(3)	2.793(4)	2.812(4)
O1W···O10#4	2.768(3)	2.714(3)	2.720(2)	2.716(3)	2.717(3)	2.717(2)	2.760(6)	2.709(4)
O2W···O11#4	2.754(4)	2.815(3)	2.822(2)	2.817(4)	2.818(3)	2.818(2)	2.796(9)	2.809(4)
O2W···O11	2.808(4)	2.790(4)	2.796(3)	2.792(4)	2.782(3)	2.780(2)	2.748(3)	2.779(7)
O3WA···O15#5	2.751(10)	2.758(5)	2.768(3)	2.750(6)	2.739(3)	2.726(3)	2.767(9)	2.708(10)
O3WB···O15#5	2.84(3)	2.72(3)	2.711(16)	2.79(3)	2.83(3)	2.87(3)	2.78(2)	2.88(3)
O3WA···O5	2.836(10)						2.787(6)	
O3WB···O5	2.76(3)						2.82(2)	
O3WA···O5A		2.808(6)	2.822(3)	2.819(6)	2.806(4)	2.797(3)		2.783(5)
O3WB···O5B		2.68(2)	2.713(17)	2.68(3)	2.71(3)	2.74(3)		2.66(3)
O4W···O2#6	3.055(4)						2.960(8)	
O4W···O2A#6		3.026(12)	3.021(5)	3.015(14)	2.986(7)	2.965(4)		2.947(8)
O4W···O2B#6		2.97(4)	2.96(2)	3.00(5)	2.99(5)	2.98(4)		2.95(3)
O4W···O8	2.920(4)	2.892(4)	2.903(3)	2.894(4)	2.893(3)	2.893(3)	2.864(3)	2.878(4)
O5W···O8#7	2.870(5)	2.774(5)	2.792(3)	2.775(5)	2.786(4)	2.784(3)	2.854(3)	2.759(4)
O5W···O8#8	2.924(5)	2.978(6)	2.975(4)	2.980(6)	2.944(4)	2.923(3)	2.886(3)	2.910(4)
O6W···O3WA	2.960(14)	3.127(7)	3.116(4)	3.110(7)	3.079(5)	3.011(3)	2.849(7)	2.988(5)
O6W···O3WB	2.72(3)	2.74(2)	2.708(15)	2.68(3)	2.65(3)	2.56(3)	3.17(2)	2.59(2)
O6W···O3	3.389(6)						3.439(12)	
O6W···O3A		2.933(6)	2.942(4)	2.930(6)	2.936(4)	2.918(3)		2.897(13)
O6W···O3B		3.66(2)	3.616(13)	3.74(2)	3.80(2)	3.74(2)		3.94(2)
O6W···O9	3.374(7)	3.819(6)	3.865(4)	3.838(6)	3.938(5)	4.013(4)	3.101(4)	4.006(5)

[a] Photoinduced high-spin (PIHS) phase; [b] Structure obtained after full relaxation of the PIHS phase. Symmetry transformations used to generate equivalent atoms: #1 x, y-1, z; #2 x, -y+1, z+1/2; #3 x, -y+1, z-1/2; #4 -x, -y, -z+1; #5 x, y+1, z; #6 -x+1, y, -z+1/2; #7 x, y, z+1; #8 -x+1, -y+2, -z+1

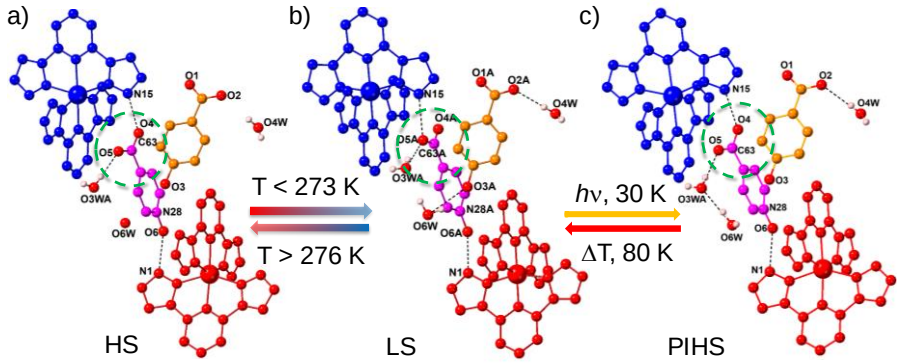

Figure 3.46. Scheme of the crystal structure of **5**·2.4H_2O showing the reversible supramolecular (H-bond) linkage isomerisation coupled to the SCO process. At 296 K (HS phase, a), O4 (isonicNO(6), magenta) is acting as H-bond acceptor, whereas at 120 K (LS phase, b) the oxygen atom that is interacting with the same bpp ligand is O5 (the other oxygen atom of the carboxylate moiety). Also, there is a rearrangement of the H-bonded network involving O3W, O4W and O6W water molecules. These structural variations can be reversed upon heating the LS phase above the SCO temperature or under laser irradiation at 30 K (PIHS phase, c). The PIHS phase relaxes back to the LS state at higher temperatures. Non-isomerised anions present in the LS phases (occupancy < 0.1) have been omitted.

These changes are mirrored in the carboxylate electron density, which is polarised towards O5 at 120 K (C63A–O5A: 1.278(3) Å; C63A–O4A: 1.236(3) Å). In addition, the negative thermal expansion observed for the *b* parameter is consequence of the rotational movement of isonicNO(6) anions. It decreases the tilt angle of the cationic layers (perpendicular to the *b* axis) with respect to the mean plane of the Fe^{2+} cations, increasing the interlayer distance. Another relevant difference concerns isonicNO(3) (orange). This anion is linking Fe1 and Fe3 sites through hydrogen bonds in both phases; however, in the LS phase it exhibits two additional interactions with water molecules (O3A···O6W: 2.918(3) Å; O2A···O4W: 2.965(4) Å) that are not present in the HS phase (O3···O6W: 3.389(6) Å; O2···O4W: 3.055(4) Å).

The question that arises now is what occurs first? The abrupt SCO or the isomerisation of this hydrogen bond? In other words, is the isomerisation of this H-bond a consequence or a cause of the SCO? In order to elucidate this situation, the crystal structure of **5**·2.4H_2O was solved at different temperatures below the transition (in the LS phase). The atomic coordinates of the cationic sublattice are similar to those observed at 120 K, without significant variations in the whole thermal range of study. Instead, considerable changes are found in the anionic sublattice with temperature. At 270 K, the isonicNO(6) is split into two positions,

A and B, with occupancy factors of 0.79 and 0.21, respectively (Figure 3.47.a). In position B (minor contribution), the anion is H-bonded through O4B, as in the original anion described in the HS phase (Figure 3.47.b). Instead, position A is H-bonded through O5A, just like the isomerised anion present in the 120 K structure. Therefore, below the SCO temperature, isonicNO(6) anions clearly isomerise from the B position (HS) to the A position (LS), a small contribution of B being present at all temperatures inside the LS phase. Interestingly, the residual fraction of non-isomerised H-bonds (occupancy of the B anions) decreases while the sample is cooled down. Finally, it becomes less than 10% at 120 K (92% of the H-bonds have isomerised, table 3.18).

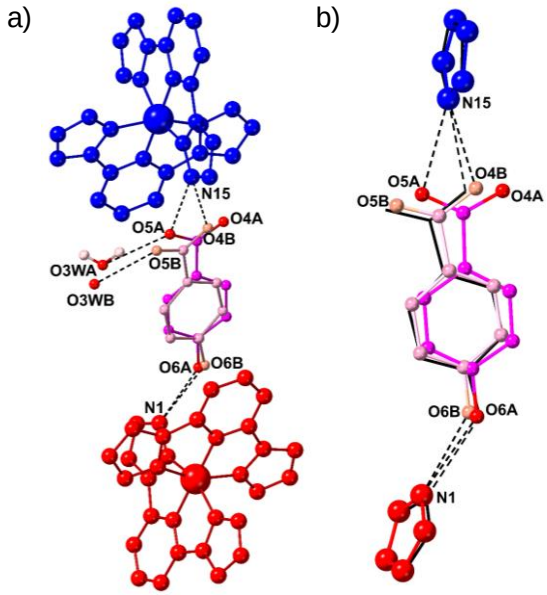

Figure 3.47. a) View of the crystal structure of **5**·2.4H_2O in the LS phase showing the two disordered positions of isonicNO(6) (magenta). The high and low occupancy contributions of this anion are illustrated in dark and light colours, respectively. b) Superposition of the crystal environment of isonicNO(6) in the X-ray structure of **5**·2.4H_2O at 296 K (HS, black sticks) and 270 K (LS, coloured balls and sticks). Dark and light colours represent the high and low occupancy subnetworks, respectively. Note the match between the HS structure and the B substructure (light coloured) of isonicNO(6) in the LS phase. Dashed lines refer to hydrogen bonds.

IsonicNO(3) is also disordered into two positions in the LS phase (Figure 3.48.a). But this time, the predominant contribution in the whole temperature range (A substructure) presents atomic coordinates that are practically equal to those observed for the HS material (Figure 3.48.b). Instead, the B position differs from that observed for the HS and LS (A sublattice) phases, appearing at 270 K and

almost vanishing at 120 K (Figure 3.48.b). All these results clearly demonstrate that the set of relevant structural transformations (hydrogen bond isomerisation, appearance of anionic disorder and the formation of new hydrogen bonds) takes place after the SCO phenomenon, and not prior nor concurrent to it.

Table 3.18. Occupancy factors of the two disordered positions (A and B, shown in Figure 3.47.a) involving isonicNO(6) in **5**·2.4H_2O at different temperatures.

T / K	296 (HS)	270 (LS)	260 (LS)	250 (LS)	200 (LS)	120 (LS)	30[a] (HS)	80[b] (LS)
A	nd	0.79	0.82	0.80	0.90	0.92	nd	0.88
B	nd	0.21	0.18	0.20	0.10	0.08	nd	0.12

[a] Photoinduced high-spin (PIHS) phase; [b] Structure obtained after complete relaxation of the PIHS phase. nd: no disorder.

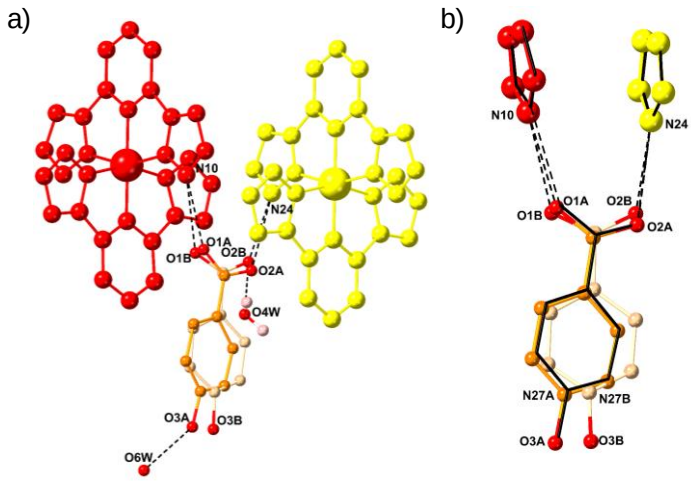

Figure 3.48. a) View of the crystal structure of **5**·2.4H_2O in the LS phase showing the two disordered positions of isonicNO(3) anion (orange). The high and low occupancy contributions of this anion are illustrated in dark and light colours, respectively. b) Superposition of the crystal environment of isonicNO(3) in the X-ray structure of **5**·2.4H_2O at 296 K (HS, black sticks) and 270 K (LS, coloured balls and sticks). Dark and light colours represent the high and low occupancy subnetworks, respectively. Note that isonicNO(3) anions do not change their position after the transition, thus, there is a good agreement between the HS structure and the A substructure (major contribution) in the LS phase. Dashed lines refer to hydrogen bonds.

In a next step, photocrystallography measurements were carried out. In order to characterise the PIHS phase, **5**·2.4H_2O was irradiated with a laser source (λ = 630 nm) for 2.5 h at 30 K. Then, the light irradiation was switched off and data

collection was performed at this temperature. The compound belongs to the same space group (*P*2/*c*) and the unit cell parameters are very similar to those obtained for the HS phase at 296 K, although slightly shorter due to thermal contraction (Table 3.14). As expected, Fe–N bond distances (mean value of 2.156 Å) and octahedral distortion parameters (Table 3.15) indicate an efficient trapping of the PIHS state. This new structure is very similar to that obtained at 296 K (Figure 3.49), without anion structural disorder and with all isonicNO(6) anions linked through O4. Undoubtedly, the hydrogen bond isomerisation has been effectively reversed under light irradiation (Figure 3.46.c). This accounts for the fact that an unusual long irradiation time was required to achieve full excitation. In addition, the O3···O6W interaction is not present after photoexcitation, just like in the structure at 296 K. Nevertheless, the hydrogen bond between O4W and O2 is preserved, in analogy to the LS phase. On the other hand, the differences involving the stacks of bpp ligands are also reversed, with stacking distances more similar to the HS phase (shorter due to thermal contraction) and higher dihedral angles (Table 3.16).

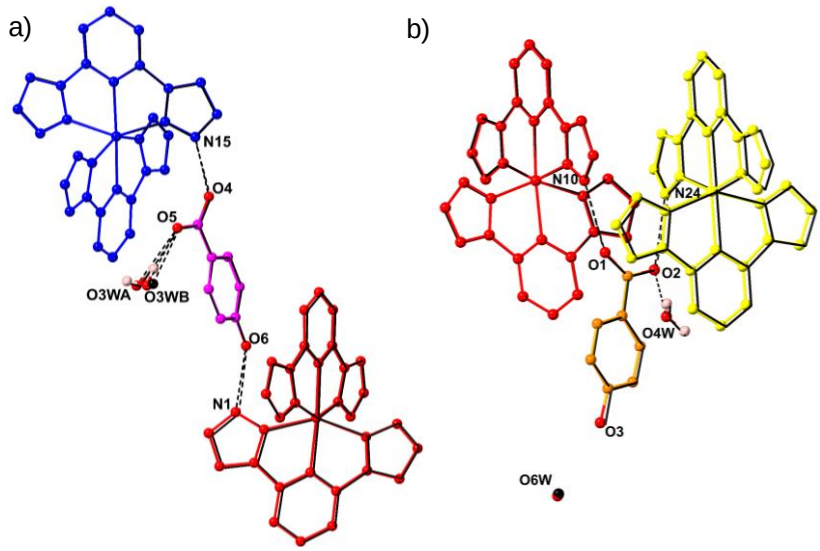

Figure 3.49. Superposition of the crystal structure of **5**·2.4H_2O measured at 296 K (HS phase, black coloured) and after irradiation at 30 K (PIHS phase, coloured balls and sticks), showing the connectivity of isonicNO(6) (a) and isonicNO(3) anions (b).

The structure of **5**·2.4H_2O was determined after relaxation of the PIHS phase at 80 K (Table 3.14). The crystal symmetry is the same (*P*2/*c*) and both the Fe–N bond lengths (mean value of 1.948 Å) and octahedral distortion parameters (Table 3.15) for the three iron centres are in agreement with a complete

relaxation to the LS state. This structure is very similar to the LS phases described previously (Figure 3.50) with the presence of anion disorder and showing that all the structural modifications obtained by light irradiation at 30 K are thermally reversed at 80 K (the onset of disorder, the formation and cleavage of hydrogen bonds and the supramolecular linkage isomerisation process).

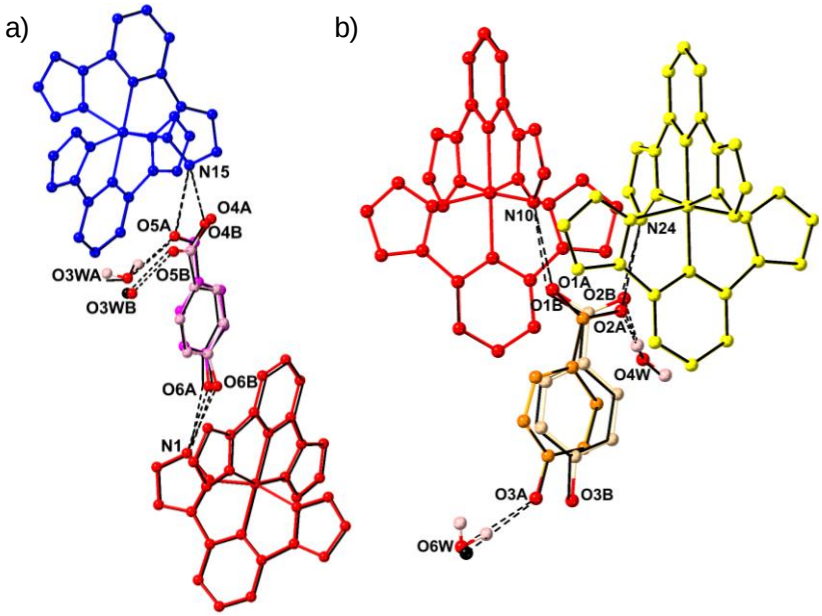

Figure 3.50. Superposition of the crystal structure of **5**·2.4H_2O measured at 270 K (LS phase, black coloured) and after thermal relaxation of the PIHS phase at 80 K (coloured balls and sticks), showing the connectivity of isonicNO(6) (a) and isonicNO(3) (b) anions.

The anhydrous material **5** was characterised in the HS (310 K) and LS (150 K) phases. The resolution of the crystal structures is very poor, however, they can afford significant information related to the SCO process. Now, the compound belongs to the triclinic *P*–1 space group (Table 3.19) and there is only one crystallographically inequivalent $[Fe(bpp)_2]^{2+}$ complex located in a general position at both temperatures. The single-crystal-to-single-crystal (SCSC) transformation takes place keeping the 2D arrangement of cationic complexes with isonicNO anions filling the space between the layers (Figure 3.51), although with relevant rearrangements concerning the anionic lattice. At 310 K, Fe–N bond distances (lying in the 2.13-2.23 Å range) and octahedral distortion parameters are indicative of a high-spin state (Table 3.20).

Table 3.19. Crystallographic data and structural refinement for anhydrous **5**.

	5 at 310 K[b]	**5** at 150 K[b]
Empirical formula	$C_{34}H_{26}FeN_{12}O_6$	$C_{34}H_{26}FeN_{12}O_6$
Formula weight	754.52	754.52
Crystallographic system	Triclinic	Triclinic
Space group	*P*–1(No. 2)	*P*–1(No. 2)
a/ Å	8.1411(5)	7.9469(3)
b/ Å	13.9346(10)	14.0674(13)
c/ Å	15.3302(10)	15.2005(5)
α/ °	82.224(6)	91.818(5)
β/ °	87.911(5)	87.371(3)
γ/ °	83.336(5)	88.410(5)
V/ Å^3	1711.1(2)	1695.93(18)
Z	2	2
R(int)[c]	?	?
ρ_{calc}/ g·cm^{-3}	1.464	1.478
μ/ mm^{-1}	0.506	0.510
Crystal dimensions/ mm	0.202 x 0. 175 x 0. 091	0.2006 x 0. 1469 x 0. 1130
T/ K	310.00(14)	150.00(10)
λ/ Å	0. 71073	0. 71073
2θ range/ °	5.04< 2θ <56.35	6.68< 2θ <56.01
Index ranges for h, k , l	-10/10, -18/18, -20/20	-10/10, -18/18, -19/19
Refinement method	Full-matrix least-squares on F^2	Full-matrix least-squares on F^2
Collected reflections	19171	18487
Unique reflections	19171	18487
Data/Restraints/Parameters	19171/52 / 445	18487 /222 / 382
Goodness-of-fit on F^2	0.936	1.053
R1, wR2 [I > 2sigma(l)][a]	0.0824/0.2106	0.1084/0.3037
R1, wR2 (all data)[a]	0.1807/0.2340	0.1718/0.3334
$\Delta\rho_{max}$ and $\Delta\rho_{min}$ (e·Å^{-3})	1.065/ -0.577	1.069/ -0.749

[a] $R1 = \Sigma(||F_o| - |F_c||)/\Sigma|F_o|$; $wR2 = \{\Sigma[w(F_o^2 - F_c^2)^2]/\Sigma[w(F_o^2)^2]\}^{1/2}$. [b] The structure of **5** is non-merohedrally twinned. The peaks were indexed by using two identical cells with different orientations related by rotation of 180° around the reciprocal b* axis. The fractional contribution of the minor twinned component refined to 0.483 and 0.497 using the BASF parameter and the HKLF5 instruction in the SHELXL program integrated in the WINGX program suite at 310 K and 150 K, respectively.[c] The Rint value is not defined for non-merohedral twins.

Table 3.20. Octahedral distortion parameters of the Fe1 centre in **5** at different temperatures.

T / K	φ / °	Σ / °
310 (HS)	170.82	149.53
150 (LS)	177.31	96.75

There are three independent isonicNO anions (denoted by the label of the corresponding NO oxygen atom, Figure 3.52): isonicNO(3) (orange) is hydrogen-bonded to two adjacent pyrazolyl NH functions in a *syn*, *syn*-bridging mode (in analogy to isonicNO(3) and isonicNO(15) in the hydrated material). This anion

connects the stacks of $[Fe(bpp)_2]^{2+}$ units along the *a* axis. Instead, the two other isonicNO anions (isonicNO(6) (magenta) and isonicNO(9) (brown)) are hydrogen-bonded to two $[Fe(bpp)_2]^{2+}$ complexes of different layers through a monodentate carboxylate anion and the N-oxide function (just like isonicNO(9) and isonicNO(6) in **5**·2.4H_2O). These isonicNO anions (brown and magenta) are statically disordered in two positions around an inversion centre, averaging the two antiparallel orientations observed in the pristine material (Figure 3.53). The process is reversible: rehydration restores the original hydrated salt, as confirmed by powder X-ray diffraction measurements (*vide infra*, Section D).

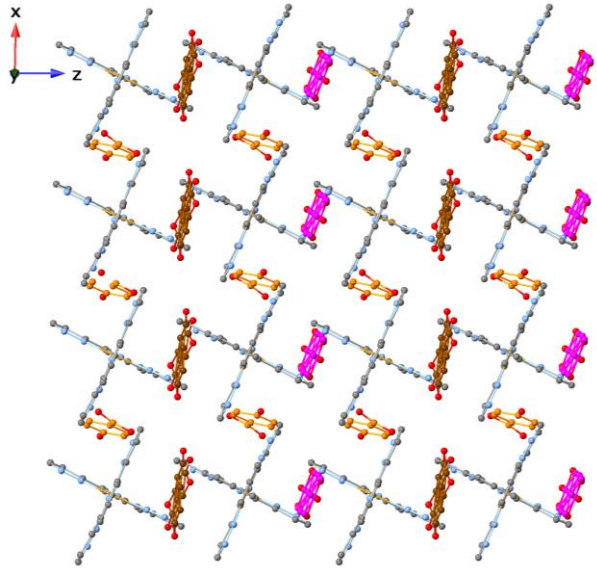

Figure 3.51. Crystal structure along the *b* axis, showing the 2D packing of $[Fe(bpp)_2]^{2+}$ complexes of **5** at 310 K.

At 150 K, Fe1–N bond distances lye in the expected range for a LS compound (2.006-1.925 Å) and octahedral distortion parameters clearly indicate a change in the spin state (Table 3.20, Figure 3.54). *a* and *c* parameters are slightly smaller and the cell volume has decreased from the value observed at 310 K about 0.89% (ΔV = 15.17 Å^3). Instead, the *b* parameter is higher than that obtained in the high-spin phase. The static disorder of isonicNO(6) and isonicNO(9) is still observed around an inversion centre (discarding a thermal motion nature), but whereas the disorder concerning isonicNO(9) is identical to that observed at 310 K, now isonicNO(6) anions change their orientation with respect to the cationic layers by as much as 23° (Figure 3.52.b). In addition, in the LS phase the inversion

centre is shifted away from the longitudinal axis of isonicNO(6) anions, resulting in a displacement along the *xy* plane.

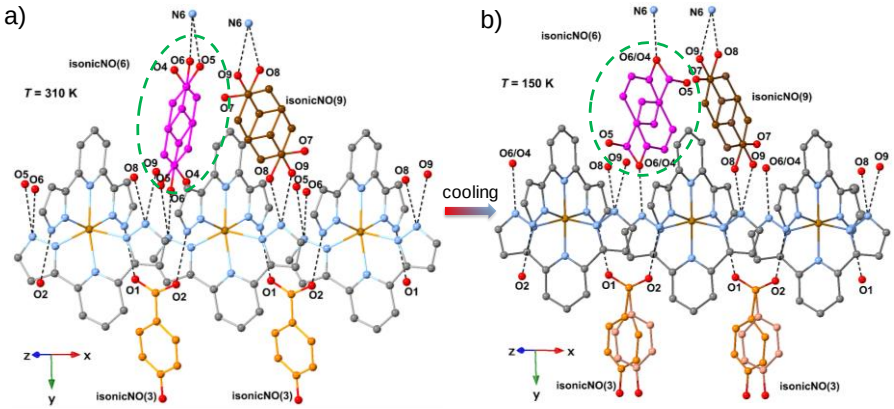

Figure 3.52. View of the X-ray crystal structure of **5** showing the crystal environment of the three isonicNO anions a) at 310 K (HS phase) and b) at 150 K (LS phase). The dashed green oval highlights the anion involved in the H bond isomerisation encompassing the SCO in **5**. Dashed lines refer to hydrogen bonds.

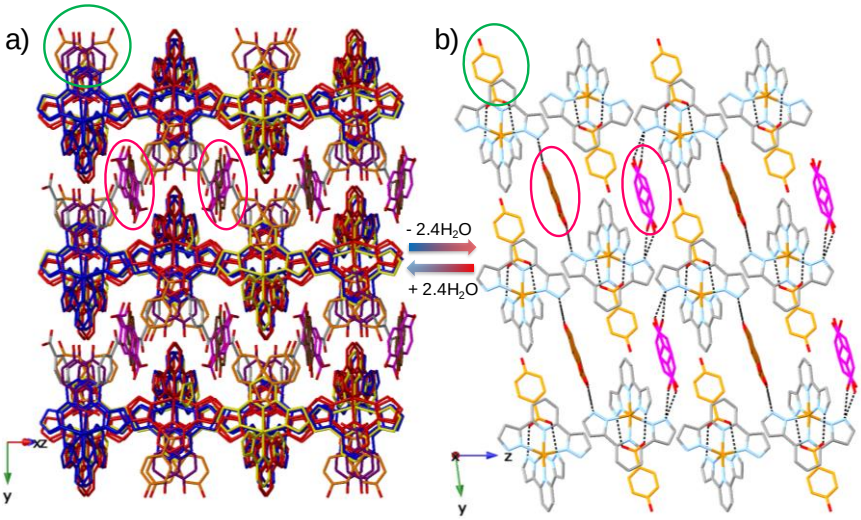

Figure 3.53. Dehydration/rehydration process. a) View of the crystal structure of **5**·2.4H_2O (T = 296 K, HS phase), showing the antiparallel orientation of magenta and brown anions within the anionic layer (pink oval). b) View of the crystal structure of **5** (T = 310 K, HS phase), showing the H-bonds between the cationic layers and isonicNO anions. Note that now the stacks of $[Fe(bpp)_2]^{2+}$ units are connected by *syn*, *syn*-bridging isonicNO anions that are all of them equivalent (green oval). And the two isonicNO anions that are hydrogen-bonded to complexes belonging to different layers are now disordered in two positions (pink oval).

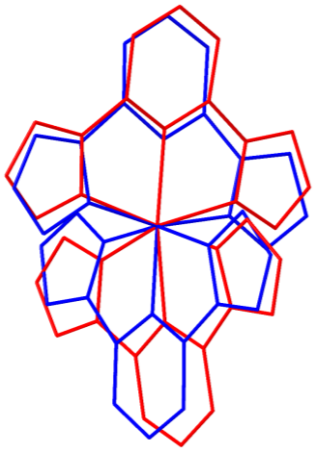

Figure 3.54. Superposition of the X-ray crystal structures of **5** at 310 K (red sticks) and 150 K (blue sticks), showing the coordination environment of the Fe1 site.

This displacement indicates that a hydrogen bond isomerisation takes place also in the anhydrous material, positioning the other oxygen atom of the carboxylate anion in a better position to act as hydrogen bond acceptor: at 310 K, O5 is forming a hydrogen bond with N6, whereas at 150 K the other oxygen atom of this carboxylate fragment (O4) is engaged in hydrogen bonds with N6 (Table 3.21). As a result of this, the position of O4 and that of O6 (the oxygen atom of the N-oxide function) become the same. On the other hand, the slight increase of the *b* parameter upon cooling reinforces that also in the anhydrous compound a hydrogen bond isomerisation takes place, involving the monodentate anions isonicNO(6) that are linking the iron sites along this direction.

Table 3.21. Intermolecular hydrogen bonds present in **5** between donors and acceptors (D-H···A) at 310 K and at 150 K.

D···A	$d_{D\cdots A}$ / Å (310 K)	$d_{D\cdots A}$ / Å (150 K)
N1···O2	2.666(9)	2.737(14)
N5···O1#1	2.684(8)	2.637(10)
N6···O6	2.639(12)	2.615(14)
N6···O4	3.454(12)	2.615(14)
N6···O5	2.622(11)	4.16(3)
N10···O9#2	2.64(9)	2.616(15)
N10···O8#2	2.54(15)	2.505(18)

Symmetry transformations used to generate equivalent atoms: #1 x + 1, y, z at 310 K and 150 K; #2 – x +1, – y + 1, – z + 1 only at 310 K.

The abrupt transformation affects also the isonicNO(3) anions (that bridge the $[Fe(bpp)_2]^{2+}$ stacks along the *a* axis), being also disordered in two positions: A (depicted in pastel red) and B (illustrated in orange), with occupancy factors of

0.50 (Figure 3.52.b). Fe1–Fe1 distances between consecutive stacked iron centres along the *c* axis decrease as the crystal is cooled (from 8.166 Å and 8.596 Å at 310 K to 8.142 Å and 8.112 Å at 150 K), as a consequence of both thermal contraction and SCO. Analogously, the intrastack distance in the *a* axis decreases from 8.141 Å at 310 K to 7.947 Å at 150 K, but this time the difference is more notable. This indicates that the contraction is more pronounced along the *a* axis, consistent with the fact that isonicNO(3) anions are connecting the iron centres in this direction. In this case, the hydrogen bonds are also lower in the LS phase with respect to the HS structure (Table 3.21). The only contact that does not follow this trend is N1···O2, which can be explained considering that this oxygen atom belongs to the bidentate anion isonicNO(3) and that the other interaction (N5···O1) is strengthened in the LS phase.

D. Powder X-ray diffraction

The purity of **5**·2.4H_2O was verified by comparing the experimental diffractogram with the simulation obtained from the single crystal X-ray data. The X-ray diffractogram of the deuterated sample was also measured and compared with that obtained for **5**·2.4H_2O, revealing that both samples are isostructural (Figure 3.55).

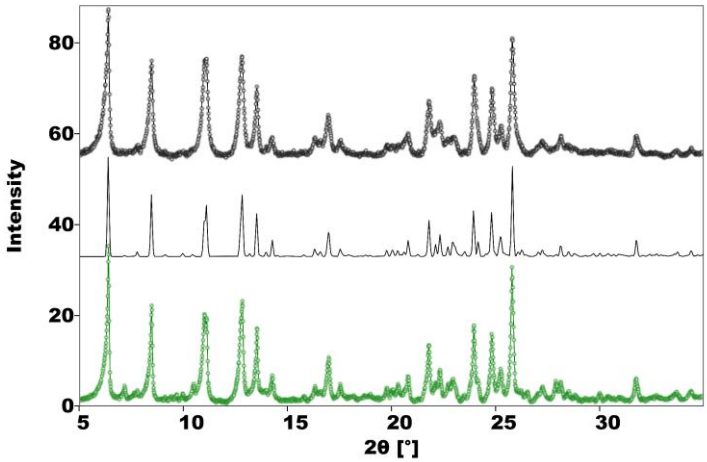

Figure 3.55. Room-temperature powder X-ray diffractograms of **5**·2.4H_2O (black points) and **5**·1.8H_2O·0.6D_2O (green points). The simulation from single crystal data for **5**·2.4H_2O at 296 K has been included for comparison (black lines).

Moreover, powder X-ray diffraction measurements of **5**·2.4H_2O were conducted at variable temperature (Figure 3.56). X-ray diffraction patterns were recorded in the 300-150 K temperature range, revealing a structural phase transition

between 300 K and 260 K, which fits in the temperature range where SCO takes place. Further cooling down to 150 K did not show any additional feature. Simulations from single crystal data in the HS and LS phases are included for comparison and the structural variations are consistent with those observed experimentally.

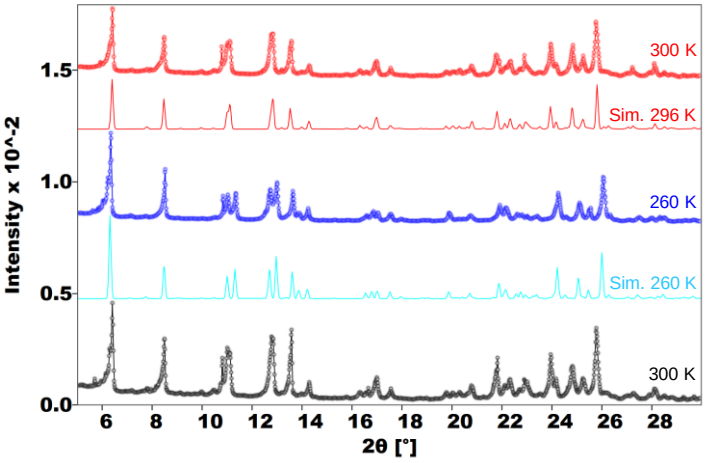

Figure 3.56. Powder X-ray diffractograms of **5**·2.4H_2O at different temperatures, together with the corresponding simulations of the LS and HS phases. A second measurement at 300 K (shown in black) after cooling down to 150 K and heating back to room temperature is shown in order to demonstrate the reversibility of the transformation.

On the other hand, diffractograms of the anhydrous material obtained by *in situ* dehydration at 400 K for 2 h were accquired in the 400-147.5 K temperature range (Figure 3.57). Cooling from 400 K to 200 K did not reveal any structural modification, showing a constant diffraction pattern that matches the simulated diffractogram for the HS phase. A phase transition was detected between 200 K and 147.5 K, which is in agreement with the SCO from the HS to the LS phase detected by DSC ($T_{anh}^{\downarrow}$) and magnetic measurements at 10 K·min^{-1}. The simulated pattern for the LS phase is in accordance with the experimental data. There is no evidence for the existence of different LS phases and the corresponding metastable LS phase at high temperatures could not be accessed in our experiments: above $T_{anh}^{\uparrow}$ the LS pattern is inevitably lost with the recovery of the HS phase, which is in agreement with DSC and magnetic measurements at high sweeping rates.

Finally, in order to study the reversibility of the dehydration-rehydration process, the powder X-ray diffractogram of the rehydrated material was also

measured at room temperature. It is compared with the diffractograms of the as-synthesised and desolvated materials, together with the corresponding simulations obtained from single crystal data (Figure 3.58). The X-ray pattern of the rehydrated sample matches perfectly with that obtained for the original product, confirming that rehydration is reversible.

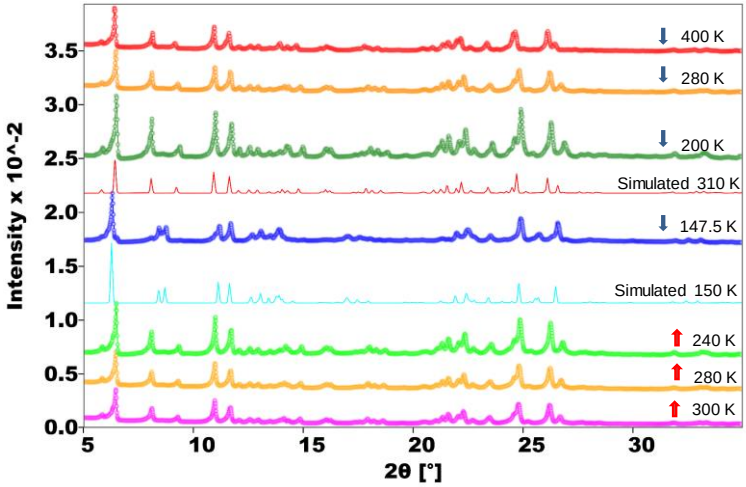

Figure 3.57. Powder X-ray patterns of **5** at different temperatures in the cooling and heating modes (blue and red arrows, respectively). The simulated diffractograms obtained from single crystal data of the HS and LS phases are shown for comparison.

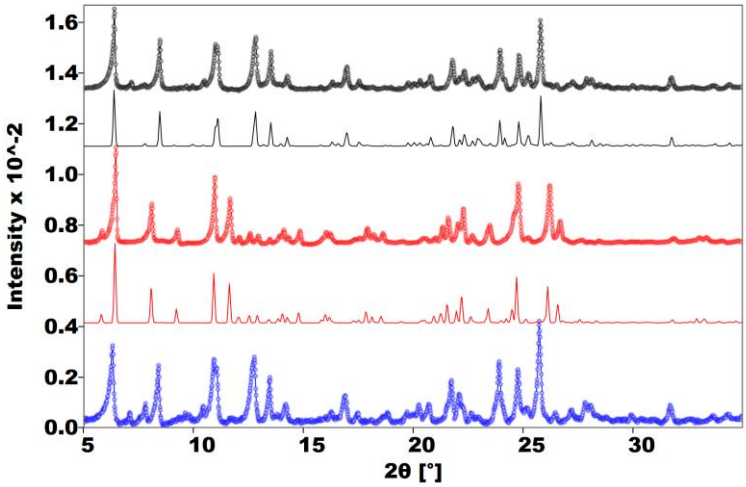

Figure 3.58. Room-temperature powder X-ray diffractograms of **5**·2.4H_2O as-synthesised (black dots), dehydrated (red dots) and rehydrated (blue dots). Simulations from single crystal data have been included for comparison (black and red lines for **5**·2.4H_2O at 296 K and **5** at 310 K, respectively).

3.4.4. Snapshots of single crystals of 5·2.4H_2O

Due to the fact that the spin transition takes place near room temperature, we were able to cool down some crystals of **5**·2.4H_2O and observe the colour changes as a consequence of the different optical absorption bands between the LS and HS states. The nucleation and growth mechanism was observed in individual single crystals (Figure 3.59), as previously investigated by means of optical microscope in SCO systems.[34]

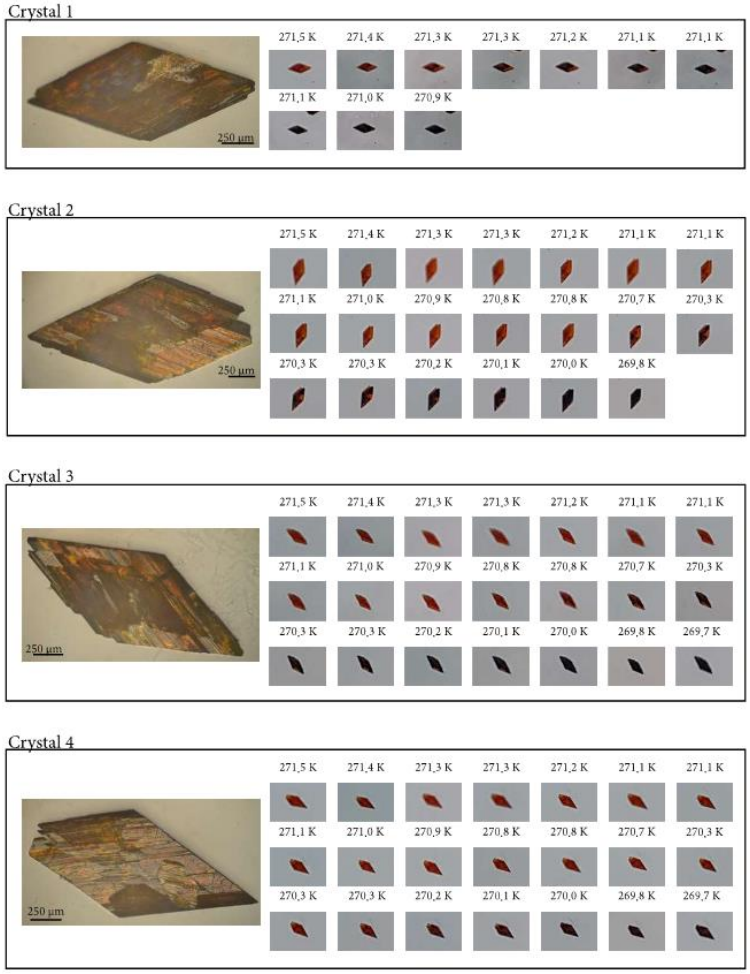

Figure 3.59. Observation of the nucleation process in single crystals of **5**·2.4H_2O during the thermally induced spin transition.

In this compound, the colour changes from dark-red in the LS phase to orange in the HS phase, in agreement with the fact that in the LS state the crystals appear darker (opaque) due to the stronger optical absorption in the visible region. Diffusion of the spin state at the nanoscale gives rise to the formation of a HS-LS interface (macroscopic barrier between the HS and LS states), which grows thanks to cooperative interactions until complete transformation of the crystal. The colour changes due to the SCO phenomenon induced by thermal variation are in agreement with the magnetic measurements and structural characterisation of **5**·2.4H_2O.

3.4.5. Conclusions and perspectives

A hydrogen-bonded network of $[Fe(bpp)_2]^{2+}$ cations and isonicNO anions has been synthesised and its structural and (photo)magnetic properties studied. In spite of not presenting the expected diamond-like structure, this material is attractive for several reasons. First of all, **5**·2.4H_2O is high-spin at room temperature and exhibits SCO without the need of prior desolvation, which is unusual for $[Fe(bpp)_2]^{2+}$ salts of simple anions in their hydrated forms.[35] For comparison, the isonicotinate salt (**3**·2H_2O) exists only in the LS state at temperatures higher than room temperature. This can be explained taking into consideration that the N-oxide function exhibits a weaker H-bond accepting character with respect to pyridines (is not always involved in hydrogen bonds with the $[Fe(bpp)_2]^{2+}$ cation). Thus, there is a decrease in the electron density of the non-coordinating nitrogen atoms that results in weaker N–Fe interactions, destabilising the low-spin state.[36] Secondly, it exhibits an extremely abrupt transition (the fraction of HS Fe^{2+} cations changes from 1 to 0 in less than 3 K at standard cooling rates) near room temperature. The cationic sublattice exhibits a similar packing to the well-known *terpyridine embrace* motif with the three iron sites present in the crystal lattice undergoing crossover almost simultaneously. More importantly, the SCO process drives a supramolecular linkage (hydrogen bond) isomerisation. The study of the crystal structure of **5**·2.4H_2O at different temperatures allows to determine unambiguously that anion disorder occurs as a result of the accommodation of some anions to the abrupt change encompassing SCO in the cationic subnetwork. This is the first time in which a drastic rearrangement of the crystal lattice influences the connectivity between the Fe(II) complexes and the anionic sublattice. Photo- and thermally induced reversible H-bond isomerisations are uncommon processes,[37] being observed in intramolecular H-bonds rather than involving more than one molecule. The modification of the H-bonded network of a compound may change its physico-chemical properties, which can be useful for

a wide variety of applications in different fields such as photoswitchable recognition or photopharmacology.[38] Therefore, the SCO phenomenon is useful for triggering reversible structural transformations in solids that might be difficult to achieve by other means. These changes are reversible with respect to temperature variation and light irradiation (Scheme 3.5).

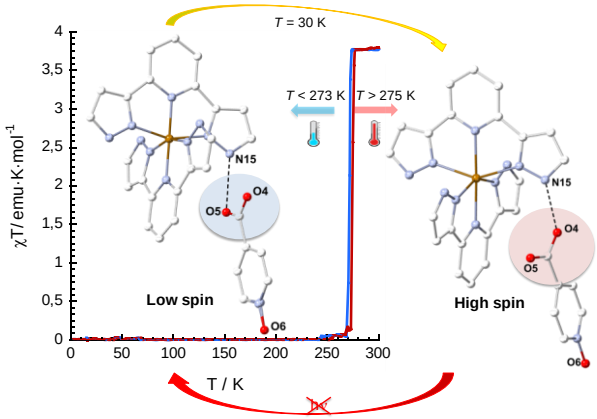

Scheme 3.5. Schematic representation of the reversible hydrogen bond isomerisation and SCO process in **5**·2.4H_2O.

On the other hand, isotopic experiments reveal that hydrogen bonding affects spin crossover behaviour. DSC and magnetic measurements show a similar behaviour for the deuterated sample with similar thermal hysteresis but with slightly different $T_{1/2}$ values. There is a 5 K decrease of the critical temperature of the phase transition for **5**·1.8H_2O·0.6D_2O, indicating a destabilisation of the low-spin phase. Since PXRD measurements show that hydrated and deuterated samples are isostructural, it is clear that the destabilisation observed has to be related to the free energy gain associated to the formation of hydrogen bonds. In particular, the hydrogen bond between O6W···O3, which is only present in the low-spin phase. It is known that hydrogen bonds become weaker upon deuteration (Ubbelohde effect),[39] as a consequence of the lower zero-point vibrational energy of O–D bonds with respect to H–O bonds. Thus, the value of the thermodynamic enthalpy (ΔH) should decrease in the deuterated material. Nevertheless, in our case a slightly higher value is obtained for the deuterated sample, which is in contrast with previous reports about isotope effects in which the SCO temperature is shifted to higher values upon deuteration.[40] Anyway, it has to be noted that in previous cases, the isotope effect compares HS and LS phases in their deuterated and non-deuterated forms, whereas in the present work we are dealing with intermolecular hydrogen bond interactions. The

important point is that there is a variation in the magnetic properties of the compound upon deuteration, demonstrating the relevant role of hydrogen bonds in defining the magnetic properties.

Furthermore, it was possible to dehydrate **5**·2.4H_2O in a reversible single-crystal-to-single-crystal transformation. The anhydrous material preserves the 2D *terpyridine embrace* motif with a strictly parallel arrangement of adjacent pyrazolyl rings along the *c* axis, suggesting that the establishment of stronger π-π stacking interactions is the driving force for this transformation. Despite the fact that the anhydrous structure in the HS and LS phases presents a high degree of anionic disorder, a hydrogen-bond isomerisation encompassing the spin transition could be detected. The removal of water molecules strengthen the bonding between the SCO cations and the isonicNO anions, which leads to strong kinetic effects in the magnetic properties and wide hysteresis loops that depend on temperature scan rate. This is a fact well-documented for SCO materials and is related to the rearrangements noticed in the anionic sublattice.[41] Furthermore, this work is another example of the dependence of SCO on the degree of hydration, which can be used in humidity sensing applications.

On the account of the $T_{1/2}$ value close to room temperature of **5**·2.4H_2O, magnetic measurements and X-ray single crystal diffraction experiments under pressure will be performed. It is well-known that the effect of increasing pressure on SCO compounds is to stabilise the low-spin phase due to its smaller volume, thus, shifting the spin equilibrum towards higher temperatures.[42] In the present work, a relatively low pressure may suffice to shift the $T_{1/2}$ from 273.8-274.8 K to RT, which is a requisite for the real application of SCO complexes.

3.5. $[Fe(bpp)_2](isonicNO)_2 \cdot HisonicNO \cdot 5H_2O$ (**6**·$5H_2O$)

3.5.1. Synthesis

Analogously to the previous compound, **6**·$5H_2O$ was synthesised by a metathesis reaction between the $[Fe(bpp)_2]SO_4$ and the barium isonicotinate N-oxide salt. It was necessary to add an excess of the second reagent in order to achieve complete removal of the sulphate anions as a consequence of the high solubility of the isonicNO anions in water. In addition, one equivalent of the free acid was also added (Scheme 3.6). **6**·$5H_2O$ was obtained as light-red cubes and contains isonicotinic acid N-oxide both in its free and deprotonated form. Heating this sample to drive off water molecules results in an amorphisation of the compound.

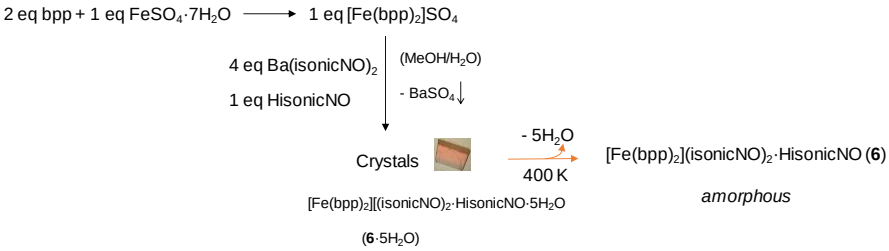

Scheme 3.6. Schematic synthesis of **6**·$5H_2O$.

Similarly, a deuterated sample was synthesised following the procedure described above but replacing H_2O and CH_3OH by deuterated solvents (D_2O and CD_3OD). IR spectrum shows a considerable fraction of non-deuterated compound. Comparative analyses based on the O–H stretching band for **6**·$5H_2O$ and the deuterated material, revealed that the approximate composition of the deuterated sample is **6**·$2.75H_2O \cdot 2.25D_2O$.

3.5.2. Magnetic characterisation

A. Magnetic properties

Magnetic susceptibility measurements of **6**·$5H_2O$ were performed in the 2-300 K temperature range. Figure 3.60.a shows that the χT product at room temperature has a value of 4.28 emu·K·mol^{-1}, above the expected value for a "spin-only" Fe^{2+} cation (χT = 3 emu·K·mol^{-1}). Nevertheless, this value corresponds to a fraction of high-spin Fe^{2+} cations (γ_{HS}) of 1. On lowering the

temperature (curve 1), the magnetic signal decreases steeply and it reaches a plateau for a χT value of 2.19 emu·K·mol^{-1} (γ_{HS} = 0.5). This indicates that the compound undergoes a partial spin transition around 167 K (inflection point where $\gamma_{HS} \approx 0.75$) to yield a mixed HS/LS state with approximately 50% of the material remaining in the high-spin state after cooling. Below 25 K, the magnetic response decreases sharply as a consequence of the zero-field splitting (ZFS) of the HS fraction present in the material. The heating process (curve 2) reveals an identical behaviour, showing that this transition is reversible and that it takes place without thermal hysteresis.

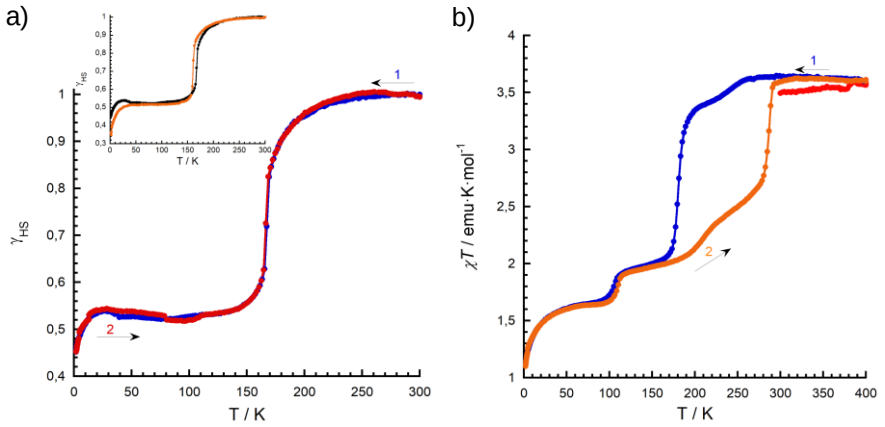

Figure 3.60. a) Thermal dependence of the χT product for **6**·5H_2O. The inset shows a comparative plot of **6**·5H_2O (black) and **6**·2.75H_2O·2.25D_2O (orange). b) Temperature dependence of the χT product for **6** after heating 2 h at 400 K (red curve). Curves 1 and 2: cooling and heating modes, respectively. A second thermal cycle revealed the same behaviour for the three compounds.

In this compound, there are also changes in H-bonding connectivity between the LS and HS phases (*vide infra*, structural characterisation); thus, isotopic effects were expected. In this context, the deuterated sample was measured and essentially an identical curve was obtained (inset Figure 3.60.a). The χT product at 300 K equals 3.68 emu·K·mol^{-1}, higher than the "spin-only" value for a 100% HS material but lower than the value registered for **6**·5H_2O. This is ascribed to the smaller size of the deuterated crystals, resulting in a decrease of orientational effects. Upon cooling, the magnetic signal decreases and a plateau for a χT value of 1.90 emu·K·mol^{-1} (γ_{HS} = 0.5) is reached, with an inflection point at 161 K (where $\gamma_{HS} \approx 0.75$). Further cooling shows an additional decrease due to ZFS effects. Again, the heating process (curve 2) is identical, demonstrating the reversibility of this transformation. Note that the SCO temperature decreases 6 K upon deuteration, in agreement with the results showed for the previous

compound (**5**·2.4H_2O) in which also a stabilisation of the HS phase was observed in the deuterated material.

Furthermore, **6**·5H_2O was dehydrated *in situ* at 400 K for 2 h (Figure 3.60.b, red curve). The χT value at room temperature is 3.63 emu·K·mol^{-1}, as expected for one high-spin Fe^{2+} cation per formula unit. On lowering the temperature (curve 1), the magnetic signal decreases smoothly and a first inflection point is observed at 222 K. This transition involves a very small fraction of iron centres (γ_{HS} = 0.95 at 206 K). Further cooling reveals a sharp transition with $T_{1/2}^{\downarrow}$ = 178 K that involves approximately 40% of the iron centres (γ_{HS} = 0.55 at 153 K). Then, the magnetic response continues decreasing and reaches a small plateau at 80 K, where χT is equal to 1.66 emu·K·mol^{-1}. This corresponds to $\gamma_{HS} \approx 0.45$. Finally, at very low temperatures, an additional decrease due to ZFS is observed. Heating now the sample (curve 2) reveals that the latter transition involving only 10% of the iron centres is reversible (T = 107 K), whereas the main transition is associated to a thermal hysteresis of ≈ 103 K ($T_{1/2}^{\uparrow}$ = 281 K) that merges heating and cooling curves and restores the complete 100% HS material. The full process is reproduced by equivalent heating and cooling curves (not shown). Further characterisation of this anhydrous phase was not conducted, due to the incomplete and gradual SCO behaviour, together with the fact that it loses its crystallinity upon dehydration, hindering the establishment of structure-property relationships.

B. Photomagnetism and excited spin-state trapping

The next step was to check if this compound presents LIESST effect. First, **6**·5H_2O was cooled down to 10 K (curve 1, Figure 3.61.a) and irradiation at this temperature with a red laser source (λ = 630 nm) resulted in an increase of the magnetic response. The magnetic signal with an initial χT value of 1.61 emu·K·mol^{-1} (mixed HS/LS state) reached saturation after 10 min of irradiation (curve 2) with a χT value of 3.56 emu·K·mol^{-1}. This indicates a fast excitation to the HS state. Then, the laser was switched off and the thermal variation of the susceptibility of **6**·5H_2O was registered in the heating mode at 0.3 K·min^{-1} (Curve 3). After an initial increase due to the ZFS of the quintet ground state, χT has a value of 4.10 emu·K·mol^{-1} at 40 K, as expected for γ_{HS} = 1. Above 60 K, the magnetic signal decreases abruptly and the 100% LS state is reached at 80 K. Surprisingly, the compound relaxes to its fully LS form, not to the HS/LS distribution found in the starting material. The sample remains in the diamagnetic state until 105 K. Further heating results in a sharp increase of χT

to reach a value of 1.93 emu·K·mol^{-1} at 118 K. Above this point, the magnetic behaviour merges with that obtained for the non-irradiated material: the mixed HS/LS phase is observed in the 120-160 K temperature range and at 167 K a transition to the fully HS phase takes place (χT value of 3.67 emu·K·mol^{-1} at 300 K). Strikingly, in the present case, the determination of T(LIESST) from the first derivative plot (inset Figure 3.61.a) reveals clearly the existence of two relaxation processes: a first one with T_1(LIESST) = 68 K, where the photoinduced HS phase relaxes to a mixed HS/LS phase, and a second process with T_2(LIESST) = 76 K, in which the remaining HS centres relax to their LS states.

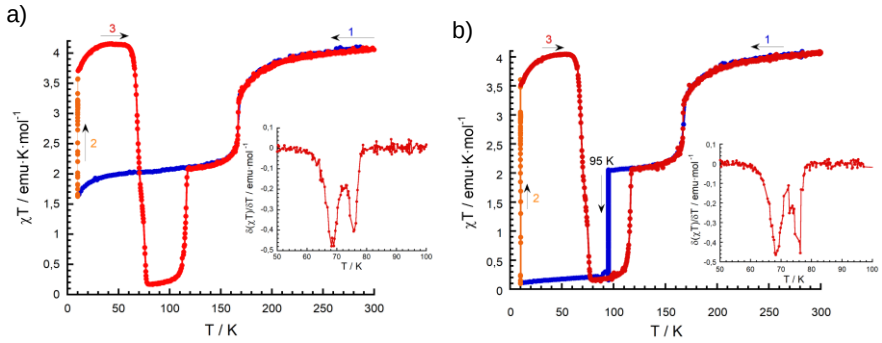

Figure 3.61. a) Temperature dependence of the χT product for **6**·5H$_2$O on cooling before irradiation (blue), under irradiation at 10 K (orange) and subsequent heating in the dark (red). The inset shows the first derivative of the LIESST plot. b) Thermal variation of χT for **6**·5H$_2$O before irradiation (curve 1, blue), including an annealing treatment at 95 K; under irradiation at 10 K (curve 2, orange) and subsequent heating in the dark (curve 3, red). The inset shows the first derivative of the LIESST plot.

The existence of more than one relaxation process in the LIESST plot is generally ascribed to the presence of inequivalent Fe centres in the structure that undergo spin crossover separately. The LIESST relaxation thus mirrors the thermomagnetic behaviour. Nevertheless, although some examples showing two separated relaxation events exist (for instance, $[Fe(L^2Me)_2](ClO_4)_2$, being L^2Me = 2,6-bis(4-methyl-pyrazol-1-yl)pyrazine),[43] LIESST plots usually exhibit an inflexion point rather than two clearly separated steps.[44] In **6**·5H$_2$O, the first relaxation process at T_1(LIESST) = 68 K is associated to the partial SCO that occurs at 167 K. Considering $T_{1/2}$ = 116 K, applying the expression that correlates the SCO temperature ($T_{1/2}$) and T(LIESST) (Eq. 3.1), a value of T(LIESST) = 115 K is obtained. As can be seen, both parameters are similar. In this situation, it has been stated that the thermal SCO depends strongly on kinetic factors, leading usually to a partial spin transition and a lower T(LIESST) parameter with respect to that predicted.[45] The behaviour described for **6**·5H$_2$O is in agreement with these facts. In addition, the photomagnetic measurements strongly suggest the

existence of three intervals of stability: 1) At T > 167 K where the HS phase is the stable one; 2) 116 K < T < 167 K, in which a HS/LS distribution is the stable phase; 3) T < 116 K, where the mixed phase becomes metastable and the most stable phase is the LS. This behaviour is very similar to that already described for an iron(II) bischelated complex of 2,6-bis(3-methylpyrazol-1-yl)pyridine.[46]

In another experiment, the sample was first cooled down from room temperature to 95 K and held at this temperature for 4 h (Figure 3.61.b). A dramatic decrease of the magnetic signal was observed during this time, reaching a final χT value of 0.20 emu·K·mol^{-1}, in agreement with an almost complete relaxation to the LS phase. The compound was then cooled further to 10 K and irradiated with red light. The behaviour of this LS phase upon laser irradiation and re-warming was identical to that observed for the metastable HS/LS form of the material with exactly the same T(LIESST) values of 68 K and 76 K. These results indicate that the same PIHS phase is reached following irradiation regardless of the LS population of the sample before irradiation. This is not always the case. In $[Fe(dpp)_2][Ni(mnt)_2]_2 \cdot MeNO_2$ (dpp = 2,6-bis(pyrazol-1-yl)pyridine, mnt = maleonitriledithiolate), that also exhibits a two-step relaxation, different photomagnetic properties are obtained depending on the low spin population of the initial phase.[47]

Moreover, photomagnetic measurements of **6**·5H$_2$O were conducted in order to check if this compound presents LITH effect (Figure 3.62.a).

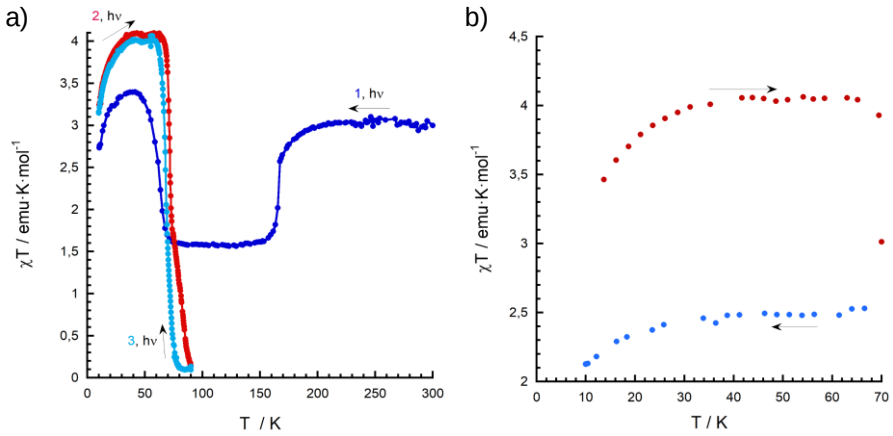

Figure 3.62. a) Temperature dependence of the χT product for **6**·5H$_2$O on the first cooling process (dark blue), and subsequent heating and cooling (red and light blue). The sample was irradiated during the whole measurement. b) Thermal variation of the χT product for **6**·5H$_2$O after heating from 10 K to 70 K the PIHS state (red), and cooling back to 10 K without irradiation (blue).

First, the temperature was decreased until 10 K under a red laser irradiation. Then, the thermal variation of the χT product was recorded without switching off the laser source both in warming and cooling modes (between 10 and 90 K). Practically it can be affirmed that there is a lack of induced thermal hysteresis, being this divergence with respect to **5**·2.4H_2O an indication of a lower degree of cooperativity in this system. After this, we have observed that it is possible to trap the compound in a mixed HS/LS phase starting from the PIHS state by heating to 70 K and cooling down back to 10 K (Figure 3.62.b).

In contrast to previous examples such as in *cis*-[Fe(picen)$(NCS)_2$] (picen = N,N'-bis(2-pyridylmethyl)1,2-ethanediamine),[48] quenching **6**·5H_2O to 10 K in a few seconds afforded a γ_{HS} fraction close to 0.5 (Figure 3.63) instead of a 100% HS material. This indicates the presence of a mixed HS/LS phase. Heating now this compound at 0.3 K·min^{-1} yields a T(TIESST) value of 96 K. The same experiment was carried out after cooling down the sample at 2 K·min^{-1} instead of quenching it. Now, a T(TIESST) value of 100 K was obtained, indicating a faster relaxation for the first experiment as a consequence of the mechanical stress induced by extremely fast cooling. In any case, both values are higher than T_2(LIESST), suggesting that the metastable mixed phase obtained by thermal quenching is different from that obtained by irradiation and subsequent partial relaxation. Further heating shows that at 114-116 K both T(TIESST) plots match perfectly with the T(LIESST) curve, revealing that the regions of stability of the LS (T < 114-116 K) and HS/LS (114-116 K < T < 167 K) phases are exactly the same irrespective of the conditions used for the spin trapping (temperature or light).

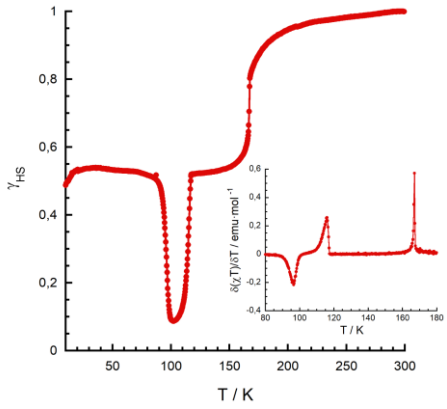

Figure 3.63. TIESST experiment: thermal dependence of the χT product for **6**·5H_2O after quenching at 10 K, then heating it at 0.3 K·min^{-1}. The inset shows the first derivative of the TIESST plot.

In general, it is not strange that metastable HS phases obtained by light irradiation (LIESST) or by thermal trapping (TIESST) present different relaxation kinetics.[48] The HS Fe^{2+} centres obtained by irradiation of the LS material at low temperatures exhibit a less distorted octahedral environment with respect to the Fe^{2+} sites obtained by an extremely fast cooling. In the latter case, the coordination environment is similar to that observed in the HS phase. As a result of the propagation of these subtle differences, the whole structure of the PIHS phase presents a closer resemblance to that of the LS phase, hence, being more favoured the HS ⟶ LS transformation.

C. Relaxation measurements

The dissimilarity observed between T(LIESST) and T(TIESST) indicates that different relaxation mechanisms for the metastable phases obtained by light irradiation and thermal quenching are present. Indeed, this can be verified by comparison of the relaxation of a precooled sample with the relaxation of the PIHS phase after light irradiation. On the one hand, the relaxation kinetics of the compound obtained after light irradiation of the metastable HS/LS material was investigated. Relaxation measurements were carried out at different temperatures between 60 K and 72 K (below T_i(LIESST)). After irradiation at 10 K until saturation of the signal, **6**·5H$_2$O was heated until the selected temperature. Then, light was switched off and the time dependence of γ_{HS} recorded (Figure 3.64.a).

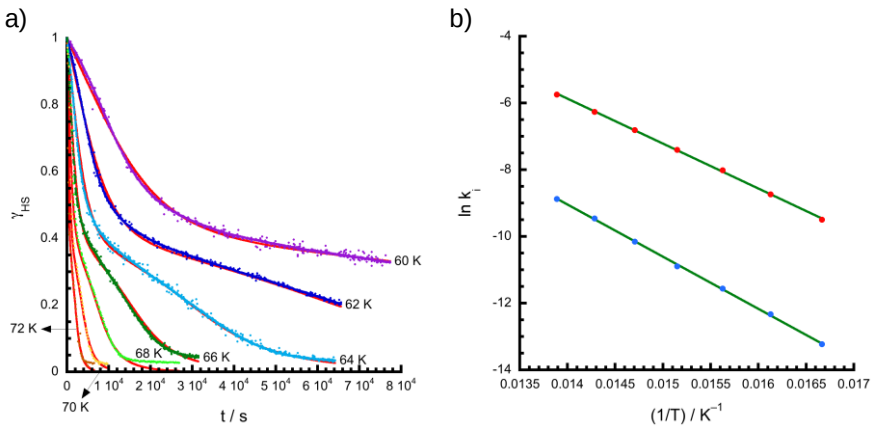

Figure 3.64. a) Time dependence of the γ_{HS} of Fe^{2+} cations obtained by light irradiation of **6**·5H$_2$O at 60 K (purple), 62 K (dark blue), 64 K (light blue), 66 K (dark green), 68 K (light green), 70 K (yellow) and 72 K (brown). Red lines represent the best fit to equation 3.5. b) Arrhenius plots corresponding to the fast (red) and slow (blue) relaxation rate constants, together with the best-fit to Arrhenius equation (green): $k_i(T) = k_i(\infty)e^{-E_{ai}/kT}$.

The relaxation curves were fitted using a sum of two exponential terms (double exponential law), based on the LIESST plot. These terms contain temperature-dependent rate constants $k_1^*(T)$ and $k_2^*(T)$, which refer to the faster and slower processes, respectively:

$$\gamma_{HS} = \frac{1}{2}e^{-k_1^*(T)t} + \frac{1}{2}e^{-k_2^*(T)t} \text{ (Eq.3.5)}$$

The shape of the relaxation curves is sigmoidal. Accordingly, due to cooperative effects, both rate constants depend on the remaining fraction of HS centres (γ_{HS}) through a self-acceleration factor, $\alpha_i(T) = (E_a^*)_i/k{\cdot}T$, that also varies with the temperature.[49] This is expressed in the following equations:

$$k_1^*(T) = k_1(T)e^{\alpha_1(T)(2-2\gamma_{HS})} \text{ (Eq. 3.6)}$$

$$k_2^*(T) = k_2(T)e^{\alpha_2(T)(1-2\gamma_{HS})} \text{ (Eq. 3.7)}$$

$k_1(T)$ and $k_2(T)$ are the intrinsic non-cooperative rate constants for the fast ($1 < \gamma_{HS} < 0.5$) and slow ($0.5 < \gamma_{HS} < 0$) processes, respectively. Values of k_i and α_i extracted from the best-fit data shown in Figure 3.64.a are gathered in Table 3.22. It can be seen that the two rate constants differ in one order of magnitude, reinforcing the existence of two different relaxation processes and justifying the inclusion of two exponential terms in equation 3.5. In comparison with **5**·2.4H_2O, the values obtained for the rate constants now are one order of magnitude lower and the self-acceleration factors have been considerably reduced.

Table 3.22. Kinetic parameters extracted from fitting the relaxation measurements of **6**·5H_2O at different temperatures.

T / K	K_1 / s^{-1}	α_1	K_2 / s^{-1}	α_2
60	$4.4{\cdot}10^{-5}$	0.90	$4.2{\cdot}10^{-6}$	0.85
62	$9.6{\cdot}10^{-5}$	0.87	$1.0{\cdot}10^{-5}$	0.55
64	$2{\cdot}10^{-4}$	0.84	$1.9{\cdot}10^{-5}$	0.86
66	$3.9{\cdot}10^{-4}$	0.82	$3.7{\cdot}10^{-5}$	0.89
68	$6{\cdot}10^{-4}$	0.79	$7.0{\cdot}10^{-5}$	1.00
70	$9.5{\cdot}10^{-4}$	0.77	$1.2{\cdot}10^{-4}$	1.20
72	$2.2{\cdot}10^{-3}$	0.75	$2.55{\cdot}10^{-4}$	1.00

The non-cooperative rate constants follow the Arrhenius law (Figure 3.64.b), indicating that both processes are thermally activated. From these plots, the apparent activation energies (E_{ai}) have been calculated: E_{a1} = 935.7 cm^{-1} and E_{a2} = 997.9 cm^{-1}, which are similar to that obtained for compound **5**·2.4H_2O and compare well with values reported for similar systems (for instance, in

$[Fe(bppSMe)_2][BF_4]_2$ and $[Fe(bppI)_2][BF_4]_2$, being bppSMe = 4-(methylsulfanyl)-2,6-di(pyrazol-1-yl)pyridine and bppI = 4-iodo-2,6-di(pyrazol-1-yl)-pyridine).[32] The preexponential factors are $k_1(\infty)$ = 2.563·10^5 s^{-1} and $k_2(\infty)$ = 1.059·10^5 s^{-1}, with a $k_1(\infty)/k_2(\infty)$ ratio close to 2. The behaviour described for the complex $[Fe(bppI)_2](BF_4)_2$ is similar,[32] with two T(LIESST) values of 65 K and 75 K. In this case, a sum of a fast exponential and a slow self-accelerated terms was used to successfully simulate the relaxation curves.

On the other hand, the relaxation curves of the thermally quenched sample were obtained between 75 K and 105 K, within the metastability region of the HS/LS phase (T < 114 K, Figure 3.65.a). The relaxation curve at 72 K of the photoinduced material decays completely after 72 min, whereas that corresponding to the thermally quenched sample at 75 K contains less than 10% LS centres even after 10.5 h, demonstrating a huge difference between the relaxation kinetics of both metastable phases. For thermally quenched samples at higher temperatures, complete relaxations were observed after 8 h at 85 K and 4 h at 95 K. However, at 102.5 K, 20% of the iron centres still remain in the HS state after 12 h and, even more, at 105 K only a subtle change in the magnetic response (1%) is observed after 3.2 h. This behaviour is surprising because at T < 114 K, the LS phase is supposed to be the stable one. Heating approximately above 95 K leads to a decrease in the relaxation rates (as observed at 97.5 K, 102.5 K and 105 K), revealing that the compound enters into the thermal range corresponding to thermodynamic equilibrium.[50]

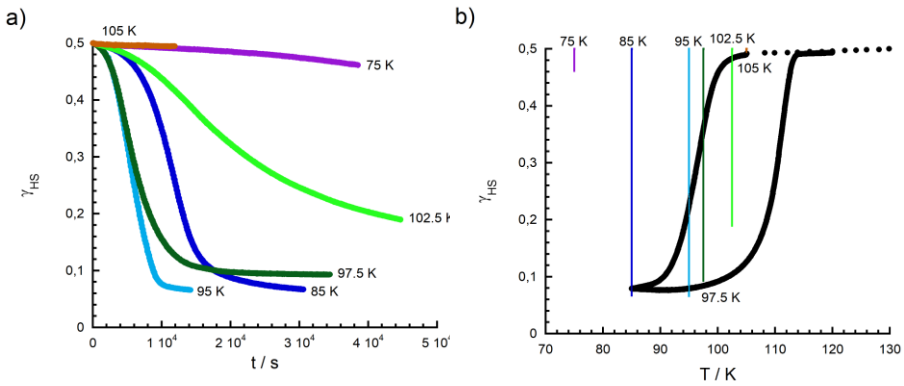

Figure 3.65. a) Time dependence of the γ_{HS} of Fe^{2+} cations in a sample of **6**·5H$_2$O thermally quenched at 75 K (purple), 85 K (dark blue), 95 K (light blue), 97.5 K (dark green), 102.5 K (light green) and 105 K (brown). b) Thermal variation of χT for **6**·5H$_2$O at a slow cooling rate (0.04 K·min^{-1}, in black) showing the thermal hysteresis. Previous isothermal relaxation experiments starting from the mixed-spin phase are also included.

All the above suggests that at T < 114 K the magnetic plot is strongly dependent on the cooling procedure. In fact, between 95 K and 114 K a thermal hysteresis should be measured if a sufficiently slow cooling rate is employed. In this regard, the thermal variation of χT was measured at a slow scan rate (0.04 K·min^{-1}, Figure 3.65.b). Upon cooling below 101 K, the magnetic signal decreases steadily, reaches an inflection point at 97 K ($T_{\downarrow}$) and decreases further until reaching a constant value of 0.17 emu·K·mol^{-1} at 85 K. In the heating mode, a fast increase of the χT product is observed around 111 K ($T_{\uparrow}$), and above 114 K the plot merges with the one obtained at higher sweeping rates. Thus, an apparent thermal hysteresis of 14 K was registered in these conditions. Nevertheless, a superposition of the isothermal relaxation experiments in the same plot reveals that kinetic effects are important even using such a slow cooling rate. At 102.5 K, complete relaxation is not achieved even after 12 h, indicating that the quasistatic hysteresis loop is thinner than the apparent one. At least, in the thermal range between 105 K and 114 K, a true bistability can be unambiguously observed.

3.5.3. Structural characterisation

A. Thermal properties

TG measurements (Figure 3.66.a) under nitrogen atmosphere show a first weight decrease at 390 K (8.89%), which is ascribed to the loss of 5 water molecules per iron cation (calculated value: 9.15%). This is consistent with the expected water content deduced from X-ray crystal structure determination and elemental analysis. Further heating above 500 K results in a decomposition of the material.

DSC measurements were carried out in the 120-300 K temperature range (Figure 3.66.b). Upon cooling the compound (curve 1), a sharp exothermic peak centred at 162 K is observed. On heating the sample (curve 2), a similar sharp endothermic peak at 167 K appears, which is exactly equal to the value determined from magnetic measurements. These features correspond to the phase transition from the HS phase to the mixed HS/LS phase. However, a small thermal hysteresis (ΔT = 5 K) is observed from DSC data, which is in contrast with the SQUID measurements that showed a lack of hysteresis. Such difference can be due to the fact that DSC analyses are performed at a higher sweeping rate (10 K·min^{-1} *vs* 2K·min^{-1}). Enthalpy and entropy changes associated to these transformations are gathered in Table 3.23. Both enthalpy values, corresponding to the cooling and heating processes, are relatively small with respect to other

complexes exhibiting also partial transitions.[51] The variation of entropy is also low in both cases.

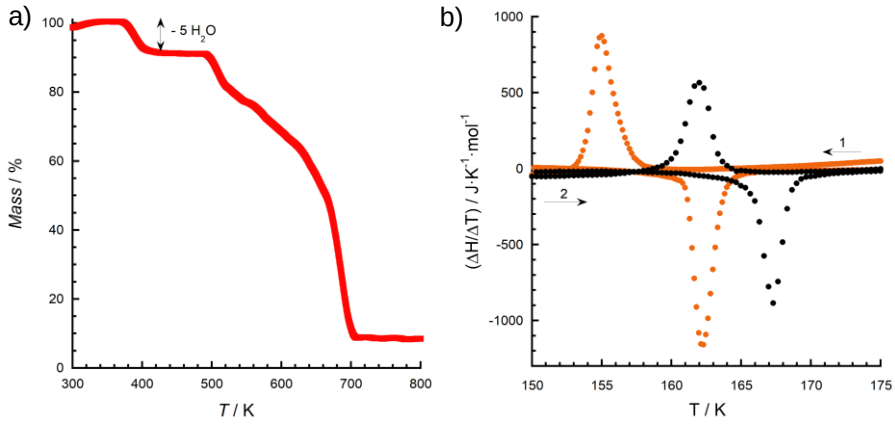

Figure 3.66. a) Thermogravimetric analysis of **6**·5H₂O. b) DSC plot of **6**·5H₂O (black) and **6**·2.75H₂O·2.25D₂O (orange). Curves 1 and 2: First cooling and heating processes, respectively. A second thermal cycle (not shown) indicates that the processes are reversible.

Table 3.23. Thermodynamic parameters ΔH and ΔS extracted from DSC measurements of **6**·5H₂O and **6**·2.75H₂O·2.25D₂O.

Compound	Curve	T_{peak}/ K	ΔH / kJ·mol^{-1}	ΔS / J·mol^{-1}·K^{-1}
6·5H₂O	1	162	-1.75	-10.8
	2	167	2.13	12.7
6·2.75H₂O·2.25D₂O	1	155	-1.73	-11.15
	2	162	2.28	14.07

DSC measurements of the deuterated sample (Figure 3.66.b) are in perfect agreement with the magnetic data, with a 6 K decrease in the SCO temperature upon deuteration that indicates a destabilisation of the mixed HS/LS phase. Now, the DSC plot shows the appearance of an exothermic peak at 155 K (curve 1) and an endothermic feature at 162 K (curve 2) with enthalpy and entropy changes similar to those obtained for **6**·5H₂O (Table 3.23). In this case, the thermal hysteresis is slightly higher (ΔT = 7 K).

B. Temperature dependence of unit cell parameters

The thermal variation of the unit cell parameters of **6**·5H₂O in the 240-120 K temperature range was investigated by single crystal X-ray diffraction (Figure 3.67). Sharp discontinuities were observed for all the parameters

between 160 K and 170 K, revealing a crystallographic phase transition in the same interval of temperature in which the SCO takes place (HS/LS ⟷ HS). The change in cell parameters is quite significant with Δa = –3.697 Å (36.98%), Δb = –5.189 (37.94%) and Δc = –2.258 (12.93%). At T < 170 K, the unit cell volume is almost doubled with respect to that obtained at higher temperatures.

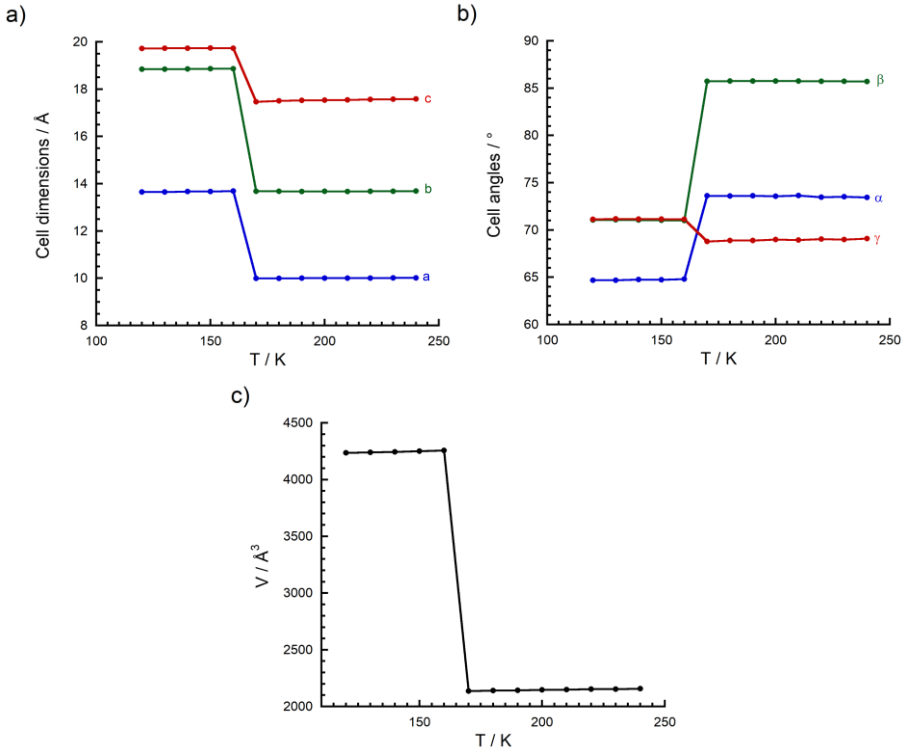

Figure 3.67. Temperature dependence of a) unit cell parameters, b) angles and c) unit cell volume for **6**·5H_2O.

C. Single crystal X-ray diffraction

The crystal structure of **6**·5H_2O was determined at 240 K and 210 K in the HS state, at 120 K in the mixed HS/LS phase and at 95 K in the LS phase (Table 3.24). Also, photocrystallography measurements of the photoinduced high-spin (PIHS) phase at 50 K after irradiation (with a laser source (λ = 630 nm) for 1h 30 min), the mixed HS/LS phase after the first relaxation step and the fully LS phase after complete relaxation from the PIHS were carried out. In all cases, the compound belongs to the triclinic P–1 space group. At 240 K and 210 K, the asymmetric unit contains only one crystallographically inequivalent $[Fe(bpp)_2]^{2+}$ complex that lies in a general position, five water molecules, two

independent isonicNO anions and one HisonicNO acid. Upon cooling at 120 K, **6**·5H_2O undergoes a crystallographic phase transition (symmetry breaking). The unit cell volume is almost doubled with respect to that observed at 240 K and 210 K (Table 3.24). Now, there are two crystallographically inequivalent metallic centres, Fe1A and Fe1B. Annealing the compound at 95 K results in a reentrant structural transition with restoration of the symmetry. The unit cell volume is halved with respect to the intermediate structure observed at 120 K (Table 3.24) and the asymmetric unit contains again a single $[Fe(bpp)_2]^{2+}$ complex.

Table 3.24. Crystallographic data and structural refinement for **6**·5H_2O at different temperatures.

	240 K (HS)	210 K (HS)	120 K (HS/LS)	95 K (LS)[b]	50 K (PIHS)[c]	50 K ($PIHS_{rel}$)[d]	95 K (LS)[e]
Empirical formula				$C_{40}H_{41}FeN_{13}O_{14}$			
Formula weight				983.71			
Crystallographic system				Triclinic			
Space group				*P*–1(No. 2)			
a/ Å	10.01048(19)	9.99242(16)	13.63358(18)	9.9953(3)	9.9402(13)	9.9614(18)	10.008(4)
b/ Å	13.6732(3)	13.64829(17)	18.8075(2)	13.6057(2)	13.5461(19)	13.577(3)	13.653(7)
c/ Å	17.5596(3)	17.4977(3)	19.6686(2)	17.1602(3)	17.384(2)	17.271(3)	17.130(6)
α/ °	73.5259(18)	73.5796(13)	64.7142(13)	76.8440(16)	73.959(6)	103.019(8)	76.955(14)
β/ °	85.7741(15)	85.7654(13)	71.0809(12)	85.770(2)	85.950(5)	94.103(8)	85.823(12)
γ/ °	69.1588(18)	69.0385(13)	71.0628(12)	110.502(3)	68.735(5)	111.280(7)	110.551(14)
V/ Å^3	2153.01(8)	2136.52(6)	4210.47(11)	2098.13(10)	2095.3(5)	2090.1(7)	2105.3(16)
Z	2	2	4	2	2	2	2
R(int)	0.0414	0.0315	0.1052	0.0949	0.0573	0.0585	0.1057
ρ_{calc}/ g·cm^{-3}	1.517	1.529	1.552	1.557	1.559	1.563	1.552
μ/ mm^{-1}	0.435	0.439	0.445	0.447	0.447	0.448	0.445
Crystal dimensions/ mm	0.550 x 0. 223 x 0. 139	0.360 x 0. 226 x 0. 166	0.360 x 0.226 x 0.166	0.486 x 0.263 x 0.146	0.494 x 0. 166 x 0. 127	0.494 x 0. 166 x 0. 127	0.494 x 0. 166 x 0. 127
T/ K	239.9(2)	210.00(14)	120.00(14)	94.9(2)	50(1)	50 (1)	95(1)
λ/ Å	0. 71073	0. 71073	0.71073	0.71073	0. 71073	0. 71073	0.71073
2θ range/ °	4.68 < 2θ < 54.85	4.93 < 2θ < 55.62	4.45 < 2θ < 55.49	4.95 < 2θ < 55.50	4.40 < 2θ < 65.34	4.40 < 2θ < 68.61	4.40 < 2θ < 65.36
Index ranges for h, k , l	-12/12, -17/17, -22/22	-12/13, -16/17, -22/22	-17/17, -24/24, -25/25	-13/12, -17/17, -22/22	-15/15, -20/20, -25/26	-14/15, -19/20, -25/26	-15/14, -20/19, -25/25
Refinement method	Full-matrix least-squares on F^2	Full-matrix least-squares on F^2	Full-matrix least-squares on F^2	Full-matrix least-squares on F^2	Full-matrix least-squares on F^2	Full-matrix least-squares on F^2	Full-matrix least-squares on F^2
Collected reflections	82160	82858	162319	77954	37908	38146	36767
Unique reflections	9117	9431	18600	9155	14987	15330	14901
Data/Restraints/Parameters	9117/0/658	9431/0/658	18600/0/1315	9155/0/658	14987/0/662	15330/0/658	14901/0/658
Goodness-of-fit on F^2	1.047	1.037	1.045	1.048	1.035	1.035	0.931
R1, wR2 [I > 2sigma(I)][a]	0.0328/0.0784	0.0298/0.0720	0.0384/0.1026	0.0459/0.0941	0.0459/0.0999	0.0482/0.1017	0.0632/0.1378
R1, wR2 (all data)[a]	0.0405/0.0836	0.0350/0.0757	0.0473/0.1125	0.0660/0.1087	0.0803/0.1113	0.0993/0.1156	0.1224/0.1658
$\Delta\rho_{max}$ and $\Delta\rho_{min}$ (e·Å^{-3})	0.24/–0.46	0.30/–0.35	0.42/–1.02	0.60/–0.68	0.66/–0.74	0.60/–0.81	1.08/–1.42

[a] $R1 = \Sigma(||F_o| - |F_c||)/\Sigma|F_o|$; $wR2 = \{\Sigma[w(F_o^2 - F_c^2)^2]/\Sigma[w(F_o^2)^2]\}^{1/2}$. [b] Temperature was held at 95 K for 4h prior to data collection. [c] Photoinduced high-spin phase. [d] Structure obtained from partial relaxation of the PIHS phase, then quenching the sample at 50 K. [e] Structure obtained from full relaxation of the PIHS phase.

On the other hand, the crystal structure of **6**·$5H_2O$ in the PIHS phase is isostructural to the structure obtained at 240 K (Table 3.24), with a 2.7% of cell volume decrease due to the thermal contraction. The structure obtained from partial relaxation of the PIHS phase and then quenching at 50 K presents similar unit cell parameters, indicating the presence of only one independent Fe(II) centre in the asymmetric unit although with lower unit cell volume than that obtained for the PIHS phase. In addition, the crystal structure of **6**·$5H_2O$ was determined after complete relaxation at 95 K, obtaining an isostructural phase to that measured at the same temperature without irradiation (Table 3.24).

As expected, the two bpp ligands are occupying the meridional positions of the iron(II) coordination sphere and are arranged in almost perpendicular planes yielding a 6-coordinate iron metal centre. The range of Fe–N bond distances decreases from 2.115-2.199 Å at 240 K to 1.940-2.006 Å at 95 K (Table 3.25), as commonly observed for spin crossover compounds as the structure goes from HS to LS. At 210 K, Fe–N bond lengths are slightly shorter with respect to the values observed at 240 K, due to thermal contraction. At 120 K, the two iron centres present very different coordination spheres. Fe1A–N bond distances (ranging from 2.116 Å to 2.188 Å) are similar to those observed at 240 K (Table 3.25, Figure 3.68), whereas Fe1B–N bond lengths (1.934-2.001 Å) are remarkably shorter and similar to those measured at 95 K (Figure 3.69). This is consistent with the mixed-spin phase 50% HS and 50% LS observed from magnetic measurements.

Table 3.25. Fe–N bond lengths (Å) for **6**·$5H_2O$ at different temperatures.

240 K (HS)	210 K (HS)	120 K (HS/LS)	120 K (HS/LS)	95 K (LS)[a]	50 K (PIHS)[b]	50 K (PIHSrel)[c]	95 K (LS)[d]
Fe1–N2	Fe1–N2	Fe1A–N2A	Fe1B–N2B	Fe1–N2	Fe1–N2	Fe1–N2	Fe1–N2
2.1618(12)	2.1534(11)	2.1539(13)	1.9982(12)	1.9933(19)	2.1541(13)	2.0816(15)	1.996(2)
Fe1–N3	Fe1–N3	Fe1A–N3A	Fe1B–N3B	Fe1–N3	Fe1–N3	Fe1–N3	Fe1–N3
2.1242(12)	2.1167(11)	2.1288(13)	1.9342(13)	1.940(2)	2.1263(13)	2.0384(16)	1.935(2)
Fe1–N4	Fe1–N4	Fe1A–N4A	Fe1B–N4B	Fe1–N4	Fe1–N4	Fe1–N4	Fe1–N4
2.1885(13)	2.1780(11)	2.1781(13)	1.9800(12)	1.9778(19)	2.1889(13)	2.0919(14)	1.971(2)
Fe1–N7	Fe1–N7	Fe1A–N7A	Fe1B–N7B	Fe1–N7	Fe1–N7	Fe1–N7	Fe1–N7
2.1904(13)	2.1822(11)	2.1870(12)	1.9905(12)	1.9921(19)	2.1949(13)	2.1007(14)	1.988(2)
Fe1–N8	Fe1–N8	Fe1A–N8A	Fe1B–N8B	Fe1–N8	Fe1–N8	Fe1–N8	Fe1–N8
2.1152(12)	2.1061(11)	2.1165(12)	1.9380(12)	1.9474(19)	2.1147(13)	2.0343(14)	1.941(2)
Fe1–N9	Fe1–N9	Fe1A–N9A	Fe1B–N9B	Fe1–N9	Fe1–N9	Fe1–N9	Fe1–N9
2.1876(13)	2.1798(11)	2.1880(12)	2.0010(12)	2.0058(19)	2.1908(13)	2.1057(15)	2.0019(19)

[a] Temperature was held at 95 K for 4h prior to data collection. [b] Photoinduced high-spin (PIHS) phase. [c] Structure obtained from partial relaxation of the PIHS phase, then quenching the sample at 50 K. [d] Structure obtained from complete relaxation of the PIHS phase.

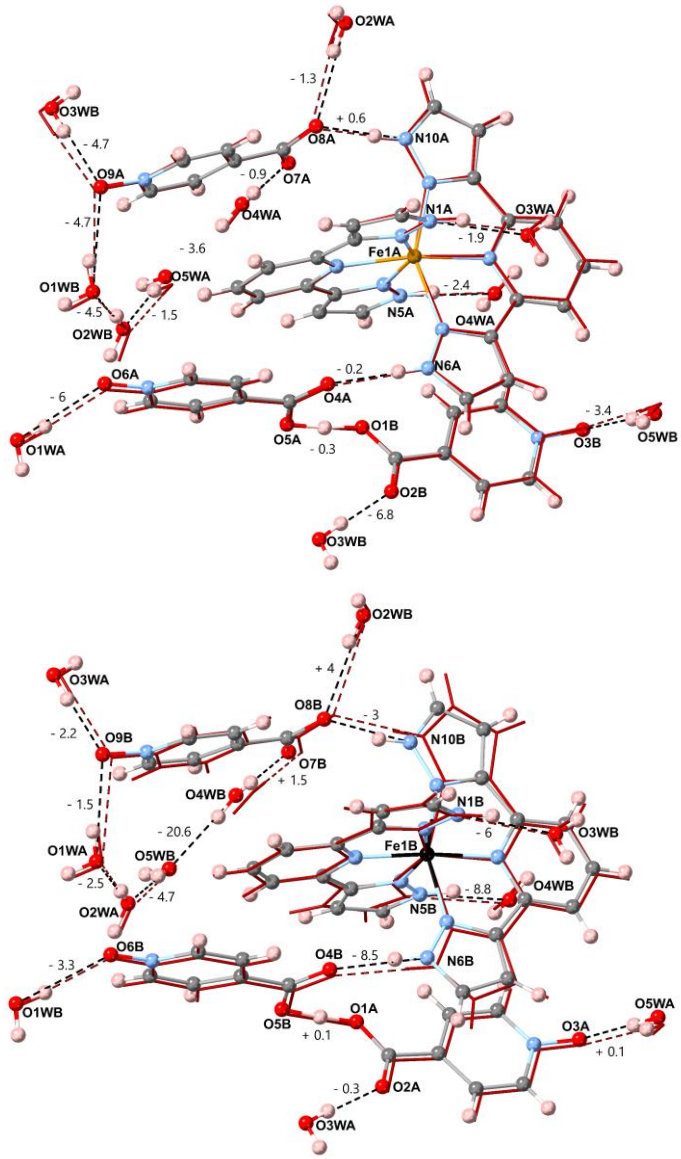

Figure 3.68. Superposition of the crystal structures of **6**·5H_2O at 240 K and 120 K. The high-temperature phase (red sticks) is compared with both sublattices present in the mixed HS/LS phase: HS (upper panel, coloured balls and sticks) and LS (lower panel, coloured balls and sticks). The variation of hydrogen-bonding distances upon cooling from 240 K to 120 K are included in the figures (expressed in picometers). Labels refer to the 120 K structure and dashed lines to hydrogen bonds.

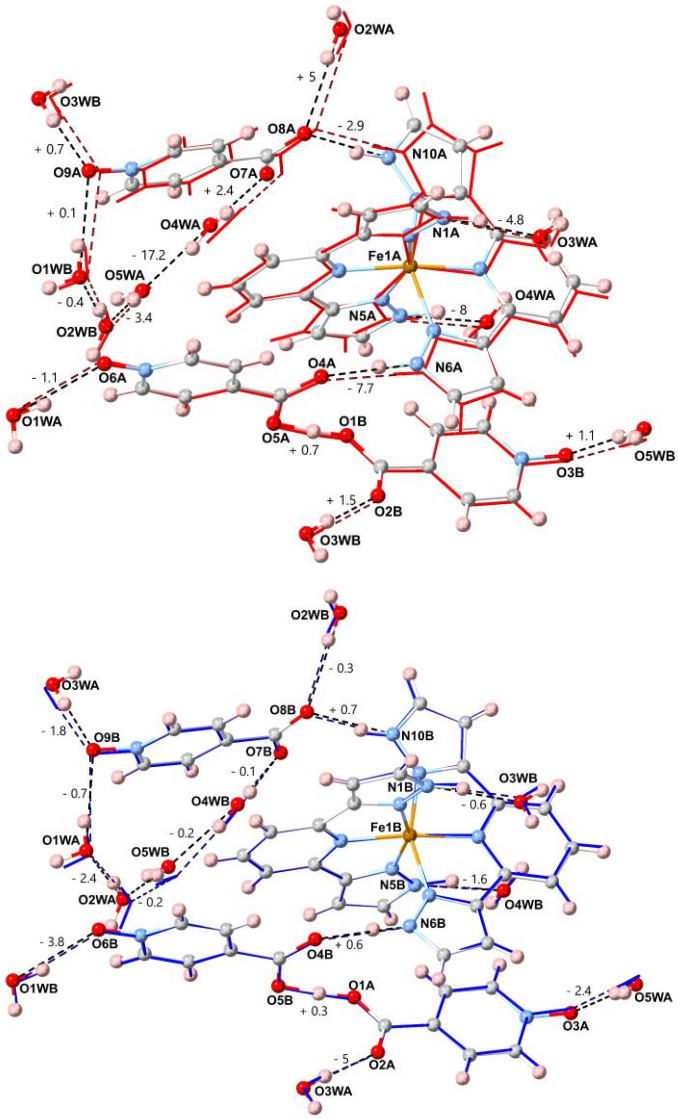

Figure 3.69. Superposition of the crystal structures of **6**·5H_2O at 120 K and 95 K. The low-temperature phase (coloured balls and sticks) is compared with both sublattices present in the mixed HS/LS phase: HS (upper panel, red sticks) and LS (lower panel, blue sticks). The variation of hydrogen-bonding distances upon cooling from 120 K to 95 K are included in the figures (expressed in picometers). Labels refer to the 120 K structure and dashed lines to hydrogen bonds.

The single inequivalent Fe(II) complex present in the PIHS phase exhibits Fe–N bond lengths characteristic of a HS state (between 2.114 Å and 2.195 Å, Figure 3.70), whereas those obtained for the structure measured from partial relaxation of the PIHS state are intermediate (mean Fe–N distance of 2.075 Å, Figure 3.71) between those corresponding to HS and LS phases (Table 3.25). In general, larger ellipsoids are observed for the atoms present in this structure (Figure 3.71), especially for those C and N atoms of pyrazol rings that experiment a higher variation with the change of the iron spin state. This is reflected in the atomic displacement parameters (Table 3.32, 3.6.3. Appendix section), which are higher than those obtained for the other structures. Several efforts were devoted to solve the crystal structure in a bigger unit cell with two inequivalent iron centres but without success. In addition, we did not observe any evidence of superstructure reflections or ordering of the two spin species in a modulated way. All the above suggest a random distribution of HS and LS iron(II) sites in the crystal structure. A possible explanation for the two-step relaxation without symmetry breaking might be the existence of a short-range interaction defining LS dimers that propagates randomly throughout the lattice.

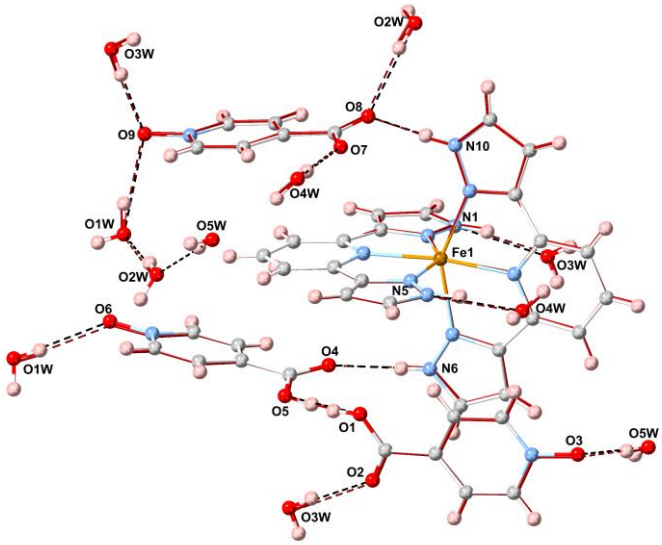

Figure 3.70. Superposition of the crystal structures of **6**·5H_2O at 240 K (red sticks) and 50 K (PIHS, coloured balls and sticks). The similarity between the thermally stable and photoinduced metastable high-spin phases can be observed.

As expected, the compound measured after complete relaxation of the PIHS phase shows Fe–N bond lengths in agreement with a LS state (mean distance of 1.972 Å, Figure 3.72). Moreover, octahedral distortion parameters (Table 3.26) are in agreement with all the spin state changes described and confirm the

efficient trapping of a mixed 1:1 HS/LS phase in the structure obtained after partial relaxation from the PIHS state.

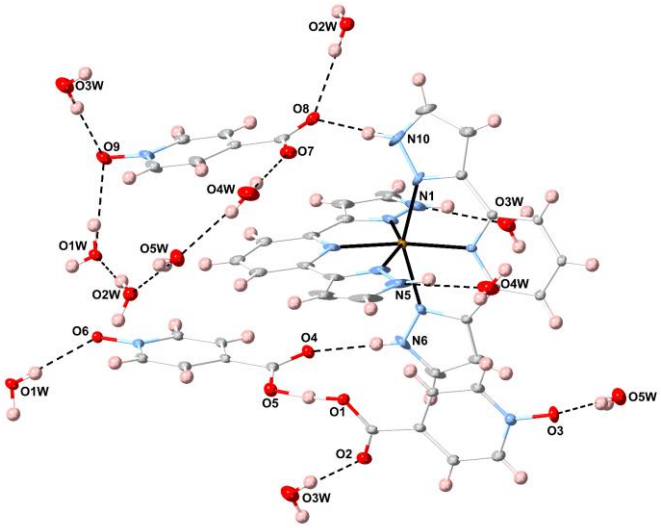

Figure 3.71. Thermal ellipsoid plot of the crystal structure of **6**·5H$_2$O at 50 K after partial relaxation of the PIHS phase. Note the ellipsoid elongation for those atoms involved in the spin crossover process (change of the bpp bite angle). Ellipsoids are drawn at 50% probability level and H atoms are shown as spheres.

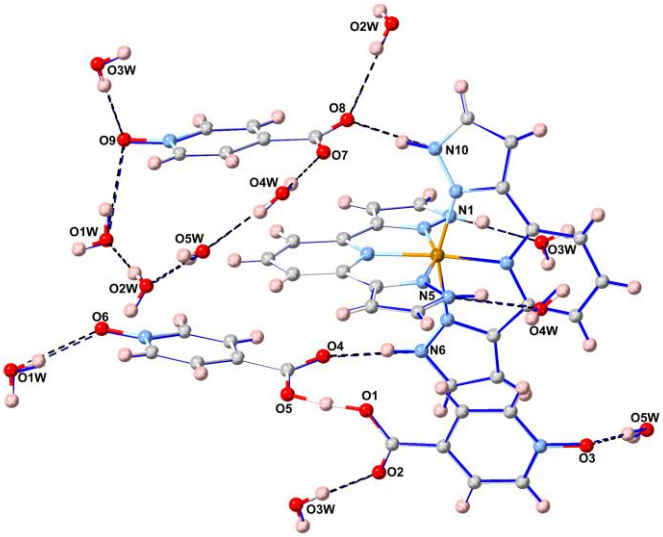

Figure 3.72. Superposition of the crystal structures of **6**·5H$_2$O at 95 K after full relaxation of the PIHS phase (coloured balls and sticks) and at 95 K without irradiation (blue sticks).

Table 3.26. Octahedral distortion parameters of the Fe^{2+} cations present in **6**·$5H_2O$ at different temperatures.

T / K	240 K Fe1 (HS)	210 K Fe1 (HS)	120 K Fe1A (HS/LS)	120 K Fe1B (HS/LS)	95 K Fe1 (LS)[a]	50 K Fe1 (PIHS)[b]	50 K Fe1 ($PIHS_{rel}$)[c]	95 K Fe1 (LS)[d]
φ / °	169.85	169.85	168.13	173.16	172.36(8)	169.10	170.46	172.62
Σ / °	140.3	139.0	142.0	100.5(6)	103(1)	140.2	123.6	100.2

[a] Temperature was held at 95 K for 4h prior to data collection. [b] Photoinduced high-spin (PIHS) phase. [c] Structure obtained from partial relaxation of the PIHS phase, then quenching the sample at 50 K. [d] Structure obtained from complete relaxation of the PIHS phase.

Regarding the crystal packing, each cationic complex interacts only with two adjacent neighbours through π-π stacking interactions, giving rise to the formation of alternating chains running along the *c* axis. The isonicNO anions are located in the space between the chains, preventing the formation of the *terpyridine embrace motif*. At 240 K, two different weak stacking contacts alternating along the chain can be distinguished (Figure 3.73): interactions between N1N2 pyrazol rings and between N4N5 pyrazolyl units, with distances between centroids defined by each pyrazol ring of 3.91(9) Å and 3.92(9) Å, respectively. The overlapping region is small in the first case and almost inexistent in the second. At 120 K, the stacks of $[Fe(bpp)_2]^{2+}$ complexes present an alternating AABB sequence (Figure 3.73). The centre of symmetry located between the N1N2 pyrazol rings is missing and a weaker overlap is observed between the planes containing N1AN2A and N1BN2B, together with a higher distance between centroid coordinates (4.01(3) Å). With respect to the second contact, it is now split into two centrosymmetric interactions: between HS units (N4AN5A rings), being very similar to that observed at 240 K, and between LS centres (N4BN5B rings), showing a stronger overlap and considerably lower distance between centroids (3.67(4) Å). At 95 K, the stacks of $[Fe(bpp)_2]^{2+}$ cations running along the *c* axis with only two different centrosymmetric contacts are restored (Figure 3.73). The interaction between N4N5 pyrazolyl fragments is considerably stronger, with a larger overlap region in comparison to those observed at 120 K and 240 K and shorter distance between centroids (3.59(9) Å). Instead, the contact between N1N2 pyrazol rings is weaker with respect to those measured at 240 K and 120 K, being the overlap region smaller and the distance between centroids much higher (4.15(7) Å).

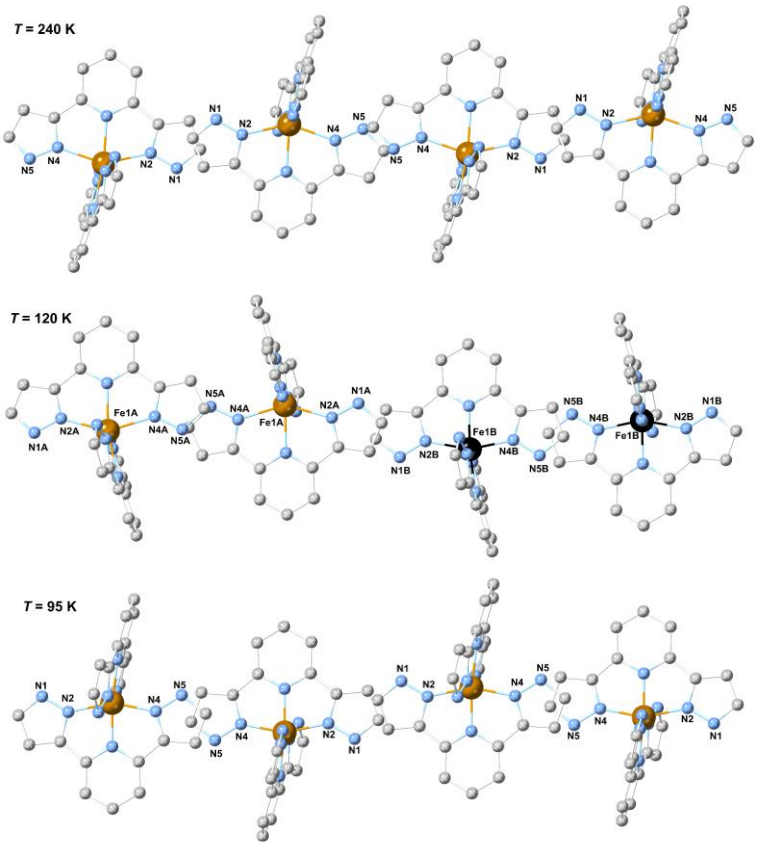

Figure 3.73. Crystal structure of **6**·5H_2O showing a comparative view of the presence of π-π stacking interactions between the bpp ligands at 240 K, 120 K and 95 K. IsonicNO anions, water molecules and H atoms are omitted.

The changes in the crystal packing and connectivity between all the structures are minor. Figure 3.74 shows the hydrogen-bonding linkage at 240 K for the following general description of the connectivity. Relevant hydrogen-bonding parameters are gathered in Table 3.27. The isonicotinate N-oxide anions are denoted as (3), (6) and (9) after the numbering of the oxygen atoms of the corresponding N-oxide groups. One of the bpp ligands is hydrogen-bonded to two different isonicNO molecules (N6···O4, N10···O8), whereas the second bpp ligand is linked through hydrogen bonds to two water molecules (N5···O4W; N1···O3W). IsonicNO(3) is hydrogen-bonded to one water molecule (O5W) through its N-oxide function, whereas the carboxylate fragment is engaged in two hydrogen bonds in a *syn*, *syn*-bridging mode: one with a water molecule (O3W) and a very strong one with isonicNO(6), being the proton of the free

isonicotinic acid N-oxide (H1O) located between O5 and O1 oxygen atoms. The carbonyl group of the second anion (isonicNO(6)) is hydrogen-bonded to one bpp ligand (N6···O4) with a relatively long distance and the N-oxide oxygen atom (O6) is interacting with one water molecule (O1W).

Table 3.27. Selected hydrogen bond distances (Å) in the crystal structure of **6**·5H_2O at different temperatures.

H-bond	240 K (HS)	210 K (HS)	120 K (HS/LS)[a]	120 K (HS/LS)[b]	95 K (LS)	*50 K (PIHS)*[c]	*50 K ($PIHS_{rel}$)*[d]	*95 K (LS)*[e]
N1···O3W	2.7031(19)	2.6982(18)	2.6845(19)	2.6427(19)	2.638(3)	2.6880(18)	2.662(2)	2.645(3)
N5···O4W	2.832(2)	2.825(2)	2.808(2)	2.7442(19)	2.727(3)	2.8188(18)	2.777(2)	2.741(3)
N6···O4	2.8357(18)	2.8320(16)	2.8335(18)	2.7507(18)	2.758(3)	2.8324(17)	2.8017(19)	2.757(3)
N10···O8	2.7179(18)	2.7155(16)	2.7235(18)	2.6883(17)	2.697(3)	2.7091(17)	2.711(2)	2.714(3)
O1W···O6	2.8488(18)	2.8402(16)	2.7889(17)	2.8158(17)	2.778(2)	2.8272(16)	2.8037(17)	2.780(3)
O1W···O9	2.838(2)	2.8311(17)	2.8231(17)	2.8153(17)	2.816(3)	2.8055(17)	2.8054(18)	2.823(3)
O2W···O1W	2.814(2)	2.8030(18)	2.7890(18)	2.7694(18)	2.765(3)	2.7955(17)	2.7780(18)	2.771(3)
O2W···O8	2.892(2)	2.8883(17)	2.8786(17)	2.9321(18)	2.928(3)	2.8616(17)	2.8857(18)	2.938(3)
O3W···O9	2.892(2)	2.8832(18)	2.8696(18)	2.8453(17)	2.853(3)	2.8579(17)	2.8503(19)	2.857(3)
O3W···O2	2.7630(18)	2.7563(16)	2.7603(17)	2.6946(17)	2.710(3)	2.7511(17)	2.7313(18)	2.713(3)
O4W···O7	2.723(2)	2.7181(17)	2.7135(18)	2.7384(17)	2.737(3)	2.7136(17)	2.7222(18)	2.736(3)
O4W···O5W	3.062(2)	3.044(2)	3.0256(19)	2.8562(19)	2.858(3)	3.0070(18)	2.934(2)	2.853(3)
O5W···O3	2.743(2)	2.7372(18)	2.7437(18)	2.7091(18)	2.722(3)	2.7397(17)	2.7313(17)	2.709(3)
O5W···O2W	2.854(2)	2.8455(19)	2.8387(19)	2.8072(18)	2.803(3)	2.8410(18)	2.8204(19)	2.802(3)

[a]Contacts within the A sublattice, except for O1WA···O9B, O3WA···O9B and O5WA···O2WB. [b]Contacts within the B sublattice, except for O1WB···O9A, O3WB···O9A and O5WB···O2WA.[c] Photoinduced high-spin (PIHS) phase.[d] Structure obtained from partial relaxation of the PIHS phase, then quenching the sample at 50 K.[e] Structure obtained from complete relaxation of the PIHS phase.

In the third anion (isonicNO(9)), the N-oxide function is acting as a ditopic hydrogen bond acceptor towards two water molecules (O1W and O3W). The carboxylate moiety exhibits three hydrogen-bonded interactions: O7 is connected to one water molecule (O4W), whereas O8 is bound in a bifurcated way to one water molecule (O2W) and one bpp ligand (N10···O8). As mentioned above, O4W is hydrogen-bonded to another bpp ligand, defining these

interactions the shortest pathway between neighbouring Fe complexes and building centrosymmetric dimeric Fe(II) units (Figure 3.75).

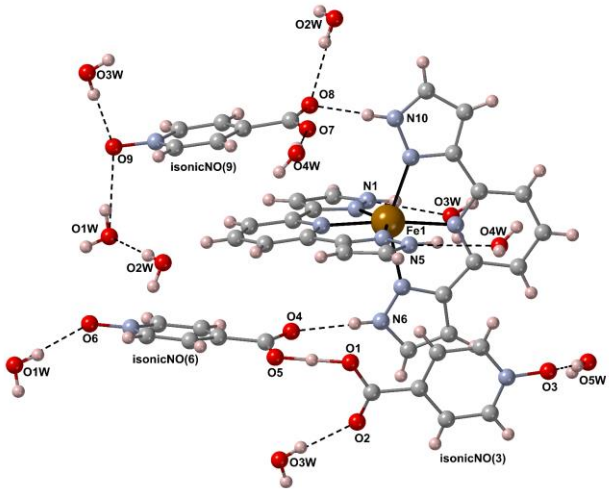

Figure 3.74. Crystal structure of **6**·5H₂O at 240 K showing the hydrogen-bonding connectivity.

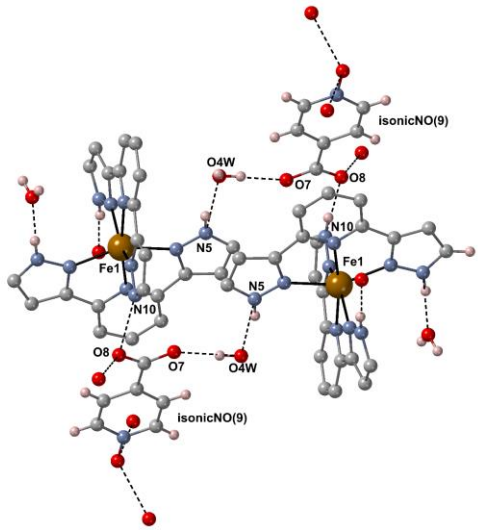

Figure 3.75. View of the crystal structure of **6**·5H₂O at 240 K showing the formation of centrosymmetric Fe(II) cyclic dimers.

At 120 K, two equivalent sublattices can be distinguished, each one associated to one iron(II) spin state. Regarding the second iron coordination sphere (Table 3.27), it is found that hydrogen bonds are stronger for the Fe1B site (LS, mean distance N···O: 2.706 Å) with respect to the Fe1A site (HS, mean distance N···O:

2.762 Å). In the latter case, those contacts are similar to the hydrogen bond distances observed in the high-temperature phase (mean value N···O: 2.772 Å at 240 K, Figure 3.68). This interesting point was also observed for compounds **1**, **3**, **5**·2.4H_2O and **5**. Thus, the examination of the hydrogen bonds between the four NH pyrazole functions and the four H-bond acceptors provides valuable information about the spin state of the iron(II) centre. In addition, a shortening of most other hydrogen bond interactions is observed due to the increase in hydrogen bond strength in the second coordination sphere of the Fe1B site with respect to the values involving the Fe1A sublattice. In few cases, elongation is observed as a consequence of the presence of bifurcated hydrogen bonds. For instance, the distance between isonicNO(9) and the LS Fe1B complex decreases at 120 K (N10B···O8B: 2.6883(17) Å vs N10A···O8A: 2.7235(18)Å), while the distance with respect to one water molecule increases (O2WB···O8B: 2.9321(18) Å vs O2WA···O8A: 2.8786(17) Å). Apart from this, the most remarkable dissimilarity between A and B sublattices is the establishment of a hydrogen bond between two water molecules only in the LS subnetwork (O4WB···O5WB: 2.8562(19) Å vs O4WA···O5WA: 3.0256(19) Å). Indeed, this interaction leads to a slight elongation of a second hydrogen bond (O4WB···O7B: 2.7384(17) Å vs O4WA···O7A: 2.7135(18) Å). At 95 K, hydrogen-bonding distances are very similar to those obtained for the B sublattice in the mixed phase at 120 K (Figure 3.69). Indeed, the mean distance between the pyrazole NH units and the H-bond acceptors has almost the same value (2.705 Å). A decrease in hydrogen bond distances is observed with respect to high temperature as a consequence of thermal contraction, except for the few cases previously pointed out (Table 3.27). Remarkably, 100% of O4W molecules are now interacting with O5W with a distance of 2.858(3) Å.

At 210 K, all the hydrogen bond distances are slightly shorter with respect to the values observed at 240 K, as expected from thermal contraction (Table 3.27). In the PIHS phase, hydrogen-bonding interactions are also very similar to those observed at 240 K (Figure 3.70) and 120 K (for the A sublattice). Indeed, the mean N···O value (2.762 Å) involving the second iron coordination sphere is identical to that calculated for the HS Fe1A site at 120 K (Table 3.27). This reinforces the correlation between the strength of the hydrogen bonds and the iron(II) spin state. In this case, the hydrogen bond between water molecules O4W and O5W is not present (distance of 3.0070(18) Å). For the mixed phase after partial relaxation, N···O distances found in the second iron coordination sphere (mean value of 2.738 Å) lie between those observed for the HS and LS phases. A similar tendency is observed for the hydrogen bond established

between water molecules O4W and O5W, with an intermediate distance of 2.934(2) Å.

The interaction between isonicNO(6) and isonicNO(3) can be described as short strong hydrogen bond (SSHB) with a marked covalent character (d(O1···O5) = 2.421-2.429 Å, Table 3.28). Although the proton that is located between the two oxygen atoms (H1O) was found in Fourier differential density maps, it presents higher atomic displacement parameters than other refined H atoms (those of water molecules) at all the temperatures (Table 3.32, appendix section). This is due to the fact that X-ray refined atomic coordinates of this type of H atom are unpredictably shifted from their real values, since the anisotropic shape of the bonding electron density cannot be properly modelled.[52] In order to locate precisely this proton, the study of Fourier differential density maps and neutron data are required. Thus, Fourier differential analyses were conducted by removing the hydrogen atom in the SSHB (H1O) and Figure 3.76 (top) shows an image of the electron density across the O1···O5 bond. At 240 K, the maximum electronic density that corresponds to H1O presents a spherical shape, suggesting that the H atom is located in one position (existence of a single potential energy well) and is not disordered in two sites with partial occupancies. Also, it exhibits similar distances within the experimental error to the two carboxylate anions (Table 3.28), being approximately halfway between them. These facts point to the presence of H1O in a single potential energy well with an energy minimum located approximately halfway between the H-bond acceptors (Figure 3.76. bottom, a). The C–O bond distances of the carboxylate anions involved in the SSHB are in agreement with this strong interaction (C23–O1: 1.281(2) Å; C29–O5: 1.279(2) Å), being longer than the distances obtained for the carbonyl groups (C23–O2: 1.233(2) Å; C29–O4: 1.235(2) Å).

At 120 K, two different short strong hydrogen bonds are observed and differential Fourier analyses revealed that the electron density distributions around the protons that are located between the two carboxylates (H1OA and H1OB) are elongated along the bonding direction and less symmetric (Figure 3.76, top). In addition, a shift in the electron density maxima is observed from O1A and O1B to O5B and O5A, respectively (Table 3.28). A possible explanation to this behaviour is the appearance of a double well potential as a consequence of the spin crossover (dynamic disorder), or the shift of the potential energy minimum towards one of the carboxylate anions below the phase transition (Figure 3.76. bottom, b). At 95 K, there is again only one short strong hydrogen bond but now the differential Fourier map (Figure 3.76, top) shows a different electron density distribution. Its shape differs from that observed at 120 K, being

more similar to that obtained for 240 K (more spherical), although being slightly unsymmetric. In accordance with a reentrant phase transition, the position of the maximum density is shifted back towards O1 (Table 3.28).

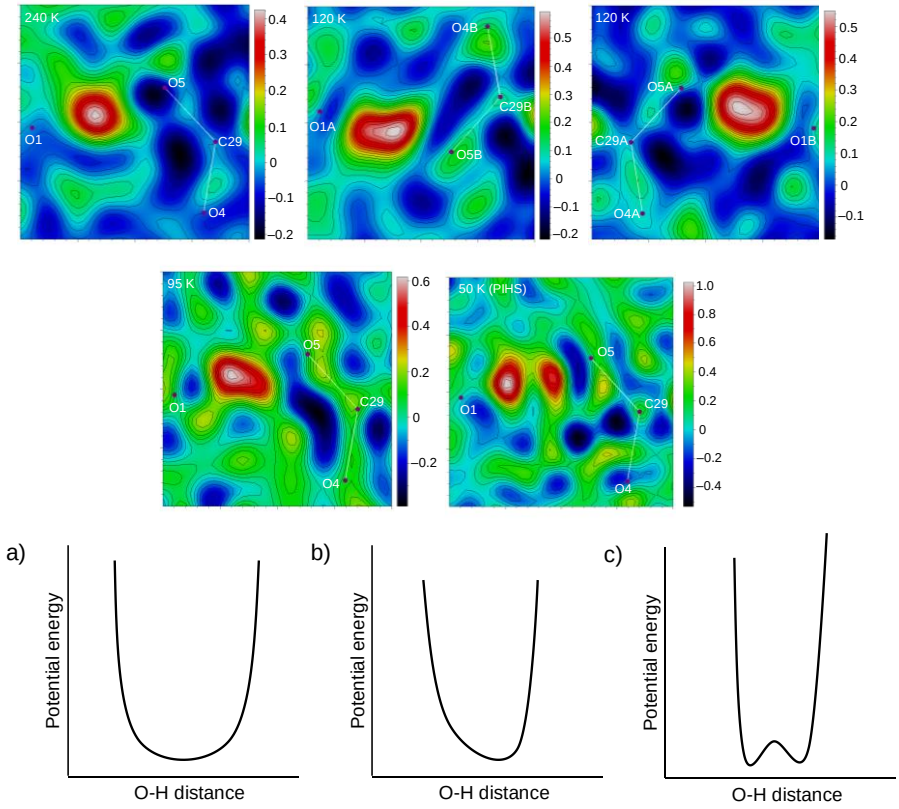

Figure 3.76. Top: X-ray Fourier difference maps (*Fo* – *Fc*) for **6**·5H$_2$O at different temperatures showing the electronic density corresponding to the H atom involved in the short-strong H-bond. The map corresponding to the photoinduced high-spin (PIHS) phase was also included for comparison. Images were calculated on a plane defined by atoms O1, O5 and C29. Note that at 120 K the interaction is split into two due to the doubling of the cell parameters. Bottom: Qualitative potential energy curves for a) symmetric and b) unsymmetric O–H···O SSHBs. c) The presence of an activation energy barrier for proton migration leading to a double-well potential.

In contrast to previous Fourier maps, two distinct maxima of electron density are clearly observed for the PIHS phase (Figure 3.76, top), being the position of each maximum closer to one oxygen atom (Table 3.28). Then, a model with two hydrogen atoms exhibiting partial occupancy factors was introduced, leading to a slight enhancement in the structural refinement parameters. This may indicate that static disorder is present at 50 K, characterised by two distinct potential minima (Figure 3.76. bottom, c) with the central hydrogen atom equally

distributed over two positions. The question that arises is if this double-well potential with a low barrier for proton migration appears as a consequence of the light irradiation or if it is already present at low temperatures. In the latter case, the energy barrier for proton migration between the two carboxylates should be low enough to be overcomed at 95 K, which would result in the observation of only one maximum in the electron density (fast exchange) at this temperature, but not at 50 K.

Both situations are very interesting, since any subtle change in the crystal structure can result in proton displacement along the SSHB or in the appearance of static disorder, being the two processes at the origin of ferroelectricity.[53] In order to elucidate this matter, a neutron crystallography study was carried out at different temperatures. The first goal was to check if there are two disordered protons at 120 K or only one well-localised between the isonicNO anions. Secondly, neutron diffraction analysis at 50 K will show if the double energy well observed in the PIHS phase appears as a consequence of the light irradiation (in this case, we will observe only one well-localised position for the proton) or due to the impossibility to overcome the activation energy barrier at 50 K (in this case, we will observe two different positions).

Table 3.28. Hydrogen bond distances (Å) for the short strong H-bond of **6**·$5H_2O$ at different temperatures obtained as distances to the maximum density peak (considering that H1O is located on the maximum of electron density) observed from difference Fourier maps (X-ray).

T / K	240 K	120 K[a]	120 K[a]	95 K[b]	50 K[c] (PIHS)	50 K[c] (PIHS)
d (O1···H1O)/Å	1.12(8)	1.33(6)	1.34(7)	1.05(5)	0.87(8)	1.67(8)
d (H1O···O5)/Å	1.30(8)	1.09(6)	1.09(7)	1.38(5)	1.55(8)	0.77(8)
d (O1···O5)/ Å	2.4247(17)	2.4216(16)	2.4257(16)	2.429(2)	2.420(4)	

[a]The O1···H1O···O5 interaction is split into two at 120 K: O1A···H1OB···O5B (left) and O1B···H1OA···O5A (right) as a consequence of the doubling of the cell volume.[b] Temperature was held at 95 K for 4h prior to data collection.[c] Photoinduced high-spin phase. The O1···H1O···O5 interaction is split into two in the PIHS phase: O1···H1O1···O5 (left) and O1···H1O2···O5 (right) as a consequence of the proton static disorder in the SSHB.

D. Neutron crystallography

First, single crystal neutron diffraction experiments of **6**·$5H_2O$ were conducted at 240 K, 120 K and 95 K (after thermal relaxation for 4 h), verifying the existence of the HS, mixed HS/LS and LS phases, respectively (Table 3.29). The coordinates of all non-hydrogen atoms are identical to those obtained from

X-ray diffraction data (within the experimental error), but significant differences are observed concerning hydrogen atoms. Therefore, a comparative study (X-ray *vs* neutron) of the hydrogen-bonding interactions involving the bpp ligands was conducted (Figure 3.77). Two conclusions can be extracted from this analysis: on the one hand, N–H distances obtained from X-ray data are understimated by 0.1-0.2 Å, whereas H···O distances are overestimated by the same amount with respect to values determined by neutron diffraction. On the other hand, as the distance between the heteroatoms increases, so does the divergence between XRD and neutron diffraction.

Table 3.29. Neutron crystal data of **6**·5H_2O at different temperatures.

	240 K (HS)	120 K (HS/LS)	95 K (LS)[b]	50 K (HS/LS)	50 K (LS)[c]
Empirical formula	$C_{40}H_{41}FeN_{13}O_{14}$	$C_{40}H_{41}FeN_{13}O_{14}$	$C_{40}H_{41}FeN_{13}O_{14}$	$C_{40}H_{41}FeN_{13}O_{14}$	$C_{40}H_{41}FeN_{13}O_{14}$
Formula weight	983.71	983.71	983.71	983.71	983.71
Crystallographic system	Triclinic	Triclinic	Triclinic	Triclinic	Triclinic
Space group	*P*–1(No. 2)	*P*–1(No. 2)	*P*–1(No. 2)	*P*–1(No. 2)	*P*–1(No. 2)
a/ Å	9.9726(3)	13.5877(3)	9.9677(4)	13.5851(9)	9.9719(3)
b/ Å	13.6198(4)	18.7535(5)	13.5502(5)	18.7551(9)	13.5419(4)
c/ Å	17.4815(5)	19.6264(5)	17.0822(5)	19.6424(8)	17.0957(5)
α/ °	73.5194(17)	64.6623(15)	76.876(2)	64.608(3)	76.716(2)
β/ °	85.7393(18)	71.0979(17)	85.729(2)	71.048(4)	85.858(2)
γ/ °	69.1085(18)	71.0863(15)	110.376(2)	71.168(4)	110.386(2)
V/ Å^3	2126.23(11)	4174.44(19)	2076.34(13)	4176.3(4)	2076.54(11)
Z	2	4	2	4	2
R(int)	0. 0473	0. 0428	0. 0417	0.0435	0. 0423
ρ_{calc}/ g·cm^{-3}	1. 536	1. 565	1. 573	1. 564	1. 573
μ/ mm^{-1}	0.190	0.193	0.194	0.193	0.194
Crystal dimensions/ mm	1.85 x 1.50 x 0.7	1.85 x 1.50 x 0.7	1.85 x 1.50 x 0.7	1.85 x 1.50 x 0.7	1.85 x 1.50 x 0.7
T/ K	240(1)	120(1)	95(1)	50(1)	50(1)
λ/ Å	1.455102	1.455102	1.455102	1.4547	1.4547
2θ range/ °	8.96 < 2θ < 121.55	9.02 < 2θ < 121.74	9.06 < 2θ < 121.60	9.02 < 2θ < 121.40	9.05 < 2θ < 121.48
Index ranges for h, k , l	-10/2, -16/16, -20/20	-16/15, -22/22, -18/23	-10/2, -15/16, -20/20	-16/15, -22/22, -18/23	-10/2, -15/16, -20/20
Refinement method	Full-matrix least-squares on F^2	Full-matrix least-squares on F^2	Full-matrix least-squares on F^2	Full-matrix least-squares on F^2	Full-matrix least-squares on F^2
Collected reflections	12723	25116	12460	24974	12440
Unique reflections	6543	12837	6404	12802	6336
Data/Restraints/ Parameters	6543/0/982	12837/0/1963	6404/0/982	12802/90/1963	6336/0/982
Goodness-of-fit on F^2	1.120	1.114	1.133	1.172	1.109
R1, wR2 [I > 2sigma(I)][a]	0.0500/0.1285	0.0639/0.1859	0.0523/0.1358	0.0916/ 0.3014	0.0782/0.2372
R1, wR2 (all data)[a]	0.0566/0.1336	0.0761/0.1992	0.0571/0.1400	0.1002/ 0.3205	0.0807/0.2423
$\Delta\rho_{max}$ and $\Delta\rho_{min}$ (e·Å^{-3})	0.66/–0.91	1.50/–1.18	0.93/–1.00	2.694/ -2.450	2.024/-1.873

[a] $R1 = \Sigma(||F_o| - |F_c||)/\Sigma|F_o|$; $wR2 = \{\Sigma[w(F_o^2 - F_c^2)^2]/\Sigma[w(F_o^2)^2]\}^{1/2}$; [b] Temperature was held at 95 K for 4 h prior to data collection; [c] Temperature was held at 95 K for 4 h prior to data collection at 50 K.

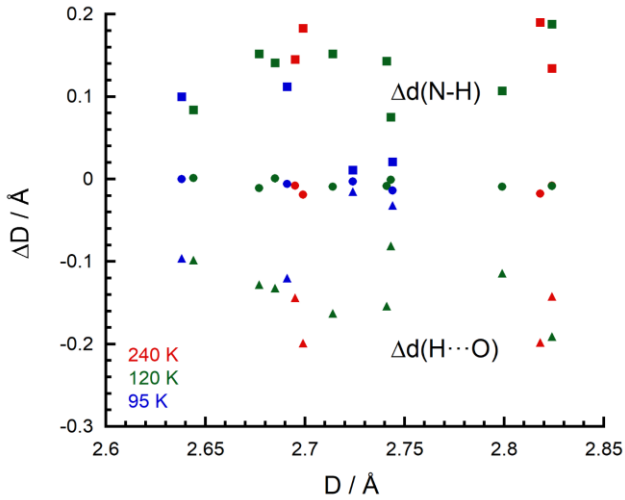

Figure 3.77. Comparative plot of H-bonding parameters obtained from neutron (*n*) and X-ray data. Circles correspond to $\Delta D = (D_n - D_{X\text{-}ray})$, where D is the distance between the heteroatoms (D_n data represent the abscissa axis). Squares and triangles refer, respectively, to $\Delta d(N{-}H) = (d_n(N{-}H) - d_{X\text{-}ray}(N{-}H))$ and $\Delta d(H\cdots O) = (d_n(H\cdots O) - d_{X\text{-}ray}(H\cdots O))$. Data have been gathered from measurements at different temperatures: 240 K (red), 120 K (green) and after annealing at 95 K (blue).

Importantly, neutron diffraction data undoubtedly confirm that hydrogen bonds found in the second iron coordination sphere are stronger for the LS species (Table 3.30): the mean NH···O distance decreases from 1.744 Å at 240 K to 1.694 Å at 95 K. In the mixed phase, the mean NH···O distances are 1.737 Å for the HS site and 1.693 Å for the LS centre. In addition, all the OH···O hydrogen bond distances involving water molecules are in agreement with the results obtained by XRD. Even the formation of the hydrogen bond between water molecules O4W and O5W only in the LS phase ((O4W)H···O5W distance decreases from 2.122(11) Å at 240 K to 1.898(8) Å at 95 K) and the few exceptions already mentioned in which distances are shorter for the HS phase.

At 240 K (HS phase) the proton involved in the SSHB is located halfway between the two oxygen atoms (Table 3.31), as suggested by XRD data. In the mixed HS/LS phase at 120 K, this interaction is split into two: the O1A···H1OB···O5B contact preserves the proton practically in the same position, whereas in the second contact, O1B···H1OA···O5A, the proton shifts slightly towards O5A. At 95 K, the proton in the LS phase still deviates from the centre of the hydrogen bond, being closer to O5. These results show that in the mixed phase only the proton that belongs to the B sublattice (the one that undergoes SCO to the LS phase) is

separated slightly from O1B, in analogy with the position of the proton in the LS phase at 95 K. Although the shift in the proton position is quite small, it is significant (eight times higher the experimental error) and of similar magnitude to variations observed in H-bonded ferroelectrics.[53-54]

Table 3.30. Selected H-bond distances (Å) in the crystal structure of **6**·5H_2O at different temperatures obtained from neutron data.

H-bond	240 K (HS)	120 K (HS/LS)[a]	120 K (HS/LS)[b]	95 K (LS)[c]	50 K (HS/LS)[a]	50 K (HS/LS)[b]	50 K (LS)[d]
N1–H···O3W	1.686(7)	1.666(7)	1.623(7)	1.604(6)	1.652(9)	1.602(9)	1.618(7)
N5–H···O4W	1.828(7)	1.827(8)	1.799(8)	1.785(6)	1.817(9)	1.766(9)	1.797(7)
N6–H···O4	1.802(6)	1.799(6)	1.717(7)	1.728(6)	1.819(9)	1.747(9)	1.725(6)
N10–H···O8	1.661(6)	1.657(6)	1.632(6)	1.660(6)	1.672(8)	1.644(9)	1.654(6)
O1W–H···O6	1.877(8)	1.827(9)	1.850(9)	1.832(8)	1.849(11)	1.879(10)	1.803(9)
O1W–H···O9	1.912(9)	1.882(8)	1.857(8)	1.868(7)	1.903(11)	1.893(11)	1.863(9)
O2W–H···O1W	1.837(8)	1.815(7)	1.793(8)	1.781(7)	1.798(9)	1.789(9)	1.761(7)
O2W–H···O8	1.921(10)	1.913(10)	1.980(10)	1.957(8)	1.916(12)	1.957(11)	1.949(8)
O3W–H···O9	1.934(8)	1.913(8)	1.879(7)	1.873(6)	1.907(8)	1.878(9)	1.890(7)
O3W–H···O2	1.794(7)	1.792(8)	1.746(8)	1.741(7)	1.796(9)	1.735(10)	1.732(8)
O4W–H···O7	1.746(7)	1.738(8)	1.769(8)	1.768(7)	1.751(10)	1.758(10)	1.757(9)
O4W–H···O5W	2.122(11)	2.079(10)	1.901(10)	1.898(8)	2.054(12)	1.887(11)	1.919(10)
O5W–H···O3	1.770(8)	1.777(8)	1.736(8)	1.740(7)	1.792(9)	1.735(9)	1.757(7)
O5W–H···O2W	1.879(8)	1.886(8)	1.850(8)	1.843(7)	1.894(9)	1.852(9)	1.858(8)

[a] Contacts within the A sublattice, except for O1WA–H···O9B, O3WA–H···O9B and O5WA–H···O2WB. [b] Contacts within the B sublattice, except for O1WB–H···O9A, O3WB–H···O9A and O5WB–H···O2WA. [c] Temperature was held at 95 K for 4 h prior to data collection. [d] Temperature was held at 95 K for 4 h prior to data collection at 50 K.

Table 3.31. Hydrogen bond distances (Å) for the short strong H-bond of **6**·5H_2O at different temperatures obtained from neutron diffraction data.

T / K	d (O1···H1O)/Å	d (H1O···O5)/Å	d (O1···O5)/ Å
240	1.203(7)	1.206(7)	2.407(4)
120[a]	1.216(7)	1.213(7)	2.427(4)
	1.221(7)	1.198(7)	2.416(4)
95[b]	1.222(6)	1.200(6)	2.420(4)
50[a]	1.213(8)	1.209(8)	2.420(5)
	1.227(8)	1.191(8)	2.414(5)
50[c]	1.237(7)	1.184(7)	2.419(4)

[a]The O1···H1O···O5 interaction is split into two at 120 K and at 50 K (direct measurement): O1A···H1OB···O5B (top line) and O1B···H1OA···O5A (bottom line) as a consequence of the doubling of the cell volume.[b] Temperature was held at 95 K for 4h prior to data collection.[c] Temperature was held at 95 K for 4 h prior to data collection at 50 K.

Unlike in X-ray data, the nuclear density of the H atom is well-localised at all temperatures (with similar atomic displacement parameters to other protons

present in the structure, Table 3.33, 3.6.3. Appendix section). In addition, differential Fourier maps reveal only one perfectly round minimum of nuclear density at all the working temperatures (Figure 3.78). Thus, this discards the existence of proton disorder resulting from the presence of a low-activation energy barrier and confirms unambiguously that SCO in **6**·5H_2O is accompanied by a proton displacement across the SSHB.[55]

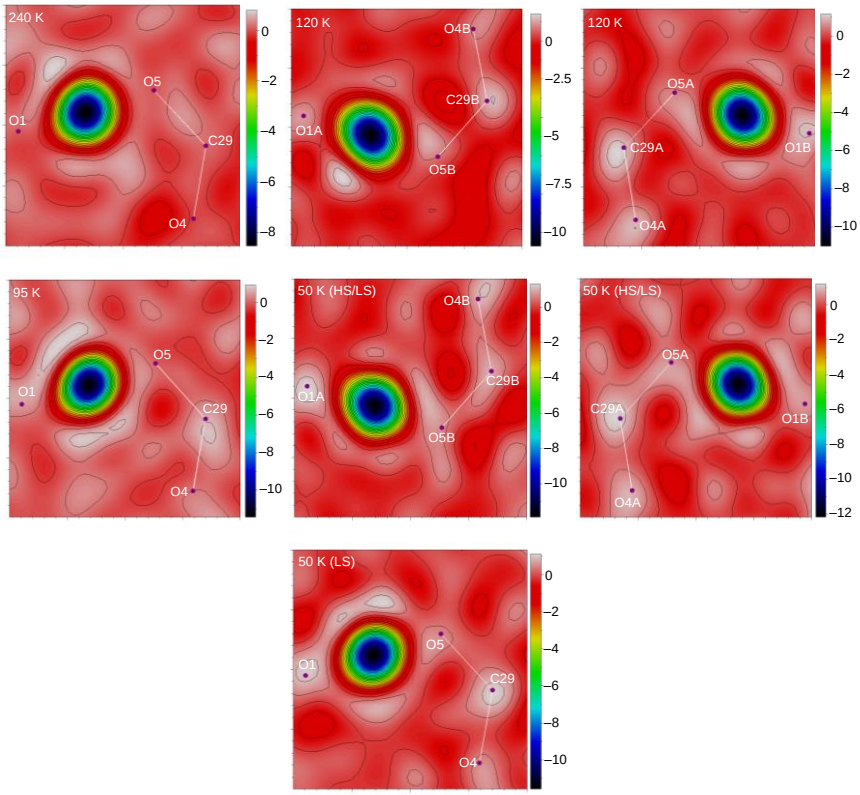

Figure 3.78. Neutron Fourier difference maps (F_0-F_c) for 6·5H_2O at different temperatures showing the nuclear density corresponding to the H atom involved in the SSHB. Images were calculated on a plane defined by atoms O1, O5 and C29. Note that at 120 K and at 50 K (direct measurement, HS/LS), the interaction is split into two due to the doubling of the cell parameters. Hydrogen peaks are negative in the neutron images due to the sign of the neutron scattering length.

Secondly, two different measurements were carried out at 50 K. First, the sample was directly cooled down to 50 K and measured in the mixed HS/LS state. Then, the temperature was increased up to 95 K in order to achieve full thermal relaxation after 4 h. At this point, the temperature was cooled down again to 50 K and the compound measured in the LS phase. Similar cell parameters (Table

3.29) to those obtained for the HS/LS phase at 120 K and for the LS phase at 95 K were obtained, respectively. Also, hydrogen bond distances parallel the results obtained for the HS/LS phase at 120 K and for the LS measured at 95 K, respectively (Table 3.30), with the formation of the hydrogen bond between O4W and O5W in the LS phase and in the B sublattice of the mixed-spin phase at 50 K. The LS phase and the LS sublattice of the mixed-spin phase exhibit a similar behaviour concerning the SSHB interaction O1···O5, as expected. In the HS/LS phase at 50 K, the O1A···H1OB···O5B contact keeps the proton practically in the middle, whereas in the O1B···H1OA···O5A interaction the proton separates slightly from O1B. For the LS phase at 50 K, the proton deviates from the centre of the hydrogen bond and approximates further towards O5 (Table 3.31). Figure 3.78 shows the neutron Fourier difference maps which also exhibit a single minimum of nuclear density in both structures measured at 50 K, discarding the existence of a double energy well with a low-activation energy barrier. Therefore, this indicates that the proton disorder present in the PIHS phase at 50 K appears as a consequence of the light irradiation that leads to a change of the potential energy surface.

E. Single crystal neutron Laue diffraction measurements

A preliminary study was performed using white-beam Laue neutron diffraction in the temperature range 320-10 K. The transition from the HS phase to the mixed-phase was reproduced at $T_{\downarrow}$ = 166 K on cooling (indicated by a shift of the Bragg reflections and the appearance of weak reflections in the low temperature measurement, Figure 3.79.a-c). Then, the thermal relaxation from the mixed-spin state to the full LS phase of **6**·5H_2O at 95 K was followed by this technique (Figure 3.79.d-e). An annealing time of approximately 4 h was needed for a complete relaxation. Further cooling to 10 K shows the absence of any structural transformation at low temperatures. Finally, during the heating process back to room temperature, two crystal phase transitions were observed at approximately 117 K (corresponding to the SCO from the LS to the mixed HS/LS phase, Figure 3.79.f) and 166 K (ascribed to the HSLS ⟶ HS transformation, Figure 3.79.g), defining the range of stability of the mixed-spin phase. Therefore, these experiments prove the existence of the three crystal phases and discard the presence of incommensurate structures or additional crystallographic phase transitions.

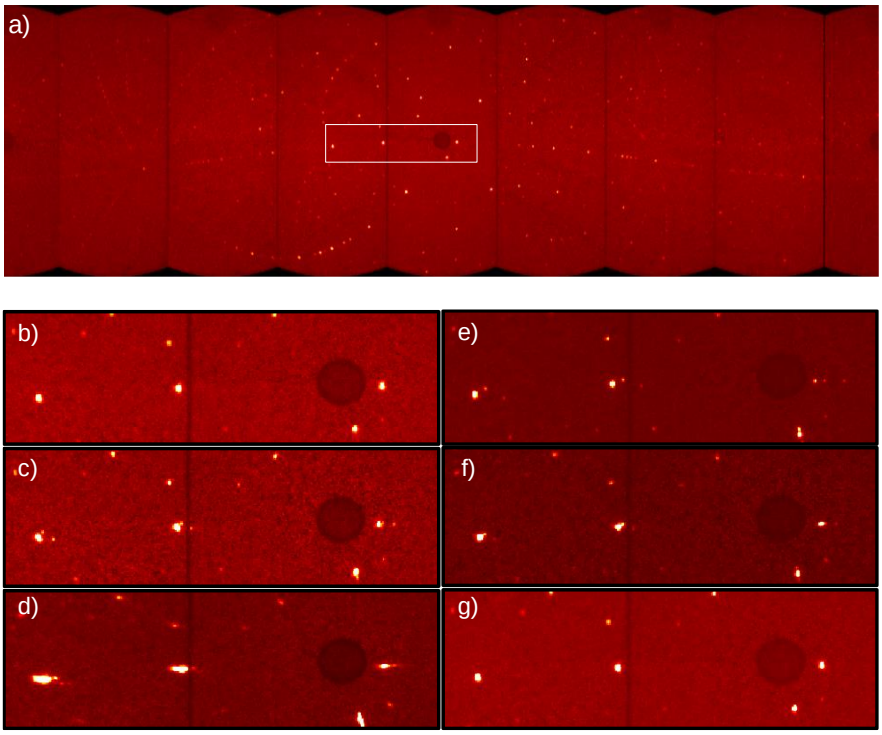

Figure 3.79. Temperature evolution of the Laue patterns of **6**·5H_2O: a) at 318 K (HS phase), b) corresponds to an enlarged area highlighted in a) with a white rectangle. The c)-g) patterns are a zoom of the same selected area at c) 166 K (HS/LS phase), d) 95 K after being 30 min at this temperature (it can be seen that the sample is relaxing to the LS phase), e) 95 K after being 4 h at this temperature (LS phase), f) at 117 K (HS/LS phase) and g) at 166 K (HS phase).

F. Powder X-ray diffraction

Figure 3.80 shows the X-ray patterns at room temperature of **6**·5H_2O as-synthesised, desolvated and rehydrated at ambient conditions. The sample was dehydrated by heating for 2 h at 400 K, which resulted in a loss of crystallinity. As observed for the adipate derivative, restoration of the original crystalline material takes place upon exposure to ambient humidity. The simulated pattern matches very well that obtained experimentally, discarding the presence of impurities and the existence of a phase transition between 240 K and room temperature. Furthermore, the powder X-ray diffractogram of the deuterated sample shows that it is isostructural to **6**·5H_2O.

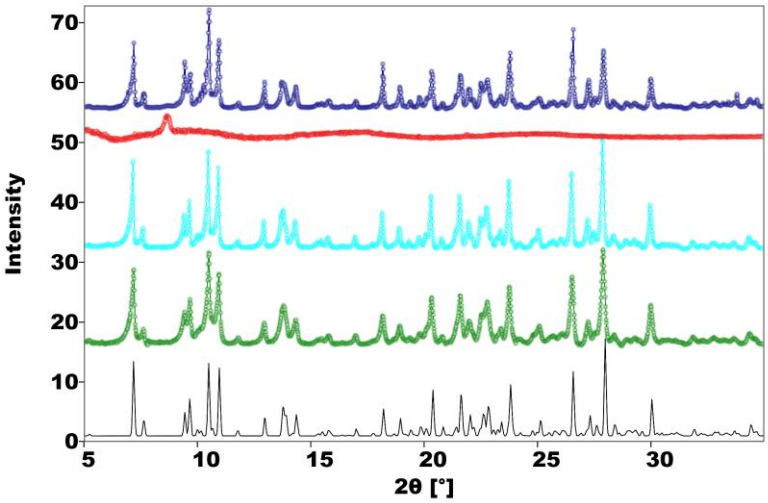

Figure 3.80. Powder X-ray diffractograms at room temperature of **6**·5H_2O as-synthesised (dark blue), dehydrated at 400 K for 2 h (red) and after rehydration at ambient conditions during 12 h (light blue). The diffractogram of the deuterated sample (green) and the simulated pattern of **6**·5H_2O from single crystal X-ray data at 240 K are shown for comparison (black lines).

3.5.4. Discussion

SSHBs with O···O distances lower than 2.45 Å are expected to exhibit proton migration as a response to different external stimuli. This interaction is consistent with very strong three-centre four-electron σ-bonding (Speakman-Hadzi bond) systems.[56] Usually, the proton is located in the middle of both heteroatoms at high temperature and it moves slightly towards one of the hydrogen bond acceptors as temperature decreases, as shown for **6**·5H_2O. Since the environment of the H atom is quite symmetric, its migration might be a consequence of a change of the potential energy surface with temperature.[55a] XRD and neutron data might show differences for hydrogen atoms bonded to electronegative elements, as it is observed in the present case. It is due to the fact that XRD deals with electron density distribution whereas neutron diffraction determines the position of nuclei.[39] SCO triggers a small displacement of the proton position but induces an important delocalisation of the electron density being shifted towards O5A and O5B in the mixed HS/LS phase. In any case, the elongated electron density observed in the mixed-spin phase might have been an indication of disorder if a double well potential have appeared below the phase transition, being neutron diffraction very useful in discarding this hypothesis. Nevertheless, this uncommon situation in SSHB appears in the

present compound as a result of the lattice expansion induced by light irradiation.

Remarkably, neutron diffraction clearly confirms that hydrogen bonds involving the second coordination sphere of $[Fe(bpp)_2]^{2+}$ cations are shorter for the LS species. This scenario is the ideal situation for comparison, because it is the first time in which HS and LS Fe(II) sites are present at the same temperature with the same second coordination sphere, thus, avoiding the ambiguities associated to temperature. As mentioned in the previous section, a simple electrostatic model can explain the increase in hydrogen-bond strength as the Fe(II) complex undergoes SCO to the LS phase. All the changes observed regarding hydrogen-bond connectivity between the LS and HS phases, are also reproduced in the B sublattice of the mixed-spin phase. Thanks to this, correlations can be established between SCO and structural properties including hydrogen bond interactions and proton migration along the SSHB. This suggests that it could be possible to trace the interaction path between the iron centres in the HS/LS phase by following the hydrogen bond cooperativity.[39] Figure 3.81.a shows the shortest hydrogen-bonding pathway between adjacent iron complexes, which defines centrosymmetric dimeric BB units. When one Fe^{2+} cation undergoes crossover to the LS site Fe1B, the distance between N10B and O8B becomes shorter in response to the increasing charge density (Table 3.27, row 4). Consequently, the hydrogen bond acceptor character of O7B decreases and the distance between O7B and O4WB increases (row 11). Then, O4WB approximates to N5B (row 2), stabilising the LS state of an adjacent iron(II) site. Instead, there is no such a short hydrogen-bonding pathway between Fe1A and Fe1B centres. Figure 3.81.b shows the shortest pathway in this case, which involves three water molecules and one carboxylate anion. As already mentioned, the presence of one LS Fe1B site increases the strength of the N5B···O4WB interaction, which induces by σ-bond cooperativity the formation of a new hydrogen bond between O4WB and O5WB water molecules. In this way, the propagation of the hydrogen-bonding cooperativity towards the A sublattice is prevented.

Undoubtedly, hydrogen-bonding cooperativity is crucial in the stabilisation of centrosymmetric LS dimers, thus, defining the magnetic properties. This is in agreement with several reports that show a clear correlation between the presence of multistep SCO in Hofmann-type frameworks and intermolecular interactions.[57] Usually, multistep transitions result from crystallographically inequivalent Fe^{2+} centres with distinct coordination environments. In our case, HS and LS states coexist in the crystal lattice in an ordered pattern as a

consequence of the presence of competing elastic interactions resulting from a structural symmetry breaking transition.

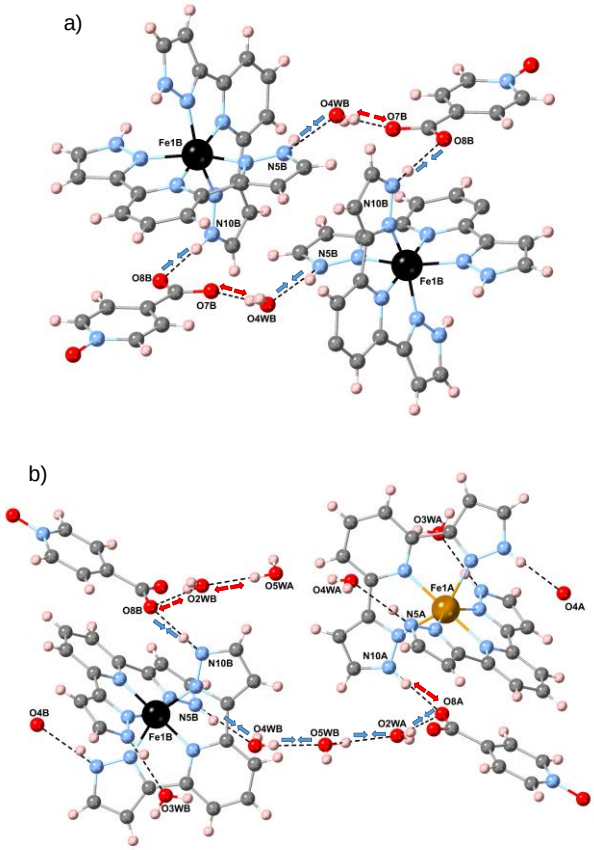

Figure 3.81. Crystal structure of **6**·5H_2O in the mixed HS/LS phase at 120 K showing the importance of hydrogen bond cooperativity in the stabilization of a) centrosymmetric LS dimers and b) the formation of a hydrogen bond between O4WB and O5WB. Blue and red arrows indicate the increase or decrease in hydrogen bonding strength, respectively.

On the other hand, the structural differences between the LS and HS phases have a direct impact in the SCO properties. It has been shown that variations in the location of solvent molecules and/or anions can result in striking changes in the magnetic behaviour.[58] In our case, the wide temperature range of metastability exhibited by the mixed-spin phase is probably related to the formation of the hydrogen bond between water molecules O4WB and O5WB.

Cooperativity of hydrogen bonds is also consistent with the analysis of the atomic displacement parameters of the atoms present in the metastable phase obtained after partial relaxation of the PIHS phase. Higher values are obtained for pyrazolyl C and N atoms that experiment a considerable displacement with the change of the bpp bite angle, for water molecules present in the second iron coordination sphere (O3W and O4W) and for those anions involved in the H-bonding cooperative pathway described in Figure 3.81 (O7 and O8, Table 3.32). This short-range interaction presumably defines LS dimers in a random fashion that would explain the two-step relaxation in the magnetic properties and the lack of a symmetry breaking event in the structural analysis of this metastable phase ($PIHS_{rel}$). Therefore, the analysis of this metastable structure is useful in the recognition of the cooperative interactions present in the material.

3.5.5. Conclusions and perspectives

A novel hydrogen-bonded complex combining a $[Fe(bpp)_2]^{2+}$ SCO typical cation and isonicotinic acid N-oxide both in its free and deprotonated form has been synthesised and its structural and (photo)magnetic properties have been studied. **6**·$5H_2O$ undergoes a crystallographic phase transition at 167 K with symmetry breaking and formation of a HS/LS mixed phase. This intermediate phase is stable between 115 K and 167 K, becoming metastable at lower temperatures. Below 115 K, the LS phase is the stable one with restoration of the original symmetry. Importantly, structural rearrangements encompass these spin transformations, including the formation of a hydrogen bond between two water molecules only in the LS (sub)lattice and a proton displacement between two isonicNO anions that form a SSHB, with formation of a photoinduced activation energy barrier for proton motion (Scheme 3.7). Furthermore, the formation of a hydrogen bond betweeen two water molecules can be reversed on heating or irradiating the sample. Recently, the first examples of coupling between proton transfer and SCO have been described.[59] In $[Fe(HL\text{-}Cl)_2](AsF_6)_2$ (HL-Cl = N‘-(di(pyridin-2-yl)-methylene)-2-chlorobenzohydrazide), an intramolecular proton transfer from a coordinated hydrazone fragment to an appended pyridine unit takes place triggered by the change in the spin state of an Fe(II) bischelated complex. Whereas in this study the driving force for proton transfer is the change in the bite angle of the chelating ligand, in our case, the effect seems to be purely electrostatic and demonstrates that the SCO can have a widespread influence even on positions located far from the Fe^{2+} cation. This opens the way to the design of SCO hydrogen-bonded complexes with ferroelectric properties.

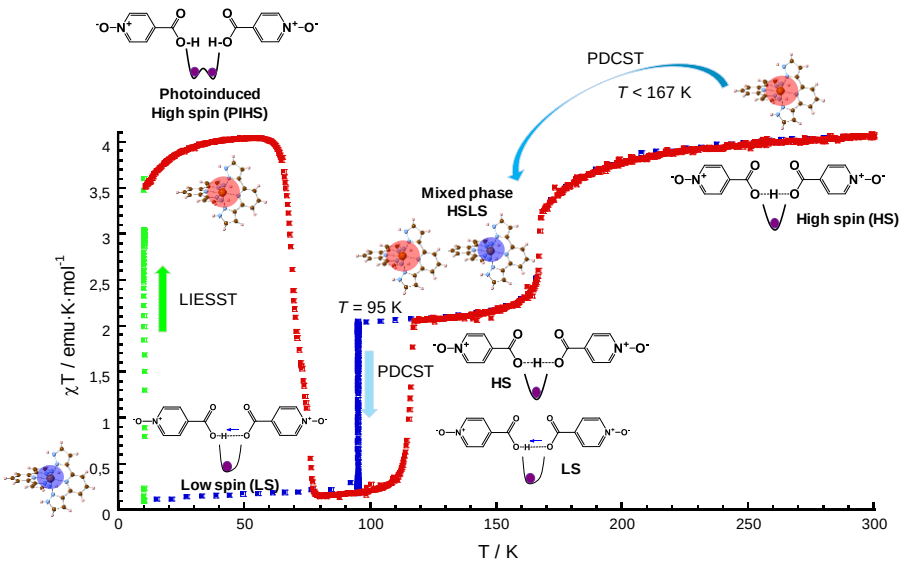

Scheme 3.7. Illustration of the reversible proton displacement coupled spin transition (PDCST) in **6**·5H$_2$O with an schematic representation of the potential energy curves for the proton migration along the short strong hydrogen bond (SSHB).

Measurements on deuterated samples show that isotope effects are present in this system, which demonstrates that hydrogen bond cooperativity plays a major role in the propagation of elastic interactions throughout the lattice. This has been also evidenced by X-ray structural analysis at different temperatures and neutron crystallography measurements, which has allowed to trace the interaction path between the iron(II) centres by looking at the hydrogen bond cooperativity.

Unlike compound **5**·2.4H$_2$O, the abruptness of the transition observed for this compound is moderate, as indicated by the value of the self-acceleration parameters (α_i) which are considerably lower for **6**·5H$_2$O. This behaviour is in agreement with the respective cationic crystal packing that consists on π-π staking interactions forming chains of $[Fe(bpp)_2]^{2+}$ complexes, whereas in the previous compound a similar packing to the well-known *terpyridine embrace* motif was present. The presence of two water molecules in the second iron coordination sphere of **6**·5H$_2$O is another reason for the lower degree of cooperativity exhibited by this system in comparison to **5**·2.4H$_2$O (in which only one water molecule was hydrogen-bonded to one of the three inequivalent Fe sites). This demonstrates that in order to increase the cooperativity of the SCO process, it is necessary to maximise the connectivity between the iron complexes and the anions. Thus, being the ideal situation that in which each $[Fe(bpp)_2]^{2+}$ is

surrounded by four anions. It is also coherent that as the number of water molecules present in the second iron coordination sphere increases, so does the likelihood of amorphisation after solvent removal. This is consistent with the fact that **6**·5H_2O losses its crystallinity during the dehydration process whereas anhydrous **5** preserves it.

3.6. Experimental Section

3.6.1. Synthesis of precursors

Synthesis of ligand bpp

Ligand bpp was prepared in two steps by the previously published procedure by Lin and Lang, which has been described in detail in the previous chapter.

Synthesis of Ag($C_6H_4NO_2$) (Ag(isonic))

A suspension of isonicotinic acid (1.230 g, 10 mmol) in 25 ml of a mixture 3:2 EtOH/H_2O was treated with a suspension of silver carbonate (1.371 g, 5 mmol) in 25 ml H_2O. Then, the mixture was refluxed for 3 h and 30 minutes until CO_2 ceased to evolve. There was a change in the colour of the solid from yellow-brown to white. The product was collected by filtration and washed with water and acetone to yield 2.062 g (90%) of the desired compound. Anal. Calcd for $AgC_6H_4NO_2$: C, 31.34; H, 1.75; N, 6.09 %. Found: C, 31.05; H, 1.81; N, 6.11 %. Selected IR (KBr, cm^{-1}): 3405.1, 1602.1, 1547.9, 1395.5, 1227.4, 1060.5, 1008.6, 866.8, 847.1, 769.0, 704.1, 689.2, 408.5. Thermogravimetric analysis (Figure 3.82, left) shows that solvent molecules of crystallisation are not present in this salt. The infrared spectrum of $Ba(C_6H_8O_4)\cdot 0.1C_6H_{10}O_4$ is shown in Figure 3.82 (right).

Synthesis of Ag($C_6H_4NO_2$) (Ag(nic))

A suspension of nicotinic acid (1.230 g, 10 mmol) was prepared in 25 ml of a mixture 3:2 EtOH/H_2O. Then, a suspension of silver carbonate (1.371 g, 5 mmol) in 25 ml H_2O was added and the mixture was refluxed for 3 h and 30 minutes (time required until CO_2 ceased to evolve). The white solid was collected by filtration and washed with water and acetone to yield 1.988 g (87%) of the desired compound. Anal. Calcd for $AgC_6H_4NO_2$: C, 31.34; H, 1.75; N, 6.09 %. Found: C, 30.58; H, 1.80; N, 6.01 %. Selected IR (KBr, cm^{-1}): 3400.4, 3042.9, 1593.9, 1549.3, 1387.4, 1196.0, 1088.4, 1022.2, 840.4, 758.4, 704.3, 511.2.

Thermogravimetric analysis (Figure 3.83, left) confirms the anhydrous character of this salt. The infrared spectrum of $Ag(C_6H_4NO_2)$ is shown in Figure 3.83 (right).

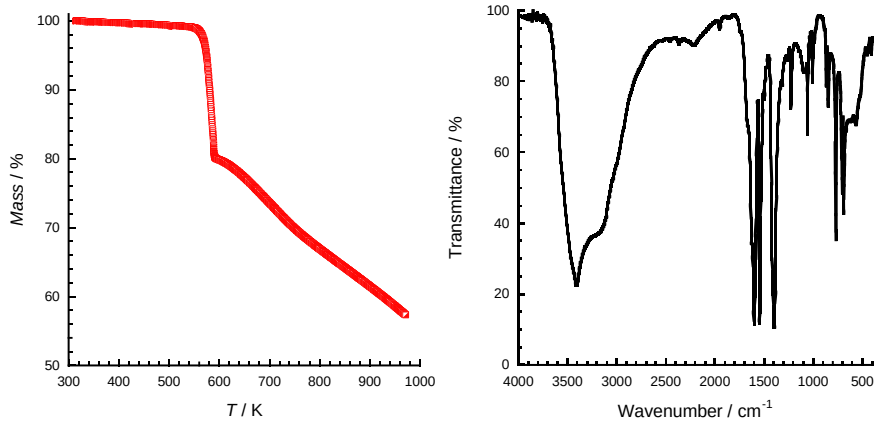

Figure 3.82. Left: Thermogravimetric analysis of $Ag(C_6H_4NO_2)$. The plot confirms the anhydrous character of this salt. Right: Infrared spectrum of $Ag(C_6H_4NO_2)$ in a KBr pellet.

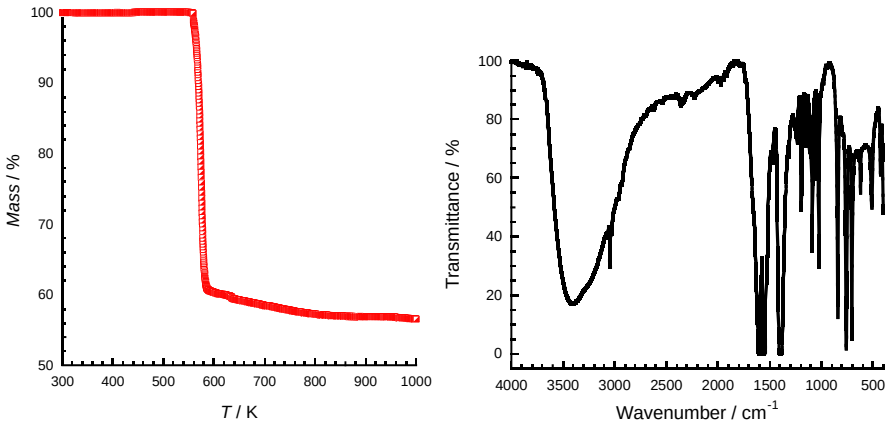

Figure 3.83. Left: Thermogravimetric analysis of $AgC_6H_4NO_2$. Right: Infrared spectrum of $AgC_6H_4NO_2$ in a KBr pellet.

Synthesis of $Ba(C_6H_4NO_3)_2{\cdot}4H_2O$

A solution of isonicotinic acid N-oxide (1.046 g, 7.52 mmol) was prepared in 40 ml H_2O. Then, a solution of barium hydroxide octahydrate (1.186 g, 3.76 mmol) in 60 ml MeOH was added and the mixture was refluxed overnight. The resulting

solution was concentrated using a rotatory evaporator until dryness. The crystalline white product was washed with water and acetone to yield 1.594 g (87%) of the desired compound. Anal. Calcd for $Ba(C_6H_4NO_3)_2{\cdot}4H_2O$: C, 29.68; H, 3.32; N, 5.77 %. Found: C, 29.42; H, 3.52; N, 5.66 %. Selected IR (KBr, cm^{-1}): 3394.53, 3108.03, 1598.03, 1545.90, 1390.56, 1225.67, 1177.57, 1139.87, 856.11, 788.13, 685.76, 641.64, 459.14. Thermogravimetric analysis (Figure 3.84, left) confirms the presence of four water molecules in this salt. The infrared spectrum of $Ba(C_6H_4NO_3)_2{\cdot}4H_2O$ is shown in Figure 3.84 (right).

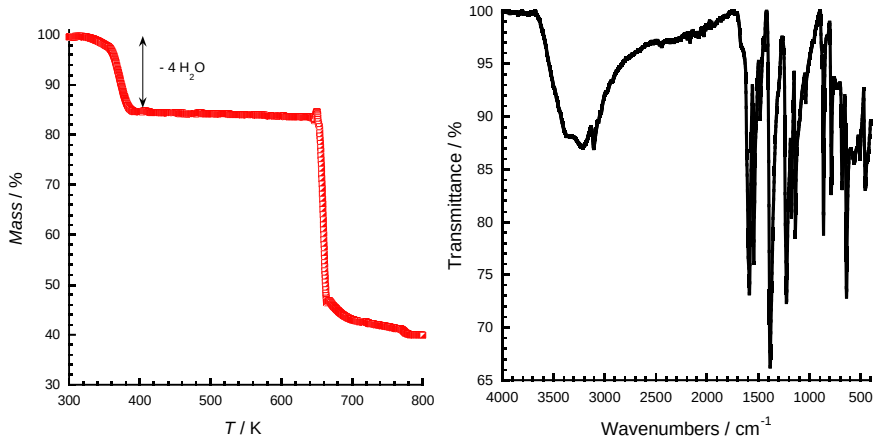

Figure 3.84. Left: Thermogravimetric analysis of $Ba(C_6H_4NO_3)_2{\cdot}4H_2O$. Right: Infrared spectrum of $Ba(C_6H_4NO_3)_2{\cdot}4H_2O$ in a KBr pellet.

3.6.2. Synthesis of complexes

Synthesis of $[Fe(bpp)_2](C_6H_4NO_2)_2{\cdot}2\ H_2O$ ($3{\cdot}2H_2O$)

$FeCl_2{\cdot}4H_2O$ (0.0994 g, 0.5 mmol) was added as a solid to a degassed solution of bpp (0.212 g, 1.0 mmol) in 20 ml of a mixture 4:1 MeOH/H_2O. A deep red colour appears. After complete dissolution of the iron reagent, a mixture of $Ag(C_6H_4NO_2)$ (Ag(isonic), 230 mg, 1 mmol) in 20 ml H_2O was added. After stirring for 1 h at 65°C, the yellowish precipitate of AgCl was filtered through a low-porosity frit. The filtrate was left undisturbed. Red prisms suitable for X-ray analysis appeared after a few days, yielding 257.2 mg (70%). Found: C, 54.03; H, 4.04; N, 22.70. $C_{34}H_{30}FeN_{12}O_6$ requires C, 53.84; H, 3.99; N, 22.16. ν_{max}/cm^{-1}: 3443.9, 3157.6, 3116.0, 1644.4, 1617.9, 1594.1, 1563.3, 1546.9, 1456.7, 1439.7, 1374.8, 1352.5, 1097.9, 1054.4, 1010.2, 836.4, 821.9, 805.1, 767.5, 708.3, 684.9, 627.9, 530.6. The infrared spectrum of **3**·$2H_2O$ is shown in Figure 3.85.

Thin film fabrication of compound 3·2H_2O

Thin films of compound **3**·2H_2O were grown by drop casting method. 11-12 mg of crystals were dissolved into 200 µl of a mixture methanol/water (160 µl MeOH and 40 µl H_2O) to form a red clear precursor solution. After filtration of the sample, 20 µl of the above solution was deposited on an FTO-coated glass substrate. Finally, the film was annealed at 35°C for 10-15 min to remove the solvent and further improve the crystallinity.

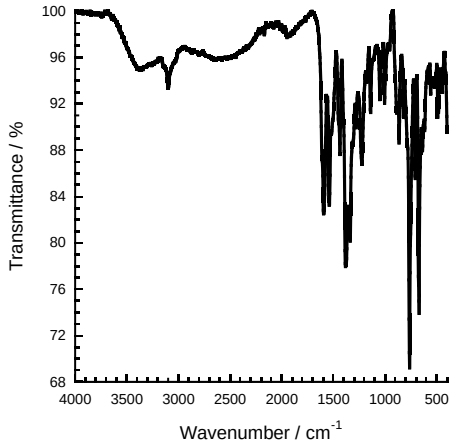

Figure 3.85. Infrared spectrum of **3**·2H_2O in a KBr pellet.

Synthesis of [Fe(bpp)$_2$]($C_6H_4NO_2$)$_2$ (3)

Dehydration of **3**·2H_2O was performed by placing a glass tube with the sample in an oil bath and heating at 453 K under vacuum for 2 h. The sample undergoes a fast rehydration to recover the pristine hydrated material. Thus, elemental analysis and infrared spectrum of anhydrous **3** could not be obtained.

Synthesis of [Fe(bpp)$_2$]($C_6H_4NO_2$)$_2$·4H_2O (4·4H_2O)

$FeCl_2$·4H_2O (0.0994 g, 0.50 mmol) was added as a solid to a degassed solution of bpp (0.212 g, 1.0 mmol) in 20 ml of a mixture 4:1 MeOH/H_2O under an argon atmosphere. A deep red colour appears after solubilisation of the iron reagent. A mixture of Ag($C_6H_4NO_2$) (230 mg, 1.0 mmol) in 20 ml H_2O was added and the resulting mixture kept under stirring for 1 h at 65°C. The yellowish precipitate of AgCl was filtered through a low-porosity frit and the filtrate was left undisturbed. Red plates of **4**·4H_2O suitable for X-ray analysis appeared after a

few days, yielding 246.3 mg (68%). Anal. Calcd for $C_{34}H_{34}FeN_{12}O_8$: C, 51.40; H, 4.31; N, 21.15 %. Found: C, 51.63; H, 4.13; N, 21.83 % (the sample is partially dehydrated, losing 0.55 H_2O molecules per formula prior to analysis). Selected IR (KBr, cm^{-1}): 3422.8, 1601.0, 1560.3, 1438.4, 1385.0, 1281.1, 1234.5, 1146.1, 1094.1, 1028.3, 897.0, 831.3, 756.8, 697.9, 619.8. The infrared spectrum of **4**·4H_2O is shown in Figure 3.86.

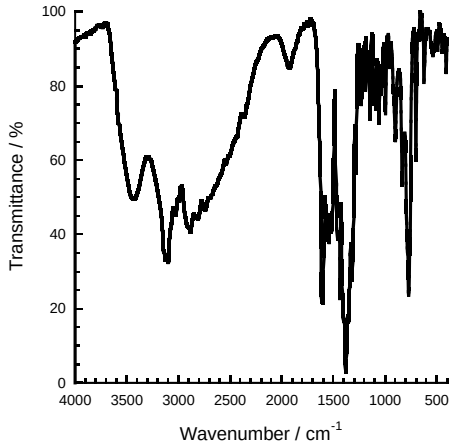

Figure 3.86. Infrared spectrum of **4**·4H_2O in a KBr pellet.

Synthesis of $[Fe(bpp)_2](C_6H_4NO_3)_2$·2.4$H_2O$ (**5**·2.4H_2O)

$FeSO_4$·7H_2O (34.75 mg, 0.125 mmol) was added as a solid to a degassed solution of bpp (53 mg, 0.25 mmol) in 5 ml MeOH yielding a deep red coloured solution after complete dissolution of the metal salt. Then, a solution of $Ba(C_6H_4NO_3)_2$·4H_2O (206.76 mg, 0.426 mmol) in 5 ml H_2O was added. After stirring for 2 h at room temperature, the yellowish precipitate of $BaSO_4$ was filtered through a low-porosity frit. The filtrate was left undisturbed in a thermostatically controlled water bath at 25 °C. Dark orange rhombuses suitable for X-ray analysis appeared after a few days, yielding 44.6 mg (45%). Found: C, 51.02; H, 3.69; N, 20.87. $C_{34}H_{30.84}FeN_{12}O_{8.4}$ requires C, 51.19; H, 3.89; N, 21.07. ν_{max}/cm^{-1}: 3426.63, 3103.77, 1611.42, 1541.58, 1436.44, 1382.85, 1362.58, 1233.40, 782.73, 636.27. The infrared spectrum of **5**·2.4H_2O is shown in Figure 3.87.

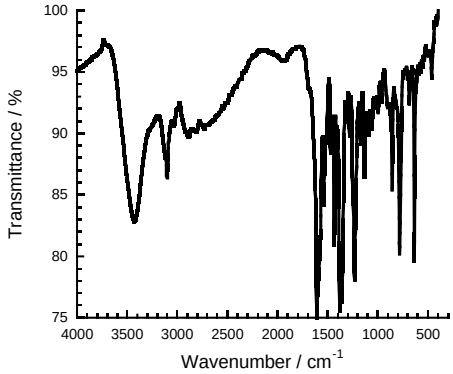

Figure 3.87. Infrared spectrum of **5**·2.4H_2O in a KBr pellet.

Synthesis of [Fe(bpp)$_2$]($C_6H_4NO_3$)$_2$·1.6H_2O·0.8D_2O (**5**·1.8H_2O·0.6D_2O)

5·1.8H_2O·0.6D_2O was prepared following the same procedure as described for compound **5**·2.4H_2O, but using deuterated solvents (D_2O and CD_3OD) instead of H_2O and CH_3OH. Elongated orange rhombuses were obtained, yielding 31 mg (31%). ν_{max}/cm^{-1}: 3420.81, 3103.30, 1611.90, 1589.89, 1575.42, 1540.88, 1437.17, 1382.68, 1233.35, 858.29, 782.91, 668.06, 636.97. IR spectrum shows that an important fraction of non-deuterated material is also present (Figure 3.88).

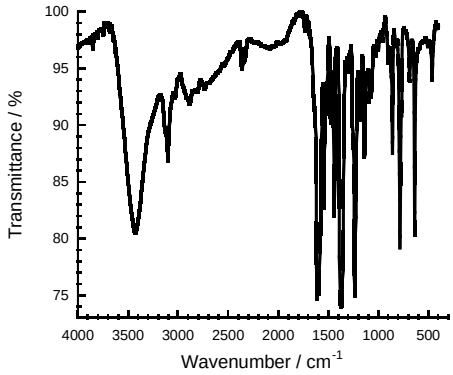

Figure 3.88. Infrared spectrum of **5**·1.8H_2O·0.6D_2O in a KBr pellet.

Synthesis of $[Fe(bpp)_2](C_6H_4NO_3)_2$ (5)

A dehydrated sample of **5** for powder X-ray diffraction measurements was obtained by heating *in situ* at 400 K for 2 h. A colour change associated to the dehydration process from orange to yellow was observed. For single crystal X-ray experiments, the sample was also dehydrated *in situ* heating at 400 K during 2 h.

Synthesis of $[Fe(bpp)_2](C_6H_4NO_3)_2(C_6H_5NO_3)\cdot 5H_2O$ (6·5H₂O)

$FeSO_4\cdot 7H_2O$ (34.75 mg, 0.125 mmol) was added as a solid to a degassed solution of bpp (53 mg, 0.25 mmol) in 5 ml MeOH, yielding a deep red coloured solution after complete dissolution of the metal salt. Then, a solution of $Ba(C_6H_4NO_3)_2\cdot 4H_2O$ (206.76 mg, 0.426 mmol) in 5 ml H_2O and a suspension of $C_6H_5NO_3$ (17.39 mg, 0.125 mmol) in 1 ml MeOH were added sequentially. After stirring for 2 h at room temperature, the off-white precipitate of $BaSO_4$ was filtered through a low-porosity frit. The filtrate was left undisturbed. Red cubes suitable for X-ray analysis appeared after three days, yielding 74.5 mg (61%). Found: C, 49.01; H, 4.14; N, 18.49. $C_{40}H_{41}FeN_{13}O_{14}$ requires C, 48.84; H, 4.20; N, 18.51. ν_{max}/cm^{-1}: 3366.92, 3232.89, 3108.88, 1611.91, 1413.76, 1374.99, 1360.52, 1248.57, 1222.25, 783.81, 775.40, 635.87. The infrared spectrum of **6**·5H₂O is shown in Figure 3.89.

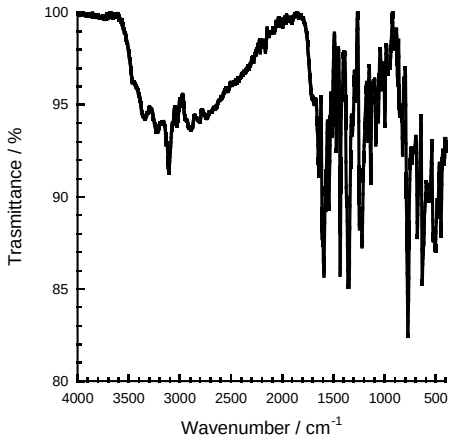

Figure 3.89. Infrared spectrum of **6**·5H₂O in a KBr pellet.

Synthesis of $[Fe(bpp)_2](C_6H_4NO_3)_2(C_6H_5NO_3)\cdot 2.75H_2O\cdot 2.25D_2O$ ($6\cdot 2.75H_2O\cdot 2.25D_2O$)

The deuterated complex was prepared following the same procedure as described for compound $\mathbf{6}\cdot 5H_2O$, using deuterated solvents (D_2O and CD_3OD) instead of H_2O and CH_3OH. Red cubes were obtained, yielding 67.7 mg (54%). ν_{max}/cm^{-1}: 3371.50, 3236.85, 3114.23, 2337.48, 2301.51, 1612.44, 1437.60, 1376.30, 1249.01, 1222.52, 1137.64, 784.33, 775.12, 635.88. IR spectrum shows only partial isotopic exchange (Figure 3.90).

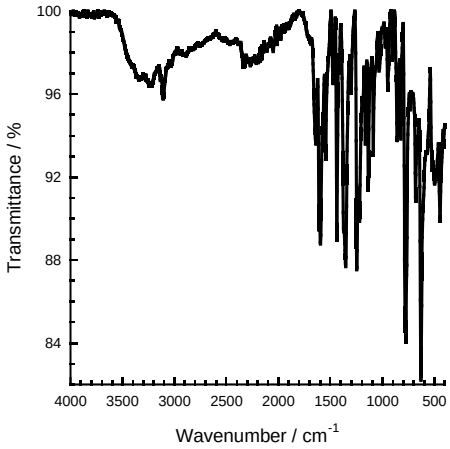

Figure 3.90. Infrared spectrum of $\mathbf{6}\cdot 2.75H_2O\cdot 2.25D_2O$ in a KBr pellet.

3.6.3. Appendix section

Table 3.32. Atomic displacement parameters ($Å^2 \cdot 10^3$) for the different X-ray structures of **6**·$5H_2O$. Equivalent isotropic displacement parameters, U(eq), defined as one third of the trace of the orthogonalized U_{ij} tensor.

atom	240 K (*HS*)	210 K (*HS*)	120 K A sublattice (*HS*/LS)	120 K B sublattice (HS/*LS*)	95 K (LS)[a]	50 K (PI*HS*)[b]	50 K ($PIHS_{rel}$)[c]	95 K (LS)[d]
Fe1	22(1)	20(1)	13(1)	12(1)	12(1)	6(1)	8(1)	8(1)
N1	30(1)	28(1)	19(1)	17(1)	16(1)	8(1)	26(1)	12(1)
N2	26(1)	24(1)	17(1)	15(1)	15(1)	7(1)	19(1)	11(1)
N3	25(1)	23(1)	16(1)	15(1)	15(1)	7(1)	15(1)	10(1)
N4	29(1)	27(1)	18(1)	16(1)	16(1)	8(1)	18(1)	11(1)
N5	35(1)	33(1)	21(1)	18(1)	19(1)	9(1)	30(1)	12(1)
N6	29(1)	28(1)	18(1)	17(1)	17(1)	8(1)	17(1)	12(1)
N7	25(1)	23(1)	15(1)	15(1)	14(1)	7(1)	11(1)	10(1)
N8	22(1)	21(1)	14(1)	13(1)	13(1)	6(1)	8(1)	9(1)
N9	25(1)	23(1)	15(1)	14(1)	14(1)	7(1)	13(1)	10(1)
N10	29(1)	26(1)	18(1)	17(1)	17(1)	8(1)	21(1)	12(1)
C1	36(1)	33(1)	23(1)	21(1)	20(1)	10(1)	30(1)	15(1)
C2	34(1)	31(1)	22(1)	19(1)	19(1)	9(1)	24(1)	14(1)
C3	25(1)	24(1)	17(1)	16(1)	15(1)	7(1)	17(1)	11(1)
C4	26(1)	24(1)	17(1)	16(1)	15(1)	7(1)	15(1)	11(1)
C5	32(1)	29(1)	21(1)	19(1)	18(1)	8(1)	17(1)	14(1)
C6	37(1)	33(1)	22(1)	21(1)	21(1)	9(1)	19(1)	16(1)
C7	35(1)	32(1)	22(1)	21(1)	19(1)	9(1)	20(1)	15(1)
C8	27(1)	26(1)	18(1)	16(1)	16(1)	7(1)	16(1)	12(1)
C9	29(1)	27(1)	19(1)	17(1)	17(1)	8(1)	20(1)	13(1)
C10	41(1)	38(1)	25(1)	23(1)	22(1)	10(1)	33(1)	16(1)
C11	44(1)	41(1)	26(1)	23(1)	22(1)	11(1)	41(1)	15(1)
C12	34(1)	32(1)	21(1)	21(1)	19(1)	9(1)	21(1)	15(1)
C13	31(1)	29(1)	19(1)	19(1)	17(1)	9(1)	16(1)	14(1)
C14	24(1)	22(1)	15(1)	15(1)	14(1)	6(1)	9(1)	11(1)
C15	24(1)	22(1)	14(1)	15(1)	13(1)	7(1)	9(1)	10(1)
C16	29(1)	27(1)	18(1)	18(1)	17(1)	8(1)	11(1)	13(1)
C17	32(1)	29(1)	19(1)	19(1)	17(1)	9(1)	11(1)	14(1)
C18	29(1)	26(1)	17(1)	17(1)	16(1)	8(1)	11(1)	13(1)
C19	23(1)	21(1)	14(1)	14(1)	13(1)	7(1)	9(1)	11(1)
C20	24(1)	22(1)	15(1)	14(1)	13(1)	7(1)	10(1)	10(1)
C21	32(1)	29(1)	18(1)	19(1)	18(1)	8(1)	18(1)	14(1)

C22	33(1)	31(1)	21(1)	20(1)	19(1)	9(1)	24(1)	14(1)
N11	36(1)	33(1)	22(1)	24(1)	19(1)	9(1)	12(1)	16(1)
O1	41(1)	37(1)	24(1)	26(1)	20(1)	10(1)	13(1)	17(1)
O2	45(1)	41(1)	29(1)	30(1)	22(1)	11(1)	16(1)	18(1)
O3	52(1)	47(1)	20(1)	21(1)	26(1)	13(1)	16(1)	23(1)
C23	33(1)	30(1)	18(1)	19(1)	17(1)	8(1)	12(1)	14(1)
C24	29(1)	27(1)	18(1)	18(1)	15(1)	7(1)	10(1)	13(1)
C25	33(1)	30(1)	20(1)	20(1)	18(1)	9(1)	13(1)	15(1)
C26	37(1)	33(1)	21(1)	22(1)	19(1)	10(1)	11(1)	15(1)
C27	40(1)	36(1)	23(1)	23(1)	21(1)	10(1)	12(1)	17(1)
C28	36(1)	33(1)	21(1)	21(1)	20(1)	9(1)	14(1)	16(1)
N12	29(1)	26(1)	23(1)	23(1)	15(1)	7(1)	10(1)	13(1)
O4	39(1)	36(1)	28(1)	26(1)	20(1)	10(1)	14(1)	16(1)
O5	51(1)	46(1)	21(1)	22(1)	23(1)	13(1)	16(1)	20(1)
O6	37(1)	34(1)	17(1)	17(1)	19(1)	10(1)	13(1)	16(1)
C29	32(1)	29(1)	19(1)	19(1)	17(1)	8(1)	11(1)	14(1)
C30	28(1)	26(1)	17(1)	18(1)	15(1)	8(1)	10(1)	13(1)
C31	31(1)	28(1)	18(1)	19(1)	16(1)	9(1)	11(1)	14(1)
C32	31(1)	29(1)	19(1)	19(1)	17(1)	9(1)	11(1)	14(1)
C33	32(1)	29(1)	19(1)	19(1)	18(1)	9(1)	12(1)	14(1)
C34	32(1)	29(1)	19(1)	18(1)	16(1)	8(1)	11(1)	14(1)
N13	30(1)	28(1)	25(1)	25(1)	17(1)	8(1)	15(1)	13(1)
O7	45(1)	41(1)	22(1)	22(1)	22(1)	11(1)	18(1)	18(1)
O8	40(1)	36(1)	22(1)	23(1)	20(1)	10(1)	17(1)	16(1)
O9	40(1)	36(1)	18(1)	18(1)	20(1)	10(1)	18(1)	16(1)
C35	31(1)	28(1)	18(1)	18(1)	17(1)	8(1)	14(1)	13(1)
C36	28(1)	25(1)	17(1)	17(1)	15(1)	8(1)	13(1)	12(1)
C37	33(1)	30(1)	19(1)	19(1)	18(1)	9(1)	15(1)	13(1)
C38	34(1)	31(1)	20(1)	20(1)	19(1)	9(1)	16(1)	15(1)
C39	37(1)	33(1)	21(1)	20(1)	19(1)	9(1)	17(1)	16(1)
C40	33(1)	30(1)	20(1)	19(1)	17(1)	9(1)	14(1)	13(1)
O1W	45(1)	40(1)	24(1)	25(1)	22(1)	12(1)	15(1)	19(1)
O2W	47(1)	42(1)	26(1)	29(1)	26(1)	13(1)	17(1)	23(1)
O3W	49(1)	45(1)	29(1)	29(1)	25(1)	13(1)	23(1)	20(1)
O4W	53(1)	48(1)	30(1)	30(1)	29(1)	13(1)	24(1)	23(1)
O5W	63(1)	55(1)	34(1)	33(1)	33(1)	15(1)	19(1)	29(1)
H1O	**106(10)**	**97(9)**	**74(9)**	**83(9)**	**79(13)**	**80(60)/21(12)**	**68(8)**	**61(12)**
H1A	55(7)	54(6)	51(7)	46(7)	42(9)	31(6)	28(6)	33(10)
H1B	68(8)	63(7)	38(6)	37(6)	41(10)	23(6)	27(6)	36(10)
H2A	66(8)	58(7)	35(6)	47(7)	26(8)	48(8)	52(8)	43(11)
H2B	64(8)	59(7)	41(7)	40(7)	45(11)	32(7)	31(6)	51(13)

H3A	61(8)	61(7)	52(7)	51(7)	48(10)	29(7)	55(8)	22(8)
H3B	76(9)	74(8)	38(6)	40(6)	37(10)	33(6)	49(7)	31(9)
H4A	78(10)	71(8)	57(8)	58(8)	49(11)	41(8)	43(7)	39(11)
H4B	84(9)	70(7)	50(7)	51(7)	85(15)	35(7)	39(8)	44(11)
H5A	54(8)	59(7)	40(6)	44(7)	78(14)	23(6)	48(8)	40(10)
H5B	70(8)	60(7)	51(7)	52(7)	41(10)	32(6)	33(7)	33(10)

[a]Temperature was held at 95 K for 4 h prior to data collection. [b]Photoinduced high-spin phase. [c]Structure obtained from partial relaxation of the PIHS phase, then quenching the sample at 50 K. [d]Structure obtained from full relaxation of the PIHS phase.

Table 3.33. Atomic displacement parameters ($Å^2 \cdot 10^3$) for the different neutron structures of **6**·$5H_2O$. Equivalent isotropic displacement parameters, U(eq), defined as one third of the trace of the orthogonalized U_{ij} tensor.

atom	240 K (*HS*)	120 K (*HS*/LS)	120 K (HS/*LS*)	95 K (*LS*)[a]	50 K (*HS*/LS)	50 K (HS/*LS*)	50 K (*LS*)[a]
Fe1	26(1)	18(1)	15(1)	14(1)	14(1)	12(1)	16(1)
N1	34(1)	24(1)	23(1)	19(1)	19(1)	17(1)	20(1)
N2	30(1)	22(1)	20(1)	18(1)	19(1)	17(1)	19(1)
N3	30(1)	21(1)	20(1)	17(1)	16(1)	15(1)	19(1)
N4	33(1)	23(1)	21(1)	18(1)	17(1)	16(1)	20(1)
N5	39(1)	26(1)	24(1)	20(1)	21(1)	19(1)	22(1)
N6	33(1)	24(1)	22(1)	20(1)	18(1)	18(1)	20(1)
N7	29(1)	20(1)	18(1)	17(1)	17(1)	16(1)	19(1)
N8	27(1)	19(1)	19(1)	16(1)	15(1)	14(1)	20(1)
N9	29(1)	21(1)	20(1)	16(1)	16(1)	15(1)	19(1)
N10	33(1)	23(1)	24(1)	19(1)	18(1)	16(1)	21(1)
C1	39(1)	28(1)	25(1)	21(1)	21(1)	20(1)	21(1)
C2	37(1)	26(1)	25(1)	20(1)	19(1)	18(1)	19(1)
C3	29(1)	20(1)	20(1)	18(1)	15(1)	15(1)	20(1)
C4	29(1)	19(1)	20(1)	17(1)	16(1)	15(1)	19(1)
C5	36(1)	25(1)	25(1)	21(1)	21(1)	20(1)	21(1)
C6	40(1)	27(1)	25(1)	23(1)	21(1)	19(1)	23(1)
C7	38(1)	27(1)	25(1)	22(1)	20(1)	20(1)	22(1)
C8	31(1)	23(1)	21(1)	18(1)	17(1)	18(1)	19(1)
C9	32(1)	21(1)	22(1)	18(1)	17(1)	16(1)	19(1)
C10	44(1)	28(1)	28(1)	22(1)	23(1)	23(1)	22(1)
C11	47(1)	32(1)	28(1)	23(1)	24(1)	21(1)	23(1)
C12	37(1)	24(1)	24(1)	22(1)	18(1)	19(1)	23(1)
C13	35(1)	23(1)	22(1)	19(1)	16(1)	17(1)	21(1)
C14	27(1)	19(1)	18(1)	17(1)	14(1)	13(1)	18(1)

C15	26(1)	19(1)	18(1)	16(1)	15(1)	14(1)	17(1)
C16	33(1)	21(1)	22(1)	19(1)	17(1)	16(1)	20(1)
C17	36(1)	23(1)	24(1)	20(1)	15(1)	16(1)	20(1)
C18	32(1)	21(1)	21(1)	19(1)	17(1)	16(1)	20(1)
C19	26(1)	18(1)	18(1)	16(1)	13(1)	14(1)	18(1)
C20	28(1)	19(1)	19(1)	16(1)	16(1)	15(1)	19(1)
C21	36(1)	23(1)	24(1)	20(1)	17(1)	18(1)	21(1)
C22	37(1)	24(1)	25(1)	20(1)	19(1)	20(1)	22(1)
N11	40(1)	25(1)	25(1)	23(1)	17(1)	17(1)	22(1)
O1	45(1)	25(1)	28(1)	22(1)	19(1)	17(1)	22(1)
O2	49(1)	29(1)	30(1)	26(1)	19(1)	20(1)	24(1)
O3	58(1)	33(1)	34(1)	29(1)	22(1)	22(1)	25(1)
C23	35(1)	22(1)	24(1)	20(1)	16(1)	17(1)	22(1)
C24	32(1)	21(1)	22(1)	19(1)	16(1)	16(1)	21(1)
C25	37(1)	24(1)	24(1)	21(1)	16(1)	18(1)	21(1)
C26	40(1)	24(1)	25(1)	21(1)	18(1)	18(1)	23(1)
C27	43(1)	26(1)	28(1)	23(1)	17(1)	18(1)	22(1)
C28	39(1)	24(1)	25(1)	22(1)	17(1)	18(1)	23(1)
N12	33(1)	21(1)	21(1)	19(1)	16(1)	16(1)	20(1)
O4	43(1)	26(1)	26(1)	22(1)	19(1)	19(1)	22(1)
O5	55(1)	33(1)	30(1)	25(1)	22(1)	20(1)	24(1)
O6	41(1)	25(1)	26(1)	23(1)	19(1)	18(1)	22(1)
C29	35(1)	22(1)	22(1)	20(1)	16(1)	15(1)	20(1)
C30	30(1)	21(1)	21(1)	18(1)	15(1)	15(1)	20(1)
C31	34(1)	20(1)	22(1)	19(1)	15(1)	16(1)	19(1)
C32	34(1)	22(1)	23(1)	21(1)	16(1)	16(1)	20(1)
C33	35(1)	22(1)	24(1)	21(1)	15(1)	17(1)	20(1)
C34	35(1)	23(1)	23(1)	20(1)	16(1)	17(1)	21(1)
N13	35(1)	24(1)	24(1)	20(1)	17(1)	18(1)	22(1)
O7	49(1)	30(1)	28(1)	24(1)	21(1)	21(1)	24(1)
O8	44(1)	28(1)	28(1)	23(1)	20(1)	19(1)	22(1)
O9	44(1)	27(1)	28(1)	23(1)	20(1)	20(1)	21(1)
C35	35(1)	23(1)	22(1)	19(1)	18(1)	16(1)	21(1)
C36	31(1)	20(1)	21(1)	18(1)	16(1)	16(1)	19(1)
C37	37(1)	25(1)	24(1)	19(1)	18(1)	18(1)	21(1)
C38	39(1)	25(1)	24(1)	21(1)	20(1)	18(1)	20(1)
C39	41(1)	27(1)	25(1)	21(1)	21(1)	21(1)	21(1)
C40	37(1)	24(1)	24(1)	19(1)	18(1)	19(1)	20(1)
O1W	47(1)	30(1)	28(1)	24(1)	23(1)	23(1)	24(1)
O2W	51(1)	30(1)	32(1)	26(1)	19(1)	22(1)	25(1)
O3W	51(1)	33(1)	33(1)	26(1)	24(1)	23(1)	26(1)

O4W	56(1)	33(1)	34(1)	30(1)	21(1)	26(1)	26(1)
O5W	66(1)	38(1)	37(1)	34(1)	24(1)	23(1)	31(1)
H1O	**62(2)**	**42(1)**	**48(1)**	**38(1)**	**32(2)**	**34(2)**	**37(1)**
H1A	60(1)	39(1)	46(2)	36(1)	36(2)	34(2)	40(1)
H1B	59(1)	41(1)	36(1)	36(1)	33(2)	31(2)	41(1)
H2A	60(2)	44(2)	44(1)	38(1)	37(2)	35(2)	37(1)
H2B	55(1)	41(1)	47(2)	42(1)	35(2)	29(2)	38(1)
H3A	55(1)	41(1)	38(1)	41(1)	34(2)	32(2)	38(1)
H3B	57(1)	42(1)	40(1)	37(1)	29(2)	35(2)	38(1)
H4A	71(2)	49(2)	46(2)	42(1)	39(2)	42(2)	45(2)
H4B	56(1)	42(1)	43(1)	43(1)	42(2)	36(2)	45(2)
H5A	65(2)	45(2)	43(1)	39(1)	31(2)	35(2)	37(1)
H5B	58(1)	43(1)	42(1)	45(1)	36(2)	34(2)	43(2)

[a]Temperature was held at 95 K for 4 h prior to data collection.

3.7. References

[1] W. Zhang, R.-G. Xiong, *Chem. Rev*. **2012**, 112, 1163-1195

[2] W.-K. Han, L.-F. Qin, C.-Y. Pang, C.-K. Cheng, W. Zhu, Z.-H. Li, Z. Li, X. Ren, Z.-G. Gu, *Dalton Trans*. **2017**, 46, 8004-8008

[3] N. A. Spaldin, R. Ramesh, *Nat. Mater*. **2019**, 18, 203-2012

[4] S. Dong, J.-M. Liu, *Mod. Phys. Lett. B*. **2012**, 26, 1-26

[5] W. Liang, G. Ya, M. Jing, *Sci. China Tech. Sci*. **2015**, 58, 2207-2209

[6] a) P.-H. Guo, Y. Meng, Y.-C. Chen, Q.-W. Li, B.-Y. Wang, J.-D. Leng, D.-H. Bao, J.-H. Jia, M.-L. Tong, *J. Mater. Chem. C*. **2014**, 2, 8858-8864. b) J. Long, J. Rouquette, J.-M. Thibaud, R. A. S. Ferreira, L. D. Carlos, B. Donnadieu, V. Vieru, L. F. Chibotaru, L. Konczewicz, J. Haines, Y. Guari, J. Larionova, *Angew. Chem. Int. Ed*. **2015**, 54, 2236-2240

[7] a) K. Asadi, M. A. v. d. V. *Eur. J. Inorg. Chem*. **2016**, 4332-4344. b) H. Cui, Z. Wang, K. Takahashi, Y. Okano, H. Kobayashi, A. Kobayashi, *J. Am. Chem. Soc*. **2006**, 128, 15074-15075

[8] a) J.-C. Liu, W.-Q. Liao, P.-F. Li, Y.-Y. Tang, X.-G. Chen, X.-J. Song, H.-Y. Zhang, Y. Zhang, Y.-M. You, R.-G. Xiong, *Angew. Chem. Int. Ed*. **2020**, 59, 3495-3499. b) P.-F. Li, Y.-Y. Tang, W.-Q. Liao, P.-P. Shi, X.-N. Hua, Y. Zhang, Z. Wei, H. Cai, R.-G. Xiong, *Angew. Chem. Int. Ed*. **2018**, 57, 11939-11942

[9] X. Zhang, T. Palamarciuc, J.-F. Létard, P. Rosa, E. V. Lozada, F. Torres, L. G. Rosa, B. Doudin, P. A. Dowbe, *Chem. Commun*. **2014**, 50, 2255-2257

[10] C. Wäckerlin, F. Donati, A. Singha, R. Baltic, S. Decurtins, S.-X. Liu, S. Rusponi, J. Dreiser, *J. Phys. Chem. C*. **2018**, 122, 8202-8208

[11] R. Akiyoshi, Y. Hirota, D. Kosumi, M. Tsutsumi, M. Nakamura, L. F. Lindoy, S. Hayami, *Chem. Sci*. **2019**, 10, 5843-5848

[12] a) M. Shatruk, H. Phan, B. A. Chrisostomo, A. Suleimenova, *Coord. Chem. Rev*. **2015**, 289-290, 62 – 73. b) N. Bréfuel, S. Imatomi, H. Torigoe, H. Hagiwara, S. Shova, J.-F. Meunier, S. B. Bonhommeau, J.-P. Tuchagues, N. Matsumoto, *Inorg. Chem*. **2006**, 45, 8126-8135. c) R. Pritchard, C. A. Kilner, M. A. Halcrow, *Chem. Commun*. **2007**, 577-579

[13] C. Wang, T. Zhang, W. Lin, *Chem. Rev*. **2012**, 112, 1084-1104

[14] H. H. Jaffé, G. O. Doak, *J. Am. Chem. Soc*. **1955**, 77, 4441-4444

[15] a) P. Guionneau, J.-F. Létard, D. S. Yufit, D. Chasseau, G. Bravic, A. E. Goeta, J. A. K. Howard, O. Kahn, *J. Mater. Chem.* **1999**, *9*, 985. b) C. Bartual-Murgui, R. Diego, S. Vela, S. J. Teat, O. Roubeau, G. Aromí, *Inorg. Chem.* **2018**, *57*, 11019. c) N. Mochida, A. Kimura, T. Ishida, *Magnetochemistry* **2015**, *1*, 17. d) F. J. Valverde-Muñoz, M. Seredyuk, M. Meneses-Sánchez, M. C. Muñoz, C. Bartual-Murgui, J. A. Real, *Chem. Sci*. **2019**, *10*, 3807. e) J. A. Rodríguez-Velamazán, M. A. González, J. A. Real, M. Castro, M. C. Muñoz, A. B. Gaspar, R. Ohtani, M. Ohba, K. Yoneda, Y. Hijikata, N. Yanai, M. Mizuno, H. Ando, S. Kitagawa, *J. Am. Chem. Soc.* **2012**, *134*, 5083.

[16] M. Szafránski, A. Katrusiak, G. J. McIntyre, *Phys*. *Rev*. *Lett*. **2002**, 89, 215507

[17] M. Schmidtmann, D. S. Middlemiss, C. C. Wilson, *CrystEngComm*. 2015, 17, 5273-5279

[18] G. A. Craig, O. Roubeau, G. Aromí, *Coord*. *Chem*. *Rev*. **2014**, 269, 13-31

[19] a) R. Pritchard, C. A. Kilner, M. A. Halcrow, *ChemComm*. **2007**, 577-579. b) T. D. Roberts, F. Tuna, T. L. Malkin, C. A. Kilner, M. A. Halcrow, *Chem*. *Sci*. **2012**, 3, 349-354

[20] P. Gütlich, H. A. Goodwin, *Top*. *Curr*. *Chem*. **2004**, 233, 1-47

[21] G. A. Craig, J. S. Costa, J. Roubeau, S. J. Teat, G. Aromí, *Chem*. *Eur*. *J*. **2012**, 18, 11703-11715

[22] S. Bonhommeau, T. Guillon, L. M. L. Daku, P. Demont, J. S. Costa, J. F. Létard, G. Molnár, A. Bousseksou, *Angew*. *Chem*. *Int*. *Ed*. **2006**, 45, 1625-1629

[23] Z.-Y. Li, J.-W. Dai, K. J. Gagnon, H.-L. Cai, T. Yamamoto, Y. Einaga, H.-H. Zhao, S. Kanegawa, O. Sato, K. R. Dunbar, R.-G. Xiong, *Dalton Trans*. **2013**, 42, 14685-14688

[24] a) H.-L. Cai, D.-W. Fu, Y. Zhang, W. Zhang, R.-G. Xiong, *Phys*. *Rev*. *Lett*. **2012**, 109, 169601. b) H.-Y. Ye, Y. Zhang, D.-W. Fu, R.-G. Xiong, *Angew*. *Chem*. *Int*. *Ed*. **2014**, 53, 11242-11247.

[25] a) Y.-Y. Tang, W.-Y. Zhang, P.-F. Li, H.-Y. Ye, Y.-M. You, R.-G. Xiong, *J*. *Am*. *Chem*. *Soc*. **2016**, 138, 15784-15789. b) D. W. Fu, H. L. Cai, Y. Liu, Q. Ye, W. Zhang, Y. Zhang, X. Y. Chen, G. Giovannetti, M. Capone, J. Li, R.-G. Xiong, *Science*. **2013**, 339, 425-428

[26] J. F. Létard, P. Guionneau, O. Nguyen, J. S. Costa, S. Marcén, G. Chastanet, M. Marchivie, L. A. Goux-Capes, *Chem*. *Eur. J.* **2005**, *11*, 4582–4589

[27] M. E. Lines, A. M. Glass. *Principles and Applications of Ferroelectric and Related Materials*, **1977**, Oxford University Press: New York

[28] M. Szafranski, A. Katrusiak, G. J. McIntyre, *Phys. Rev. Lett.* **2002**, 89, 215507

[29] M. Yamasaki, T. Ishida, *J. Mater. Chem. C.* **2015**, 3, 7784-7787

[30] A. Desaix, O. Roubeau, J. Jeftic, J. G. Haasnoot, K. Boukheddaden, E. Codjovi, J. Linares, M. Nogues, F. Varret, *Eur. Phys. J. B.* **1998**, 6, 183

[31] M. Marchivie, P. Guionneau, J. -F. Létard, D. Chasseau, J. A. K. Howard, *J. Phys. Chem. Solids.* **2004**, 65, 17-23

[32] L. J. K. Cook, H. J. Shepherd, T. P. Comyn, C. Baldé, O. Cespedes, G. Chastanet, M. A. Halcrow, *Chem. Eur. J.* **2015**, 21, 4805-4816

[33] a) C. Bartual-Murgui, C. Codina, O. Roubeau, G. Aromí, *Chem. Eur. J.* **2016**, 22, 12767-12776. b) S. Rat, K. Ridier, L. Vendier, G. Molnár, L. Salmon, A. Bousseksou, *CrystEngComm*. **2017**, 19, 3271-3280. c) L. Piñeiro-López, F. J. Valverde-Muñoz, M. Seredyuk, C. Bartual-Murgui, M. C. Muñoz, J. A. Real, *Eur. J. Inorg. Chem*. **2018**, 289-296

[34] R. Traiche, M. Sy, H. Oubouchou, G. Bouchez, F. Varret, K. Boukheddaden, *J. Phys. Chem. C.* **2017**, 121, 11700-11708

[35] M. L. Scudder, D. C. Craig, H. A. Goodwin, *CrystEngComm*. **2005**, 7, 642-649

[36] M. Clemente-León, E. Coronado, M. C. Giménez-López, F. M. Romero, *Inorg. Chem*. **2007**, 46, 11266-11276

[37] M. A. Gordillo, M. Soto-Monsalve, C. C. Carmona-Vargas, G. Gutiérrez, R. F. D'vries, J.-M. Lehn, M. N. Chaur, *Chem. Eur. J.* **2017**, *23*, 14872-14882

[38] a) J. E. Zweig, T. R. Newhouse, *J. Am. Chem. Soc.* **2017**, *139*, 10956-10959. b) Z. Kokan, M. J. Chmielewski, *J. Am. Chem. Soc.* **2018**, *140*, 16010-16014

[39] T. Steiner, *Angew. Chem. Int. Ed.* **2002**, 41, 48-76

[40] a) C. P. Köhler, R. Jakobi, E. Meissner, L. Wiehl, H. Spiering, P. Gütlich, *J. Phys. Chem. Solids.* **1990**, 51, 239-247. b) A. Bousseksou, L. Tommasi, G. Lemercier, F. Varret, J.-P. Tuchages, *Chem. Phys. Lett.* **1995**, 243, 493-499

[41] S. Brooker, *Chem. Soc. Rev.* **2015**, *44*, 2880-2892

[42] A. B. Gaspar, G. Molnár, A. Rotaru, H. J. Shepherd, *C. R. Chimie*, **2018**, 21, 1095-1120

[43] R. Mohammed, G. Chastanet, F. Tuna, T. L. Malkin, S. A. Barrett, C. A. Kilner, J.-F. Létard, M. A. Halcrow, *Eur. J. Inorg. Chem*. **2013**, 819-831

[44] D. Zhang, E. Trzop, F. J. Valverde-Muñoz, L. Piñeiro-López, M. C. Muñoz, E. Collet, J. A. Real, *Cryst. Growth Des.* **2017**, 17, 2736-2745

[45] a) N. F. Sciortino, S. M. Neville, C. Desplanches, J.-F. Létard, V. Martínez, J. A. Real, B. Moubaraki, K. S. Murray, C. J. Kepert, *Chem. Eur. J.* **2014**, 20, 7448-7457. b) J.-F. Létard, S. Asthana, H. J. Shepherd, P. Guionneau, A. E. Goeta, N. Suemura, R. Ishikawa, S. Kaizaki, *Chem. Eur. J.* **2012**, 18, 5924-5934

[46] V. A. Money, C. Carbonera, J. Elhaik, M. A. Halcrow, J. A. K. Howard, J.-F. Létard, *Chem. Eur. J.* **2007**, 13, 5503-5514

[47] M. Nihei, H. Tahira, N. Takahashi, Y. Otake, Y. Yamamura, K. Saito, H. Oshio, *J. Am. Chem. Soc.* **2010**, 132, 3553-3560

[48] a) G. A. Craig, J. S. Costa, O. Roubeau, S. J. Teat, G. Aromí, *Chem. Eur. J.* **2011**, 17, 3120-3127. b) G. A. Craig, J. S. Costa, S. J. Teat, O. Roubeau, D. S. Yufit, J. A. K. Howard, G. Aromí, *Inorg. Chem.* **2013**, 52, 7203-7209

[49] A. Hauser, J. Jeftic, H. Romstedt, R. Hinek, H. Spiering, *Coord. Chem. Rev.* **1999**, 471, 190-192

[50] C. Enachescu, F. Varret, E. Codjovi, J. Linarès, S. Floquet, P. Manikandan, P. T. Manoharan, *J. Phys. Chem. B.* **2006**, 110, 5883-5888

[51] E. König, *Struct. Bonding*. **1991**, 76, 51-152

[52] A. Parkin, S. M. Harte, A. E. Goeta, C. C. Wilson, *New. J. Chem.* **2004**, 28, 718-721

[53] a) S. Horiuchi, R. Kumai, Y. Tokunaga, Y. Tokura, *J. Am. Chem. Soc.* **2008**, 130, 13382-13391. b) S. Horiuchi, R. Kumai, Y. Tokura. *Angew. Chem. Int. Ed.* **2007**, 46, 3497-3501

[54] R. Kumai, S. Horiuchi, H. Sagayama, T. Arima, M. Watanabe, Y. Noda, Y. Tokura, *J. Am. Chem. Soc.* **2007**, 129, 12920-12921

[55] a) A. O. F. Jones, M.-H. Lemée-Cailleau, D. M. S. Martins, G. J. McIntyre, I. D. H. Oswald, C. R. Pulham, C. K. Spanswick, L. H. Thomas, C. C. Wilson, *Phys. Chem. Chem. Phys.* **2012**, 14, 13273-13283. b) A. O. F. Jones, N. Bladgen, G. J. McIntyre, A. Parkin, C. C. Seaton, L. H. Thomas, C. C. Wilson, *Cryst. Growth Des.* **2013**, 13, 497-509

[56] J. C. Speakman, *J. Chem. Soc.* **1949**, 3357-3365

[57] N. F. Sciortino, F. Ragon, Y. M. Klein, C. E. Housecroft, C. G. Davies, G. N. L. Jameson, G. Chastanet, S. M. Neville, *Inorg. Chem.* **2018**, 57, 11068-11076

[58] M. Weselski, M. Ksiazek, D. Rokosz, A. Dreczko, J. Kusz, R. Bronisz, *Chem*. *Commun*. **2018**, 54, 3895-3898

[59] a) T. Nakanishi, Y. Hori, H. Sato, S.-Q. Wu, A. Okazawa, N. Kojima, T. Yamamoto, Y. Einaga, S. Hayami, Y. Horie, H. Okajima, A. Sakamoto, Y. Shiota, K. Yoshizawa, O. Sato, *J*. *Am*. *Chem*. *Soc*. **2019**, 141, 14384-14393. b) T. Nakanishi, Y. Hori, S. Wu, H. Sato, A. Okazawa, N. Kojima, Y. Horie, H. Okajima, A. Sakamoto, Y. Shiota, K. Yoshizawa, O. Sato, *Angew*. *Chem*. *Int*. *Ed*. **2020**, 59, 14781-14787

Part II. Coordination polymers containing ethynyl-bridged picolinate ligands with luminescent, magnetic and/or catalytic properties

Chapter 4: Introduction to coordination polymers

Coordination polymers (CPs) are extended crystalline materials containing both inorganic and organic components linked to form multidimensional networks. Materials of this kind have a well-defined structure with a periodic arrangement formed by the self-assembly of metallic centres (metal-containing clusters or metal ions as nodes) and multi-coordinating organic molecules as bridging ligands through metal-ligand bonds (Figure 4.1).[1] The term coordination polymer was introduced by the first time in 1964.[1b] At that time CPs were synthesised by simple mixing of components, giving rise to the formation of hopelessly insoluble materials which were regarded by a figurative expression as "vaguely defined insoluble materials at the bottom of your vessel that spell death for your reaction".[2] However, even if the term had been not used at the end of the 19th century, CPs were widely in use in daily life, for instance, in the preparation of pigments (e.g. Prussian blue) and dyes (e.g. alizarin).[3] The first CPs were crystallised by Saito et al.[4] in 1959. The obtained compounds were bis(alkylnitrilo)copper(I) complexes whose structures were analysed by single crystal X-ray diffraction. They consisted on tetrahedral $Cu(-CN)_4$ subunits connected by organic ligands with different length. Depending on the length of the linker, one-dimensional chains (in the case of succinonitrile, SUC), two-dimensional grid networks (in the case of glutaronitrile, GLU) or three-dimensional structures (in the case of adiponitrile, ADI) were obtained (Figure 4.2).[5] Fortunately, in 1990s new synthetic techniques were developed (such as the solvothermal method) which enable the synthesis of crystalline CPs and the study of their crystal structures by X-ray diffraction analysis.

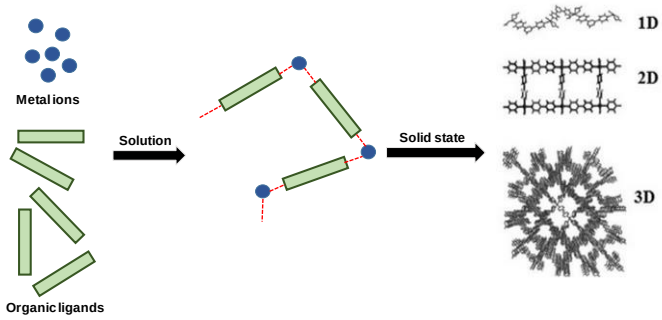

Figure 4.1. Schematic representation of the formation of CPs. Extracted and adapted from reference [1b].

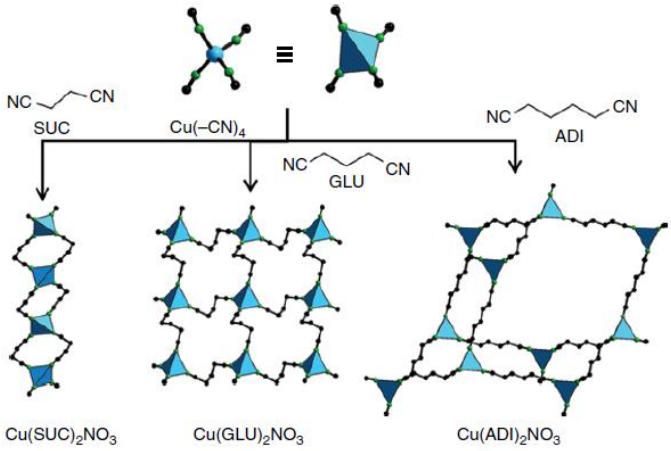

Figure 4.2. Bis(alkylnitrilo)copper(I) structures containing succinonitrile (SUC), glutaronitrile (GLU) and adiponitrile (ADI) anions. Hydrogen atoms, anions and interpenetrating networks are omitted for clarity. Color code: black, C; green, N; blue polyhedral, Cu. Extracted from reference [5].

A potential feature of CPs is that both organic and inorganic components can contribute to the chemical and physical properties of the resulting material. Thus, by controlling the self-assembly process, functional architectures with modulated properties and structures can be obtained.[6] In addition, it has been shown that these materials can be structurally modified without disruption of their crystallinity in single-crystal-to-single-crystal (SCSC) transformations,[7] proving to be versatile scaffolds to enhance the properties of the original CPs. For instance, the metal ions can be replaced, in a partial or in a total way, through cation exchange;[8] also the ligands can be exchanged in post-synthetic processes[9], or even both consecutively.[10] This can be considered as a novel avenue for the development of new multifunctional and multimetallic CPs that are difficult to obtain by direct synthetic methods.

On the other hand, a particular subclass of coordination polymers makes reference to those materials presenting potential voids of size enough for incorporation of different guest molecules in a reversible way. These compounds are regarded as porous coordination polymers (PCPs), although another acronym frequently used to describe them is metal-organic frameworks (MOFs), which dates back to 1995.[11] It was used for the first time to make reference to a compound with formula $Cu(bipy)_{1.5}(NO_3)$ (being bipy= 4,4'-bipyridine), whose structure is described as diamond-like composed of Cu(I) ions and bipy ligands (Figure 4.3). Since then, thousands of MOFs have been reported and they raise an ongoing interest due to their ultrahigh porosity (up to 90% of free volume) and huge internal surface areas (beyond 6000 m^2/g).[12]

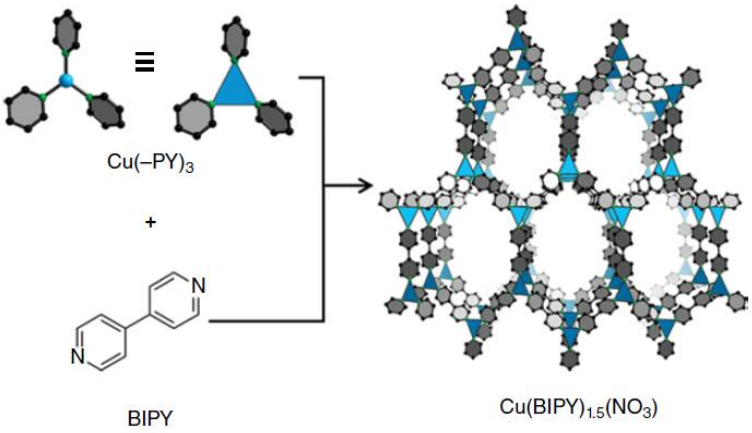

Figure 4.3. Crystal structure of $Cu(bipy)_{1.5}(NO_3)$ showing the triangular Cu(I) building blocks bridged by 4,4'-bipyridine ligands (left). Illustration of the 3D cationic network (right). Extracted from reference [5].

The field of coordination chemistry has shown a remarkable progress from "polymer disposal" to "materials of future"[13,1b] thanks to the possibility of preparation of new crystalline materials with given practical properties. The common interest focused on these compounds has been driven by their promising applications in fields such as ion exchange, adsorption, drug delivery, luminescence, sensing, catalysis, magnetism, biomedical applications and separation processes.[14] Currently, amongst the most studied fields, gas adsorption and separation for PCPs and catalysis and sensing of metal and organic molecules for CPs in general are worth noting.

4.1. Molecular assembly. Modulated synthesis

Metal ions and bridging ligands present different geometries and coordination modes, respectively, giving rise to a huge number of possible combinations through coordination bonds. In principle, since metal ions exhibit coordination preference, a specific regular structure can be formed by using appropriate nodes and linkers. Nonetheless, many reaction parameters, such as pH, solvent, counter ions, and reaction or crystallisation temperature, play a decisive role in the formation of the CP structure. Therefore, it is challenging to predict the product or mixture of products simply by the choice of the starting materials. Indeed, for a given set of metal and ligands in a solvent medium, different CPs can be generated by subtle modifications in the reaction conditions. Usually, if different products are formed from a single reaction, the thermodynamic product presents a higher activation energy (Figure 4.4) and, in general, high concentration and low temperature favour the formation of the

kinetic product, whereas low concentration and high temperature yields the thermodynamic one.[15] Moreover, there are a lot of strategies to control the degree of interpenetration of CPs involving the optimisation of the reaction parameters and template-directed synthesis.[16] Specifically, it has been shown that interpenetration can be avoided through variation of temperature and concentration of reagents during the synthesis.[17] High temperature and concentration favour an interpenetrated structure which can be understood in terms of more thermodynamic stable, denser crystal forms affordable in these conditions.

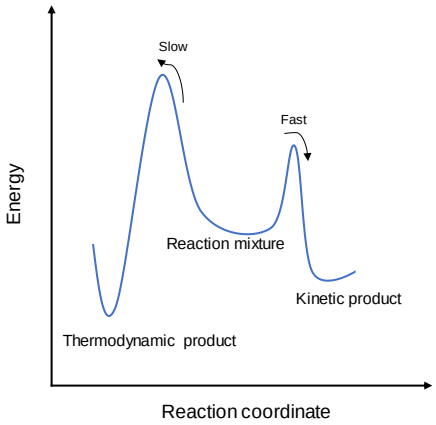

Figure 4.4. Schematic representation of the energy barrier for the synthesis of a thermodynamic and a kinetic product. Extracted and adapted from reference [15].

On the other hand, the main issue in this field arises from the difficulty in obtaining single crystals of extended coordination polymers. Generally, direct reaction or even slow diffusion of the precursors results in a fast precipitation of the material, due to the high insolubility of the final products. The crystallisation process requires an equilibrium between crystal formation and dissolution in order to generate an appropriate structure reorganisation and/or defect reparation. Therefore, in some cases it is necessary to develop hydro/solvothermal methods at high temperatures. A modulated synthesis is sometimes required. This term is based on the regulation of the coordination equilibrium by modulators or structural directing agents that competitively coordinate to the metal centres and/or hinder the deprotonation of the ligands. As a consequence of this competitive reaction between the ligands and the modulators, the rate of the nucleation process is considerably reduced and so does crystal growth.[18] Strong monoprotic acids with weakly coordinating counterions are usually used as modulators (HBF_4, HNO_3, acetic acid, etc). In

addition, the use of aminoacids as modulators for the synthesis of zirconium derivatives has resulted in the formation of several new porous coordination polymers.[19]

It is believed that the mechanism of modulated synthesis is the *in situ* construction of coordination complexes between the cations and the carboxylic moieties of the modulators. In this way, coordination polymer assembly can be considered as a series of consecutive ligand substitution reactions on this intermediate cluster, enabling the synthesis of the desired compound (Figure 4.5).[18]

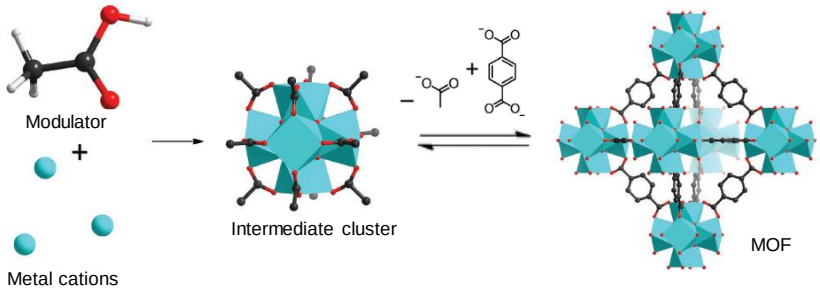

Figure 4.5. Scheme of modulated synthesis showing the formation of an intermediate cluster and subsequent ligand substitution reaction. Extracted and adapted from reference [18a].

4.2. Charged coordination polymers

Most of the hybrid materials are based on neutral CPs since typical carboxylic acid ligands compensate the positive charge of the metal ions. Nonetheless, charged frameworks present better performance in diverse applications thanks to the post-synthetic ion exchange with functional guests that is not possible in neutral compounds. For instance, $[Ag_2(btr)_2]_2ClO_4{\cdot}3H_2O$ (being btr = 4,4'-bis(1,2,4-triazole)) is a cationic CP that presents nanoscale cages filled by perchlorate anions and exhibits fast anion exchange, high trapping capacity and good selectivity for separation of $Cr_2O_7^{2-}$ in water. The selectivity may be ascribed to stronger interactions of $Cr_2O_7^{2-}$ with the cationic lattice with respect to other anions.[20a] Further studies in the field of catalysis indicate that anion-exchange improves the catalytic activity of CPs considerably, for example, as has been proven by comparison of the oxidation of diphenylmethane catalysed by $[Cu^{II}(bped)_2(H_2O)_2(SiF_6)]I{\cdot}4H_2O$ (being bped = meso-1,2-bis(4-pyridyl)-1,2-ethandiol) and by the exchanged-derivative with NO_3^-.[20b]

Firstly, charged CPs can be anionic in which a negative charge of the skeleton requires additional guest cations to ensure electroneutrality. And, secondly, there are cationic CPs that exhibit positively charged framework with a demand for extra anions in order to compensate the overall charge. In order to design a charged framework, the choice of metal ions, organic ligands and solvents is of vital importance.[21] For instance, some solvents like N,N-dimethylformamide (DMF), N,N-dimethylacetamide (DMA) and N,N-diethylformamide (DEF) under solvothermal conditions generate $[(NH_2(CH_3)_2]^+$ or $[NH_2(CH_2CH_3)_2]^+$ cations, giving rise to the formation of anionic MOFs. The first anionic MOF with $[NH_2(CH_3)_2]^+$ cations occupying the cavities was reported by Rosi and co-workers in $Zn_8(ad)_4(BPDC)_6O{\cdot}_2(CH_3)_2NH_2{\cdot}8DMF{\cdot}11H_2O$ (ad = adeninate, BPDC = biphenyldicarboxylate).[22] On the other hand, post-synthetic modification (PSM) approaches have shown to be effective in converting neutral CPs into anionic CPs. Regarding the synthesis of cationic CPs, the method widely used consists on binding metal cations to neutral nitrogen donor ligands, with the presence of extra anions to compensate the charge. Also, it is possible to obtain new cationic CPs by anion exchange processes from neutral networks in a single-crystal-to-single-crystal transformation and the charge-balancing anions play a very important role on the structural assembly.[21] Another method used to develop cationic CPs is based on ligands containing imidazolium cations.[23] Figures 4.6 and 4.7 show schematically the mentioned design strategies of charged CPs.

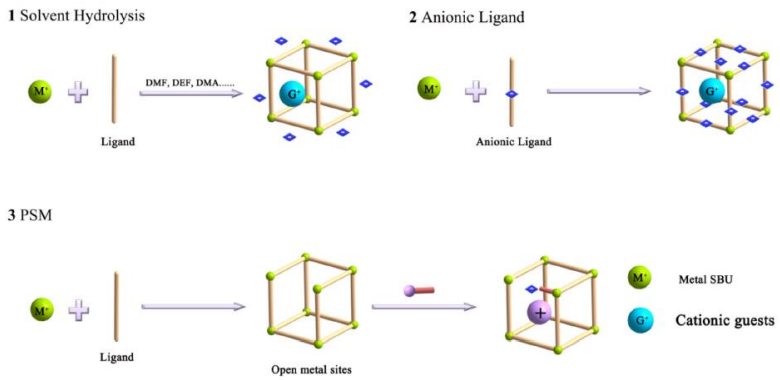

Figure 4.6. Scheme showing the representative design strategies of anionic CPs. Extracted from reference [21].

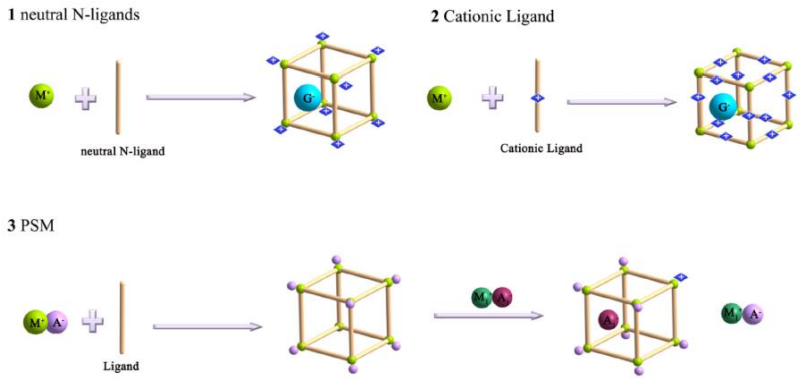

Figure 4.7. Scheme showing the representative design strategies of cationic CPs. Extracted from reference [21].

4.3. Applications of coordination polymers

The potential applications of these materials in different fields has led to an impressive number of compounds reported over the last two decades, which is still growing. Among these, magnetic, luminescent and catalytic processes are those in which this part of the thesis has been focused on. Thus, the next sections are devoted to give a brief overview of these fields in the context of coordination chemistry.

4.3.1. Magnetism

Molecular magnetism involves magnetic properties of isolated molecules, that may contain one or more magnetic centres, and also assemblies of molecules. These magnetic moment carriers may be metal complexes containing unpaired *d*- or *f*-electrons or organic radicals containing unpaired *p*-electrons. The whole meaning of the term magnetism encompasses the assembly of the paramagnetic molecular centres in such a way that they interact ferro- or antiferromagnetically, resulting in long-range magnetic order.[24] The publication in the mid-seventies by Kahn[25] was a milestone in molecular magnetism and it pointed out the key role of the overlap between the magnetic orbitals in defining magnetic interactions: when there is a net overlap between the magnetic orbitals, an antiferromagnetic interaction is observed, whereas if these orbitals are orthogonal, a ferromagnetic coupling is the resulting interaction. More importantly, Kahn's model gave an explanation to the fact that most of the magnetic complexes are coupled antiferromagnetically according to the overlap between the magnetic orbitals, and to the relative weakness of the ferromagnetic interactions.

Molecular magnetism is evolving towards the emerging field of molecular electronics,[26] for example, for the preparation of devices and electronic circuits thanks to the fact that they preserve their intrinsic magnetic properties even when deposited onto substrates.[27] Simultaneously, in the past 25 years or so, single-molecule magnets (SMMs) and multifunctional magnetic materials have been dominating this field. In the first case, the characteristic feature of these magnetic molecules is that they display slow relaxation of the magnetisation after removal of the external magnetic field used to magnetise the molecule. In order to exhibit SMM behaviour, the molecule should present a bistable magnetic ground state and an energy barrier (associated with magnetic anisotropy) preventing fast reorientation of the spins. There is a double-well potential energy curve for reversal of the magnetisation (Figure 4.8.a) and the magnetic relaxation is thermally activated, following an Arrhenius law:

$$\tau = \tau_0 \cdot \exp(U_{eff}/K_B T) \text{ (Eq. 4.1)},$$

where τ is the experimentally-determined relaxation time, U_{eff} is the effective energy barrier and τ_0 is the preexponential factor.[28]

The energy barrier is usually used as an indicator of the SMM behaviour and table 4.1 compiles some reported SMMs with their corresponding U_{eff} and τ_0 values.[29-36] In 1993, a compound composed by 12 manganese ions (known as Mn_{12}-acetate, Figure 4.8.b) showed a large magnetic hysteresis at low temperatures and quantum-tunnelling effects, being the first example of a SMM.[37] This means that in addition to thermal activation over the barrier, the reversal of the direction of the magnetisation takes place by tunnelling the energy barrier through excited states (as evidenced by the observation of steps in the magnetisation hysteresis loops, Figure 4.8.c).

Table 4.1. U_{eff} and τ_0 values for selected SMMs.

Compound	U_{eff}/ cm^{-1}	τ_0 / s
$[Dy_7(OH)_6(thmeH_2)_5(thmeH)(tpa)_6(MeCN)_2](NO_3)_2$ [29]	97	$7.2\cdot10^{-9}$
$[Dy_5O(OiPr)_{13}]$ [30]	367	$4.7\cdot10^{-10}$
$[(NMe_4)_3Na(Co_4(cit)_4[Co(H_2O)_5]_2)]\cdot11H_2O$ [31]	18	$8.2\cdot10^{-9}$
$[Mn_{21}DyO_{20}(OH)_2(Bu^tCO_2)_{20}(HCO_2)_4(NO_3)_3(H_2O)_7]$ [32]	51	$2.0\cdot10^{-12}$
$[Mn_6O_2(Et\text{-}sao)_6(O_2CPh(Me)_2)_2(EtOH)_6]$ [33]	86.4	$2.0\cdot10^{-10}$
$[Mn_{12}O_{12}(O_2CCH_3)_{16}(CH_3OH)_4]\cdot CH_3OH$ [34]	50	$9.8\cdot10^{-9}$
$[Mn_{84}O_{72}(O_2CMe)_{78}(OMe)_{24}(MeOH)_{12}\text{-}(H_2O)_{42}(OH)_6]$ [35]	12.5	$5.7\cdot10^{-9}$
$[Fe_8O_2(OH)_{12}(tacn)_6]^{8+}$ [36]	17	$3.4\cdot10^{-8}$

$thmeH_3$: tris(hydroxymethyl)ethane; tpa: triphenylacetic acid; OiPr: isopropoxide; cit: citrate; Bu^t: terc-butanol; sao: 2-hydroxybenzaldehyde oxime; tacn: 1,4,7-triazacyclononane.

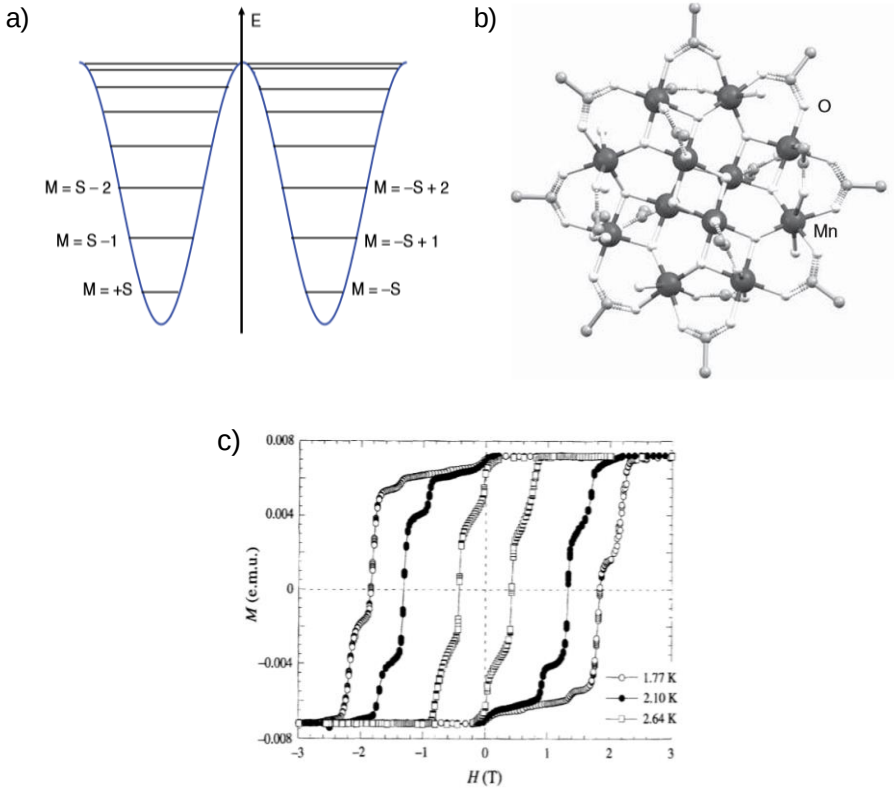

Figure 4.8. a) Energies of the ground manifold spin levels *M*, from -*S* to +*S*. The highest level is *M* = 0. b) Crystal structure of dodecakis(μ_3-oxo)-hexadecakis(μ_2-perdeuteroacetato-O,O')-dodeca-manganese. c) Magnetisation hysteresis loop of Mn12-acetate measured at 1.77 K, 2.10 K and 2.64 K. Extracted from references [28] and [37b].

More recently, analogue compounds to SMMs but based on mononuclear complexes containing a single magnetic ion (usually an *f*-block metal) were developed. In 2003, a compound in which a lanthanide ion (Ln) is sandwiched between two dianions of phthalocyanine (Pc^{-}) with formula [(Bu_4N)][$LnPc_2$] (being Bu_4N tetrabutylammonium cations, Figure 4.9.a), showed slow magnetic relaxation (Ln = Tb and Dy).[38] These materials are called single-ion magnets (SIMs) and both, SIMs and SMMs, present potential applications in ultra-high-density data storage, spintronics and quantum information processing.[39]

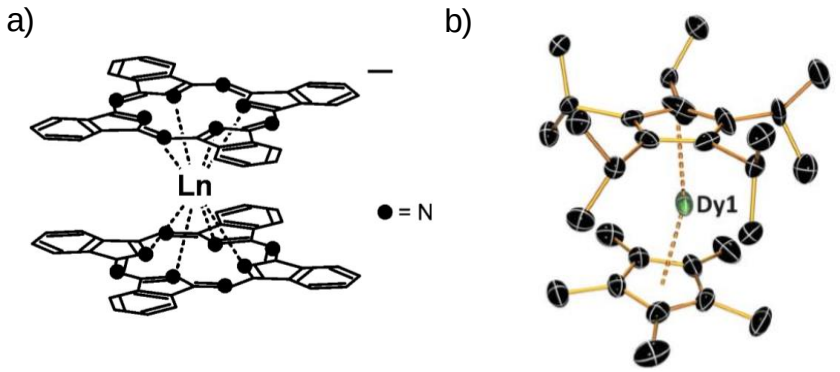

Figure 4.9. a) View of the crystal structure of $[Pc_2Ln]^-$ (Ln = Tb, Dy, Ho, Er, Tm or Yb). b) Thermal ellipsoid representation of the molecular structure of the cationic subunit in $[(\eta^5\text{-}Cp^{iPr5})Dy(\eta^5\text{-}Cp^*)][B(C_6F_6)_4]$. Extracted from references [38] and [40].

To date, lanthanide ions with strong single-ion anisotropy still represent the most efficient tool to develop SMM with higher energy barriers and blocking temperatures compared with transition metal ions. This is mainly because of the larger spin-orbit coupling energy relative to the electrostatic crystal-field interactions which results in the large unquenched orbital angular moment and high magnetic anisotropy. Consequently, magnetic hysteresis at temperatures as high as 80 K have been reported for a Dy metallocene ($[\eta^5\text{-}Cp^{iPr5})Dy(\eta^5\text{-}Cp^*)][B(C_6F_6)_4]$, being Cp^{iPr5} = penta-iso-propylcyclopentadienyl and Cp* = pentamethylcyclopentadienyl, Figure 4.9.b).[40]

4.3.2. Luminescence

The term "luminescence" originates from the Latin "lumen" meaning light and was first introduced in 1888 by the physicist Eilhardt Wiedemann to define any kind of phenomenon in which light is emitted from an electronically excited state without heating being involved. In particular, photoluminescence stands for the emission of light due to direct photoexcitation of the emitting species and the term luminescence comprises both fluorescence and phosphorescence, being the two terms differentiated by spin selection rules whether the transition is allowed (fluorescence, from an excited singlet state to the singlet ground state) or forbidden (phosphorescence, from excited triplet state to singlet ground state).[41] The first phosphorescent materials date back to the Middle Ages and the most popular one was the Bolognian phosphor, a heavy stone discovered in Bologna in 1602. Whereas the term fluorescence was introduced by Sir George Gabriel Stokes in the middle of the nineteenth century, the first notice of fluorescence was taken by a Spanish physician in 1565. In 1852, Stokes also

demonstrated that the phenomenon was an emission of light upon absorption of light. Later on, generations of scientists such as Kasha, Jablonsky, Becquerel, and many others have made impressive contributions to this field and, nowadays, the fascination of the scientific community towards luminescence has not been diminished. The wide variety of technological advances that this field offers are behind this, for instance, the development of light sources and lasers, photomultipliers and monochromators.[42] Moreover, medical and biological applications are highly exploited.[43]

Luminescent compounds can be of different kinds, distinguishing between purely organic (for exemple, naphthalene or anthracene), inorganic (for instance, ZnS or CdSe) and metal-organic compounds (such as complexes with transition metal ions or lanthanide ions). CPs are located within the latter context, being luminescent lanthanide (Ln) coordination polymers the most widely investigated during the last years, thanks to their large Stokes shift, long lifetimes (ms range) and narrow line-like emission bands (10-20 nm bandwidth).[44] The pioneering work in spectroscopic studies of lanthanide ions in solution dates back to 1930s and early 1940s. Freed et al. discovered in 1939 that the absorption spectra of Eu^{3+} in different solvents presented a change in the relative intensity of the signals.[45] Next, in 1942, Weissman found out that complexes of Eu(III) were markedly luminescent when excited with ultraviolet light, varying notably its intensity with the nature of the organic ligand, temperature and solvent.[46] As a solution of Eu^{3+} ions was not very luminescent, it was clear that some organic ligands could photosensitise the luminescence of lanthanide ions. Those observations were the starting point for the development of luminescent Ln-CPs.

4.3.2.1. Luminescent Ln-CPs. Antenna effect

The ground state electronic configuration of Ln(III) ions is $[Xe]4f^n$ (n = 0-14) and it is well separated energetically from the $[Xe]4f^{(n-1)}5d^1$, resulting in little interaction between both states. Thus, 4*f* orbitals are like "inner orbitals" since they are shielded from the environment by the $5s^2$ $5p^6$ subshells. Consequently, they are not really involved in bonding and this results in uniform chemical and spectroscopic properties of the series. When a photon is absorbed by a lanthanide ion, three different types of transitions can occur: sharp 4*f*-4*f* transitions, broader 4*f*-5*d* transitions and broad charge-transfer transitions. Transitions from 4*f* to 5*d* orbitals and charge-transfer reactions are parity allowed, whereas Ln electronic transitions (between states of f^n configurations in which the emitting excited state and the ground state have the same *f*

electronic configuration) are forbidden by the Laporte rule (transitions that do not involve a change in parity are forbidden, $\Delta l = \pm 1$), having weak absorbance, low quantum yields and characteristic line-like emission bands with long lifetimes.[47]

Complexation of the desired lanthanide ion with an appropriate absorbing ligand can solve this situation. The linker can act as antenna (light collector) transferring the absorbed energy to the lanthanide cation (emitter), resulting in an enhanced lanthanide luminescence that is widely known as *antenna effect* or *luminescence sensitisation* (Figure 4.10).[47]

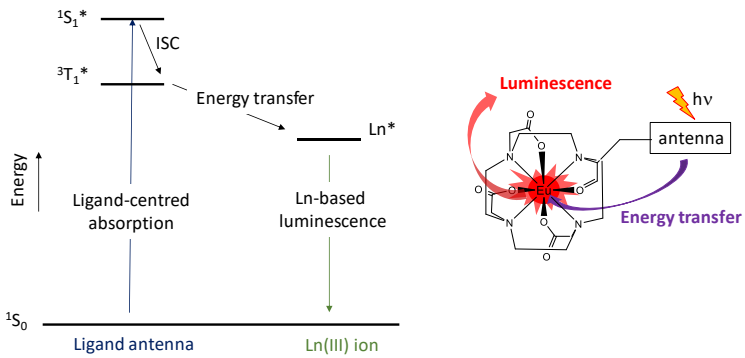

Figure 4.10. Schematic representation of the "antenna effect" that takes place between an absorbing organic ligand and an emitting Ln ion.

The main migration path involves ligand absorption, then, intersystem crossing (ISC) from an excited singlet state ($^1S^* \rightarrow {}^3T^*$) to the ligand triplet state. Next, energy transfer occurs from this state ($^3T^* \rightarrow Ln^*$), followed by spontaneous metal-centred emission. Subsequent regeneration of the Ln(III) ground state is spin forbidden (due to different multiplicity of implied states), leading to a slow release of the energy with a long lifetime of the photoinduced state. For example, it has been reported an enhancement of Tb(III) luminescence more than 10^4-fold by using dipicolinic acid as a light collector, and Eu(III) signal is similarly enhanced by diketonates.[48]

It has to be noted that a luminescent system in its excited state, can also go back to its ground state without emitting radiation, which is known as non-radiative transition (encompassing internal conversion, vibrational relaxation and intersystem crossing, Figure 4.11). There is always competition between radiative emission deactivation paths (fluorescence and phosphorescence) and radiationless processes; therefore, the latter processes must be minimised in

order to achieve a high quantum yield (Φ). This parameter can be defined as the ratio between the total number of photons that are released in the emission process and the total number of molecules promoted to the excited state.[49] This parameter, together with the characteristic relaxation time (lifetime, τ) that indicates the time that the molecule remains in its excited state prior to the emission of a photon, allows for comparison between the luminescent performance of different compounds. Table 4.2 compiles some Ln-CPs reported with the corresponding values of these parameters, presenting $[EuKL1_4(H_2O)_2]\cdot H_2O$ (HL1 = chloro-1-cyclopropyl-6-fluoro-4-oxo-1,4-di-hydroquinoline-3-carboxylic acid) the highest luminescence quantum yield among the synthesised Ln-CPs.[50]

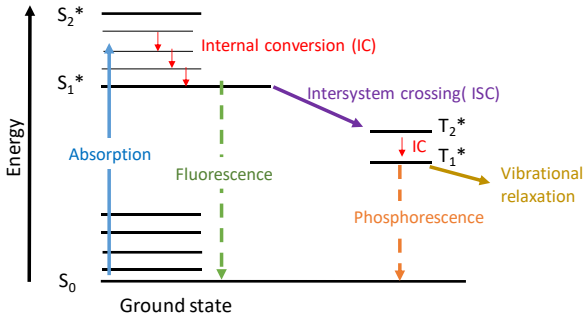

Figure 4.11. Schematic representation of non-radiative transitions, fluorescence and phosphorescence.

Table 4.2. Quantum yield and lifetime values for some Ln-CPs measured at room temperature.

Compound	Quantum yield/ %	Lifetime/ ms
$[LnNaL1_4(H_2O)_3]\cdot H_2O$ (Ln = Eu/Tb) [50]	77/2	0.97/0.52
$[LnKL1_4(H_2O)_2]\cdot H_2O$ (Ln = Eu/Tb) [50]	92/12	0.94/0.24
$Eu(TTA)_3(DBSO)_2$ [51]	85	0.38
$Eu(TTA)_3(TPPO)_2$ [51]	73	0.35
$Eu(TTA)_3(H_2O)_2$ [51]	23	0.19
$Eu(TTA)_3\cdot 2PTSO$ [52]	57	0.598
$Eu(TTA)_3PHEN$ [52]	69	0.976
$[Ln_3(bcpb)_4(\mu\text{-}HCOO)(\mu\text{-}H_2O)(H_2O)_2(DEF)]$ (Ln = Eu/Tb [53]	16/71	0.53/0.98

HL1= chloro-1-cyclopropyl-6-fluoro-4-oxo-1,4-di-hydroquinoline-3-carboxylic acid; TTA= thenoyltrifluoroacetonate; DBSO= dibenzyl sulfoxide; TPPO = triphenylphosphine oxide; PTSO= p-tolyl sulfoxide; PHEN = 1,10-phenantroline; H_2bcpb= 3,5-bis(3-carboxyphenyl)pyridine; DEF= N,N-diethylformamide.

The high values of the quantum yield indicate that sensitisation is effective, which can be explained on the basis of the energy difference between the triplet state of the corresponding ligand and the emissive level of Ln^{3+} ions (ΔE). In

particular, it has been reported that for optimal energy transfer, ΔE must be around 2500-4000 cm^{-1} for Eu^{3+} and Tb^{3+}.[54a] In $(Eu_{0.5}Gd_{0.5})_2(BDC)_3(H_2O)_4$ and $(Tb_{0.5}Gd_{0.5})_2(BDC)_3(H2O)_4$ (BDC^{2-} = benzene-1,4-dicarboxylate), the energy differences of ΔE are 6341 cm^{-1} and 3241 cm^{-1}, respectively. Thus, the improved photophysical properties of the second complex (τ = 0.81 ms and Φ = 22%) with respect to the first one (τ = 0.28 ms and Φ = 2.4%) can be explained taking into account that the ideal ΔE is only achieved for the Tb-containing compound.[54b]

Two different mechanistic pathways have been proposed for the energy transfer and are depicted in Figure 4.12. The first one is known as Dexter (or exchange) mechanism and involves a double-electron transfer. In the second one, called Förster (or dipole-dipole), the dipole moment associated with the excited triplet state of the ligand couples with the dipole moment of the 4*f* orbitals.

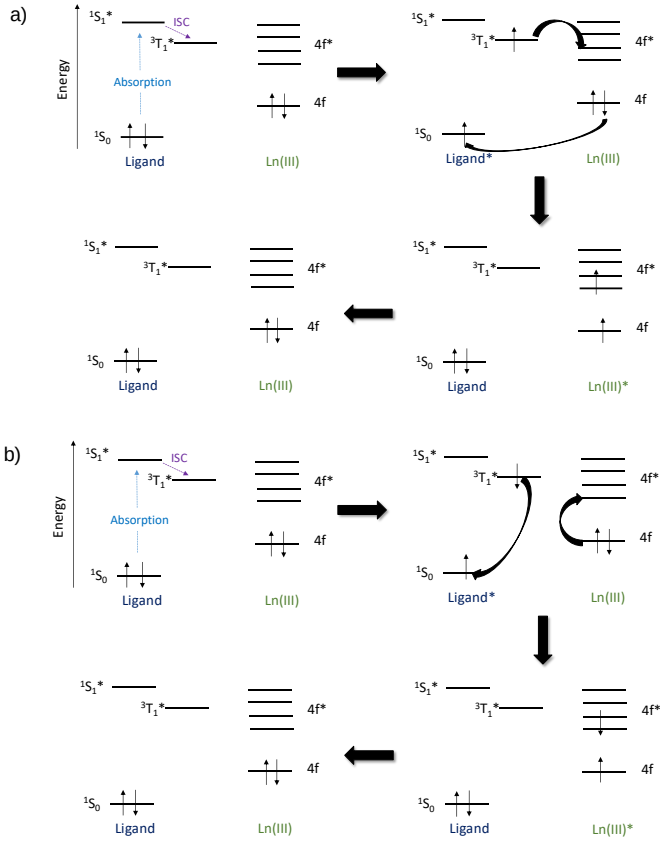

Figure 4.12. Schematic representation of a) triplet-triplet Dexter and b) singlet-singlet Förster energy transfer mechanisms.

In both cases, the energy is transferred from the sensitiser (ligand) to the acceptor (Ln) by a non-radiative process (without an emission and reabsorption of a photon). Singlet-singlet energy transfer may occur at short distances by the Dexter mechanism and at long distances by dipole-dipole interactions through the Förster mechanism. In addition, Dexter triplet-triplet energy transfer is also possible and exchanges both spin and energy between the donor and the acceptor.

A partial energy diagram showing the ligand-sensitised europium and terbium emission is shown in Figure 4.13. Emission takes place from one electronic state to multiple *J* levels (being *J* the total momentum derived from the sum of the total orbital momentum *L* and the total spin momentum *S*), leading to a series of bands on emission to the ground state.

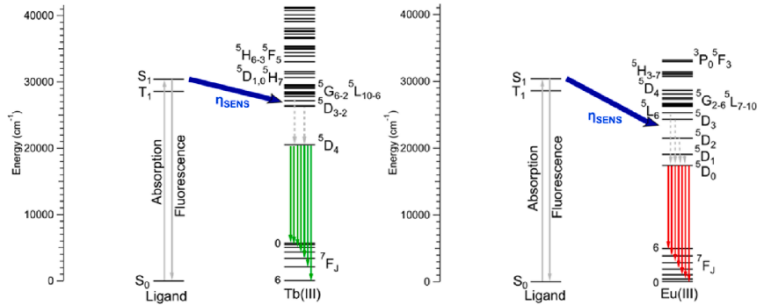

Figure 4.13. Energy level diagram showing the energy transfer pathway involving the antenna ligand and Ln(III) ions (Eu and Tb). Extracted from reference [55].

4.3.2.2. Luminescence quenching

The use of coordination polymers as fluorescent probes is based on the variation in luminescence intensity before and after their interaction with different analytes present in the reaction medium. Enhancement or quenching of luminescence can occur due to involvement of these components, which are called sensitizers or quenchers, respectively. These species absorb the exciting radiation and transfer it to the fluorophore or, contrary, avoid that the fluorophore itself absorbs that energy without transferring it. In particular, fluorescence quenching is the most usual response and any process that causes a decrease in intensity can be considered to be quenching, even if this process leads to a fluorescent species (the word quenching is referred only to the initially excited molecule). For instance, a Ln-CP with 2D structure and formula [Eu(BTB)(H_2O)$_2$·solvent] (being H_3BTB = 4,4',4''-benzene-1,3,5-triyl-tribenzoic

acid), shows Eu^{3+} characteristic fluorescent emission which can be selectively quenched by acetone with high efficiency.[56] In another example, the strong emission of [Eu_3(bcpb)$_4$(μ-HCOO)(μ-H2O)(H_2O)$_2$(DEF)] (being H_2bcpb = 3,5-bis(3-carboxyphenyl)pyridine and DEF = N,N-diethylformamide) could be efficiently quenched by Cu^{2+} ions and trinitrophenol.[57]

In collisional (dynamic) quenching, the quencher approaches to the luminescent molecule when it is in its excited state, collision takes place between them and, finally, the luminescent probe goes back to the ground state without emitting light. In other cases, these collisions may result in the formation of a ground-state non-luminescent complex or in the formation of a sphere of effective quenching (static quenching). In the last scenario, when the excited molecule and the quencher species are not able to modify their positions in the space during the excited state lifetime, a sphere of quencher molecules is formed surrounding the fluorophore. There is a decrease in the fluorescence intensity, nevertheless, the excited-state lifetime of the uncomplexed fluorophore is unaffected, in contrast to dynamic quenching. For dynamic quenching processes, the Stern-Volmer equation stands for the description of the luminescence interaction:

$$\frac{I_0}{I} = 1 + K_D \cdot [Q] = 1 + k_q \cdot \tau_0 [Q] \quad \text{(Eq. 4.2)}$$

in which K_D is the dynamic quenching constant (or Stern-Volmer constant, K_{sv}), k_q is the bimolecular rate constant, τ_0 is the observed lifetime in absence of quencher, [Q] is the quencher concentration and I_0 and I are the emission intensities in absence and in presence of quencher, respectively. For static quenching, an analogous equation can be applied, being K_S the static quenching constant (the association constant of the complex):

$$\frac{I_0}{I} = 1 + K_S \cdot [Q] \quad \text{(Eq. 4.3)}$$

When both quenching processes are present simultaneously, the corresponding equation is given by:

$$\frac{I_0}{I} = (1 + K_D \cdot [Q]) \cdot (1 + K_S [Q]), \quad \frac{I_0}{I} - 1 = (K_D + K_S)[Q] + K_D \cdot K_S \cdot [Q]^2 \quad \text{(Eq. 4.4)}$$

At the light of these equations, it is to be stressed that if the Stern-Volmer plot ($\frac{I_0}{I}$ vs [Q]) is linear, it indicates the presence of only one quenching process, either dynamic or static. Therefore, in order to distinguish between both quenching processes, dependence on temperature or lifetime (τ) measurements are

required. If both processes take place simultaneously with the same quencher, a quadratic term appears and deviation of the plot of I_0/I against $[Q]$ from linearity is observed at high concentrations of quencher. This can be observed in S-V plots by un upward curvature[58] as illustrated in Figure 4.14.

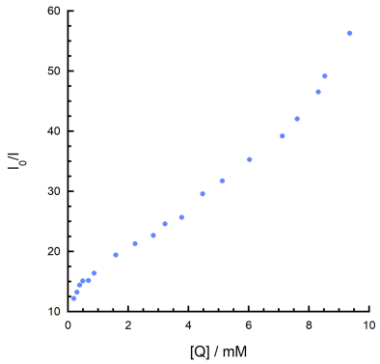

Figure 4.14. The Stern-Volmer plot showing the quencher (Q) concentration influence on the fluorescence intensity of the fluorophore, with upward curvature at higher concentrations.

Quenching luminescence involves many factors and processes and, in general, might be consequence of basically four mechanisms: excimers and exciplexes formation, photoinduced electron transfer (PET), energy transfer (radiative and non-radiative) and the collapse of the framework after introducing quencher molecules.[58] Regarding the first case, excimers are dimers in the excited state that are built up by collision between an excited molecule (^{1}M*) and an identical molecule (^{1}M) in its ground state: $^1M^* + {}^1M \leftrightarrow {}^1(MM)^*$

Whereas exciplexes are excited-state complexes that are constructed thanks to collisional interactions between an excited molecule (^{1}M*) and a different unexcited molecule (N): $^1M^* + N \leftrightarrow {}^1(MN)^*$

In both cases, their presence can be detected from the appearance of new emission bands at higher wavelengths than that of the monomer which do not present vibronic bands. Secondly, PET is often responsible for fluorescence quenching and it is involved in many organic photochemical reactions related to molecules containing donor-acceptor subunits integrated into the same entity. In PET systems, the fluorescence is quenched due to electron transfer between the excited fluorophore (^{1}D*) and the quencher (A). This leads to the formation of a charge separate state consisting in the ligand radical cation ($D^{\cdot+}$) and the quencher radical anion ($A^{\cdot-}$) or viceversa, depending on oxidation and reduction potentials:

$$D^* + A \longrightarrow D^{\cdot +} + A^{\cdot -}$$

$$A^* + D \longrightarrow A^{\cdot -} + D^{\cdot +}$$

Generally, this radical pair relaxes to the ground state via charge recombination and this results in non-radiative dissipation of excited-state energy. Thus, the subsequent ligand to metal energy transfer is hindered and this results in Ln luminescence quenching (Figure 4.15).

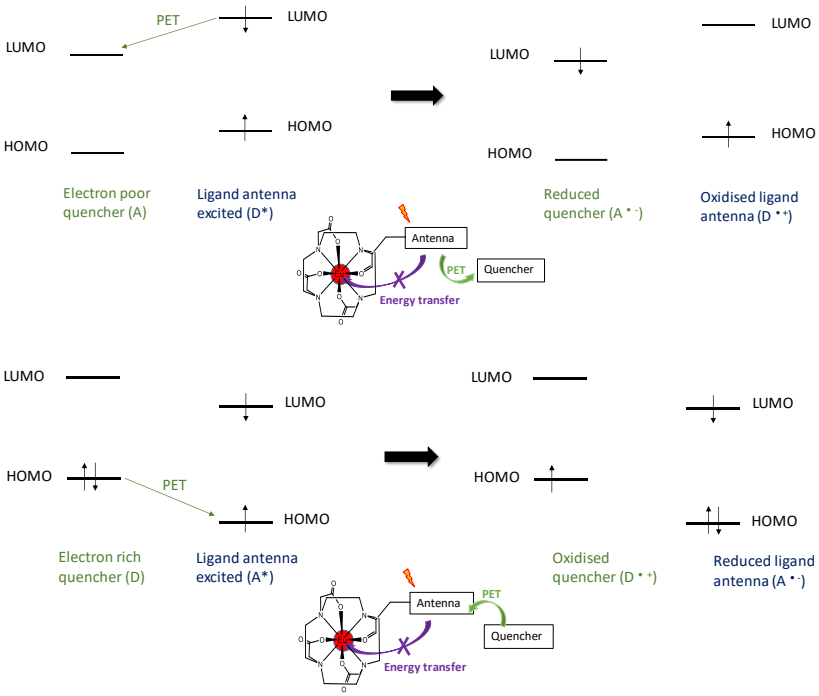

Figure 4.15. HOMO and LUMO energy scheme of a quencher and an antenna ligand showing the oxidative (top) or reductive (bottom) electron transfer.

On the other hand, in a radiative energy transfer process (also known as emission-reabsorption process, 'trivial' transfer), the sensitiser (or donor, D) absorbs energy, emits a photon and then there is a reabsorption of this photon by the quencher (or acceptor, A):

$$D^* \rightarrow D + h\nu$$

$$h\nu + A \rightarrow A^*$$

If the excited acceptor is a fluorophore molecule, it will emit a second photon. Both entities are independent of each other and the interaction between them is not direct. Thus, their lifetimes will be not altered by the presence of the other and the distance between them should be larger than the wavelength in order to be accomplished the absorption of the emitted photon. Nevertheless, a spectral overlap between the emission of the molecule and the absorption of the quencher is required for radiative energy transfer to occur. Non-radiative energy transfer requires also spectral overlap between the emission spectrum of the donor and the absorption spectrum of the acceptor, in such a way that several vibronic transitions in the donor have almost the same energy as the corresponding transitions in the acceptor. Therefore, such transitions are coupled and the term *resonance energy transfer* (RET) is usually used (Figure 4.16).

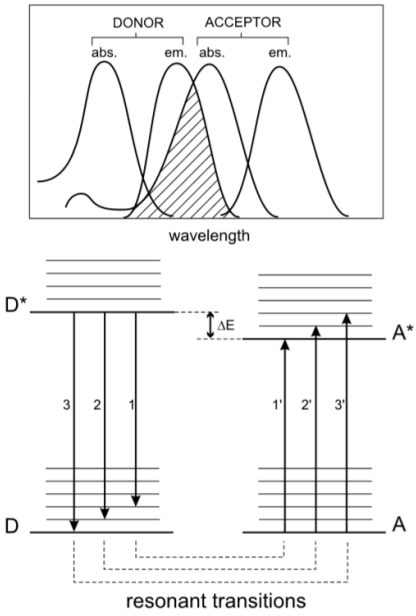

Figure 4.16. Schematic representation of the energy level of donor and acceptor molecules showing the coupled transitions. At the top is included an illustration of the integral overlap between the absorption spectrum of the acceptor and the emission spectrum of the donor. Extracted from reference [58].

From the mechanistic point of view, Coulombic interactions or intermolecular orbital overlap can be at the origin of energy transfer. In the first case, long-range dipole-dipole interactions and short-range multi-polar interactions are established (Förster's mechanism). In the second case, only short-range

interactions are formed (mainly involving covalent bonds between the two species), encompassing electron exchange (Dexter's mechanism). Corresponding mechanisms are analogous to those described for the non-radiative energy transfer involved in the antenna effect and are detailed in Figure 4.12. It has to be stressed that whereas Förster resonance energy transfer exhibits a characteristic inverse sixth power dependence on the distance between the sensitiser and the quencher (α $1/R^6$) and can be effective at large distances (up to 80-100 Å), Dexter's mechanism shows an exponential dependence and is only present at distances < 10 Å.[58]

Regarding the disruption of the crystal structure, several compounds have been reported to undergo this process upon interaction with different analytes. For instance, $[EuNaL_4(H_2O)_3]\cdot H_2O$ (being HL = 7-chloro-1-cyclopropyl-6-fluoro-4-oxo-1,4-dihydroquinoline-3-carboxylic acid) displays a variation in its luminescence intensity as a function of pH (sensing of H^+). The strongest luminescence was registered at pH = 7, indicating PXRD measurements that the fluorescence quenching is induced by the collapse of the crystal structure at pH = 1-4 and pH = 11-14 (Figure 4.17). Moreover, there is a linear relationship between the luminescence response and the pH in a range comprised between 7 and 11, which allows quantitative determination of pH.[59]

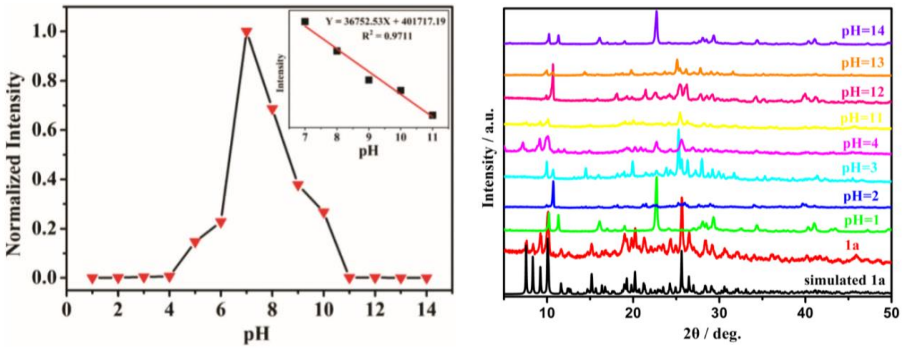

Figure 4.17. Left: Luminescence intensity of $[EuNaL_4(H_2O)_3]\cdot H_2O$ in function of the pH. Right: PXRD of the same compound soaked in solutions of various pH values. Extracted from reference [59].

4.3.2.3. Luminescent molecular sensing

Nowadays the design of luminescent sensors remains a hot topic due to its high demand in a wide variety of fields, such as analytical chemistry, medicine, clinical biochemistry and environmental science. Supramolecular

interactions of luminescent CPs with the analyte may increase or decrease the luminescence response, resulting in a turn-on or turn-off display, respectively.[60] Different types of analytes can be detected by this method, including cations, anions, neutral molecules and gases, probing its excellent versatility. Indeed, there are already many commercially fluorescent molecular sensors available, however, their selectivity, limit of detection and toxicity should be improved. At the same time, luminescent sensing exhibits major advantages for its success in comparison with other techniques (for instance, chromatographic and other spectroscopic methods) in terms of response time, selectivity, ease in its detection by the naked eye and sensitivity, which justify its widespread use.

Detecting cations is of great interest in several disciplines. For instance, in medicine, it is of vital importance to monitor metal ions like Na^{+}, K^{+}, Ca^{2+}, Li^{+} and Mg^{2+} in blood and urine for diagnosis. These metal ions are involved in biological processes as important as muscle contraction, transmission of nerve impulses or regulation of cell activity. Regarding environment, early detection of toxic metal ions such as Pb^{2+}, Cd^{2+}, Hg^{2+}, Al^{3+} and Fe^{3+} is highly recommended, due to their accumulation as pollutants in water. In addition, Fe(III) is one of the most common and relevant components in the Earth's crust and is also present in biological systems, developing an important role in metabolic processes. Its presence in an appropriate amount is essential for regular growth and development progress, nevertheless, an excess of iron(III) can lead to physical illnesses. Hence, an enormous attention is paid to its effective and selective detection. Recently, Ln-CPs have been found to be promising candidates in this regard, being its main drawback that they have been applied in organic solvents as a consequence of their poor stability in aqueous medium. The first example of europium(III) fluorescent sensor for Fe^{3+} detection was developed by Dang et al. in 2012 (EuL, being H_4L = tetrakis[(4-carboxyphenyl)oxamethyl]methane acid). Nonetheless, the selective quenching mechanism consisted on cation exchange between the original metal ion and Fe^{3+} cations rather than in a specific interaction (Figure 4.18).[61] Later on, more Eu-CPs have been applied for the sensing of Fe^{3+} ions and Table 4.3 contains some examples with corresponding K_{sv} and *LOD* (limit of detection) values. The main quenching mechanisms are based on cation exchange between Fe^{3+} and Eu^{3+}, competitive absorption of excitation wavelength energy and the interaction between Fe^{3+} and the organic ligand.[62-72]

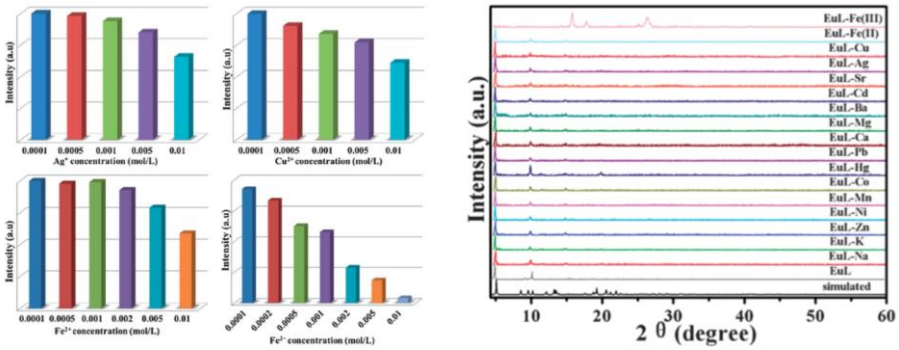

Figure 4.18. Left: Luminescence intensity of EuL after soaking in aqueous solutions of different concentrations of various metal ions (Ag^{+}, Cu^{2+}, Fe^{2+} and Fe^{3+}). Right: PXRD patterns of EuL and EuL after immersion in solutions containing different metal ions. Extracted from reference [61].

Table 4.3. Limit of detection (*LOD*) and Stern-Volmer constant (K_{sv}) of Fe^{3+} ions by Eu-CPs in different media.

Complex	Solvent	K_{sv}/M^{-1}	*LOD*/M
Eu^{3+}@MIL-124 [62]	H_2O	$3.87\cdot10^{4}$	$1\cdot10^{-2}$
$[Ln(Hpzbc)_2](NO_3)]\cdot H_2O$ [63]	EtOH	---	$1\cdot10^{-3}$
$[Eu(BTPCA)(H_2O)]$ [64]	DMF	---	$1\cdot10^{-5}$
$[Eu(H_2O)_2(BTMIPA)]$ [65]	DMF	---	$1\cdot10^{-5}$
$Eu(L)_3$ [66]	H_2O	$4.1\cdot10^{3}$	$1\cdot10^{-4}$
$[Eu_2(N\text{-}BDC)_3(dmf)_4]$ [67]	DMF	$2.88\cdot10^{4}$	---
$[(NH_2CH_3)][Eu(C_{33}H_{24}O_{12})(H_2O)]$ [68]	H_2O	$3.874\cdot10^{4}$	$1\cdot10^{-2}$
$[Eu(HL')(H_2O)_2]\cdot 2H_2O$ [69]	H_2O	---	$1\cdot10^{-6}$
$[Eu(atpt)_{1.5}(phen)(H_2O)]$ [70]	EtOH	$7.60\cdot10^{3}$	$1\cdot10^{-3}$
$[Me_2NH_2][Eu(CPA)_2(H_2O)_2]$ [71]	H_2O	$1.041\cdot10^{4}$	10^{-7}
$[Eu(bpda)_{1.5}]\cdot H_2O$ [72]	H_2O	$1.25\cdot10^{4}$	10^{-7}

MIL-124: $Ga_2(OH)_4(C_9O_6H_4)$; H_2pzbc: 3-(1H-pyrazol-3-yl)benzoic acid; H_3BTPCA: 1,1,1-(benzene-1,3,5-triyl)tripiperidine-4-carboxylic acid; H_4BTMIPA: 5,5′-methylenebis(2,4,6-trimethylisophthalic acid); L: 4′-(4-carboxyphenyl)-2,2′: 6′,2″-terpyridine; BDC: benzene-1,4-dicarboxylate; H_4L': tetrakis[4-carboxyphenyl)-oxamethyl]methane acid; H_2atpt: 2-aminoterephthalic acid; phen: 1,10-phenanthroline; H_2CPA: 5-(4-carboxy phenyl)picolinic acid; BPDA: biphenyl-2,2'-dicarboxylic acid

Zn-based coordination complexes have also been extensively applied in the field of fluorescence detection of cations and organic molecules, following mainly PET, metal binding interactions, energy transfer mechanisms and competition of the excitation energy by the analyte and fluorophore.[73] In this case, luminescence arises from direct organic ligand excitation, showing an intense and broad absorption band in the short wavelength ultraviolet. Most of the current linkers used in coordination chemistry are π-conjugated organic molecules and are functionalised with multi-carboxylate groups or heterocyclic groups for metal-ligand coordination. Commonly, the fluorescence emission of organic ligands corresponds to the transition from the lowest excited singlet state to the singlet ground state, being the transitions $\pi \rightarrow \pi^*$ or $n \rightarrow \pi^*$ in nature.

However, it has to be noted that there are still some doubts about the exact nature of the optical absorption transition. It is ascribed to a charge-transfer transition from the ligand to an antibonding orbital which is located partly on the d^{10} ion and partly on the ligands, explaining the large width and high intensity of the absorption band.[74] Upon ligand coordination to the metal centre, the organic ligands are stabilised and there is a reduction in the non-radiative decay rates. This leads to an increased fluorescence intensity, lifetime and quantum yield. This effect is termed as *aggregation-induced emission* (AIE), in which coordinated ligands lose their freedom to move and, hence, their non-radiative decay. Moreover, the crystalline packing of the resulting coordination polymer affects the fluorescent properties, since different intermolecular or intramolecular interactions among organic linkers are established. For instance, $Zn_3(\mu_5\text{-pta})_2(\mu_2\text{-}H_2O)_2$ (being pta = 2,4,6-pyridinetricarboxylate) exhibits luminescence properties with a fluorescent enhancement and red shift of the maximum emission in comparison with the free linker. This is associated to the maximisation of the interactions among the organic ligands upon metal coordination that allows ligand-to-ligand $\pi \rightarrow \pi^*$ charge transfer (LLCT) transition emission.[75]

Different hazardous metal cations have been detected by Zn(II)-CPs in aqueous phase and, specifically, Table 4.4 compiles some Zn(II)-CPs used for detection of Fe^{3+} ions in different solvents. It can be seen that all of them present very high quenching constant values and low detection limits comparable to those observed for Eu-CPs.

Table 4.4. A comparison of *LOD* and K_{SV} of Zn-CPs used for detecting Fe^{3+} ions.[76-81]

Complex	Solvent	K_{sv} / M^{-1}	*LOD* / M
$[Zn_2(tpt)(tda)_2]\cdot H_2O$ [76]	H_2O	$4.6\cdot10^4$	$4.72\cdot10^{-6}$
$[Zn_2(NO_3)_2(bpy)_2(TBA)]$ [77]	H_2O	$7.48\cdot10^3$	$7.18\cdot10^{-6}$
$[Zn_6(L^{15})_2(H_2O)_7]\cdot(DMF)_2$ [78]	DMA	$3.58\cdot10^4$	$2.5\cdot10^{-7}$
$[Zn(H_4L^{15})(bpy)0.5(H_2O)_2]\cdot H_2O$ [78]	DMA	$1.57\cdot10^4$	$1.9\cdot10^{-7}$
$[(Zn_2(BDPO)\cdot 3H_2O]\cdot H_2O$ [79]	DMF	$2.45\cdot10^4$	---
$[Zn_2(TPOM)(NDC)_2]\cdot 3.5H_2O$[80]	H_2O	$1.90\cdot10^4$	$2\cdot10^{-6}$
$[Zn_2(L^{16})_2(bpe)_2(H_2O)_2]$ [81]	H_2O	$2.39\cdot10^3$	$2.5\cdot10^{-5}$

tpt: 2,4,6-tri(pyridin-4-yl)-1,3,5triazine; H_2tda: 2,5-thiophene dicarboxylic acid; H_2TBA: 4-(1Htetrazol-5-yl)-benzoic acid; bpy: 4,4′-bipyridine; H_6L^{15}: 5,5′(propane-2,2-diyl)bis(2-hydroxyisophthalic acid); H_4BDPO: N,N′-Bis(3,5-discarboxyphenyl)oxalamide; TPOM: tetrakis(4-pyridyloxymethylene)methane, H_2NDC: 2,6-naphthalenedicarboxylic acid; L^{16}: 4,4′-((1,2-phenylenebis(methylene))bis(oxy))dibenzoic acid; bpe: (E)-1,2-di(pyridin-4-yl)ethene

On the other hand, nitroaromatic compounds (NACs) represent serious sources of pollution of soils and groundwater, mainly because of their high toxicity. This term includes 2,4,6-trinitrophenol (TNP), trinitrotoluene (TNT), 2,4-dinitrophenol (2,4-DNP), dinitrotoluene (DNT), *p*-nitrophenol (4-NP), 1,3-

dinitrobenzene (1,3-DNB), nitrotoluene (NT) and nitrobenzene ($PhNO_2$). Highly sensitive and efficient materials able to detect trace amounts of explosive NACs in water are in strong demand for environmental applications. Such materials are also frequently used as explosive materials in terrorism and cause harmful effects on human health. As in metal sensing, efficient detective methods of NACs are usually expensive and difficult to manipulate. Thus, new technologies are needed for both security issues and pollution regulation. Luminescent Ln-CPs and Zn(II) complexes have been applied in this regard. A quenching process is usually observed and the sensing mechanism mainly is based on the interaction between electron rich fluorescent CPs and electron deficient NACs. The pioneering work applying fluorescent CPs on the detection of NACs was conducted by Li et al. in 2009.[82] This work was based on $[Zn_2(bpdc)_2(bpee)]\cdot 2DMF$ (bpdc = 4,4'-biphenyldicarboxylate; bpee = 1,2-bipyridylethene, Figure 4.19.a) and, following this, a series of fluorescent CPs containing Zn^{2+} and Cd^{2+} ions were reported with the same purpose.

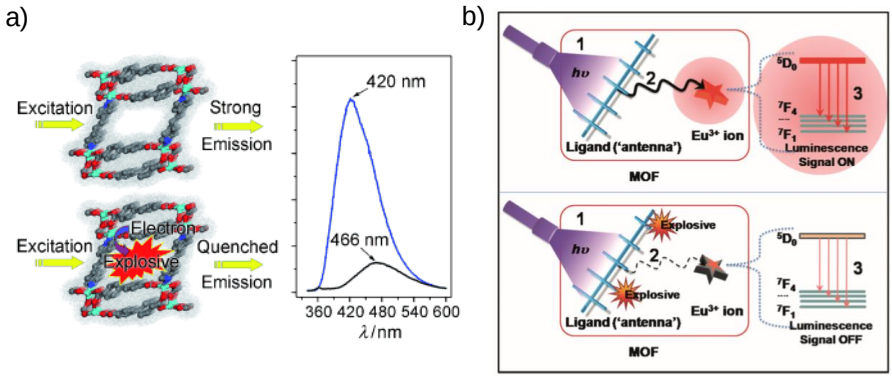

Figure 4.19. a) Schematic representation of the redox quenching mechanism in $[Zn_2(bpdc)_2(bpee)]\cdot 2DMF$ responsible for the selective detection of explosives. b) Scheme of the ligand-sensitised europium luminescence in the absence of NACs (upper panel) and in its presence (lower panel). Process 1 represents the UV light absorption of the ligand. Process 2 shows the energy transfer from the antenna ligand to the Eu^{3+} centre. Process 3 illustrates Eu^{3+} emission. Extracted from references [82] and [83].

It was not until 2015 that Ln-CPs were applied as fluorescent sensors for NACs detection (in particular, $[Y_{1.8}Eu_{0.2}(PDA)_3(H_2O)]$ being PDA = 1,4-phenylenediacetate), exhibiting quenching in the presence of nitro explosives with estimated K_{SV} values amongst the highest known for CPs ($15.9\cdot10^4$-$1.1\cdot10^4$ M^{-1} for TNP (2,4,6-trinitrophenol) and NT (4-nitrotoluene), respectively).[83] Figure 4.19.b shows a schematic representation of the antenna effect in the absence of explosive NACs (upper panel) and in its presence (lower panel) and

Table 4.5 contains a list of selected metallic complexes used for detection of nitrobenzene (chosen as a representative nitroaromatic compound), together with the K_{sv} and *LOD* achieved. Zn(II)-CPs are those which present the best parameters (higher K_{SV} and lower *LOD*) in this context.

Table 4.5. Comparison of *LOD* and K_{sv} values of metallic CPs used for nitrobenzene detection.[84-90]

Compound	K_{sv} / M^{-1}	*LOD* / M	Solvent
$[Eu(pdba)_3(H_2O)_3]\cdot 2H_2O$[84]	$3.00\cdot10^3$	---	H_2O
$[Eu_3(pdba)_4(H_2O)_4]\cdot 5H_2O$ [84]	$1.64\cdot10^3$	---	H_2O
$[Cd_2(L^{10})(DMA)][H_2N(Me)_2]$[85]	$2.70\cdot10^3$	$2.54\cdot10^{-3}$	DMA
$[(N_3)Zn(L^{11})_2Zn]$[86]	$1.95\cdot10^4$	$2.66\cdot10^{-7}$	DMF
$[(SCN)Zn(L^{11})_2Zn]$ [86]	$1.14\cdot10^4$	$3.18\cdot10^{-7}$	DMF
$[(SCN)Zn(L^{12})_2Zn]$ [86]	$1.50\cdot10^4$	$3.18\cdot10^{-7}$	DMF
$[(N_3)Zn(L^{12})_2Zn]$ [86]	$1.04\cdot10^4$	$3.71\cdot10^{-7}$	DMF
$[(N_3)Zn(L^{13})_2Zn]\cdot CH_2Cl_2$ [86]	$0.94\cdot10^4$	$3.56\cdot10^{-7}$	DMF
$[Zn(H_2L^{14})(H_2O)]$ [87]	$3.26\cdot10^3$	$7.2\cdot10^{-6}$	DMF
$[Eu(pdba)_3(H_2O)_3]\cdot 2H_2O$[88]	$3.00\cdot10^3$	---	H_2O
$[Eu_3(pdba)_4(H_2O)_4]\cdot 5H_2O$ [88]	$1.64\cdot10^3$	---	H_2O
$[Eu_2(pypymba)_6\cdot 4H_2O]\cdot 2H_2O$[89]	$4.83\cdot10^3$	$1.0\cdot10^{-3}$	H_2O
$[H_2N(Me)_2]_2[Eu_6(\mu^3\text{-}OH)_8(BPDC)_6(H_2O)_6]\cdot(solv)_x$[90]	$5.42\cdot10^3$	$4.06\cdot10^{-5}$-$5.69\cdot10^{-4}$	H_2O

H_2pdba: 4'-(1H-pyrazol-3-yl)-[1,1'-biphenyl]-3,5-dicarboxylic acid; H_5L^{10}: 2,4-di(3',5'-dicarboxylphenyl)benzoic acid; H_2L^{11}: 2,20-[(1,3-propanediyl)bis(iminomethylene)]bis[6-ethoxyphenol]; H_2L^{12}: 2,20-[(2,2-dimethyl-1,3-propanediyl)bis(iminomethylene)]bis[6-methoxyphenol]; H_2L^{13}: 2,20-[(2,2-dimethyl-1,3-propanediyl)bis(iminomethylene)]bis[6-ethoxyphenol]; H_4L^{14}: 3-(3 ,5 -dicarboxyphenyl)pyridine-2,6-dicarboxylic acid; DMA: N,N-dimethylacetamide; DMF: N,N-dimethylformamide; H_2pdba: 4'-(1H-pyrazol-3-yl)-[1,1'-biphenyl]-3,5-dicarboxylic acid; Hpypymba = 4-((3-(pyrazin-2-yl)-1H-pyrazol-1-yl) methyl) benzoic acid; H_2BPDC: biphenyl-4,4'-dicarboxylic acid

4.3.3. Catalysis

Among the most important developments in the field of coordination chemistry in recent years are those concerning catalytic reactions in which CPs act as catalysts, both in homogeneous and in heterogeneous systems. To date, CPs have shown catalytic performance in a broad range of organic transformations, for instance, the formation of C-C bonds, aldol condensations, oxidations, cyclisation and epoxidations, among others.[91] Heterogeneous catalysts present relevant advantages with regards to separation and recycling. Besides, solid CPs catalysts are more selective than corresponding homogeneous catalysts in some cases.[92] For this reason, preferential efforts are devoted to their development for application in different transformations. The functionalisation of hydrocarbons is of great technological interest due to their abundance in nature and at the same time is tricky because of the kinetically inert nature of C–H bonds, despite of being the conversion of C–H into C–O bonds thermodynamically favourable. Thus, highly reactive oxidising agents are

needed and a major challenge is to achieve chemo and regioselective transformations while operating under mild and sustainable conditions.

Specifically, oxidation of alkanes C–H bonds is a prominent area for the chemical industry because of the convenience of producing oxygen-containing materials from fossil hydrocarbons.[93] In particular, the selective oxidation of cyclohexane under mild conditions with molecular oxygen or hydrogen peroxide occupies a prominent position due to the fact that the product of this reaction generates a mixture of cyclohexanol and cyclohexanone (*KA-oil*) that is an intermediate in the petrochemical industry.[94] Moreover, this mixture can be further applied to the fabrication of adipic acid and ε-caprolactam, which are essential materials for the production of Nylon-6,6 and Nylon-6, respectively (Figure 4.20).[95]

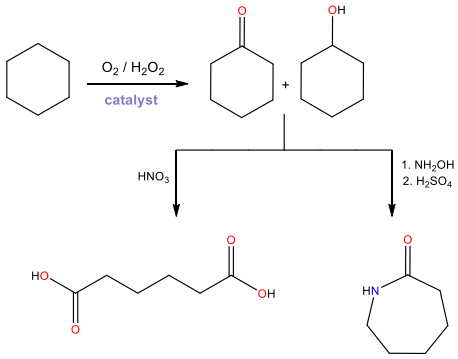

Figure 4.20. Conversion of cyclohexane to adipic acid or ε-caprolactam.

In this context, most industrial processes are based on the use of soluble Co(II) salts as catalysts, thus, requiring an additional catalyst separation step[96a] and usually require high pressure (15 bar) and temperature (~160°C), obtaining high selectivity for the mixture of cyclohexanol and cyclohexanone (80%, with a cyclohexanol/cyclohexanone molar ratio of 2:1) but at a low conversion (as low as 4%).[96b] Therefore, there is a need to develop new catalysts that improve current conversions and CPs have shown significant potential towards this goal.[97] A wide variety of transition metal catalysts have proven efficient performance for the oxidation of alkane C–H bonds, such as chromium, manganese, cobalt, nickel, copper, iron, ruthenium, rhenium, osmium and iridium complexes.[97] In particular, iron complexes are the most widely studied, as they are constituents of enzymes that catalyse C-H oxidative transformations, in conjunction with its lack of toxicity and availability. Over the last decade, iron CPs have emerged as powerful oxidation catalysts in terms of product yields and

selectivities and significant progress has been made. Therefore, this section is focused in iron-based systems.

Since 1993, it was noted that the oxidation of cyclohexane must be the least efficient of all major industrial processes, producing 10^6 tons per year of cyclohexanone and cyclohexanol for conversion to Nylon-6 and Nylon-6,6. At the same time, a series of reagents for the oxygenation of hydrocarbons were developed by D. Barton and co-workers between 1983 and 1998, and named as Gif-reagents in reference to the research-oriented town (Gif-sur-Yvette) at the outskirts of Paris.[98] The reagents consist on a redox-active metal (usually iron) and an oxo-donor system (Table 4.6).

Table 4.6. Barton's Gif oxygenation systems. Extracted from reference [98].

System	Precatalyst	Oxidant	Reductant	Solvent [c]
Gif^{I}	None added [a]	O_2	Fe^0/Na_2S	Py/AcOH (10:1 v/v)
Gif^{II}	None added [a]	O_2	Fe^0/Na_2S	Py/AcOH/H_2O (6.6%)
Gif^{III}	None added [a]	O_2	Fe^0	Py/AcOH/H_2O (6.6%)
Gif^{IV}	$Fe^{II/III}$ [b]	O_2	Zn	Py/AcOH/H_2O [d] (6.6%)
GO	$Fe^{II/III}$ [b]	O_2	Hg cathode	Py/CF_3COOH
$GoAgg^{I}$	Fe^{II}	KO_2 [e]		Py/AcOH
$GoAgg^{II}$	Fe^{III} [f]	H_2O_2 (30%) [g]		Py/AcOH
$GoAgg^{III}$	Fe^{III} [f]/picH (1:3)	H_2O_2 (30%) [g]		Py/AcOH (or py)
$GoChAgg^{I}$	Cu^{II}	H_2O_2 (30%) [g]		Py/AcOH (or py)
$GoChAgg^{II}$	None added [a]	O_2	Cu^0	Py/AcOH
$GoAgg^{IV}$ [h]	Fe^{III} [i]	*t*-BuOOH (90%) [g]		Py/AcOH, 60°C
$GoAgg^{V}$ [h]	Fe^{III} [d]/picH (1:3)	*t*-BuOOH (90%) [g]		Py/AcOH, 60°C

[a] Although no compound is added, the zero-valent metal partially dissolves in solution. [b] Usually $[Fe_3O(OAc)_6(py)_3]\cdot 0.5py$. [c] At room temperature, unless otherwise noted. [d] Addition of H_2O is optional. [e] Under inert gas (Ar, N_2). [f] Usually $[FeCl_3]\cdot 6H_2O$. [g] Under inert gas or O_2. [h] Later expelled from the GoAgg family. [i] Usually $Fe(NO_3)_3\cdot 9H_2O$

Conventional *Gif^{IV}* oxidation systems form mainly cyclohexanone with a conversion of cyclohexane of 40% but require large quantities of zinc and were declared as non-suitable for cyclohexane oxidation because coupling products with pyridine were formed, which reduced the selectivity for the KA-oil.[99] The *$GoAgg^{II}$* system does not form any side products but is too slow for any industrial use. Nonetheless, an adapted *$GoAgg^{II}$* system in which picolinic acid was added as a ligand to the iron catalyst, proved to be faster while maintaining the same

selectivity in the oxidation of cyclohexane and yielded a similar concentration of oxidised products to that obtained in the industrial process. The problem found in this system is the use of pyridine (attempting to substitute pyridine by acetonitrile or tert-butanol resulted in a strong decrease in the selectivity) and the rapid deactivation of the catalyst.[99] For these reasons, nowadays there is a pressing interest in the development of heterogeneous catalysts and, in particular, for the enhancement in the conversion for selective oxidation of alkanes at room temperature without pressure in hydrogen peroxide as oxidant (since it only produces water as a by-product in an environmentally friendly reaction [95]).

Even though there is uncertainty with respect to the reaction mechanism of the catalytic process, detailed experimental investigations provide evidence to support oxygen- and carbon-centred radical chemistry.[100] For instance, Gif oxygenation of DMSO by H_2O_2 catalised by $[Fe(pic)_2(py)_2]$ provides pyridine-trapped methyl radicals under argon which is an indicative of the addition reaction of OH· to DMSO. In addition, the reaction is inhibited by the progressive addition of EtOH that generates pyridine-captured $CH_3{\cdot}CHOH$ and $\cdot CH_2CH_2OH$ radicals.[101] Catalysed decomposition of hydrogen peroxide would generate hydroxyl radicals (HO·), and catalysed decomposition of intermediate alkyl hydroperoxide would generate alkoxyl radicals (RO·) (Figure 4.21.a).

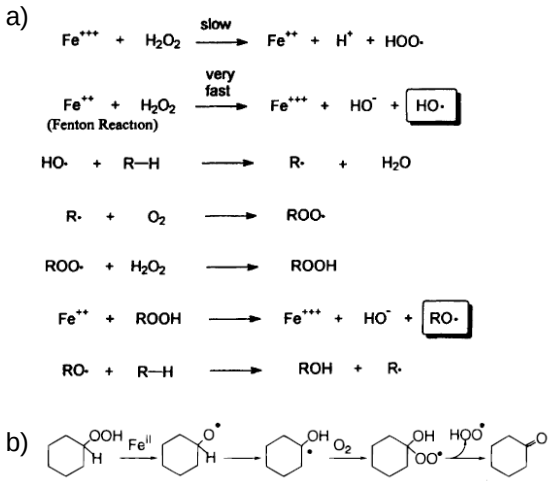

Figure 4.21. a) Scheme of the radical mechanism in Gif reactions. b) 1,2-hydrogen shift explaining the formation of the ketone derivative. Extracted from references [101] and [102].

Both types of radicals are able to abstract hydrogen from alkanes, leading to the formation of the product ROH. The unusually high ketone/alcohol ratio, suggests

that decomposition of alkylperoxyl radicals may occur through metal-dependent pathways (Figure 4.21.b)

The vast majority of iron CPs that have been applied in the catalysis field present an Fe(II) centre with two cis coordination positions occupied by labile ligands, which allow a fast reaction with the oxidant. Simple iron salts such as $Fe(ClO_4)_2$, $Fe(BF_4)_2$ and $FeCl_3$ have proven their potential to catalyse cyclohexane oxidation to a mixture of cyclohexanol and cyclohexanone by hydrogen peroxide with high yields (Table 4.7, entries 1-3). The selectivity of the reaction is improved upon addition of a tridentate ligand dapb or a pentadentate ligand dapab (Table 4.7, entries 4-7, Figure 4.22).[97]

Table 4.7. Catalytic oxidation of cyclohexane with different iron catalysts and hydrogen peroxide.

Entry	Catalyst	Conversion[f]	Products (A/K) [a]	Products yield / %
1	$Fe(ClO_4)_2$ [b]	100	0.46	87
2	$Fe(BF_4)_2$ [b]	100	1.55	81
3	$FeCl_3$ [b]	99	0.45	79
4	$Fe(BF_4)_2$ + dapab [b]	100	1.11	**100**
5	$Fe(BF_4)_2$ + dapb [b]	100	0.77	81
6	$Fe(ClO_4)_2$ + dapb [b]	100	0.68	91
7	$FeCl_3$ + dapb [b]	93	0.61	93
8	$[L^1Fe^{II}(NCMe)_2]^{2+}$ [c]	---	1.1	---
9	$[L^2Fe^{II}(NCMe)]^{2+}$ [c]	---	1.1	---
10	$[L^3Fe^{II}(NCMe)]^{2+}$ [c]	---	0.8	---
11	$[Fe^{III}(dpaq)(H_2O)]^{2+}$ [d]	---	11.3	---
12	$[Fe^{II}(CF_3SO_3)_2(^{Me2}PyTACN)]$ [e]	65	**12**	---
13	$[Fe^{II}(BPMEN)(CH_3CN)_2]^{2+}$ [c]	63	8	---
14	$Fe(OTf)_2$	---	1	7
15	1·$Fe(OTf)_2$	---	0.11	60
16	2·$Fe(OTf)_2$	---	0.13	64
17	3·$Fe(OTf)_2$	---	0.36	30

[a] Ratio Cyclohexanol/Cyclohexanone. [b] The reactions take place at 50℃ under air in acetonitrile. [c] The reactions take place at 25℃ under air in acetonitrile. [d] The reaction takes place at room temperature in acetonitrile. [e] The reaction takes place at 25 ℃ under air in acetonitrile/H_2O. [f] Efficiency in the conversion of H_2O_2 into products.

Furthermore, a series of rigid pentadentate iron complexes constructed from bispidine derivatives ($[L^1Fe^{II}(NCMe)_2]_2$, $[L^2Fe^{II}(NCMe)_2]$ and $[L^3Fe^{II}(NCMe)_2]$, Table 4.7, entries 8-10, Figure 4.22) has shown good performance as catalyst in the oxidation of cyclohexane (up to 35% cyclohexanol and cyclohexanone) and the selectivity is markedly improved (in acetone/Ar, alcohol/ketone ratio up to 4).[103] More recently, a new Fe(III) system based on the pentadentate H-dpaq ligand (being dpaq = 2-[bis-(pyridine)-2-ylmethyl)]amino-*N*-quinolin-8-yl-acetamidate, Table 4.7, entry 11) shows catalytic activity for the same oxidation reaction[104] with an efficient stereospecific alkane hydroxylation performance

(A/K ≈ 11). A/K selectivity exhibited by this complex is comparable to values reported for $[Fe^{II}(CF_3SO_3)_2(^{Me2}PyTACN)]$[105] and $[Fe^{II}(BPMEN)(CH_3CN)_2]^{2+}$[106] (Table 4.7, entries 12 and 13, Figure 4.22). The catalytic activity of $Fe(OTf)_2$ (OTf = trifluoromethanesulfonate) and three derivatives, $1{\cdot}Fe(OTf)_2$, $2{\cdot}Fe(OTf)_2$ and $3{\cdot}Fe(OTf)_2$, has been also investigated. For $Fe(OTf)_2$, low reactivity and no selectivity are observed, while the remaining three catalysts are much more effective (Table 4.7, entries 14-17, Figure 4.22).[107] Some catalytic parameters describing the catalytic activity of these iron reagents towards cyclohexane oxidation reaction with hydrogen peroxide are summarised in Table 4.7, being this a selection of relevant contributions.

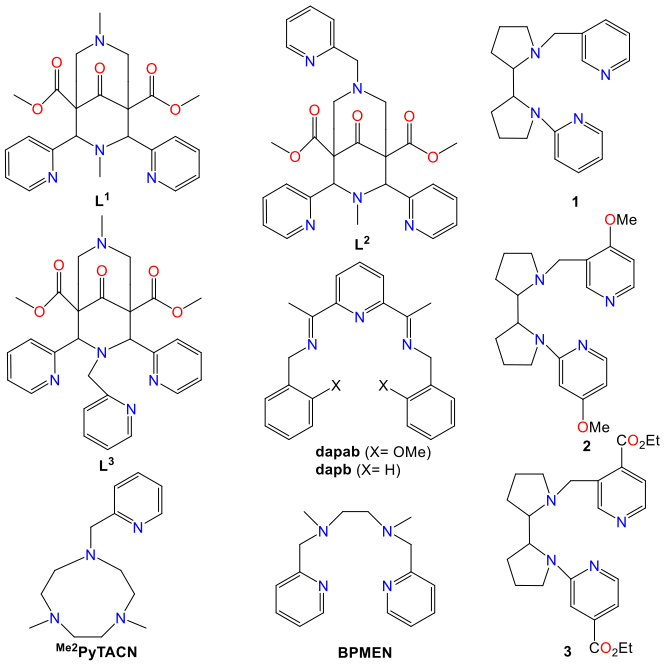

Figure 4.22. Molecular structure of the ligands used for the development of the iron catalysts mentioned in the text.

In view of the above results, it has to be highlighted that the iron(II) complex containing the pentadentate ligand dapab is able to convert completely cyclohexane to the corresponding cyclohexanol/cyclohexanone mixture within 12 hours. However, there is a low selectivity as indicated by the alcohol/ketone ratio close to 1. On the other hand, the catalyst that achieves a higher selectivity is $[Fe^{II}(CF_3SO_3)_2(^{Me2}PyTACN)]$, which is very efficient for the hydroxylation of cyclohexane. Analysis of the data compiled in Table 4.7 shows that most efficient complexes contain ligands that form chelate metalocycles and they must be

oxidatively robust and form stable complexes under oxidative and acidic reaction conditions.

4.4. Stability of CPs. Ethynyl-bridged picolinate systems

Most coordination frameworks are easily hydrolysed, as they are based on organic polytopic carboxylate ligands. The stability of CPs is affected by several factors such as the nature of the organic ligands, the metal ions and the metal-ligand coordination geometry. Their degradation can be schematically viewed as consecutive substitution reactions in which the linkers are replaced by water or hydroxide molecules (Scheme 4.1). Therefore, in order to construct stable complexes, strong coordination bonds are needed or, alternatively, steric hindrance to prevent the approximation of guest molecules to the metal nodes.[108]

Scheme 4.1. Decomposition mechanism of coordination polymers in water.

In order to increase the stability of these systems, several strategies are currently being developed. For the same set of ligands and coordination sphere, high-valent metal ions that present higher charge density establish stronger coordination bonds. This trend is in agreement with Pearson's hard/soft acid/base (HSAB) principle (Scheme 4.2).[109]

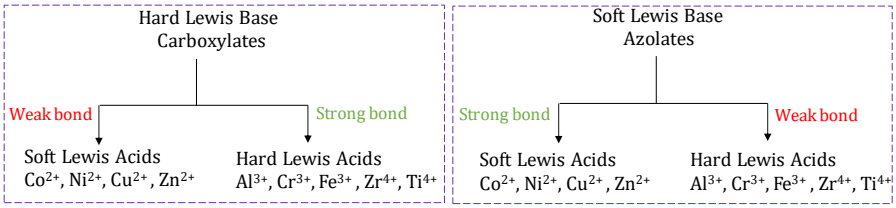

Scheme 4.2. Application of HSAB principle to the construction of stable coordination polymers.

According to this principle, stable complexes can be assembled by the combination of carboxylate-based ligands (hard bases) and high-valent metal ions (Ti^{4+}, Zr^{4+}, Al^{3+}, Fe^{3+} and Cr^{3+}). Alternatively, stable frameworks can also be constructed by soft azolate ligands (imidazolates, pyrazolates, triazolates and tetrazolates) and soft divalent metal ions (Zn^{2+}, Cu^{2+}, Ni^{2+}, Mn^{2+} and Ag^{+}). A well-

known series of the first group is the Material Institute Lavoisier (MIL) series, as a representative example, MIL-53 is built up from Cr^{3+} cations and terephthalate anions.[110] On the other hand, the zeolitic imidazolate frameworks (ZIF) are representative examples for the second group and are constructed by Zn^{2+} cations and imidazolate ligands.[111] Additionally, post-synthetic modification of labile complexes with hydrophobic coatings has proven to be an efficient strategy to obtain stable networks,[112] as well as direct enhancement of water stability by introducing hydrophobic groups onto the ligands.[113]

Another approach is focused on using chelating anionic ligands, which is an almost unexplored alternative to that based on high-valent complexes. There are only a few examples related to tetraanionic bisbidentate dioxidobenzenedicarboxylate ligands[114-116] and catecholates[117] (Figure 4.23). The M_2(dobdc)[115] (where M = Mg, Mn, Fe, Co, Ni, Cu, Zn and dobdc = 2,5-dioxido-1,4-benzenedicarboxylate) series has been extensively studied because of its high concentration of coordinately unsaturated metal sites upon evacuation of the solvent molecules present in the voids of the structure. A series of compounds with the *meta*-substituted 4,6-dioxo-1,3-benzenedicarboxylate ligand (M_2(m-dobdc), M = Mn, Mg, Fe, Co and Ni) has also been synthesised.[116] 1D hexagonal voids are formed in both series of materials, however, there are minor structural changes between both crystal packings that result in markedly different H_2 binding enthalpies and, therefore, gas storage properties. M-CATS[117] (M = Co, Ni and CAT = triphenylene-2,3,6,7,10,11-hexakis(olate)) present a 2D porous extended framework, high chemical and thermal stability, electrical conductivity and charge storage capacity.

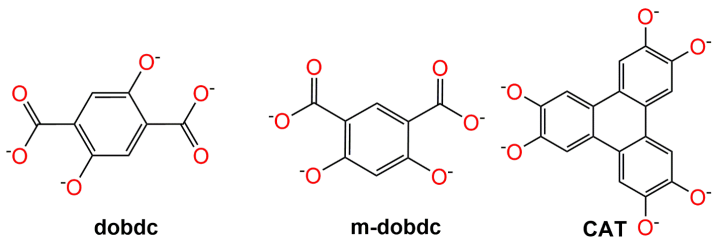

Figure 4.23. Molecular structure of chelating anionic ligands used in the chelating-CPs field.

In this context, the picolinate (pic) ligand is a promising chelating anionic fragment for the design of robust CPs with high stability. On the other hand, ethynylene bridges have been incorporated in the design of some organic linkers because they provide rigidity, linear connectivity and electron delocalisation.[118] Despite the fact that the picolinate ligand is an universal chelating anionic entity,

only a few segmented polytopic picolinate ligands have been reported (L1-L3, Figure 4.24).[119-123] In particular, only Zn(II), Fe(II) and Pb(II) complexes of L1, L2 and L3 have been described, respectively. The Zn(II) complex of L1 presents a tetranuclear core with $[Zn_4(L1)_4(X)_4]^{n+}$ formula. Each metallic centre is bound to two nitrogen and four oxygen atoms, coordinating two picolinate subunits in a bidentate mode and the remaining oxygen atoms coming from water and/or perchlorate anions are highly disordered in the structure (Figure 4.25).[119]

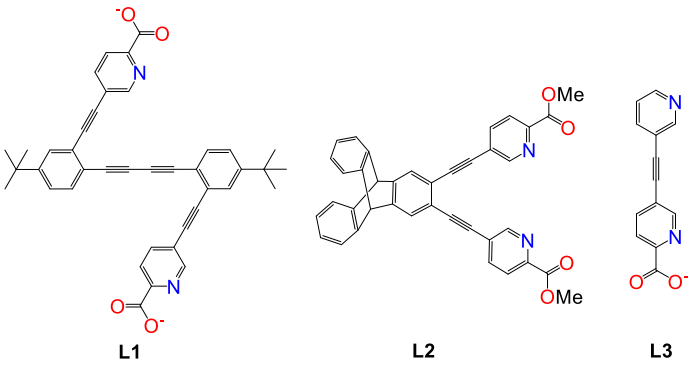

Figure 4.24. Molecular structure of segmented polytopic picolinate ligands reported up to date.

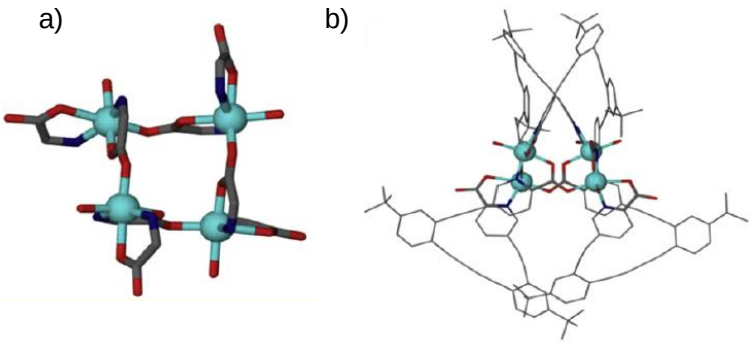

Figure 4.25. (a) Schematic representation of the tetrazinc(II) core. Picolinate ligands are shown as N-C-C(=O)-O fragments and the X ligand is either ClO_4^- or H_2O, showing only the oxygen atom coordinated to the zinc cation for clarity. (b) Representation of the $[Zn_4(L1)_4(X)_4]^{n+}$ fragment. Extracted and adapted from reference [119].

In the diiron(II) complex $[Fe_2(\mu\text{-}OTf)_2(L2)_2](BARF)_2$ (OTF = trifluoromethanesulfonate and BARF = tetrakis[3,5-bis(trifluoromethyl)phenyl]borate),[120] each iron centre is coordinated to two N,O-chelating picolinate ester groups and two oxygen atoms from the bridging triflates (Figure 4.26). With the same ligand, a heterodinuclear sodium-iron

complex of formula [NaFe(L2)(μ-O_2CTrp)$_3$] (Trp = 9-triptycenyl) has been reported.[121] The iron and sodium cations are bridged by three triptycene carboxylates and each of them is linked to a picolinate subunit in a chelating bidentate mode. This results in a distorted trigonal-bipyramidal coordination geometry for both cations (Figure 4.27). Coordination of L3 to Pb(II) cations results in the isolation of the mononuclear [Pb(L3)$_2$(H_2O)$_2$] entity.[122] Two picolinate subunits coordinate to the Pb(II) cation in a bidentate chelating mode and the axial positions of the coordination sphere are occupied by two water molecules in *cis* arrangement (Figure 4.28). In addition, the corresponding 5-ethynylpyridine-2-carboxylic acid was prepared and employed in the synthesis of a luminescent silver salt and an iridium(III)-polyoxometalate with charge-transfer properties.[123]

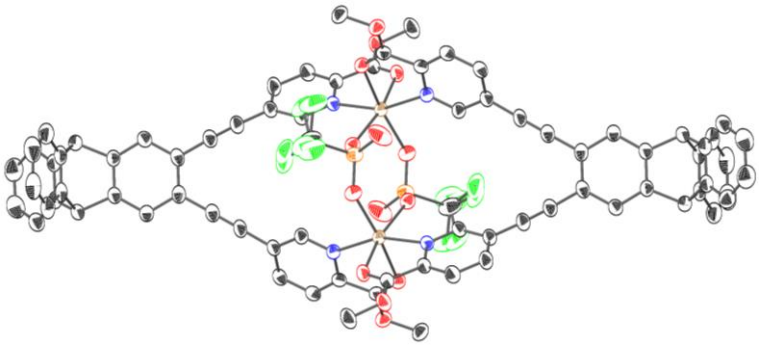

Figure 4.26. ORTEP representation of the dinuclear entity present in the compound [Fe_2(μ-OTf)$_2$(L2)$_2$](BARF)$_2$, showing 50% probability thermal ellipsoids for all non-hydrogen atoms. C, F, Fe, N, O and S atoms are illustrated as black, green, brown, blue, red and orange spheres, respectively. Hydrogen atoms are omitted for clarity. Redrawn from CCDC 681359.

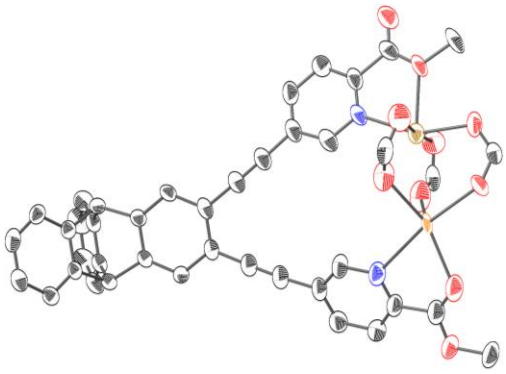

Figure 4.27. ORTEP diagram of [NaFe(L2)(μ-O_2CTrp)$_3$], showing 50% probability thermal ellipsoids for all non-hydrogen atoms. The triptycene units of the bridging carboxylates are simplified for

clarity and H atoms are omitted. C, Fe, N, Na and O atoms are illustrated as black, brown, blue, orange and red spheres, respectively. Redrawn from CCDC 292311.

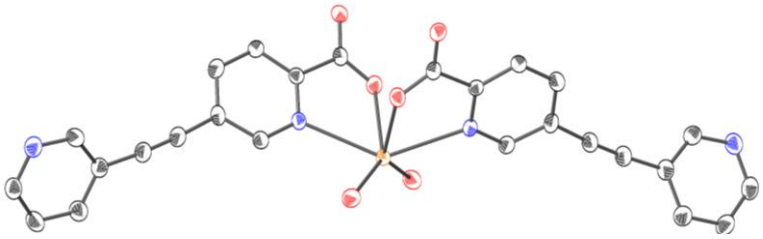

Figure 4.28. Representation of the coordination sphere of the Pb(II) cations in $[Pb(L3)_2(H2O)_2]$. C, Pb, N and O atoms are illustrated as black, orange, blue and red spheres, respectively. Hydrogen atoms are omitted for clarity. Redrawn from CCDC 864784.

As described in these examples, the picolinate ion coordinates to metal ions in a N,O-chelating mode, through an oxygen atom of the carboxylate moiety and the N atom of the pyridine ring, forming five-membered chelate rings that provide stability to the system. A recent study in the Cambridge Structural Database (CSD) revealed that there are until 33 possible coordination modes for picolinate-based ligands.[124] 92% of the deposited structures present a N,O chelating ring, being the most frequently observed coordination mode that in which the coordination involves only the chelating ring (56%). The second most common coordination mode (20%) relies on a picolinate ligand that links two metal centres through both oxygen atoms of its carboxylato group while presenting a N,O-chelating ring. In addition, further comparison between bridged and non-bridged structures showed that the picolinate ligand tends to form non-bridged structures (87)%.

4.5. References

[1] a) J. Zhao, X. Qu, B. Yan, *J. Photochem. Photobiol. A. Chem*. **2020**, 390, 112296. b) G. I. Dzhardimalieva, I. E. Uflyand, *Chemistry of Polymeric Metal Chelates*. **2018**, Springer Series in Materials Science.

[2] G. B. Kauffmann, Alfred Werner, *Founder of Coordination Chemistry*. **1966**, Springer -Verlag, Berlin.

[3] C.-H. Wunderlich, G. Bergerhoff, *Chem. Ber.* **1994**, 127, 1185–1190

[4] a) Y. Kinoshita, I. Matsubara, Y. Saito, *Bull. Chem. Soc. Jpn*. **1959**, 32, 1216-1221. b) Y. Kinoshita, I. Matsubara, T. Higuchi, Y. Saito, *Bull. Chem. Soc. Jpn*. **1959**, 32, 1221-1226. c) Y. Kinoshita, I. Matsubara, Y. Saito, *Bull. Chem. Soc. Jpn*. **1959**, 32, 741-747

[5] R. M. Izatt, *Macrocyclic and Supramolecular Chemistry*. **2016**, John Wiley & Sons

[6] W. Lu, Z. Wei, Z.-Y. Gu, T.-F. Liu, J. Park, J. Park, J. Tian, M. Zhang, Q. Zhang, T. Gentle, M. Boscha, H.-C. Zhou, *Chem. Soc. Rev*. **2014**, 43, 5561-5593

[7] H. A. Al-Mohsin, A. Almousa, S. A. Oladepo, A. S. Jalilov, M. Fettouhi, A. M. P. Peedikakkal, *Inorg. Chem*. **2019**, 58, 10167-10173

[8] C. K. Brozek, M. Dincä, *Chem. Soc. Rev*. **2014**, 43, 5456-5467

[9] T. Li, M. T. Kozlowski, E. A. Doud, M. N. Blakely, N. L. Rosi, *J. Am. Chem. Soc*. **2013**, 135, 11688-11691

[10] H. Fei, J. F. Cahill, K. A. Prather, S. M. Cohen, *Inorg. Chem*. **2013**, 52, 4011-4016

[11] O. M. Yaghi, H. Li, *J. Am. Chem. Soc*. **1995**, 117, 10401–10402.

[12] H. C. Zhou, J. R. Long, O. M. Yaghi, *Chem. Rev*. **2012**, 112, 673-674

[13] A. U. Czaja, N. Trukhan, U. Müller, *Chem. Soc. Rev*. **2009**, 38, 1284-1293

[14] a) Z. Ma, B. Moulton, *Coord. Chem. Rev*. **2011**, 255, 1623-1641. b) H. Li, Y. Wang, Y. He, Z. Xu, X. Zhao, Y. Han, *New. J. Chem*. **2017**, 41, 1046- 1056. c) T.

Sherstobitova, K. Maryunina, S. Tolstikov, G. Letyagin, G. Romanenko, S. Nishihara, K. Inoue, *ACS Omega*. **2019**, 4, 17160-17170. d) A. Geersing, N. Ségaud, M. G. P. van der Wijst, M. G. Rots, G. Roelfes, *Inorg. Chem*. **2018**, 57, 7748-7756. e) Y.-P. Zhao, Y. Li, C.-Y. Cui, Y. Xiao, R. Li, S.-H. Wang, F.-K. Zheng, G.-C. Guo, *Inorg. Chem*. **2016**, 55, 7335-7340. f) J. S. Seo, D. Whang, H. Lee, S. I. Jun, J. Oh, Y. J. Jeon, K. Kim, *Nature*. **2000**, 404, 982-986. g) S. Hasegawa, S. Horike, R. Matsuda, S. Furukawa, K. Mochizuki, Y. Kinoshita, S. Kitagawa, *J. Am. Chem. Soc*. **2007**, 129, 2607-2614. g) M. Fujita, Y. J. Kwon, S. Washizu, K. Ogura, *J. Am. Chem. Soc*. **1994**, 116, 1151-1152

[15] X.-M. Chen, *Modern Inorganic Synthetic Chemistry*, DOI: 10.1016/B978-0-444-53599-3.10010-1

[16] O. Shekhah, H. Wang, M. Paradinas, C. Ocal, B. Schüpbach, A. Terfort, D. Zacher, R. A. Fischer, C. Wöll, *Nat. Mat*. **2009**, 8, 481-484

[17] J. Zhang, L. Wojtas, R. W. Larsen, M. Eddaoudi, M. J. Zaworotko, *J. Am. Chem. Soc*. **2009**, 131, 17040-17041

[18] a) S. Yuan, L. Feng, K. Wang, J. Pang, M. Bosch, C. Lollar, T. Sun, J. Qin, X. Yang, P. Zhang, Q. Wang, L. Zou, Y. Zhang, L. Zhang, Y. Fang, J. Li, H.-C. Zhou, *Adv. Mater*. **2018**, 30, 1704303. b) R. S. Forgan, *Chem*. *Sci*. **2020**, 11, 4546-4562

[19] a) O. V. Gutov, S. Molina, E. C. Escudero-Adán, A. Shafir, *Chem. Eur. J*. **2016**, 22, 13582-13587. b) S. Wang, M. Wahiduzzaman, L. Davis, A. Tissot, W. Shepard, J. Marrot, C. Martineau-Corcos, D. Hamdane, G. Maurin, S. Devautour-Vinot, C. Serre, *Nat. Commun*. **2018**, 9, 4937

[20] a) X. Li, H. Xu, F. Kong, R. Wang, *Angew. Chem. Int. Ed*. **2013**, 52, 13769–13773. b) S. Wang, L. Li, J. Zhang, X. Yuan, C. Y. Su, Mater. Chem. 2011, 21, 7098-7104

[21] S.-N. Zhao, Y. Zhang, S.-Y. Song, H.-J. Zhang, *Coord. Chem. Rev*. **2019**, 398, 113007

[22] J. An, S. J. Geib, N. L. Rosi, *J. Am. Chem. Soc*. *Commun*. **2009**, 131, 8376-8377

[23] R. S. Crees, M. L. Cole, L. R. Hanton, C. J. Sumby, *Inorg. Chem.* **2010**, 49, 1712-1719

[24] Y. Journaux, J. Ferrando-Soria, E. Pardo, R. Ruiz-Garcia, M. Julve, F. Lloret, J. Cano, Y. Li, L. Lisnard, P. Yu, H. Stumpf, C. L. M. Pereira, *Eur. J. Inorg. Chem*. **2018**, 228-247

[25] a) O. Kahn, B. Briat, *J. Chem. Soc., Faraday Trans*. **1976**, 72, 268–281. b) O. Kahn, B. Briat, *J. Chem. Soc., Faraday Trans.* **1976**, 72, 1441–1446. c) J. J. Girerd, Y. Journaux, O. Kahn, *Chem. Phys. Lett*. **1981**, 82, 534–538

[26] O. Kahn, *Molecular magnetism*. **1993**, VCH Publishers

[27] K. Diller, A. Singha, M. Pivetta, C. Wäckerlin, R. Hellwig, A. Verdini, A. Cossaro, L. Floreano, E. Vélez-Fort, J. Dreiser, S. Rusponi, H. Brune, *RSC Adv*. **2019**, 9, 34421-34429

[28] C. Benelli, D. Gatteschi, *Introduction to Molecular Magnetism*. **2016**, Wiley-VCH

[29] J. W. Sharples, Y.-Z. Zheng, F. Tuna, E. J. L. McInnes, D. Collison, *Chem. Commun.* **2011**, 47, 7650-7652

[30] R. J. Blagg, C. A. Muryn, E. J. L. McInnes, F. Tuna, R. E. P. Winpenny, *Angew. Chem. Int. Ed*. **2011**, 50, 6530-6533

[31] M. Murrie, S. J. Teat, H. Stoeckli-Evans, H. U. Güdel, *Angew. Chem. Int. Ed.* **2003**, 42, 4653-4656

[32] C. Papatriantafyllopoulou, W. Wernsdorfer, K. A. Abboud, G. Christou, *Inorg. Chem*. **2011**, 50, 421-423

[33] C. J. Milios, R. Inglis, A. Vinslava, R. Bagai, W. Wernsdorfer, S. Parsons, S. P. Perlepes, G. Christou, E. K. Brechin, *J. Am. Chem. Soc.* **2007**, 129, 12505-12511

[34] G. Redler, C. Lampropoulos, S. Datta, C. Koo, T. C. Stamatatos, N. E. Chakov, G. Christou, S. Hill, *Phys. Rev. B*. **2009**, 80, 094408

[35] A. J. Tasiopoulos, A. Vinslava, W. Wernsdorfer, K. A. Abboud, G. Christou, *Angew. Chem. Int. Ed*. **2004**, 43, 2117-2121

[36] C. Sangregorio, T. Ohm, C. Paulsen, R. Sessoli, D. Gatteschi, *Phys. Rev. Lett*. **1997**, 78, 4645-4648

[37] a) R. Sessoli, D. Gatteschi, A. Caneschi, M. A. Novak, *Nature*. **1993**, 365, 141-143. b) L. Thomas, F. Lionti, R. Ballou, D. Gatteschi, R. Sessoli, B. Barbara, *Nature*. **1996**, 383, 145-147

[38] N. Ishikawa, M. Sugita, T. Ishikawa, S.-y. Koshihara, Y. Kaizu, *J. Am. Chem. Soc*. **2003**, 125, 8694-8695

[39] S. G. McAdams, A.-M. Ariciu, A. K. Kostopoulos, J. P. S. Walsh, F. Tuna, *Coord. Chem. Rev*. **2017**, 346, 216-239

[40] F.-S. Guo, B. M. Day, Y.-C. Chen, M.-L. Tong, A. Mansikkamäki, R. A. Layfield, *Science*. **2018**, 362, 1400-1403

[41] D. Singh, V. Tanwar, S. Bhagwan, I. Singh, *Recent Advances in Luminescent Materials and Their Potential Applications*. **2016**, Wiley.

[42] K. K.-W. Lo, L. J. Charbonnière, *Eur. J. Inorg. Chem*. **2017**, 5055-5057

[43] a) H. Tan, T. Wang, Y. Shao, C. Yu, L. Hu, *Front. Chem*. **2019**, 7, 387. b) X. Zhu, Q. Su, W. Feng, F. Li, *Chem. Soc. Rev*. **2017**, 46, 1025-1039

[44] B. Li, H.-M. Wen, Y. Cui, G. Qian, B. Chen, *Prog. Polym. Sci*. **2015**, 48, 40-84

[45] S. Freed, S. I. Weissman, F. E. Fortess, H. F. Jacobson, *J. Chem. Phys*. **1939**, 7, 824-828

[46] S. I. Weissman, *J. Chem. Phys*. **1942**, 10, 214-217

[47] J.-C. G. Bünzli, C. Piguet, *Chem. Soc. Rev*. **2005**, 34, 1048-1077

[48] J. B. Lamture, Z. H. Zhou, A. S. Kumar, T. G. Wensel, *Inorg. Chem*. **1995**, 34, 864-869

[49] Y. Cui, B. Chen, G. Qian, *Luminescent Properties and Applications of Metal-Organic Frameworks*. **2013**, Springer-Verlag

[50] K. Zheng, Z. Liu, Y. Jiang, P. Guo, H. Li, C. Zeng, S. W. Ng, S. Zhong, *Dalton Trans*. **2018**, 47, 17432

[51] N. B. D. Lima, S. M. C. Gonçalves, S. A. Júnior, A. M. Simas, *Sci. Rep*. **2013**, 3, 2395

[52] F. R. G. e Silva, J. F. S. Menezes, G. B. Rocha, S. Alves, H. F. Brito, R. L. Longo, O. L. Malta, *J. Alloys Compd.* **2000**, 364-370

[53] L.-Z. Yang, J. Wang, A. M. Kirillov, W. Dou, C. Xu, R. Fang, C.-L. Xu, W.-S. Liu, *CrystEngComm*. **2016**, 18, 6425-6436

[54] a) M. Latva, H. Takalo, V. Mukkala, C. Matachescu, J. Rodriguez-Ubis, J. Kankare, *J. Lumin*. **1997**, 75, 149–169. b) T. Alammar, I. Z. Hlova, S. Gupta, A.

Biswas, T. Ma, L. Zhou, V. Balema, V. K. Pecharsky, A.-V. Mudring, *New J. Chem*. **2020**, 44, 1054-1062

[55] R. Maouche, S. Belaid, B. Benmerad, S. Bouacida, S. Freslon, C. Daiguebonne, Y. Suffren, G. Calvez, K. Bernot, C. Roiland, L. L. Pollès, O. Guillou, *Inorg. Chim. Acta*. **2020**, 501, 119309

[56] M. Zhao, Z.-Q. Yao, Y.-L. Xu, Z. Chang, X.-H. Bu, *RSC Adv*. **2017**, 7, 2258-2263

[57] L.-Z. Yang, J. Wang, A. M. Kirillov, W. Dou, C. Xu, R. Fang, C.-L. Xu, W.-S. Liu, *CrystEngComm*. **2016**, 18, 6425-6436

[58] B. Valeur, *Molecular Fluorescence Principles and Applications*. **2001**, Wiley-VCH

[59] K. Zheng, Z. Liu, Y. Jiang, P. Guo, H. Li, C. Zeng, S. W. Ng, S. Zhong, *Dalton Trans*. **2018**, 47, 17432-17440

[60] J.-C. G. Bünzli, C. Piguet, *Chem. Soc. Rev*. **2005**, 34, 1048-1077

[61] S. Dang, E. Ma, Z.-M. Sun, H. Zhang, *J. Mater. Chem*. **2012**, 22, 16920-16926

[62] X.-Y. Xu, B. Yan, *ACS Appl*. *Mater*. *Interfaces*. **2015**, 7, 721-729

[63] G.-P. Li, G. Liu, Y.-Z. Li, L. Hou, Y.-Y. Wang, Z. Zhu, *Inorg*. *Chem*. **2016**, 55, 3952-3959

[64] Q. Tang, S. Liu, Y. Liu, J. Miao, S. Li, L. Zhang, Z. Shi, Z. Zheng, *Inorg*. *Chem*. **2013**, 52, 2799-2801

[65] Z. Chen, Y. Sun, L. Zhang, D. Sun, F. Liu, Q. Meng, R. Wang, D. Sun, *Chem*. *Commun*. **2013**, 49, 11557-11559

[66] M. Zheng, H. Tan, Z. Xie, L. Zhang, X. Jing, Z. Sun, *ACS Appl*. *Mater*. *Interfaces*. **2013**, 5, 1078-1083

[67] J.-N. Hao, B. Yan, *J. Mater*. *Chem*. *C*. **2014**, 2, 6758-6764

[68] S. Dang, E. Ma, Z.-M. Sun, H. Zhang, *J. Mater*. *Chem*. **2012**, 22, 16920-16926

[69] Y.-T. Liang, G.-P. Yang, B. Liu, Y.-T. Yan, Z.-P. Xi, Y.-Y. Wang, *Dalton Trans*. **2015**, 44, 13325-13330

[70] Y. Kang, X.-J. Zheng, L.-P. Jin, *J Colloid Interf Sci*. **2016**, 471, 1-6

[71] Y.-P. Wu, G.-W. Xu, W.-W. Dong, J. Zhao, D.-S. Li, J. Zhang, X. Bu, *Inorg*. *Chem*. **2017**, 56, 1402-1411

[72] J. Wang, J. Wang, Y. Li, M. Jiang, L. Zhang, P. Wu, *New*. *J*. *Chem*. **2016**, 40, 8600-8606

[73] R. Pandey, A. Kumar, Q. Xu, D. S. Pandey, *Dalton Trans*. **2020**, 49, 542-568

[74] G. Blasse, B. C. Grabmaier, *Luminescent Materials*. **1994**, Springer-Verlag

[75] X. Li, X.-W. Wang, Y.-H. Zhang, *Inorg. Chem. Commun*. **2008**, 11, 832-834

[76] X. Zhuang, X. Zhang, N. Zhang, Y. Wang, L. Zhao, Q. Yang, *Cryst. Growth Des*. **2019**, 19, 5729-5736

[77] X. Zhang, X. Zhuang, N. Zhang, C. Ge, X. Luo, J. Li, J. Wu, Q. Yang, R. Liua, *CrystEngComm*. **2019**, 21, 1948-1955

[78] X.-D. Duan, F.-Y. Ge, H.-G. Zheng, *Inorg. Chem. Commun*. **2019**, 107, 107479-107484

[79] S. Dong, J. Hu, X. Zhang, M. Zheng, *Inorg*. *Chem. Commun*. **2018**, 97, 180-186

[80] R. Lv, H. Li, J. Su, X. Fu, B. Yang, W. Gu, X. Liu, *Inorg. Chem*. **2017**, 56, 12348−12356

[81] F.-l. Hu, Y.-X. Shi, H.-H. Chen, J.-P. Lang, *Dalton Trans*. **2015**, 44, 18795-18003

[82] A. Lan, K. Li, H. Wu, D. H. Olson, T. J. Emge, W. Ki, M. Hong, J. Li, *Angew. Chem. Int. Ed*. **2009**, 48, 2334-2338

[83] D. K. Singha, P. Majee, S. K. Mondal, P. Mahata, *Eur. J. Inorg. Chem*. **2015**, 1390-1397

[84] H. Li, Y. Han, Z. Shao, N. Li, C. Huang, H. Hou, *Dalton Trans*. **2017**, 46, 12201-12208

[85] Y.-T. Yan, J. Liu, G.-P. Yang, F. Zhang, Y.-K. Fan, W.-Y. Zhang, Y.-Y. Wang, *CrystEngComm*. **2018**, 20, 477-486

[86] M. Karmakar, S. Roy, S. Chattopadhyay, *New. J. Chem*. **2019**, 43, 10093-10102

[87] Q. Zhao, C.-D. Si, *Cryst. Res. Technol*. **2019**, 54, 1800155

[88] H. Li, Y. Han, Z. Shao, N. Li, C. Huang, H. Hou, *Dalton Trans*. **2017**, 46, 12201-12208

[89] Y.-Y. Tang, S. Chen, C.-J. Wang, Z.-X. Zhu, D.-N. Liu, *J. Coord. Chem*. **2018**, 71, 3207-3221

[90] M.-L. Gao, X.-M. Cao, Y.-Y. Zhang, M.-H. Qi, S.-M. Wang, L. Liu, Z.-B. Han, *RSC Adv*. **2017**, 7, 45029-45033

[91] a) A. Dhakshinamoorthy, M. Alvaro, P. Horcajada, E. Gibson, M. Vishnuvarthan, A. Vimont, J.-M. Grenèche, C. Serre, M. Daturi, H. Garcia, *ACS Catal*. **2012**, 2, 2060-2065. b) J. M. Roberts, B. M. Fini, A. A. Sarjeant, O. K. Farha, J. T. Hupp, K. A. Scheidt, *J. Am. Chem. Soc*. **2012**, 134, 3334-3337. c) C. Huang, H. Wang, X. Wang, K. Gao, J. Wu, H. Hou, Y. Fan, *Chem. Eur. J*. **2016**, 22, 6389-6396. d) F. Carson, S. Agrawal, M. Gustafsson, A. Bartoszewicz, F. Moraga, X. Zou, B. Martín-Matute, *Chem. Eur. J*. **2012**, 18, 15337-15344. e) F. Song, C. Wang, J. M. Falkowski, L. Ma, W. Lin, *J. Am. Chem. Soc*. **2010**, 132, 15390-15398. f) L. Ma, X. Wang, D. Deng, F. Luo, B. Ji, J. Zhang, *J. Mater. Chem. A*. **2015**, 3, 20210-20217

[92] M. Yoon, R. Srirambalaji, K. Kim, *Chem. Rev*. **2012**, 112, 1196-1231

[93] G. Dyker, *Handbook of C–H transformations*. **2005**, Wiley-VCH

[94] H.-X. Yuan, Q.-H. Xia, H.-J. Zhan, X.-H. Lu, K.-X. Su, *Appl. Catal. A.* **2006**, 304, 178-184

[95] U. Schuchardt, D. Cardoso, R. Sercheli, R. Pereira, R. S. da Cruz, M. C. Guerreiro, D. Mandelli, E. V. Spinacé, E. L. Pires, *Appl. Catal. A*. **2001**, 211, 1-17

[96] a) Y. Hong, D. Sun, Y. Fang, *Chem. Cent. J*. **2018**, 12, 1-9. b) R. Bechara, D. Balloy, J. Y. Dauphin, J. Grimblot, *Chem. Mater*. **1999**, 11, 1703-1711

[97] J. Lloret, A. Company, L. Gómez, M. Costas, *Alkane C–H activation by single-site metal catalysis*. **2013**, Springer

[98] D. Crich, *Handbook of reagents for organic synthesis. Reagents for radical and radical ion chemistry*. **2008**, Wiley

[99] a) U. Schuchardt, W. A. Carvalho, E. V. Spinacé, *Synlett*. **1993**, 713-718. b) D. H. R. Barton, A. E. Martell, D. T. Sawyer, *The activation of Dioxygen and homogeneous catalytic oxidation*. **1993**, Plenum Press

[100] P. Stavropoulos, R. Çelenligil-Çetin, A. E. Tapper, *Acc. Chem. Res*. **2001**, 34, 745-752

[101] S. Kiani, A. Tapper, R. J. Staples, P. Stavropoulos, *J. Am. Chem. Soc.* **2000**, 122, 7503-7517

[102] M. J. Perkins, *Chem. Soc. Rev.* **1996**, 25, 229-236

[103] P. Comba, M. Maurer,P. Vadivelu, *Inorg. Chem.* **2009**, 48, 10389-10396

[104] Y. Hitomi, K. Arakawa, T. Funabiki, M. Kodera, *Angew. Chem. Int. Ed.* **2012**, 51, 3448-3452

[105] A. Company, L. Gómez, M. Güell, X. Rivas, J. M. Luis, L. Que, Jr., M. Costas, *J. Am. Chem. Soc.* **2007**, 129, 15766-15767

[106] K. Chen, L. Que, Jr. *J. Am. Chem. Soc.* **2001**, 123, 6327-6337

[107] G. Olivo, O. Lanzalunga, L. Mandolini, S. D. Stefano, *J. Org. Chem.* **2013**, 78, 11508-11512

[108] S. Yuan, L. Feng, K. Wang, J. Pang, M. Bosch, C. Lollar, Y. Sun, J. Qin, X. Yang, P. Zhang, Q. Wang, L. Zou, Y. Zhang, L. Zhang, Y. Fang, J. Li, H.-C. Zhou, *Adv. Mater.* **2018**, 30, 1704303

[109] R. G. Pearson, *J. Am. Chem. Soc.* **1963**, 85, 3533-

[110] C. Serre, F. Millange, C. Thouvenot, M. Nogue, G. Marsolier, D. Louër, G. Férey, *J. Am. Chem. Soc.* **2002**, 124, 13519-13526

[111] K. S. Park, Z. Ni, A. P. Côté, J. Y. Choi, R. Huang, F. J. Uribe-Romo, H. K. Chae, M. O'Keeffe, O. M. Yaghi, *PNAS.* **2006**, 103, 10186-10191

[112] W. Zhang, Y. Hu, J. Ge, H.-L. Jiang, S.-H. Yu, *J. Am. Chem. Soc.* **2014**, 136, 16978-16981

[113] C. Yang, U. Kaipa, Q. Z. Mather, X. Wang, V. Nesterov, A. F. Venero, M. A. Omary, *J. Am. Chem. Soc.* **2011**, 133, 18094-18097

[114] S. R. Caskey, A. G. Wong-Foy, A. J. Matzger, *J. Am. Chem. Soc.* **2008**, 130, 10870-10871

[115] E. D. Bloch, L. J. Murray, W. L. Queen, S. Chavan, S. N. Maximoff, J. P. Bigi, R. Krishna, V. K. Peterson, F. Grandjean, G. J. Long, B. Smit, S. Bordiga, C. M. Brown, J. R. Long, *J. Am. Chem. Soc.* **2011**, 133, 14814-14822

[116] M. T. Kapelewski, S. J. Geier, M. R. Hudson, D. Stück, J. A. Mason, J. N. Nelson, D. J. Xiao, Z. Hulvey, E. Gilmour, S. A. FitzGerald, M. Head-Gordon, C. M. Brown, J. R. Long, *J. Am. Chem. Soc*. **2014**, 136, 12119-12129

[117] M. Hmadeh, Z. Lu, Z. Liu, F. Gándara, H. Furukawa, S. Wan, V. Augustyn, R. Chang, L. Liao, F. Zhou, E. Perre, V. Ozolins, K. Suenaga, X. Duan, B. Dunn, Y. Yamamto, O. Terasaki, O. M. Yaghi, *Chem. Mater*. **2012**, 24, 3511-3513

[118] a) N. Zhu, M. J. Lennox, T. Düren, W. Schmitt, *Chem. Commun*. **2014**, 50, 4207-4210. b) J. Cui, Y.-L. Wong, M. Zeller, A. D. Hunter, Z. Xu, *Angew. Chem. Int. Ed*. **2014**, 53, 14438-14442. c) R. J. Marshall, S. L. Griffin, C. Wilson, R. S. Forgan, *Chem. Eur. J*. **2016**, 22, 4870-4877

[119] B. G. Park, M. Pink, D. Lee, *J. Organomet. Chem*. **2011**, 696, 4039-4045

[120] J. J. Kodanko, S. J. Lippard, *Inorg. Chim. Acta*. **2008**, 361, 894-900

[121] J. J. Kodanko, D. Xu, D. Song, S. J. Lippard, *J. Am. Chem. Soc*. **2005**, 127, 16004-16005

[122] R. C. Severance, E. S. Rountree, M. D. Smith, H.-C. z. Loye, *Solid State Sci*. **2012**, 14, 1512-1519

[123] a) B. Matt, J. Moussa, L.-M. Chamoreau, C. Afonso, A. Proust, H. Amouri, G. Izzet, *Organometallics*. **2012**, 31, 35-38. b) B. Matt, X. Xiang, A. L. Kaledin, N. Han, J. Moussa, H. Amouri, S. Alves, C. L. Hill, T. Lian, D. G. Musaev, G. Izzet, A. Proust, *Chem. Sci*. **2013**, 4, 1737-1745. c) Z. Zhang, B. Li, X. Meng, X. Yin, T. Zhang, *Dalton Trans.* **2013**, 42, 4306-4312

[124] Z. Mardani, V. Golsanamlou, Z. Jabbarzadeh, K. Moeini, C. Carpenter-Warren, A. M. Z. Slawin, J. D. Woollins, *J. Korean Chem. Soc*. **2018**, 62, 372-376

Chapter 5: Synthesis and characterisation of rigid ethynyl-bridged polytopic picolinate ligands

This chapter describes the synthesis and characterisation of a novel family of segmented ethynyl-bridged picolinate ligands. These compounds are classified in homopolytopic (**H_2L1**-**H_2L5**) and heteroditopic (**HL6**-**H_2L8**), the latter containing an additional non-chelating functional group like pyridine or benzoate. First of all, an illustration of the molecular structure of each compound is presented. Then, the experimental conditions for the ligand preparation and subsequent characterisation are included. In addition, the reaction mechanism is briefly described.

5.1. Synthesis of rigid ethynyl-bridged polytopic picolinate ligands

As presented in the introduction, the picolinate ligand is a chelating anionic species that is able to coordinate to any kind of metal, providing a versatile scaffold for a wide variety of applications and drawing the attention of the scientific community. Concerning the synthetic methodology, the Sonogashira cross-coupling reaction[1] was applied, in a similar way to that previously used in the construction of polytopic α-diimine ligands.[2] The reaction name arises from the discovery in 1975 by Sonogashira, Tohda and Hagihara that a terminal *sp* hybridised carbon from an alkyne could be coupled with a sp^2 carbon of an aryl or vinyl halide. This process gives rise to the formation of a C–C bond and is catalysed by palladium, originally, Pd^{II} in combination with a co-catalytic amount of Cu^{I} in the presence of an amine.[3] Following this methodology, a family of ligands in which the chelating picolinate subunits are separated by different rigid spacers with variable dimension has been obtained. Within this family of ligands, two different groups can be separated. The first one encompasses segmented homopolytopic ligands that consist of a rigid central arylene platform, ethynylene spacers and terminal chelating picolinate subunits (Figure 5.1, **H_2L1**-**H_2L5**). Whereas the second embraces heteroditopic ligands (Figure 5.2, **HL6**-**H_2L8**) that present picolinate and a second non-chelating pyridine or benzoate functional group.

5.1.1. Synthesis of ligands H_2L1, H_2L3, H_3L4, H_2L5, HL7 and H_2L8

Homopolytopic ligands **H_2L1**, **H_2L3**, **H_3L4** and **H_2L5** and heteroditopic ligands **HL7** and **H_2L8** have been synthesised in a two-step procedure involving a Sonogashira-type cross coupling reaction between the commercially available

5-bromopyridine-2-carboxylate methyl ester (**a**) and several arylacetylenes, followed by basic hydrolysis of the resulting methyl picolinates.

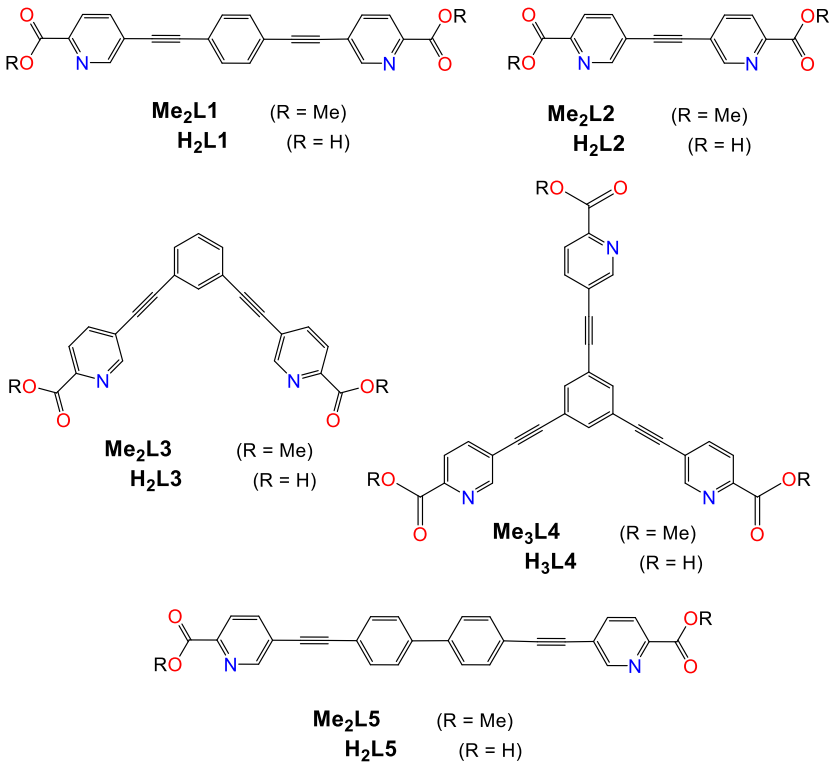

Figure 5.1. Molecular structure of homopolytopic ligands (**H_2L1**-**H_2L5**).

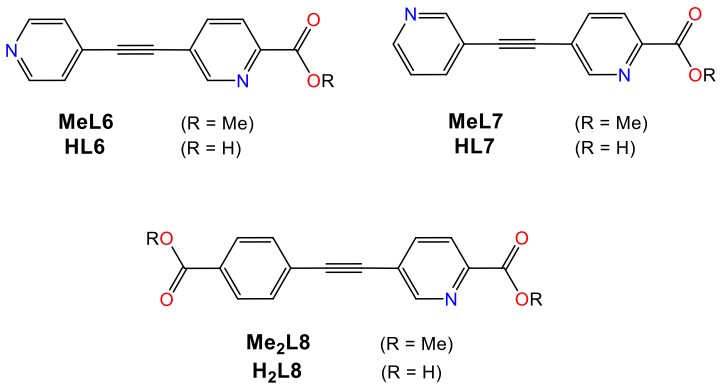

Figure 5.2. Molecular structure of heteroditopic ligands (**HL6**-**H_2L8**).

In a first step, treatment of ester **a** with aromatic compounds that have different terminal acetylenes yielded several aryleneethynylene-bridged polypicolinate esters (**Me_2L1**, **Me_2L3**, **Me_3L4**, **Me_2L5**, **MeL7** and **Me_2L8**). Upon basic hydrolysis and subsequent protonation, ligands **H_2L1**, **H_2L3**, **H_3L4**, **H_2L5, HL7** and **H_2L8** were obtained. These reactions are shown in Scheme 5.1. The cross-coupling reactions take place using $Pd(PPh_3)_4$ as catalyst and NEt_3 as base in THF at 75 °C in an argon atmosphere.

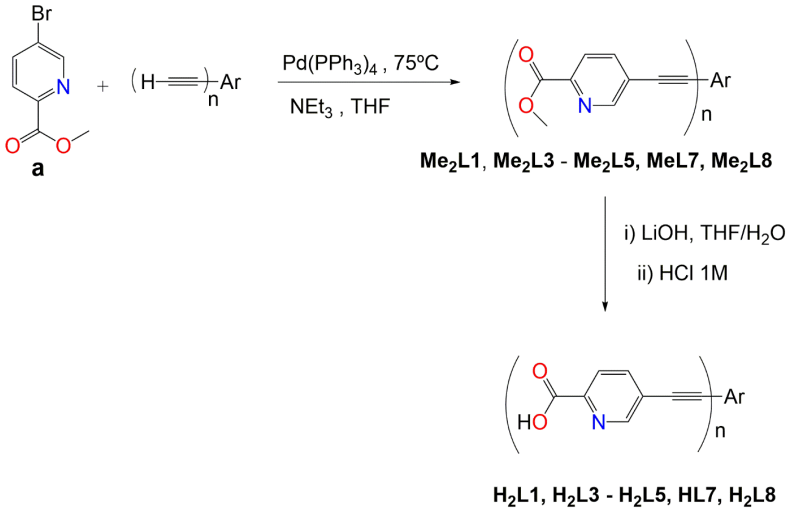

Scheme 5.1. Synthesis of compounds **H_2L1**, **H_2L3**, **H_3L4**, **H_2L5** and **HL7**, **H_2L8** by Pd-catalysed cross-coupling reactions.

Esters obtained can be isolated by filtration in good yields (72-85 %) after 19-48 h of reaction. However, in some cases, column chromatography on silica was used for further purification. The basic hydrolysis is performed using lithium hydroxide in a THF/H_2O (3:1) mixture. After completion of the reaction (3-5 h), THF was evaporated and 1M HCl solution was added to the mixture in order to protonate the different lithium picolinates. The corresponding acids precipitate in this aqueous medium and can be easily and quantitatively isolated by filtration.

5.1.2. Synthesis of ligands H_2L2 and HL6

Initially, ligand **HL6** was attempted to be obtained by direct reaction between the 5-bromopyridine-2-carboxylate methyl ester and 4-ethynyl pyridine, but polymerisation of the second reagent made it impossible. For this reason, as an alternative, we explored the possibility of performing the cross-

coupling reaction inverting the ethynyl and bromide starting reagents, which has proven to be successful. Therefore, ligands **H_2L2** and **HL6** were obtained from the 5-ethynylpicolinate methyl ester (**b**), which is prepared in a two-step procedure involving a Sonogashira-type cross coupling reaction between the 5-bromopyridine-2-carboxylate methyl ester (**a**) and ethynyltrimethylsilane, followed by deprotection with potassium fluoride (Scheme 5.2).

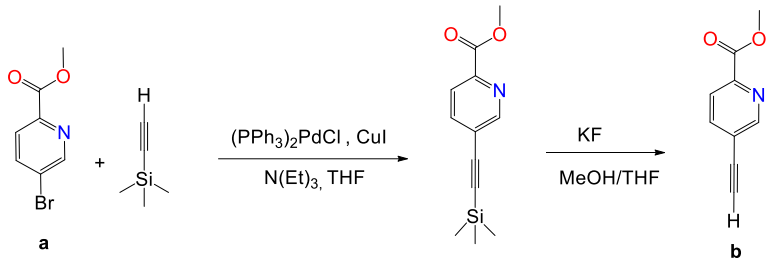

Scheme 5.2. Synthesis of compound **b** by Sonogashira-type cross coupling reaction and subsequent deprotection with KF.

Then, cross-coupling between the ester **b** and 4-bromopyridine or ester **a** gave ester **MeL6** or diester **Me_2L2**, respectively. The corresponding picolinic acids **HL6** and **H_2L2** were obtained by basic hydrolysis and protonation with high yields (78-80%), as shown in Scheme 5.3.

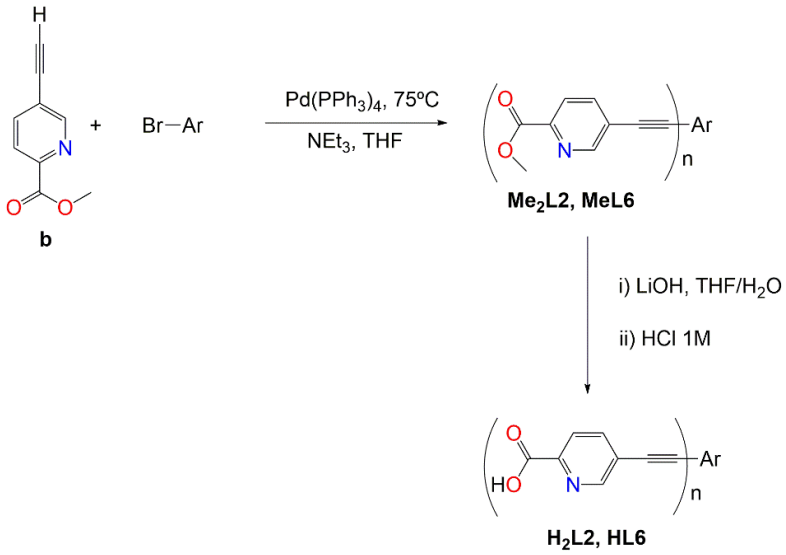

Scheme 5.3. Synthesis of compounds **H_2L2** and **HL6** by Pd-catalysed cross-coupling reactions starting from **b**.

On balance, seven novel picolinate ethynyl-bridged ligands have been prepared. Compound **HL7** was obtained before the development of this thesis from 3-iodopyridine and 5-bromo-2cyanopyridine in two steps.[4] Our synthesis also proceeds in two steps, however, the overall yield has notably been increased from 15.3% to 71%, providing our strategy a much more convenient synthetic approximation.

5.1.3. Mechanism of the synthesis

Despite the thorough study and great success of the Sonogashira cross-coupling reaction, providing a powerful tool for the formation of carbon-carbon bonds, its mechanism still remains unclear. Depending on the use of co-catalysts, two main approaches for Pd-catalysed alkynylations have been developed. The original Sonogashira reaction is based on the use of a Cu(I) salt in addition to the palladium reagent. In this case, a consensus is reached regarding the mechanistic pathway, which involves two coupled catalytic cycles (A and B), as depicted in Figure 5.3.b.[5-6] The real catalyst is thought to be the bis(triphenylphosphine)palladium(0)complex, generated in situ by reduction of different palladium (II) complexes depending on the reaction conditions or by ligand loss of the tetrakis(triphenylphosphine)palladium (0) complex. On the one hand, the Pd^0 reagent experiments oxidative addition of the C(sp^2)–Br bond of aryl bromide species to give a Pd^{II} compound (complex **A**, cycle A). On the other hand, a copper acetylide reagent is generated from the acetylene substrate as shown in cycle B. Then, in a transmetallation process, the bromide ligand is replaced by the acetylene group of the copper acetylide reagent to provide σ-alkynylpalladium(II) species (**B**). The final step involves reductive elimination, in which the acetylene cross-coupling product is released and the Pd^0 reagent is regenerated. Regarding the Cu-free Sonogashira reaction, it is not fully established. The formation of the complex **B** was proposed to take place through reversible π-coordination of the alkyne reagent to the oxidative adduct **A**, instead of a transmetallation step. This would give rise to an intermediate complex **C** and, by deprotonation of the terminal acetylenic proton, **B** would be obtained (Figure 5.3.c).[7] However, it has not been possible to validate and answer several questions concerning this currently accepted model. Recently, it has been proposed that the Cu-free Sonogashira reaction proceeds through a tandem Pd/Pd mechanism involving two catalytic cycles (shown in Figure 5.3.d). This mechanism is analogous to the Pd/Cu pathway, replacing the major role of the copper co-catalyst by a Pd complex. Experimental evidence and computational investigations support the existence of this palladium-palladium trasmetallation.[8]

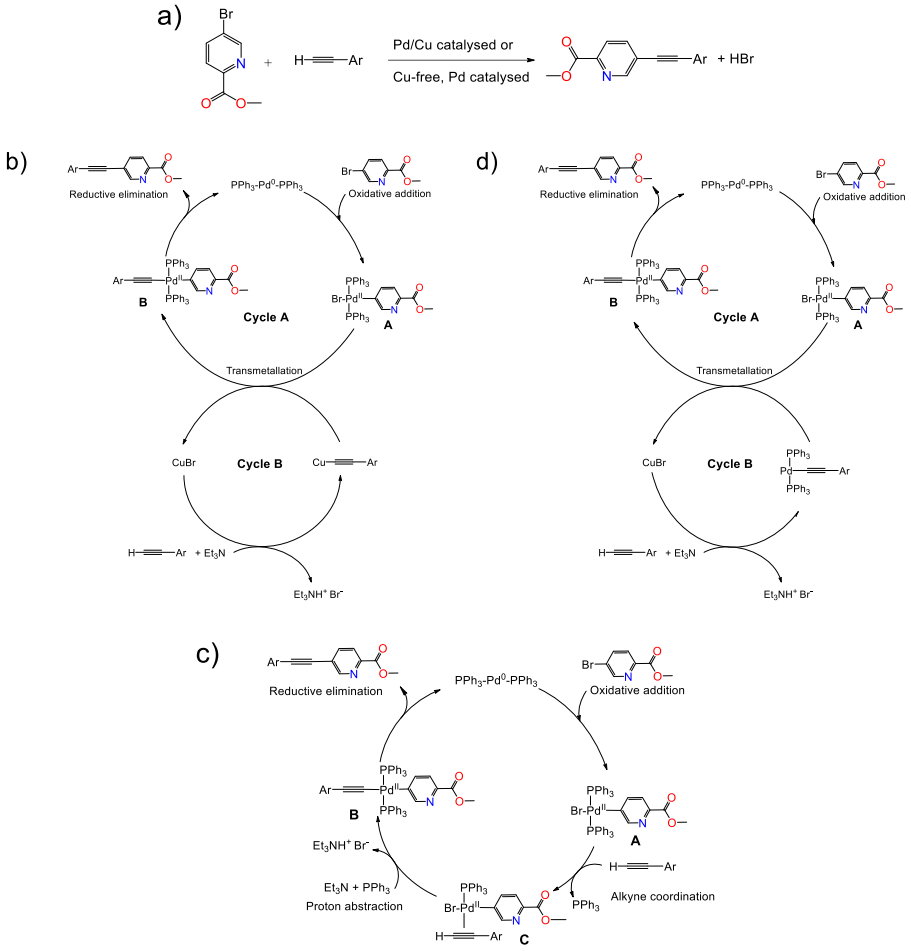

Figure 5.3. a) General representation of Sonogashira reaction for the synthesis of ethynyl-bridged polytopic picolinate esters. b) Textbook mechanism for Pd/Cu catalysed Sonogashira cross-coupling reaction. c) Textbook mechanism for Cu-free Sonogashira reaction. d) Novel mechanistic pathway proposed for Cu-free Sonogashira reaction.[8]

A schematic representation of the synthetic mechanism for obtaining the acidic derivatives is shown in Figure 5.4. The methodology is based on the well-known nucleophilic acyl substitution.[9] The first step involves basic hydrolysis of the synthesised esters using lithium hydroxide that acts as a nucleophile attacking the carbonyl carbon. Then, loss of the methoxide leaving group (CH_3O^-) takes place and a very fast acid/base reaction where the CH_3O^- deprotonates the carboxylic acid leading to the formation of the corresponding lithium salt. Finally, protonation with HCl affords the desired products.

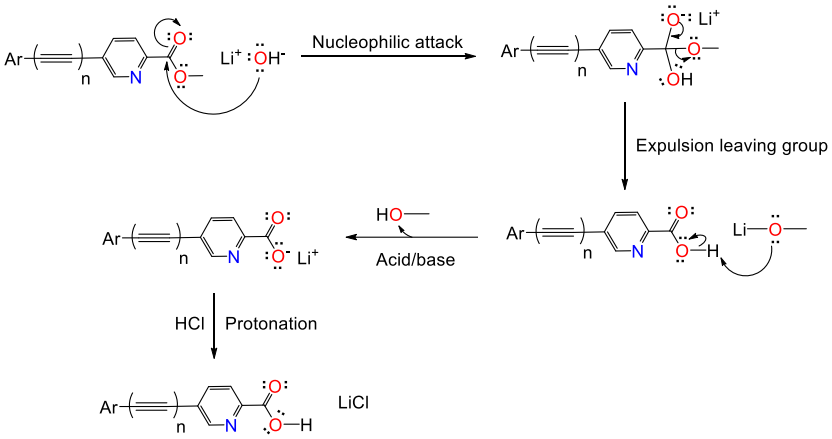

Figure 5.4. General mechanism for the synthesis of the acid ligands.

5.2. Conclusions and future prospects

Sonogashira-type cross-coupling reactions have been successfully applied for the synthesis of polytopic ligands that contain a rigid central arylene platform, ethynylene spacers and terminal chelating picolinate subunits. In all the reactions developed, the yields achieved are very high and ligands **H_2L1**-**H_2L8** have been isolated as pure compounds. All the members of this new family of ligands are potential organic linkers for the development of robust coordination polymers (CPs). In chapter 6, the exploitation of these ligands in the field of coordination chemistry with divalent metal transition ions will be addressed. Next, chapter 7 will focus on the synthesis, characterisation and applications of lanthanide coordination complexes containing ethynyl-bridged picolinate ligands.

5.3. Experimental part. Characterisation of ligands

The progress of the reactions was monitored, in all cases, by thin-layer chromatography (TLC). Elemental analyses of the percentage in weight of C, N and H were carried out for all the synthesised compounds. Three independent measurements were conducted which were consistent between them and the best experimental result is included in the following description, together with the calculated values. Also, the infrared spectra of all the ligands were registered, as well as the electrospray ionisation time-of-flight (ESI-TOF) mass spectra and the nuclear magnetic resonance spectra (*vide infra*).

Dimethyl 5,5'-(1,4-phenylenebis(ethyne-2,1-diyl))dipicolinate, Me_2L1

Methyl 5-bromopicolinate (216 mg, 1 mmol) and 1,4-diethynylbenzene (60 mg, 0.48 mmol) were introduced in a Schlenk flask containing 8 mL of dry degassed THF. $Pd(PPh_3)_4$ (38 mg, 0.033 mmol) and NEt_3 (0.2 mL, 1.435 mmol) were then added and the reaction mixture was stirred for 10 h. The precipitate was filtered and washed with water and methanol to afford 162 mg of **Me_2L1** as a pale yellow solid. Yield: 85%. Scheme 5.4 shows the corresponding reaction. Data for **Me_2L1**: Anal. Calcd for $C_{24}H_{16}N_2O_4 \cdot 0.15H_2O$: C, 72.23; H, 4.12; N, 7.02. Found: C, 72.08; H, 3.95; N, 6.96. ^{1}H-NMR (CD_2Cl_2): δ = 8.85 (dd, ^4J = 1.8Hz, ^5J = 0.9Hz, 2H), 8.11 (dd, ^3J = 8.1Hz, ^5J = 0.6Hz, 2H), 7.98 (dd, ^3J = 8.1Hz, ^4J = 2.1Hz, 2H), 7.61 (s, 4H), 3.97 (s, 6H) ppm. ^{13}C-NMR ($CDCl_3$): δ = 165.39, 152.28, 146.57, 139.50, 132.05, 124.73, 123.78, 123.06, 95.07, 87.86, 53.33 ppm. ESI-TOF MS: m/z 397.12 and 419.10, attributed to $[M+H]^+$ and $[M+Na]^+$, respectively. Selected IR (KBr, cm^{-1}): 1716.3, 1440.1, 1404.0, 1366.3, 1317.4, 1236.4, 1135.9, 1116.3, 1016.2, 957.9, 866.6, 829.0, 819.7, 793.7, 698.2. ^{1}H- and ^{13}C-NMR, IR and MS spectra are included in Figures 5.5-5.8, respectively.

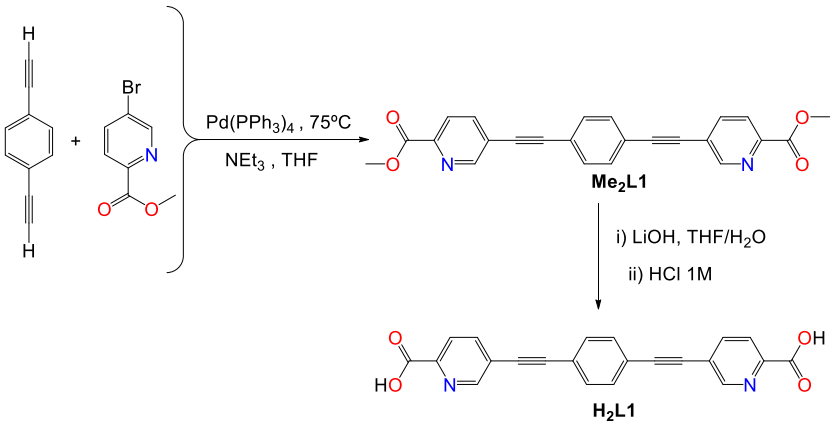

Scheme 5.4. Synthesis of compounds **Me_2L1** and **H_2L1** by Pd-catalysed cross-coupling reaction and subsequent basic hydrolysis.

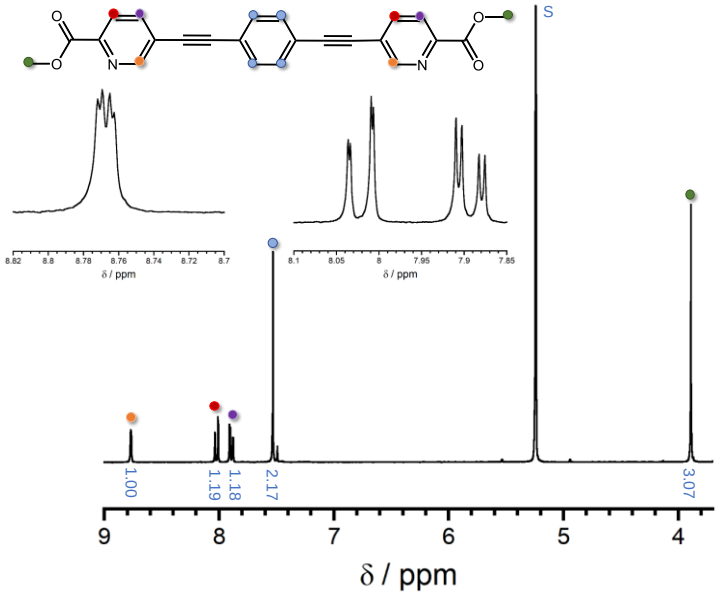

Figure 5.5. ^{1}H-NMR spectrum of compound **Me$_2$L1**. Values in blue refer to the integration of signals and S to solvent.

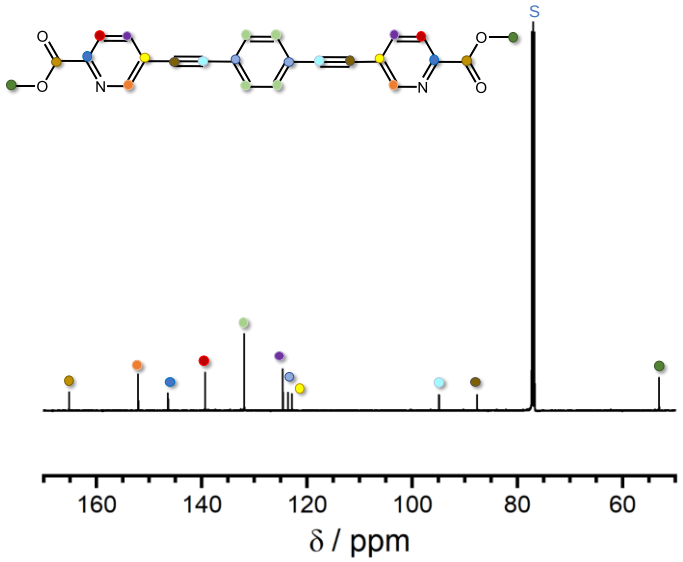

Figure 5.6. ^{13}C-NMR spectrum of compound **Me$_2$L1**. S refers to solvent.

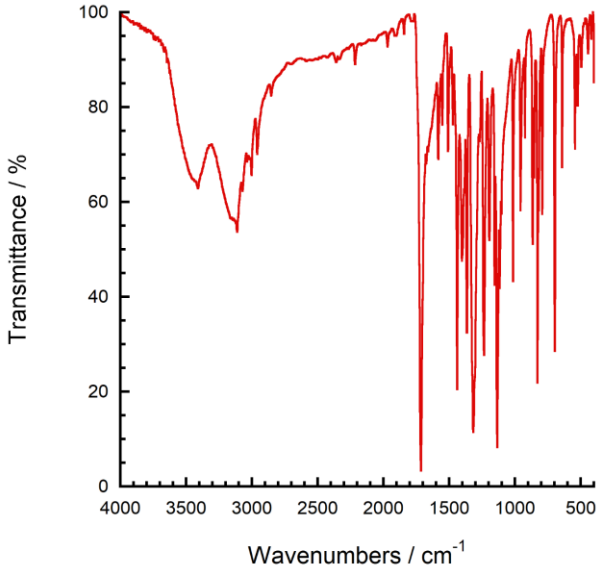

Figure 5.7. Infrared spectrum of **Me_2L1** in a KBr pellet.

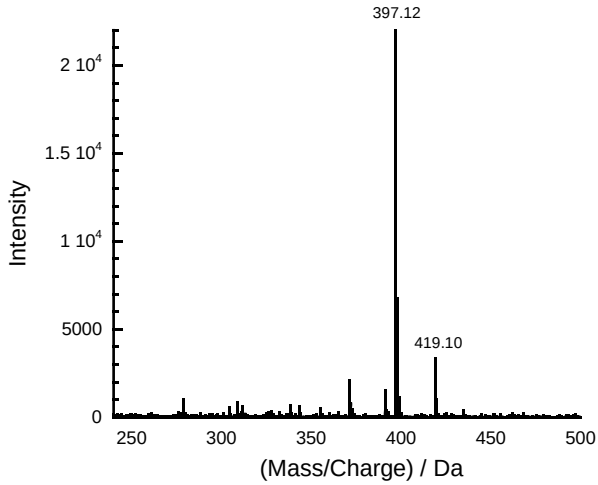

Figure 5.8. ESI-TOF mass spectrum of **Me_2L1** showing $[M+H]^+$ and $[M+Na]^+$ at 397.12 and 419.10 m/z, respectively.

5,5'-(1,4-phenylenebis(ethyne-2,1-diyl))dipicolinic acid, H_2L1

Me_2L1 (101 mg, 0.25 mmol) was suspended in 20 mL of a THF/H_2O (3/1) mixture. $LiOH{\cdot}H_2O$ (21 mg, 0.5 mmol) was added and the suspension was stirred for 5 h. Then, THF was evaporated and the pH of the resulting aqueous suspension was adjusted to 2.70 using 1M HCl. The slightly yellow solid was filtered, washed with cold water and dried under vacuum (Scheme 5.4). Yield: 96 % (88 mg). Data for **H_2L1**: Anal. Calcd for $C_{22}H_{12}N_2O_4{\cdot}1.1LiCl$: C, 63.68; H, 2.91; N, 6.75. Found: C, 63.60; H, 3.09; N, 6.58. ESI-TOF MS: m/z 367.07 $[M–H]^-$. Selected IR (KBr, cm^{-1}): 3454.0, 1691.3, 1317.6, 1241.7, 844.4, 793.7, 698.5. Infrared and ESI-TOF mass spectra are shown in Figures 5.9 and 5.10. The corresponding picolinic acid was insoluble in all common solvents and its NMR spectra could not be recorded.

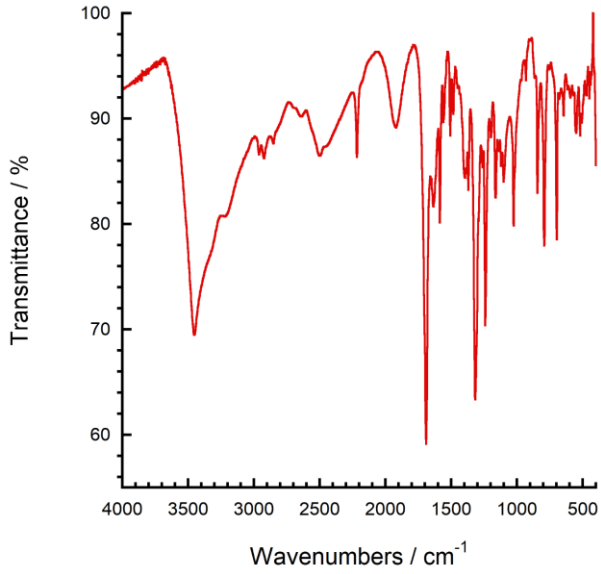

Figure 5.9. Infrared spectrum of **H_2L1** in a KBr pellet.

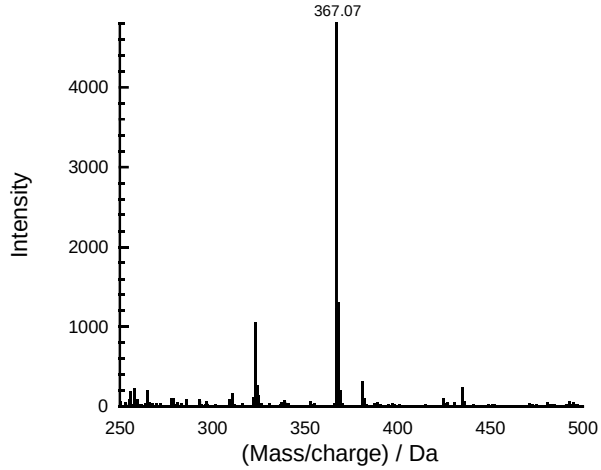

Figure 5.10. ESI-TOF mass spectrum of **H_2L1** showing $[M-H]^-$ at 367.07 m/z.

Dimethyl 5,5'-(ethyne-1,2-diyl)dipicolinate, Me_2L2

Methyl 5-ethynylpicolinate (173.5 mg, 1.08 mmol) and methyl 5-bromopicolinate (233 mg, 1.08 mmol) were introduced in a Schlenk flask containing 8 mL of dry degassed THF. $Pd(PPh_3)_4$ (38 mg, 0.033 mmol) and NEt_3 (0.4 mL, 2.87 mmol) were then added and the reaction mixture was stirred for 41 h. The yellow suspension was concentrated to dryness and the crude product was purified by flash column chromatography (7% MeOH in CH_2Cl_2) to afford 254 mg of **Me_2L2** as a white solid. Yield: 80%. Scheme 5.5 shows the corresponding reaction.

Data for **Me_2L2**: Anal. Calcd for $C_{16}H_{12}N_2O_4$: C, 64.86; H, 4.08; N, 9.46. Found: C, 64.67; H, 4.09; N, 9.52. ^{1}H-NMR ($CDCl_3$): δ = 8.86 (dd, ^4J = 2.08 Hz, ^5J = 0.82 Hz, 2H), 8.13 (dd, ^3J = 8.14 Hz, ^5J = 0.85 Hz, 2H), 7.97 (dd, ^3J = 8.14 Hz, ^4J = 2.09 Hz, 2H), 3.99 (s, 6H) ppm. ^{13}C-NMR ($CDCl_3$): δ = 165.48, 152.65, 147.52, 140.26, 124.99, 123.25, 91.60, 53.83 ppm. ESI-TOF MS: m/z 318.9 $[M+Na]^+$. Selected IR (KBr, cm^{-1}): 3411.3, 1716.4, 1441.0, 1370.6, 1330.4, 1321.6, 1305.6, 1239.6, 1197.8, 1137.8, 1018.2, 958.8, 866.0, 794.4, 698.1. ^{1}H- and ^{13}C-NMR, IR and MS spectra are included in Figures 5.11-5.14, respectively.

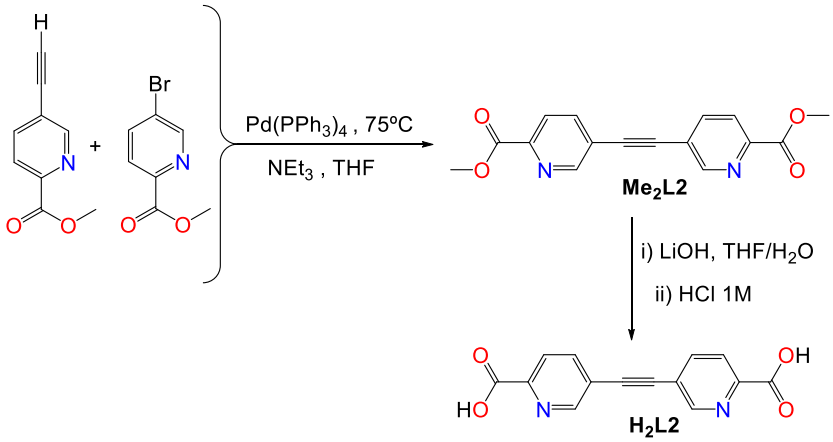

Scheme 5.5. Synthesis of compounds **Me_2L2** and **H_2L2** by Pd-catalysed cross-coupling reaction and subsequent basic hydrolysis.

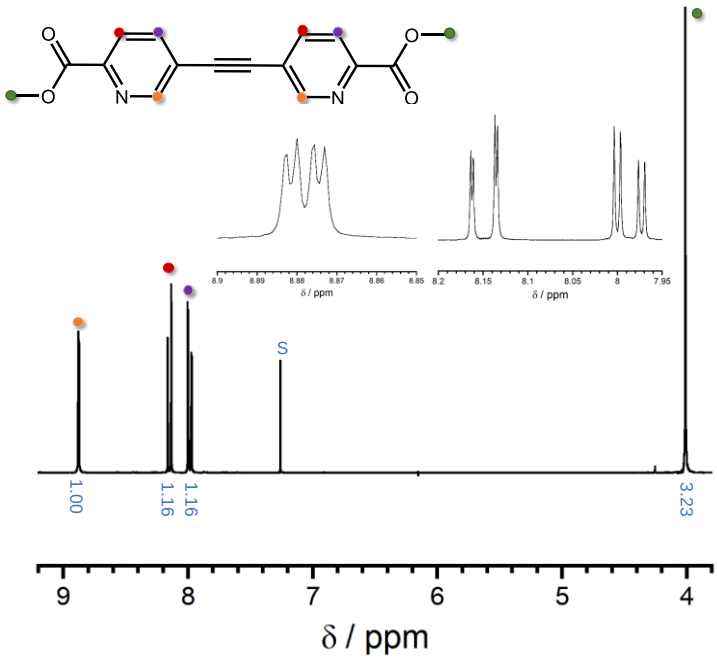

Figure 5.11. ^{1}H-NMR spectrum of compound **Me_2L2**. Values in blue refer to the integration of signals and S to solvent.

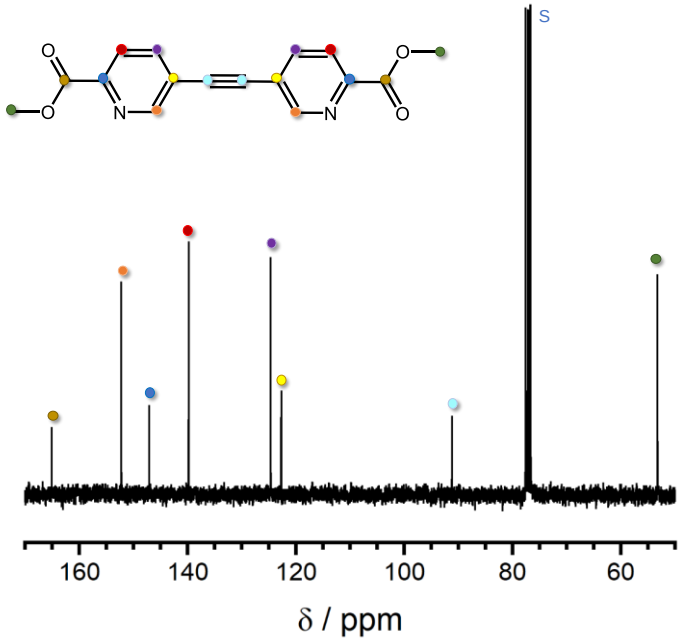

Figure 5.12. ^{13}C-NMR spectrum of compound **Me$_2$L2**. S refers to solvent.

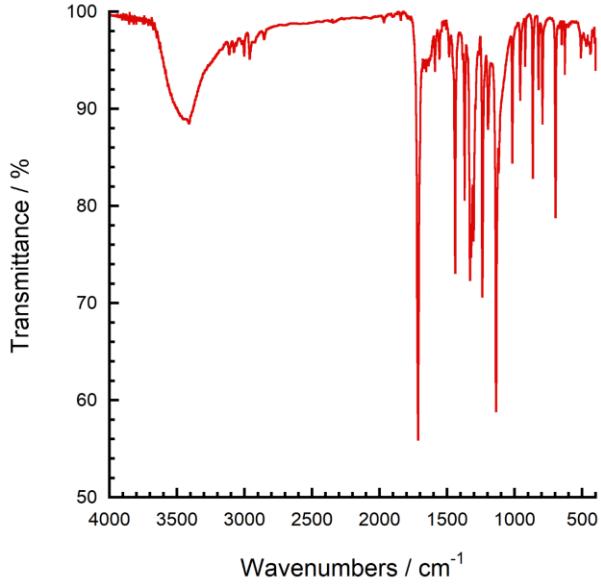

Figure 5.13. Infrared spectrum of **Me$_2$L2** in a KBr pellet.

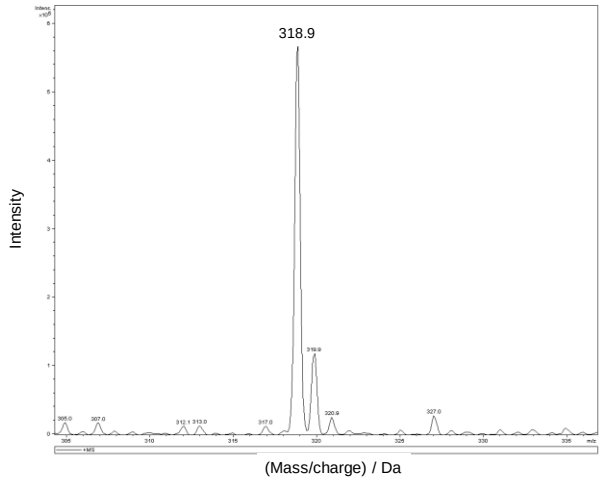

Figure 5.14. ESI-TOF mass spectrum of **Me_2L2** showing $[M+Na]^+$ at 318.9 m/z.

5,5'-(ethyne-1,2-diyl)dipicolinic acid, H_2L2

Me_2L2 (178 mg, 0.6 mmol) was suspended in 23 mL of a THF/H_2O (2/1) mixture. $LiOH{\cdot}H_2O$ (50 mg, 1.2 mmol) was added and the suspension was stirred for 4 h. Then, THF was evaporated and the pH was adjusted to 3.48 using 1M HCl. The white solid was filtered, washed with cold water and dried under vacuum (Scheme 5.5). Yield: 93 % (152 mg).

Data for **H_2L2**: Anal. Calcd for $C_{14}H_8N_2O_4{\cdot}2H_2O$: C, 55.27; H, 3.98; N, 9,21. Found: C, 55.17; H, 3.91; N, 9.19. ^{1}H-NMR (D_2O/KOH): δ = 8.77 (dd, ^4J = 2.08 Hz, ^5J = 0.82 Hz, 2H), 8.12 (dd, ^3J = 8.14 Hz, ^5J = 0.85 Hz, 2H), 7.96 (dd, ^3J = 8.14 Hz, ^4J = 2.09 Hz, 2H) ppm. ^{13}C-NMR (D_2O/KOH): δ = 172.58, 152.82, 151.14, 140.75, 123.53, 121.21, 90.24 ppm. ESI-TOF MS: m/z 291.1 $[M+Na]^+$. Selected IR (KBr, cm^{-1}): 3461.3, 1691.9, 1322.6, 1306.4, 1241.0, 1027.0, 788.6, 698.1. ^{1}H- and ^{13}C-NMR, IR and MS spectra are included in Figures 5.15-5.18, respectively.

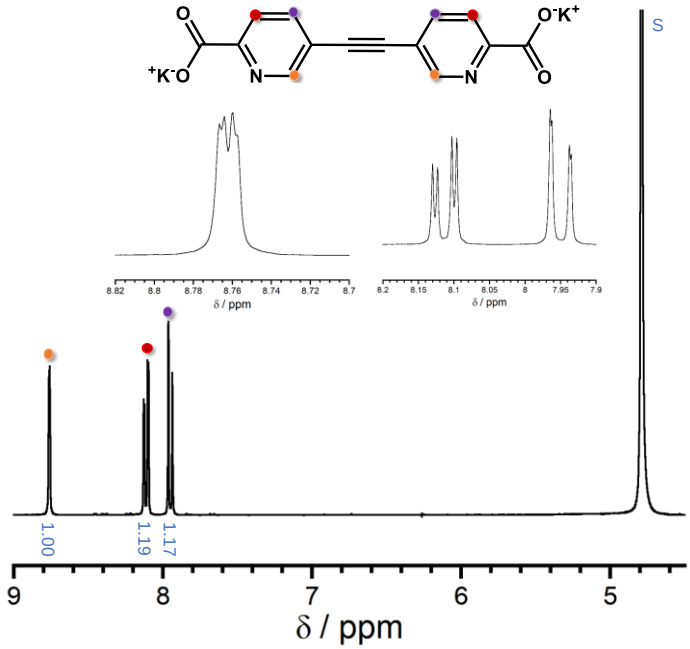

Figure 5.15. ^{1}H-NMR spectrum of compound **H_2L2** as a potassium salt. Values in blue refer to the integration of signals and S to solvent.

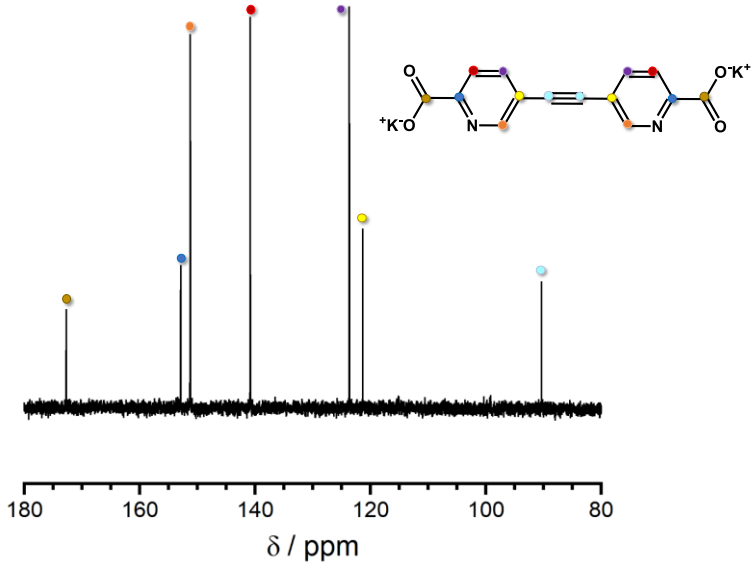

Figure 5.16. ^{13}C-NMR spectrum of compound **H_2L2** as a potassium salt.

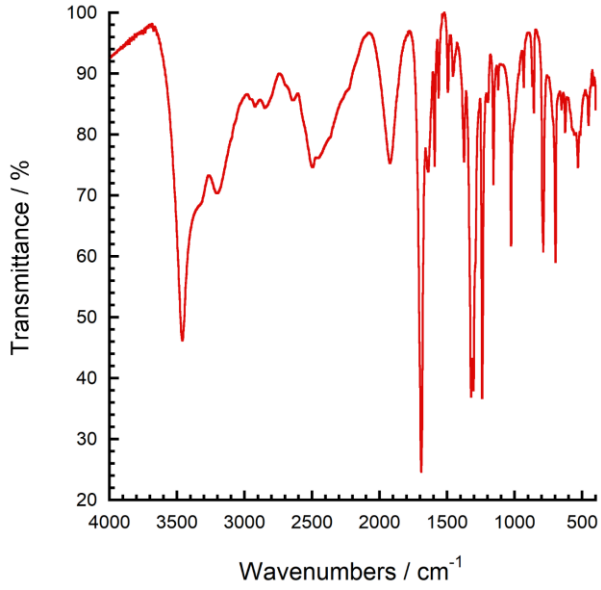

Figure 5.17. Infrared spectrum of **H_2L2** in a KBr pellet.

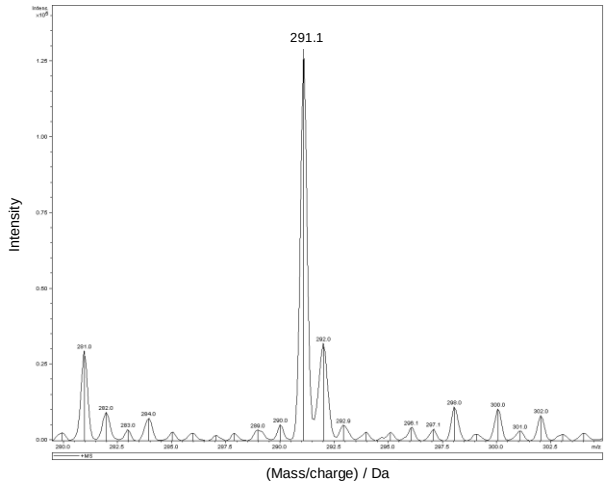

Figure 5.18. ESI-TOF mass spectrum of **H_2L2** showing $[M+Na]^+$ at 291.1 m/z.

Dimethyl 5,5'-(1,3-phenylenebis(ethyne-2,1-diyl))dipicolinate, Me_2L3

Methyl 5-bromopicolinate (216 mg, 1 mmol) and 1,3-diethynylbenzene (57 mg, 0.45 mmol) were introduced in a Schlenk flask containing 8 mL of dry degassed THF. $Pd(PPh_3)_4$ (38 mg, 0.033 mmol) and NEt_3 (0.2 mL, 1.435 mmol) were then

added and the reaction mixture was stirred for 24 h. The precipitate was filtered and washed with water and methanol to afford 128 mg of **Me_2L3** as a white solid. Yield: 72%. Scheme 5.6 shows the corresponding reaction.

Data for **Me_2L3**: Anal. Calcd for $C_{24}H_{16}N_2O_4$: C, 72.72; H, 4.07; N, 7.07. Found: C, 72.58; H, 4.02; N, 6.93. ^{1}H-NMR ($CDCl_3$): δ = 8.84 (dd, ^4J = 2.018Hz, ^5J = 0.786 Hz, 2H), 8.12 (dd, ^3J = 8.115 Hz, ^5J = 0.798 Hz, 2H), 7.93 (dd, ^3J = 8.117 Hz, ^4J = 2.077 Hz, 2H), 7.77 (t, J = 1.35 Hz, 1H), 7.56 (dd, ^3J = 7.737 Hz, ^4J = 1.56 Hz, 2H), 7.40 (t, J = 7.772 Hz, 1H), 4.00 (s, 6H) ppm. ^{13}C-NMR ($CDCl_3$): δ = 165.38, 152.23, 146.53, 139.56, 135.16, 132.59, 129.10, 124.77, 123.70, 122.84, 94.47, 86.45, 53.27 ppm. ESI-TOF MS: m/z 397.12 $[M+H]^+$. Selected IR (KBr, cm^{-1}): 3113.7, 1716.2, 1438.6, 1400.8, 1367.5, 1314.9, 1237.6, 1195.4, 1136.5, 1016.0, 867.3, 801.5, 698.3, 685.3. ^{1}H- and ^{13}C-NMR, IR and MS spectra are included in Figures 5.19-5.22, respectively.

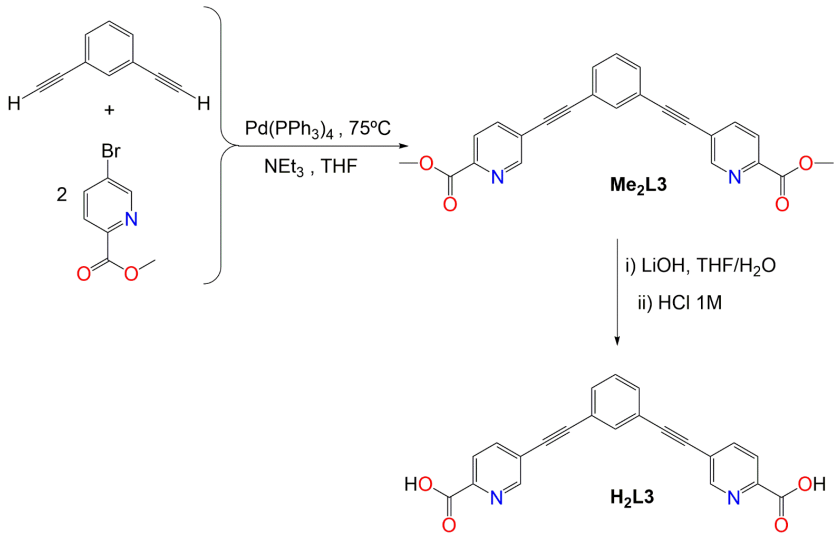

Scheme 5.6. Synthesis of compounds **Me_2L3** and **H_2L3** by Pd-catalysed cross-coupling reaction and subsequent basic hydrolysis.

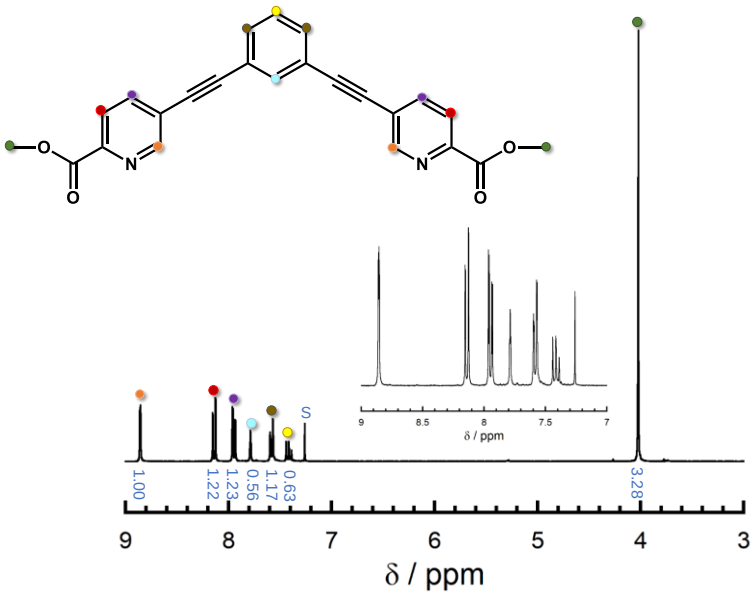

Figure 5.19. ^{1}H-NMR spectrum of compound **Me$_2$L3**. Values in blue refer to the integration of signals and S to solvent.

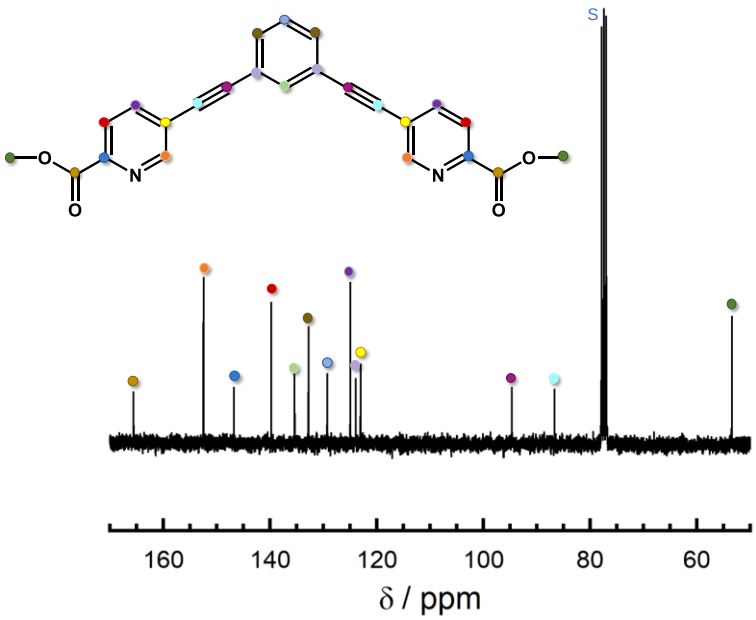

Figure 5.20. ^{13}C-NMR spectrum of compound **Me$_2$L3**. S refers to solvent.

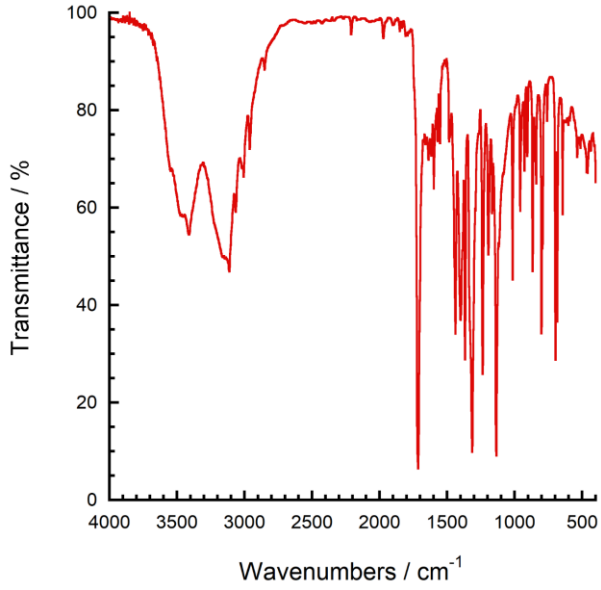

Figure 5.21. Infrared spectrum of **Me_2L3** in a KBr pellet.

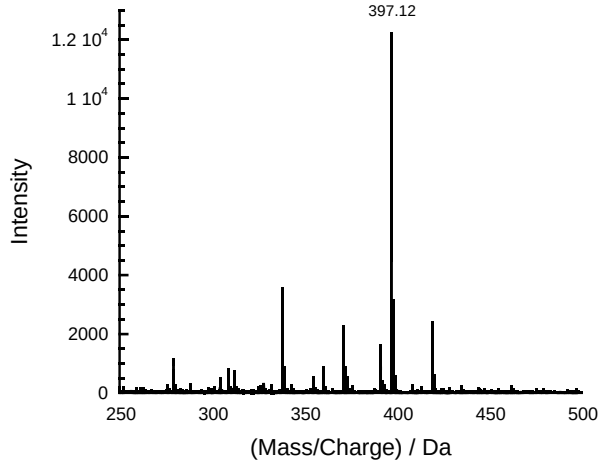

Figure 5.22. ESI-TOF mass spectrum of **Me_2L3** showing $[M+H]^+$ at 397.12 m/z.

5,5'-(1,3-phenylenebis(ethyne-2,1-diyl))dipicolinic acid, H_2L3

Me_2L3 (101 mg, 0.25 mmol) was suspended in 20 mL of a THF/H_2O (3/1) mixture. LiOH·H_2O (21 mg, 0.5 mmol) was added and the suspension was stirred for 75 min. Then, THF was evaporated and the pH of the resulting aqueous

suspension was adjusted to 3.21 using 1M HCl. The white precipitate was filtered, washed with cold water and dried under vacuum (Scheme 5.6). Yield: 96% (88 mg).

Data for **H_2L3**: Anal. Calcd for $C_{22}H_{12}N_2O_4 \cdot 0.95H_2O$: C, 68.55; H, 3.63; N, 7.27. Found: C, 68.39; H, 3.39; N, 7.19. ^{1}H-NMR (CD_3CN/TBAOH): δ = 8.91 (dd, ^4J = 2.08 Hz, ^5J = 0.8 Hz, 2H), 8.15 (dd, ^3J = 8.05 Hz, ^5J = 0.83 Hz, 2H), 8.06 (dd, ^3J = 8.06 Hz, ^4J = 2.13 Hz, 2H), 7.97 (t, ^4J = 1.365 Hz, 1H), 7.81 (dd, ^3J = 7.4 Hz, ^4J = 1.62 Hz, 2H), 7.67 (t, ^3J = 7.75 Hz, 1H) ppm. ^{13}C-NMR (CD_3CN/TBAOH): δ = 150.36, 138.03, 133.81, 131.47, 128.88, 122.68 ppm (only CH carbon atoms are observed). ESI-TOF MS: m/z 367.07 $[M-H]^-$. Selected IR (KBr, cm^{-1}): 3046.3, 1698.0, 1313.8, 799.5, 685.1. ^{1}H- and ^{13}C-NMR, IR and MS spectra are included in Figures 5.23-5.26, respectively.

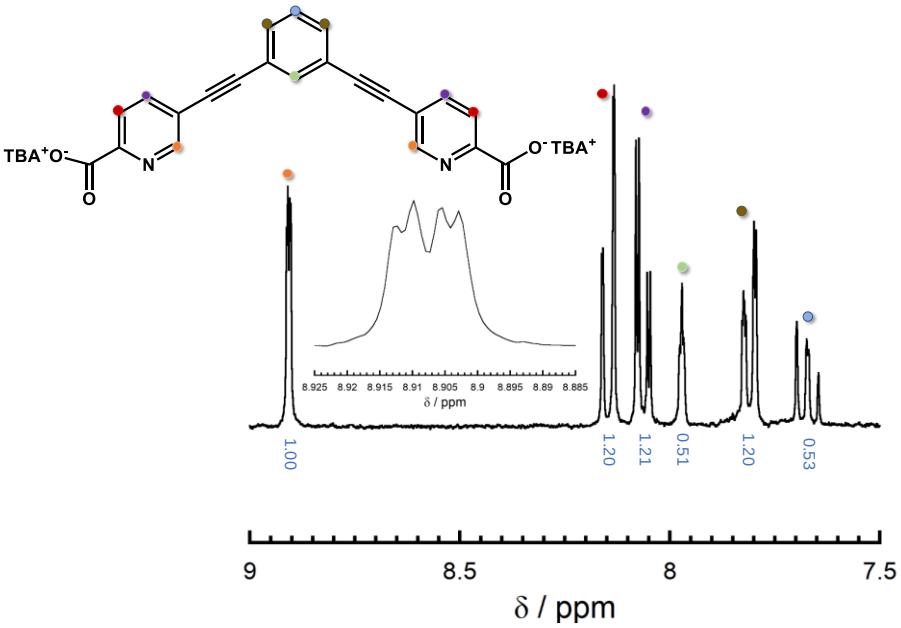

Figure 5.23. ^{1}H-NMR spectrum of compound **H_2L3** as a tetrabutylammonium salt. Values in blue refer to the integration of signals.

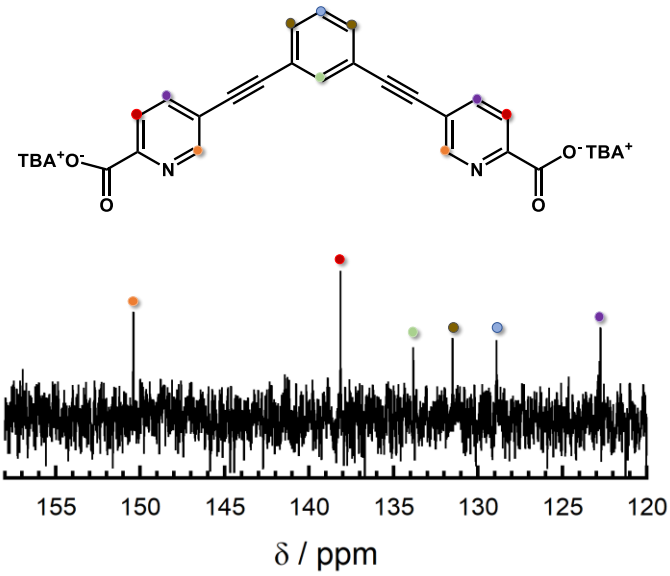

Figure 5.24. ^{13}C-NMR spectrum of compound **H_2L3** as a tetrabutylammonium salt.

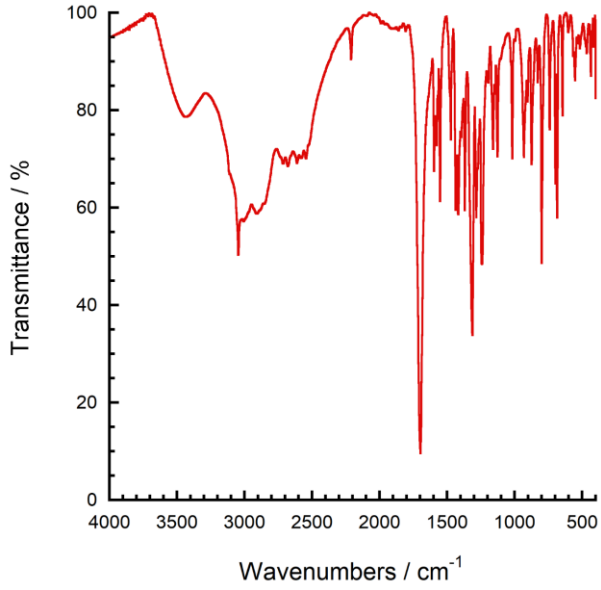

Figure 5.25. Infrared spectrum of **H_2L3** in a KBr pellet.

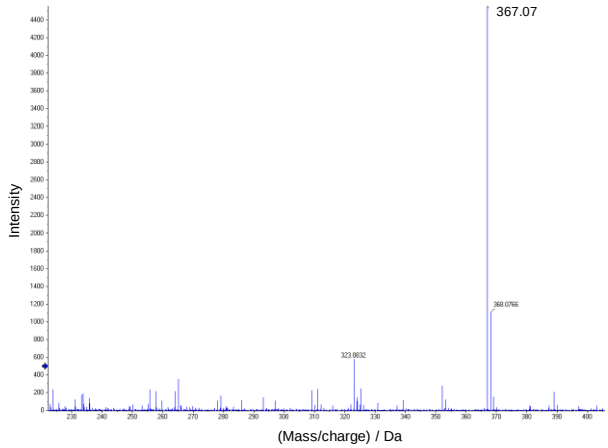

Figure 5.26. ESI-TOF mass spectrum of **H_2L3** showing $[M-H]^-$ at 367.07 m/z.

Trimethyl 5,5',5''-(benzene-1,3,5-triyltris(ethyne-2,1-diyl))tripicolinate, Me_3L4

Methyl 5-bromopicolinate (216 mg, 1 mmol) and 1,3,5-triethynylbenzene (45 mg, 0.3 mmol) were introduced in a Schlenk flask containing 8 mL of dry degassed THF. $Pd(PPh_3)_4$ (38 mg, 0.033 mmol) and NEt_3 (0.4 mL, 2.87 mmol) were then added and the reaction mixture was stirred for 28 h. The precipitate was filtered and washed with water and methanol to afford 124.8 mg of **Me_3L4** as a beige solid. Yield: 75%. Scheme 5.7 shows the corresponding reaction.

Data for **Me_3L4**: Anal. Calcd for $C_{33}H_{21}N_3O_6 \cdot 0.8H_2O$: C, 69.54; H, 4.00; N, 7.37. Found: C, 69.29; H, 3.73; N, 7.30. ^{1}H-NMR ($CDCl_3$): δ = 8.84 (dd, ^4J = 2.054 Hz, ^5J = 0.706 Hz, 3H), 8.13 (dd, ^3J = 8.118 Hz, ^4J = 0.716 Hz, 3H), 7.93 (dd, ^3J = 8.109 Hz, ^4J = 2.082 Hz, 3H), 7.76 (s, 3H), 4.00 (s, 9H) ppm. ^{13}C-NMR ($CDCl_3$): δ = 165.30, 152.26, 146.83, 139.67, 135.32, 124.77, 123.56, 123.32, 93.26, 87.28, 53.29 ppm. ESI-TOF MS: m/z 556.15, 578.13 attributed to $[M+H]^+$ and $[M+Na]^+$. Selected IR (KBr, cm^{-1}): 1742.0, 1721.0, 1588.7, 1435.5, 1311.8, 1278.4, 1234.1, 1194.1, 1135.5, 1115.5, 1022.9, 700.1. ^{1}H- and ^{13}C-NMR, IR and MS spectra are included in Figures 5.27-5.30, respectively.

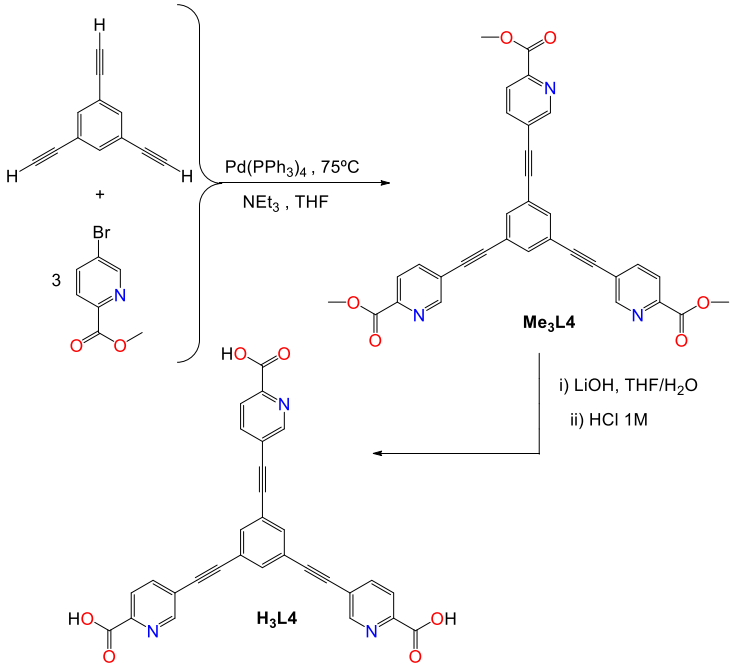

Scheme 5.7. Synthesis of compounds **Me_3L4** and **H_3L4** by Pd-catalysed cross-coupling reaction and subsequent basic hydrolysis.

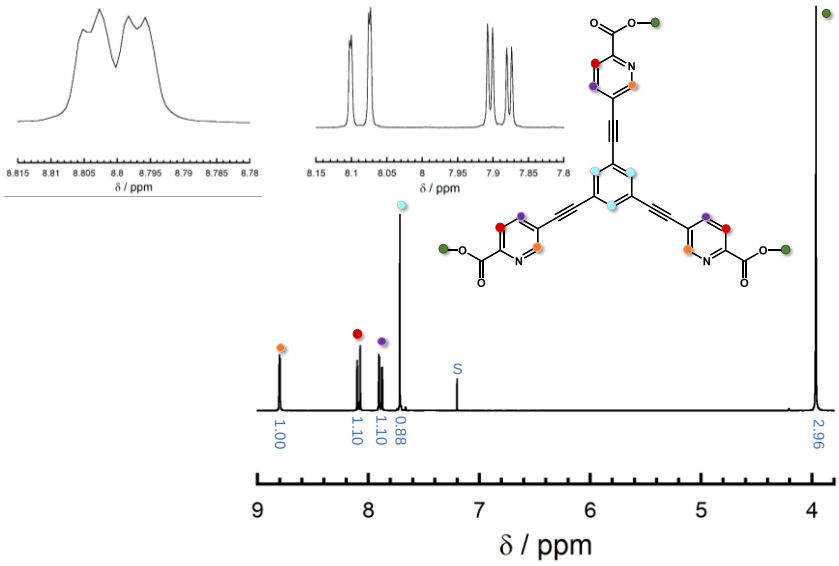

Figure 5.27. ^{1}H-NMR spectrum of compound **Me_3L4**. Values in blue refer to the integration of signals and S to solvent.

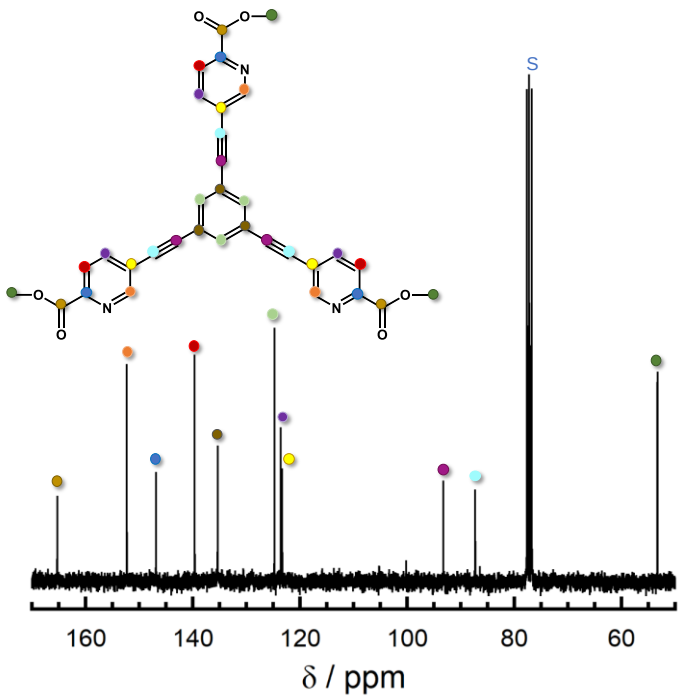

Figure 5.28. ^{13}C-NMR spectrum of compound **Me$_3$L4**. S refers to solvent.

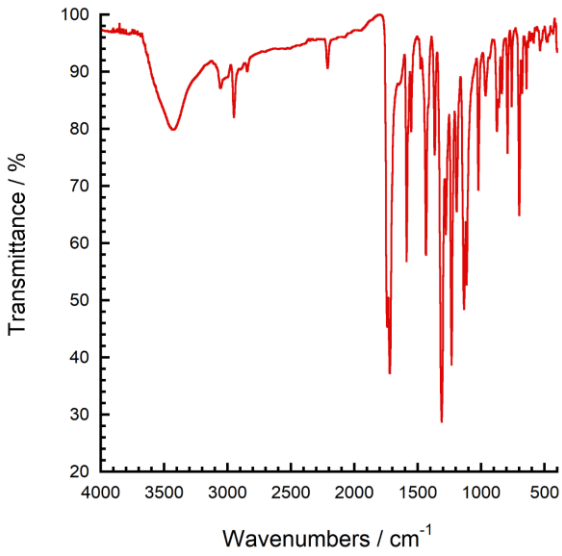

Figure 5.29. Infrared spectrum of **Me$_3$L4** in a KBr pellet.

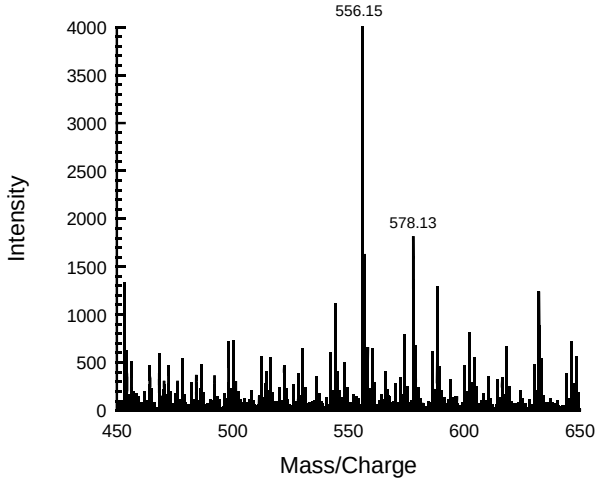

Figure 5.30. ESI-TOF mass spectrum of **Me_3L4** showing $[M+H]^+$ and $[M+Na]^+$ at 556.15 and 578.13 m/z, respectively.

5,5',5''-(benzene-1,3,5-triyltris(ethyne-2,1-diyl))tripicolinic acid, H_3L4

Me_3L4 (101 mg, 0.18 mmol) was suspended in 20 mL of a THF/H_2O (3/1) mixture. After addition of LiOH·H_2O (23 mg, 0.54 mmol), the initial solid dissolved and a reprecipitation was observed. After stirring for 2 h, THF was evaporated and the pH of the resulting aqueous suspension was adjusted to 2.65 using 1M HCl. The beige precipitate was filtered, washed with cold water and dried under vacuum (Scheme 5.7). Yield: 91% (84 mg).

Data for **H_3L4**: Anal. Calcd for $C_{30}H_{15}N_3O_6$·0.15 LiCl·2.0 H_2O: C, 64.82; H, 3.45; N, 7.56. Found: C, 64.98; H, 3.38; N, 7.38. MALDI-TOF: m/z 514.07 $[M + H]^+$. Selected IR (KBr, cm^{-1}): 1708.3, 1637.7, 1590.4, 1372.8, 1360.1, 1283.4, 1233.1, 1148.7, 1120.2. As the corresponding picolinic acid was insoluble in all common solvents, its NMR spectra could not be recorded and ESI-TOF mass spectra was not successful. Instead, the sample was mixed with a matrix (CHCA: α-cyano-4-hydroxycinnamic acid, Bruker) in solid[10] and the resulting mixture was analysed in a MALDI-TOF (matrix-assisted laser desorption ionization time-of-flight) experiment. Infrared and MALDI-TOF mass spectra are shown in Figures 5.31 and 5.32, respectively.

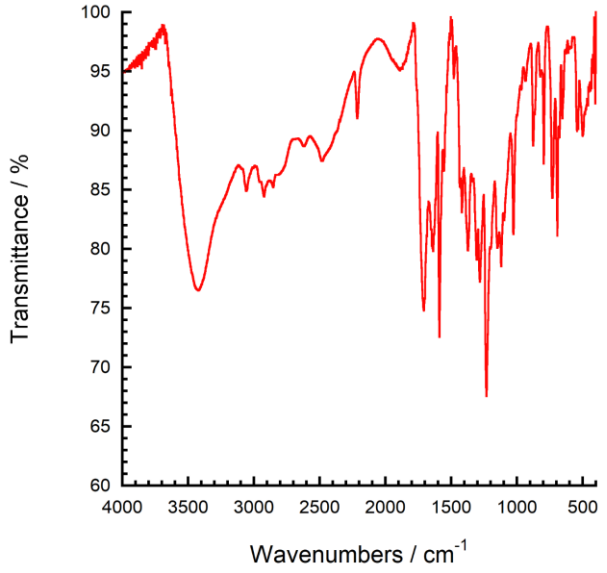

Figure 5.31. Infrared spectrum of **H_3L4** in a KBr pellet.

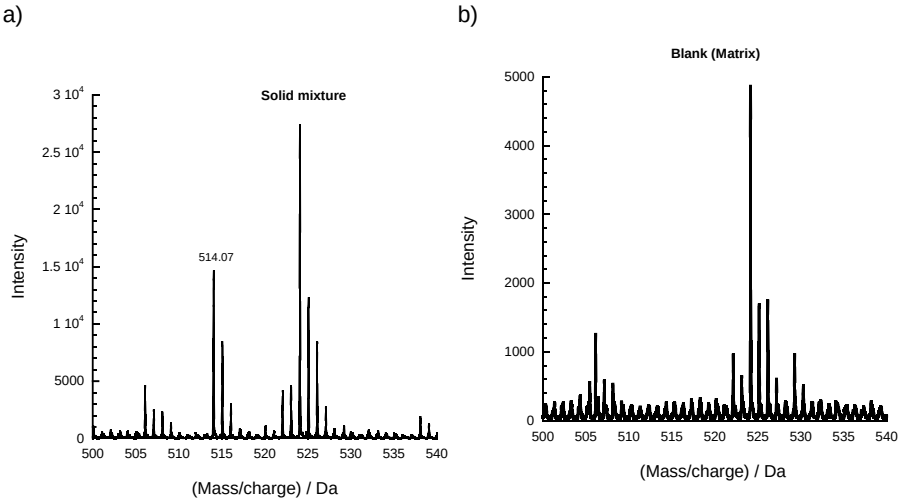

Figure 5.32. a) MALDI-TOF mass spectrum of the solid mixture containing **H_3L4**. The signal at 514.07 m/z is ascribed to $[M+H]^+$. b) MALDI-TOF mass spectrum of the matrix (blank).

Dimethyl 5,5'-([1,1'-biphenyl]-4,4'-diylbis(ethyne-2,1-diyl))dipicolinate, Me_2L5

Methyl 5-bromopicolinate (216 mg, 1 mmol) and 4,4'-diethynyl-1,1'-biphenyl (101 mg, 0.5 mmol) were introduced in a Schlenk flask containing 8 mL of dry degassed THF. $Pd(PPh_3)_4$ (38 mg, 0.033 mmol) and NEt_3 (0.2 mL, 1.435 mmol) were then added and the reaction mixture was stirred for 23 h. The precipitate was filtered and washed with water and methanol to afford 184 mg of **Me_2L5** as a white solid. Yield: 78%. Scheme 5.8 shows the corresponding reaction.

Data for **Me_2L5**: Anal. Calcd for $C_{30}H_{20}N_2O_4 \cdot 0.45H_2O$: C, 74.97; H, 4.38; N, 5.83. Found: C, 74.63; H, 3.94; N, 5.84. ^{1}H-NMR ($CDCl_3$): δ = 8.89 (d, J = 1.36 Hz, 2H), 8.14 (dd, ^3J = 8.15 Hz, ^5J = 0.56 Hz, 2H), 7.96 (dd, ^3J = 8.13 Hz, ^4J = 2.05 Hz, 2H), 7.64 (s, 8H), 4.03 (s, 6H) ppm. ^{13}C-NMR ($CDCl_3$): δ = 166.37, 153.2, 147.16, 141.88, 140.34, 133.52, 128.24, 125.77, 124.84, 122.67, 96.48, 87.48, 53.47 ppm. ESI-TOF MS: m/z 473.15 and 495.13 attributed to $[M+H]^+$ and $[M+Na]^+$, respectively. Selected IR (KBr, cm^{-1}): 3444.7, 1716.7, 1436.2, 1318.5, 1308.5, 1237.9, 1137.5, 1114.6, 823.4, 702.0. ^{1}H- and ^{13}C-NMR, IR and MS spectra are included in Figures 5.33-5.36, respectively.

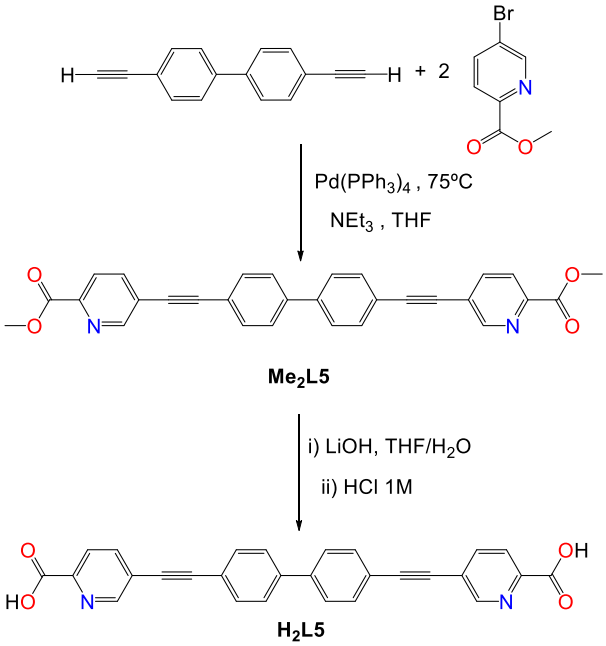

Scheme 5.8. Synthesis of compounds **Me_2L5** and **H_2L5** by Pd-catalysed cross-coupling reaction and subsequent basic hydrolysis.

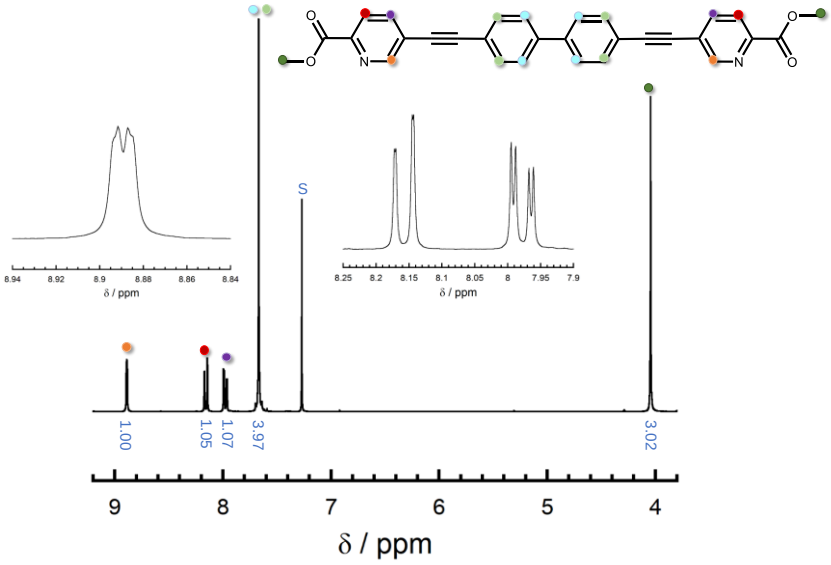

Figure 5.33. ^{1}H-NMR spectrum of compound **Me$_2$L5**. Values in blue refer to the integration of signals and S to solvent.

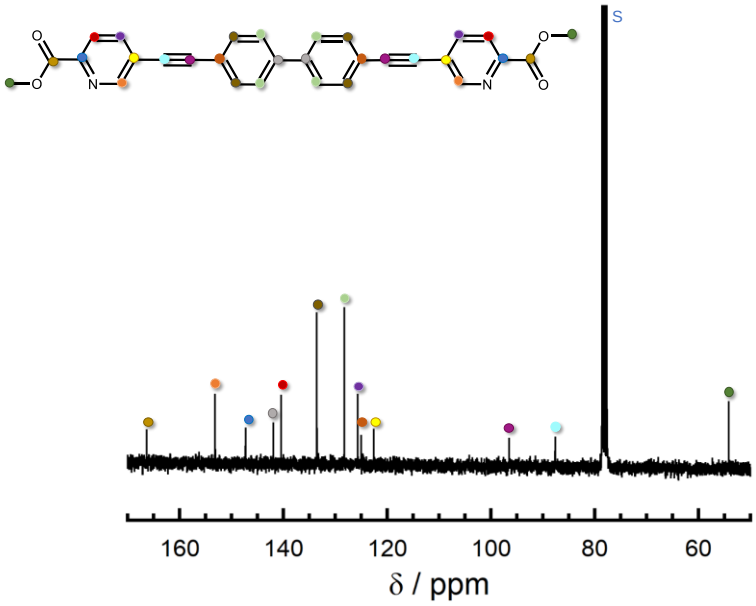

Figure 5.34. ^{13}C-NMR spectrum of compound **Me$_2$L5**. S refers to solvent.

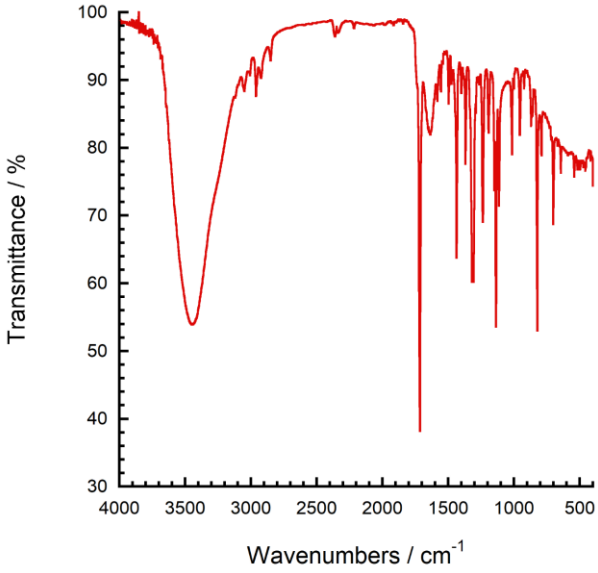

Figure 5-35. Infrared spectrum of **Me_2L5** in a KBr pellet.

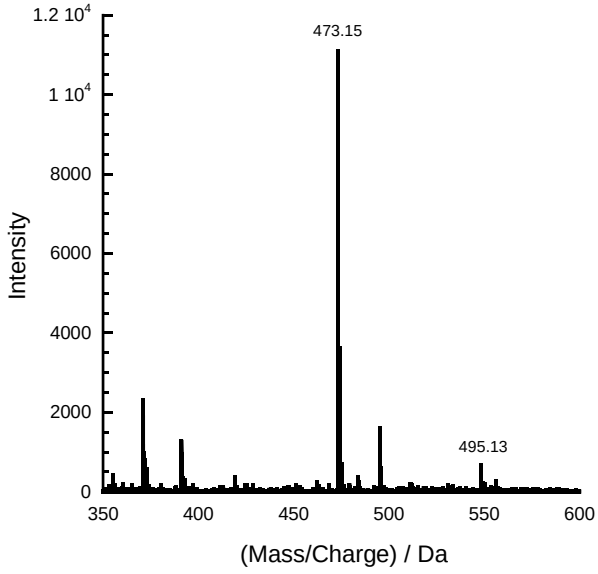

Figure 5.36. ESI-TOF mass spectrum of **Me_2L5** showing $[M+H]^+$ and $[M+Na]^+$ at 473.15 and 495.13 m/z, respectively.

5,5'-([1,1'-biphenyl]-4,4'-diylbis(ethyne-2,1-diyl))dipicolinic acid, H_2L5

Me_2L5 (101 mg, 0.21 mmol) was suspended in 8 mL of a THF/H_2O (3/1) mixture. LiOH·H_2O (18 mg, 0.43 mmol) was added and the suspension was stirred for 3 h. Then, THF was evaporated and the pH of the resulting aqueous suspension was adjusted to 5.11 using 1M HCl. The yellowish precipitate was filtered, washed with cold water and dried under vacuum (Scheme 5.8). Yield: 97% (94 mg).

Data for **H_2L5**: Anal. Calcd for $C_{28}H_{16}N_2O_4$·1.3H_2O: C, 71.88; H, 4.01; N, 5.99. Found: C, 71.78; H, 3.87; N, 5.86. ESI-TOF MS: m/z 445.11 $[M+H]^+$. Selected IR (KBr, cm^{-1}): 1698.0, 1581.2, 1316.9, 1242.1, 822.2. Infrared and ESI-TOF mass spectra are shown in Figures 5.37 and 5.38, respectively. The corresponding picolinic acid was insoluble in all common solvents and its NMR spectra could not be recorded.

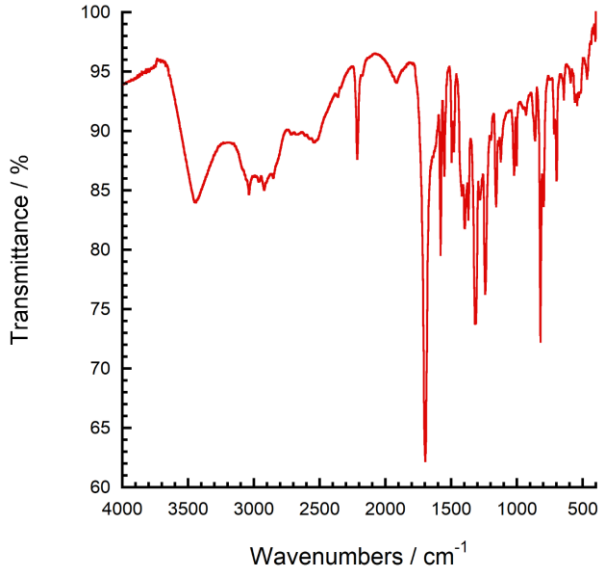

Figure 5.37. Infrared spectrum of **H_2L5** in a KBr pellet.

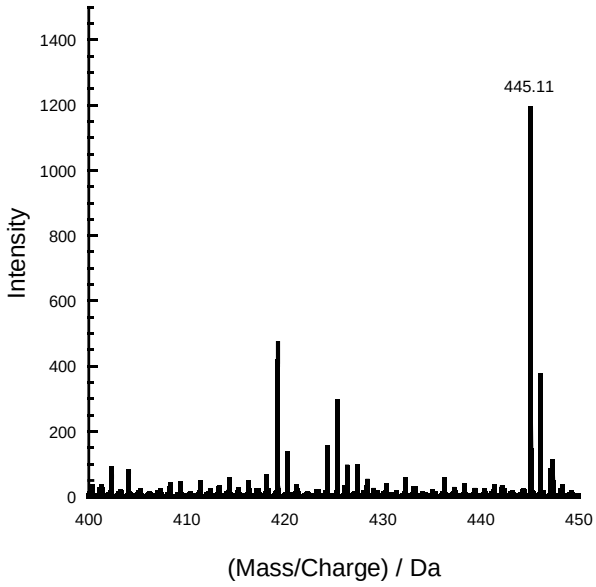

Figure 5.38. ESI-TOF mass spectrum of **H_2L5** showing $[M+H]^+$ at 445.11 m/. The remaining signals are due to the solvent (CH_2Cl_2/CH_3OH) and are also present when the blank is measured.

Methyl 5-(pyridin-4-ylethynyl)picolinate, MeL6

Methyl 5-ethynylpicolinate (173.5 mg, 1.08 mmol) and 4-bromopyridine hydrochloride (210 mg, 1.08 mmol) were introduced in a Schlenk flask containing 8 mL of dry degassed THF. $Pd(PPh_3)_4$ (38 mg, 0.033 mmol) and NEt_3 (0.4 mL, 2.87 mmol) were then added and the reaction mixture was stirred for 24 h. The yellow suspension was concentrated to dryness and the crude product was purified by flash column chromatography (ethyl acetate) to afford 254 mg of **MeL6** as crystalline yellowish solid. Yield: 98%. Scheme 5.9 shows the corresponding reaction.

Data for **MeL6**: Anal. Calcd for $C_{14}H_{10}N_2O_2 \cdot 0.45C_4H_8O_2$: C, 68.29; H, 4.93; N, 10.08. Found: C, 67.87; H, 4.44; N, 9,80. ^{1}H-NMR ($CDCl_3$): δ = 8.86 (dd, ^4J = 2.06 Hz, ^5J = 0.78 Hz, 1H), 8.64 (dd, ^3J = 4.45 Hz, ^4J = 1.61 Hz, 2H), 8.14 (dd, ^3J = 8.11 Hz, ^5J = 0.85 Hz, 1H), 7.96 (dd, ^3J = 8.12 Hz, ^4J = 2.08 Hz, 1H), 7.40 (dd, ^3J = 4.43 Hz, ^4J = 1.64 Hz, 2H), 4.01(s, 3H) ppm. ^{13}C-NMR ($CDCl_3$): δ = 165.62, 152.77, 150.68, 147.57, 140.29, 130.71, 126.12, 125.14, 123.36, 92.92, 90.02, 53.74 ppm. ESI-TOF MS: m/z 238.9 $[M+H]^+$, 260.8 $[M + Na]^+$. Selected IR (KBr, cm^{-1}): 3448.1, 1738.4, 1724.0, 1593.5, 1304.8, 1276.1, 1236.2, 1218.7, 1191.9, 1154.5, 1114.1, 1020.2, 820.6, 698.3. ^{1}H- and ^{13}C-NMR, IR and MS spectra are included in Figures 5.39-5.42, respectively.

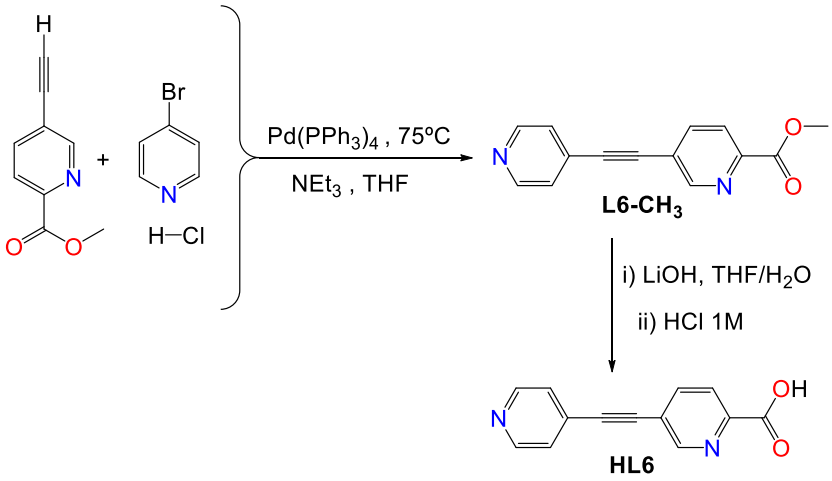

Scheme 5.9. Synthesis of compounds **MeL6** and **HL6** by Pd-catalysed cross-coupling reaction and subsequent basic hydrolysis.

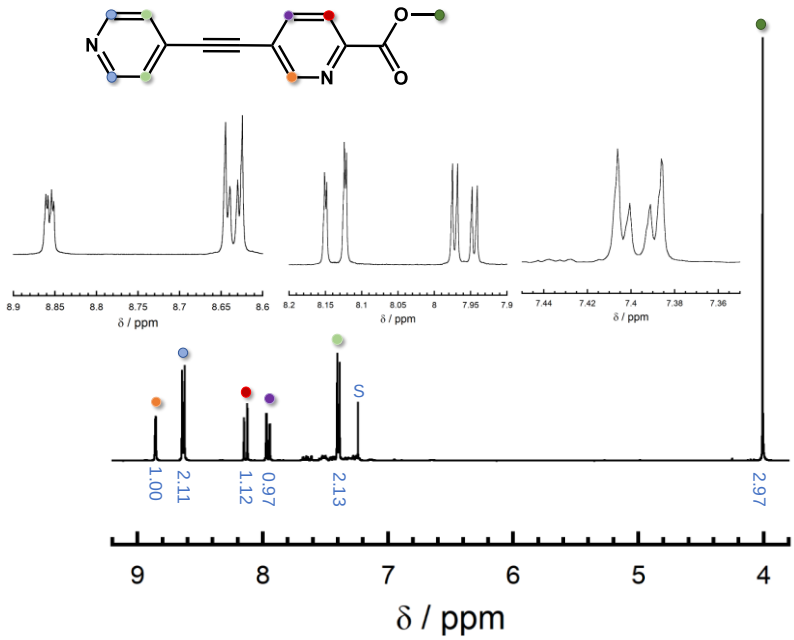

Figure 5.39. ^{1}H-NMR spectrum of compound **MeL6**. Values in blue refer to the integration of signals and S to solvent.

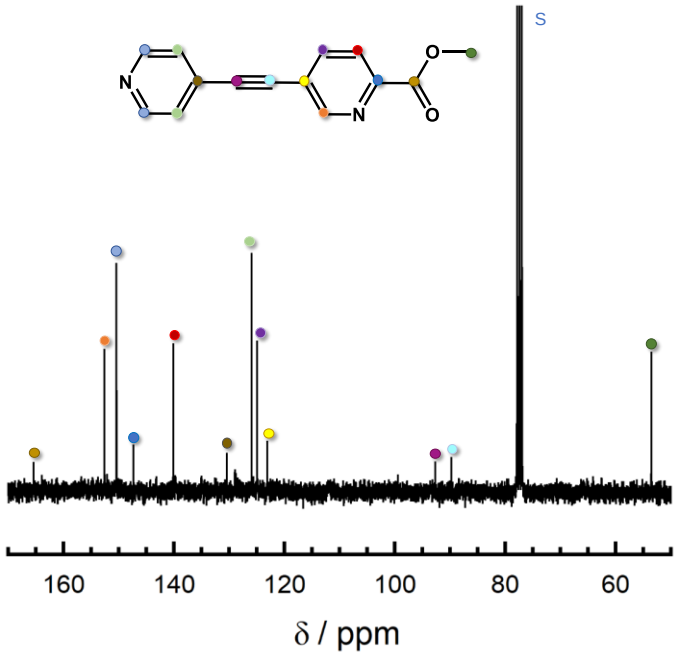

Figure 5.40. ^{13}C-NMR spectrum of compound **MeL6**. S refers to solvent.

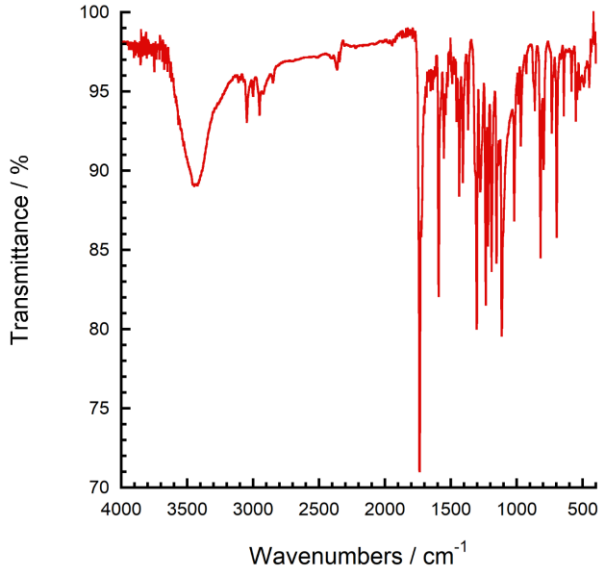

Figure 5.41. Infrared spectrum of **MeL6** in a KBr pellet.

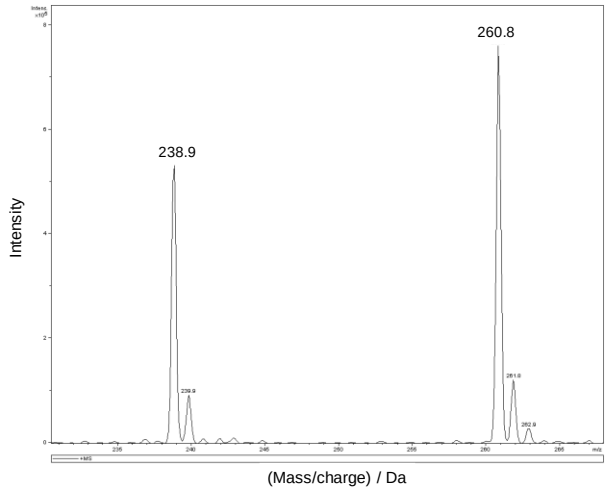

Figure 5.42. ESI-TOF mass spectrum of **MeL6** showing $[M+H]^+$ at 238.9 and $[M+Na]^+$ at 260.8 m/z.

5-(pyridin-4-ylethynyl)picolinic acid, HL6

MeL6 (144 mg, 0.60 mmol) was dissolved in 11 mL of a THF/H_2O (1/1) mixture. $LiOH{\cdot}H_2O$ (25 mg, 0.60 mmol) was added and the solution was stirred for 3 h. Then, THF was evaporated and the pH of the resulting aqueous solution was adjusted to 5.5 using 1M HCl. The white precipitate was filtered, washed with cold water and dried under vacuum (Scheme 5.9). Yield: 78%, 105 mg.

Data for **HL6**: Anal. Calcd for $C_{13}H_8N_2O_2{\cdot}0.5H_2O$: C, 66.95; H, 3.89; N, 12.01. Found: C, 67.31; H, 3.77; N, 11.56. ^{1}H-NMR (D_2O/KOH): δ = 8.74 (dd, ^4J = 2.05 Hz, ^5J = 0.78 Hz, 1H), 8.55 (dd, ^3J = 4.61 Hz, ^4J = 1.62 Hz, 2H), 8.09 (dd, ^3J = 8.12 Hz, ^5J = 2.08 Hz, 1H), 7.93 (dd, ^3J = 8.13 Hz, ^{5}J=0.83 Hz, 1H), 7.58 (dd, ^3J = 4.62 Hz, ^4J = 1.61 Hz, 2H) ppm. ^{13}C-NMR (D_2O/KOH): δ = 172.27, 153.02, 151.25, 149.11, 140.85, 131.56, 126.24, 123.74, 120.86, 90.92, 90.73 ppm. ESI-TOF MS: m/z 225.7 $[M+H]^+$. Selected IR (KBr, cm^{-1}): 1716.2, 1603.7, 1314.3, 1234.0, 1210.9, 1162.2, 1021.7, 825.9, 723.7. ^{1}H- and ^{13}C-NMR, IR and MS spectra are included in Figures 5.43-5.46, respectively.

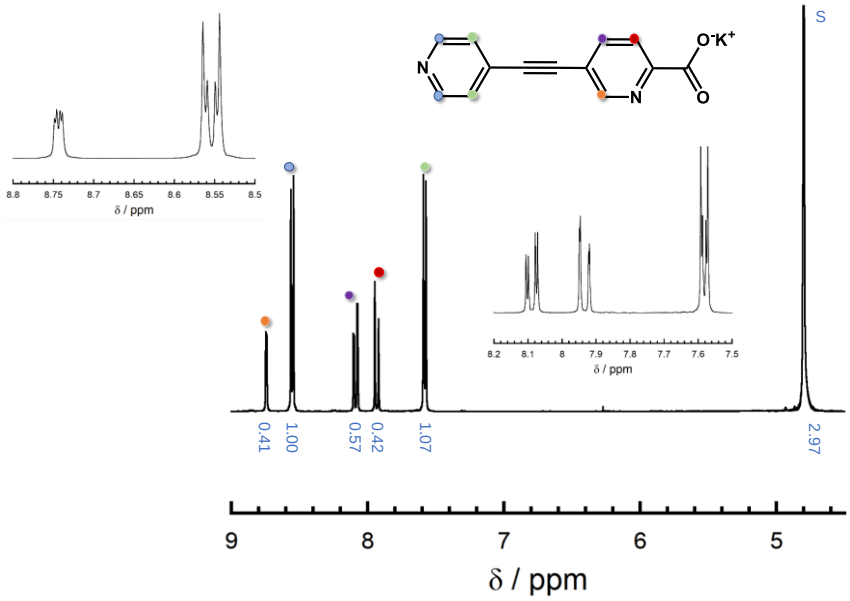

Figure 5.43. [1]H-NMR spectrum of compound **HL6** as a potassium salt. Values in blue refer to the integration of signals and S to solvent.

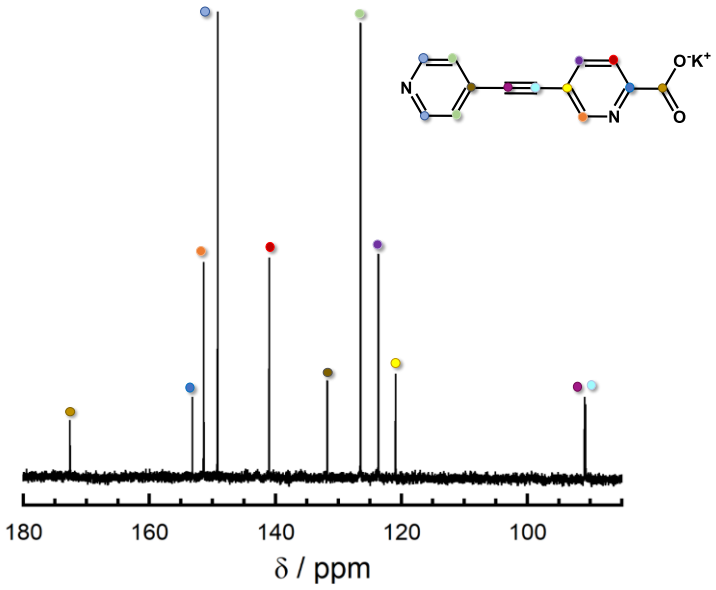

Figure 5.44. [13]C-NMR spectrum of compound **HL6** as a potassium salt.

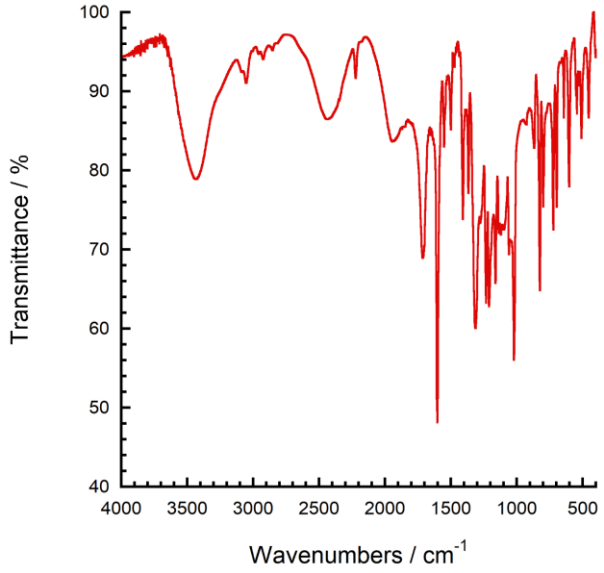

Figure 5.45. Infrared spectrum of **HL6** in a KBr pellet.

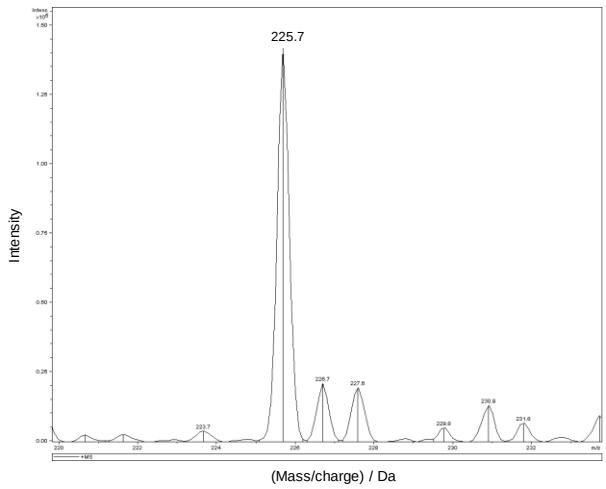

Figure 5.46. ESI-TOF mass spectrum of **HL6** showing $[M+H]^+$ at 225.7 m/z.

Methyl 5-(pyridin-3-ylethynyl)picolinate, MeL7

Methyl 5-bromopicolinate (216 mg, 1 mmol) and 3-ethynylpyridine (103 mg, 1 mmol) were introduced in a Schlenk flask containing 8 mL of dry degassed THF. $Pd(PPh_3)_4$ (38 mg, 0.033 mmol) and NEt_3 (0.2 mL, 1.435 mmol) were then added

and the reaction mixture was stirred for 46 h. The reaction mixture was filtered and the filtrate was concentrated to dryness. Flash column chromatography (ethyl acetate:hexane, 1:2) yields 224 mg of **MeL7** as a pure white solid. Yield: 94%. Scheme 5.10 shows the corresponding reaction.

Data for **MeL7**: Anal. Calcd for $C_{14}H_{10}N_2O_2 \cdot 0.2H_2O$: C, 69.53; H, 4.33; N, 11.58. Found: C, 69.79; H, 4.26; N, 11.54. ^{1}H-NMR ($CDCl_3$): δ = 8.86 (dd, ^4J = 2.05 Hz, ^5J = 0.73 Hz, 1H), 8.80 (dd, 1H), 8.60 (dd, 1H), 8.14 (dd, ^3J = 8.12 Hz, ^5J = 0.74 Hz, 1H), 7.96 (dd, ^3J = 8.12 Hz, ^4J = 2.08 Hz, 1H), 7.84 (m, 1H), 7.32 (m, 1H), 4.02 (s, 3H) ppm. ^{13}C-NMR ($CDCl_3$): δ = 165.40, 152.68, 152.26, 149.81, 146.77, 139.69, 138.94, 124.79, 123.26, 119.44, 100.39, 92.27, 88.80, 53.31 ppm. ESI-TOF MS: m/z 239.08 and 261.06 attributed to $[M+H]^+$ and $[M+Na]^+$, respectively. Selected IR (KBr, cm^{-1}): 1719.3, 1560.2, 1441.7, 1406.7, 1366.8, 1319.2, 1239.0, 1197.2, 1153.8, 1137.0, 1016.8, 865.6, 794.9, 697.6. ^{1}H- and ^{13}C-NMR, IR and MS spectra are included in Figures 5.47-5.50, respectively.

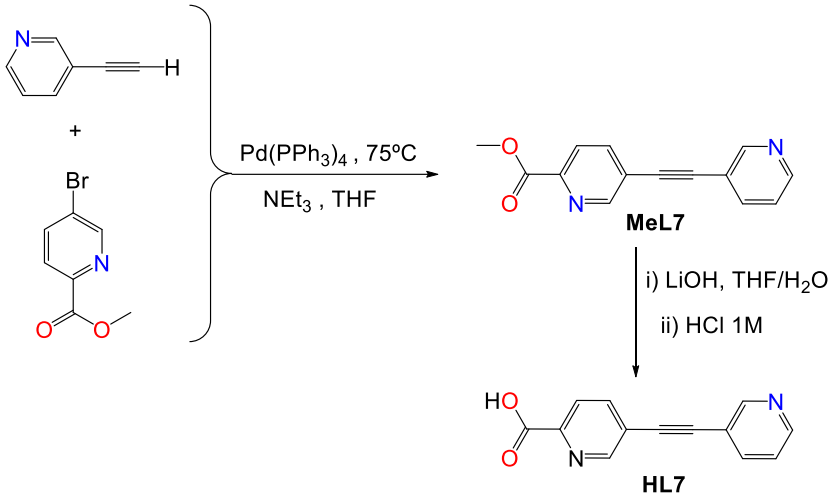

Scheme 5.10. Synthesis of compounds **MeL7** and **HL7** by Pd-catalysed cross-coupling reaction and subsequent basic hydrolysis.

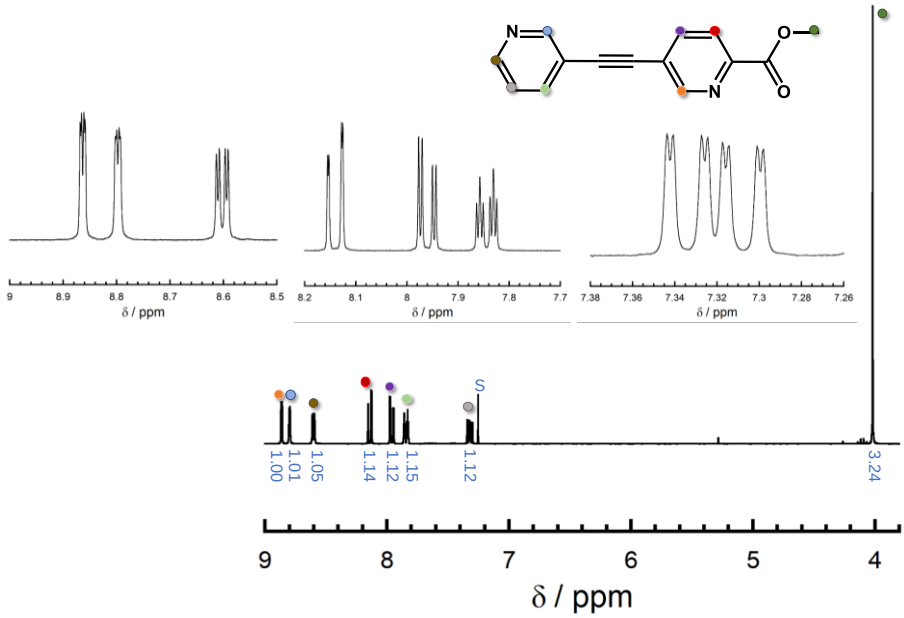

Figure 5.47. ^{1}H-NMR spectrum of compound **MeL7**. Values in blue refer to the integration of signals and S to solvent.

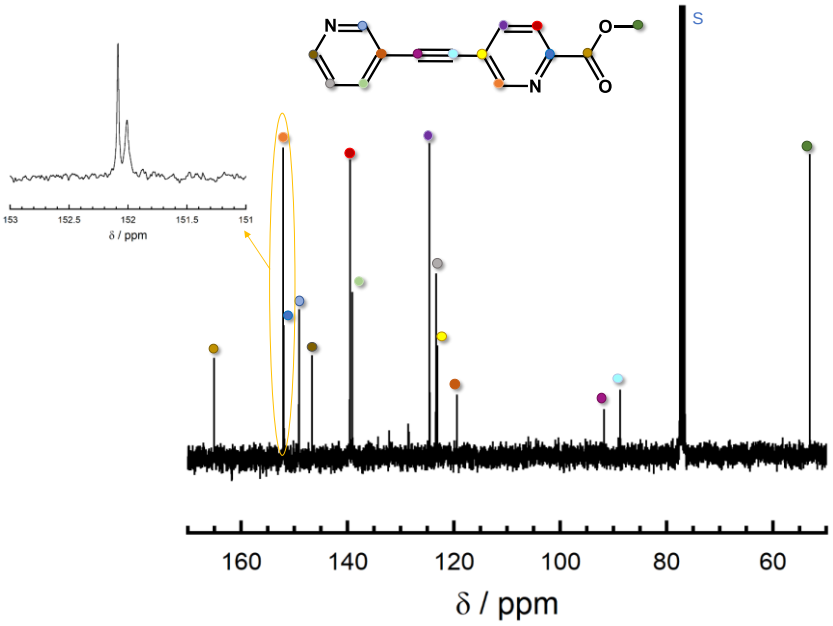

Figure 5.48. ^{13}C-NMR spectrum of compound **MeL7**. S refers to solvent.

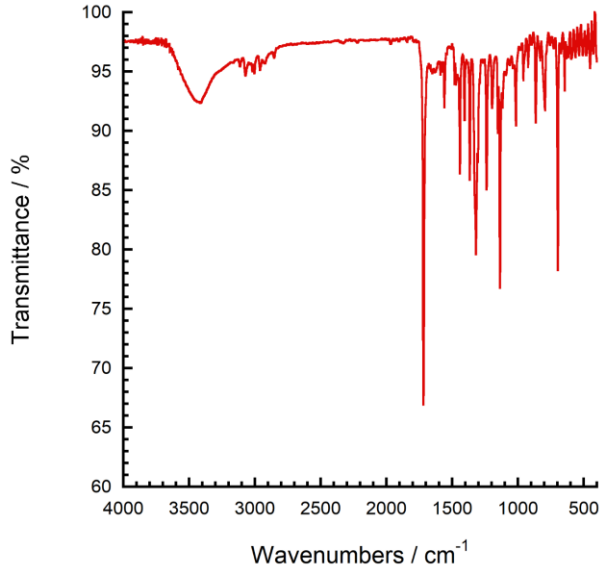

Figure 5.49. Infrared spectrum of **MeL7** in a KBr pellet.

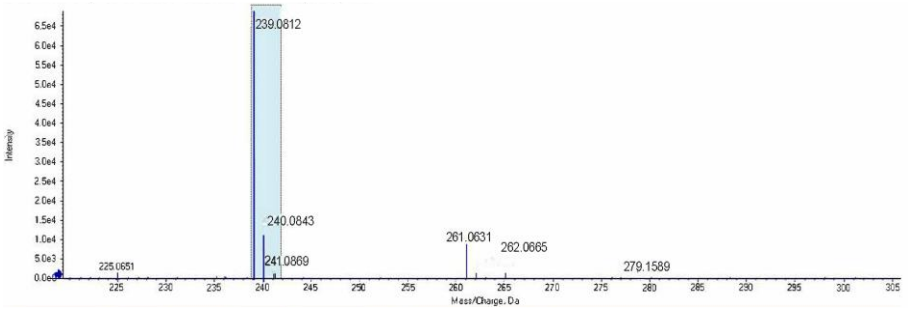

Figure 5.50. ESI-TOF mass spectrum of **MeL7**showing $[M+H]^+$ and $[M+Na]^+$ at 239.08 and 261.06 m/z, respectively.

5-(pyridin-3-ylethynyl)picolinic acid, HL7

MeL7 (200 mg, 0.84 mmol) was dissolved in 14 mL of a THF/H_2O (1/1) mixture. $LiOH{\cdot}H_2O$ (35 mg, 0.84 mmol) was added and the solution was stirred for 4 h. Then, THF was evaporated and the pH of the resulting aqueous solution was adjusted to 5.20 using 1M HCl. The yellowish precipitate was filtered, washed with cold water and dried under vacuum (Scheme 5.10). Yield: 76% (144 mg).
Data for **HL7**: Anal. Calcd for $C_{13}H_8N_2O_2$: C, 69.64; H, 3.60; N, 12.49. Found: C, 69.92; H, 3.34; N, 12.39. ^{1}H-NMR (D_2O/KOH): δ = 8.83 (m, 1H), 8.81 (m, 1H), 8.62 (dd, 1H), 8.17 (dd, ^3J = 8.14 Hz, 1H), 8.12 (dt, ^3J = 8.03 Hz, 1H), 8.02 (m, 1H), 7.59

(m, 1H) ppm. ^{13}C-NMR (D_2O/KOH): δ = 172.59, 152.70, 151.37, 151.14, 148.66, 140.70, 140.31, 124.39, 123.63, 121.29, 120.03, 90.42, 89.24 ppm. ESI-TOF MS: m/z 225.06 $[M+H]^+$. Selected IR (KBr, cm^{-1}): 1707.4, 1407.1, 1310.1, 1232.7, 1190.0, 1128.3, 1045.3, 810.6, 699.3, 648.8. ^{1}H- and ^{13}C-NMR, IR and MS spectra are included in Figures 5.51-5.54, respectively.

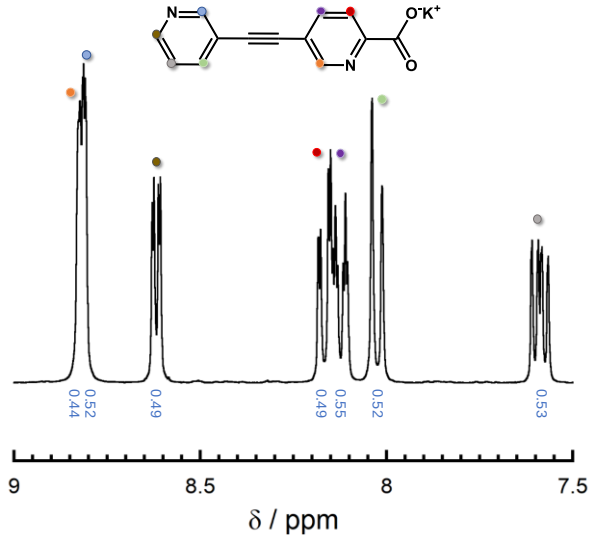

Figure 5.51. ^{1}H-NMR spectrum of compound **HL7** as a potassium salt. Values in blue refer to the integration of signals.

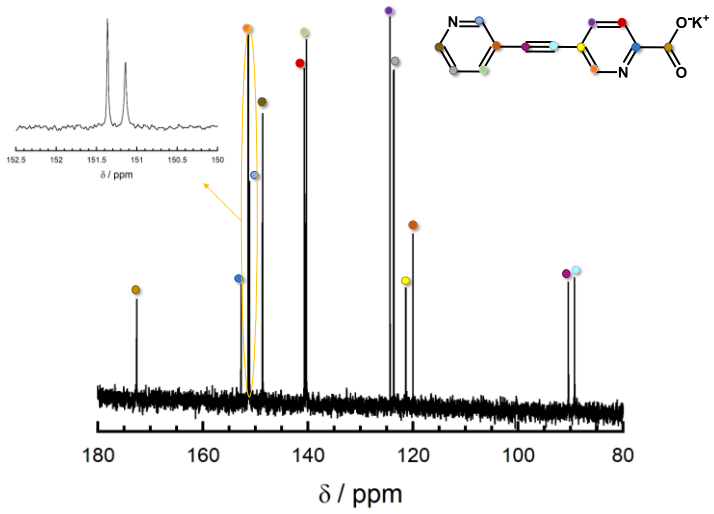

Figure 5.52. ^{13}C-NMR spectrum of compound **HL7** as a potassium salt.

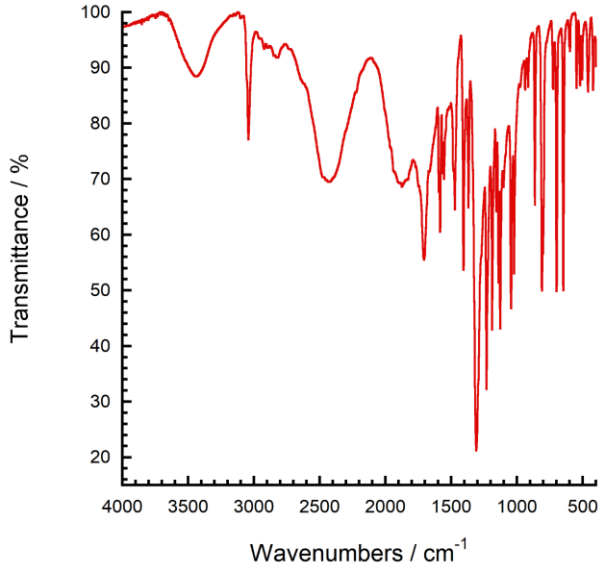

Figure 5.53. Infrared spectrum of **HL7** in a KBr pellet.

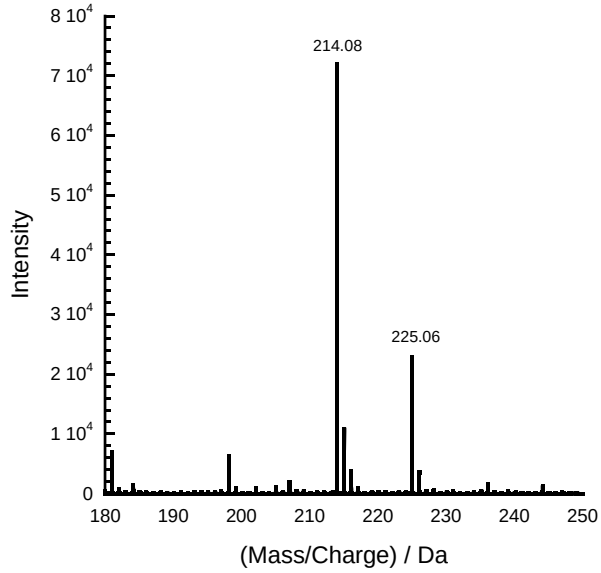

Figure 5.54. ESI-TOF mass spectrum of **HL7** showing $[M+H]^+$ at 225.06 m/z. At 214.08 m/z a signal due to the solvent appears (CH_2Cl_2/CH_3OH), which is also present when the blank is measured.

Methyl 5-((4-(methoxycarbonyl)phenyl)ethynyl)picolinate, Me_2L8

Methyl 5-bromopicolinate (216 mg, 1 mmol) and methyl 4-ethynylbenzoate (160 mg, 1 mmol) were introduced in a Schlenk flask containing 8 mL of dry degassed THF. $Pd(PPh_3)_4$ (38 mg, 0.033 mmol) and NEt_3 (0.4 mL, 2.87 mmol) were then added and the reaction mixture was stirred for 48 h. The yellow suspension was concentrated to dryness and the crude product was purified by flash column chromatography (ethyl acetate:hexane 1:2) to afford 181 mg of **Me_2L8** as a crystalline yellowish solid. Yield: 61%. The corresponding reaction is shown in Scheme 5.11.

Data for **Me_2L8**: Anal. Calcd for $C_{17}H_{13}NO_4 \cdot 0.15C_4H_8O_2$: C, 68.52; H, 4.64; N, 4.54. Found: C, 68.41; H, 4.35; N, 4.24. ^{1}H-NMR ($CDCl_3$): δ = 8.85 (dd, ^4J = 2.05 Hz, ^5J = 0.73 Hz, 1H), 8.12 (dd, ^3J = 8.11 Hz, ^5J = 0.76 Hz, 1H), 8.03 (dt, ^3J = 8.54 Hz, ^4J = 1.71 Hz, 2H), 7.94 (dd, ^3J = 8.13 Hz, ^4J = 2.08 Hz, 1H), 7.61 (dt, ^3J = 8.53 Hz, ^4J = 1.71 Hz, 2H), 4.01 (s, 3H), 3.92 (s, 3H) ppm. ^{13}C-NMR ($CDCl_3$): δ = 166.55, 165.33, 152.26, 146.77, 139.69, 131.90, 130.75, 129.85, 126.73, 124.74, 123.61, 94.73, 88.14, 53.27, 52.52 ppm. ESI-TOF MS: m/z 296.09 $[M+H]^+$. Selected IR (KBr, cm^{-1}): 1720.2, 1607.5, 1438.7, 1403.8, 1367.7, 1319.6, 1275.7, 1237.8, 1195.9, 1178.7, 1134.4, 1116.7, 1107.7, 1016.7, 957.6, 862.3, 853.5, 816.5, 793.5, 768.4, 698.4. ^{1}H- and ^{13}C-NMR, IR and MS spectra are included in Figures 5.55-5.58, respectively.

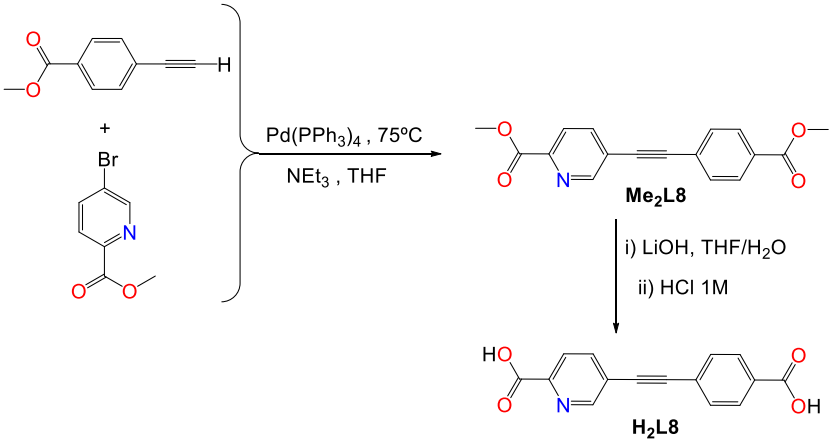

Scheme 5.11. Synthesis of compounds **Me_2L8** and **H_2L8** by Pd-catalysed cross-coupling reaction and subsequent basic hydrolysis.

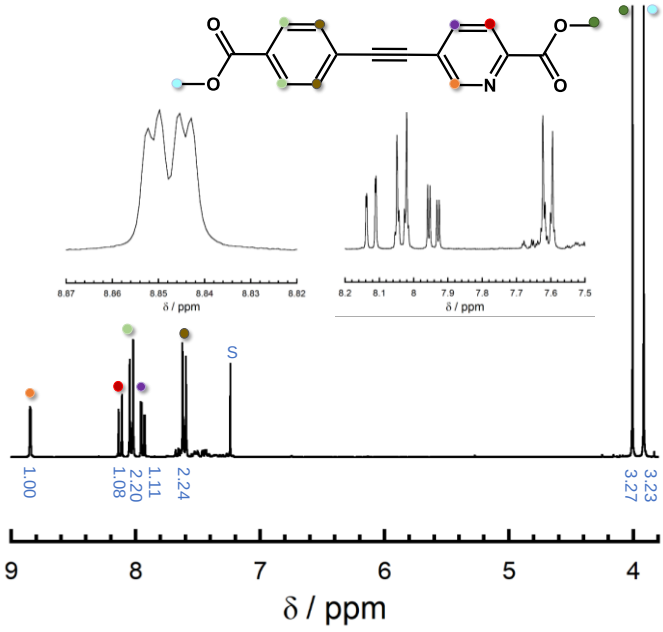

Figure 5.55. ^{1}H-NMR spectrum of compound **Me$_2$L8**. Values in blue refer to the integration of signals and S to solvent.

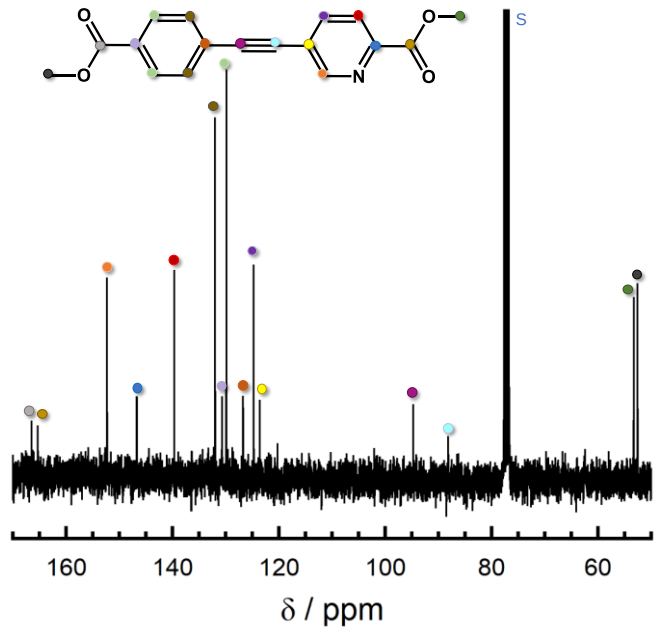

Figure 5.56. ^{13}C-NMR spectrum of compound **Me$_2$L8**. S refers to solvent.

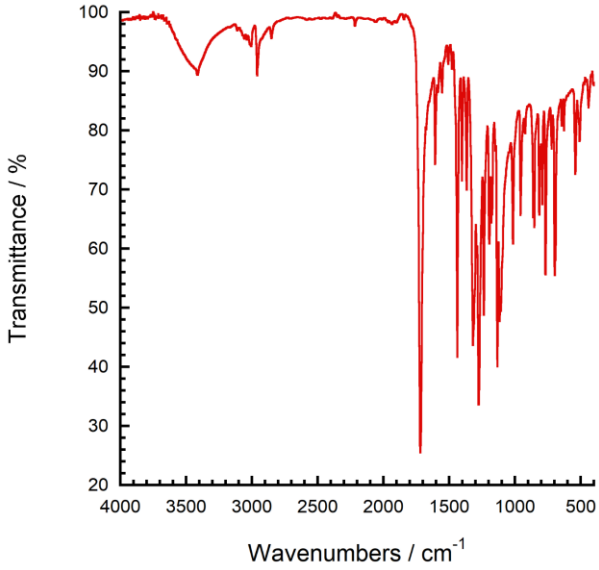

Figure 5.57. Infrared spectrum of **Me_2L8** in a KBr pellet.

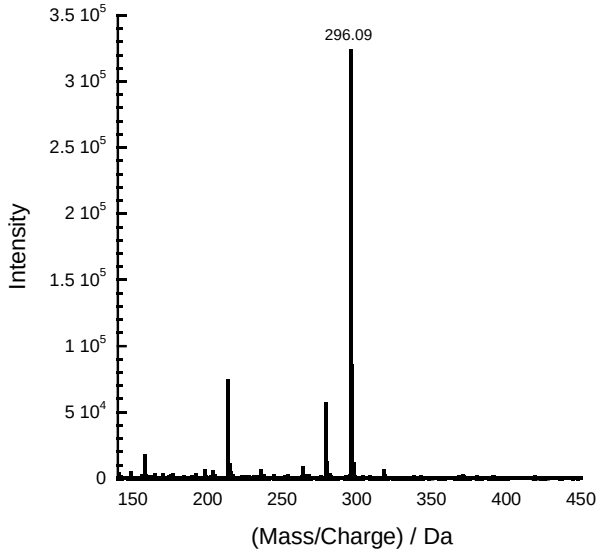

Figure 5.58. ESI-TOF mass spectrum of **Me_2L8** showing $[M+H]^+$ at 296.09 m/z.

5-((4-carboxyphenyl)ethynyl)picolinic acid, H_2L8

Me_2L8 (100 mg, 0.34 mmol) was suspended in 10 mL of a THF/H_2O (2/1) mixture. After addition of LiOH·H_2O (29 mg, 0.68 mmol), the initial solid dissolved. After stirring for 3 h, THF was evaporated and the pH was adjusted to 3.98 using 1M HCl. The white precipitate was filtered, washed with cold water and dried under vacuum (Scheme 5.11). Yield: 77% (73 mg).

Data for **H_2L8**: Anal. Calcd for $C_{15}H_9NO_4$·0.6 H_2O: C, 64.8; H, 3.70; N, 5.04. Found: C, 64.76; H, 3.52; N, 4.86. ^{1}H-NMR (D_2O/KOH): δ = 8.63 (dd, ^4J = 2.09 Hz, ^5J = 0.81 Hz, 1H), 7.98 (dd, ^3J = 8.14 Hz, ^4J = 2.06 Hz, 1H), 7.83 (dd, ^3J = 8.14 Hz, ^5J = 0.68 Hz, 1H), 7.78 (dt, ^3J = 8.45 Hz, ^4J = 1.74 Hz, 2H), 7.58 (dt, ^3J = 8.43 Hz, ^4J = 1.75 Hz, 2H) ppm. ^{13}C-NMR (D_2O/KOH): δ = 174.86, 172.46, 152.09, 150.75, 140.25, 136.72, 131.51, 128.91, 124.33, 123.20, 121.43, 93.34, 87.12 ppm. ESI-TOF MS: m/z 268.06 $[M+H]^+$. Selected IR (KBr, cm^{-1}): 1701.0, 1696.8, 1685.7, 1605.6, 1420.3, 1316.3, 1281.9, 1240.9, 858.1, 771.9. ^{1}H- and ^{13}C-NMR, IR and MS spectra are included in Figures 5.59-5.62, respectively.

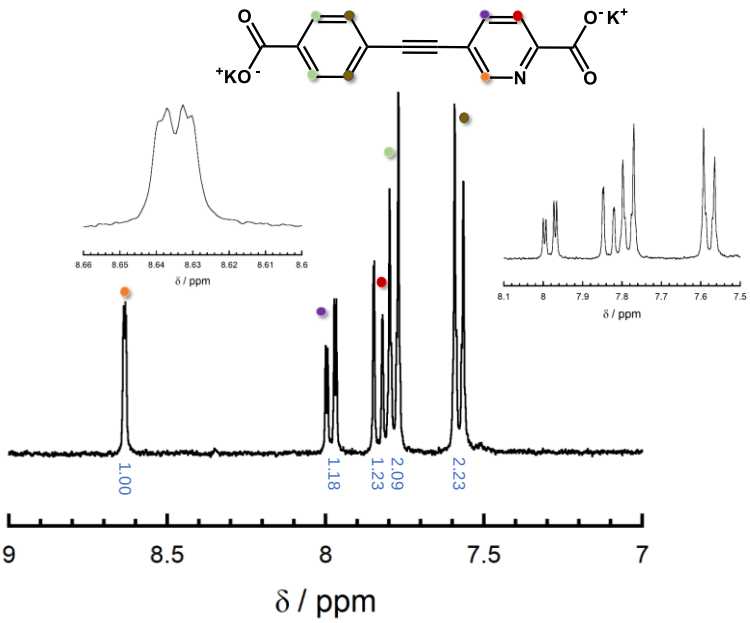

Figure 5.59. ^{1}H-NMR spectrum of compound **H_2L8** as a potassium salt. Values in blue refer to the integration of signals.

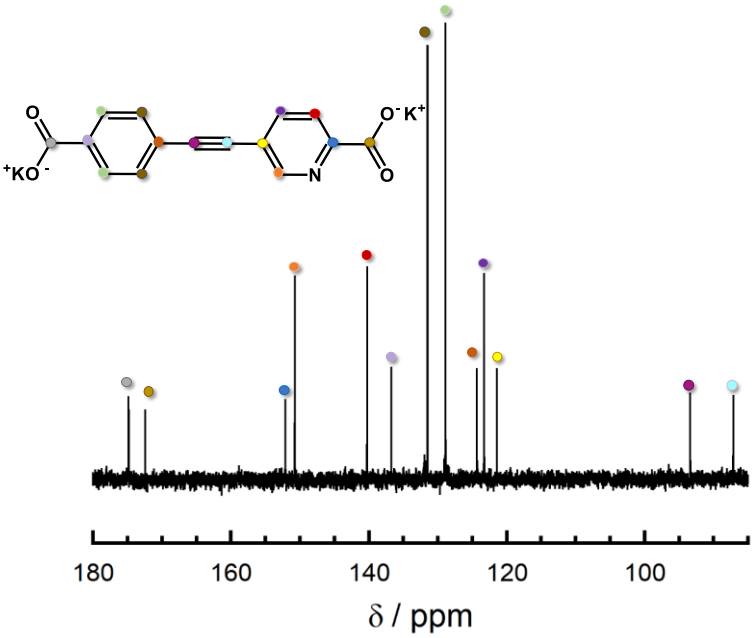

Figure 5.60. ^{13}C-NMR spectrum of compound **H_2L8** as a potassium salt.

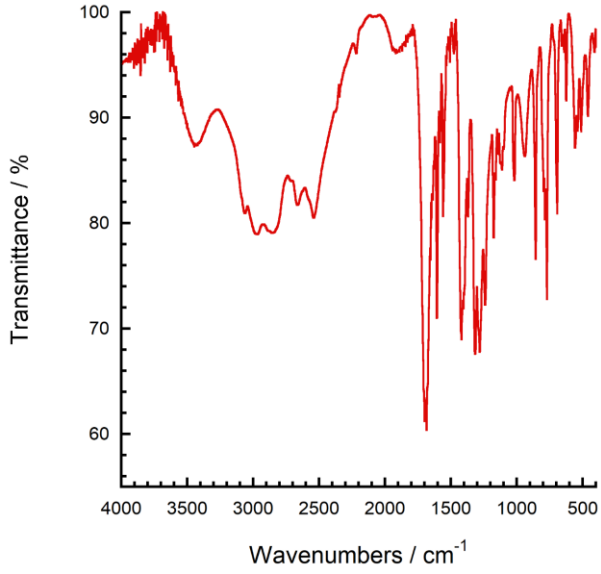

Figure 5.61. Infrared spectrum of **H_2L8** in a KBr pellet.

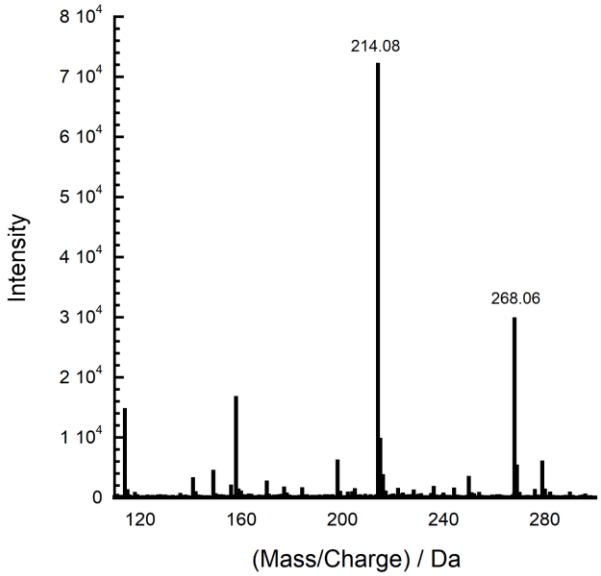

Figure 5.62. ESI-TOF mass spectrum of **H_2L8** showing $[M + H]^+$ at 268.06 m/z. At 214.08 m/z a signal due to the solvent appears (CH_2Cl_2/CH_3OH), which is also present when the blank is measured.

In general, the infrared spectra show the presence of O-H stretching (3600-2500 cm^{-1}, alcohol or carboxylic acid), C-H stretching (3100-2800 cm^{-1}, alkene or alkane), C≡C stretching (2260-2150 cm^{-1}, alkyne), C-H bending (2000-1650 cm^{-1}, aromatic compound), C=O stretching (1760-1670 cm^{-1}, carboxylic acid or ester), O-H bending (1440-1395 cm^{-1}, carboxylic acid or alcohol), C=C stretching (1670-1600 cm^{-1}, alkene), C-H bending (1450 cm^{-1}, alkane), C-N stretching (1340-1260 cm^{-1}, aromatic amine), C=N stretching (≈1628 cm^{-1}, aromatic amine), C-O stretching (1250-1100 cm^{-1}, ester), C-H bending (700-610 cm^{-1}, aromatic compound) and C=C bending (990-660 cm^{-1}, alkene). C≡C stretching signal is a good indicator of the presence of an alkyne functional group, since very few organic compounds show an absorption in this region (2260-2150 cm^{-1}). However, in some compounds, there is a lack of this signal due to its weak intensity or to the fact that if the molecule has centre of symmetry, the transition associated to this vibration mode is forbidden and, therefore, no vibrational mode can appear (compounds **Me_2L2** and **H_2L2**). A signal only appears in IR spectrum if the dipole moment of the molecule changes during the vibration (selection rule), and C≡C group has already a small difference in electronegativity, giving rise to weak peaks in those cases in which the ligand is "infrared-active".[11]

5.4. References

[1] R. Chinchilla, C. Nájera, *Chem. Rev*. **2007**, 107, 874-922

[2] V. Grosshenny, F. M. Romero, R. Ziessel, *J. Org. Chem*. **1997**, 62, 1491-1500

[3] K. Sonogashira, Y. Tohda, N. Hagihara,*Tetrahedron Lett*. **1975**, 50, 4467-4470

[4] R. C. Severance, E. S. Rountree, M. D. Smith, H.-C. z. Loye, *Solid State Sci*. **2012**, 14, 1512-1519

[5] R. Chinchilla, C. Nájera, *Chem. Soc. Rev*. **2011**, 40, 5084-5121

[6] a) X. Wang, Y. Song, J. Qu, Y. Luo, *Organometallics*. **2017**, 36, 1042-1048. b) A. J. Burke, C. S. Marques, *Catalytic Arylation Methods – From the Academic Lab to Industrial Processes*. **2015**, Wiley-VCH

[7] A. Soheili, J. Albaneze-Walker, J. A. Murry, P. G. Dormer, D. L. Hughes, *Org*. *Lett*. **2003**, 5, 4191-4194

[8] M. Gazvoda, M. Virant, B. Pinter, J. Kosmrlj, *Nat*. *Commun*. **2018**, 9, 4814

[9] Organic Chemistry Study Guide: Key Concepts, Problems, and Solutions http://dx.doi.org/10.1016/B978-0-12-801889-7.00021-2 Copyright © **2015** Elsevier Inc.

[10] R. Skelton, F. Dubois, R. Zenobi, *Anal*. *Chem*. **2000**, 72, 1707-1710

[11] B. H. Stuart, *Infrared Spectroscopy: Fundamentals and Applications*. **2004**, United States (USA), John Wiley & Sons

Chapter 6: Structural and thermal study of divalent polynuclear coordination complexes based on ethynyl-bridged picolinate ligands

This chapter is devoted to describe the progress achieved in the coordination chemistry of the novel family of picolinate ligands with divalent metal transition ions. First, the preparation and schematic representation of divalent complexes of zinc, copper and iron are detailed, as well as their structural and thermal characterisation. Furthermore, their magnetic and luminescent properties have been analysed, with special emphasis in the luminescent detection of small organic molecules and metal sensing. In addition, the catalytic activity of an Fe(II) complex has been studied in cyclohexane oxidation.

6.1. Divalent polynuclear picolinate-bridged complexes

Synthesis of coordination complexes with first-row transition-metal ions such as Mn^{2+}, Cu^{2+}, Ni^{2+}, Co^{2+} or Fe^{2+} can give rise to the incorporation of bridging units across paramagnetic metal centres and result in interesting magnetic properties. The expansion in this field has been notable and a wide variety of chains, layers and three-dimensional ordered structures with magnetic metal ions have been obtained. Furthermore, isolated or even weakly interacting metal complexes that present a slow relaxation of the magnetisation represent appealing materials for quantum information data storage and processing.[1] Since the picolinate anion is able to transmit magnetic interactions in a more or less efficient way, we have explored its coordination with this kind of metals. In this context, we have been successful in the synthesis of two copper(II) and one iron(II) compounds with a chain structure: $[Cu_2(\mathbf{L7})_4]$ (**7**), $[Cu_3(\mathbf{MeL8})_6]$ (**8**) and $[Fe(H_2O)_2(\mathbf{L2})]$ (**9**).

In parallel, the field of coordination polymers has grown towards the design of luminescent inorganic-organic hybrid materials, due to their potential applications in sensing, solid-state lasers and optical signal amplifiers.[2] In this context, emission can be directly from the linker (typically conjugated organic compound) or can be associated to a charge transfer with the coordinated metal ions, among other modes for generating luminescence.[3] Transition-metal ions with unpaired electrons can quench ligand-based luminescence. Nevertheless, in the case of Cd(II) and Zn(II) complexes which have filled, core-like *d*-orbitals, no *d-d* transitions are possible and, therefore, linker-based luminescence can be

observed. In this regard, two zinc(II) compounds with a layer and a chain structure have been prepared: [Zn(**L7**)$_2$] (**10**) and [Zn(H_2O)$_2$(**L8**)] (**11**), respectively.

6.2. Synthesis

The compounds synthesised during this part of the thesis have been prepared using solvothermal methods. The low solubility of the starting polypicolinate ligands has limited their synthetic versatility and, among all the synthetic available techniques, the solvothermal method has led to complexation of these ligands. A solvothermal process can be regarded as a chemical reaction in a closed system in the presence of a solvent at a temperature higher than its boiling point.[4] Therefore, solvothermal synthesis involves high pressures and enables the solubilisation of the reactive mixture, allowing ligand coordination and crystallisation. Following this methodology, new crystalline picolinate-bridged complexes (**7**-**11**) have been prepared starting from the corresponding picolinate ligands either in their methyl ester or acid form by careful optimisation of synthetic parameters such as temperature, concentration, solvent, reaction time, rate of heating and cooling, etc.

A general strategy that consists in a solvothermal complexation reaction of M(NO_3)$_2$·xH_2O (M = Cu or Zn) with methyl 5-(pyridine-3-ylethynyl)picolinate (**MeL7**), methyl 5-((4-(methoxycarbonyl)phenyl)ethynyl)picolinate (**Me$_2$L8**) or 5-((4-carboxyphenyl)ethynyl)picolinic acid (**H$_2$L8**) in a mixed solvent (water/ethanol/pyridine) has been employed for the synthesis of compounds **7**, **8**, **10** and **11** (Scheme 6.1). The mixture was placed inside an oven at 96 °C during 96 h, with cooling and heating rates of 0.2 °C/min. In the reaction medium (basic pH due to the presence of pyridine), these picolinate esters and acid **H$_2$L8** were hydrolysed or deprotonated to yield the anionic ligands. It has to be noted that the methyl benzoate ester moiety of **MeL8** was not hydrolysed in these conditions, indicating that the driving force for hydrolysis is complexation to the metal(II) cation.

Secondly, complex **9** has been prepared using a solvothermal synthesis between 5,5'-(ethyne-1,2-diyl)dipicolinic acid (**H$_2$L2**) and Fe(NO_3)$_3$·9H_2O in a mixed solvent (DMF/H_2O). The mixture was held inside an oven at 130 °C during 3 days, with cooling and heating rates of 0.09 °C/min. In this case, acetic acid was used as a modulator in order to obtain single crystals suitable for X-ray diffraction measurements (Scheme 6.2). It has to be noted that in the reaction medium, iron(III) was reduced to yield iron(II) cations as a part of a redox reaction.[5]

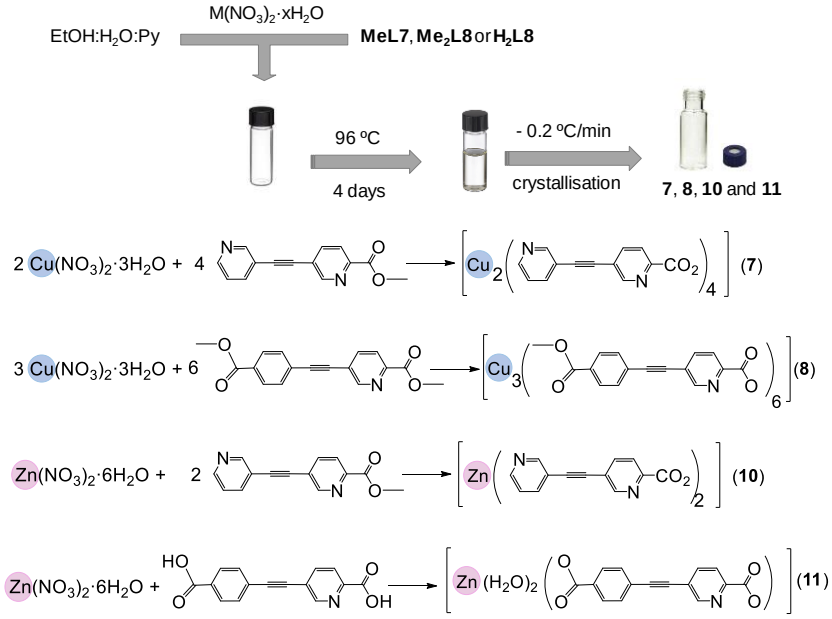

Scheme 6.1. Schematic representation for the preparation of complexes **7**, **8**, **10** and **11**.

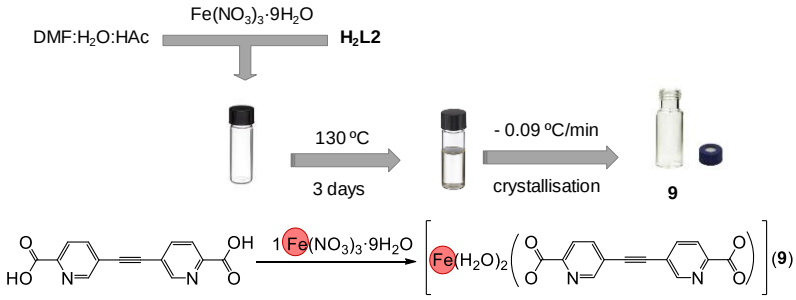

Scheme 6.2. Schematic representation for the synthesis of complex **9**.

6.3. $[Cu_2(\mathbf{L7})_4]$ (**7**) and $[Cu_3(\mathbf{MeL8})_6]$ (**8**)

6.3.1. Structural characterisation

A. Single crystal X-ray diffraction

7 crystallises in the triclinic space group *P*–1 and the corresponding unit cell parameters can be found in Table 6.1. The asymmetric unit contains a single Cu^{2+} cation and two crystallographically inequivalent picolinate anions. The first one is coordinated to one copper cation binding the equatorial positions of the metal ion through atoms N3 and O3 in a bidentade mode, and also binds to an adjacent copper cation using O4 in an axial position. This results in the formation of centrosymmetric copper(II) dinuclear entities, where the two metal ions are bound through double *syn*, *anti*-out-of-plane carboxylato bridges with a Cu–Cu distance of 5.2040(11) Å (Figure 6.1).

Table 6.1. Crystallographic data and structural refinement for $Cu_2(\mathbf{L7})_4$ (**7**).

Empirical formula	$C_{26}H_{14}CuN_4O_4$
Formula weight	509.95
Crystallographic system	Triclinic
Space group	P–1 (no. 2)
a/ Å	9.3748(8)
b/ Å	10.6145(9)
c/ Å	11.6674(10)
α/ °	70.226(8)
β/ °	88.843(7)
γ/ °	74.446(7)
V/ Å³	1049.35(17)
Z	2
R(int)	0.0951
ρ_{calc}/ g·cm^{-3}	1.614
μ/ mm^{-1}	1.086
Crystal dimensions/ mm	0.1382 x 0.0569 x 0.0328
T/ K	120.00(10)
λ/ Å	0.71073 A
2θ range/ °	5.777< 2θ < 59.8314
Index ranges for h, k , l	-12/13,-14/14,-16/16
Completeness to θ = 26.00° (%)	99.9
Refinement method	Full-matrix least-squares on F^2
Collected reflections	25443
Unique reflections	5604
Data/Restraints/Parameters	5604/ 0 / 316
Goodness-of-fit on F^2	0.890
R, wR [I > 2sigma(I)] [a]	R1 = 0.0610, wR2 = 0.1443
R, wR (all data) [a]	R1 = 0.1154, wR2 = 0.1833
$\Delta\rho_{max}$ and $\Delta\rho_{min}$ (e·Å^{-3})	1.166, -0.836

[a] $R = \Sigma(||F_o| - |F_c||)/\Sigma|F_o|$; $wR = \{\Sigma[w(F_o^2 - F_c^2)^2]/\Sigma[w(F_o^2)^2]\}^{1/2}$

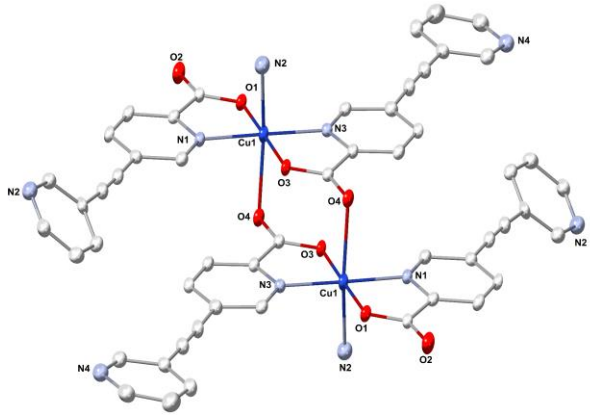

Figure 6.1. ORTEP view of the doubly-bridged dinuclear unit of **7**. Thermal ellipsoids are drawn at the 50% probability level. H atoms have been omitted for clarity.

Dinuclear copper(II) compounds bridged by carboxylate spacers have been extensively studied due to their interesting magnetic properties.[6] The variable bridging modes of the carboxylate groups can result in a wide variety of magnetic properties and, in particular, the formation of the *syn*, *anti*- (axial-equatorial) carboxylato bridge is very frequent in copper(II) coordination chemistry.[7] In fact, a high number of single-bridged[8] and double-bridged[9] picolinato complexes have been reported.

The second anion coordinates the equatorial positions of the copper cation in a bidentade mode using atoms N1 and O1 and connects the dinuclear complexes into a chain of dimers through the pyridine nitrogen atom N2. It can be noted that the mean planes of the ditopic ligands lie parallel to each other in this chain of dimers (Figure 6.2).

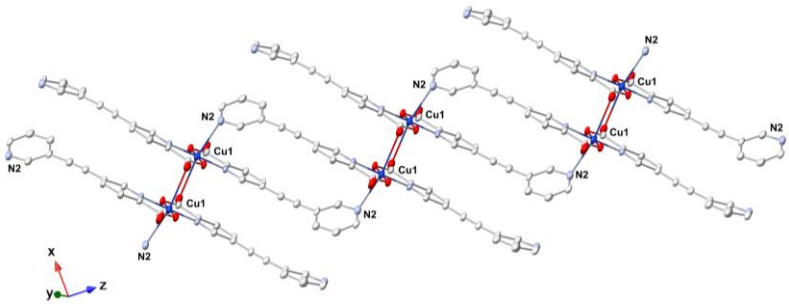

Figure 6.2. ORTEP view of the dimeric copper(II) picolinate chains of **7** running along the [0–11] direction. Thermal ellipsoids are drawn at the 50% probability level. H atoms have been omitted for clarity.

These doubly-bridged chains are further packed into layers by the establishment of π-π stacking interactions involving the free pyridine moiety between adjacent chains (Figure 6.3).

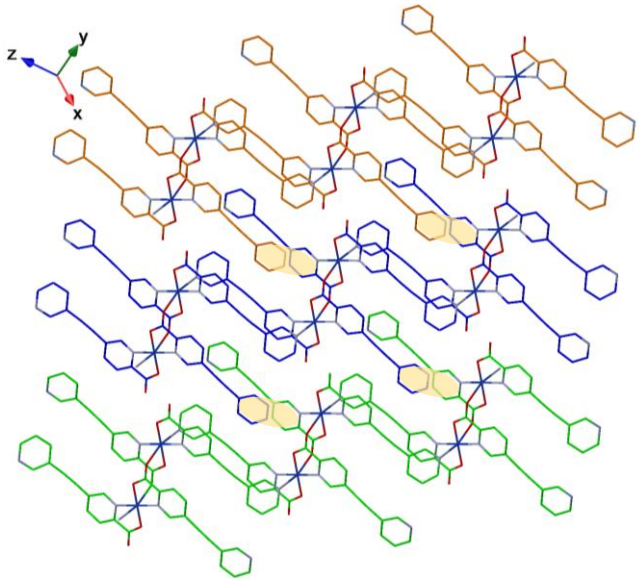

Figure 6.3. Representation of the layered structure of **7**. Each chain is shown in a different colour and π-π stacking interactions between adjacent chains of dimers are indicated in yellow. H atoms have been omitted for clarity.

As it is shown in Figure 6.1, the metal ion presents a CuN_3O_3 tetragonally distorted octahedral environment. Two carboxylate oxygen atoms and two nitrogen atoms from two chelate picolinate subunits are present in the equatorial plane. Copper-carboxylate Cu–O bond distances (mean value: 1.943 ± 0.008 Å) are shorter than copper-pyridine Cu–N bonds (mean value: 1.975 ± 0.006 Å), as expected from electrostatic considerations. There is a slight difference between the two Cu–O distances (Cu1–O1: 1.935(3) Å *vs* Cu1–O3: 1.951(3) Å) due to the higher nucleating character of the bridging picolinate N3O3 ligand in comparison to the terminal picolinate N1O1. Instead, the copper-pyridine Cu–N distances are more similar (Cu1–N1: 1.980(3) Å *vs* Cu1–N3: 1.969(3) Å). It has to be noted that the two picolinate chelate rings are almost planar in order to maximise the electronic delocalisation. On the other hand, the axial positions in the coordination sphere are occupied by the bridging picolinate (Cu1–O4: 2.738(3) Å) and pyridine (Cu1–N2: 2.543(3) Å) ligands. In both cases, the distances are higher than the equatorial ones, as a common feature from the Jahn-Teller effect. The torsion angle between the pyridine and carboxylate units

in the terminal picolinate anion indicates less geometric constraints in comparison to the bridging one (α = 2.2 *vs* 6.0°). In addition, the binding of this pyridine moiety (N2) to an axial position of the copper cation results in a notable deviation from planarity. For this anion, the dihedral angle between the two pyridine rings is 37.6°, whereas the first ligand presents a nearly planar conformation with a smaller dihedral angle between the two pyridine rings (11.1°). Regarding the bending of the triple bond, the terminal picolinate ligand also exhibits a higher deviation from the ideal 180° geometries (C-C≡C and C≡C-C angles of 176.38 and 177.29 *vs* 177.07 and 178.47°, respectively).

8 crystallises in the triclinic space group *P*–1 and the corresponding unit cell parameters are listed in Table 6.2. The asymmetric unit contains two crystallographically inequivalent Cu^{2+} cations, Cu1 and Cu2, and three independent anions. Cu1 lies on a centre of symmetry and presents a distorted (elongated) octahedral environment: it is coordinated by two picolinate ligands in equatorial positions (Cu1–O1: 1.950(2) Å; Cu1–N1: 1.972(3) Å) whereas the two axial sites (Cu1–O10: 2.689(3) Å) are occupied by bridging picolinate ligands that bind also to Cu2 in a *syn*, *anti*- mode of the carboxylate moiety (Figure 6.4).

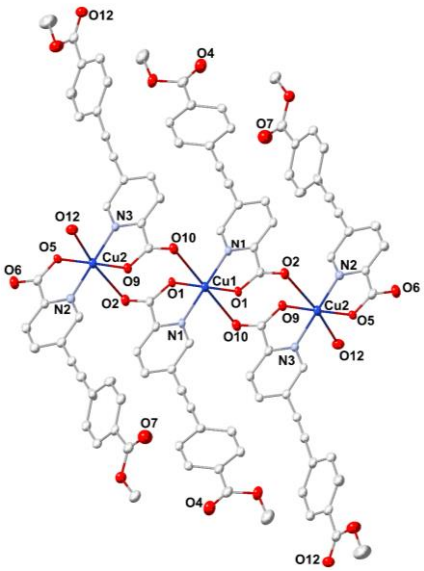

Figure 6.4. ORTEP view of the trimeric unit of **8**, showing the coordination environment around both metal cations. Thermal ellipsoids are drawn at the 50% probability level. H atoms have been omitted for clarity.

Table 6.2. X-ray crystallographic data and structural refinement for Cu_3(**MeL8**)$_6$ (**8**).

Empirical formula	$C_{96}H_{60}Cu_3N_6O_{24}$
Formula weight	1872.19
Crystallographic system	Triclinic
Space group	P–1 (no. 2)
a/ Å	10.5778(3)
b/ Å	10.7471(3)
c/ Å	18.2489(6)
α/ °	98.429(3)
β/ °	102.475(3)
γ/ °	98.574(2)
V/ Å^3	1968.29(11)
Z	1
R(int)	0.1001
ρ_{calc}/ g·cm^{-3}	1.579
μ/ mm^{-1}	0.893
Crystal dimensions/ mm	0.278x 0.080x 0.065
T/ K	120.00(10)
λ/ Å	0.71073 A
2θ range/ °	4.8976 < 2θ < 59.9662
Index ranges for h, k , l	-14/14,-15/14,-25/23
Completeness to θ = 26.00° (%)	99.9
Refinement method	Full-matrix least-squares on F^2
Collected reflections	48495
Unique reflections	10514
Data/ Restraints/Parameters	10514/ 0 / 586
Goodness-of-fit on F^2	1.033
R, wR [I > 2sigma(I)] [a]	R1 = 0.0639, wR2 = 0.1337
R, wR (all data) [a]	R1 = 0.1327, wR2 = 0.1721
$\Delta\rho_{max}$ and $\Delta\rho_{min}$ (e·Å^{-3})	0.857, -0.809

[a] $R = \Sigma(||F_o| - |F_c||)/\Sigma|F_o|$; $wR = \{\Sigma[w(F_o^2 - F_c^2)^2]/\Sigma[w(F_o^2)^2]\}^{1/2}$

The second Cu^{2+} cation is located on a general position and also presents an elongated octahedral environment: it is surrounded by two chelating picolinate ligands lying on equatorial sites (mean values, Cu2–O: 1.948 ± 0.004 Å *vs* Cu2–N: 1.972 ± 0.01 Å). One axial position is filled by another independent bridging picolinate ligand (Cu2–O2: 2.747(3) Å) and the remaining axial site is capped by a carbonyl group of the methyl ester moiety (Cu2–O12: 2.676(3) Å). Again, Cu–O bond distances are shorter than Cu–N, as expected from electrostatic considerations, and axial distances are clearly larger than the equatorial ones due to Jahn-Teller distortion.

This connectivity leads to the formation of a linear centrosymmetric copper(II) trinuclear complex, where the metal ions are connected through double *syn*, *anti*-carboxylato bridges, with an intermetallic distance (Cu1–Cu2) of 5.047(4) Å. This value is slightly shorter in comparison to that obtained for compound **7**, being the axial-equatorial binding mode of the bridged carboxylate moiety the

same in both compounds. Despite the fact that a relatively high number of linear copper(II) trinuclear complexes have been reported, most of them are triazolato,[10] pyrazolato,[11] and alkoxo[12]-bridged systems. Only a few of the published compounds contain a bridging carboxylate anion[13] and it has to be highlighted that the axial-equatorial binding mode has never been observed before in this kind of complexes.

Regarding the three independent ligands, the first one coordinates to the central Cu1 ion through atoms N1 and O1 in a chelating centrosymmetric environment. In addition, it binds to external copper centres (Cu2) *via* O2. The second one coordinates to Cu2 through atoms N2 and O5 (Cu2–N2: 1.962(3) Å; Cu2–O5: 1.945(2) Å) in the equatorial sites as a terminal ligand. The third anion binds equatorially to Cu2 cation *via* atoms N3 and O9 (Cu2–N3: 1.982(3) Å; Cu2–O9: 1.950(2) Å), and also acts as a bridging picolinate *via* O10 connecting to Cu1 ions. The latter ligand enables the linking of the trinuclear complexes into a chain of trimers (Figure 6.5) through the ester function (O12).

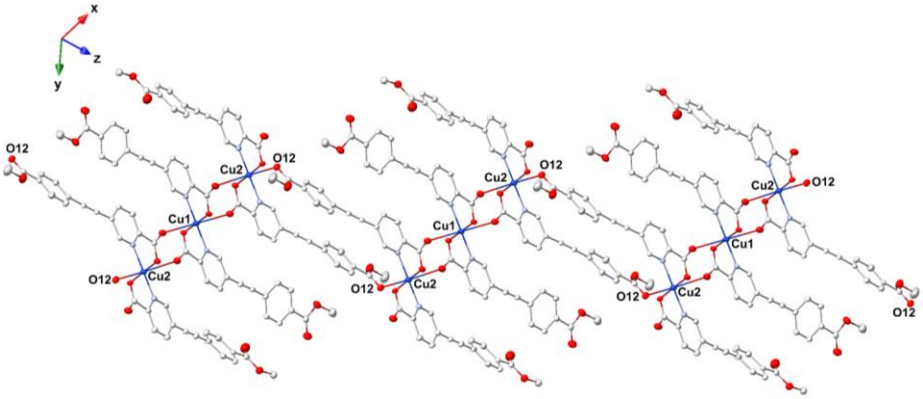

Figure 6.5. ORTEP view of the doubly-bridged copper(II) picolinate chains of **8** running along the [101] direction. Thermal ellipsoids are drawn at the 50% probability level. H atoms have been omitted for clarity.

Despite the differences observed in the coordination modes of the three independent ligands, all of them present a twisted conformation, with a strong deviation from planarity as indicated by the dihedral angles between the two aromatic rings (27.28, 27.02 and 29.87°). In addition, as observed for compound **7**, the torsion angles between the pyridine and carboxylate units in the bridging picolinate anions are higher in comparison to the terminal one (α = 6.69 and 8.08° *vs* 0.05°). Also, the bending of the triple bond is more pronounced for the bridging picolinate ligands (C-C≡C and C≡C-C angles of 177.99 and 177.68° for

the first anion, 175.04 and 177.56° for the third anion *vs* 178.02 and 178.64° for the second one, respectively).

Further insight into the structure shows that the chains of trimers are packed by π-π stacking interactions in the three dimensions of the space, keeping the equatorial planes of all the copper(II) ions parallel to each other (Figure 6.6).

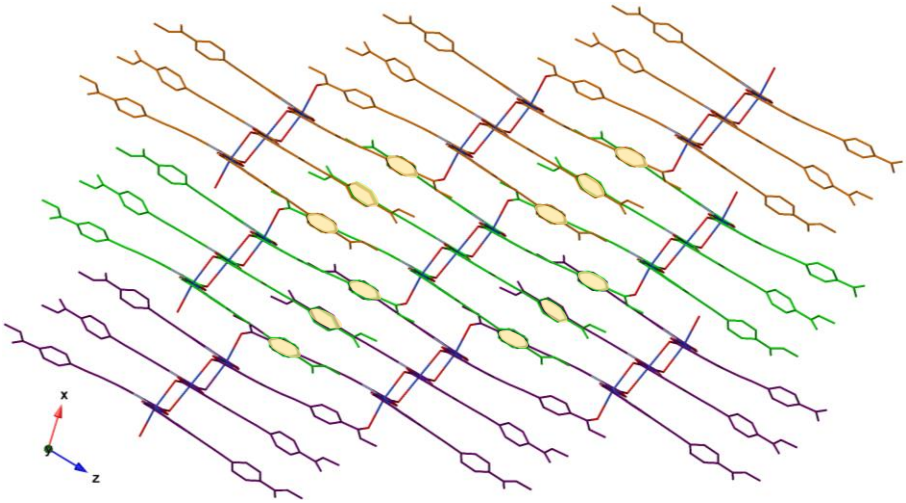

Figure 6.6. Representation of the crystal structure of **8**, emphasising the presence of π–π stacking interactions (yellow spheres) between adjacent chains of trimers that are shown in different colour. H atoms have been omitted for clarity.

B. Powder X-ray diffraction and thermogravimetric analysis

Figure 6.7 shows the comparison between the powder X-ray diffractograms measured at room temperature of the bulk samples and the simulated patterns from the X-ray single crystal data recorded at 120 K for compounds **7** and **8**. In the first case, there is a good agreement between both patterns, discarding the presence of impurities. In the second case there is a reasonable agreement between both patterns, with just the appearance of an additional peak at low angles ($2\theta \approx 6.45°$) in the experimental pattern with respect to the simulated one. This may indicate the presence of a small amount of crystalline impurities, however, the corresponding elemental analysis is consistent with the formulation assigned for the pure sample.

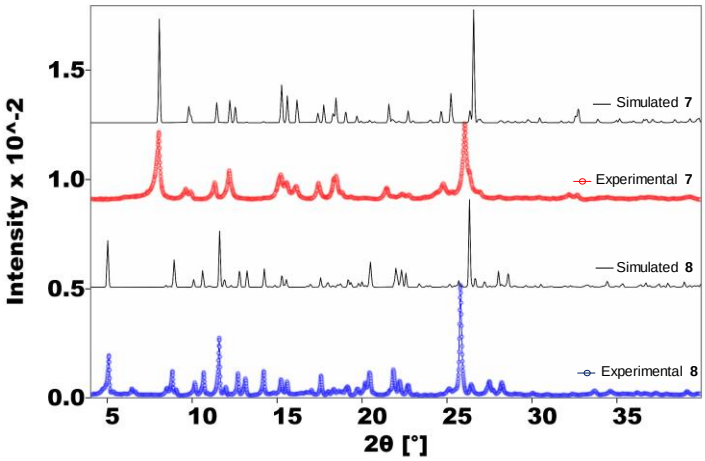

Figure 6.7. Powder X-ray diffractograms of **7** and **8** collected at room temperature (in red and blue, respectively). The simulated patterns (in black) obtained using *CrystalDiffract* software at 120 K are shown for comparison.

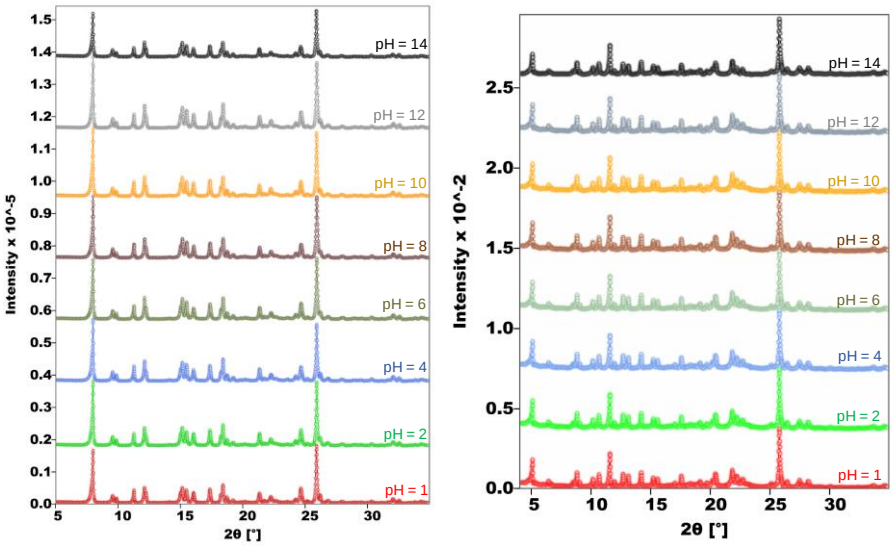

Figure 6.8. Powder X-ray diffractograms of **7** (left) and **8** (right) collected at room temperature at different pH values ranging from 1 to 14.

Moreover, powder samples of both compounds were soaked in aqueous solutions at different pH values for 2 h, filtered, air dried and their powder X-ray diffractogram measured. Figure 6.8 shows the results of these studies, confirming the high stability of both copper complexes under all pH values. In addition, thermogravimetric analyses were performed in order to determine the

temperature range of stability of both solid materials (Figure 6.9). Compound **7** is stable up to 565 K whereas complex **8** shows a slightly higher stability (up to 575 K). Further increase of the temperature results in decomposition of both samples. The lack of loss of solvent molecules at lower temperatures is in agreement with the anhydrous formulation determined from X-ray crystal structure experiments in both cases.

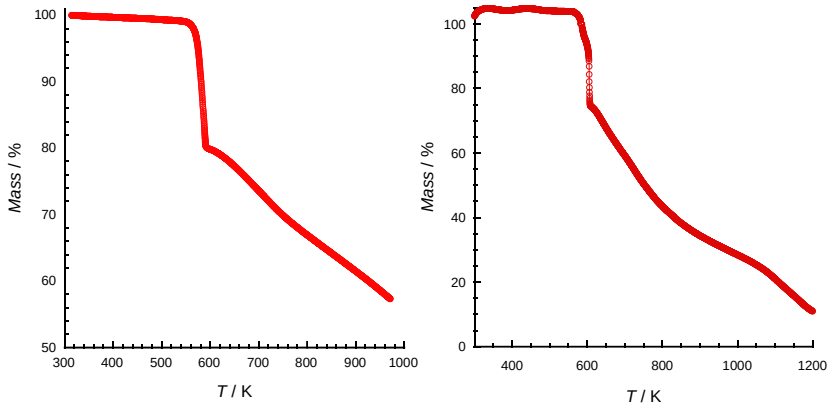

Figure 6.9. Thermogravimetric analyses of complexes **7** (left) and **8** (right). The plots confirm the anhydrous character of these salts.

6.3.2. Magnetic characterisation

A. Magnetic properties

In order to determine if there is any magnetic interaction between the Cu(II) centres, variable temperature magnetic susceptibility measurements were performed at 1000 Oe applied DC field in 2-300 K temperature range. The thermal variation of the χT product (χ = molar magnetic susceptibility per two copper(II) ions; T = absolute temperature) of complex **7** is shown in Figure 6.10.a. It presents a nearly constant value of 0.85 emu·K·mol^{-1} between 300 and 20 K, a value slightly higher than that expected for two uncorrelated S = ½ spins with a Landé factor g = 2 (0.75 emu·K·mol^{-1}). Upon further cooling below 20 K, the χT product decreases continuously and at 1.95 K the χT product reaches a value of 0.62 emu·K·mol^{-1}. This behaviour indicates antiferromagnetic coupling between Cu^{2+} ions in the dinuclear unit, the most common behaviour with about 95% of copper(II) dinuclear compounds presenting an antiferromagnetic interaction.

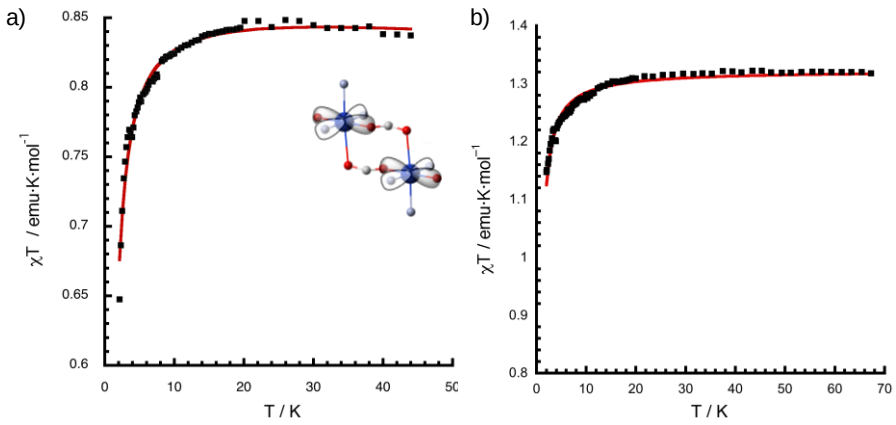

Figure 6.10. a) Temperature dependence of the χT product of **7** with an applied field of 1000 Oe. The red line shows the best-fit to the Bleaney-Bowers equation. The inset represents a schematic illustration of the d_{x2-y2} type magnetic orbital in centrosymmetric Cu(II) dimers present in **7**. b) Thermal variation of the χT product of **8**. The red line shows the best-fit to a linear trimer of **S** = ½ spins.

In agreement with the dinuclear structure of **7**, its magnetic susceptibility data were fitted to a simple dimer model (Bleaney-Bowers equation, Eq. 6.1, spin Hamiltonian: $\mathbf{H} = -2J\mathbf{S}_{Cu}\mathbf{S}_{Cu}$),[6] yielding a weak antiferromagnetic coupling constant $J = -0.59$ cm^{-1} and $g = 2.17$. The solid line obtained with these calculated values reproduces the results within the experimental accuracy (Figure 6.10.a).

$$\chi T = \frac{2 \cdot N_A \cdot g^2 \cdot \mu_B{}^2}{k_B\left(3+\exp\left(-\frac{2J}{T}\right)\right)} \text{ (Eq. 6.1)}$$

N_A corresponds to the Avogadro number, k_B is the Boltzmann constant, μ_B is the Bohr magneton, g is the Landé factor and J is the exchange coupling constant.

The temperature dependence of χT (χ = molar magnetic susceptibility per three copper(II) ions; T = absolute temperature) product for complex **8** (Figure 6.10.b) presents a practically constant value of 1.31 emu·K·mol^{-1} between 300 K and 20 K, slightly higher than that expected for three uncorrelated $S = 1/2$ spins with a Landé factor $g = 2$ (1.125 emu·K·mol^{-1}). Further cooling below 20 K shows a continuous decrease of the magnetic signal until reaching a value of 1.15 emu·K·mol^{-1} at 2 K. This behaviour reveals antiferromagnetic coupling between copper ions in the trinuclear unit. A linear symmetric trimer model with $\mathbf{H} = -2J(\mathbf{S}_{Cu1}\mathbf{S}_{Cu2}+\mathbf{S}_{Cu2}\mathbf{S}_{Cu1})$ was used to fit the magnetic properties (results shown in Figure 6.10.b. The interaction between terminal Cu^{2+} ions has been set equal to

zero), yielding a weak antiferromagnetic exchange coupling constant J = –0.30cm^{-1} and g = 2.17.

The magnitude of the antiferromagnetic coupling constant (J) is proportional to the overlap integral between the magnetic orbitals. The unpaired electron on each axially distorted Cu(II) ion is in a d_{x2-y2} type magnetic orbital, which mainly points towards the equatorial sites (see inset in Figure 6.10.a). Therefore, only a very small spin density is concentrated in the axial positions. Besides, the magnetic interaction in both compounds takes place through the picolinate group of the ligand in a *syn-anti* coordination mode, linking an equatorial position of a metal centre with an axial position on the neighbouring metal centre. Thus, this exchange pathway provides a very weak overlap between the magnetic orbitals that results in very weak interactions and small values of the corresponding exchange coupling constant.

B. EPR spectroscopy

Powder EPR spectra have been recorded on polycrystalline powder samples at room temperature at the X- (0-5000 G) and Q-band frequencies (0-15000 G). The X-band EPR spectra of **7** and **8** (Figure 6.11) both display typical axial features, giving the following values of the g parameters: g_{II} = 2.242 (parallel transition); $g_{\perp}$ = 2.070 (perpendicular transition) for **7**, and g_{II} = 2.227; $g_{\perp}$ = 2.072 for **8**. The g values are those expected for copper atoms exhibiting a very elongated octahedral environment, and indicate a basically d_{x2-y2} ground state for the Cu(II) ion.[14,15] The lack of half-field transition signals, usually observed in the case of dinuclear species,[14,16] may indicate a very weak interaction between the copper(II) centres.

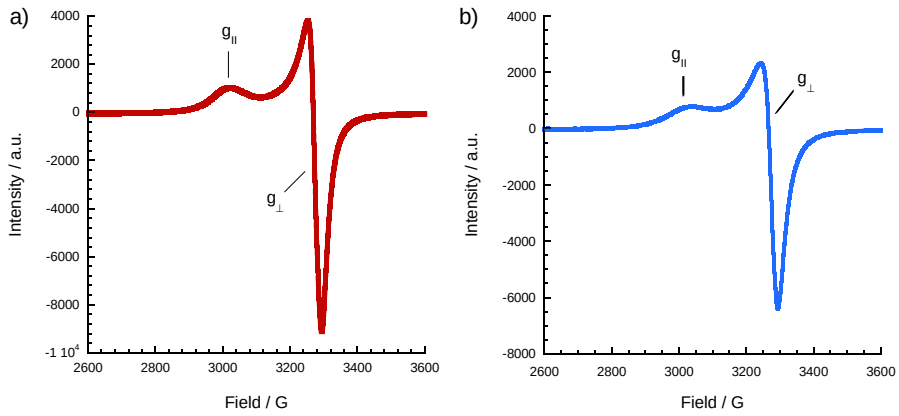

Figure 6.11. a) X-band EPR spectrum of **7**. b) X-band EPR spectrum of **8**.

The Q-band EPR spectra of compounds **7** and **8** exhibit a quasi-axial pattern with a slight rhombicity (Figure 6.12). The three principal components of the *g* tensor are $g_1 = 2.263$; $g_2 = 2.080$ and $g_3 = 2.067$ for the dimer **7** and $g_1 = 2.243$; $g_2 = 2.065$ and $g_3 = 2.0654$ for the trimer **8**, being very close values to those observed for similar systems.[16]

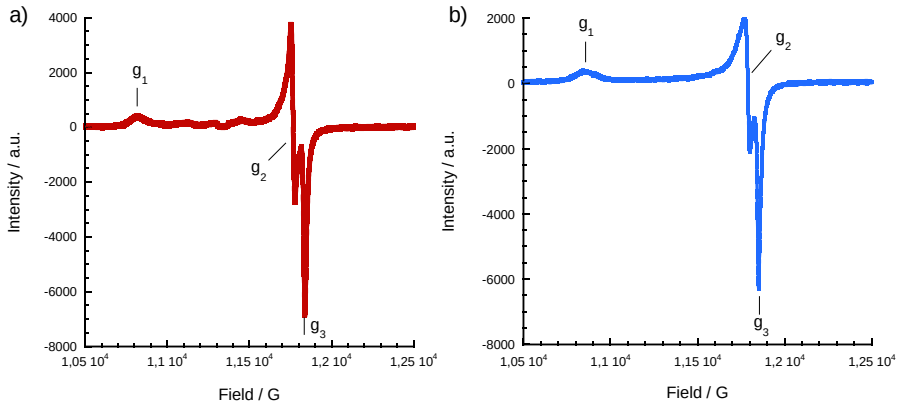

Figure 6.12. a) Q-band EPR spectrum of **7**. b) Q-band EPR spectrum of **8**.

The average *g* factor is g_{av} = 2.137 and 2.121 for compounds **7** and **8**, respectively, which compare well with that obtained from magnetic susceptibility measurements (*g* = 2.17 for both complexes). The axial signal of **7** appears to present hyperfine splitting due to the coupling with the copper nucleus ($I = 3/2$). In this case, the Zeeman line is split into four lines (m_I= 3/2, 1/2, -1/2, -3/2), separated by a hyperfine coupling constant (*A*) of 170 G. Nevertheless, despite the fact of observing hyperfine splitting in other weakly coupled Cu(II) dimers,[17] the position of the split band and the value of the coupling constant suggest the presence of some monomeric impurities in the sample.

6.3.3. Discussion

There is a common and important feature in both compounds, which is the presence of an out-of-plane carboxylate double-bridge between copper(II) ions. Nevertheless, compound **7** forms dimers whereas compound **8** stabilises trimeric units. Now, the question that arises is why these different topological arrangements have been adopted for the copper complexes? What prompted copper picolinate units to exhibit such variations? Since the pyridine nitrogen atoms present a stronger σ-donor ability with respect to the oxygen atom of methyl benzoate, the axial distance in compound **7** (Cu1–N2: 2.543(3) Å) is

shorter than the equivalent axial distance in complex **8** (Cu2–O12: 2.676(3) Å). This implies that axial capping of the doubly-bridged picolinate entities is more favoured in **7** than in **8** and may be a possible explanation for the fact that 50% of the pyridine moieties are bound to the copper ions in **7** whereas only 33% of the methyl benzoate subunits bind in **8**. As a result, complex **8** yields trimers instead of dimers.

The magnetic interaction in both compounds is very small as indicated by magnetic susceptibility and EPR measurements. In the latter context, the simple pattern and marked similarity between the spectra of both compounds are attributed to the coplanar arrangement of the equatorial planes of the copper(II) centres, resulting in similar exchange pathways. Furthermore, the EPR measurements are in good accordance with the fact that the greater the spin coupling, the greater the intensity of the EPR line, showing the spectra of compound **7** a slightly increased intensity. The only difference between both patterns is the apparent presence of hyperfine splitting in compound **7**. However, due to the value of the coupling constant and to the position of the split signals, it may be best regarded as the signature of some monomeric impurities in the sample. This would explain why trimer **8** lacks of any hyperfine splitting band, despite of showing a weaker exchange interaction between adjacent copper(II) ions. In general, weak antiferromagnetic interactions are observed in carboxylate bridged copper(II) complexes in which the carboxylate moiety adopts the *syn-anti* coordination mode. This behavior can be explained taken into account the small overlap between the magnetic orbitals of the copper atoms through the *syn-anti* carboxylato bridge. This kind of small interaction can produce either antiferromagnetic or ferromagnetic exchange pathways.[18,19] In general, ferromagnetic interactions have been observed for malonato bridged systems[20] and other carboxylate salts.[21] On the other hand, antiferromagnetic coupling has been associated to several squarato-,[7a] oxamato-,[22] and oxalato-bridged complexes,[23] in addition to other bridging carboxylates.[24] A Cu(II) chain structure exhibiting double picolinate bridges has been reported with a J = –1.04cm^{-1}.[9a] This value is similar in sign and magnitude to the values calculated in this thesis for compounds **7** and **8**.

6.4. $[Fe(H_2O)_2(\mathbf{L2})]$ (**9**)

6.4.1. Structural characterisation

A. Single crystal X-ray diffraction

9 crystallises in the triclinic space group *P*–1 and the corresponding unit cell parameters are included in Table 6.3. The asymmetric unit contains only one crystallographically inequivalent Fe^{2+} cation located in an inversion centre, half independent anion and one water molecule.

Table 6.3. X-ray crystallographic data and structural refinement for $[Fe(H_2O)_2(\mathbf{L2})]$ (**9**).

Empirical formula	$C_7H_5Fe_{0.5}0NO_3$
Formula weight	179.04
Crystallographic system	Triclinic
Space group	P–1 (no. 2)
a/ Å	5.119(12)
b/ Å	6.55(3)
c/ Å	10.63(4)
α/ °	84.44(18)
β/ °	83.04(15)
γ/ °	69.18(19)
V/ Å^3	330(3)
Z	2
R(int)	0.0969
ρ_{calc}/ g·cm^{-3}	1.801
μ/ mm^{-1}	1.178
Crystal dimensions/ mm	0.137x 0.043x 0.030
T/ K	120(2)
λ/ Å	0.71073 A
2θ range/ °	6.6640 < 2θ < 70.878
Index ranges for h, k , l	-8/8,-10/10,-16/17
Completeness to θ = 25.242° (%)	99.9
Refinement method	Full-matrix least-squares on F^2
Collected reflections	15875
Unique reflections	2656
Data/Restraints/Parameters	2656/ 0 / 114
Goodness-of-fit on F^2	1.045
R, wR [I > 2sigma(I)] [a]	R1 = 0.0766, wR2 = 0.1315
R, wR (all data) [a]	R1 = 0.1181, wR2 = 0.1474
$\Delta\rho_{max}$ and $\Delta\rho_{min}$ (e·Å^{-3})	0.897, -1.088

[a] $R = \Sigma(||F_o| - |F_c||)/\Sigma|F_o|$; $wR = \{\Sigma[w(F_o^2 - F_c^2)^2]/\Sigma[w(F_o^2)^2]\}^{1/2}$

The iron centre presents a slightly distorted octahedral N_2O_4 coordination environment: it is coordinated by two picolinate ligands in equatorial positions (Fe1–O1: 2.121(7) Å; Fe1–N1: 2.167(7) Å), whereas the two axial sites (Fe1–O1W: 2.094(7) Å) are occupied by two water molecules in *trans*. As observed in

previous compounds, Fe–O bond distances are shorter than Fe–N, as expected from electrostatic considerations. Fe–N bond lengths are typical for high-spin iron(II) ions (Table 6.4) and this is consistent with the magnetic susceptibility measurements (Section 6.4.2, *vide infra*).[25] Each ligand binds to two metallic centres in a bis (bidentate) chelating mode, resulting in the formation of a wave-like iron(II) chain network, with an intermetallic distance (Fe1–Fe1) of 12.345 Å (Figure 6.13).

Table 6.4. Fe–N, Fe–O bond lengths and O–Fe–O, O–Fe–N bond angles for Fe1 centre in compound **9**.

Bond lengths/Å		Bond angles/°	
Fe1–O1W	2.094(7)	N1–Fe1–O1	77.64(19)
Fe1–O1	2.121(7)	O1–Fe1–O1W	90.8(3)
Fe1–N1	2.167(7)	O1W–Fe1–N1	88.5(3)

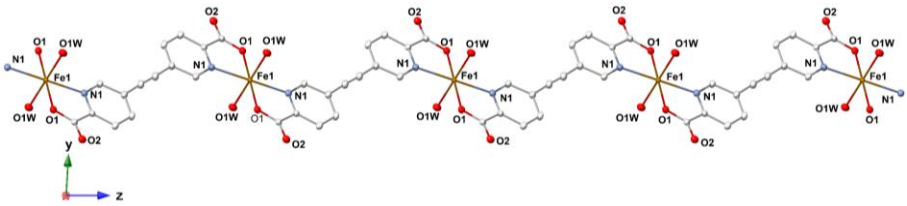

Figure 6.13. ORTEP view of the bridged iron(II) picolinate chain structure of **9** running along the [–120] direction. Thermal ellipsoids are drawn at the 50% probability level. H atoms have been omitted for clarity.

This bis (bidentate) coordination mode has been observed previously in a pyridazine-3,6-dicarboxylate based dinuclear complex of iron(II).[26] Nevertheless, there is a lack of reports concerning iron(II) complexes with extended picolinate ligands. It is worth noting that all the atoms of the ligand lie in the same plane (the dihedral angle between the two aromatic rings is zero), maximising the electronic delocalisation and adopting a linear conformation with an *anti*-alignment of the picolinate moieties (transoid conformation). Moreover, the torsion angle between the pyridine and the carboxylate unit has a value of 2.617°, which is lower than those obtained for bridging picolinate anions in compounds **7** and **8**. However, C-C≡C and C≡C-C angles show similar values (177.49°) to those measured for bridging picolinate ligands in complexes **7** and **8**, indicating that the bending of the triple bond is still present.

The bridged iron(II) picolinate chains are connected through hydrogen bonds between water molecules bound to the iron centre and oxygen atoms of the

carboxylate groups directly linked to the metal centres (O1W–O1: 2.718(7) Å) as shown in Figure 6.14. Further insight into the structure shows that these chains are packed by π-π stacking interactions, keeping the equatorial planes of all the iron(II) ions parallel to each other (Figure 6.15).

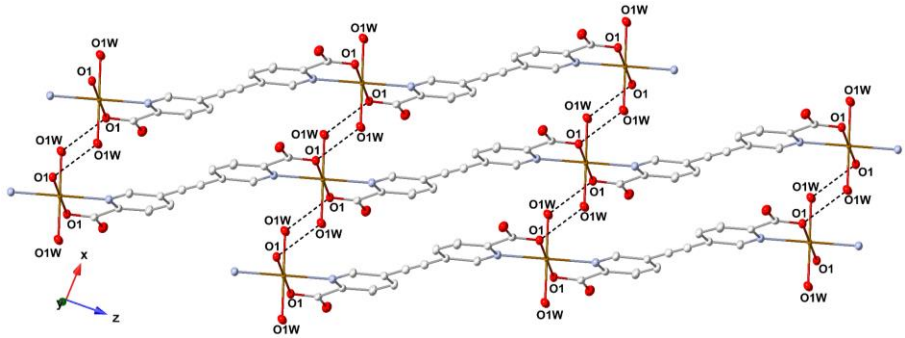

Figure 6.14. ORTEP view of the H-bonded iron(II) layered structure of **9** running along the [0–10] direction. H-bonds are depicted by dashed lines. Thermal ellipsoids are drawn at the 50% probability level. H atoms have been omitted for clarity.

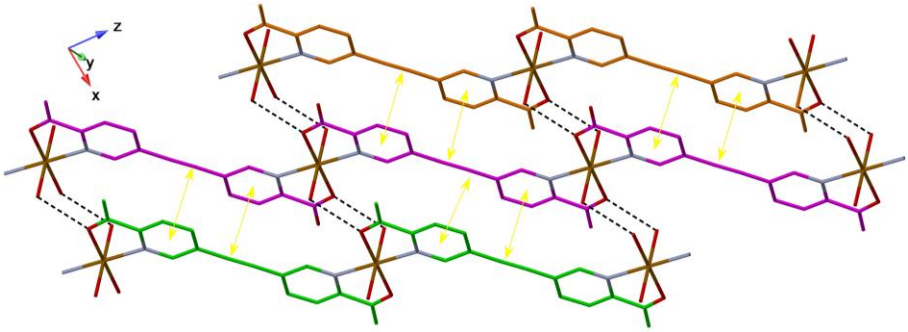

Figure 6.15. Stick representation of the H-bonded iron(II) layered structure of **9** showing the presence of π-π stacking interactions between adjacent chains that are shown in different colour. H-bonds are depicted by dashed lines and π-π interactions by yellow arrows. H atoms have been omitted for clarity.

These supramolecular layers are doubly connected by additional hydrogen bonds (O1W–O2 = 2.664(8)) that are established between water molecules and free oxygen atoms of the carboxylate units (Figure 6.16).

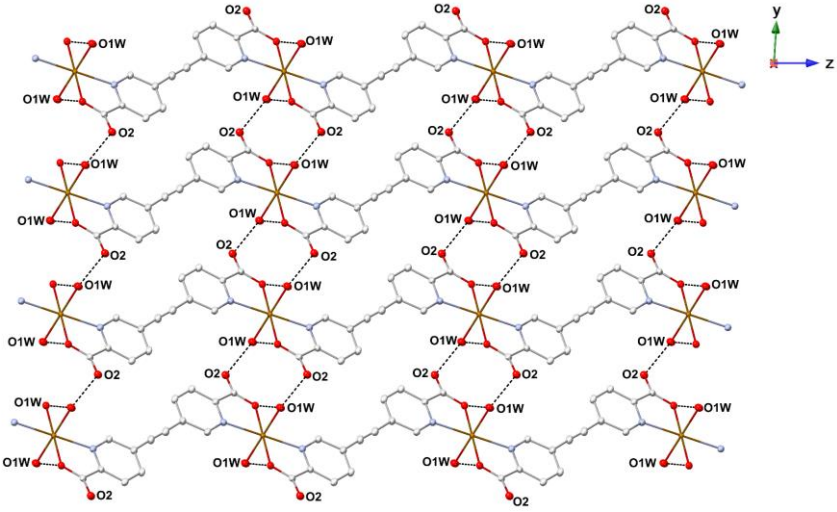

Figure 6.16. ORTEP view of the 3D supramolecular packing of **9** along the b axis. H-bonds are depicted by dashed lines. Thermal ellipsoids are drawn at the 50% probability level. H atoms have been omitted for clarity.

B. Powder X-ray diffraction and thermogravimetric analysis

The comparison between the powder X-ray diffractogram measured at room temperature of the bulk sample and the simulated diffractogram from the X-ray single crystal data recorded at 120 K is presented in Figure 6.17. There is a good agreement between both patterns, discarding the presence of impurities. Although the experimental pattern shows broad diffraction peaks that indicate a low crystalline quality, this could be improved by adding one equivalent of 4,4'-bipyridine or two equivalents of pyridine (red and green patterns shown in Figure 6.17, respectively). It has been shown that these ligands can act as a coordinative unit to participate in the formation of the final structure or serve as a template agent to direct the formation of the final product during the *in situ* assembly process, being the last scenario our case.[27]

Thermogravimetric (TG) analysis of **9** was carried out under nitrogen atmosphere in the temperature range 300-900 K. As shown in Figure 6.17, this sample is stable up to 475 K and the TG plot exhibits a multi-step weight loss. The initial weight loss between 475 and 545 K is due to the release of approximately one water molecule per iron cation (observed: 4.79%, and expected 5.03%). Further heating gives rise to a gradual and continuous weight loss until 737 K: between 545 and 632 K, a second step of weight loss ascribable to the removal of two water molecules per iron cation takes place (observed:

11.60%, and expected: 10.58%). Further heating leads to decomposition of organic moieties and subsequent decomposition of the structure. The first weight loss is associated to the removal of one water molecule absorbed from the environment, indicating that compound **9** is hygroscopic. This result has been verified by elemental analysis (section 6.7) that shows that the best fitting between experimental and calculated values of C, N and H (in %) is obtained with the inclusion of 0.75 additional water molecules to the molecular formula. The second weight loss is ascribed to the removal of two water molecules per iron cation that corresponds to coordinated water molecules. Thus, removal of these strongly bound water molecules takes place at very high temperatures and this fact is in agreement with the crystal structure described for compound **9**. Once these water molecules are lost, fast collapse of the structure occurs.

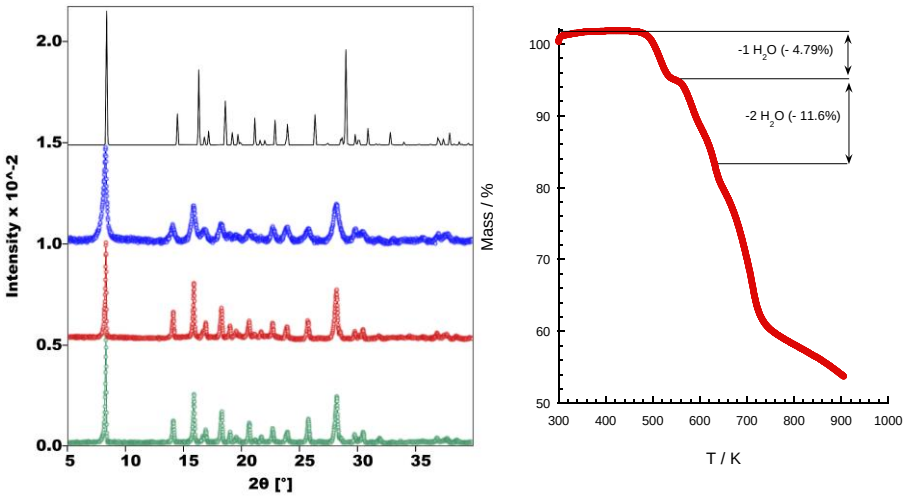

Figure 6.17. Left: Powder X-ray diffractogram of **9** collected at room temperature (in blue). The simulated diffractogram (in black) obtained using *Crystaldiffract* software at 120 K is shown for comparison. Moreover, the experimental diffractogram of **9** obtained from a mixture containing an additional equivalent of 4,4'-bipyridine or 2 equivalents of pyridine are included (shown in red and green, respectively). Right: Thermogravimetric analysis of **9**, showing a multi-step weight loss.

Finally, the stability of suspensions of compound **9** was studied in aqueous medium at different pH values. Figure 6.18 reveals that this compound is stable in a wide pH range (1-12), observing the appearance of additional peaks only at pH = 14.

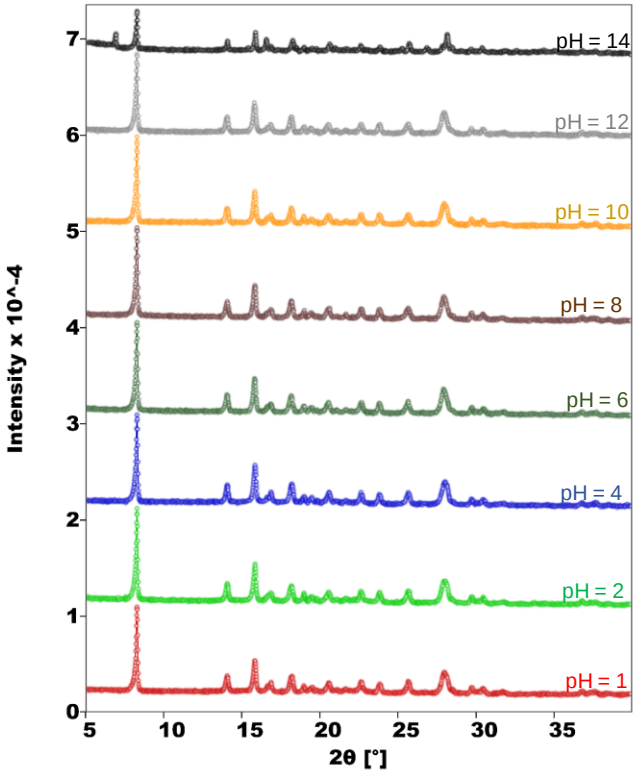

Figure 6.18. Powder X-ray diffractograms of **9** collected at room temperature at different pH values ranging from 1 to 14. The samples were soaked in aqueous solutions at different pH values for 2 h, filtered and air dried previously to their measurement.

6.4.2. Magnetic properties

Magnetic susceptibility measurements per Fe(II) atom in the 2-300 K temperature range were performed for a polycrystalline sample of **9**. As shown in Figure 6.19, between 300 and 60 K, the value of χT remains practically constant at around 3.76 emu·K·mol^{-1}. This value is very close to that expected for the spin-only value for one Fe(II) **S** = 2 high-spin (with $g \approx 2$) and is in agreement with the spin state configuration determined by X-ray crystallography. Below 50 K, there is an abrupt decrease in the χT product until reaching a value of 1.62 emu·K·mol^{-1} at 2 K. Assuming that the coupling between the iron(II) centres is negligible due to the large separation between them, this behaviour is likely ascribed to zero-field splitting effects.[25]

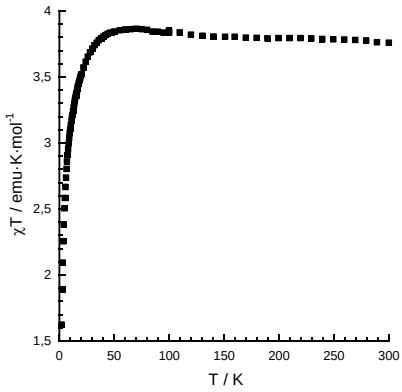

Figure 6.19. Temperature dependence of the χT product of **9** with an applied field of 1000 Oe.

6.4.3. Catalytic activity toward cyclohexane oxidation

The catalytic performance of compound **9** was evaluated in cyclohexane oxidation, using H_2O_2 as oxidant in a catalyst:oxidant:substrate ratio of 1:300:100. The reactions were performed employing acetonitrile and pyridine as deuterated solvents at ambient temperature and pressure. Preliminary results were obtained from ^{1}H- and ^{13}C-NMR spectroscopy (Figure 6.20.a-b) for 72 h of reaction. Cyclohexanol and cyclohexanone were formed during the oxidation process and were detected in ^{1}H-NMR experiments, whereas ^{13}C-NMR spectra only showed the presence of some signals of cyclohexanone, the major oxidation product. Integration of the signals associated to the cyclohexane (1.4 ppm) that remains after the reaction and to the different products (cyclohexanone at 2.27 ppm and cyclohexanol at 3.60 ppm) that have been formed allows evaluation of the catalyst selectivity and conversion (Table 6.5). A total conversion of ~ 14% was obtained, with a selectivity of 97% for cyclohexanone. The cyclohexanone yields a similar substrate conversion (13.6%) to that obtained by E. H. de Faria et al with iron complexes supported on clays.[28]

Table 6.5. Conversion (%) of cyclohexane to cyclohexanone (ONE) and cyclohexanol (OL) using **9** as a catalyst. The cyclohexanone selectivity was calculated as ONE/(ONE+OL).

ONE	OL	ONE+OL
13.6	0.3	~ 14

Control experiments (Figure 6.20.c-d) in the absence of compound **9** did not show the presence of oxidised products, revealing the catalytic efficiency of

compound **9** in promoting cyclohexane oxidation. The same experiment was carried out with an increased reaction time of 96 h, however, the conversion of cyclohexane in products was almost the same to that reached with 72 h.

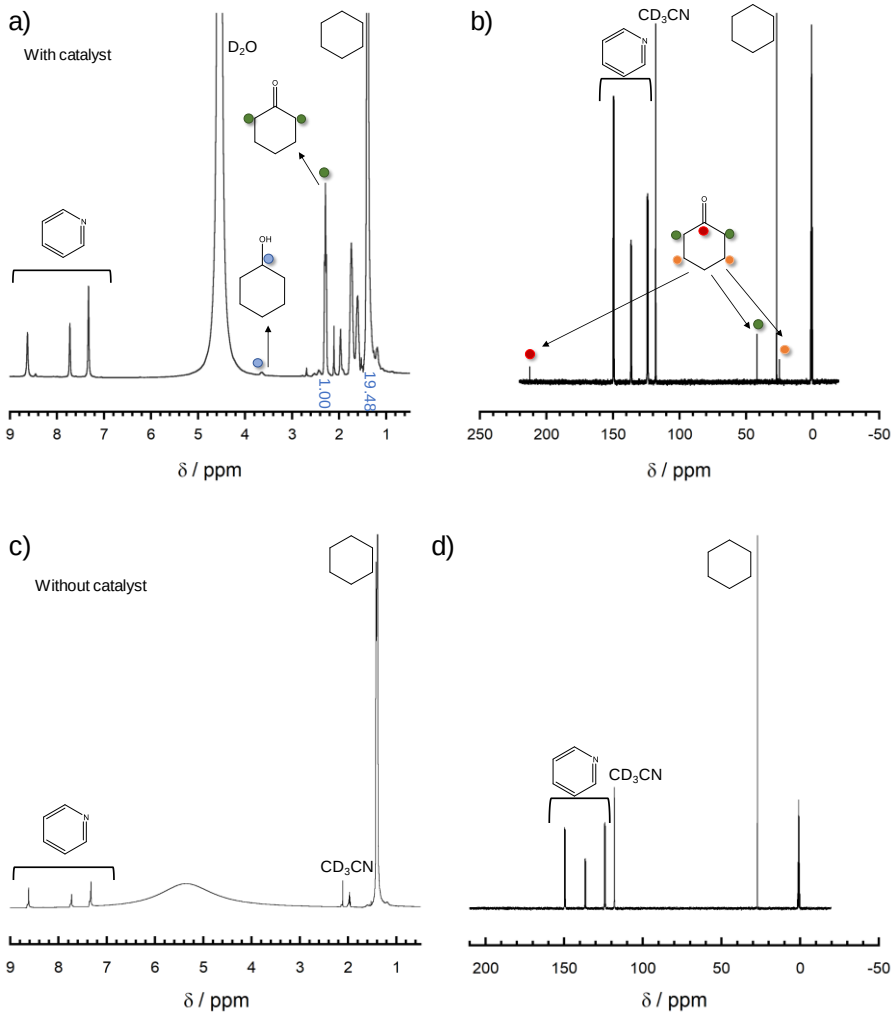

Figure 6.20. ^{1}H- and ^{13}C-NMR spectra for the cyclohexane oxidation with the presence (a and b) and absence (c and d) of compound **9** as heterogeneous catalyst after 72 h of reaction.

6.4.4. Conclusions and outlook

The synthesis, structural, magnetic and thermal characterisation of compound **9** have been described. It is a 1D iron(II)picolinate wave-like chain polymer with an extended H-bonded network in the three dimensions of the

space. It exhibits a good thermal stability in the solid state and a remarkable stability in aqueous medium at different pH values (1-12). Unfortunately, the large separation between the paramagnetic Fe(II) HS centres prevents the existence of magnetic interactions.

Prompted by several reports concerning the synthesis of 3D or 2D structures starting from 2D or 1D materials,[29] we started a systematic study in order to extend the dimensionality of compound **9**. After addition of different amounts of a second N-donor coordinating ligand (pyridine and/or 4,4'bipyridine) to the initial reaction mixture or to the previously synthesised crystals of compound **9**, no change in the appearance of the crystals nor in the diffraction pattern were observed. Even after the addition of 20 equivalents of pyridine or 10 equivalents of 4,4'-bipyridine and with long reaction times at high temperatures (130°C during 3 days). The only worth mentioning feature is that a notable increase in the intensity of the diffracted peaks was observed, indicating that these ligands act as template agents (as previously mentioned in section 6.4.1.B, Figure 6.17) but are not included in the crystal structure of the final compound.

Compound **9** is the first compound that combines iron(II) centres and ethynylene-bridged picolinate ligands. Iron-catalysed oxidation reactions based on the combination of an iron-picolinate complex and hydrogen peroxide have been extensively studied for the oxidation of saturated hydrocarbons, as mentioned in the introduction.[30-32] Apart from oxidation of hydrocarbons, it has been shown that oxidation of allylic alcohols to α,β-unsaturated carbonyl groups proceeds efficiently using this kind of systems and, in addition, that steric hindrance of the picolinate ligands around the iron centres might influence the selectivity of the reaction pathways.[30] In general, sustainable C–H activation represents a remarkable possibility to directly convert a relatively inert C–H group into a desired moiety without the need to prior implement a more reactive functional group, reducing considerably the number of synthetic steps. In light of the progress achieved using iron-picolinate complexes in this field, the catalytic activity of compound **9** was studied. Preliminary results show that this complex is efficient and highly selective in promoting cyclohexane oxidation, although more accurate experiments that allow precise quantification of the products are needed (gas chromatography using the internal standard method), as well as optimisation of the reaction conditions in order to reduce reaction time. The main advantage of this strategy is the easy separation of compound **9** from the reaction mixture by simple filtration of the solid, allowing catalyst reuse.

6.5. $[Zn(\mathbf{L7})_2]\cdot 0.5H_2O$ (**10**) and $[Zn(H_2O)_2(\mathbf{L8})]$ (**11**)

6.5.1. Structural characterisation

A. Single crystal X-ray diffraction

10 crystallises in the monoclinic space group $P2_1/n$ and corresponding crystallographic data are shown in Table 6.6. The asymmetric unit contains two crystallographically inequivalent Zn^{2+} cations located in an inversion centre (Zn1A and Zn1B), two independent **L7** anions and one uncoordinated water molecule with a partial occupancy factor of 0.5.

Table 6.6. X-ray crystallographic data and structural refinement for $[Zn(\mathbf{L7})_2]\cdot 0.5H_2O$ (**10**).

Empirical formula	$C_{26}H_{14}N_4O_{4.5}Zn$
Formula weight	519.78
Crystallographic system	Monoclinic
Space group	$P2_1/n$ (no. 14)
a/ Å	13.0702(8)
b/ Å	12.8461(7)
c/ Å	13.1323(9)
α/ °	90
β/ °	96.934(6)
γ/ °	90
V/ Å^3	2188.8(2)
Z	4
R(int)	0.0552
ρ_{calc}/ g·cm^{-3}	1.577
μ/ mm^{-1}	1.168
Crystal dimensions/ mm	0.17x 0.145 x 0.06
T/ K	120.10(14)
λ/ Å	0.71073 A
2θ range/ °	5.662 < 2θ < 59.574
Index ranges for h, k , l	-17/18,-17/16,-17/18
Completeness to θ = 25.242° (%)	99.9
Refinement method	Full-matrix least-squares on F^2
Collected reflections	31343
Unique reflections	5847
Data/Restraints/Parameters	5847/ 0 / 328
Goodness-of-fit on F^2	1.046
R, wR [I > 2sigma(l)] [a]	R1 = 0.0447, wR2 = 0.0783
R, wR (all data) [a]	R1 =0.0727, wR2 = 0.0874
$\Delta\rho_{max}$ and $\Delta\rho_{min}$ (e·Å^{-3})	0.351 and -0.385

[a] $R = \Sigma(||F_o| - |F_c||)/\Sigma|F_o|$; $wR = \{\Sigma[w(F_o^2 - F_c^2)^2]/\Sigma[w(F_o^2)^2]\}^{1/2}$

Both zinc centres present a slightly distorted octahedral N_4O_2 coordination environment. The equatorial positions are occupied by two chelating picolinate ligands (Zn1A–O1A: 2.0475(15) Å; Zn1A–N1A: 2.1392(17) Å; Zn1B–O1B:

2.0594(15) Å; Zn1B–N1B: 2.1354(17) Å) whereas the axial sites are filled by two nitrogen atoms from two pyridine moieties (Zn1A–N2A: 2.2018(17) Å; Zn1B–N2B: 2.2242(18) Å). Only crystallographically equivalent **L7** anions coordinate to a particular zinc centre (Figure 6.21). As observed in previous compounds, Zn–O bond distances are shorter than Zn–N, as expected from electrostatic considerations. The coordination mode of both ligands is identical: each one binds to two equivalent metallic centres in a (bidentate) chelating/pyridine (monodentate) mode, resulting in the formation of a layered structure for each subnetwork (Figure 6.22).

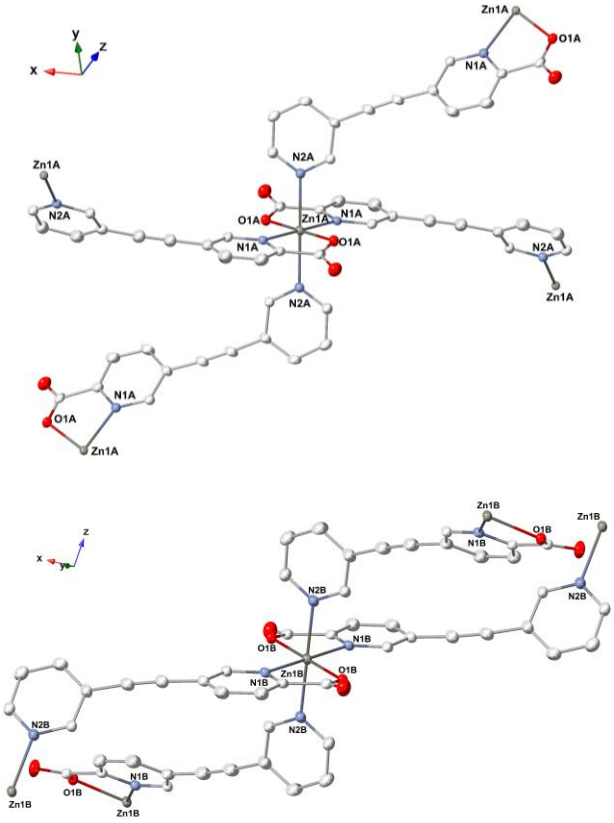

Figure 6.21. ORTEP view of the octahedral coordination environment around both zinc centres in **10**. Thermal ellipsoids are drawn at the 50% probability level. H atoms have been omitted for clarity.

N-containing polycarboxylates such as pyrazine- and pyridine-carboxylates have diverse coordination modes to bridge or chelate metal centres. In particular, similar coordination manners to that observed in compound **10** with one chelated picolinate moiety and one monodentate carboxylate fragment have

been previously reported in zinc(II) compounds.[33] Nevertheless, the presence of a second pyridine subunit instead of a carboxylate fragment could be considered as an uncommon situation.

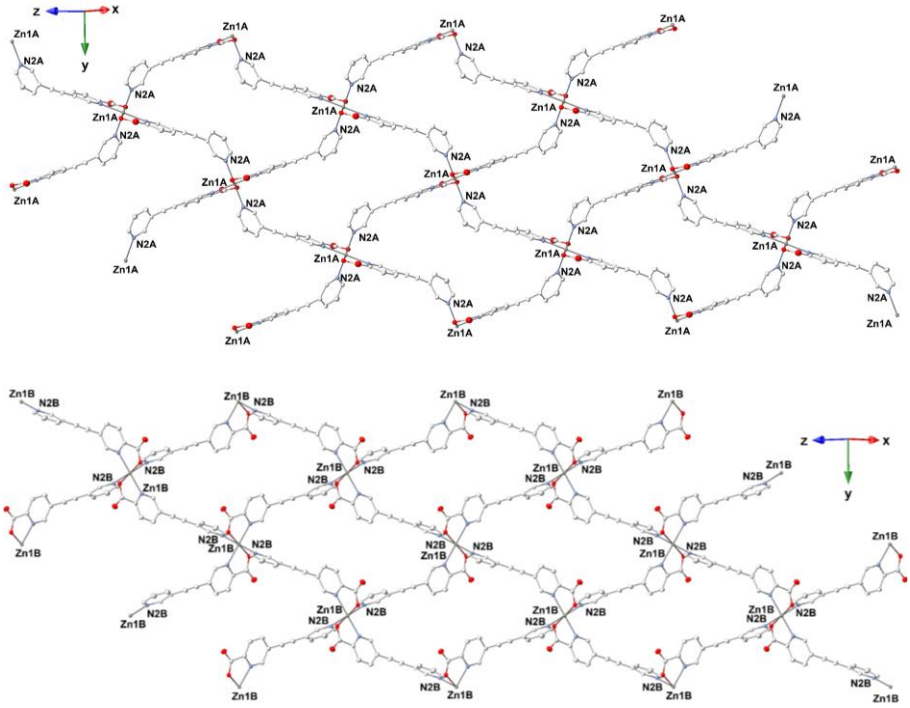

Figure 6.22. ORTEP view of the picolinate-bridged zinc(II) layers in **10** for Zn1A (top) and Zn1B (bottom). Thermal ellipsoids are drawn at the 50% probability level. H atoms have been omitted for clarity.

Both ligands adopt a transoid conformation and exhibit a severe deviation from planarity (with dihedral angles between the two pyridine rings of 42.42° and 48.85° for the A and B sublattices, respectively). Indeed, the torsion angle between the carboxylate fragment and the pyridine ring has a value of 10.35° and 11.27° for the A and B substructures, respectively. The triple bond is markedly bended, presenting also the B sublattice the more distorted values with C-C≡C and C≡C-C angles of 176.11°; 176.26° and 174.77°;175.64° for the A and B sublattices, respectively. This strong deviation from planarity is adopted in order to maximise the number of coordination bonds and results in a loss of electron delocalisation.

Sublattices A and B are arranged alternatively, so that the cavities of each subnetwork are filled by the second subnetwork (Figure 6.23).

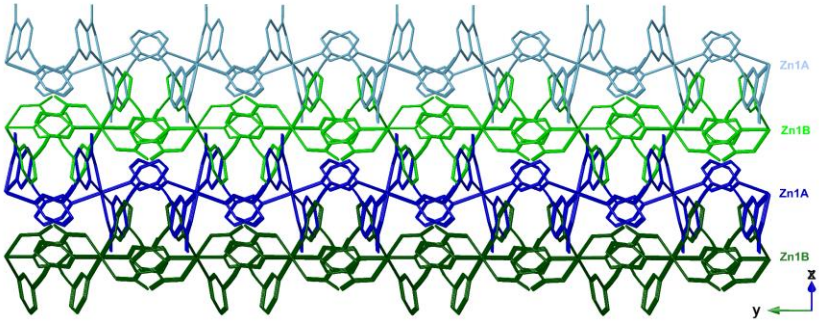

Figure 6.23. Structure of **10** in stick mode, showing the two different zinc(II) sublattices in different colour. H atoms have been omitted for clarity.

Furthermore, these sublattices are linked to each other by several π-π stacking interactions between pyridyl and picolinate rings of adjacent layers as shown in Figure 6.24.

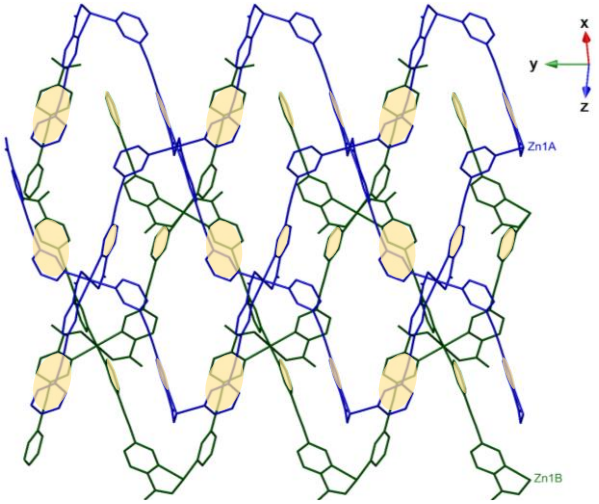

Figure 6.24. Stick representation of the zinc(II) layered structure of **10** showing the presence of π-π stacking interactions between A and B subnetworks that are illustrated in different colour. π-π interactions are represented by yellow spheres. H atoms have been omitted for clarity.

This packing results in the formation of a flower-shaped structure (Figure 6.25). In addition, there are crystallisation water molecules (one water molecule per

two zinc ions) occupying the voids of this structure thanks to the establishment of hydrogen bonds with free oxygen atoms of the picolinate subunit only from the B sublattice (O2B–O1W: 2.855(5) Å). Therefore, the difference between the two zinc subnetworks is the formation of intermolecular interactions with water molecules (Figure 6.25).

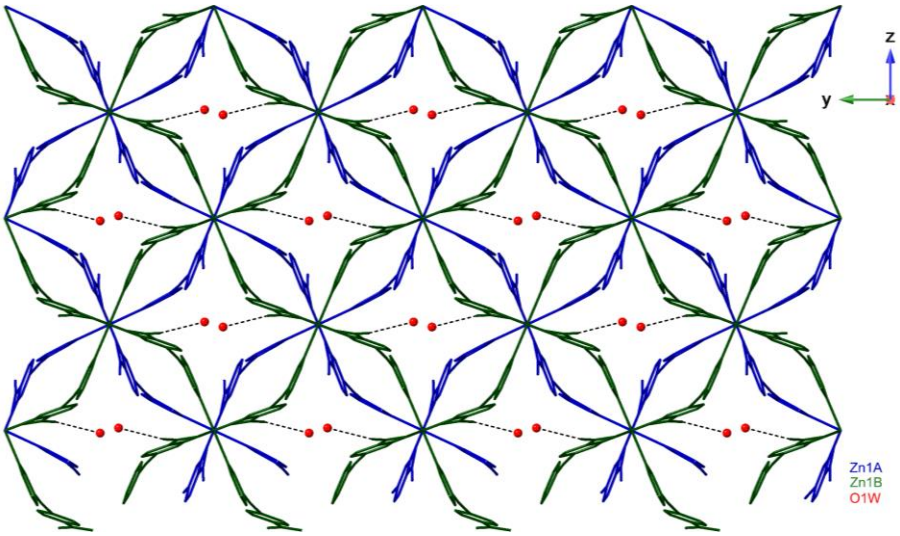

Figure 6.25. Packing of compound **10** showing the presence of water molecules hydrogen-bonded to the zinc(II) B sublattice. H-bonds are represented by dashed lines. H atoms have been omitted for clarity.

11 crystallises in the triclinic space group *P*–1 and corresponding structural and crystallographic data are shown in Table 6.7. The asymmetric unit contains only one crystallographically inequivalent Zn^{2+} cation, one independent **L8** anion and two coordinated water molecules. The zinc(II) ion is coordinated by two ligands and two water molecules (Zn1-O1W= 2.0063(18) Å; Zn1–O2W: 2.0404(18) Å), with a N_1O_4 coordination environment. The only inequivalent ligand in the asymmetric unit coordinates to one zinc ion in a chelating picolinate mode (Zn1–O1: 2.1137(16) Å; Zn1–N1: 2.1091(18) Å) and it also binds to a second zinc ion through an oxygen atom from the carboxylate group at position 4 (Zn1–O4: 2.0002(16) Å). Zn–O bond length in average (2.0402(18) Å) is shorter than Zn–N distance (2.1091(18) Å), in agreement with the distances obtained for **10**. Five-coordinate geometries for transition metal ions are generally found to be between square pyramidal or trigonal bipyramidal.[34] Indeed, the tau (τ) parameter, introduced by Addison and co-workers,[35] is used in order to distinguish between both geometries. This parameter ranges between 0 and 1 at

the extreme values, leading to an ideal square pyramidal geometry and a perfect trigonal bipyramidal structure, respectively. Thus, a structure that does not present any of those ideal geometries will have a τ value between 0 and 1. $\tau = (\beta - \alpha)/60°$, where β and α are the first and second largest possible basal angles, respectively.

Table 6.7. X-ray crystallographic data and structural refinement for $[Zn(H_2O)_2(\mathbf{L8})]$ (**11**).

Empirical formula	$C_{15}H_{11}NO_6Zn$
Formula weight	366.62
Crystallographic system	Triclinic
Space group	*P*–1 (no. 2)
a/ Å	7.1331(4)
b/ Å	7.3839(4)
c/ Å	14.3093(6)
α/ °	80.730(4)
β/ °	88.395(4)
γ/ °	63.232(5)
V/ Å^3	663.27(7)
Z	2
R(int)	0.0495
ρ_{calc}/ g·cm^{-3}	1.836
μ/ mm^{-1}	1.886
Crystal dimensions/ mm	0.099x 0.077 x 0.068
T/ K	120.00(10)
λ/ Å	0.71073 A
2θ range/ °	7.148 < 2θ < 55.808
Index ranges for h, k , l	-9/9,-9/9,-18/18
Completeness to θ = 25.242° (%)	99.8
Refinement method	Full-matrix least-squares on F^2
Collected reflections	25602
Unique reflections	2970
Data/Restraints/Parameters	2970/ 0 / 220
Goodness-of-fit on F^2	1.066
R, wR [I > 2sigma(I)] [a]	R1 = 0.0309, wR2 = 0.0666
R, wR (all data) [a]	R1 = 0.0406, wR2 = 0.0718
$\Delta\rho_{max}$ and $\Delta\rho_{min}$ (e·Å^{-3})	0.473 and -0.473

[a] $R = \Sigma(||F_o| - |F_c||)/\Sigma|F_o|$; $wR = \{\Sigma[w(F_o^2 - F_c^2)^2]/\Sigma[w(F_o^2)^2]\}^{1/2}$

In our case, the Zn(II) ion has a distorted square pyramidal environment with τ = (158.56-152.73)/60 = 0.097. The pseudo square plane is formed by O1, O4, N1 and O2W atoms whereas the apical position is occupied by O1W (Figure 6.26). The relevant bond angles are O1-Zn1-O2W = 152.73(7)° and N1-Zn1-O4 = 158.56(7)°.

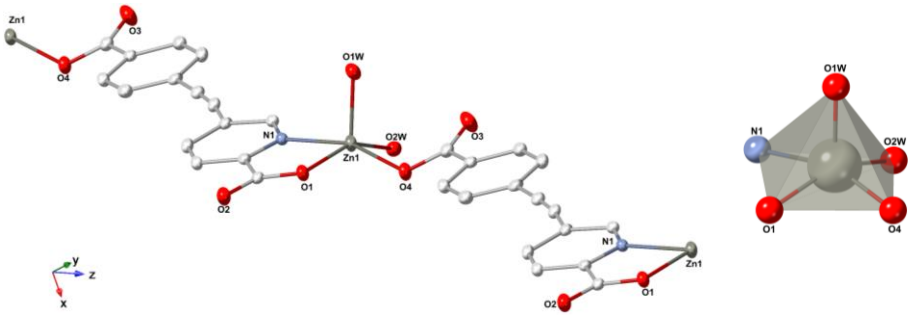

Figure 6.26. Left: ORTEP view of the square pyramidal coordination environment of Zn(II) ions in **11**. Thermal ellipsoids are drawn at the 50% probability level. H atoms have been omitted for clarity. Right: Detail of the Zn(II) square pyramid geometry.

Several Zn(II) complexes bearing the 2,5-pyridinedicarboxylate dianion, which presents an analogous connectivity to ligand **L8** (linear linker with one picolinate fragment and one carboxylate subunit), exhibit an equivalent tridentate bridging coordination mode.[36] The **L8** ligand presents a transoid conformation and connects two zinc(II) ions, giving rise to the formation of a one-dimensional wave-like chain structure (Figure 6.27). Unlike compound **10**, the dihedral angle between the two aromatic rings indicates almost a negligible deviation from planarity (with a value of 3.68°). Furthermore, the carboxyl group involved in chelation is almost coplanar with the pyridine ring with a torsion angle between pyridine and carboxylate subunits in the picolinate ligand of 0.097°. Instead, the torsion angle involving the another carboxylate fragment is 12.56°, being this value very similar to that measured for compound **10**. The bending of the triple bond is also comparable to those observed for the previous compound, exhibiting C-C≡C and C≡C-C angles of 176.66° and 169.95°.

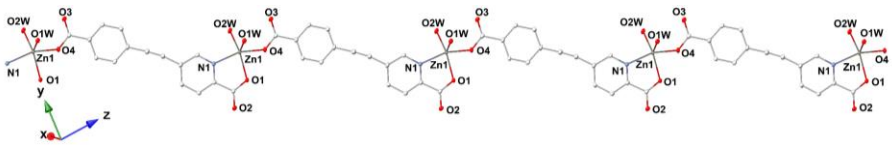

Figure 6.27. ORTEP view of the bridged zinc(II) picolinate chain structure of **11** running along the [7–20] direction. Thermal ellipsoids are drawn at the 50% probability level. H atoms have been omitted for clarity.

These chains are linked through several hydrogen bonds between water molecules bound to the zinc centre and oxygen atoms of carboxylate groups directly linked to the metal centres (O1), as well as with non-coordinated carboxylate oxygen atoms (O3 and O2). Intermolecular interactions O1W–O3

(2.640(2) Å) result in the formation of H-bonded centrosymmetric Zn(II) double chains running along the z axis (Figure 6.28).

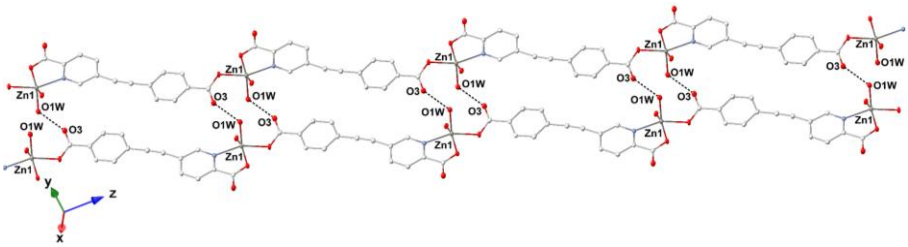

Figure 6.28. ORTEP view of the H-bonded Zn(II) double chains of **11** running along the [7–20] direction. Thermal ellipsoids are drawn at the 50% probability level. H bonds are shown as dashed lines. H atoms have been omitted for clarity.

H-bonded double chains are further linked by additional hydrogen bonds (d(O1W–O1) = 2.867(2) Å, d(O2W–O2) = 2.630(2) Å) in the y direction, and π-π stacking interactions between picolinate and benzoate fragments of consecutive double-chains. These interactions give rise to the formation of supramolecular layers in the xz plane and the equatorial planes of all the zinc(II) ions are kept parallel to each other (Figure 6.29). Further insight into the structure shows that these layers are connected through O2W–O1 (2.885(2) Å) hydrogen bonds and π-π stacking interactions between picolinate and benzoate subunits of adjacent layers (Figure 6.30).

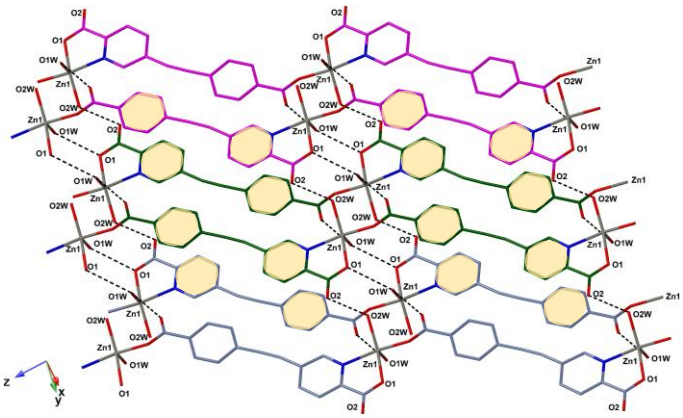

Figure 6.29. Stick view of the H-bonded Zn(II) layers of **11**. Each Zn(II) double chain is shown in different colour. H bonds are shown as dashed lines. π-π interactions are represented by yellow spheres. H atoms have been omitted for clarity.

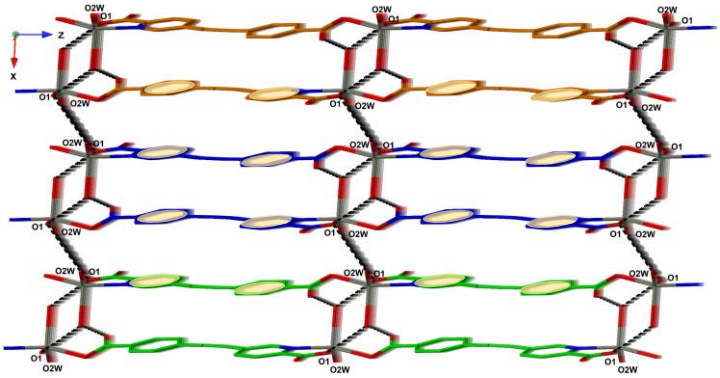

Figure 6.30. Stick view of the 3D supramolecular packing of **11** in the xz plane. Each H-bonded layer is shown in different colour. H bonds are shown as dashed lines whereas π-π interactions are represented by yellow spheres. H atoms have been omitted for clarity.

B. Powder X-ray diffraction and thermogravimetric analysis

Figure 6.31 shows the comparison between the powder X-ray diffractogram measured at room temperature of the bulk sample and the simulated diffractogram from the X-ray single crystal data recorded at 120 K for compounds **10** and **11**. It can be seen that there is a good agreement between both patterns, discarding the presence of impurities.

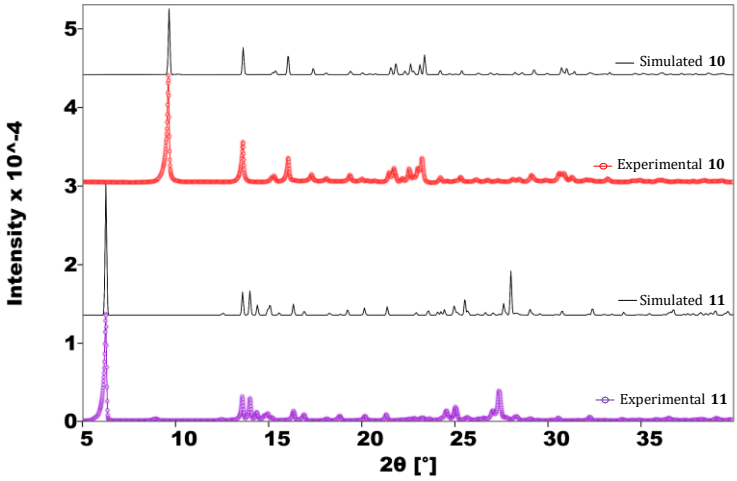

Figure 6.31. Powder X-ray diffractograms of **10** (red) and **11** (purple) collected at room temperature. The simulated patterns (in black) obtained using *CrystalDiffract* software at 120 K are shown for comparison.

Furthermore, the stability of both compounds was studied by soaking the materials in aqueous solutions at different pH values (Figure 6.32). Compound **10** is stable in aqueous suspensions ranging from pH 1 to pH 12. At pH > 12, a complete solubilisation is observed. Instead, complex **11** is less stable at extreme acid pH values (stable at pH values between 3 and 12), probably due to the protonation of the carboxylate moiety of the benzoate that is not present in compound **10**. At pH = 13, it starts to decompose and at pH = 14 a completely different pattern is registered. In any case, both compounds exhibit a remarkable stability in aqueous medium.

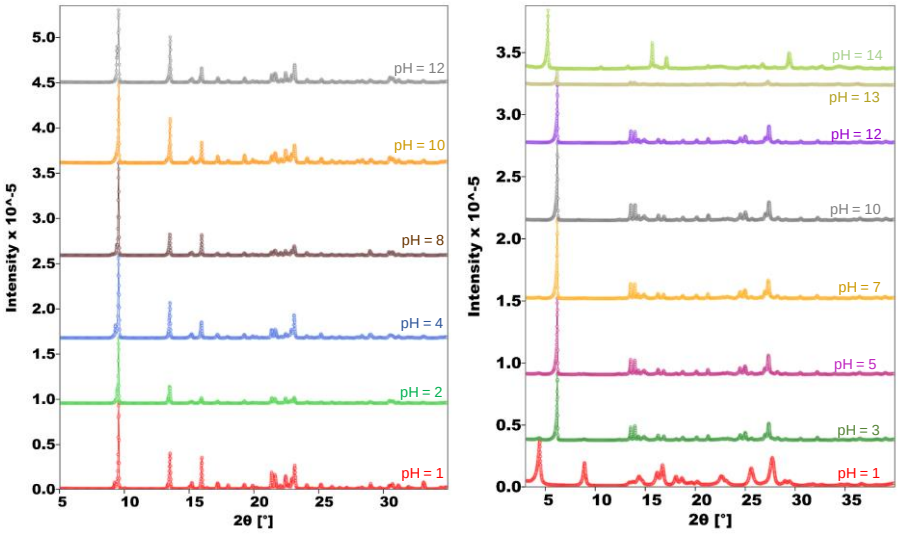

Figure 6.32. Powder X-ray diffractograms of **10** (left) and **11** (right) collected at room temperature at different pH values ranging from 1 to 14. The samples were soaked in aqueous solutions at different pH values for 2 h, filtered and air dried previously to their measurement.

To examine the thermal stability of the complexes, TG analyses were carried out in the temperature range 300-980 K for compound **10** and from 300 to 1280 K for compound **11** (Figure 6.33). The first compound is stable up to 650 K and the initial weight loss between 300 and 565 K is due to the release of approximately half water molecule per zinc cation (observed: 1.76%, and expected 1.73%). The remaining framework is decomposed at higher temperatures. This result is in agreement with the crystal structure described for compound **10**, in which a water molecule with an occupancy factor of 0.5 is included. On the other hand, the TG curve for compound **11** shows three steps of weight loss. This sample is stable up to 400 K and the initial weight loss between 410 and 500 K can be attributed to the release of approximately two water molecules per zinc cation

(observed: 9.15%, and expected 9.81%). Further heating results in a multi-step decomposition process of the compound. This observation is in accordance with the fact that the crystal structure described for compound **11** shows two water molecules in the first coordination sphere of the zinc(II) centre.

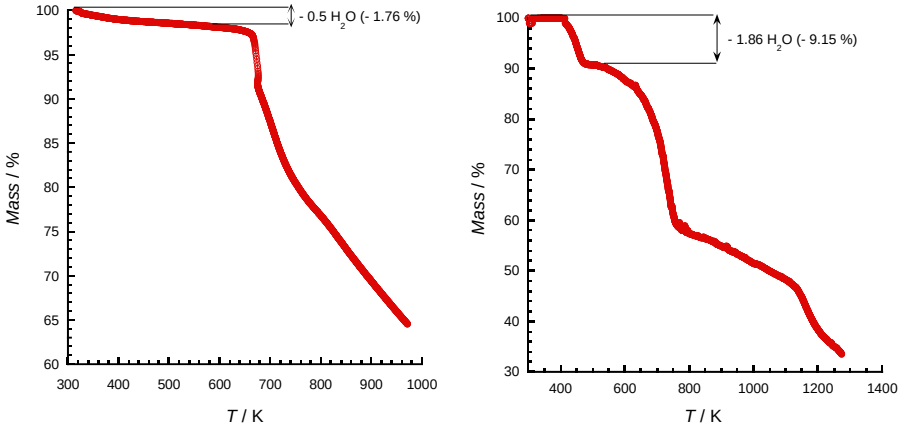

Figure 6.33. Left: Thermogravimetric analysis of **10**. Right: Thermogravimetric analysis of **11**.

6.5.2. Photoluminescence

Luminescent coordination polymers have been widely employed in sensing for detecting various chemical species, such as metal ions, organic solvents and explosives, among others. As mentioned in the introduction, in comparison to traditional analytical methods, such as gas chromatography, inductively coupled plasma (ICP) mass spectrometry, Raman spectroscopy and cyclic voltammetry, luminescent probes do not require difficult pre-treatment steps and provide remarkably low detection limits, high selectivity and portability, together with the possibility to detect signal changes by the naked eye.[37] The main disadvantage of typical detective methods is that they are usually expensive and not very easy to manipulate. Therefore, new technologies that allow low cost, rapid, easy-to-use and efficient detection need to be developed and, within this context, fluorescent materials have been prepared and used in the past decade. All the measurements included in the following sections have been, at least, measured twice in order to ensure reproducibility of the results.

A. Photoluminescent properties

Photophysical properties of complexes **10** and **11** were investigated at room temperature. Both compounds exhibit an intense and broad absorption band at 202-400 nm and 215-465 nm, respectively (Figure 6.34). These bands are also similarly present in the free ligands, hence, are assigned to intraligand $\pi \rightarrow \pi^*$ and $n \rightarrow \pi^*$ transitions.

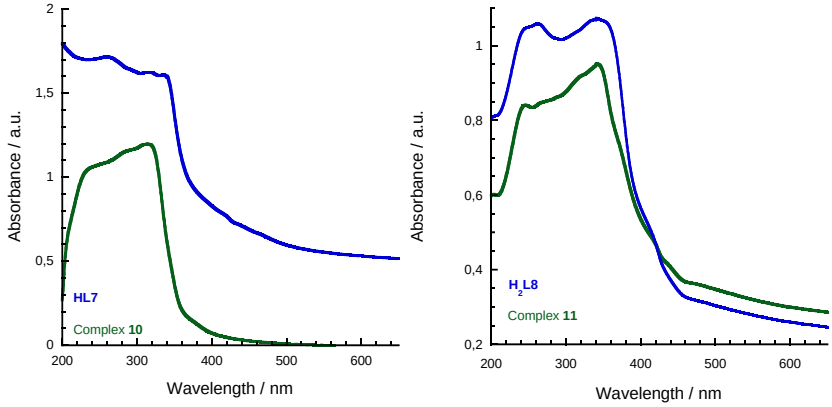

Figure 6.34. Left: UV/VIS absorption spectra of complex **10** and ligand **HL7** in the solid state. Right: UV/VIS spectra of complex **11** and ligand **H_2L8** in the solid state.

The photoluminescence properties of suspensions of compounds **10** and **11** in water were investigated at room temperature. Complex **10** exhibits weak blue fluorescent emission band centred at 406 nm under excitation at 339 nm (Figure 6.35). An aqueous suspension of the free ligand **HL7** shows a similar emission peak in shape and coincident in position, centred at 412 nm, under photo-excitation at 339 nm. On the other hand, complex **11** exhibits intense blue photoluminescent emission at 446 nm upon excitation at 350 nm (Figure 6.36). The free ligand **H_2L8** displays weaker emission at 415 nm (λ_{exc} = 350 nm).

Strong blue-emitting metal complexes are still rare, unlike the other basic components of white emission (red and green). Among d^{10} metal complexes, Zn(II) complexes are relevant candidates for electroluminescent emitters due to their excellent light-emitting nature and low cost in comparison with other d^{10} metal complexes. The d^{10} Zn(II) ion is electrochemically inert, therefore, it cannot accept an electron from the ligand nor donate an electron to the ligand. This indicates that the luminescence of complexes **10** and **11** is ascribed to ligand-centred transitions rather than metal to ligand charge transfer (MLCT), in

agreement with other Zn(II) complexes reported.[38-39] In both cases, the enhancement of fluorescence may be attributed to the chelation of the ligand to the metal centre (chelation-enhanced fluorescence, CHEF). Even though no net charge transfer takes place between Zn(II) ions and ligands, the coordination enhances the rigidity of the ligand and enlarges virtually the delocalisation range of electrons of ligands. As a result, there is a significant decrease in the loss of energy through radiationless pathways.[38]

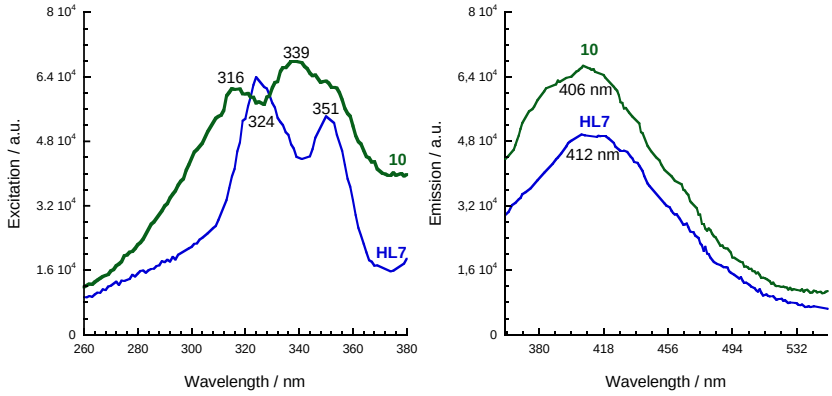

Figure 6.35. Excitation (left) and emission (right) spectra of **10** and ligand **HL7**.

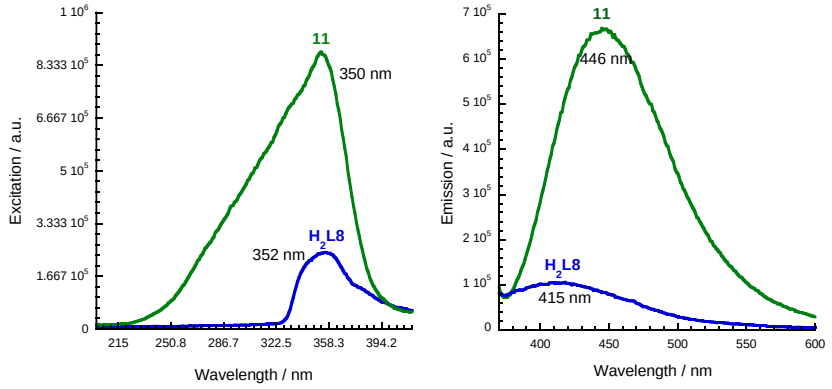

Figure 6.36. Excitation (left) and emission (right) spectra of **11** and ligand **H_2L8**.

B. Luminescence decay

The lifetime and quantum yield of both complexes in the solid-state were measured at room temperature on the basis of the maximum emission and

excitation signals. The decay curves (Figure 6.37) were successfully fitted by a bi-exponential function:

$$I = A_1 \cdot \exp(-t/\tau_1) + A_2 \cdot \exp(-t/\tau_2) \quad \text{(Eq. 6.2)}$$

where τ_i is the lifetime and A_i is the pre-exponential factor.

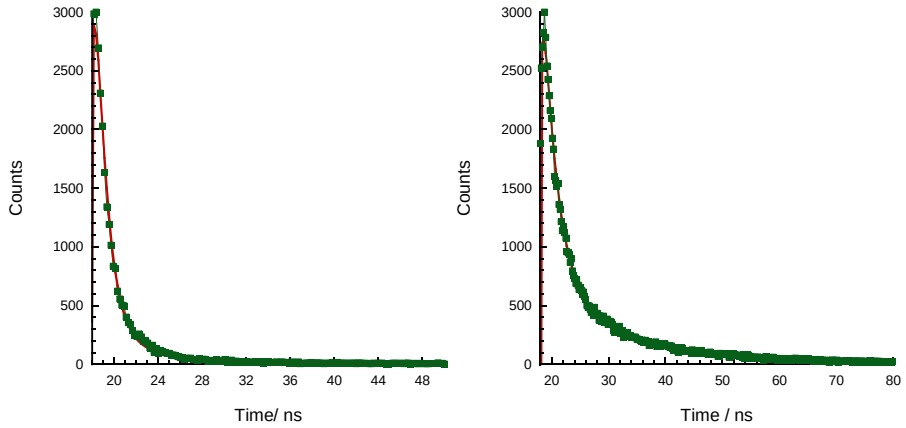

Figure 6.37. Left: Lifetime spectrum of **10** with the corresponding fitted decay curve (red). Right: Lifetime spectrum of **11** with the corresponding fitted decay curve (red).

The fitting results show τ_1 = 0.925 ns, τ_2 = 5.259 ns (average lifetime of 1.931 ns) with A_1 = 1042.16 (94.95 %) and A_2 = 55.43 (5.05 %), respectively, and a χ^2 value of 1.370 for compound **10**. Compound **11** presents the best fit for τ_1 = 2.749 ns, τ_2 = 16.211 ns (average lifetime of 9.740 ns) with A_1 = 627.71 (84.52 %), A_2 = 114.98 (15.48 %) and χ^2 = 1.243. The calculated values lye in the nanosecond range, which is typical for fluorescent zinc(II) complexes (Table 6.8).[40-43] Compound **11** displays higher lifetime values in agreement with the better planarity of **L8** ligands compared with **L7**, resulting in an increased π conjugation length and electron delocalisation energy.[38a, 44]

On the other hand, the luminescence quantum yield (ϕ) was measured by the absolute method using an integrating sphere and a value of 0.0224(3) and 0.3019(8) for compounds **10** and **11** were obtained, respectively. The value obtained for the first complex is in the lower part of the range observed for other zinc(II) compounds (~2%, Table 6.8), being the small magnitude of this parameter in agreement with the weak emission signal registered for **10** and with the distortion of the planarity observed for **L7** ligands, implying more efficient nonradiative deactivation pathways. The magnitude of this parameter for complex **11** is considerably higher, which is expected from its intense blue

emission. Indeed, it is worth noting that the quantum yield achieved is high enough to compare this compound with other recently reported as promising for emitting materials in the development of OLEDs (Organic Light Emitting Diodes).[40]

Table 6.8. Photophysical properties of some Zn(II) CPs.

Complex	τ/ ns	Φ / %
$[Zn(L^1)Cl_2]$[40]	1.50	39.8
$[Zn(L^2)Cl_2]$ [40]	1.23; 4.92	28.3
$[Zn(L^3)Cl_2]$ [40]	2.18; 8.73	7.5
$[Zn(L^4)Cl_2]$ [40]	2.04, 8.19	11.3
$[Zn(L^5)Cl_2]$ [40]	1.74	30.6
$[Zn_2(L^6)_2(OH_2)_2](ClO_4)_4$ [41]	< 1	1.90
$[Zn_3(L^7)_3(ClO_4)_2(OH_2)_2](ClO_4)_4$ [41]	< 1	3.1
$[Zn(L^8)_2(ClO_4)](ClO_4)$ [41]	< 1	4.9
$[Zn(pbm)_2]$[42]	1.90	---
$[Zn(apbm)_2]\cdot C_2H_5OH\cdot H_2O$ [42]	1.21	---
$[H_3O][Zn(L^9)_2]ClO_4$ [43]	2.30; 6.0	7.8
$[Zn_2(\mu\text{-}L^9)_2(NCS)_2]$ [43]	2.47; 6.27	32.0
$[Zn_3(\mu\text{-}L^9)_2(\mu\text{-}N_3)_4]$ [43]	2.46; 5.01	13.0
Complex **10** (This thesis)	0.93; 5.26	2.2
Complex **11** (This thesis)	2.75; 16.21	30.2

L^1: 5-(pyridine-2-yl)-3-phenyl-1,2,4-triazole; L^2: 5-fluoro-2-(3-phenyl-1H-1,2,4-triazol-5-yl)pyridine; L^3: 5-methyl-2-(3-phenyl-1H-1,2,4-triazol-5-yl)pyridine; L^4: 1-(6-(3-phenyl-1H-1,2,4-triazol-5-yl)pyridin-3-yl)ethan-1-one; L^5: 4-(3-phenyl-1H-1,2,4-triazol-5-yl)pyrimidine; L^6: 1,2-Bis((1,10-phenanthrolin-2-yl)oxy)ethane; L^7: 1,2-Bis((1,10-phenanthrolin-2-yl)oxy)propane; L^8: 2-Ethoxy-1,10-phenanthroline; HL^9: (2-hydroxybenzyl-2-tetrahydrofurylmethyl)imine; Hpbm: 2-(2-hydroxyphenyl)benzimidazole; Hapbm: 5-amino-2-(1H-benzoimidazol-2-yl)phenol.

C. Luminescent sensing of organic solvent molecules

Recently, special emphasis has been devoted to the detection of nitroaromatic compounds (NACs) and heavy metal ions,[45] as pointed out in the introduction. In this thesis, nitrobenzene solvent molecule was chosen as a representative nitroaromatic compound and sensing experiments for the detection of organic solvent molecules were conducted. Our study has been focused on complex **11** due to the striking increase in emission signal observed in comparison with that of the free ligand. In addition, there is a significant red-shift of 31 nm upon ligand complexation. Since photophysical properties of complex **10** only show a slight enhancement with respect to those of the free ligand, its further employment in this context has been discarded. The sensing ability of **11** for organic solvent molecules was investigated at room temperature. Compound **11** (1 mg) was added to different solvents (1 ml, Figure 6.38) and the resulting mixtures vigorously ultrasonicated in order to form stable and homogeneous suspensions. As shown in Figure 6.38, the luminescence spectra in different solvents are similar to that of compound **11**

(Figure 6.36) with an excitation at 350 nm. In general, there are small variations in the fluorescence signal of **11** upon dispersion in different solvents. However, it has to be highlighted that **11** exhibits complete fluorescence quenching in $PhNO_2$ and DMSO suspensions and a partial quenching in MeOH. This indicates that the luminescence intensity of **11** depends markedly on the nature of the solvent.[46]

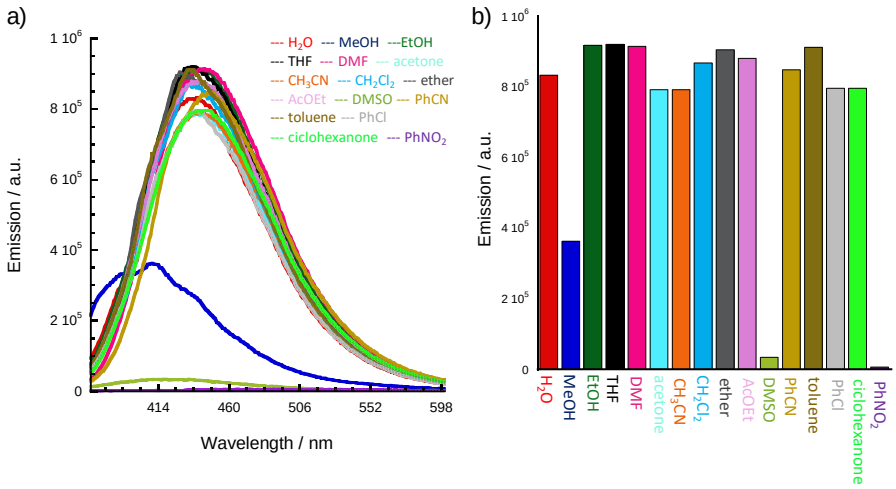

Figure 6.38. a) Emission spectra of **11** dispersed in different solvents when excited at 350 nm. b) Summary column plot of corresponding emissive intensities.

As explained in Chapter 4, the common quenching mechanisms are the collapse of the framework after introducing analytes, photoinduced electron transfer (PET), Dexter or Förster non-radiative energy transfer and 'trivial' energy transfer.[47] On the one hand, compound **11** is completely solubilised in DMSO, indicating that the luminescence quenching induced by this solvent is likely due to the collapse of the framework rather than caused by a PET or an energy transfer. On the other hand, in order to verify that the sample is stable in MeOH and in $PhNO_2$, powder X-ray diffraction (PXRD) patterns were obtained after soaking during 2 hours in these solvents. The PXRD pattern of **11** in $PhNO_2$ matches well with the experimental pattern obtained for the original complex, demonstrating that this compound is stable in $PhNO_2$, although the intensity of the signals has been considerably reduced (Figure 6.39). After soaking in MeOH, the intensity of the registered diffractogram is even lower, and a broad new peak is detected at low angles (2θ = 8.24°). Consequently, the partial luminescence quenching caused by MeOH might be mostly attributed to the collapse of the framework.

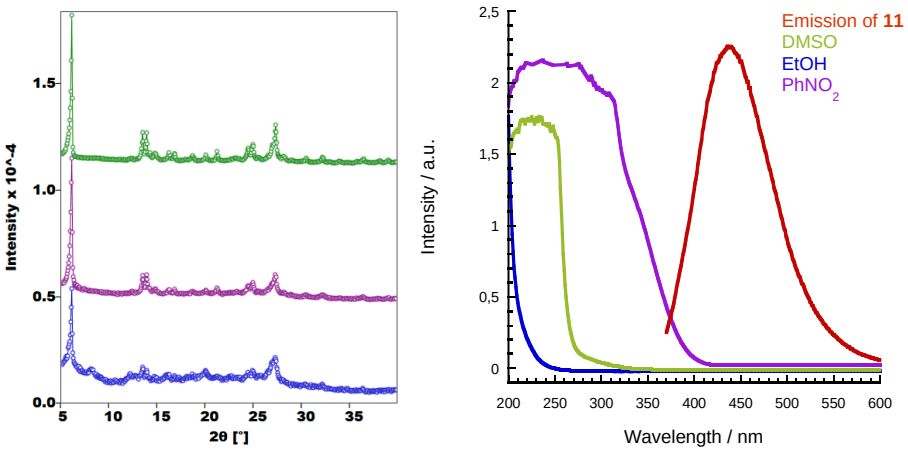

Figure 6.39. Left: Powder XRD patterns at room temperature of **11** as synthesised, after soaking in nitrobenzene and after soaking in MeOH (shown in green, purple and blue, respectively). Right: Spectral overlap between absorbance spectra of selected solvents and emission spectrum of **11**.

On the other hand, energy transfer depends on the degree of overlap between the absorption capacity of analytes and the emission signal of the fluorophore. In this context, the UV-VIS spectra of selected solvents were recorded (Figure 6.39). The results show that there is a considerable spectral overlap only between the absorption spectra of $PhNO_2$ and the fluorescence emission spectrum of compound **11**. This demonstrates that **11** can selectively detect $PhNO_2$ partially due to Förster resonance energy transfer.[47-48] Moreover, another contribution to the quenching effect is the fact that $PhNO_2$ solvent molecules absorb energy at the excitation wavelength used in this experiment (λ_{exc} = 350 nm), competing with **11** for absorption of the light source energy.

To quantitatively investigate the quenching effect of nitrobenzene towards emission of **11**, a suspension was prepared by immersing 1 mg of the complex in 1 ml of water. Then, increasing amounts of $PhNO_2$ in an ethanol solution were gradually added. With an increase in the volume of $PhNO_2$ (from 0 to 600 µl of 0.1 mol·L^{-1} nitrobenzene ethanol solution), the fluorescent intensity of **11** gradually decreased (Figure 6.40). When the volume of nitrobenzene solution added was 400 µl, the fluorescence efficiency reached was 83 %. The plot of I_0/I *vs* [$PhNO_2$] can be well-fitted by the Stern-Volmer equation:

$$I_0/I = 1 + K_{sv}\,[PhNO_2] \quad \text{(Eq. 6.3)},$$

being I the emission intensity in presence of $PhNO_2$ and I_0 the blank, without the quencher molecules. K_{sv} is the quenching constant and [$PhNO_2$] the molar concentration of the quencher.

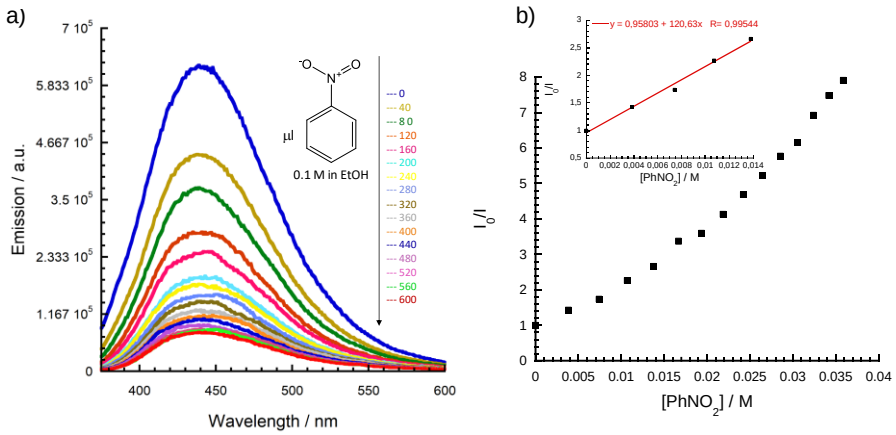

Figure 6.40. a) Comparison of the luminescence intensity of **11** upon addition of different amount of $PhNO_2$ (0.1 M in EtOH), with λ_{exc} = 350 nm. b) Stern-Volmer plots of the luminescence intensity of **11** upon addition of $PhNO_2$ (0.1 M in EtOH). The inset shows the linear fit at low concentrations of $PhNO_2$.

Figure 6.40.b shows that the plot is nearly linear in the low concentrations range. However, a characteristic upward curvature is observed at high concentrations of $PhNO_2$, suggesting a combination of static and dynamic quenching.[49] The Stern-Volmer constant (K_{sv}) was calculated from the slope of the linearly fitted curve (inset in Figure 6.40.b) to be $1.21 \cdot 10^2$ M^{-1}, indicating a moderate ability for $PhNO_2$ detection in comparison with values reported for other compounds in this context (Table 4.5, Chapter 4).

Moreover, the detection limit (LOD) of compound **11** was calculated on the basis of the equation: $LOD = 3\delta/s$ (Figure 6.41, being s the slope of the plot between fluorescence intensity and $PhNO_2$ concentration and δ the standard deviation for ten repeated luminescence measurements of the blank solution). The detection limit was as low as $4.23 \cdot 10^{-3}$ M, which is in the upper range of reported values for some other compounds (Table 4.5). This indicates that complex **11** displays a moderate detection sensitivity towards nitrobenzene.

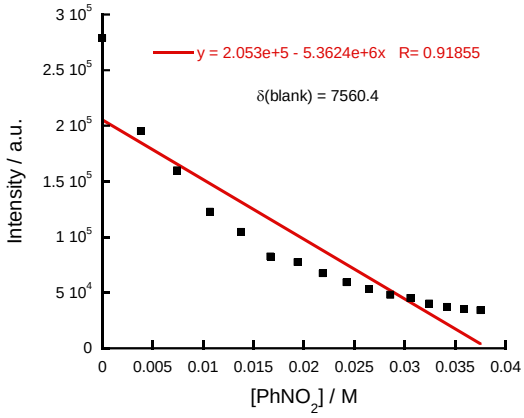

Figure 6.41. The fitting curve of the luminescence intensity of **11** at different $PhNO_2$ concentration.

D. Luminescent sensing of metal ions

As mentioned in the introduction, the design of suitable systems capable of Fe^{3+} luminescent sensing in water is extremely urgent in terms of both human and environmental frameworks.[48] Thus, in order to explore the ability of **11** to sense metal ions, aqueous solutions of 0.01 M MCl_x or $M(NO_3)_x$ (M = Li^+, Na^+, K^+, Ca^{2+}, Zn^{2+}, Ni^{2+}, Co^{2+}, Cd^{2+}, Ba^{2+}, Mn^{2+}, Mg^{2+}, Pb^{2+}, Al^{3+} and Fe^{3+}) were added to 1 mg of this compound and emission spectra recorded. As shown in Figure 6.42, the emission intensity of **11** is slightly enhanced by Li^+, K^+, Zn^{2+}, Co^{2+} and In^{3+}, whereas metal ions such as Na^+, Ca^{2+}, Cd^{2+}, Ba^{2+}, Ni^{2+}, Mn^{2+}, Mg^{2+}, Pb^{2+}, Al^{3+}, Fe^{3+}, Cu^{2+}, Dy^{3+}, Tb^{3+} and Sm^{3+} result in different degrees of luminescence quenching effects. The one that stands out is Fe^{3+}, producing a remarkable quenching effect (up to 76%).

In addition, in order to determine the sensitivity and limit of detection of compound **11** for Fe^{3+} ions, a suspension of **11** (1 mg in 1 ml H_2O) was titrated with a 25 mM aqueous solution containing Fe^{3+} ions. The luminescence intensity of **11** was gradually quenched with the increase in concentration of the Fe^{3+} ions (Figure 6.43.a). As the Fe^{3+} concentration increased from $10 \cdot 10^{-5}$ M to $8.5 \cdot 10^{-3}$ M, the quenching efficiency increases up to 86 %. Next, a suspension of **11** with a total volume of water equivalent to that obtained in the final point of the titration experiment was prepared. The emission spectrum was measured and compared with the spectrum obtained at the final point of the corresponding titration (Figure 6.44). It is clear that the intensity signal is much lower when Fe^{3+} ions are added, indicating that a quenching process is present and discarding the simple presence of dilution effects.

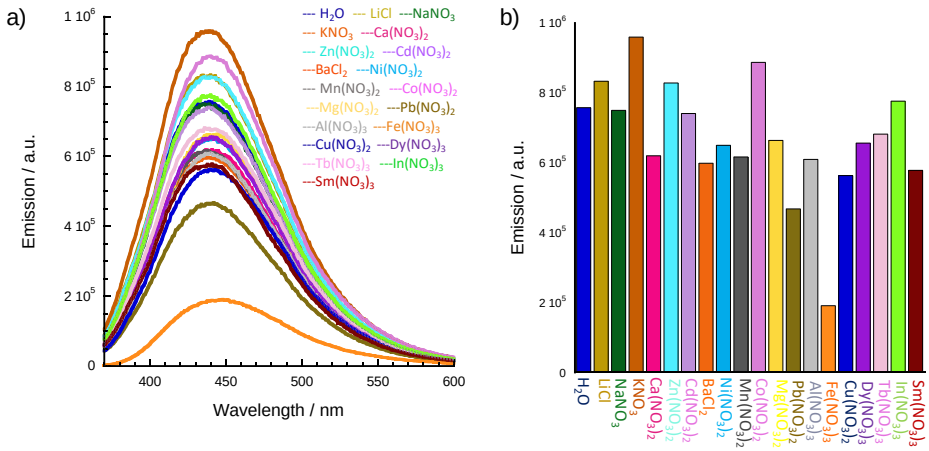

Figure 6.42. a) Fluorescence spectra of compound **11** (1 mg) in metal aqueous solutions (1ml, 0.01 M) with λ_{exc} = 350 nm. b) Summary column plot of corresponding emissive intensities.

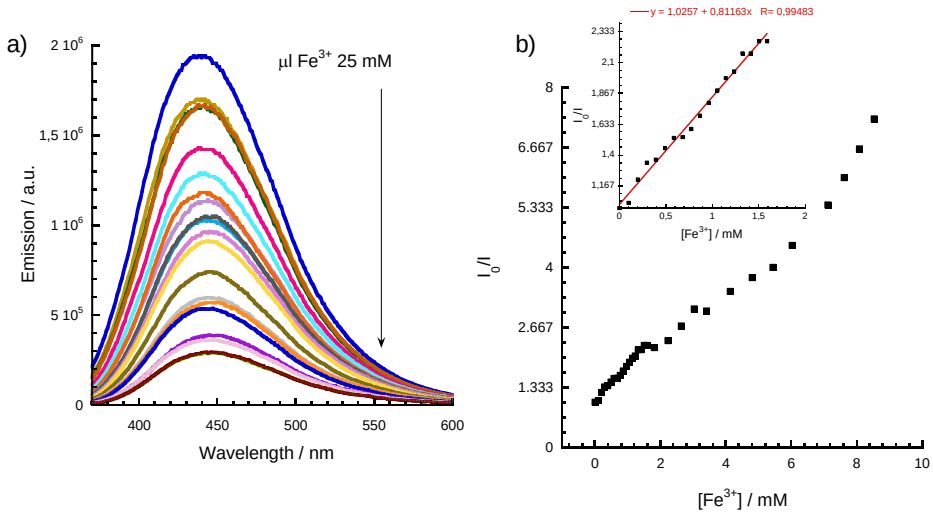

Figure 6.43. a) Comparison of the luminescence intensity of **11** upon addition of differents amounts of Fe^{3+} ions (25 mM), with λ_{exc} = 350 nm. b) Stern-Volmer plots of the luminescence intensity of **11** upon addition of Fe^{3+} ions (25 mM). The inset shows the linear fit at low concentrations of Fe^{3+} ions.

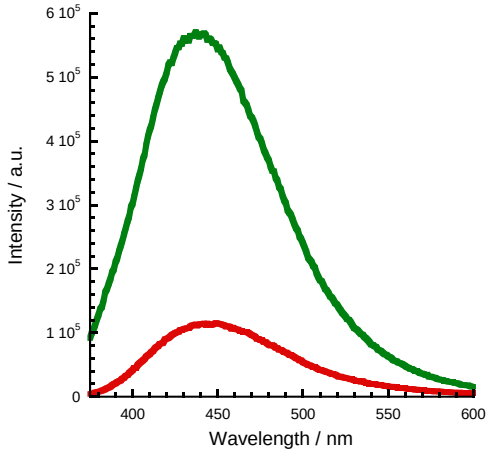

Figure 6.44. Emission spectra (λ_{exc} = 350 nm) of suspensions of **11** prepared in 1 ml of water after addition of 520 μl of H_2O extra (shown in green) and after addition of 520 μl of an aqueous solution containing 25 mM Fe^{3+} ions (shown in red).

The Stern-Volmer (S-V) plot ($I_0/I = f[Fe^{3+}]$, Figure 6.43.b) exhibits a good linear correlation (I is the emission intensity in presence of Fe^{3+} and I_0 is the blank, without Fe^{3+} ions) at low concentrations of Fe^{3+} ions. As in the previous subsection, a characteristic upward curvature at high concentrations of Fe^{3+} ions suggests a combination of static and dynamic quenching. Using S-V equation (Eq. 6.3), the quenching constant (K_{sv}) of Fe^{3+} ions for fluorescence intensity of **11** can be calculated. This parameter has a value of $8.1163 \cdot 10^2$ M^{-1}, which is comparable with that of other Zn(II) fluorescence sensing materials for Fe^{3+} previously reported.[47-49] This result indicates that **11** could be used as a selective fluorescence probe for detecting Fe^{3+} by fluorescence quenching in aqueous media. Moreover, the corresponding detection limit obtained from 3δ/s (δ: standard deviation of 10 consecutive blank measurements and s: slope of the plot between fluorescence intensity and Fe^{3+} ion concentration) has a value of $7.08 \cdot 10^{-4}$ M (Figure 6.45), which gives the lowest concentration of Fe^{3+} ions that can be detected (yielding a signal-to-noise ratio of 3:1). This value is higher than those calculated for other fluorescent sensing Zn complexes (Table 4.4, Chapter 4). Therefore, the detection limit of **11** towards Fe^{3+} ions is not enhanced.

In order to elucidate the luminescence quenching mechanism for Fe^{3+} detection, powder X-ray diffraction, energy-dispersive X-ray (EDX) microanalysis carried out on a scanning electron microscopy (SEM) and UV-VIS spectra were recorded (Figure 6.46 and Table 6.9).

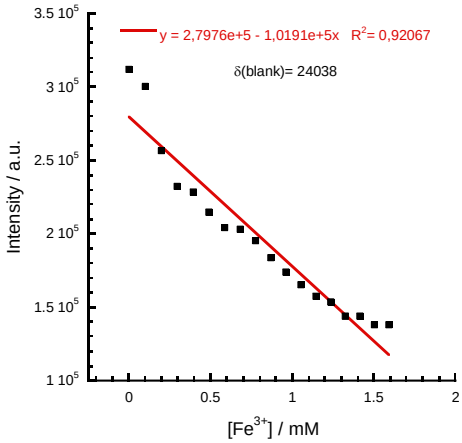

Figure 6.45. The fitting curve of the luminescence intensity of **11** at different Fe^{3+} concentration.

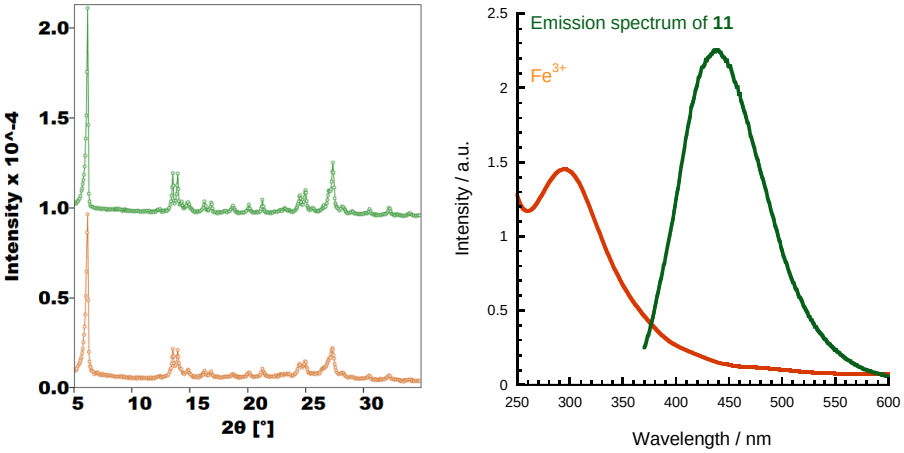

Figure 6.46. Left: Powder XRD patterns of **11** and compound **11** after soaking in an Fe^{3+} aqueous solution (shown in green and orange, respectively). Right: Spectral overlap between the absorbance spectrum of $Fe(NO_3)_3$ and the emission spectrum of **11**.

On the one hand, PXRD measurements show that the framework remains unaltered after soaking in an aqueous solution of Fe^{3+}, discarding a collapse of the crystal structure. EDX microanalysis indicates that in the sample soaked in an aqueous solution of Fe^{3+} ions, iron is not present in the composition of the final material, ruling out the existence of a cation exchange process (Table 6.9). On the other hand, the UV-VIS absorption spectrum of $Fe(NO_3)_3$ was registered and a significant degree of overlap with the emission spectrum of the

fluorophore was observed (Figure 6.46). Furthermore, competition between excitation of **11** and absorption of metallic ions is only present in the case of Fe^{3+} (Figure 6.47). Therefore, a Förster resonance energy transfer mechanism, together with the absorption of Fe^{3+} ions at the excitation wavelength used in these experiments (350 nm) play a significant role in the detection of Fe^{3+} ions by **11**.

Table 6.9. SEM-EDX analyses for **11** soaked in Fe^{3+} aqueous solution. Three independent measurements were conducted, which were consistent between them and only one result is shown for simplicity.

	SEM/EDX Analyses (atomic %)				
Sample	C	N	O	Zn	Fe
11 soaked in Fe^{3+}	60.17	6.59	29.97	1.93	0.02

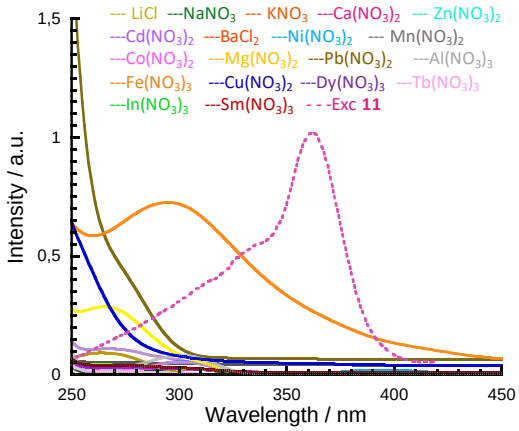

Figure 6.47. UV-VIS spectra of 0.01 M aqueous metallic solutions used for metal sensing experiments. Excitation spectrum of **11** is shown for comparison.

E. Effect of pH

Luminescence measurements were carried out in order to determine the effect of pH on the spectroscopic properties and stability of **11**. Figure 6.48.a shows the emission of this complex after immersion in aqueous solutions at different pH values ranging from 1 to 14. The sample immersed in a solution of pH=10 has the highest emission, practically constant between the pH range comprised between 7 and 10 (Figure 6.48.b). Then, the luminescence decreases as the pH shifts from 7 to 1, and from 10 to 14, with an almost complete quenching at pH = 14. The peaks are shifted towards lower wavelengths at acid

pH of 1 and 2 whereas at pH values of 11 and 12 are shifted to higher wavelengths. At pH of 13, the signal reproduces the centred emission similar to that observed for pH values between 7 and 10.

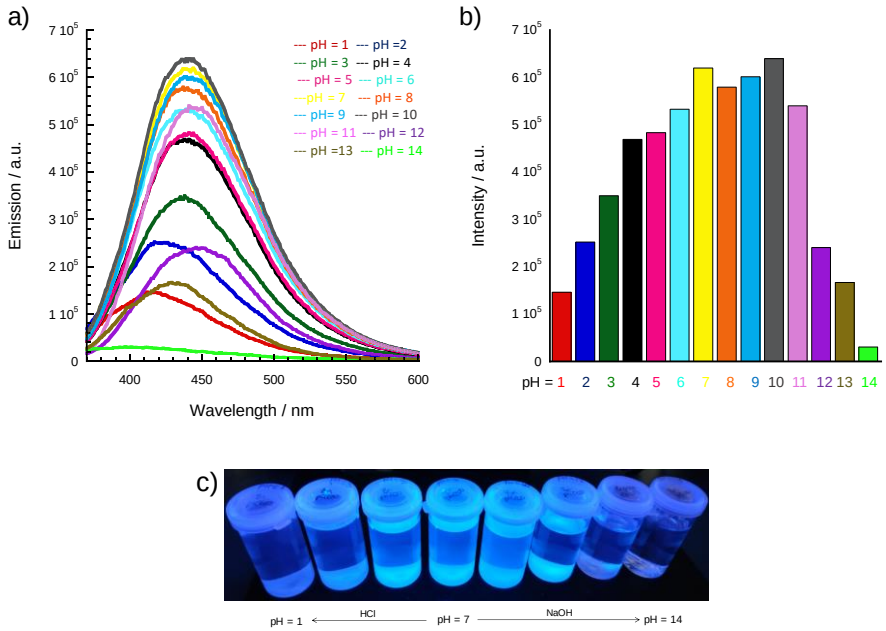

Figure 6.48. a) pH dependence of the emission spectrum of **11** with λ_{exc} = 350 nm. b) A summary column plot of maximum emission band. c) pH-dependent colour-switching of **11** under UV (λ_{exc} = 365 nm) lamp showing naked eye intensity changes.

The drop of emission at very acid or basic pH values is probably ascribed to changes in the crystal structure of the compound after protonation/deprotonation of the carboxylate oxygen atoms and pyridinic groups. PXRD measurements of **11** after soaking in aqueous solutions at different pH values (Figure 6.32, right) showed that the crystal structure changes at pH = 1 and pH = 13-14, whereas the original diffraction pattern is preserved at pH values comprised between 2 and 12. This reveals a broad interval of pH stability and indicates that the fluorescence quenching is induced by dissociation of the pristine complex at very acid or basic conditions. The characteristic intensity of **11** is reduced as the H^+ ion (pH < 3) can break the five-membered chelate ring built by coordination of the picolinate ligand to the Zn^{2+} ion. This results in a less efficient chelation-enhanced fluorescence (CHEF). The same situation is found in strong alkaline solutions (pH > 12). Dissociation of the complex might give rise to the displacement of the **L8** ligands by solvent

molecules or Cl^- ions (coming from the HCl solution used in the preparation of acid aqueous solutions at different pH values) and this would result in the emission quenching process.

6.5.3. Discussion

As a common feature in both compounds, **L8** and **L7** ligands present a tridentate bridging coordination mode with one chelating picolinate moiety and a second monodentate carboxylate or pyridine subunit. In addition, in both cases the ligands adopt a transoid conformation in order to maximise the number of coordination bonds. Nevertheless, there is a notable difference between the connectivity provided by both ligands. In compound **11**, the dihedral angle between benzoate and pyridine rings is 3.68°, indicating that both aromatic rings are almost planar and a wave-like chain structure is formed. Whereas in compound **10**, both aromatic rings exhibit higher deviation from planarity (dihedral angle between aromatic rings of 42.42°). This distortion together with the meta-position of the N atom favour the formation of a layered network.

The blue fluorescence emission in compound **10** is very weak whereas compound **11** shows an intense blue emission band, being in both cases ligand-based emissions. This trend is also reflexed in the quantum yield and lifetime measurements, obtaining for compound **10** values of Φ = 0.022 and τ_{av} = 1.93 ns whereas compound **11** yields higher values (Φ = 0.30 and τ_{av} = 9.74 ns), even though the absorption of light in both cases is similar (**10**: 48%, **11**: 53%). This can be explained taking into account that compound **11** presents a tighter molecular packing compared with complex **10**. The 'SQUEEZE' option of PLATON[50] shows that compound **10** exhibits a potential solvent area volume of 37.1 $Å^3$ (1.7 % per unit cell volume 2188.8 $Å^3$), whereas in compound **11** the same test results in no residual solvent accessible void. Thus, the increase in planarity and rigidity in compound **11** promotes more efficient electron delocalisation, reducing the number of rotational degrees of freedom that contribute to the non-radiative decays of the excited state. Consequently, the emission signal of the molecule, the quantum yield and the average lifetime increase with respect to compound **10** with more distorted and flexible ligands.

Complex **11** is a 1D coordination compound, presents two water molecules in its first coordination sphere and is further linked by hydrogen bonds and π-π stacking interactions giving rise to the formation of a 3D supramolecular network. Therefore, its aggregation-deaggregation process is affected by the properties of solvent. In fact, we have observed a complete quenching of the

emission signal in DMSO and $PhNO_2$. In the first case, interaction with the solvent might be the explanation of this fact, resulting in a deaggregation of the zinc(II) building blocks and leading to the disruption of the crystal structure. Whereas it has been shown that in the second case, absorption of $PhNO_2$ solvent molecules occurs in the range of emission of compound **11**. Therefore, the moderate overlap area explains the huge quenching effect and the corresponding mechanism was attributed to Förster resonance energy transfer between both components, together with the competitive absorption of the excitation energy between the ligand and $PhNO_2$ molecules. Moreover, complex **11** is able to selectively detect Fe^{3+} cations *via* fluorescence quenching and the main possible mechanism is again Förster resonance energy transfer due to the partial overlap between the emission of **11** and the absorption of Fe^{3+} ions. Simultaneously, a competitive absorption of the excitation energy between Fe^{3+} ions and **L8** ligand takes place. Besides, **11** can be used as a pH probe due to quenching of its emission intensity as the pH change to critical values (1 or 13-14) leads to protonation or deprotonation of the carboxylic and pyridinic groups and disruption of the original chelate complex.

6.6. Conclusions and future prospects

The coordination of the new polytopic family of ligands described in the previous chapter with divalent metals has been investigated. Herein, we have described our achievements in this context that encompass the synthesis of five novel polynuclear complexes and the description of their structural, thermal, magnetic and luminescent properties.

Compounds **7** and **8** are two copper(II) coordination polymers that exhibit a chain structure built up from dinuclear or trinuclear units, respectively, in which the metal centres are linked by double *syn*, *anti*- out-of-plane picolinate bridges. This connectivity implies a weak overlap between magnetic orbitals, consequently, the magnetic susceptibility and EPR measurements indicate that the exchange interactions are rather weak in both cases. In order to increase the interaction between the magnetic orbitals, a strong overlap between them is required, which is only possible to achieve if another kind of bridge exists between the metal centres. Several efforts are currently concentrated in obtaining new copper(II) polymers combining **L7** or **L8** ligands with a second bridging component that may allow a higher overlap between the copper centres.

Compound **9** is an iron(II) coordination complex that has a wave-like chain structure thanks to the bis(bidentate) chelating coordination mode of the ditopic **L2** ligands. Magnetic susceptibility measurements show a high-spin state for the iron centre, which is in agreement with Fe–N bond distances extracted from single crystal X-ray diffraction data. Preliminary results show that it can be used as heterogeneous catalyst in the oxidation of cyclohexane at ambient temperature and pressure with almost 100% selectivity for cyclohexanone and 14% substrate conversion. Further application of **9** in the catalysis field is in study.

Compounds **10** and **11** are two new zinc(II) coordination compounds with a layered and wave-like chain structures, respectively. Both complexes exhibit blue-luminescence when irradiated with UV light. Fluorescence spectroscopy measurements reveal a weak signal in the former case, whereas in the latter compound an excellent emission response is registered. This is ascribed to the different planar nature of involved ligands, which affects their rigidity, electron delocalisation and the subsequent loss of energy through radiationless pathways. Further measurements show that **11** displays selective detection performance of $PhNO_2$ and Fe^{3+} ions *via* fluorescence quenching. The mechanism of quenching is attributed to resonance energy transfer between compound **11** and the quenchers, as well as to a competitive excitation absorption process between them. In order to achieve a real sensing application, the selective detection of a specific metal ion in presence of a mixture of them is required. Thus, the selective sensing detection of **11** for Fe^{3+} ions and $PhNO_2$ molecules is being investigated by competitive experiments. At the same time, it is clear from these results that planarity is essential in order to obtain systems with enhanced emissive and photophysical properties. Therefore, new systems are being designed with the aim of increasing conjugation (promoting electron delocalisation) while keeping planarity.

It is well-known that higher thermal stability results when metals like copper and zinc are used than if metals capable of changing their ionic valency are involved. In water, also the stability of coordination polymers correlates well with the standard reduction potentials, leading the use of more inert metals to larger robustness.[51] In the present case, complexes **7**-**11** exhibit a high stability in aqueous medium in a wide pH range, avoiding ligand displacement by water and a coordination polymer hydrolysis. This represents a considerable improvement in comparison to coordination polymers constructed from labile linkers, which justifies the further use of the corresponding ligands in the coordination chemistry field.

6.7. Experimental part

Synthesis of complex [$Cu_2(L7)_4$] (7)
A mixture of $CuCl_2{\cdot}2H_2O$ (42.6mg, 0.25 mmol) and methyl 5-(pyridine-3-ylethynyl)picolinate (L7-CH_3, 120 mg, 0.5 mmol) was combined with water (0.36 ml), ethanol (0.11 ml) and pyridine (0.14 ml) in a glass vial. After sonication, the resulting solution was placed inside an oven at 96°C for 96 h with heating and cooling rates of 0.2 K·min^{-1}. Blue plate-like crystals suitable for X-ray single diffraction were obtained upon decanting the mother liquor. Yield: 79% (100.1 mg).

Elemental analysis (% in weight) of C, N and H for this sample was obtained and the result is consistent with the values calculated for the anhydrous material: Calcd for $C_{26}H_{14}CuN_4O_4$ (%): C, 61.24; H, 2.77; N, 10.99. Found: C, 61.26; H, 2.58; N, 10.58.

Synthesis of complex [$Cu_3(MeL8)_6$] (8)
A mixture of $CuCl_2{\cdot}2H_2O$ (3.41 mg, 0.019 mmol) and methyl 5((4-(methoxycarbonyl)phenyl)ethynyl)picolinate (L8-CH_3, 12 mg, 0.0374 mmol) was combined with water (0.36 ml), ethanol (0.11 ml) and pyridine (0.28 ml) in a glass vial. After sonication, the resulting solution was placed inside an oven at 96°C for 72 h, then the mixture was allowed to cool until room temperature at 0.2 K·min^{-1}. Pale blue needles suitable for X-ray single diffraction were obtained upon decanting the mother liquor. Yield: 73% (8.6 mg).

The phase purity of the sample was determined by elemental analysis (% in weight of C, N and H) and this measurement is in agreement with the anhydrous nature of compound **8**: Calcd for $C_{32}H_{20}CuN_2O_8$ (%): C, 61.59; H, 3.23; N, 4.49. Found: C, 61.70; H, 2.88; N, 4.54.

Synthesis of complex [$Fe(H_2O)_2(L2)$] (9)
A mixture of $Fe(NO_3)_3{\cdot}9H_2O$ (22.62 mg, 0.056 mmol) and 5,5'-(ethyne-1,2-diyl)dipicolinic acid (HL2, 15 mg, 0.056 mmol) was combined with water (0.50 ml) and dimethylformamide (4.0 ml) in a glass vial. After sonication, 1100 μl of acetic acid were added to the resulting suspension. The mixture was placed inside an oven at 130°C for 72 h with a cooling rate of 0.09 K·min^{-1}. Red plate-like crystals suitable for X-ray single diffraction were obtained upon filtration. Yield: 74% (14.8 mg).

Elemental analysis (% in weight) of C, N and H measurements reveal that this sample absorbs water molecules from the environment. Calcd for

$C_{14}H_{10}FeN_2O_6 \cdot 0.75H_2O$ (%): C, 45.25; H, 3.12; N, 7.54. Found: C, 45.53; H, 2.86; N, 7.13.

Synthesis of complex [Zn(L7)$_2$] (10)
A mixture of $ZnCl_2$ (10.22 mg, 0.075 mmol) and methyl 5-(pyridin-3-ylethynyl)picolinate (36 mg, 0.15 mmol) was thoroughly mixed with water (0.36 mL), ethanol (0.11 mL) and pyridine (0.14 mL) in a glass tube. This tube was placed inside an oven at 96 °C during 96 hours (heating and cooling rates were 0.2°/min). After decanting the mother liquor, yellowish block crystals were obtained. Yield: 47% (18 mg).

Elemental analysis (% in weight) of C, N and H measurements verify the phase purity of the material and its anhydrous character. Calcd for $C_{26}H_{14}ZnN_4O_4$ (%): C, 61.02; H, 2.76; N, 10.95. Found: C, 61.34; H, 2.72; N, 10.75.

Synthesis of complex [Zn(H$_2$O)$_2$(L8)] (11)
A mixture of $ZnCl_2$ (19.30 mg, 0.14 mmol) and 5-((4-carboxyphenyl)ethynyl)picolinic acid (37.8 mg, 0.0.14 mmol) was thoroughly mixed with water (1.80 mL), ethanol (0.55 mL) and pyridine (0.70 mL) in a glass tube. This tube was placed inside an oven at 96 °C during 96 hours (heating and cooling rates were 0.2°/min). After decanting the mother liquor, colourless rhombohedral crystals were obtained. Yield: 34% (17.6 mg).

Elemental analysis (% in weight) of C, N and H measurements are consistent with the formulation deduced for **11** from single crystal X-ray diffraction. Calcd for $C_{15}H_{11}ZnNO_6$ (%): C, 49.14; H, 3.02; N, 3.82. Found: C, 49.43; H, 2.79; N, 3.87.

The infrared spectra for complexes **7**-**11** are shown in Figure 6.49. In all of them the more intense bands are attributed to C=O stretching (1760-1670 cm^{-1}, carboxylic acid or ester), C=C stretching (1670-1600 cm^{-1}, alkene), C=N stretching (≈1628 cm^{-1}, aromatic amine) and C-N stretching (1340-1260 cm^{-1}, aromatic amine), due to the presence of pyridine aromatic rings and carboxylate subunits. In addition, weak C≡C stretching (2260-2150 cm^{-1}, alkyne) signal is present, which is the most characteristic band for the existence of the triple bond. Moreover, O-H stretching (3600-2500 cm^{-1}, water molecules), C-H stretching (3100-2800 cm^{-1}, alkene or alkane), C-H bending (2000-1650 cm^{-1}, aromatic compound overtones), traces of CO_2 (doublet of bands at ≈ 2341 cm^{-1}), C-H bending (1450 cm^{-1}, alkane), C-O stretching (1250-1100 cm^{-1}, ester), C-H bending (700-610 cm^{-1}, aromatic compound out-of-plane) and C=C bending (990-660 cm^{-1}, alkene) signals are observed, among others.

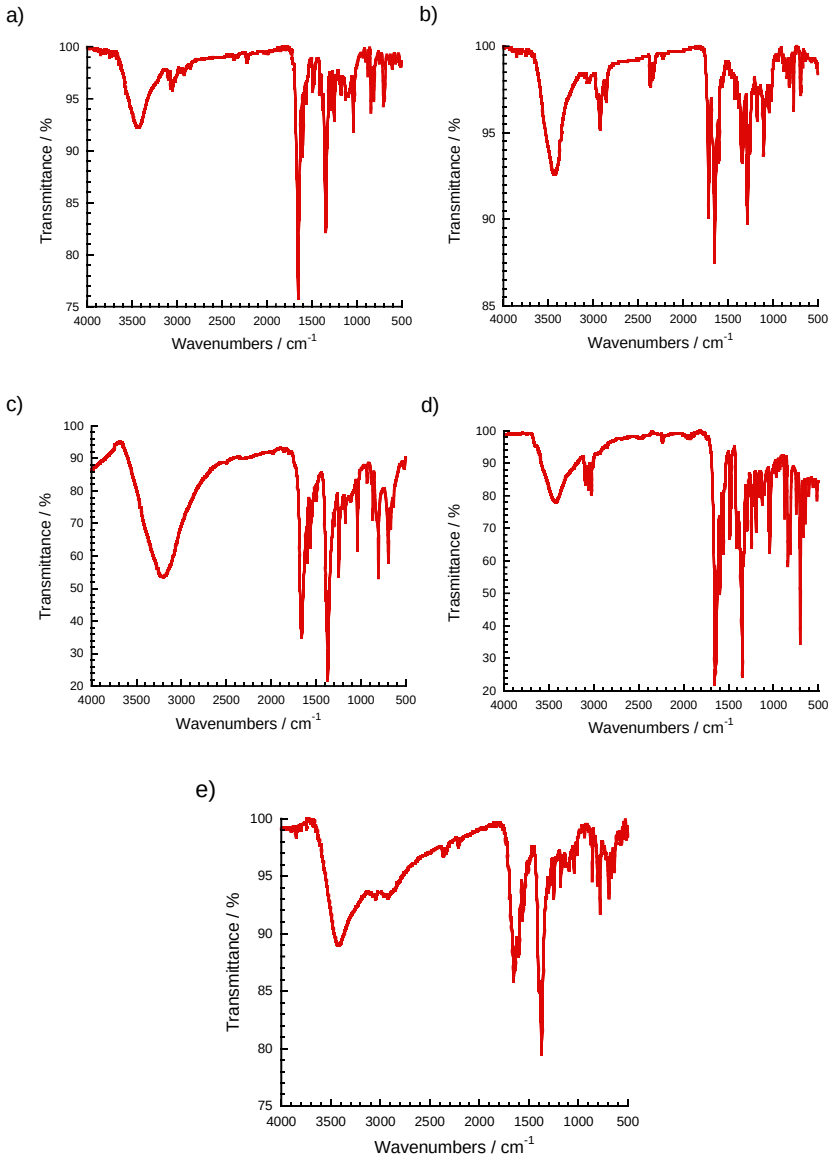

Figure 6.49. Infrared spectrum of complexes **7**-**11** in a KBr pellet, from a) to e), respectively.

6.8. References

[1] J. Ferrando-Soria, J. Vallejo, M. Castellano, J. Martínez-Lillo, E. Pardo, J. Cano, I. Castro, F. Lloret, R. Ruiz-García, M. Julve, *Coord. Chem. Rev*. **2017**, 339, 17-103

[2] Y. Zhang, S. Yuan, G. Day, X. Wang, X. Yang, H.-C. Zhou, *Coord. Chem. Rev*. **2018**, 354, 28-45

[3] M. D. Allendorf, C. A. Bauer, R. K. Bhakta, R. J. T. Houk, *Chem. Soc. Rev*. **2009**, 38, 1330-1352

[4] G. Demazeau, *J. Mater. Sci. Lett*., **2008**, 43, 2104-2114

[5] Y. Xu, L. Han, Z.-Z. Lin, C.-P Liu, D.-Q. Yuan, Y.-F. Zhou, M.-C. Hong, *Eur. J. Inorg. Chem*. **2004**, 4457-4462

[6] a) O. Kahn, *Molecular Magnetism*.**1942**, VCH publishers. b) R. Baggio, R. Calvo, M. T. Garland, O. Peña, M. Perec, L. D. Slep, *Inorg. Chem. Commun*. **2007**, 10, 1249-1252

[7] a) S. C. Manna, J. Ribas, E. Zangrando, N. R. Chaudhuri, *Inorg. Chim. Acta*. **2007**, 360, 2589-2597. b) E. Coronado, C. Giménez-Saiz, F. M. Romero, A. Tarazón, *Inorg. Chem*. **2009**, 48, 2205-2214

[8] C. Biswas, P. Mukherjee, M. G. B. Drew, C. J. Gómez-García, J. M. Clemente-Juan, A. Ghosh, *Inorg. Chem*. **2007**, 46, 10771-10780

[9] a) B. Zurowska, J. Mrozinski, K. Slepokura, *Polyhedron*. **2007**, 26, 3379-3387. b) Z. Han, Y. Zhao, J. Peng, C. J. Gómez-García, *Inorg. Chem*. **2007**, 46, 5453-5455

[10] a) J.-K. Tang, H.-M. Wang, P. Cheng, X. Liu, D.-Z. Liao, Z.-H. Jiang, S.-P. Yan, *Polyhedron*. **2001**, 20, 675-680. b) G. A. Senchyk, A. B. Lysenko, E. B. Rusanov, A. N. Chernega, J. Jezierska, K. V. Domasevitch, A. Ozarowski, *Eur. J. Inorg. Chem*. **2012**, 5802-5813

[11] F. Klongdee, J. Boonmak, B. Moubaraki, K. S. Murray, S. Youngme, *Polyhedron*. **2017**, 126, 8-16

[12] P. Seppala, E. Colacio, A. J. Motab, R. Sillanpaa, *Dalton Trans*. **2012**, 41, 2648-2658

[13] a) Z. Boulsourani, V. Tangoulis, C. P. Raptopoulou, V. Psycharisb, C. Dendrinou-Samara, *Dalton Trans*. **2011**, 40, 7946-7956. b) W.-G. Wang, J. Zhang,

L.-J. Song, Z.-F. Ju, *Inorg. Chem. Com*mun. **2004**, 7, 858-860. c) K. C. Thatipamula, G. Bhargavi, M. V. Rajasekharan, *ChemistrySelect*, **2019**, 4, 3344-3350

[14] H. Núñez, J.-J. Timor, J. Server-Carrió, L. Soto, E. Escrivà, *Inorg. Chim. Acta*. **2001**, 318, 8-14

[15] O. Castillo, A. Luque, S. Iglesias, C. Guzmán-Miralles, P. Román, *Inorg. Chem. Commun.* **2001**, 4, 640-642

[16] E. Aznar, S. Ferrer, J. Borrás, F. Lloret, M. Liu-González, H. Rodríguez-Prieto, S. García- Granda, *Eur. J. Inorg. Chem*. **2006**, 5115-5125

[17] I. Unamuno, J. M. Gutiérrez-Zorrilla, A. Luque, P. Román, L. Lezama, R. Calvo, T. Rojo, *Inorg. Chem*. **1998**, 37, 6452-6460[18] A. Das, B. Dey, A. D. Jana, J. Hemming, M. Helliwell, H. M. Lee, T.-H. Hsiao, E. Suresh, E. Colacio, S. R. Choudhury, S. Mukhopadhyay, *Polyhedron*. **2010**, 29, 1317-1325

[19] J. Carranza, H. Grove, J. Sletten, F. Lloret, M. Julve, P. E. Kruger, C. Eller, D. P. Rillema, *Eur. J. Inorg. Chem*. **2004**, 4836-4848

[20] F. S. Delgado, J. Sanchiz, C. Ruiz-Pérez, F. Lloret, M. Julve, *Inorg. Chem*. **2003**, 42, 5938-5948

[21] D. Yoneyama, T. Kodama, K. Kikuchi, T. Fujisawa, A. Yamaguchi, A. Sumiyama, Y. Shuku, S. Aoyagid, W. Fujita, *Dalton Trans*. **2016**, 45, 16774-16778

[22] R. A. A. Cassaro, S. Ciattini, S. Soriano, H. S. Amorim, N. L. Speziali, M. Andruh, M. G. F. Vaz, *Cryst. Gowth Des*. **2013**, 13, 2711-2715

[23] J. Nenwa, E. D. Djomo, E. N. Nfor, P. L. Djonwouo, M. Mbarki, B. P. T. Fokwa, *Polyhedron*. **2015**, 99, 26-33

[24] Y. Han, Z. Zheng, C. Wang, J. Sun, X. Li, J. Zhang, J. Xiao, G. He, L. Li, *J. Mol. Struct*. **2015**, 1079, 163-166

[25] B. Schneider, S. Demeshko, S. Neudeck, S. Dechert, F. Meyer, *Inorg. Chem*. **2013**, 52, 13230-13237

[26] A. Chatterjee, L. K. Thompson, S. K. Dey, *Magnetochemistry*. **2018**, 4, 53

[27] a) Y.-J. Ma, S.-D. Han, Y. Mu, J. Pan, J.-H. Li, G.-M. Wang, *Dalton Trans*. **2018**, 47, 1650-1656. b) M. Lanchas, D. Vallejo-Sánchez, G. Beobide, O. Castillo, A. T. Aguayo, A. Luque, P. Román, *Chem. Commun*. **2012**, 48, 9930-9932

[28] E. H. de Faria, G. P. Ricci, L. Marçal, E. J. Nassar, M. A. Vicente, R. Trujillano, A. Gil, S. A. Korili, K. J. Ciuffi, P. S. Calefi, *Catal*. *Today*. **2012**, 187, 135-149

[29] a) T. K. Maji, K. Uemura, H.-C. Chang, R. Matsuda, S. Kitagawa, *Angew. Chem. Int. Ed*. **2004**, 43, 3269-3272. b) R. Kitaura, R. Matsuda, Y. Kubota, S. Kitagawa, M. Takata, T. C. Kobayashi, M. Suzuki, *J. Phys. Chem. B*. **2005**, 109, 23378-23385

[30] S. Tanaka, Y. Kon, T. Nakashima, K. Sato, *RSC Adv*. **2014**, 4, 37674-37678

[31] D. H. R. Barton, *Tetrahedron*. **1998**, 54, 5805-5817

[32] P. Stavropoulos, R. Çelenligil-Çetin, A. E. Tapper, *Acc. Chem. Res*. **2001**, 34, 745-752

[33] X.-M. Lin, L. Chen, H.-C. Fang, Z.-Y. Zhou, X.-X. Zhou, J.-Q. Chen, A.-W. Xu, Y.-P. Cai, *Inorg. Chim. Acta*. **2009**, 362, 2619-2626

[34] D. C. Crans, M. L. Tarlton, C. C. McLauchlan, *Eur. J. Inorg. Chem*. **2014**, 4450-4468

[35] A. W. Addison, T. N. Rao, *J. Chem. Soc. Dalton Trans*. **1984**, 1349-1356

[36] a) J. He, G.-P. Tan, J.-X. Zhang, Y.-N. Zhang, Y.-G. Yin, *Inorg. Chem. Commun*. **2008**, 11, 1094-1096. b) Y.-X. Chi, S.-Y. Niu, J. Jin, *Inorg. Chim. Acta*. **2009**, 3821-3828. d) A. T. Çolak, O. Z. Yesilel, O. Büyükgüngör, *J. Inorg. Organomet. Polym*. **2010**, 20, 26-31. c) X. Wang, C. Qin, E. Wang, C. Hu, L. Xu, *J. Mol. Stru*ct. **2004**, 698, 75-80. e) P. Mahata, S. Natarajan, *Eur. J. Inorg. Chem*. **2005**, 2156-2163

[37] a) W. Wang, J. Yang, R. Wang, L. Zhang, J. Yu, D. Sun, *Cryst. Growth Des*. **2015**, 15, 2589-2592. b) S. Shaligram, P. P. Wadgaonkar, U. K. Kharul, *J. Mater. Chem. A.* **2014**, 2, 13983-13989[38] a) Y.-P. Tong, S.-L. Zheng, X.-M. Chen, *Eur. J. Inorg. Chem*. **2005**, 3734-3741. b) J. He, J.-X. Zhang, G.-P. Tan, Y.-G. Yin, D. Zhang, M.-H. Hu, *Cryst. Growth Des*. **2007**, 7, 1508-1513

[39] a) S.-L. Zheng, J.-P. Zhang, X.-M. Chen, Z.-L. Huang, Z.-Y. Lin, W.-T. Wong, *Chem. Eur. J.* **2003**, 9, 3888-3896. b) Y.-P. Tong, S.-L. Zheng, X.-M. Chen, *Inorg. Chem*. **2005**, 44, 4270-4275

[40] A. Gusev, E. Braga, E. Zamnius, M. Kiskin, M. Kryukova, A. Baryshnikova, B. Minaev, G. Baryshnikov, H. Ågren, W. Linert, *RSC Adv*. **2019**, 9, 22143

[41] P. Levín, D. Escudero, N. Díaz, A. Oliver, A. G. Lappin, G. Ferraudi, L. Lemus, *Inorg. Chem*. **2020**, 59, 1660-1674

[42] Y.-P. Tong, S.-L. Zheng, X.-M. Chen, *Eur. J. Inorg. Chem*. **2005**, 3734-3741

[43] H. Mandal, S. Chakrabartty, D. Ray, *RSC Adv*. **2014**, 4, 65044-65055

[44] Y. Yamaguchi, Y. Matsubara, T. Ochi, T. Wakamiya, Z.-i. Yoshida, *J. Am. Chem. Soc.* **2008**, 130, 13867-13869

[45] Y. Salinas, R. Martínez-Máñez, M. D. Marcos, F. Sancenón, A. M. Costero, M. Parra, S. Gil, *Chem. Soc. Rev*. **2012**, 41, 1261-1296

[46] N. B. Shustova, B. D. McCarthy, M. Dinca, *J. Am. Chem. Soc*. **2011**, 133, 20126-20129

[47] X. Zhuang, X. Zhang, N. Zhang, Y. Wang, L. Zhao, Q. Yang, *Cryst. Growth Des*. **2019**, 19, 5729-5736

[48] X. Zhang, X. Zhuang, N. Zhang, C. Ge, X. Luo, J. Li, J. Wu, Q. Yang, R. Liua, *CrystEngComm*. **2019**, 21, 1948-1955

[49] R. Lv, H. Li, J. Su, X. Fu, B. Yang, W. Gu, X. Liu, *Inorg. Chem*. **2017**, 56, 12348−12356

[50] a) A. L. Spek, *Acta. Cryst*. **2015**, C71, 9-18. b) A. L. Spek, *Acta Cryst*. **2009**, D65, 148-155

[51] a) A. P. Terzyk, A. Bieniek, P. Bolibok, M. Wisniewski, P. Ferrer, I. da Silva, P. Kowalczyk, *Adsorption*. **2019**, 25, 1-11. b) E. A. Tomic, *J. Appl. Polym. Sci*. **1965**, 9, 3745-3752

Chapter 7: Synthesis, characterisation and luminescent properties of lanthanide coordination complexes containing ethynyl-bridged picolinate ligands

This chapter describes the synthesis and characterisation of eleven anionic lanthanide coordination complexes constructed from ligands **H_2L8** ($[NH_2(CH_3)_2][Ln(H_2O)_2(\mathbf{L8})_2]$, Ln = Eu(**12**), Gd(**13**), Tb(**14**), Dy(**15**), Ho(**16**) and Er(**17**)) and **H_2L2** ($[NH_2(CH_3)_2][Ln(\mathbf{L2})_2]\cdot 1H_2O\cdot 1HAc$, Ln = Eu(**18**), Gd(**19**), Tb(**20**), Dy(**21**) and Ho(**22**)). First of all, experimental conditions for the preparation of the complexes, as well as their thermal and structural characterisation are described. Then, their magnetic and luminescent properties are detailed with special emphasis in their solvatochromic behaviour and sensing of metal ions.

As presented in chapter 5, **H_2L8** is a linear heteroditopic ligand containing a picolinate and a carboxylate functional group, whereas **H_2L2** is a linear homopolytopic ligand exhibiting two picolinate subunits. As expected, the different topology and coordination modes of the organic ligands lead to significant variations in the crystal structure of the resulting materials that have been addressed by means of single crystal X-ray diffraction. Moreover, the europium derivatives present striking emissive properties, which were further studied by fluorescence spectroscopy.

7.1. Introduction to Lanthanide coordination networks

The design and synthesis of lanthanide coordination polymers (Ln-CPs) still remains a hot topic due to their unusual coordination characteristics and appealing photophysical and magnetic properties.[1,2] In particular, most trivalent lanthanide ions show line-like, narrow emission bands associated to *f-f* transitions in the visible to near-infrared region of the optical spectrum.[3-5] Furthermore, in comparison with transition metals, lanthanides have higher coordination numbers, more flexible coordination geometry and, therefore, a wide variety of beautiful and interesting topological networks have been reported: 1D chains,[6] 2D grids,[3] 3D porous structures[7] and interpenetrating architectures.[8] For these reasons, coordination polymers based on lanthanides have great potential applications in different fields, such as catalysis, adsorption, magnetic materials, separation sensors and luminescent sensors among

others.[9-13] However, their coordination spheres and structures are hard to predict and the design of high-dimensional Ln-CPs remains challenging.[5,13]

Rigid benzenedicarboxylate-type ligands have been widely employed in the preparation of Ln-CPs, for instance 5-(4-pyridyl)-isophthalic acid (H_2IP-Py), isophthalic acid (H_2IP) and terephthalic acid (H_2TP).[5] Compared with benzenedicarboxylate ligands, the use of benzenedipicolinate or ligands combining picolinate and carboxylate moieties is still scarcely investigated. In fact, only two 3D cerium(III) and erbium(III) salts with pyrazine-2,5-dicarboxylic acid,[14] and a family of anionic networks prepared from 5-(4-carboxyphenyl) picolinic acid and lanthanide ions (Ln = Ce, Pr, Nd, Sm, Eu, Gd, Tb, Dy, Ho and Er) have been reported.[15-18] Even more, concerning ethynyl-bridged benzenedicarboxylate ligands, the number of reports involving Ln(III) ions are considerably lower than those with transition metal ions. In particular, to the best of our knowledge, there are sixteen coordination polymers based on the ligand 4,4'-ethynylbenzenedibenzoate (edb^{2-}), being only three of them lanthanide compounds.[19,20]

Recently, Ln-CPs with charged frameworks have attracted a great deal of attention due to the exchangeability between the compensating charged ions and a wide variety of external guest species.[21] In this context, using an appropriate host, immobilisation of different kinds of metal ions is possible through ion-exchange processes. For instance, a recent work shows that *in situ* reduction of ion-exchanged Ag(I) to Ag nanoparticles in an anionic Ln-CP is possible.[18] Another example shows that tunable luminescent properties can be achieved by means of reversible ion exchange in a 1D lanthanide coordination polymer.[22] The ion size and charge, as well as the dimensions of the host channel are of outmost importance, thus, careful optimisation of these factors is crucial.

7.2. Synthesis of a family of 2D lanthanide complexes based on the rigid ligand H_2L8

Complexes **12**-**17** were prepared by the reaction of lanthanide nitrates or chlorides with **H_2L8** under hydrothermal conditions. Suitable crystals were not obtained when we tried to synthesise the complexes by traditional methods such as slow evaporation and diffusion at room or low temperature. In such situations a fast irreversible precipitation of the compounds was observed. On the other hand, we found that the addition of an acid modulator was necessary in order to

obtain single crystals of the corresponding complexes and avoid the formation of powder.

A general strategy that consists in a solvothermal complexation reaction of $LnX_3 \cdot xH_2O$ (X = NO_3^- or Cl^-, Ln = Eu(**12**), Gd(**13**), Tb(**14**), Dy(**15**), Ho(**16**) or Er(**17**)) with 5-((4-carboxyphenyl)ethynyl)picolinic acid (**H_2L8**) in a mixed solvent (DMF/water, 3:2) has been employed for the synthesis of compounds **12**-**17** (Scheme 7.1). The mixture was held inside an oven at 130 °C during 3 days, with heating and cooling rates of 2 and 0.2 °C/min, respectively. In all cases nitric acid was used as a modulator in order to obtain single crystals suitable for X-ray diffraction measurements.

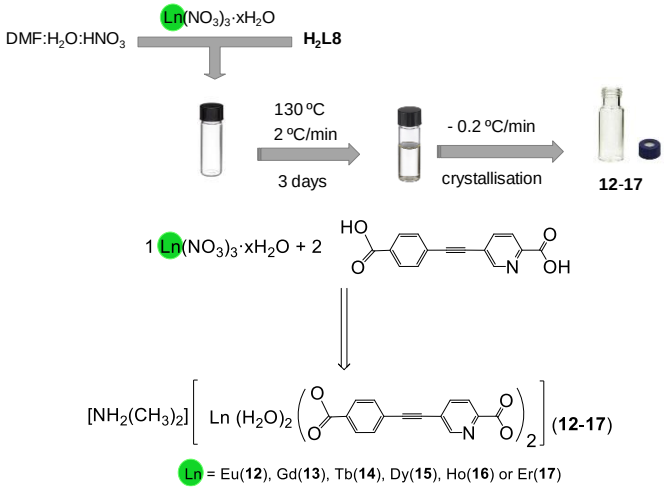

Scheme 7.1. Synthetic route employed to obtain complexes **12**-**17**.

7.3. Synthesis of a family of 3D lanthanide complexes based on the rigid ligand H_2L2

Complexes **18**-**22** were prepared by direct reaction between the corresponding lanthanide nitrate and ligand **H_2L2** or diester **Me_2L2** under hydrothermal conditions. Although important efforts have been devoted to obtain single crystals of the erbium derivative, its isolation as a pure phase was not possible. Just as in compounds **12**-**17**, crystalline material was not obtained when traditional synthetic methods were used. In these cases, an immediate precipitation of the compounds was observed after mixing the precursors. The addition of an acid modulator was also necessary in order to obtain single crystals.

A solvothermal general reaction of $Ln(NO_3)_3 \cdot xH_2O$ (Ln = Eu(**18**), Gd(**19**), Tb(**20**), Dy(**21**) or Ho(**22**)) with 5,5'-(ethyne-1,2-diyl)dipicolinate acid (**H_2L2**) or dimethyl 5,5'-(ethyne-1,2-diyl)dipicolinate (**Me_2L2**) in a mixed solvent (DMF/water, 8:1) has been developed for the synthesis of compounds **18**-**22** (Scheme 7.2). Different amounts of acetic acid (ranging from 1000 to 1300 μl) were added as a modulator depending on the lanthanide metal ion. The mixture was held inside an oven at 130 °C during 3 days, with heating and cooling rates of 1.7 and 0.2 °C/min, respectively.

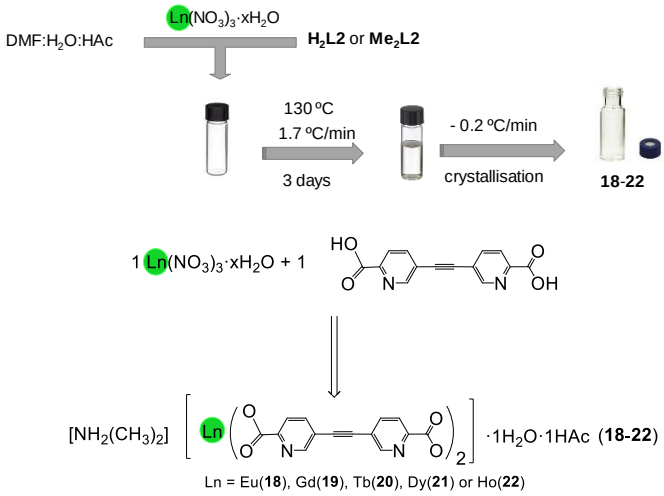

Scheme 7.2. Synthetic route employed to obtain complexes **18**-**22**.

7.4. $[NH_2(CH_3)_2][Ln(H_2O)_2(\mathbf{L8})_2]$ (**12**-**17**) and $[NH_2(CH_3)_2][Ln(\mathbf{L2})_2]\cdot 1H_2O\cdot 1HAc$ (**18**-**22**)

7.4.1. Structural characterisation

A. Single crystal X-ray diffraction

Single crystal X-ray analysis revealed that complexes **12**-**17** are isostructural (the corresponding unit cell parameters are gathered in Table 7.1.), crystallising in the monoclinic space group *I*2/*a*. Therefore, only the structure of **14** will be discussed in detail as a representative example. Its asymmetric unit contains half Tb(III) cation, one **L8** anion fully deprotonated, one coordinated water molecule and half dimethylammonium cation ($[NH_2(CH_3)_2]^+$). This guest molecule is required in order to balance the negative charge of the host framework and comes from the hydrolysis of dimethylformamide molecules

present as a solvent in the reaction medium (Scheme 7.3): DMF is decomposed in formic acid and dimethylamine that acts as a base deprotonating the **H_2L8** ligand and giving rise to dimethylammonium cations. This situation has been previously noted. In fact, there are several compounds in which dimethylammonium cations are observed in the final structure and come from the decomposition of DMF molecules.[17,23]

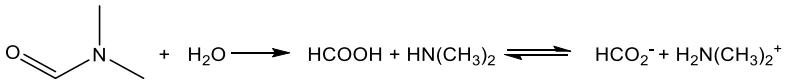

Scheme 7.3. Hydrolysis of DMF forming $[NH_2(CH_3)_2]^+$ cations.

The Tb cation sits on a twofold axis and displays an eight-coordinated distorted square antiprism geometric configuration (Figure 7.1). It is coordinated by two carboxylate oxygen atoms (Tb1–O3: 2.3920(10) Å) and two nitrogen atoms (Tb1–N1: 2.5608(12) Å) from two chelating picolinate subunits, two oxygen atoms (Tb1–O1: 2.3294(9) Å) from monodentate benzoate groups and two oxygen atoms (Tb1–O1W: 2.3479(11) Å) from water molecules. The continuous shape measure (CShM) calculations using SHAPE 2.1 confirm that the coordination geometry is a distorted square antiprism (D_{4d}, with a minimum CShM value of 9.174, Table 7.2).[24] A CShM calculation of a molecular entity indicates its distance to an ideal shape, regardless of its size and orientation and is given by the following expression:

$$S(G) = min\frac{\sum_{k=1}^{N}|Q_k - P_k|^2}{\sum_{k=1}^{N}|Q_k - Q_0|^2} \cdot 100 \text{ (eq. 7.1)}$$

The vectors Q_k (k = 1, 2…N) indicate the coordinates of the N vertices of a given structure, G is a specific and perfect symmetry group with coordinates P_k (k = 1, 2…N) and, then, the distances between the vertices of the two objects are calculated until a set of P_k coordinates is found that minimises the distances (Q_0 is the coordinate vector of the centre of mass of the investigated structure and the denominator is a size normalisation factor). The lower the CShM parameter, the better the agreement between the investigated and reference coordination geometry.[25] According to eq. 7.1, CShM measures must lie within the range 100 ≥ S ≥0. In compound **14**, a value of 9.174 suggests a strong distortion from the ideal geometry. In fact, the skew angle (Φ), described as the offset between the two squares defined by the mean planes through the coordination atoms (Figure 7.1), has a value of 38.21°. This angle is quite different to that expected for an ideal D_{4d} symmetry (Φ = 45°).

Table 7.1. Crystallographic data and structural refinement for $[NH_2(CH_3)_2][Ln(H_2O)_2(\mathbf{L8})_2]$ (**12**-**17**).

	12	**13**	**14**	**15**	**16**	**17**
Empirical formula	$C_{32}H_{26}EuN_3O_{10}$	$C_{32}H_{26}GdN_3O_{10}$	$C_{32}H_{26}TbN_3O_{10}$	$C_{32}H_{26}DyN_3O_{10}$	$C_{32}H_{26}HoN_3O_{10}$	$C_{32}H_{26}ErN_3O_{10}$
Formula weight	764.52	769.81	771.48	775.06	777.49	779.82
Crystallographic system	Monoclinic	Monoclinic	Monoclinic	Monoclinic	Monoclinic	Monoclinic
Space group	*I*2/*a* (no. 15)	*I*2/*a* (no. 15)	*I*2/*a* (no. 15)	*I*2/*a* (no. 15)	*I*2/*a* (no. 15)	*I*2/*a* (no. 15)
a/ Å	11.97630(10)	11.9735(2)	11.9538(1)	11.95380(10)	11.9306(2)	11.93380(10)
b/ Å	10.67410(10)	10.7027(2)	10.7164(1)	10.71640(10)	10.7799(2)	10.72770(10)
c/ Å	24.7299(3)	24.6745(4)	24.5755(2)	24.5755(2)	24.3559(4)	24.4262(3)
α/ °	90	90	90	90	90	90
β/ °	98.0830(10)	98.214(2)	98.361(1)	98.3610(10)	98.763(2)	98.6390(10)
γ/ °	90	90	90	90	90	90
V/ Å^3	3129.97(6)	3129.57(9)	3114.70(5)	3114.70(5)	3095.86(9)	3091.62(5)
Z	4	4	4	4	4	4
R(int)	0.0249	0.0251	0.0244	0.0364	0.0517	0.0300
ρ_{calc}/ g·cm^{-3}	1.622	1.634	1.645	1.653	1.668	1.675
μ/ mm^{-1}	2.066	2.182	2.333	2.462	2.619	2.778
Crystal dimensions/ mm	0.224 x 0.151 x 0.104	0.390 x 0.281 x 0.150	0.324 x 0.194 x 0.118	0.336 x 0.154 x 0.085	0.121 x 0.105 x 0.083	0.340 x 0.203 x 0.106
T/ K	120.2(3)	119.9(3)	119.9(3)	119.95(10)	119.9(3)	120.00(10)
λ/ Å	0.71073	0.71073	0.71073	0.71073	0.71073	0.71073
2θrange/ °	6.378< 2θ <59.506	6.674< 2θ <55.256	6.704< 2θ< 55.480	6.396< 2θ <55.516	6.770< 2θ <55.474	6.748< 2θ <59.642
Index ranges for h, k , l	-16/16, -14/14, -34/34	-14/15, -13/13, -31/32	-15/15, -14/14, -32/31	-15/15, -13/13, -31/30	-15/15, -14/13, -30/31	-16/16, -13/14, -33/33
Completeness to θ= 25.242° (%)	99.8	99.7	99.8	99.8	99.8	99.8
Refinement method	Full-matrix least-squares on F^2	Full-matrix least-squares on F^2	Full-matrix least-squares on F^2	Full-matrix least-squares on F^2	Full-matrix least-squares on F^2	Full-matrix least-squares on F^2
Collected reflections	37152	26278	40403	58070	28851	36543
Unique reflections	4273	3421	3519	3495	3414	4193
Data/Restraints/Parameters	4273/ 0/ 218	3421/ 0/ 218	3519/ 0/ 218	3495/ 0/ 218	3414/ 0/ 218	4193/ 0/ 218
Goodness-of-fit on F^2	1.153	1.165	1.092	1.215	1.029	1.145
R1, wR2 [I > 2sigma(I)][a]	R1 = 0.0145, wR2 = 0.0356	R1 = 0.0143, wR2 = 0.0357	R1 = 0.0128, wR2 = 0.0312	R1 = 0.0159, wR2 = 0.0358	R1 = 0.0258, wR2 = 0.0521	R1 = 0.0149, wR2 = 0.0352
R1, wR2 (all data)[a]	R1 = 0.0158, wR2 = 0.0363	R1 = 0.0153, wR2 = 0.0362	R1 = 0.0140, wR2 = 0.0319	R1 = 0.0184, wR2 = 0.0375	R1 = 0.0318, wR2 = 0.0553	R1 = 0.0167, wR2 = 0.0362
$\Delta\rho_{max}$ and $\Delta\rho_{min}$ (e·Å^{-3})	0.444, -0.238	0.638, -0.244	0.414, -0.278	0.851, -0.367	0.730, -0.423	0.736, -0.588

[a] $R1 = \Sigma(||F_o| - |F_c||)/\Sigma|F_o|$; $wR2 = \{\Sigma[w(F_o^2 - F_c^2)^2]/\Sigma[w(F_o^2)^2]\}^{1/2}$

Figure 7.2 shows that each anion acts as a tridentate ligand and links to two Tb(III) ions through the picolinate group (N1O3) in a bidentate manner and using the benzoate group (O1O2) in a monodentate fashion. This connectivity results in the formation of a 2D rhombus grid layer that presents channels (7.270 x 20.588 Å) along the *a* axis. These voids are occupied by dimethylammonium cations (one cation per channel) thanks to the establishment of hydrogen bonds with the non-coordinated carboxylate oxygen atoms (N2···O4: 2.7230(10) Å).

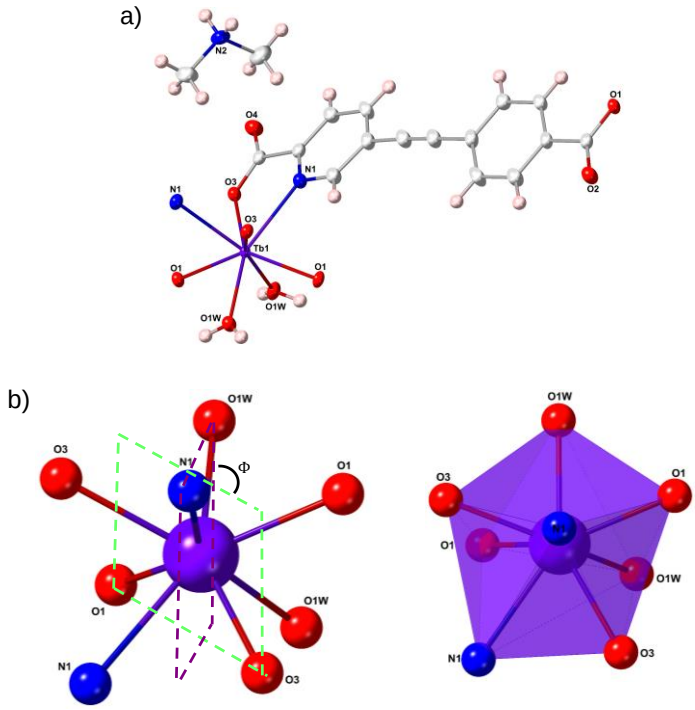

Figure 7.1. a) ORTEP view of coordination environment of Tb(III) in **14**. Thermal ellipsoids are drawn at the 50% probability level. b) The distorted square antiprism first coordination sphere of Tb^{3+} in **14**.

Table 7.2. Continuous shape measures (CShM) for **14** using SHAPE 2.1

	14	
OP-8	Octagon (D_{8h})	20.194
HPY-8	Heptagonal pyramid (C_{7v})	17.786
HBPY-8	Hexagonal bipyramid (D_{6h})	21.264
CU-8	Cube (Oh)	17.002
SAPR-8	**Square antiprism (D_{4d})**	**9.174**
TDD-8	Triangular dodecahedron (D_{2d})	10.444
JGBF-8	Johnson gyrobifastigium J26 (D_{2d})	22.450
JETBPY-8	Johnson elongated triangular bipyramid J14 (D_{3h})	24.721
JBTPR-8	Biaugmented trigonal prism J50 (C_{2v})	10.886
BTPR-8	Biaugmented trigonal prism (C_{2v})	10.920
JSD-8	Snub diphenoid J84 (D_{2d})	12.486
TT-8	Triakis tetrahedron (Td)	17.069
ETBPY-8	Elongated trigonal bipyramid (D_{3h})	21.471

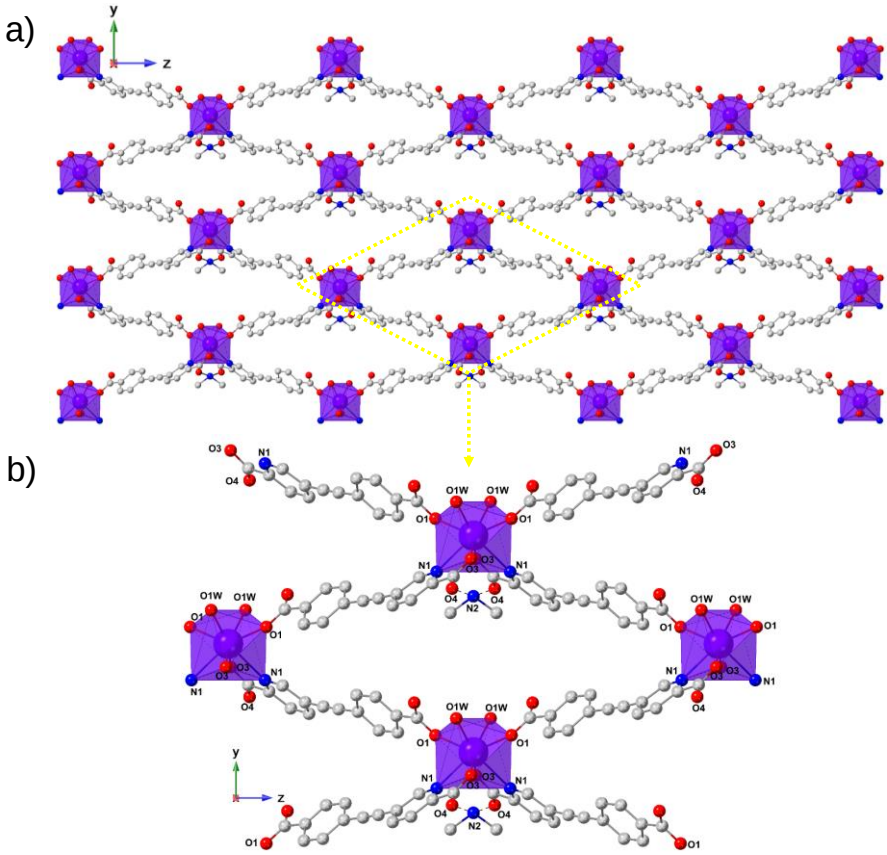

Figure 7.2. a) Representation of the layered structure of **14** in the *yz* plane. b) A zoom showing the label code. H atoms have been omitted for clarity.

Tb–O bond distances range from 2.3920(10) to 2.3294(9) Å and are lower than the Tb–N distance (2.5608(12) Å), in agreement with those values reported for Ln(III) complexes based on pyridyl-carboxylate ligands.[15,16] In addition, there is a notable difference between the two carboxylate Tb–O distances (Tb1–O3: 2.3920(10) Å *vs* Tb1–O1: 2.3294(9) Å) as a consequence of the higher nucleating character of the picolinate N1O3 moiety with respect to the O1O2 benzoate unit.

Furthermore, additional hydrogen bonds between water molecules coordinated to the metal and carboxylate oxygen atoms (O1W···O3: 2.7750(14) Å, O1W···O2: 2.5978(15)) are established. On the one hand, hydrogen bonds between coordinated water molecules (O1W) and carboxylate O3 oxygen atoms bridge consecutive layers, leading to the formation of a 3D doubly H-bonded network with an ABAB arrangement (Figure 7.3). In addition, π-π stacking interactions

are observed between pyridine and benzene aromatic rings of adjacent layers, with a mean value of 3.48(8) Å. On the other hand, hydrogen bonds between O1W and O2 oxygen atoms are only observed within each layer. Also, hydrogen bonds involving dimethylammonium cations are linking layers, but in this case of the same type (Figure 7.4).

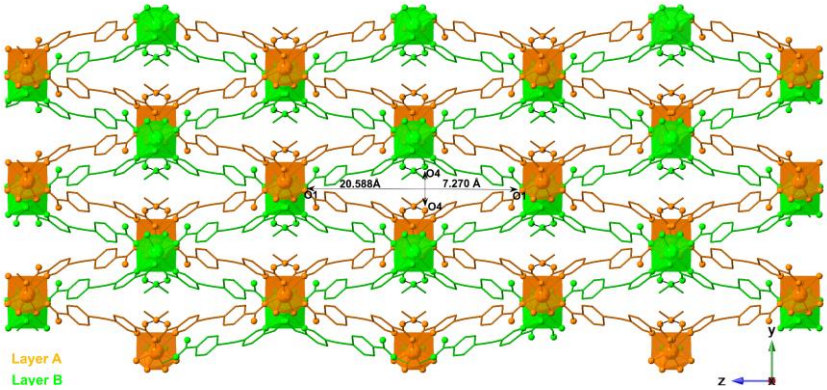

Figure 7.3. Representation of the layered structure of **14** in the *yz* plane showing the ABAB arrangement (each layer is illustrated in a different colour). H atoms have been omitted for clarity.

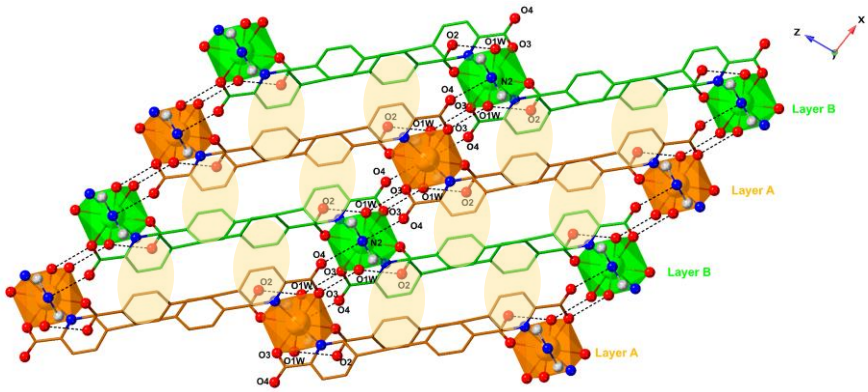

Figure 7.4. Representation of the 3D supramolecular structure of **14** showing the different type of hydrogen bonds found. Each layer is presented in different colour and π-π stacking interactions between adjacent layers are indicated in yellow. The dashed lines represent the hydrogen bonds. H atoms have been omitted for clarity.

The anion exhibits an almost planar conformation, with a small dihedral angle between the pyridine and benzene rings (12.90°) that allows coordination to two different metal cations. In addition, the carboxylate group involved in chelation presents a low torsion angle of 6.84° and the geometry of the triple bond is only

slightly distorted (-C-C≡C- and -C≡C-C- angles of 177.45° and 177.86°, respectively in comparison with the ideal value of 180°).

It is tempting to compare **14** with $[(CH_3)_2NH_2][Ln(H_2O)_2(C_{13}O_4N_1H_7)_2]$ (Ln = Eu, Gd, Er, Ho, Dy, Tb, Sm, Nd, Pr and Ce), a related family of lanthanide complexes based on 5-(4-carboxyphenyl)picolinate dianions (CPA^{2-}).[15] These isostructural compounds crystallise in the monoclinic *C*2/*c* space group, nevertheless, the lanthanide coordination sphere is analogous to that described for complex **14** and CPA^{2-} ligands adopt the same coordination mode to form an equivalent 2D rhombus grid layer. Even more, these layers are assembled into 3D supramolecular networks via similar H-bonding and π-π stacking interactions. In this family, when the counter cations are removed, the 'SQUEEZE' option of PLATON[26] indicates an empty volume of the anionic complex of 558.8 $Å^3$ for $[(CH_3)_2NH_2][Eu(H_2O)_2(C_{13}O_4N_1H_7)_2]$, corresponding to 20% of the total crystal volume. In compounds **12**-**17**, values slightly lower are obtained (Table 7.3). With respect to the inner surface of the rhombus channel, a value of 7.517 Å (inner carboxylate O···O separation) is found for $[(CH_3)_2NH_2][Eu(H_2O)_2(C_{13}O_4N_1H_7)_2]$ along the shortest direction, and those observed for compounds **12**-**17** are in agreement (Table 7.3). As expected, for compounds **12**-**17**, the inner surface of the channel along its longest direction is notably higher in comparison with that obtained for $[(CH_3)_2NH_2][Eu(H_2O)_2(C_{13}O_4N_1H_7)_2]$ (16.495 Å), due to the presence of two additional carbon atoms in **H_2L8** *vs* H_2CPA.

Table 7.3. Empty volume of the anionic Ln CPs **12**-**17** (calculated using PLATON software after removal of $[(CH_3)_2NH_2]^+$ counter cations)[26] and dimensions of the 1D channels found along the z and y axis.

Compound	Empty volume($Å^3$)/% of the total crystal volume	Dimension of the channel along z axis (d(O1···O1))/ Å	Dimension of the channel along y axis (d(O4···O4))/ Å
$[(CH_3)_2NH_2][Eu(H_2O)_2($**L8**$)_2]$ (**12**)	442.4/14.1	20.718	7.242
$[(CH_3)_2NH_2][Gd(H_2O)_2($**L8**$)_2]$ (**13**)	445.1/14.2	20.667	7.261
$[(CH_3)_2NH_2][Tb(H_2O)_2($**L8**$)_2]$ (**14**)	448.0/14.4	20.588	7.270
$[(CH_3)_2NH_2][Dy(H_2O)_2($**L8**$)_2]$ (**15**)	448.5/14.4	20.590	7.285
$[(CH_3)_2NH_2][Ho(H_2O)_2($**L8**$)_2]$ (**16**)	452.6/14.6	20.382	7.297
$[(CH_3)_2NH_2][Er(H_2O)_2($**L8**$)_2]$ (**17**)	443.8/14.4	20.472	7.292

Moreover, it is worth noting that the channel may present hydrophilic character, due to the fact that it is internally surrounded by non-coordinated carboxylate oxygen atoms that may allow specific interactions between guest molecules and the host framework in post-synthetic cation exchange processes. These post-

synthetic processes allow the fabrication of new materials with enhanced properties that may be not possible to obtain by direct methods. For instance, the replacement of dimethylammonium cations by Li^+ ions in $[(NH_2)(CH_3)_2]_2[Zn_2(BDC)_3(DMA)_2]\cdot 6DMF$ (BDC^{2-} = 1,4-benzenedicarboxylate and DMA = dimethylamine) results in an increase in its internal surface area and methane sorption capacity.[27] In another case, exchange of the nickel(II) cations located in the pores of $Ni_2[Ni_4[Cu_2\text{-}(Me_3mpba)_2]_3]\cdot 54H_2O$ (Me_3mpba^{4-} = N,N'-2,4,6-trimethyl-1,3-phenylenebis(oxamate) ligand) with barium cations produces a novel coordination polymer that presents improved features for SO_2 adsorption.[28]

Lanthanide chemistry generally results in the formation of isostructural compounds since lanthanide ions exhibit common chemical properties. Nevertheless, lanthanide contraction can lead to slightly structural changes or result in full structural rearrangements that influences the physical properties of the materials. In the latter scenario, the structure of the polymers varies systematically with increasing atomic number of lanthanide ions. For instance, the complexes $[Ln_2(HL)_3(H_2O)_n]\cdot XH_2O$ (being HL^{2-} = 3,5-pyrazoledicarboxylate and Ln = Pr, Nd, Sm, Eu, Gd, Tb, Dy, Ho and Er) range from porous 3D frameworks (Ln = Pr, Nd and Sm) and 2D double decker-structures (Ln = Eu, Gd and Tb) to 2D monolayer frameworks (Ln = Dy, Ho and Er), with a formula of $[Ln(HL)(H_2L)(H_2O)_2]_n$ in the latter situation.[29] In our case, Table 7.4 contains Ln-O and Ln-N bond lengths for complexes **12**-**17** and it can be seen that for increasing atomic number, as the ionic radii of the lanthanide ions decreases, so does the corresponding bond length values. This is a clear signature of the lanthanide contraction effect (Figure 7.5).

Table 7.4. Selected bond lengths in Å for Ln-CPs **12**-**17**.

Compound	**12** (Eu)	**13** (Gd)	**14** (Tb)	**15** (Dy)	**16** (Ho)	**17** (Er)
Ln-O1	2.3512(9)	2.3448(11)	2.3293(9)	2.3248(12)	2.3073(19)	2.3037(10)
Ln-O3#1	2.4183(9)	2.4106(11)	2.3920(10)	2.3818(11)	2.3737(18)	2.3638(10)
Ln-O5	2.3799(10)	2.3670(12)	2.3479(11)	2.3300(13)	2.319(2)	2.3064(12)
Ln-N1#1	2.5919(11)	2.5790(14)	2.5609(12)	2.5480(15)	2.528(2)	2.5232(13)

Symmetry code: #1 -x+1, y+1/2, -z+1/2

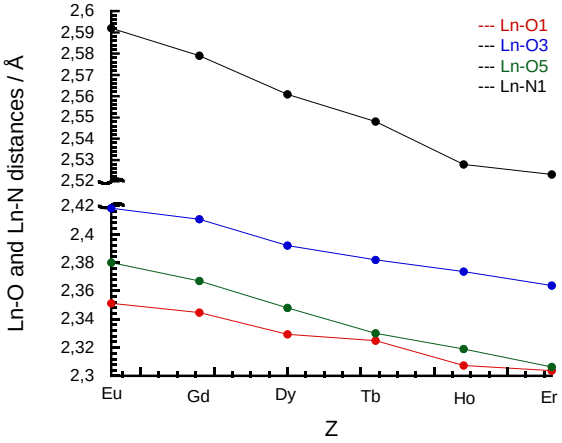

Figure 7.5. Variation of the Ln-O and Ln-N bond lengths with the increasing atomic number (*Z*) of lanthanide ions for **12**-**17**.

Regarding the second family of lanthanide complexes based on **L2** ligand, only the crystal structure of the Tb complex is described in detail as a representative example of the isostructural series (corresponding single crystal X-ray data are gathered in Table 7.5). Compound **20** crystallises in the orthorhombic $Pna2_1$ space group and its asymmetric unit contains a Tb(III) cation, two crystallographically independent **L2** anions, one dimethylammonium cation and crystallisation solvent molecules (one water molecule and one acetic acid). The Flack parameter is close to zero (Table 7.5), implying that none of the crystals are in the inverted form and the model has the correct absolute structure.[30] Like in the previous family of lanthanide complexes, dimethylammonium cations are needed in order to balance the negative charges of the host framework and they arise from the hydrolysis of dimethylformamide used as a solvent during the synthesis.

The Tb cation is located in a general position and exhibits a nine-coordinated tricapped trigonal prismatic structure that has been determined by continuous shape measure (CShM) calculations (Table 7.6 presents the CShM values for all the possible nine coordinated-polyhedra, with a minimum CShM value of 3.853 for a tricapped trigonal prism). As Figure 7.6 shows, four picolinate subunits coordinate in a bidentate fashion (Tb1–O1: 2.333(3) Å), Tb1–N1: 2.580(4) Å; Tb1–O5: 2.390(4) Å), Tb1–N3: 2.673(4) Å; Tb1–O4: 2.344(4) Å), Tb1–N2: 2.684(4) Å; Tb1–O8: 2.340(3) Å), Tb1–N4: 2.607(4) Å) and the ninth position is occupied by a carboxylate oxygen atom (Tb1–O6: 2.335(4) Å). The triangular faces of the tricapped trigonal prism are defined by O1O5N1 and O6O8O4 atoms,

whereas the "caps" over each rectangular face are formed by N2, N3 and N4 nitrogen atoms. The angle between the trigonal faces is 175.76°, indicating that they are almost parallel.

Table 7.5. Crystallographic data and structural refinement for $[NH_2(CH_3)_2][Ln(\mathbf{L2})_2]\cdot 1H_2O\cdot 1HAc$ (**18**-**22**).

	18	**19**	**20**	**21**	**22**
Empirical formula	$C_{32}H_{26}EuN_5O_{11}$	$C_{32}H_{26}GdN_5O_{11}$	$C_{32}H_{26}TbN_5O_{11}$	$C_{32}H_{26}DyN_5O_{11}$	$C_{32}H_{26}HoN_5O_{11}$
Formula weight	808.54	813.83	815.50	819.08	821.51
Crystallographic system	Orthorhombic	Orthorhombic	Orthorhombic	Orthorhombic	Orthorhombic
Space group	$Pna2_1$ (no. 33)	$Pna2_1$ (no. 33)	$Pna2_1$ (no. 33)	$Pna2_1$ (no. 33)	$Pna2_1$ (no. 33)
a/ Å	19.6440(2)	19.6404(2)	19.70340(10)	19.63920(10)	19.6233(2)
b/ Å	12.35500(10)	12.36350(10)	12.32080(10)	12.33990(10)	12.3460(2)
c/ Å	13.21490(10)	13.18630(10)	13.14510(10)	13.10680(10)	13.0756(2)
α/ °	90	90	90	90	90
β/ °	90	90	90	90	90
γ/ °	90	90	90	90	90
V/ Å^3	3207.28(5)	3201.95(5)	3191.13(4)	3176.38(4)	3167.82(8)
Z	4	4	4	4	4
R(int)	0.0975	0.0810	0.0435	0.0748	0.1617
ρ_{calc}/ g·cm^{-3}	1.674	1.688	1.697	1.713	1.723
μ/ mm^{-1}	2.025	2.141	2.286	2.423	2.568
Crystal dimensions/ mm	0.124x 0.105x 0.073	0.108x 0.095x 0.058	0.180× 0.136 × 0.122	0.145x 0.108x 0.084	0.080x 0.057x 0.048
T/ K	119.7(8)	120.00(10)	120.00(10)	120.0(6)	119.95(10)
λ/ Å	0.71073	0.71073	0.71073	0.71073	0.71073
2θrange/ °	6.60<2θ<56.21	6.59<2θ<55.34	6.61<2θ<55.42	6.60<2θ<55.48	6.60<2θ<56.05
Index ranges for h, k , l	-25/24, -16/16, -16/17	-25/24, -16/16, -17/17	-25/25, -16/15, -17/17	-25/25, -15/15, -16/16	-25/25, -16/16, -17/16
Completeness to θ = 25.242° (%)	99.7	99.7	99.7	99.7	99.7
Refinement method	Full-matrix least-squares on F^2	Full-matrix least-squares on F^2	Full-matrix least-squares on F^2	Full-matrix least-squares on F^2	Full-matrix least-squares on F^2
Collected reflections	118251	99746	116487	116555	116736
Unique reflections	7383	7154	7172	7094	7285
Data/Restraints/parameters	7383 / 33 / 453	7154 / 6 / 422	7172 / 9 / 428	7094 / 31 / 447	7285 / 31 / 447
Goodness-of-fit on F^2	1.073	1.743	1.106	1.063	1.062
Final R indices [I > 2sigma(I)][a]	R1 = 0.0386, wR2 = 0.0757	R1 = 0.0904, wR2 = 0.2195	R1 = 0.0307, wR2 = 0.0708	R1 = 0.0352, wR2 = 0.0719	R1 = 0.0508, wR2 = 0.0859
R indices (all data)[a]	R1 = 0.0625, wR2 = 0.0876	R1 = 0.1083, wR2 = 0.2314	R1 = 0.0355, wR2 = 0.0741	R1 = 0.0488, wR2 = 0.0781	R1 = 0.0979, wR2 = 0.1004
Absolute structure parameter	-0.039(6)	-0.02(4)	-0.026(4)	-0.035(5)	-0.031(8)
$\Delta\rho_{max}$ and $\Delta\rho_{min}$ (e·Å^{-3})	2.284, -1.104	6.928, -3.794	1.705, -1.043	1.418, -0.962	2.925, -1.475

[a] $R1 = \Sigma(||F_o| - |F_c||)/\Sigma|F_o|$; $wR2 = \{\Sigma[w(F_o^2 - F_c^2)^2]/\Sigma[w(F_o^2)^2]\}^{1/2}$

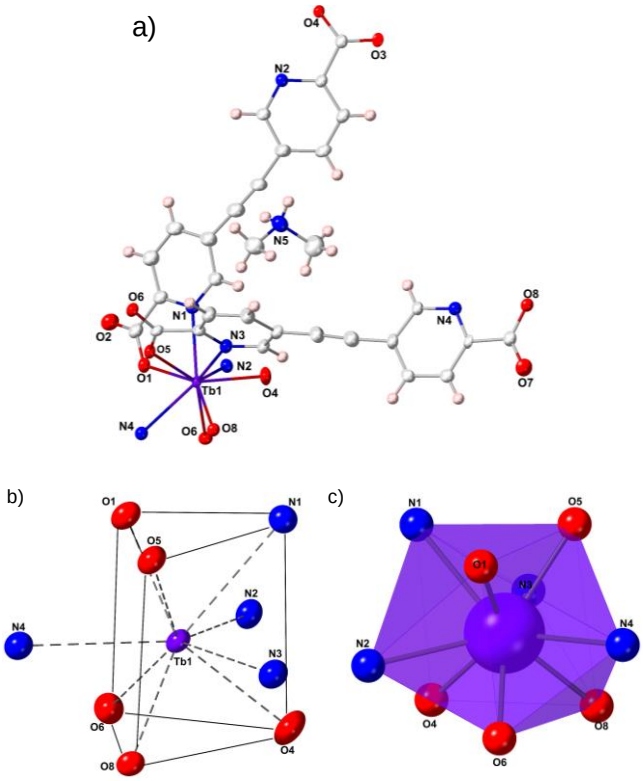

Figure 7.6. a) ORTEP view of coordination environment of Tb(III) in **20**. Thermal ellipsoids are drawn at the 50% probability level. b) and c) The distorted trigonal geometry of Tb^{3+} in **20**.

Table 7.6. Continuous shape measures (CShM) for **20** using SHAPE 2.1

	20	
EP-9	Enneagon (D_{9h})	29.233
OPY-9	Octagonal pyramid (C_{8v})	19.518
HBPY-9	Heptagonal bipyramid (D_{7h})	16.985
JTC-9	Johnson triangular cupola J3 (C_{3v})	15.250
JCCU-9	Capped cube J8 (C_{4v})	10.261
CCU-9	Spherical-relaxed capped cube (C_{4v})	10.813
JCSAPR-9	Capped square antiprism J10 (C_{4v})	4.605
CSAPR-9	Spherical capped square antiprism (C_{4v})	4.341
JTCTPR-9	**Tricapped trigonal prism J51 (D_{3h})**	**3.853**
TCTPR-9	Spherical tricapped trigonal prism (D_{3h})	4.106
JTDIC-9	Tridiminished icosahedron J63 (C_{3v})	14.612
HH-9	Hula-hoop (C_{2v})	11.012
MFF-9	Muffin (Cs)	4.372

There are two independent **L2** ligands that adopt different coordination modes: one as a terminal chelating ligand and the other as a bridging anion. Thus, wave-like chains running parallel to the *c* axis are formed, in which the metal ions are bridged by *anti*, *anti*-carboxylate groups (O5O6) with intrachain metal-metal distances of 6.656 Å (Figure 7.7). This coordination mode has been already described in oxalate-bridged lanthanide complexes, as well as in multi-dimensional frameworks containing pyrazine, imidazole and thiophene carboxylates.[31] As observed in compounds **12**-**17**, Tb–O bond distances (ranging from 2.333(3) to 2.390 (4) Å) are lower than Tb–N distances (from 2.580(4) to 2.684(4) Å), and are also in agreement with previously values reported for Ln(III) complexes based on picolinate ligands.[15,16] It has to be noted that among the four chelating picolinate Tb–O distances found, Tb1–O5 is the biggest as a consequence of the higher nucleating character of this picolinate moiety.

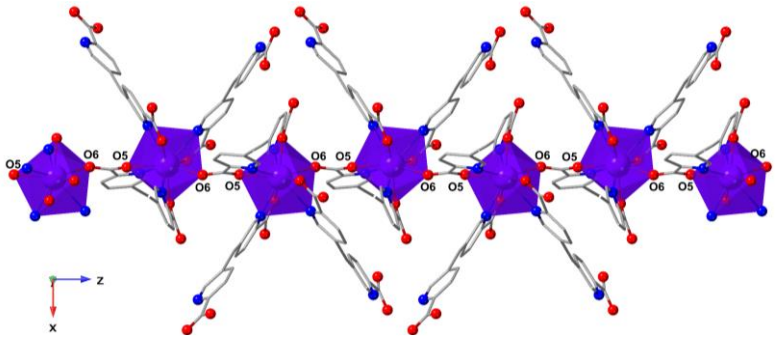

Figure 7.7. View of the carboxylate-bridged chain structure of **20** in the xz plane. H atoms have been omitted for clarity.

In addition, the same bridging ligand adopts a bis-bidentate coordination mode (N3O5 and N4O8), linking to Tb(III) centres of adjacent chains. In this way, metal centres are connected along the *b* axis (Figure 7.8.a). Therefore, the first anion (depicted in orange in Figure 7.8) acts as a pentadentate ligand and coordinates to two Tb(III) ions through two picolinate groups in a bidentate manner (*transoid*-alignment of the picolinate subunits) and to a third anion in a monodentate fashion using the another oxygen atom from one picolinate group. This connectivity results in the formation of a 2D layered structure.

On the other hand, the second **L2** anion exhibits a bis-bidentate coordination mode with a *transoid*-alignment of the picolinate groups (depicted in green in Figure 7.8), linking metal centres in a zigzag chain structure with intrachain

metal-metal distances of 12.815 Å. Figure 7.9 shows the resulting 3D structure that presents triangular channels along the *b* axis. These small voids are occupied by H-bonded water solvent molecules, acetic acid and dimethylammonium cations, one of each molecule per channel. Dimmetylammonium cations are forming H-bonds with coordinated carboxylate oxygen atoms (N5···O8: 2.742(9) Å) and water molecules (N5···O1W: 2.702(14) Å). O1W is interacting as a H-bond donor with non-coordinated carboxylate oxygen atoms (O1W···O3: 2.739(14) Å) and with acetic acid (O1W···O10: 3.03(2) Å). In addition, acetic acid is H-bonded to O2 carboxylate atom with a very short hydrogen bond distance of 2.486(18) Å.

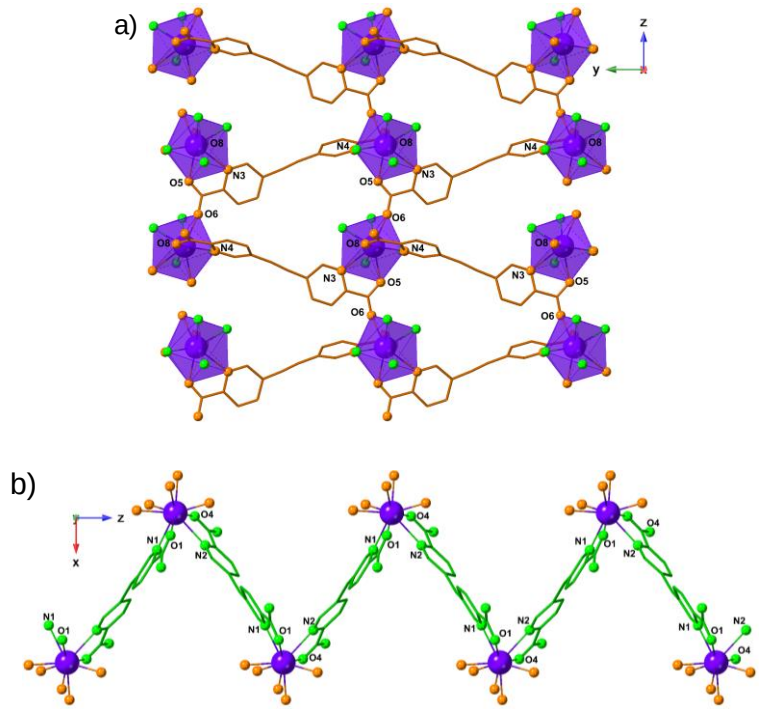

Figure 7.8. a) Crystal structure of **20** showing the connectivity of the first ligand in the yz plane. The second ligand has been omitted for clarity. b) Crystal network of **20** presenting the connectivity of the second ligand. The first ligand has been omitted for clarity.

Both anions are markedly distorted, being the dihedral angle between the two pyridine rings of 99.35° and 26.70° for the first (depicted in orange) and the second (depicted in green) ligand, respectively. In fact, the first ligand displays a higher deviation from planarity, which may be attributed to the binding of the bridging carboxylate (O5O6) to a second Tb^{3+} centre. For the same reason, the

torsion angle involving O5 carboxylate oxygen atom (12.40°) is higher than those obtained for the other carboxylate moieties (0.49°-8.51°), being the lowest values obtained for the ligand that only shows the bis(bidentate) coordination mode. With respect to the bending of the triple bond, it is similar in both cases with a maximum deviation of 7.34° to the ideal –C-C≡C- and -C≡C-C- angles of 180° (175.91°; 174.28° and 174.72°; 172.67° for the first and the second ligand, respectively).

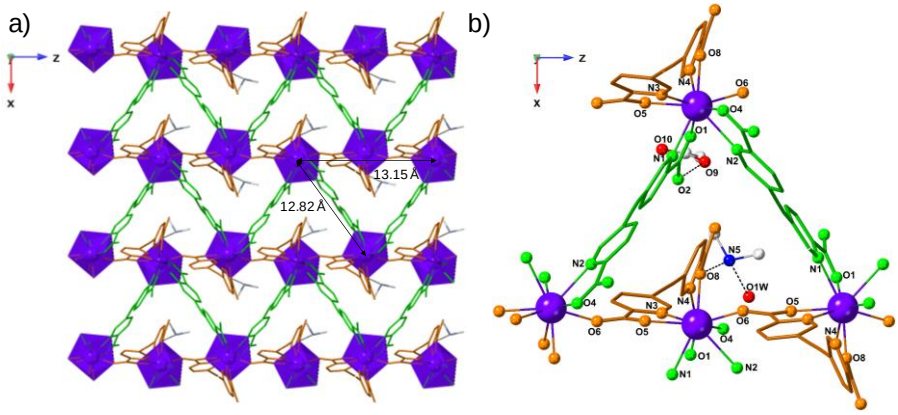

Figure 7.9. a) Representation of the 3D structure of **20** in the xz plane. Each independent ligand is shown in a different colour. b) A zoom showing the label code. H atoms have been omitted for clarity.

Analogously to compounds **12**-**17**, the voids present in this family of lanthanide complexes are surrounded by non-coordinated carboxylate oxygen atoms. This confers hydrophilic character to the channels which may be exploited in post-synthetic cation exchange processes.[16] For compound **20**, after removal of the counter cations and the solvent molecules, the PLATON/VOID calculation[26] indicates an empty volume of the anionic complex of 893.5 $Å^3$, corresponding to 28.0% of the total crystal volume (3191.1 $Å^3$). Similar values are found for compounds **18**, **19**, **21** and **22**, which are included in Table 7.7. Compounds **18**-**22** present a solvent accessible void higher than that associated to complexes **12**-**17**, nevertheless, the dimensions of the channel are smaller. This indicates that the family of lanthanide complexes **12**-**17** exhibits a more condensed structure in comparison to the 3D crystal lattice described for complexes **18**-**22**.

Table 7.7. Empty volume of the anionic Ln-CPs **18**-**22** (calculated using PLATON software after removal of $[(CH_3)_2NH_2]^+$ counter cations and the solvent molecules) and dimensions of the 1D channels found along the z and y axis.

Compound	Empty volume($Å^3$)/% of the total crystal volume	Dimension of the channel along x axis (d(Ln1···Ln1))/ Å	Dimension of the channel along z axis (d(Ln1···Ln1))/ Å
$[NH_2(CH_3)_2][Eu(\mathbf{L2})_2]\cdot 1H_2O\cdot 1HAc$ (**18**)	928.2/28.9	12.837	13.215
$[NH_2(CH_3)_2][Gd(\mathbf{L2})_2]\cdot 1H_2O\cdot 1HAc$ (**19**)	853.1/27.1	12.789	13.241
$[NH_2(CH_3)_2][Tb(\mathbf{L2})_2]\cdot 1H_2O\cdot 1HAc$ (**20**)	893.5/28.0	12.815	13.145
$[NH_2(CH_3)_2][Dy(\mathbf{L2})_2]\cdot 1H_2O\cdot 1HAc$ (**21**)	879.5/27.7	12.803	13.107
$[NH_2(CH_3)_2][Ho(\mathbf{L2})_2]\cdot 1H_2O\cdot 1HAc$ (**22**)	869.4/27.4	12.797	13.076

Complexes **18**-**22** are isostructural with Ln-O and Ln-N distances following the trend of lanthanide contraction: in general, with increasing atomic number, the average distance decreases (Table 7.8, Figure 7.10).

Table 7.8. Selected bond lengths in Å for Ln-CPs **18**-**22**.

Compound	**18** (Eu)	**19** (Gd)	**20** (Tb)	**21** (Dy)	**22** (Ho)
Ln-O1	2.354(6)	2.339(12)	2.334(4)	2.319(6)	2.320(7)
Ln-O5	2.419(8)	2.414(14)	2.388(5)	2.385(8)	2.367(11)
Ln-N1	2.603(9)	2.589(14)	2.583(6)	2.561(8)	2.549(10)
Ln-N3	2.692(9)	2.696(15)	2.668(6)	2.659(8)	2.656(10)
Ln-O6#1	2.360(7)	2.350(13)	2.332(5)	2.318(7)	2.315(10)
Ln-O8#2	2.377(6)	2.367(10)	2.339(4)	2.332(5)	2.319(6)
Ln-O4#3	2.372(8)	2.369(12)	2.347(5)	2.329(7)	2.320(9)
Ln-N2#3	2.672(9)	2.673(15)	2.679(6)	2.661(8)	2.655(10)
Ln-N4#2	2.626(8)	2.622(13)	2.608(6)	2.608(8)	2.582(9)

Symmetry code: #1 1-x, -y, ½+z; #2 x, -1+y, z; #3 3/2-x, -1/2+y, ½+z

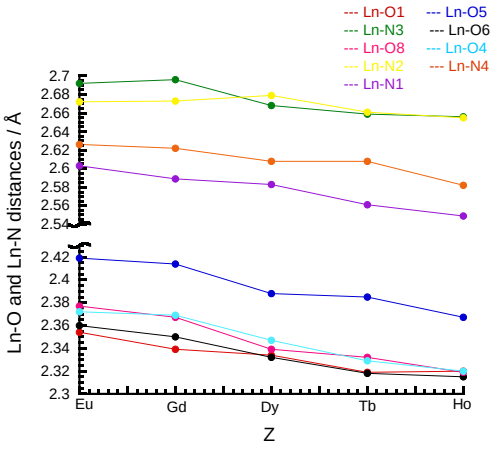

Figure 7.10. Variation of the Ln-O and Ln-N bond lengths with the increasing atomic number (*Z*) of lanthanide ions for **18**-**22**.

B. Powder X-ray diffraction and thermogravimetric analysis

In order to confirm the phase purity of the bulk materials, powder X-ray diffraction measurements were undertaken (Figure 7.11). The experimental patterns recorded at room temperature for compounds **12**-**17** and **18**-**22** are compared with the simulated diffractogram for **14** and for **20** from the single crystal data at 120 K, respectively. There is a perfect agreement between both subsets of patterns, discarding the presence of impurities.

Next, thermogravimetric analyses were performed under nitrogen atmosphere (Figure 7.12). TG curves for **12**-**17** (Figure 7.12.a) resemble each other and present three separated steps of weight loss. The first one takes place between 416-435 K and is ascribed to the release of two coordinated water molecules (calcd: 4.71-4.62 %). Observed values for this weight loss are summarised in Table 7.9. The second and third steps occur above 515 K and are attributed to the decomposition of dimethylammonium cations and **L8** ligands. These results are consistent with the formulation deduced from single crystal X-ray diffraction measurements that show the presence of two water molecules per lanthanide ion.

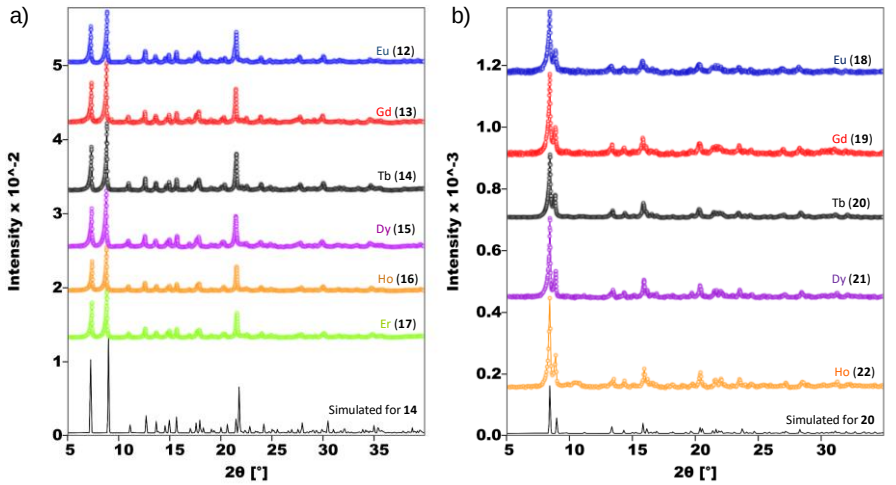

Figure 7.11. a) Comparison of the powder diffractograms of **12**-**17** with the simulation obtained from single crystal X-ray data for **14** using *CrystalDiffract* software. b) Comparison of the powder diffractograms of **18**-**22** with the simulation obtained from single crystal X-ray data for **20** using *CrystalDiffract* software.

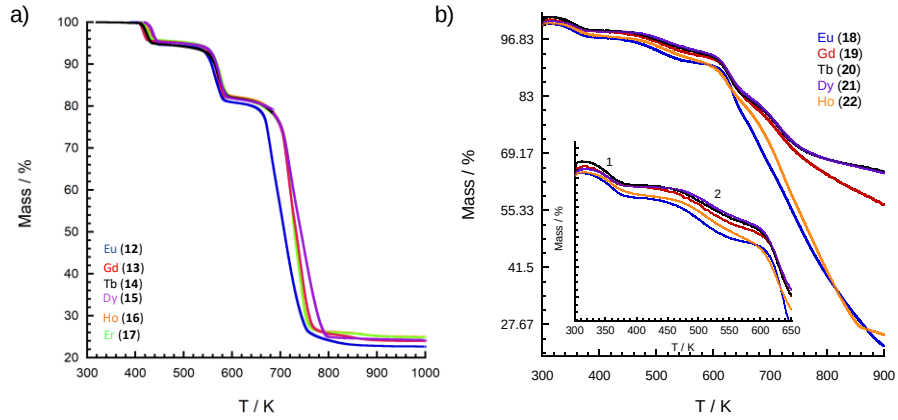

Figure 7.12. a) Thermogravimetric analysis of **12**-**17**. b) Thermogravimetric analysis of **18**-**22.**

Table 7.9. Experimental values and temperature of decomposition for the first step of weight loss in TG plots for **12**-**17**.

Compound	First weight loss/ %	First decomposition temperature/ K
$[(CH_3)_2NH_2][Eu(H_2O)_2(\mathbf{L8})_2]$ (**12**)	5.27	435
$[(CH_3)_2NH_2][Gd(H_2O)_2(\mathbf{L8})_2]$ (**13**)	4.60	416
$[(CH_3)_2NH_2][Tb(H_2O)_2(\mathbf{L8})_2]$ (**14**)	5.04	422
$[(CH_3)_2NH_2][Dy(H_2O)_2(\mathbf{L8})_2]$ (**15**)	4.75	435
$[(CH_3)_2NH_2][Ho(H_2O)_2(\mathbf{L8})_2]$ (**16**)	4.40	426
$[(CH_3)_2NH_2][Er(H_2O)_2(\mathbf{L8})_2]$ (**17**)	4.40	422

For compounds **18**-**22**, the TG curves (Figure 7.12.b) are very similar in the low temperature regime (below 600 K) and exhibit a multi-step weight loss. Between RT and 390 K, a first weight loss associated to the release of water molecules present in the voids of the structure takes place. Then, a second step ascribed to the loss of acetic acid molecules is detected between 425 and 590 K. These observations are consistent with the release of two different types of solvent molecules that are present in the voids of the structure. Observed and calculated values for the loss of the ascribed solvent are summarised in Table 7.10. These values indicate a solvent content in agreement with the formulation deduced from single crystal X-ray diffraction in the case of the europium and holmium derivatives. For the rest of the members of the family, the observed values are lower than the expected ones. This difference is consistent with the fast loss of solvent molecules that are placed within the voids of the structure upon their extraction from the mother liquor (the crystals were filtered and air kept several days prior to TG measurements, whereas for single crystal XRD experiments all of them were kept in the solution until the crystal was mounted in the diffractometer). Then, above 590 K decomposition of dimethylammonium cations and **L2** ligands occurs.

Table 7.10. Data extracted for the solvent weight loss (between 320 and 575 K) in TG plots for **18**-**22**.

Compound	Solvent weight loss (RT-590 K) (obs/calc[a])/ %
$[NH_2(CH_3)_2][Eu(\mathbf{L2})_2]\cdot 1H_2O\cdot 1HAc$ (**18**)	9.26/9.65
$[NH_2(CH_3)_2][Gd(\mathbf{L2})_2]\cdot 1H_2O\cdot 1HAc$ (**19**)	7.33/9.59
$[NH_2(CH_3)_2][Tb(\mathbf{L2})_2]\cdot 1H_2O\cdot 1HAc$ (**20**)	6.83/9.57
$[NH_2(CH_3)_2][Dy(\mathbf{L2})_2]\cdot 1H_2O\cdot 1HAc$ (**21**)	6.50/9.65
$[NH_2(CH_3)_2][Ho(\mathbf{L2})_2]\cdot 1H_2O\cdot 1HAc$ (**22**)	9.18/9.50

[a]calculated considering the molecular weight of the original solvate deduced from X-ray single crystal diffraction measurements ($\cdot 1H_2O\cdot 1HAc$)

7.4.2. Magnetic characterisation

Magnetic susceptibility measurements were carried out on bulk samples of **12**-**22** at 1000 Oe in a direct current (dc) field in the temperature range of 2-300 K in order to probe any possible interaction between the Ln(III) ions (Figure 7.13). Without considering the europium derivatives, at room temperature, the samples show χT values close to those expected for the free trivalent ion (Table 7.11)[32]: χT = 7.56 and 7.82 emu·K·mol^{-1} for **13** and **19**, respectively (Gd^{3+} (S = 7/2, g = 2) ion, $\chi T_{\text{free ion}}$ = 7.87); 12.50 and 12.49 emu·K·mol^{-1} for **14** and **20**, respectively (Tb^{3+} (S = 3) ion, g = 3/2, $\chi T_{\text{free ion}}$ = 11.82); 14.18 and 14.95 emu·K·mol^{-1} for **15** and **21**, respectively (Dy^{3+} (S = 5/2, g = 4/3) ion, $\chi T_{\text{free ion}}$ = 14.17); 14.04 and 12.86 emu·K·mol^{-1} for **16** and **22**, respectively (Ho^{3+} (S = 2, g

= 5/4) ion, $\chi T_{\text{free ion}}$ = 14.05) and 11.98 emu·K·mol^{-1} for **17** (Er^{3+} (S = 3/2, g = 6/5) ion, $\chi T_{\text{free ion}}$ = 11.48).

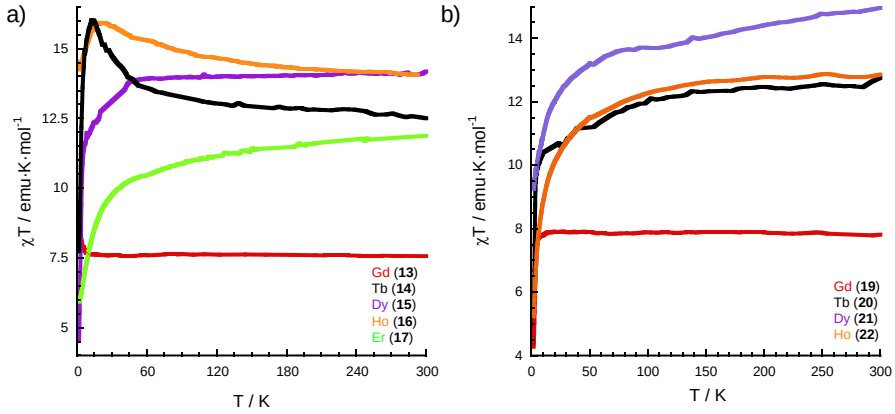

Figure 7.13. a) Temperature dependence of the χT values for **13**-**17** at 1000 Oe dc magnetic field. b) Temperature dependence of the χT values for **19**-**22** at 1000 Oe dc magnetic field.

Table 7.11. Direct current magnetic data for complexes **12**-**22**. χT is the product of magnetic susceptibility and temperature, C is the Curie constant and θ is the Weiss constant.

Compound	Experimental χT_{300K} / emu·K·mol^{-1}	Theoretical χT / emu·K·mol^{-1}	C / emu·K·mol^{-1}	θ / K
$[(CH_3)_2NH_2][Eu(H_2O)_2(\mathbf{L8})_2]$ (**12**)	1.35	0 (1.50)	---	---
$[(CH_3)_2NH_2][Gd(H_2O)_2(\mathbf{L8})_2]$ (**13**)	7.56	7.87	7.576	0.172
$[(CH_3)_2NH_2][Tb(H_2O)_2(\mathbf{L8})_2]$ (**14**)	12.50	11.82	12.577	2.876
$[(CH_3)_2NH_2][Dy(H_2O)_2(\mathbf{L8})_2]$ (**15**)	14.18	14.05	14.207	-1.945
$[(CH_3)_2NH_2][Ho(H_2O)_2(\mathbf{L8})_2]$ (**16**)	14.04	14.04	14.056	2.757
$[(CH_3)_2NH_2][Er(H_2O)_2(\mathbf{L8})_2]$ (**17**)	11.98	11.48	11.867	-5.935
$[NH_2(CH_3)_2][Eu(\mathbf{L2})_2]\cdot 1H_2O\cdot 1HAc$ (**18**)	1.32	0 (1.50)	---	---
$[NH_2(CH_3)_2][Gd(\mathbf{L2})_2]\cdot 1H_2O\cdot 1HAc$ (**19**)	7.82	7.87	7.85	-0.041
$[NH_2(CH_3)_2][Tb(\mathbf{L2})_2]\cdot 1H_2O\cdot 1HAc$ (**20**)	12.49	11.82	12.63	-2.90
$[NH_2(CH_3)_2][Dy(\mathbf{L2})_2]\cdot 1H_2O\cdot 1HAc$ (**21**)	14.95	14.05	14.83	-4.32
$[NH_2(CH_3)_2][Ho(\mathbf{L2})_2]\cdot 1H_2O\cdot 1HAc$ (**22**)	12.86	14.04	13.05	-5.02

The value reported in brackets is obtained by including first-order and second-order contributions as extracted from reference [32].

With lowering the temperature, the χT values of **15** ($[(CH_3)_2NH_2][Dy(H_2O)_2(\mathbf{L8})_2]$), **17** ($[(CH_3)_2NH_2][Er(H_2O)_2(\mathbf{L8})_2]$) and **20**-**22** ($[NH_2(CH_3)_2][Ln(\mathbf{L2})_2]\cdot 1H_2O\cdot 1HAc$, Ln = Tb, Dy and Ho, respectively) decrease

gradually from 300 to 50 K and then drop sharply to a minimum value of 4.59 emu·K·mol^{-1}, 5.9 emu·K·mol^{-1}, 4.67 emu·K·mol^{-1}, 9.31 emu·K·mol^{-1} and 5.31 emu·K·mol^{-1} at 2.0 K, respectively. For compounds **15** ([$(CH_3)_2NH_2$][Dy(H_2O)$_2$(**L8**)$_2$]) and **17** ([$(CH_3)_2NH_2$][Er(H_2O)$_2$(**L8**)$_2$]), the decrease of χT values may be attributed to the progressively thermal depopulation of the highest ground-state Ln^{3+} sublevels that arise from the splitting of the ground term by the ligand field, together with the possible existence of intermolecular dipolar interactions.[33,34] For complexes **20**-**22** ([$NH_2(CH_3)_2$][Ln(**L2**)$_2$]·1H_2O·1HAc, Ln = Tb, Dy and Ho, respectively), the decrease of χT values may be attributed to a combination of weak antiferromagnetic interactions between the metal centres through the carboxylate bridges and to the progressively thermal depopulation of the highest crystal-field levels.[35] The χT value of **13** ([$(CH_3)_2NH_2$][Gd(H_2O)$_2$(**L8**)$_2$]) remains essentially constant while cooling down the sample until 25 K before increasing abruptly to 8.93 emu·K·mol^{-1} at 2 K. This small increase of χT can be related to very weak ferromagnetic dipolar interactions or with the reorientation of the crystals in the presence of magnetic field.[32] Instead, compound **19** (([$NH_2(CH_3)_2$][Gd(**L2**)$_2$]·1H_2O·1HAc) maintains its χT product approximately constant until 6 K. Further cooling shows an abrupt decrease of the signal up to 4.31 emu·K·mol^{-1} at 2.0 K, which indicates the presence of weak antiferromagnetic interaction between Gd^{3+} ions.[36] With respect to compounds **14** ([$(CH_3)_2NH_2$][Tb(H_2O)$_2$(**L8**)$_2$]) and **16** ([$(CH_3)_2NH_2$][Ho(H_2O)$_2$(**L8**)$_2$]), χT values increase gradually on decreasing the temperature to reach the highest value of 16.0 emu·K·mol^{-1} at 14.39 K and 15.92 emu·K·mol^{-1} at 21.68 K, respectively. At lower temperatures, χT values decrease abruptly to 7.74 and 14.25 emu·K·mol^{-1} at 2 K, respectively. The increase of χT values suggests ferromagnetic dipolar interactions whereas the decrease of χT at lower temperatures may be due to antiferromagnetic intermolecular interactions and/or the thermal depopulation of the Ln(III) highest ground-state sublevels.[37] In this context, the main possible interaction paths are those provided by H-bonds: the shortest H-bond pathway between neighbouring Ln complexes involves the coordinated water molecule O1W and the carboxylate oxygen atom O3 with a Ln···Ln distance of 6.124 and 6.113 Å for the Tb and Ho derivatives, respectively.

Observed χT values for europium derivatives **12** ([$(CH_3)_2NH_2$][Eu(H_2O)$_2$(**L8**)$_2$]) and **18** ([$NH_2(CH_3)_2$][Eu(**L2**)$_2$]·1H_2O·1HAc) are 1.35 and 1.32 emu·K·mol^{-1} at room temperature, respectively. The ground state of europium(III) is non-magnetic, thus, this indicates that magnetic excited states are populated at room

temperature because of the small difference between the ground state and excited multiplets. In general, lanthanide ions present a ground state multiplet level well separated from the excited ones because of the large spin-orbit coupling energies, except for Eu^{III} and Sm^{III}.[38] The inclusion of both the first-order contribution of the excited states and the second-order effects due to the coupling of the ground J state with the excited states, gives an estimation of the room temperature of χT of 1.5 emu·K·mol^{-1}[32], which is similar to those observed for compounds **12** and **18**. The temperature dependence of the magnetic susceptibility on cooling down both samples (Figure 7.14) shows a decrease due to the thermal depopulation of the magnetic excited states until reaching an approximate value of 0 emu·K·mol^{-1} at 2 K, which is characteristic of the diamagnetic ground state $^7F_0$ of europium(III) ion. This behaviour is in agreement with the χT thermal variation observed for other Eu^{III} complexes.[39]

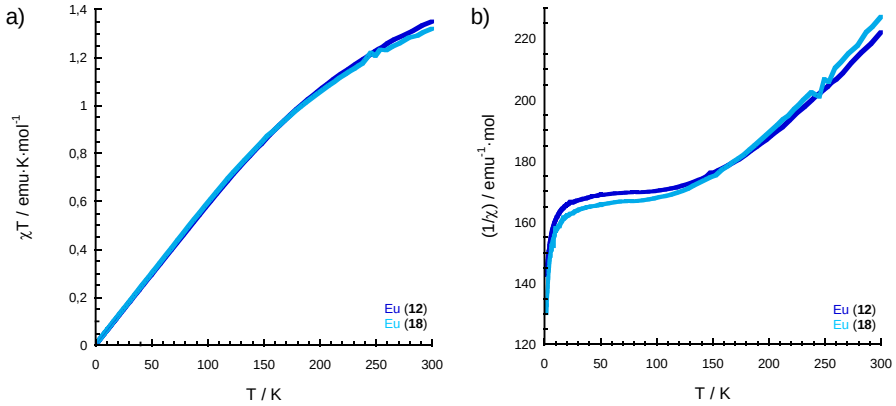

Figure 7.14. a) Temperature dependence of the χT values for the europium derivatives (**12** and **18**) at 1000 Oe dc magnetic field. b) Plot of temperature dependence of reciprocal χ for compounds **12** and **18** showing the deviation from the Curie-Weiss law.

$(1/\chi)$ *vs* T data has been fitted to the Curie-Weiss law (Equation 7.2) for complexes **13**-**17** and **19**-**22** (Figure 7.15).

$$\chi = C/(T - \theta) \quad \text{(Eq. 7.2)}$$

The values obtained are shown in Table 7.11. Similar to the χT values at room temperature, the Curie constant values are coincident with the expected values for the corresponding Ln^{3+} ions. Small positive values of the Weiss constant suggest the presence of weak dipolar ferromagnetic interactions (**13**, **14** and **16**) whereas small negative values indicate the existence of weak dipolar

antiferromagnetic interactions (**15**, **17** and **19**-**22**),[2,3] which are consistent with the thermal variation of the χT product described previously for each compound.

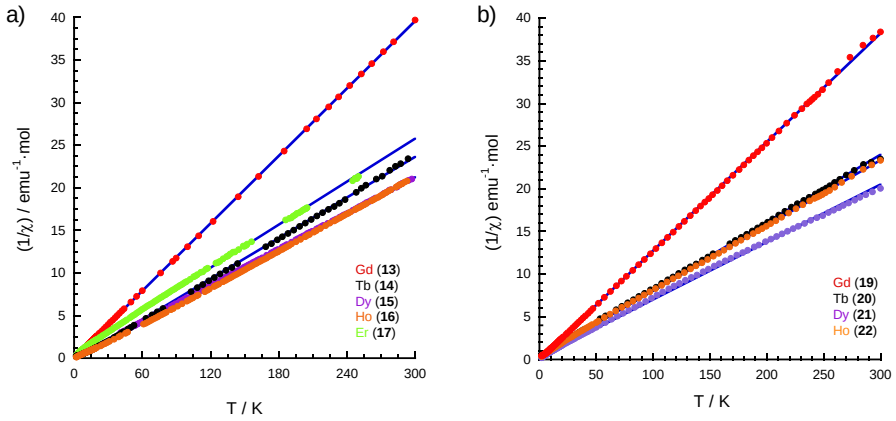

Figure 7.15. a) Plots of temperature dependence of reciprocal χ for compounds **13**-**17**. Solid blue lines represent the best fit to the data. b) Plots of temperature dependence of reciprocal χ for compounds **19**-**22**. Solid blue lines represent the best fit to the data.

On the other hand, europium derivatives do not follow the Curie-Weiss law, which has been derived considering only the population of the ground state multiplet.[40] Thus, deviations from the linear relationship between $(1/\chi)$ and T are observed (Figure 7.14.b).

The AC (alternating current) susceptibility was measured under a zero direct current field, 1000 and 2000 Oe with different frequencies (1, 10, 110, 332 and 997 Hz) to study the low-temperature magnetic relaxation behaviour of the anisotropic magnetic moments (in presence of an oscillating ac field of 3.95 Oe). The two prerequisites for observing slow relaxation of magnetisation are the following: 1) The electronic ground state must be bistable, which arises from the spin-orbit coupling in the case of lanthanide complexes. 2) Magnetic anisotropy must be present, being inherent of lanthanide ions.[41a] Tb^{III}, Dy^{III} and Ho^{III} exhibit oblate $4f$ charge distributions, whereas the distribution of Er^{III} is prolate and that for Gd^{III} is spherical.[40] Europium and gadolinium derivatives were not included in these experiments due to the presence of low-lying excited states and isotropic electronic distribution, respectively.[41b] Under a zero direct current field, none of the compounds show any out-of-phase AC (χ'') signal, mainly due to the fast quantum tunnelling of the magnetisation and to the small energy barrier which could not prevent the inversion of the spin.[2b,41] Both in-phase (χ') and out-of-phase (χ'') AC signals did not show any frequency dependence for

complexes **14-16** ([$(CH_3)_2NH_2$][Ln$(H_2O)_2$(**L8**)$_2$], Ln = Tb, Dy and Ho, respectively). For compound **20** ([$NH_2(CH_3)_2$][Tb(**L2**)$_2$]·1H_2O·1HAc), a maximum in the in-phase (χ') signal is observed applying a magnetic field (500-4000 Oe). However, no noticeable maximum or shoulder in the out-of-phase susceptibility was observed above 2 K (Figure 7.16), even when using a magnetic field of 4000 Oe. Compound **22** ([$NH_2(CH_3)_2$][Ho(**L2**)$_2$]·1H_2O·1HAc) does not show neither any out-of phase signal even under an applied dc field of 3000 Oe (Figure 7.17).

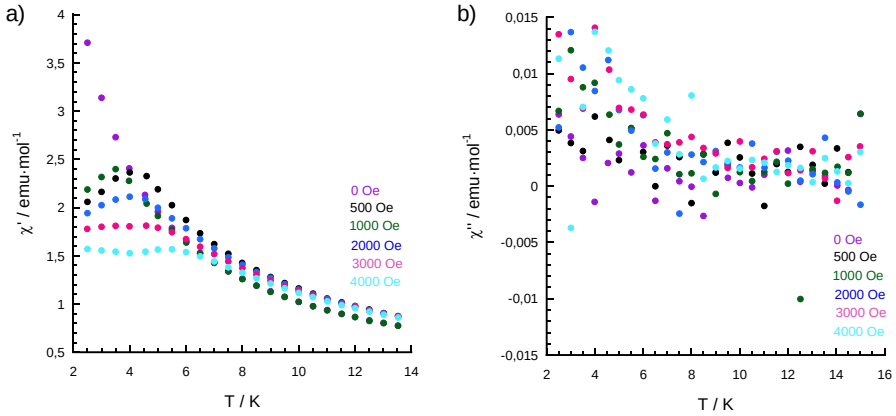

Figure 7.16. Temperature dependence of a) in-phase AC susceptibility and b) out-of-phase AC susceptibility under different DC fields and a frequency of 110 Hz for **20** ([$NH_2(CH_3)_2$][Tb(**L2**)$_2$]·1H_2O·1HAc).

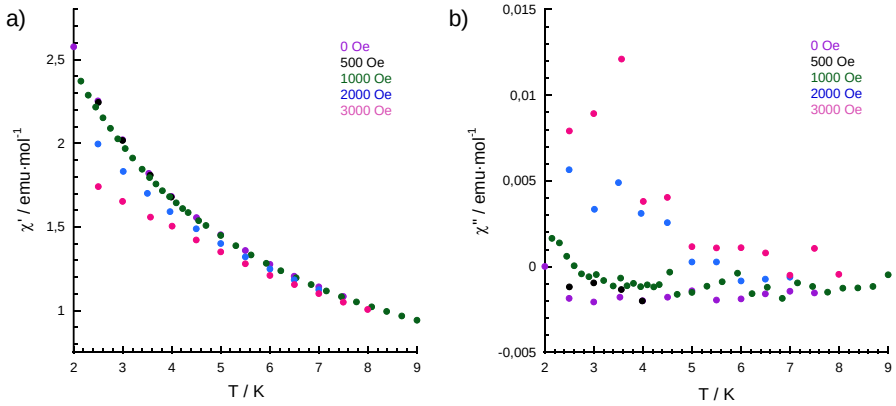

Figure 7.17. Temperature dependence of a) in-phase AC susceptibility and b) out-of-phase AC susceptibility under different DC fields and a frequency of 110 Hz for **22** ([$NH_2(CH_3)_2$][Ho(**L2**)$_2$]·1H_2O·1HAc).

For compound **17** ([$(CH_3)_2NH_2$][Er(H_2O)$_2$(**L8**)$_2$]), χ' and χ'' signals show strong frequency dependence under the application of a DC field of 1000 and 2000 Oe (Figure 7.18), suggesting a slow relaxation of the magnetisation.[2b,41] In compound **21** ([$NH_2(CH_3)_2$][Dy(**L2**)$_2$]·1H_2O·1HAc, Figure 7.19), a maximum in the χ' signal is observed when applying a magnetic field and a shoulder can be appreciated in χ'' for a field of 3000-4000 Oe at 3-4 K (for a frequency of 110 Hz). A magnetic field of 3000 Oe was selected as the optimised one (it supresses the fast quantum tunnelling of the magnetisation) and frequency-dependent out-of-phase signals were observed below 3 K, indicating the presence of slow magnetic relaxation involving an energy barrier for the reversal of the magnetisation (Figure 7.20).

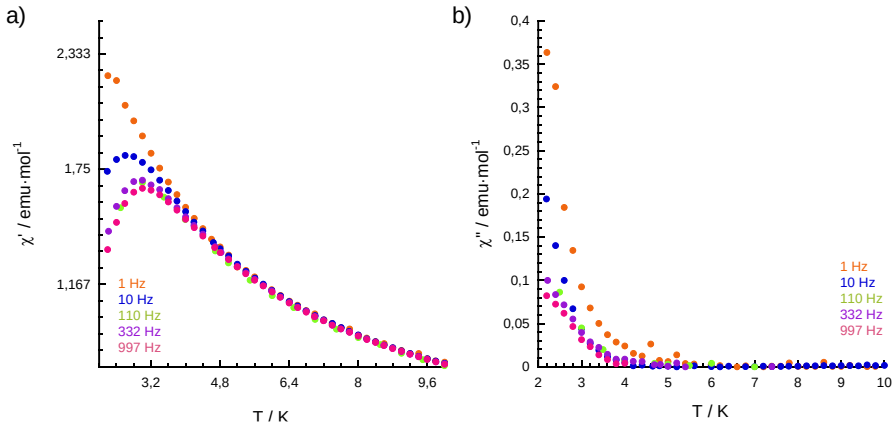

Figure 7.18. Temperature dependence of a) in-phase AC susceptibility and b) out-of-phase AC susceptibility under a 2000 Oe DC field for **17** ([$(CH_3)_2NH_2$][Er(H_2O)$_2$(**L8**)$_2$]).

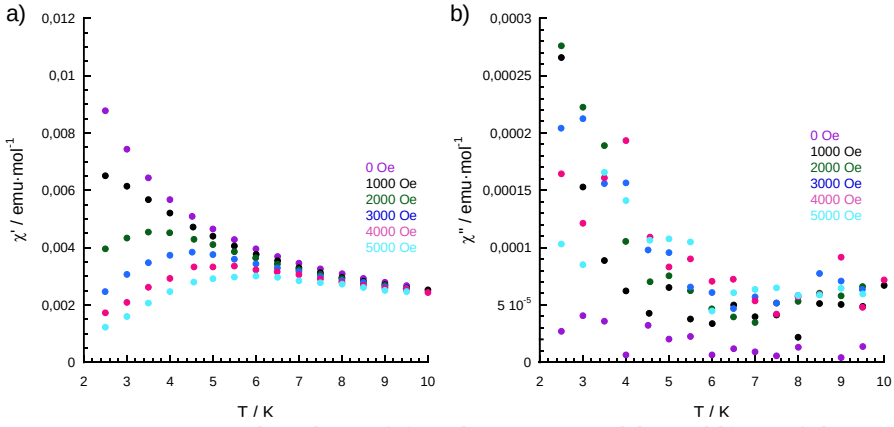

Figure 7.19. Temperature dependence of a) in-phase AC susceptibility and b) out-of-phase AC susceptibility under different DC fields and a frequency of 110 Hz for **21** ([$NH_2(CH_3)_2$][Dy(**L2**)$_2$]·1H_2O·1HAc).

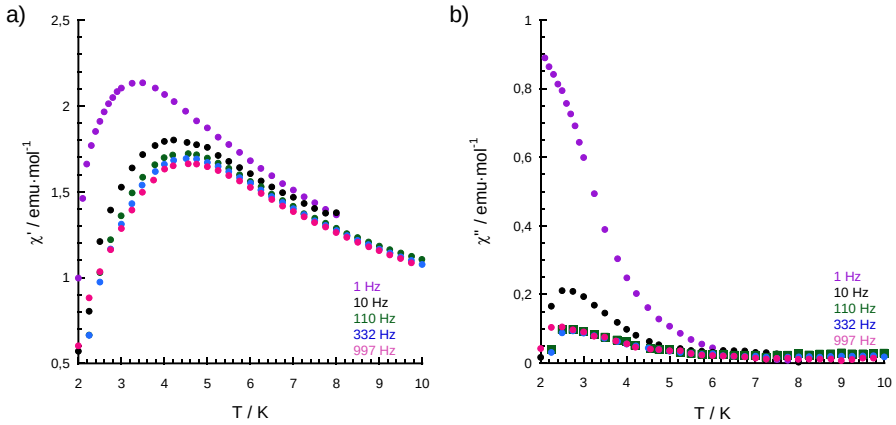

Figure 7.20. Temperature dependence of a) in-phase AC susceptibility and b) out-of-phase AC susceptibility at the indicated frequencies for **21** ($[NH_2(CH_3)_2][Dy(\mathbf{L2})_2]\cdot 1H_2O\cdot 1HAc$, in a 3000 Oe dc field).

These observations can be explained using the simple oblate-prolate electrostatic model developed by Long.[41c] For example, the 4*f* electron density of Dy(III) in its ground state has an oblate shape (it extends into the *xy* plane). Therefore, the anisotropy is enhanced when using ligands that provide a strongly axial field to diminish electrostatic repulsions between donor atoms of the ligands and the oblate *f*-electron charge cloud. In contrast, the equatorial coordination environment generates effective Er(III)-SMM due to the prolate paramagnetic centre. Within the oblate group, Dy-SMM are the most common because dysprosium(III) is a Kramers' ion (the ground state will always be bistable regardless of the ligand field symmetry), whereas Tb(III) and Ho(III) are non-Kramers' ions (the ground state is only bistable when the ligand field has axial symmetry).[41a] There are two shortest Dy–O distances (greater electron density) that result in axial-like ligand field for the second family of compounds (**18**-**22**), whereas there are four shortest Er–O distances located closer to the lanthanide ion and leading to an equatorial-like ligand field for the first family of ligands (**12**-**17**).

Due to the limited number of points and to the lack of clear maxima in the χ'' *vs* T graphs, a method employed by Bartolomé et al.[42] was applied in order to describe the kinetics of spin relaxation, assuming that there is only one Debye-type relaxation process with a characteristic relaxation time (τ_0) and an effective energy barrier (E_a/K_B) at a given frequency (ω) to reverse the magnetisation. Based on the following relationship:

$$\ln(\chi''/\chi') = \ln(\omega \cdot \tau_0) + E_a/K_B \cdot T \text{ (Eq. 7.3)},$$

both parameters have been roughly evaluated from $\ln(\chi''/\chi')$ versus $1/T$ plots (Figure 7.21). These yield E_a/K_B = 15.10 K and $\tau_0 \approx 9.65 \cdot 10^{-8}$ s at a frequency of 997 Hz for complex **17**, whereas for compound **21**, $E_a/K_B \approx 8.36$ K and $\tau_0 \approx 4.49 \cdot 10^{-6}$ s at 997 Hz were obtained. These values are in the expected range for compounds presenting slow magnetic relaxation of the magnetisation (expected value of $\tau_0 = 10^{-6}$-10^{-11} s, Table 4.1, Chapter 4).[3]

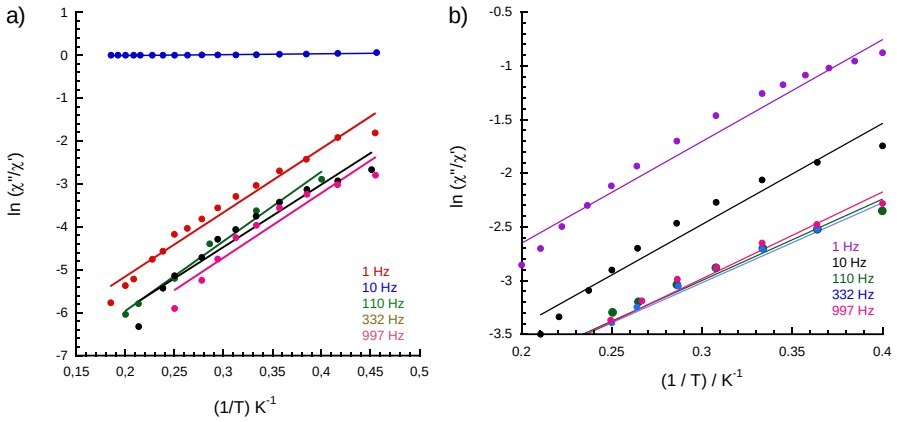

Figure 7.21. a) Plot of $\ln(\chi''/\chi')$ versus $1/T$ for **17** ([$(CH_3)_2NH_2$][$Er(H_2O)_2$(**L8**)$_2$]). b) Plot of $\ln(\chi''/\chi')$ versus $1/T$ for **21** ([$NH_2(CH_3)_2$][Dy(**L2**)$_2$]·$1H_2O$·1HAc). The solid lines represent the fitting results in the range of 2.2-5.4 K and 2.5-5.0 K, respectively.

7.4.3. Photoluminescence

As pointed out previously, the luminescent detection of nitroaromatic compounds (NACs) and heavy metal ions is a pressing issue as a consequence of their high toxicity and pollution load in aqueous solution that has led to a serious threat to ecosystems and human health. On the other hand, lanthanide CPs are potential luminescent materials since they usually exhibit narrow, sharp and well-separated emission bands. Among all the lanthanide family, the most studied in this context are the terbium, dysprosium and europium derivatives. This can be explained taking into consideration the energy gap between the lowest excited (emissive) state of the metal ion and the highest sublevel of its ground multiplet. The smaller this gap, the more probable is that deactivation processes take place, for instance through vibrations of bound ligands. Figure 7.22 shows a partial energy diagram for the lanthanide aqua ions and it can be seen that Eu(III), Gd(III), Tb(III) and Dy(III) have the highest energy gaps, therefore, representing the best candidates. In addition, the other ions present

all very low quantum yield in aqueous solution, reducing their interest in this field. Gd(III) emits in the UV, which is not very convenient for luminescent probe applications due to luminescence interference issues with the organic part of the complex.[43] Consequently, the photoluminescence properties of Tb, Dy and Eu derivatives of both families in water and in the solid-state were investigated at room temperature. The excitation spectra of Tb ($[(CH_3)_2NH_2][Tb(H_2O)_2(\mathbf{L8})_2]$ (**14**) and ($[NH_2(CH_3)_2][Tb(\mathbf{L2})_2]\cdot 1H_2O\cdot 1HAc$ (**20**)) and Dy complexes ($[(CH_3)_2NH_2][Dy(H_2O)_2(\mathbf{L8})_2]$ (**15**) and ($[NH_2(CH_3)_2][Dy(\mathbf{L2})_2]\cdot 1H_2O\cdot 1HAc$ (**21**)) were obtained by monitoring the 550 nm line of the $^5D_4 \rightarrow {}^7F_5$ emission and the 575 nm line of the $^4F_{9/2} \rightarrow {}^6H_{13/2}$ emission, respectively. Next, both derivatives were found to present an obvious broad band in the purple spectral region associated to ligand-centred emission, being the most intensive emission (section 7.6.2). This fact suggests a partial and inefficient ligand-to-metal energy transfer (antenna effect) process from the ligand to the Ln^{III} ions. For the europium derivatives no sign of the ligand emission indicates almost complete energy transfer from the ligand π excited states to the Eu f excited states. Therefore, the following sections are devoted to study the luminescent properties of compounds **12** ($[(CH_3)_2NH_2][Eu(H_2O)_2(\mathbf{L8})_2]$) and **18** ($[NH_2(CH_3)_2][Eu(\mathbf{L2})_2]\cdot 1H_2O\cdot 1HAc$), which exhibit a metal-centred luminescence, and their capability to detect organic molecules and different metal ions within the context of improving current sensors for detection of NACs and Fe^{3+} ions.

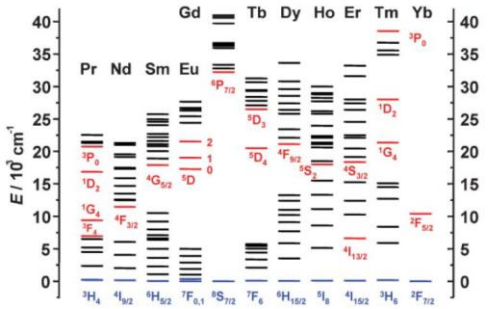

Figure 7.22. Partial energy diagram for the lanthanide ions, extracted from reference [43]. The fundamental level is illustrated in blue, while the main luminescent levels are indicated in red.

A. Photoluminescent properties

The electronic absorption spectra of ligands **H_2L8**, **H_2L2** and their europium complexes have been measured in the solid state at room temperature (Figure 7.23). The UV absorption spectra of both europium complexes show an

intense absorption band at about 250-255 nm and a second absorption band at about 331-334 nm with the same intensity. These features are practically identical to those observed for the free ligands and are attributed to $\pi \rightarrow \pi^*$ and $n \rightarrow \pi^*$ electronic transitions of the pyridine and benzoate rings in the ligands. The similarity observed between these patterns indicates that absorption takes place on the ligand rather than directly in the metal centre.

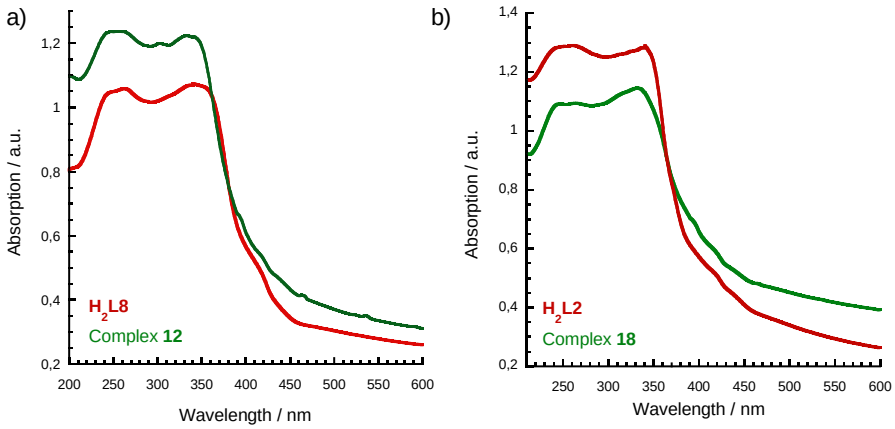

Figure 7.23. a) UV absorption spectra of **H₂L8** (red trace) and [$(CH_3)_2NH_2$][Eu(H_2O)$_2$(**L8**)$_2$] (**12**, green trace). b) UV absorption spectra of **H₂L2** (red trace) and [$NH_2(CH_3)_2$][Eu(**L2**)$_2$]·1H_2O·1HAc (**18**, green trace).

The photoluminescence properties of suspensions of compounds **12** ([$(CH_3)_2NH_2$][Eu(H_2O)$_2$(**L8**)$_2$]) and **18** ([$NH_2(CH_3)_2$][Eu(**L2**)$_2$]·1H_2O·1HAc) and ligands **H₂L8** and **H₂L2** in water were investigated at room temperature (Figures 7.24 and 7.25). The free **H₂L8** ligand exhibits an intense emission at 432 nm, which is attributed to $\pi^* \rightarrow \pi$ and $\pi^* \rightarrow n$ electronic transitions when excited at 350 nm. Under excitation at 344 nm, **12** exhibits a typical red emission of the Eu^{3+} ion, with fluorescence emission peaks attributed to transitions between $^5D_0 \rightarrow {}^7F_j$ (j = 0, 1, 2, 3, 4), at: λ = 578 nm ($^5D_0 \rightarrow {}^7F_0$), λ = 593 nm ($^5D_0 \rightarrow {}^7F_1$), λ = 614 nm ($^5D_0 \rightarrow {}^7F_2$), λ = 653 nm ($^5D_0 \rightarrow {}^7F_3$), λ = 705 nm ($^5D_0 \rightarrow {}^7F_4$). The free **H₂L2** ligand shows a broad intense emission between 410 and 435 nm, assigned to $\pi^* \rightarrow \pi$ and $\pi^* \rightarrow n$ electronic transitions when excited at 356 nm. Upon UV excitation at 340 nm, complex **18** exhibits a strong and characteristic red emission of the Eu^{3+} ion, with five typical narrow peaks at 580, 592, 615, 653 and 690-696 nm, which corresponds to the $^5D_0 \rightarrow {}^7F_j$ (j = 0, 1, 2, 3, 4) transitions of the Eu^{III} centres.[44]

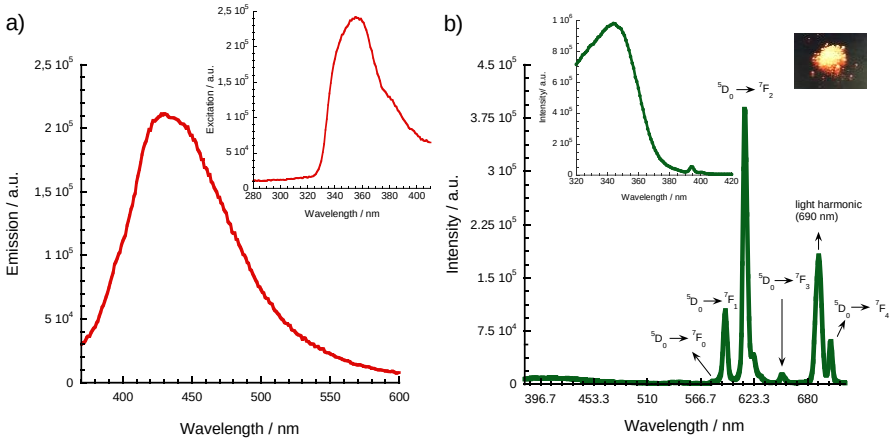

Figure 7.24. a) Emission spectrum of **H_2L8** under excitation at 350 nm. b) Emission spectrum of **12** under excitation at 344 nm. At 690 nm appears a signal due to light harmonic. The insets show the excitation spectra of **H_2L8** and **12**, with a λ_{em}= 434 and 614 nm, respectively. A photograph of red emissive **12** excited at 365 nm is also shown.

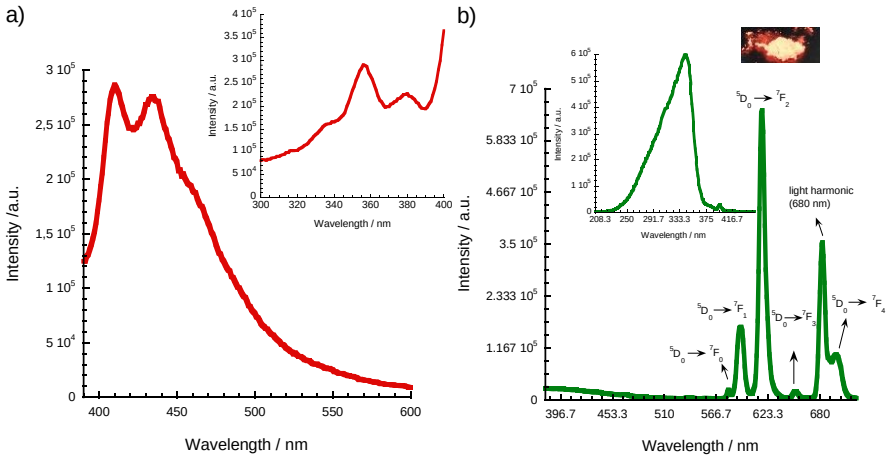

Figure 7.25. a) Emission spectrum of **H_2L2** under excitation at 356 nm. b) Emission spectrum of **18** under excitation at 340 nm. At 680 nm appears a signal due to light harmonic. The insets show the excitation spectra of **H_2L2** and **18**, with a λ_{em}= 408 and 614 nm, respectively. A photograph of red emissive **18** excited at 365 nm is also shown.

In both complexes, the emission spectrum is dominated by the most intense band at 615 nm ascribed to $^5D_0 \longrightarrow {}^7F_2$ transition, which is responsible for the strong red emission. In fact, the intensity ratio of the $^5D_0 \rightarrow {}^7F_2$ transition and the $^5D_0 \rightarrow {}^7F_1$ transition gives an indication about the symmetry of the first coordination environment of the Eu(III) ions and has a value of 3.6 for **12** and

3.8 for **18**. These values together with the very low intensity of the $^5D_0 \rightarrow {}^7F_0$ transition band, suggest the non-existence of an inversion centre.[44] This is in agreement with the assignation of $I2/a$ and $Pna2_1$ space groups for compounds **12** and **18**, respectively. The values of this ratio are very similar to those obtained for previous europium(III) complexes. For instance, $[EuL(HL)H_2O]\cdot 6H_2O$ (being H_2L bis(5-(pyridine-2-yl)-1,2,4-triazol-3-yl)methane ligand) presents a ratio value of 3.4 and crystallises in the monoclinic space group $C2/c$.[45]

It is worth noting that there is a negligible contribution below 500 nm coming from the ligand in the emission spectrum of complexes **12** and **18**. Therefore, both ligands have proven to be suitable for absorbing light efficiently and for transferring this energy to the europium cations with high efficiency. In fact, the excitation spectra of both complexes (inset of Figures 7.24.b and 7.25.b) monitored within the Eu^{3+} more intense transition ($^5D_0 \rightarrow {}^7F_2$) are dominated by a broad band from 310 to 390 nm and from 220 to 375 nm, respectively, assigned to intraligand transitions. There are also two weak signals (at 395 and 465 nm) attributed to transitions between the $^7F_0$ and excited states of Eu^{3+}. The very low relative intensity of the latter lines compared with that of the ligand related broad band suggests a more efficient ligand-sensitisation process than direct intra-$4f^6$ excitation.

B. Luminescence decay

In order to obtain the lifetime, the luminescence decay curves of complexes **12** and **18** in the solid-state were measured at room temperature by monitoring the strongest emission of $^5D_0 \rightarrow {}^7F_2$ (Figure 7.26). In both cases, the decrease in the number of excited fluorophores with time following optical excitation with a short light pulse was successfully fitted using a second-order exponential function (Eq. 7.4), suggesting the existence of different interaction possibilities for luminescence decay:

$$I = A_1 \cdot \exp(-t/\tau_1) + A_2 \cdot \exp(-t/\tau_2) \quad \text{(Eq. 7.4)}$$

where τ_i is the lifetime and A_i is the pre-exponential factor that allows quantitative assignment of the relative contribution of each component with a characteristic lifetime. The fitting results show τ_1 = 227 μs, τ_2 = 390 μs with A_1 = 1625 (14.64 %) and A_2 = 5529 (85.36 %), respectively, and a χ^2 value of 1.006 for compound **12**. The average lifetime τ_{av} is calculated as 366 μs based on the following formula:[46]

$$\tau_{av} = \frac{A_1 \cdot \tau_1^2 + A_2 \cdot \tau_2^2}{A_1 \cdot \tau_1 + A_2 \cdot \tau_2} \text{ (Eq. 7.5)}$$

Compound **18** presents the best fit for τ_1 = 427 μs, τ_2 = 1330 μs (average lifetime of 1183 μs calculated according to equation 7.5) with A_1 = 1577 (16.29 %), A_2 = 2601 (83.71 %) and χ^2 = 1.204. Luminescence lifetimes on the micro- to millisecond timescale are typical for *f-f* transitions that involve very long lived excited states and the values obtained for compounds **12** and **18** are within this range (Table 7.12).[47-52] However, there is a big difference between registered lifetime values for both complexes, showing compound **18** higher lifetime values than **12**. This can be explained taking into account that only complex **12** presents solvent molecules (two H_2O molecules per europium centre) in the first coordination sphere, which leads to quenching of the europium luminescence. It is well-known that the luminescence of lanthanide-based complexes is markedly influenced by the denticity of the ligand, being polydentate ligands useful for increasing the stability of the complexes and allowing the metal centre to be protected from solvent molecules. Non-radiative decay of the excited state *via* vibronic coupling of the europium energy level with the vibrational modes of O–H bonds in the surroundings of the europium ion takes place (with the subsequent reduction of the lifetime of the excited state).[53a]

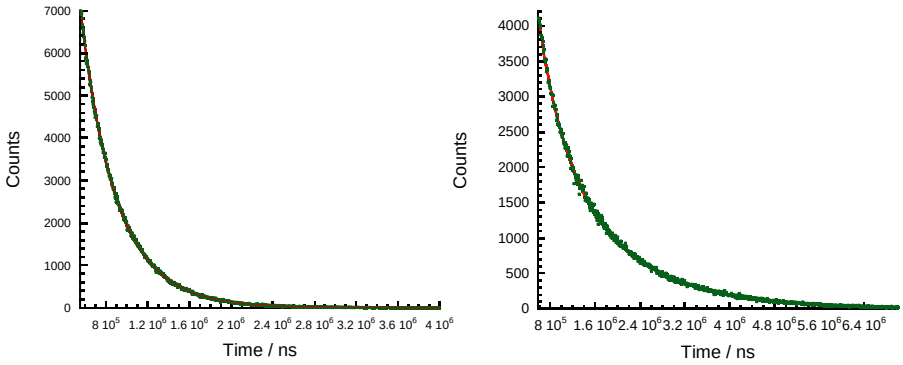

Figure 7.26. Left: Lifetime spectrum of **12** ([$(CH_3)_2NH_2$][Eu$(H_2O)_2$(**L8**)$_2$]) at 614 nm and the lifetime fitted decay curve (red). Right: Lifetime spectrum of **18** ([$NH_2(CH_3)_2$][Eu(**L2**)$_2$]·1H_2O·1HAc) at 614 nm and the lifetime fitted decay curve (red).

On the other hand, the luminescence quantum yield (ϕ) was measured by the absolute method using an integrating sphere and has a value of 0.229 and 0.292 with an absorption of 48% and 42% for complexes **12** and **18**, respectively. These values are typical for europium(III) CPs (Table 7.12), presenting complex **18** improved quantum yield due to the lack of coordinating water molecules which contribute to non-radiative luminescence quenching. This behaviour has

been well documented for many of the hydrated europium β-diketonate complexes.[53b] Nonetheless, a recent compound with formula $[EuKL_4(H_2O)_2]\cdot H_2O$ (being HL = 7-chloro-1-cyclopropyl-6-fluoro-4-oxo-1,4-dihydroquinoline-3-carboxylic acid), presents an ultrahigh quantum yield value of 92%, which is much higher than most lanthanide complexes.[54] Europium complexes present higher lifetimes in comparison to those values registered for the zinc complexes in the previous chapter. This is due to the fact that in zinc complexes the mechanism associated with luminescence is fluorescence (τ = 1-100 ns), whereas for Eu(III) compounds phosphorescence is the way to return to the ground state, resulting in long excited lifetimes (τ > 100 μs). In addition, despite the fact that ligands **L2** exhibit a severe deviation from planarity in **18** (dihedral angle of 27.14° and 100.06° between aromatic rings) *vs* ligands **L8** in **12** (dihedral angle of 12.23° between aromatic rings), which favours radiationless deactivation pathways, complex **18** displays enhanced quantum yield and lifetime values, in agreement with the metal-based luminescence nature of these compounds.

Table 7.12. Values of quantum yield (ϕ) and lifetime (τ_0) for selected europium(III) complexes.

Compound	ϕ / %	τ_0 /ms
Eu-L1 [48]	32	1.25
[Eu(tta)4(DEASPI)] [49]	28	---
Eu-L2 [47]	12	1.65
Eu-L3 [47]	25	1.16
$[Eu(dpq)(DMF)_2(NO_3)_3]$ [50]	32.5	0.47
$[Eu(dppz)_2(NO_3)_3]$ [50]	38.5	0.49
$Eu(PBI)_3\cdot C_2H_5OH\cdot H_2O$ [51]	26	0.25
$Eu(PBI)_3$·bpy [51]	68	0.98
$Eu(PBI)_3$·dmbpy [51]	72	1.18
$Eu(PBI)_3$·phen [51]	57	1.03
$Eu(PBI)_3$·bath [51]	71	1.01
$Eu(MPPD)_3$ [52]	8.2	0.12
$Eu(MPPD)_3$·bpy [52]	25.2	0.25
$Eu(MPPD)_3$·phen [52]	38.8	0.46
Complex **12** (This thesis)	22.9	0.37
Complex **18** (This thesis)	29.2	1.18

L1: 2,2'-(8-(3-(N-maleimido)-1-carboxylatopropyl)-5,8,11-triaza-1,2,3(2,6)tripyridinacyclododecaphane-5,11-diyl)diacetate; tta: trans-4-[p-(N,N-diethylamino)styryl]-N-methylpyridinium tetrakis(a-thenoyltrifluoroacetonato); DEASPI: trans-4-[p-(N,Ndiethylamino)styryl]-N-methylpyridinium; L2: Pyridine-2,6-dicarboxylic acid; L3: Dipotassium salt of 4-(thien-2-yl)pyridine-2,6-dicarboxylic acid; dpq: dipyrido[3,2-d:2',3'-f]quinoxaline; dppz: dipyrido[3,2-a:2',3'-c]phenazine; dppz: dipyrido[3,2-a:2',3'-c]phenazine; HPBI: 3-phenyl-4-benzoyl-5-isoxazolone; bpy: 2,2'-bipyridine; dmbpy: 4,4'-dimethoxy-2,2'-bipyridine; phen: 1,10-phenanthroline; bath: 4,7-diphenyl-1,10-phenanthroline; MPPD: 1-(4-methoxyphenyl)-3-phenylpropane-1,3-dione.

C. Luminescent sensing of organic solvent molecules

The luminescence sensing response of both europium derivatives for organic solvent molecules was studied at room temperature. The as-synthesised crystals (1 mg) were ground and suspended in different solvents (1 ml), as shown in Figures 7.27-7.28. The strongest peak that corresponds to the $^5D_0 \rightarrow {}^7F_2$ transition was taken for comparison. The luminescence signal of **12** ([$(CH_3)_2NH_2$][Eu(H_2O)$_2$(**L8**)$_2$]) is enhanced by solvents like MeOH, EtOH, CH_3CN, DMF and DMSO, presenting in the last case a huge increase of 72 % (I(DMSO)/I(H_2O) ≈ 1.72). On the other hand, most solvent molecules present a slight degree of luminescent quenching effect. However, nitrobenzene could almost quench completely the luminescence of **12**, standing out from the rest. For **18** ([$NH_2(CH_3)_2$][Eu(**L2**)$_2$]·1H_2O·1HAc), enhancement of the luminescence signal is observed when a solvent different to water was used, except for $PhNO_2$ solvent that exhibits an almost complete luminescent quenching effect (Figure 7.28). Also, a remarkable feature is that when **18** is dispersed in DMSO, a striking luminescent increase is reached (I(DMSO)/I(H_2O) ≈ 3.6). All the above suggests that **12** and **18** could be used as specific luminescent sensors for $PhNO_2$ solvent molecules and, in both cases, the strongest emission is registered in DMSO.

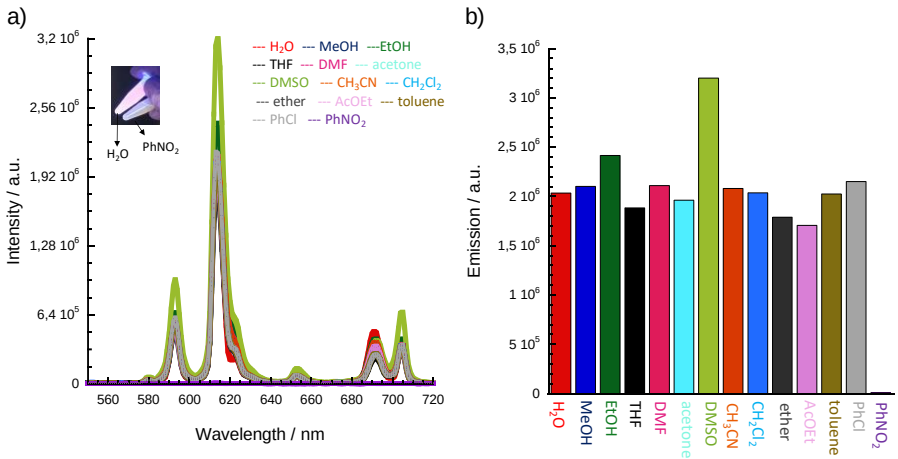

Figure 7.27. a) Emission spectra of **12** ([$(CH_3)_2NH_2$][Eu(H_2O)$_2$(**L8**)$_2$]) dispersed in different solvents when excited at 344 nm. The inset shows an image of a suspension of **12** in water and in $PhNO_2$ under UV light at 365 nm. b) Summary column plot of corresponding emissive intensities considering the peak height at 614 nm.

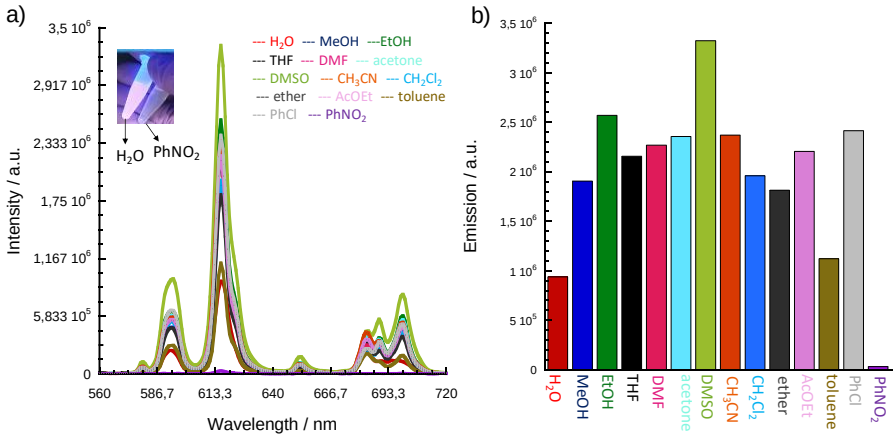

Figure 7.28. a) Emission spectra of **18** ([$NH_2(CH_3)_2$][Eu(**L2**)$_2$]·1H_2O·1HAc) dispersed in different solvents when excited at 340 nm. The inset shows an image of a suspension of **18** in water and in $PhNO_2$ under UV light at 365 nm. b) Summary column plot of corresponding emissive intensities considering the peak height at 614 nm.

Powder X-ray diffraction (PXRD) measurements were carried out in order to investigate this luminescence modulation (Figure 7.29). There is a perfect agreement between the original diffractograms and those corresponding to the samples soaked in DMSO and in $PhNO_2$, indicating that their crystal structures are retained after interaction with these solvent molecules.

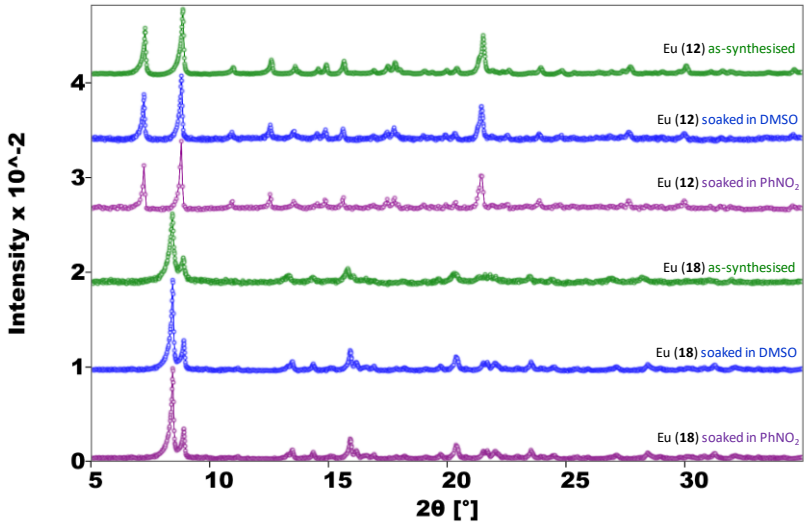

Figure 7.29. PXRD patterns at room temperature of **12** and **18** as-synthesised and after soaking in DMSO and $PhNO_2$ (shown in green, blue and purple, respectively).

An increase of emission intensity after soaking in DMSO has been previously noted in Eu^{3+} complexes and ascribed to energy transfer from organic DMSO solvent to the antenna ligand.[55] However, in this case DMSO molecules do not absorb energy at the excitation wavelengths used (340 and 344 nm, Figure 7.30), discarding this hypothesis. Thus, the possible explanation for this fact relies on the exchange of inner-sphere coordinating water molecules or hydrogen-bonded water molecules by DMSO in the surface of the particles, which would preserve their crystal integrity. In this way, non-radiative decay of the excited states through vibronic coupling with the vibrational modes of O–H bonds would be reduced, with the corresponding enhancement in the europium emission.

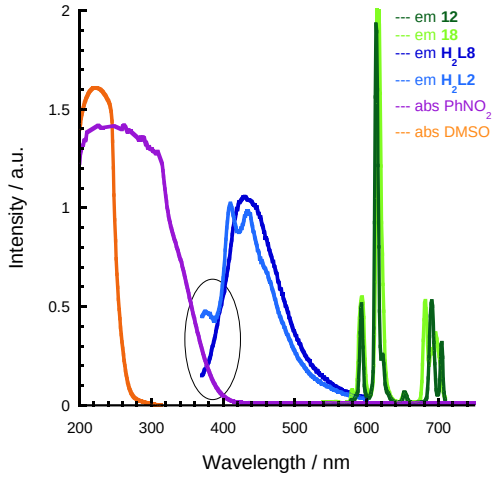

Figure 7.30. Comparison between the absorbance spectra of $PhNO_2$ and DMSO and the emission spectra of **12, 18**, **H_2L2** and **H_2L8**.

Regarding nitrobenzene quenching, the disruption of the crystal structure and the Dexter energy transfer that requires a covalent bond between the quencher and the fluorophore can be excluded since the diffraction patterns show a lack of structural changes in both frameworks. The absorption spectrum of $PhNO_2$ was compared with the emission spectra of **12** and **18** (Figure 7.30). It can be seen a lack of spectral overlap between absorption and emission patterns, discarding a resonance energy transfer from Eu^{3+} ions to $PhNO_2$. Nevertheless, there is a spectral overlap between the absorption spectrum of $PhNO_2$ and the emission of ligands **H_2L8** and **H_2L2** (Figure 7.30), indicating that a Förster energy transfer (FRET) is feasible between them. Therefore, **12** and **18** can selectively detect $PhNO_2$ mainly thanks to the fact that $PhNO_2$ solvent molecules absorb energy at the excitation wavelength used in these experiments (344 and

340 nm, respectively), competing with the corresponding ligands for energy transfer to the Eu^{3+} ions, together with the FRET process from ligands to $PhNO_2$. Energy competition between Eu complexes and nitroaromatic compounds has been already noted as possible mechanism of luminescence quenching.[56]

Furthermore, to explore the sensitivity of both europium complexes towards nitrobenzene, titration experiments were undertaken by adding increasing amounts of $PhNO_2$ in an ethanol solution to suspensions of **12** and **18** in water (1 mg in 1 ml). Both complexes have similar response behaviours toward nitrobenzene, decreasing gradually the luminescence intensity with an increase in the concentration of $PhNO_2$ (Figures 7.31 and 7.32). When the volume of nitrobenzene reached 400 µl, the quenching efficiency (Q) was 85% and 87% respectively for complexes **12** and **18**, calculated according to equation 7.6:

$$Q = \frac{I_0 - I}{I_0} \cdot 100\ (\%)\ \text{(Eq. 7.6)},$$

being I and I_0 the fluorescence intensity at 614 nm with and without quencher molecules, respectively.

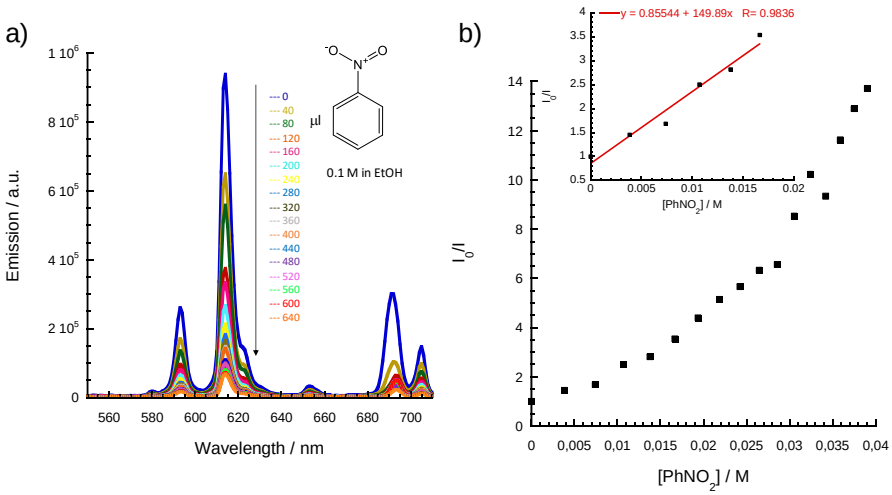

Figure 7.31. a) Comparison of the luminescence intensity of **12** ($[(CH_3)_2NH_2][Eu(H_2O)_2(\mathbf{L8})_2]$) upon addition of different amount of $PhNO_2$ (0.1 M in EtOH), with λ_{exc} = 344 nm. b) Stern-Volmer plots of the luminescence intensity of **12** upon addition of $PhNO_2$ (0.1 M in EtOH). The inset shows the linear fit at low concentrations of $PhNO_2$.

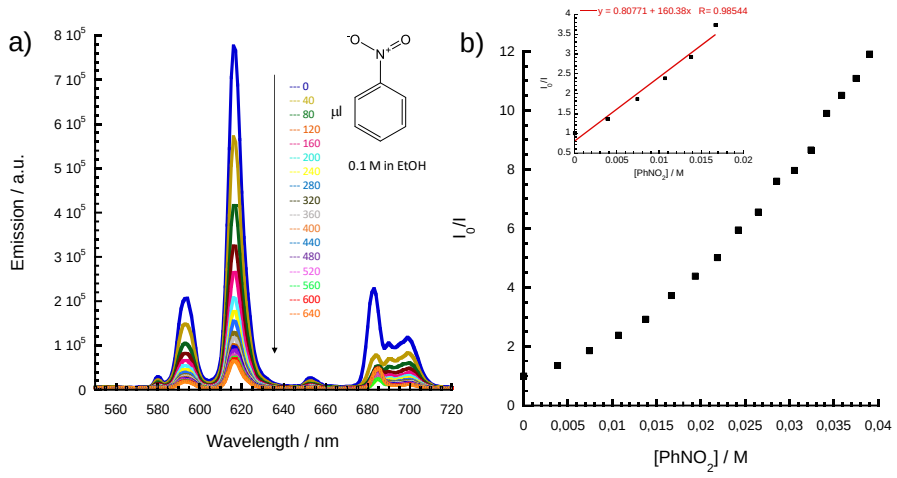

Figure 7.32. a) Comparison of the luminescence intensity of **18** ($[NH_2(CH_3)_2][Eu(\mathbf{L2})_2]\cdot 1H_2O\cdot 1HAc$) upon addition of different amount of $PhNO_2$ (0.1 M in EtOH), with λ_{exc} = 340 nm. b) Stern-Volmer plots of the luminescence intensity of **18** upon addition of $PhNO_2$ (0.1 M in EtOH). The inset shows the linear fit at low concentrations of $PhNO_2$.

The linear luminescence intensity versus $PhNO_2$ concentration plot was fitted by using the well-known Stern-Volmer equation (Figures 7.31 and 7.32): [57,58]

$$I_0/I_i = 1 + K_{SV}[PhNO_2] \text{ (Eq. 7.7)},$$

The Stern-Volmer plots display a linear relation at low concentration of quencher, while they present upward bending trend at high concentration of quencher (a quadratic dependence appears). This indicates the existence of two different relaxation mechanisms, static and dynamic quenching.[58] The Stern-Volmer quenching constant (K_{SV}) was calculated to be $1.50\cdot 10^2$ M^{-1} and $1.60\cdot 10^2$ M^{-1} for compounds **12** and **18**, respectively, indicating that both compounds show a moderate nitrobenzene sensing ability in comparison with the performance achieved for other Eu(III) luminescent sensors to detect $PhNO_2$ (Table 4.5, Chapter 4). Moreover, the detection limit (*LOD*) for detecting $PhNO_2$ was calculated based on the following equation (Eq. 7.8):

$$LOD = \frac{3\delta}{s} \text{ (Eq. 7.8)},$$

being s the slope of the plot of luminescence intensity against $PhNO_2$ concentration (Figure 7.33) and δ the standard deviation for ten repeated luminescence measurements of the blank solution. The results show detection limits of $5.37\cdot 10^{-4}$ M and $6.57\cdot 10^{-4}$ M for complexes **12** and **18**, respectively.

These values compare well with those reported for Eu(III) complexes exhibiting luminescent $PhNO_2$ sensing (Table 4.5).

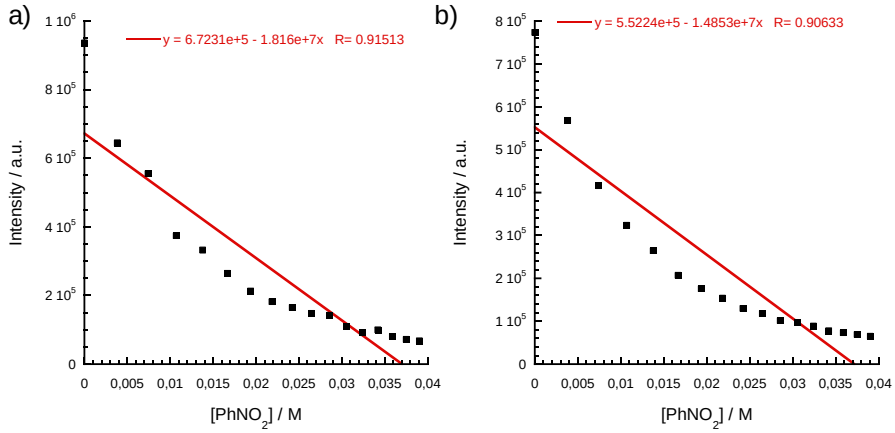

Figure 7.33. Fitting curves of the luminescence intensity (at 614 nm) at different $PhNO_2$ concentration for a) **12** ($[(CH_3)_2NH_2][Eu(H_2O)_2(\mathbf{L8})_2]$) and b) **18** ($[NH_2(CH_3)_2][Eu(\mathbf{L2})_2]\cdot 1H_2O\cdot 1HAc$).

D. Luminescent sensing of metal ions

Compounds **12** and **18** (1 mg) were dispersed in 1 ml of aqueous solutions containing 0.01 M of MCl_x or $M(NO_3)_x$ (M = Li^+, Na^+, K^+, Mg^{2+}, Ca^{2+}, Mn^{2+}, Fe^{3+}, Co^{2+}, Ni^{2+}, Cu^{2+}, Zn^{2+}, Cd^{2+}, Al^{3+}, In^{3+}, Pb^{2+}, Sm^{3+}, Tb^{3+} and Dy^{3+}) and then the luminescence spectra recorded (Figures 7.34 and 7.35). Again, in order to analyse the degree of change, the strongest peak, corresponding to the $^5D_0 \rightarrow {}^7F_2$ transition, was taken as an indicator. For compound **12** ($[(CH_3)_2NH_2][Eu(H_2O)_2(\mathbf{L8})_2]$), all metal ions exhibit varying degrees of luminescent quenching effects. Noteworthy is the fact that Fe^{3+} and Pb^{2+} ions could almost completely quench its luminescence, being Fe^{3+} more effective than Pb^{2+} ions (up to 80% and 72%, respectively). On the other hand, metals like Li^+, Na^+, Mg^{2+} and Ca^{2+} increase the luminescence signal of **18** ($[NH_2(CH_3)_2][Eu(\mathbf{L2})_2]\cdot 1H_2O\cdot 1HAc$), whereas the remaining metal ions result in varying degrees of luminescent quenching effects. Fe^{3+}, Cd^{2+} and Zn^{2+} metal ions stand out with quenching efficiencies of 82, 68 and 69%, respectively. These results are consistent with the fact that Pb^{2+} ions present higher affinity for oxygen donor ligands than for nitrogen-based ligands. That means that Pb^{2+} ions exhibit a greater competition for **L8** ligand coordination with respect to **L2** ligand, because the former contains an additional carboxylate functional group that is not present in the latter anion. This results in a more pronounced decrease in emission intensity for **12** than for **18**. Moreover, transition metals

like Co, Ni, Cu, Zn and Cd exhibit competition for ligand coordination in both cases. In particular, their quenching effect is stronger for compound **18** due to the fact that all of them present more affinity for nitrogen donor ligands and ligand **L2** has one additional picolinate group in comparison with ligand **L8**. Lanthanide(III) ions present higher affinity for oxygen donor ligands, as well as Mg^{2+} and Ca^{2+} ions. Therefore, the decrease in the emission signal is higher for compound **12** in these cases. In general, compound **18** which contains the bis(picolinate) ligand, shows a better stability in these metal sensing experiments than **12**.

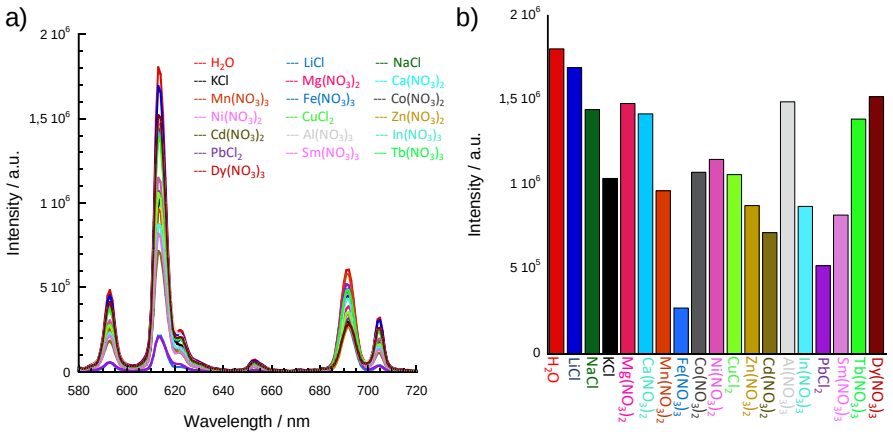

Figure 7.34. a) Emission spectra of compound **12** ([$(CH_3)_2NH_2$][Eu(H_2O)$_2$(**L8**)$_2$]), 1 mg) in metal aqueous solutions (1ml, 0.01 M) with λ_{exc} = 344 nm. b) Summary column plot of the $^5D_0 \rightarrow {}^7F_2$ emission in metal aqueous solutions.

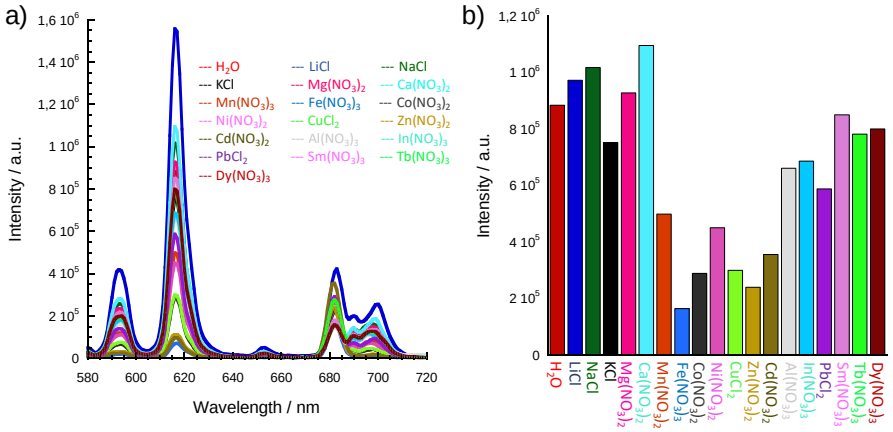

Figure 7.35. a) Emission spectra of compound **18** ([$NH_2(CH_3)_2$][Eu(**L2**)$_2$]·1H_2O·1HAc), 1 mg) in metal aqueous solutions (1ml, 0.01 M) with λ_{exc} = 340 nm. b) Summary column plot of the $^5D_0 \rightarrow {}^7F_2$ emission in metal aqueous solutions.

The most significant change for both complexes is observed when Fe^{3+} is used. In addition, for complex **12**, Pb^{2+} ions also result in a significant quenching effect. Thus, in order to check if the crystalline frameworks are preserved after interaction with these metal ions, powder X-ray diffraction measurements were conducted (Figure 7.36). PXRD patterns of both samples suspended in aqueous solutions of Fe^{3+} cations are consistent with the original frameworks, whereas the pattern of compound **12** suspended in an aqueous solution of Pb^{2+} ions is completely different. The latter situation indicates that collapse of the original network takes place and this might possibly result from the interaction between Pb^{2+} ions and the uncoordinated carboxylate groups in the channel, which could reduce energy transfer from the ligand to Eu^{3+}ions, or even from a cation exchange process. Energy-dispersive X-ray (EDX) microanalysis carried out on a scanning electron microscopy (SEM) shows that this sample contains both Pb^{2+} and Eu^{3+} ions after suspension in an aqueous solution of Pb^{2+} ions, with a Pb^{2+}/Eu^{3+} ratio of 1.3. The same analysis for the compounds soaked in aqueous solutions of Fe^{3+} ions indicates that Fe^{3+} ions are not present in the composition of the soaked materials (Table 7.13). Therefore, the collapse of the framework of **12** induces the variation of the luminescence intensity after immersion in Pb^{2+} aqueous solution but this can be ruled out for the Fe^{3+}sensing.

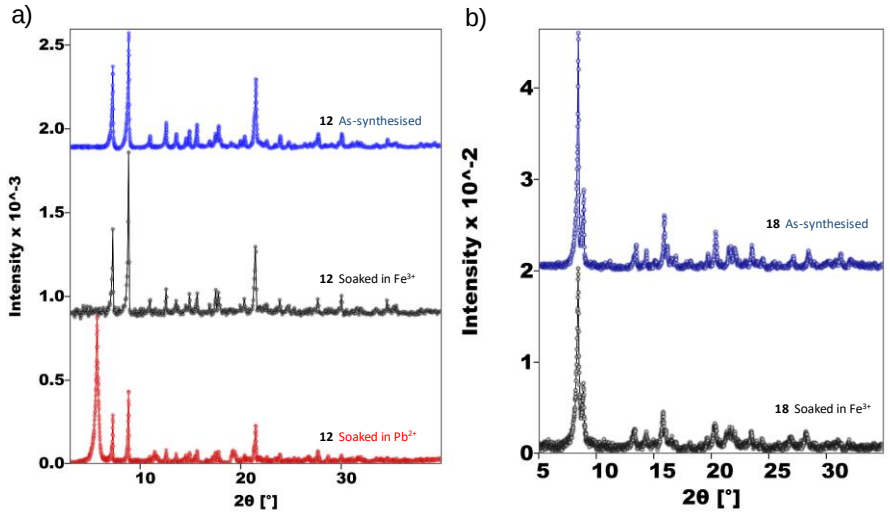

Figure 7.36. a) Powder XRD patterns of **12** as-synthesised and **12** after soaking in an Fe^{3+} and Pb^{2+} aqueous solutions (shown in blue, black and red, respectively). b) Powder XRD patterns of **18** as-synthesised and **18** after soaking in an Fe^{3+} aqueous solution (shown in blue and black, respectively).

Table 7.13. SEM-EDX analyses for **12** and **18** after soaking in 0.01 M metallic aqueous solutions. Three independent measurements were conducted, which were consistent between them. Here only one is shown for simplicity.

SEM/EDX Analyses (atomic %)						
Sample	C	N	O	Eu	Pb	Fe
12 soaked in Pb^{2+}	66.05	6.31	23.73	1.70	2.20	---
12 soaked in Fe^{3+}	65.78	8.08	25.19	0.93	---	0.02
18 soaked in Fe^{3+}	60.39	12.55	24.53	1.59	---	0.07

In order to get more insight into the iron(III) quenching mechanism, UV/VIS spectra measurements were carried out for all metallic aqueous solutions and compared with the emission spectra of complexes **12** and **18**, together with those of corresponding ligands (Figure 7.37).

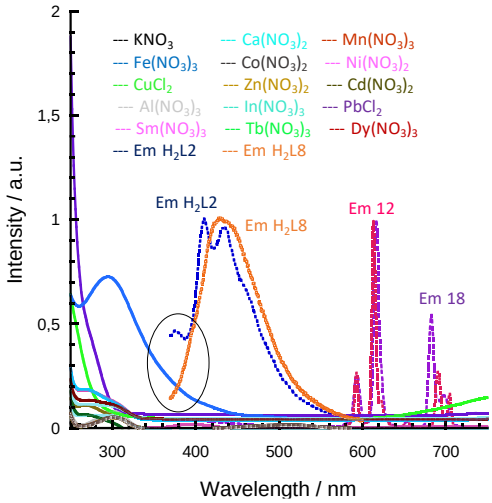

Figure 7.37. UV-VIS spectra of 0.01 M aqueous metallic solutions used for metal sensing experiments. Emission spectra of **H_2L2**, **H_2L8**, **12** and **18** are shown for comparison.

On the one hand, it can be seen a lack of spectral overlap between absorption spectra of metallic ions and emission spectra of the complexes, discarding a resonance energy transfer mechanism between them. Nonetheless, there is a considerable overlap between the absorption spectrum of Fe^{3+} ions and the emission spectra of ligands **H_2L8** and **H_2L2**. Instead of Eu^{3+} sensitisation, energy transfer from excited levels of the ligand to the Fe^{3+} ions takes place, being this an important contribution to the observed quenching effect. On the other hand, the wide absorption band of Fe^{3+} ions ranging from 430 to 260 nm covers the wavelength used for excitation of **12** and **18** (344 and 340 nm, respectively),

while other metal ions such as Pb^{2+} have no obvious absorption in this range. Therefore, some of the excitation energy is absorbed by Fe^{3+} ions, being a second contribution to the quenching process.

The sensitivity of both complexes towards Fe^{3+} ions was also studied. A suspension of each complex (1mg in 1ml H_2O) was titrated with a 25 mM and 50 mM aqueous solution containing Fe^{3+} ions, respectively for **12** and **18**. The luminescence intensities were gradually quenched, reaching a quenching efficiency (*Q*, calculated according to equation 7.6) of 83% and 92% when the concentration of Fe^{3+} was 9.35 mM and 20.80 mM, respectively (Figure 7.38 and 7.39). Simultaneously, in order to exclude that the decrease observed in the luminescence signals upon addition of Fe^{3+} ions is only due to dilution effects, the emission signal of both suspensions prepared in an equivalent volume of water has been registered (Figure 7.40). There is a clear difference between the intensities registered in the presence and in the absence of Fe^{3+} ions, verifying that a quenching process is present.

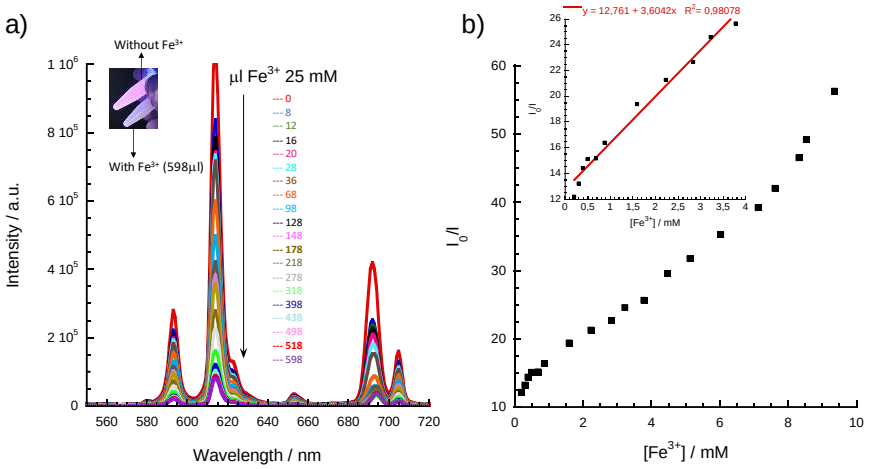

Figure 7.38. a) Comparison of the luminescence intensity of **12** ($[(CH_3)_2NH_2][Eu(H_2O)_2(\mathbf{L8})_2]$) upon addition of differents amounts of Fe^{3+} ions (25 mM), with λ_{exc} = 344 nm. The inset shows an image of a suspension of **12** in water without and with the addition of Fe^{3+} cations (598 µl) under UV light at 365 nm. b) Stern-Volmer plots of the luminescence intensity of **12** upon addition of Fe^{3+} ions. The inset shows the linear fit at low concentrations of Fe^{3+} ions.

The quenching efficiency was quantitatively evaluated using the Stern-Volmer equation (Eq. 7.7), being in this case $[Fe^{3+}]$ the quencher concentration. As shown in Figures 7.38.b and 7.39.b, the Stern-Volmer plots present again an upward bending trend at high concentration of quencher, characteristic of the existence of static and dynamic quenching relaxation mechanisms.[58] From the fit of the

experimental data at low concentration of Fe^{3+} ions (from 0.19 to 3.77 mM and from 0 to 6.9 mM, respectively) to the Stern-Volmer equation (inset of Figures 7.38.b and 7.39.b), K_{SV} values of $3.60 \cdot 10^3$ M^{-1} and $7.06 \cdot 10^2$ M^{-1} are obtained for complexes **12** and **18**, respectively. The first value is comparable to those obtained for the sensing of Fe^{3+} ions by reported Eu-CPs (10^3-10^4 M^{-1}, Table 4.3)[16,59], whereas the second one is one order of magnitude lower.

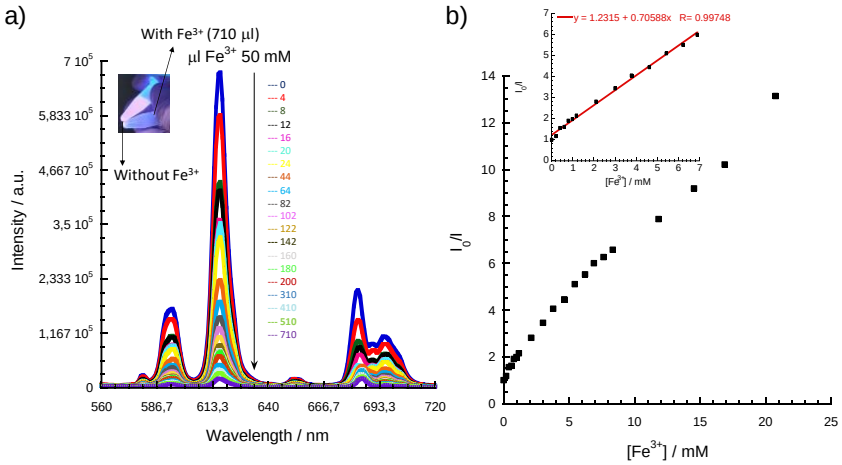

Figure 7.39. a) Comparison of the luminescence intensity of **18** ($[NH_2(CH_3)_2][Eu(\mathbf{L2})_2]\cdot 1H_2O\cdot 1HAc$) upon addition of increasing amounts of Fe^{3+} ions (50 mM), with λ_{exc} = 340 nm. The inset shows an image of a suspension of **18** in water without and with the addition of Fe^{3+} cations (710 µl) under UV light at 365 nm. b) Stern-Volmer plots of the luminescence intensity of **18** upon addition of Fe^{3+} ions. The inset shows the linear fit at low concentrations of Fe^{3+} ions.

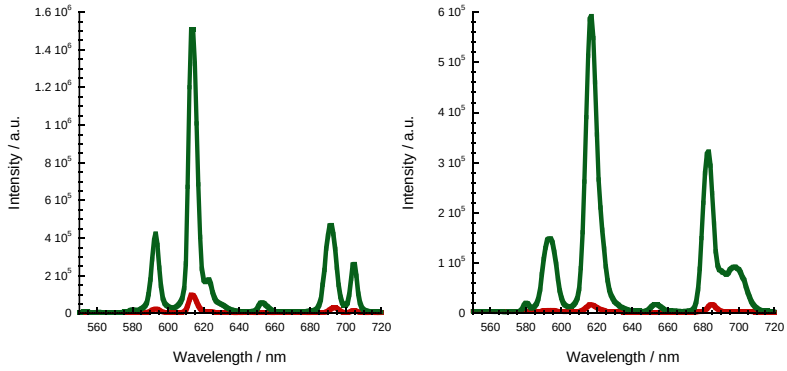

Figure 7.40. Left: Emission spectra of suspensions of **12** prepared in 1 ml of water after addition of 600 µl of H_2O extra (shown in green) and after addition of 598 µl of an aqueous solution containing 25 mM Fe^{3+} ions (shown in red). Right: Emission spectra of suspensions of **18** prepared in 1 ml of water after addition of 700 µl of H_2O extra (shown in green) and after addition of 710 µl of an aqueous solution containing 50 mM Fe^{3+} ions (shown in red).

Furthermore, the limit of detection (*LOD*) was calculated from $3\delta/s$ (Eq. 7.8, where δ is the standard deviation of ten consecutive blank measurements and s is the slope of the plot of luminescence intensity against Fe^{3+} concentration), giving a value of $1.72 \cdot 10^{-4}$ M and $3.26 \cdot 10^{-4}$ M for complexes **12** and **18** (Figure 7.41).

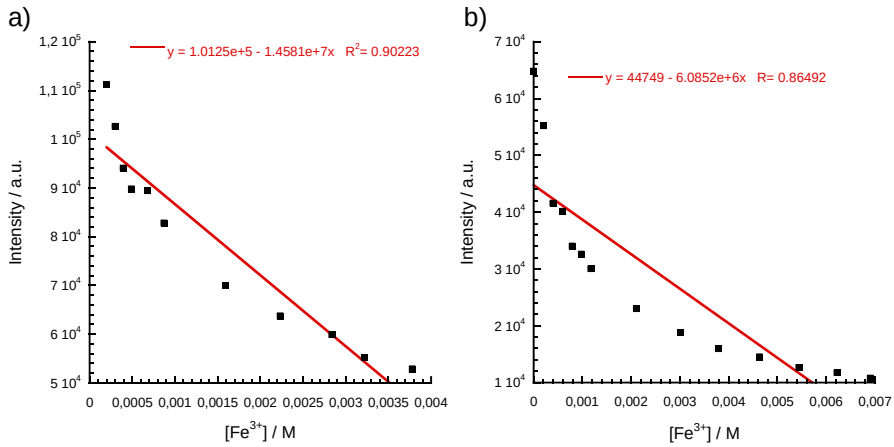

Figure 7.41. Fitting curves of luminescence intensity at different Fe^{3+} concentration for a) complex **12** ([$(CH_3)_2NH_2$][$Eu(H_2O)_2$(**L8**)$_2$]) and b) compound **18** ([$NH_2(CH_3)_2$][Eu(**L2**)$_2$]·$1H_2O$·1HAc).

Both values are very similar and within the range observed for reported Eu-CPs sensors in different sytems (Table 4.3). Nevertheless, the *LOD* calculated for [$(CH_3)_2NH_2$][$Eu(CPA)_2(H_2O)_2$] (CPA^{2-} = 5-(4-carboxy phenyl)picolinate dianion) has a value of 10^{-7} M,[16] which is clearly enhanced compared with the values obtained for compounds **12** and **18**.

E. Effect of pH

pH-sensitive luminescent studies were carried out for both complexes in water suspensions. The emission was registered after immersion in aqueous solutions at different pH values ranging from 1 to 14. The pH of each aqueous solution was adjusted by the addition of HCl or NaOH solution. It was found that, for compound **12** ([$(CH_3)_2NH_2$][$Eu(H_2O)_2$(**L8**)$_2$], Figure 7.42), Eu-based emission is practically constant in the pH range comprised between 3 and 12, whereas at extreme acid or basic pH values there is a complete disappearance of the luminescence. At pH < 3 and pH > 12, a significant molecular fluorescence emission (λ_{max} = 396-432 nm) is registered, which is attributed to the

decomposition of the complex and release of the free ligand in its protonated or fully deprotonated forms.[45]

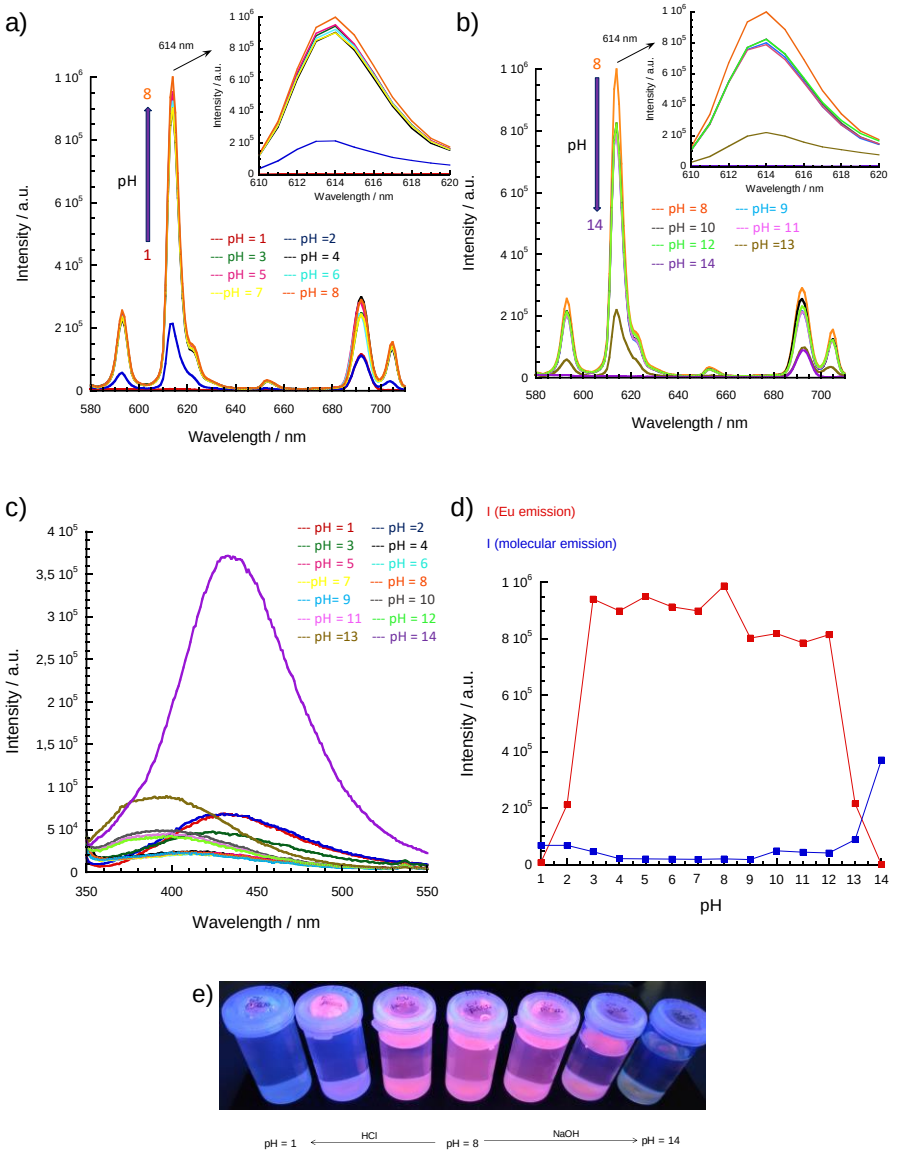

Figure 7.42. Luminescence spectra of **12** in 580-710 nm range (λ_{exc} = 344 nm) at pH values a) 1-8 and b) 8-14. The insets show a zoom in the 614 nm signal. c) Luminescence spectra of **12** with different pH values in 350-550 nm range (λ_{exc} = 344 nm). d) Intensity variation of luminescence of **12** at 614 nm and at 396-432 nm upon increasing the pH value. e) pH-dependent colour-switching of **12** under UV (λ_{exc} = 365 nm) lamp showing naked eye intensity changes.

Accordingly, PXRD experiments (Figure 7.43) show the collapse of the crystal structure at pH = 1 and pH = 13-14, which is the reason for the luminescence quenching of **12**.

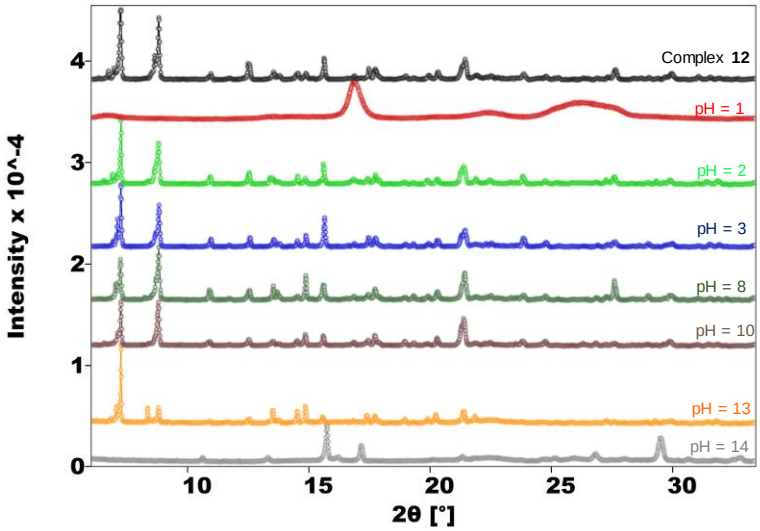

Figure 7.43. PXRD of **12** ($[(CH_3)_2NH_2][Eu(H_2O)_2(\mathbf{L8})_2]$) at different pH values.

Complex **18** ($[NH_2(CH_3)_2][Eu(\mathbf{L2})_2]\cdot 1H_2O\cdot 1HAc$) displays a practically constant luminescence in the pH range comprised between 3 and 8 (Figure 7.44). Above this pH value, the Eu(III) luminescence response decreases gradually until complete quenching at pH = 14. Analogously, below pH = 3, there is a smooth drop in the luminescence signal until a complete disappearance at pH = 1. A molecular-based emission (at 400-376 nm) is observed in a relevant way at pH = 1, 13 and 14, which is ascribed to the release of free ligand at extreme pH values. PXRD measurements (Figure 7.45) reveal that the crystalline integrity of the material is completely lost at pH = 1 and pH = 14. At pH < 3 and pH > 8, additional peaks are registered, suggesting that the compound is being decomposed and new species are formed. Therefore, the luminescence quenching observed for **18** at different pH values is also attributed to the disruption of the crystal structure. The characteristic emission of Eu^{3+} ion ($^5D_0 \longrightarrow {}^7F_2$) is reduced immediately as the chelate ring built by the picolinate ligands and Eu^{3+} ions is broken at extreme pH values. This results in a sensitisation mechanism of ligands **L8** and **L2** less effective and, consequently, poor energy transfer to the Eu^{3+} ion.

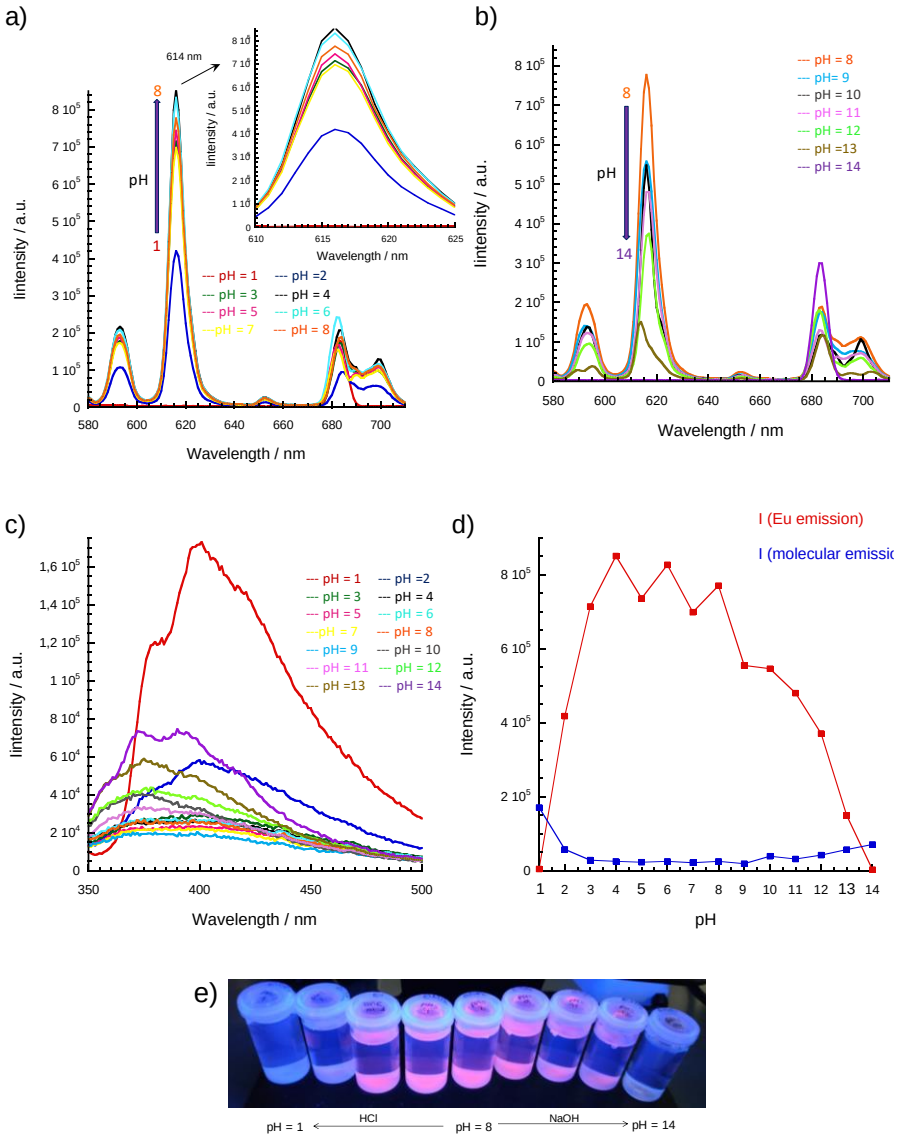

Figure 7.44. Luminescence spectra of **18** in 580-710 nm range (λ_{exc} = 340 nm) with pH values a) 1-8 and b) 8-14. The inset shows a zoom in the 614 nm signal for pH values between 1 and 8. c) Luminescence spectra of **18** with different pH values in 350-550 nm range (λ_{exc} = 340 nm). d) Intensity variation of luminescence of **18** at 614 nm and at 400-376 nm upon increasing the pH value. e) pH-dependent colour-switching of **18** under UV (λ_{exc} = 365 nm) lamp showing naked eye intensity changes.

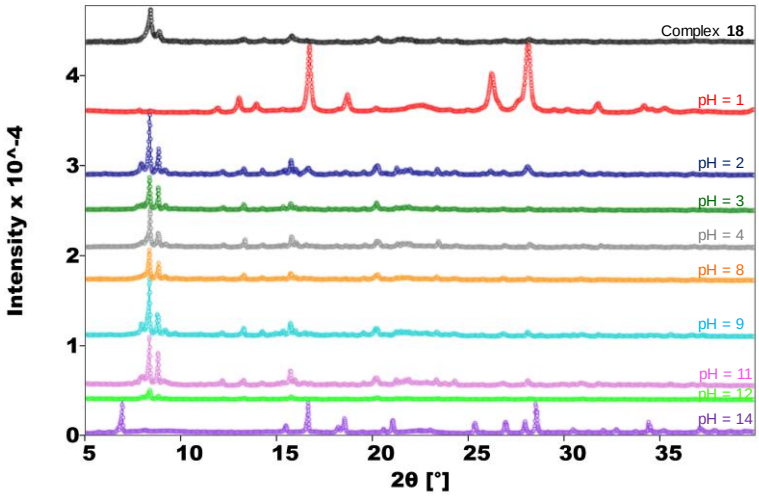

Figure 7.45. PXRD of **18** ($[NH_2(CH_3)_2][Eu(\mathbf{L2})_2]\cdot 1H_2O\cdot 1HAc$) at different pH values.

A compound reported recently, $[EuNaL_4(H_2O)_3]\cdot H_2O$ (being HL = 7-chloro-1-cyclopropyl-6-fluoro-4-oxo-1,4-dihydroquinoline-3-carboxylic acid), exhibits a similar behaviour with the strongest luminescence observed at pH = 7.[54] Between pH 7 and 11, its luminescence intensity decreases gradually until complete quenching due to collapse of the crystal structure at pH values > 11, as well as at pH values between 1 and 4. In our case, both compounds show an improved stability, standing out complex **12** with a wider pH range of stability and crystal structure integrity.

7.5. Conclusions

Solvothermal reactions of hydrated lanthanide (III) nitrates or chlorides and ligand **H_2L8** or **H_2L2** have provided access to two isostructural families of complexes depending on the ligand used: compounds **12**-**17** and compounds **18**-**22**, respectively. In compounds **12**-**17**, the Ln(III) centres exhibit an eight-coordinated distorted square antiprism geometric configuration and **L8** ligand presents a nearly planar conformation, providing both carboxylate-monodentate and picolinate-chelating coordination sites. Bridging of Ln(III) metal ions through monodentate and bidentate chelation in an alternative way results in the formation of a 1D chain network. A 2D anionic layered structure is formed by further linking of the remaining coordination sites available on the Ln^{3+} metal centres between adjacent chains. For compounds **18**-**22**, the Ln(III) cations exhibit a nine-coordinated tricapped trigonal prismatic structure and the two independent **L2** ligands present a strong deviation from planarity. In

addition, the bending of the triple bond is more pronounced for this ligand. *Anti*, *anti*-carboxylate bridged Ln(III) chains are formed, which are further connected by bis-bidentate chelating coordination sites from the same ligand, yielding a 2D layered structure. The second ligand provides bis-bidentate coordination mode and builts up a 3D anionic structure. In all compounds, the resulting anionic frameworks exhibit one-dimensional hydrophilic channels that contain dimethylammonium cations. With the aim of exchanging these cations located in the voids of the structure for magnetic ions (Ni^{2+}, Co^{2+}, Fe^{2+}), several attempts were conducted in different solvents (DMF, EtOH and water) for compounds **12**-**17** (complexes **18**-**22** were not considered due to the fact that the crystallinity of the first family of compounds is markedly higher). These trials consisted in soaking the as-synthesised single crystals in solutions of concentration ranging from 0.1 to 0.001 M of $MCl_2{\cdot}xH_2O$ (M = Ni^{2+}, Co^{2+}, Fe^{2+}) with different immersion time (from 1 to 10 days). When EtOH or DMF were used as a solvent, cation exchange processes were not observed (as deduced from SEM analysis), regardless of the concentration or immersion time. If water was used as a solvent, even with the smallest concentration and from the second day, new crystals were formed. However, SEM analysis showed that the Ln(III) ion was replaced by the divalent cation and single crystal XRD experiments revealed that a mononuclear complex of formula $[M(H_2O)_4(\mathbf{L8})]$ was obtained instead of taking place the desired cation exchange process.

Magnetic measurements show a progressively thermal depopulation of the ground-state Ln(III) sublevels for coordination polymers **15** ($[(CH_3)_2NH_2][Dy(H_2O)_2(\mathbf{L8})_2]$) and **17** ($[(CH_3)_2NH_2][Er(H_2O)_2(\mathbf{L8})_2]$), whereas complexes **13**, **14** and **16** ($[(CH_3)_2NH_2][Ln(H_2O)_2(\mathbf{L8})_2]$, Ln = Gd, Tb and Ho, respectively) exhibit very weak ferromagnetic dipolar interactions. Compounds **19**-**22** ($[NH_2(CH_3)_2][Ln(\mathbf{L2})_2]{\cdot}1H_2O{\cdot}1HAc$, Ln = Gd, Tb, Dy and Ho, respectively) exhibit a weak antiferromagnetic coupling between the metal centres through the bridging carboxylate moiety and/or progressively thermal depopulation of the ground-state Ln(III) sublevels. For europium derivatives ($[(CH_3)_2NH_2][Eu(H_2O)_2(\mathbf{L8})_2]$(**12**) and $[NH_2(CH_3)_2][Eu(\mathbf{L2})_2]{\cdot}1H_2O{\cdot}1HAc$ (**18**)), the presence of thermally populated excited states is revealed by DC measurements. On lowering the temperature, these states are depopulated and at 2 K the ground state is mostly populated. On the other hand, AC magnetic studies showed that complexes **17** ($[(CH_3)_2NH_2][Er(H_2O)_2(\mathbf{L8})_2]$) and **21** ($[NH_2(CH_3)_2][Dy(\mathbf{L2})_2]{\cdot}1H_2O{\cdot}1HAc$) exhibit field-induced slow magnetic relaxation of the magnetisation, while the remaining complexes do not display such properties. The values obtained for the energy effective barrier (E_a/K_B) of magnetisation reversal are 15.10 K for **17** and 8.36 K for **21**. These values

indicate an enhancement in the energy barrier for compound **17** compared to **21**, being ascribed to the fact that the lanthanide centres are better isolated in **17** than in **21**. Despite the fact that the shortest distance between the lanthanide centres is similar, in compound **17** (d(Er···Er) = 6.115 Å) the linkage is through doubly hydrogen-bonded chains, whereas in **21** (d(Dy···Dy) = 6.635 Å) it is through the *anti*, *anti*-bidentate bridging carboxylate moiety.

Solid complexes **12** and **18** emit red light upon excitation at 365 nm and luminescence investigations demonstrate that **L8** and **L2** ligands can effectively sensitise the europium derivatives (acting as organic antennas). The quantum yield value measured for compound **18** (ϕ = 0.29) is higher than that obtained for compound **12** (ϕ = 0.23). Luminescence decay experiments showed a higher lifetime value for compound **18** (τ_{av} = 1.18 ms) in comparison with compound **12** (τ_{av} = 0.37 ms), which can be explained considering the non-radiative quenching process *via* O–H oscillators of coordinating water molecules in **12**.

Both complexes are promising luminescent sensors to detect selectively $PhNO_2$ molecules and Fe^{3+} ions through luminescence quenching. Compounds **12** and **18** exhibit comparable quenching efficiency of both analytes on Eu-based emission, with quite similar limits of detection. The quenching mechanism caused by $PhNO_2$ and Fe^{3+} ions might be explained by a combination of two factors: first, the competitive absorption of excitation energy between the quenchers and the fluorophores. And, secondly, the energy transfer from the excited state of the ligands to the quencher molecules, which hinders the Eu(III)-sensitisation process. Furthermore, both europium derivatives show a significant quenching of their emission intensity when the pH reaches critical acid or basic values (1-2 or 13-14) as a consequence of the disruption of the original crystal structure. Therefore, they present a striking stability in aqueous solutions within a wide pH range. The visible colour changes allow distinction by the naked eye and paves the way for their further application in the field of detection.

The question that arises is why only the europium derivatives show an efficient energy transfer from ligands **L8** and **L2** to the lanthanide centre despite the fact that the dysprosium and terbium analogues are isostructural and well-known luminescent probes have been described with these metal ions? The energy of the triplet excited state in the ligand should be appropriate to match well with the emitting energy level of the lanthanide ion. Thus, it is not possible for only one ligand to match well with different lanthanide ions because their energy levels are not the same. Based on this, a possible explanation relies on the fact

that if the LUMO orbital of the corresponding Ln complex lies at low energy enough, the fluorophore can transfer energy into the excited 4*f* states of the corresponding Ln(III). Nevertheless, in the scenario in which the energy of the excited state of the ligand is close to the energy of the emitting level of the corresponding Ln(III) ion, the ligand itself acts as an efficient quencher of the 4*f* luminescence.[43] Considering the partial energy diagrams for the lanthanide aqua ions (Figure 7.22), it can be seen that the emitting level of Eu(III) is lower in energy with respect to that of Tb(III), and this latter is slightly lower than that of Dy(III). Therefore, is not unreasonable that the energy of the excited states of **L8** and **L2** ligands lie high enough in comparison with the excited state of compounds **12** and **18** for a charge-transfer process, whereas they are energetically too close to the excited states of terbium and dysprosium derivatives for allowing an efficient charge-transfer, thus, leading to a drop in the 4*f*-luminescence.

7.6. Experimental Section

7.6.1. Synthesis

A. Synthesis of complexes $[NH_2(CH_3)_2][Ln(H_2O)_2(L8)_2]$ (12-17)

A solution of $Eu(NO_3)_3{\cdot}6H_2O$ (11.15 mg, 0.025 mmol) and 5-((4-carboxyphenyl)ethynyl)picolinic acid (13.35 mg, 0.05 mmol) in 2.5 ml of DMF/H_2O (ratio 3:2) was placed in a 4 ml glass vial and stirred for 30 min. Next, 2 drops of acid nitric (65%, aq.) were added and the resulting suspension was placed in an oven. The mixture was heated at 130°C for 3 days and then cooled to room temperature at a cooling rate of 0.2°/min. Colourless spearhead-shaped crystals were obtained, filtered and air dried to give compound **12**. Yield: 79% (15.1 mg), based on $Eu(NO_3)_3{\cdot}6H_2O$. The other compounds of the family were prepared in a similar way to that described for complex **12**. Exact amount of reagents, solvents, modulator, as well as the synthetic yields achieved are included in Table 7.14. Isostructural compounds were obtained when methyl 5-((4-(methoxycarbonyl)phenyl)ethynyl)picolinate was used instead of 5-((4-carboxyphenyl)ethynyl)picolinic acid. It has to be noted that the amount and type of modulator added during the synthesis is crucial. For example, for the europium derivative, if no modulator is used, only crystalline powder is obtained, whose structure was not possible to determine by single-crystal X-ray diffraction. If the amount of nitric acid is increased, two different types of crystals are obtained: needles (unknown phase) and spearhead-shaped (isostructural to

compound **12**) crystals. In this case, the optimal volume of nitric acid for obtaining **12** as a pure phase was found to be 2 drops.

Table 7.14. Synthetic details for the preparation of compounds **12**-**17**.

Compound	$LnX_3 \cdot 6H_2O$	**H_2L8**	Solvent (DMF/H_2O, 3:2)	HNO_3	Yield
12	$Eu(NO_3)_3 \cdot 6H_2O$ (11.15 mg, 0.025 mmol)	13.35 mg (0.05 mmol)	2.5 ml	2 drops	15.1 mg (79%)
13	$GdCl_3 \cdot 6H_2O$ (18.59 mg, 0.05 mmol)	26.7 mg (0.1 mmol)	5 ml	3 drops	24.6 mg (64%)
14	$TbCl_3 \cdot 6H_2O$ (18.67 mg, 0.05 mmol)	26.7 mg (0.1 mmol)	5 ml	3 drops	33.6 mg (87%)
15	$DyCl_3 \cdot 6H_2O$ (18.85 mg, 0.05 mmol)	26.7 mg (0.1 mmol)	5 ml	3 drops	32.9 mg (85%)
16	$HoCl_3 \cdot 6H_2O$ (13.78 mg, 0.036 mmol)	19.4 mg (0.073 mmol)	3.65 ml	2 drops	22.0 mg (79%)
17	$ErCl_3 \cdot 6H_2O$ (19.09 mg, 0.05 mmol)	26.7 mg (0.1 mmol)	5 ml	3 drops	29.3 mg (75%)

Elemental analysis of the percentage in weight of C, N and H were carried out for the as-synthesised crystals. Three independent measurements were conducted which were consistent between them and the best experimental result is included in Table 7.15, together with the calculated values. These results indicate that some of the samples absorb water molecules (0.5 H_2O per formula) from the environment (TG measurements were carried out just after filtration of the compounds, prior to their elemental analysis, for this reason they do not reflect this water absorption).

Table 7.15. Data of weight percent of C, H and N for compounds **12**-**17**.

Compound	% C exp (calc.)	% N exp (calc.)	% H exp (calc.)
($C_{32}H_{26}EuN_3O_{10}$) (**12**)	49.86 (50.27)	5.36 (5.50)	3.38 (3.43)
($C_{32}H_{26}GdN_3O_{10}$) (**13**)	49.87 (49.93)	5.46 (5.46)	3.47 (3.40)
($C_{32}H_{26}TbN_3O_{10}$)·0.5H_2O (**14**)	49.01 (49.24)	5.43 (5.38)	3.69 (3.49)
($C_{32}H_{26}DyN_3O_{10}$) (**15**)	49.21 (49.59)	5.47 (5.42)	3.38 (3.38)
($C_{32}H_{26}HoN_3O_{10}$)·0.5H_2O (**16**)	48.56 (48.87)	5.44 (5.34)	3.21 (3.46)
($C_{32}H_{26}ErN_3O_{10}$) (**17**)	49.45 (49.29)	5.53 (5.39)	3.25 (3.36)

The infrared spectra of compounds **12**-**17** are shown in Figure 7.46. The most intense signals are associated to –C=O, –C=N and –C=C- stretching bands (1630, 1589, 1530, 1475, 1375 and 1355cm^{-1} for **12**), and the presence of the triple bond is demonstrated by a stretching C≡C signal around 2220 cm^{-1}, due to the

ligand **L8**. The weak intensity of the broad band observed in the 4000-3000 cm^{-1} range is associated to O-H stretching signal and indicates that the samples contain water molecules, which is in agreement with the crystal structure described for these compounds and with elemental analysis results. The spectra obtained are almost coincident with those reported for $[(CH_3)_2NH_2][Ln(H_2O)_2(C_{13}O_4N_1H_7)_2]$ (Ln = Eu, Gd, Er, Ho, Dy, Tb, Sm, Nd, Pr and Ce), a related family of lanthanide complexes, except for the presence of the C≡C signal around 2220 cm^{-1}.[15]

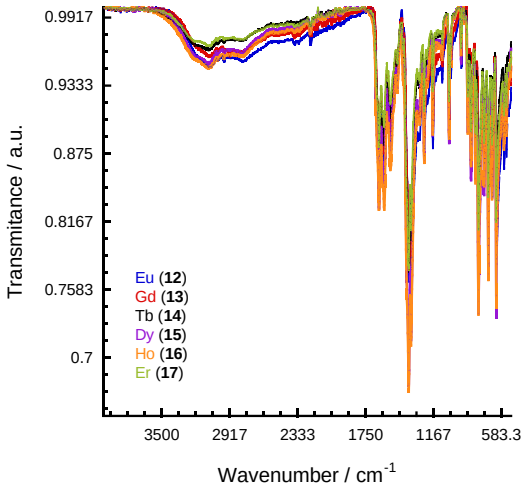

Figure 7.46. Infrared (IR) spectra of complexes **12**-**17** recorded in an attenuated total reflection (ATR) apparatus.

B. Synthesis of complexes $[NH_2(CH_3)_2][Ln(L2)_2]\cdot 1H_2O\cdot 1HAc$ (18-22)

A mixture of $Eu(NO_3)_3\cdot 6H_2O$ (24.9 mg, 0.056 mmol) and 5,5'-(ethyne-1,2-diyl)dipicolinic acid (15 mg, 0.056 mmol) was thoroughly mixed with water (0.5 ml) and DMF (4 ml) in a glass vial and stirred for 30 min until a solution is formed. Then, acetic acid (1100 μl) was added and the mixture was placed in an oven at 130°C for 3 days. A cooling rate of 0.2°/min was applied to cool down the sample until room temperature. After decanting the liquid, colourless aggregated crystals were obtained. The final mass of the crystals after washing and drying in air was 14.3 mg (yield: 60%). Complexes (**19**-**22**) were synthesised in a similar way to that described for complex **18**. The corresponding synthetic details are gathered in Table 7.16. It is worth mentioning that the amount and type of modulator used for the synthesis of the complexes is of vital importance. For instance, when formic acid was used only

crystalline powder was obtained. If nitric acid is used instead of acetic acid, thin needles were obtained. In both cases, these products were new phases and their crystal structure determination was not possible due to the small size of the crystals if present.

When starting from dimethyl 5,5'-(ethyne-1,2-diyl)dipicolinate instead of 5,5'-(ethyne-1,2-diyl)dipicolinic acid, isostructural compounds were obtained and formic acid was proven to be more effective for obtaining single crystals than acetic acid.

Table 7.16. Synthetic details for the preparation of compounds **18**-**22**.

Compound	$Ln(NO_3)_3 \cdot 6H_2O$	**H_2L2**	Solvent (DMF/H_2O, 8:1)	HAc (μl)	Yield
18	Eu (24.9 mg, 0.056 mmol)	15 mg (0.056 mmol)	4.5 ml	1100	14.3 mg (63%)
19	Gd (25.28 mg, 0.056 mmol)	15 mg (0.056 mmol)	4.5 ml	1100	14.3 mg (63%)
20	Tb (24.3 mg, 0.056 mmol)	15 mg (0.056 mmol)	4.5 ml	800	17.2 mg (75%)
21	Dy (25.5 mg, 0.056 mmol)	15 mg (0.056 mmol)	4.5 ml	1000	16.7 mg (73%)
22	Ho (24.62 mg, 0.056 mmol)	15 mg (0.056 mmol)	4.5 ml	1300	10.2 mg (44%)

The weight percent of C, N and H was determined by elemental analysis for the as-synthesised samples. Three independent measurements show consistent results, and the best result is shown in Table 7.17, as well as with the calculated values for each element. These results indicate that these compounds absorb water molecules from the environment (1-2 water molecules) upon exposure to ambient conditions for several days.

Table 7.17. Data of weight percent of C, H and N for compounds **18**-**22**.

Compound	% C exp (calc.)	% N exp (calc.)	% H exp (calc.)
$(C_{32}H_{26}EuN_5O_{11})\cdot 2H_2O$ (**18**)	45.22 (45.51)	8.29 (8.29)	3.11 (3.58)
$(C_{32}H_{26}GdN_5O_{11})\cdot 1H_2O$ (**19**)	45.98 (46.20)	8.49 (8.42)	3.03 (3.39)
$(C_{32}H_{26}TbN_5O_{11})\cdot 1.5H_2O$ (**20**)	45.67 (45.62)	8.38 (8.31)	3.08 (3.47)
$(C_{32}H_{26}DyN_5O_{11})\cdot 1H_2O$ (**21**)	45.68 (45.91)	8.47 (8.37)	3.08 (3.37)
$(C_{32}H_{26}HoN_5O_{11})\cdot 1H_2O$ (**22**)	45.76 (45.78)	8.56 (8.34)	3.10 (3.36)

The infrared spectra of compounds **18**-**22** were registered (Figure 7.47). As in the previous family of compounds, the most relevant signals correspond to –C=O, -C=N and –C=C- stretching bands (1607, 1556 and 1388 cm^{-1} for **18**), ascribed to the presence of ligand **L2**. A weak signal in the 4000-3000 cm^{-1} range indicates that crystallisation water molecules (O–H stretching) are present in these compounds, which is in agreement with the thermogravimetric measurements

and elemental analyses results. In this case, the lack of the triple bond signal around 2200 cm^{-1} is due to the fact that the ligand is symmetric, and it is well-known that the intensity of this signal is reduced as symmetry increases (compounds **12**-**17** crystallise in the monoclinic space group whereas complexes **18**-**22** in the orthorhombic). For the same reason, the IR spectra recorded for compounds **18**-**22** have less peaks in comparison to those registered for complexes **12**-**17**.

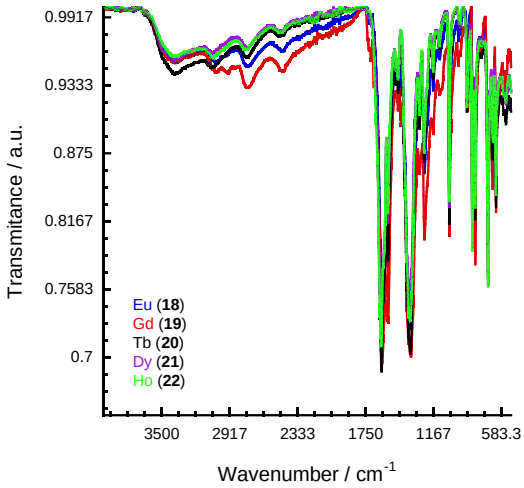

Figure 7.47. Infrared (IR) spectra of complexes **18**-**22** recorded in an attenuated total reflection apparatus (ATR).

7.6.2. Luminescent properties of Dy and Tb derivatives

A. Terbium complexes

The excitation spectra of complexes **14** ($[(CH_3)_2NH_2][Tb(H_2O)_2(\mathbf{L8})_2]$) and **20** ($[NH_2(CH_3)_2][Tb(\mathbf{L2})_2]\cdot 1H_2O\cdot 1HAc$) were obtained by monitoring the 556-545 nm line of the characteristic $^5D_4 \rightarrow {}^7F_5$ emission for Tb^{3+} complexes.[15] The excitation spectrum of **14** (λ_{em} = 545 nm) shows a weak broad band located at 373 nm. Upon excitation at 373 nm, the emission spectrum presents a broad band ascribed to ligand-centred emission that is overlapped with the light harmonic that appears at 373 nm. Therefore, excitation was carried out at 325 nm and the resulting spectrum reveals a broad band due to the ligand-centred emission at 420 nm and two weak signals at 592 and 615 nm. These two peaks may be ascribed to the characteristic bands for the Tb^{3+} emission associated to $^5D_4 \rightarrow {}^7F_4$ and $^5D_4 \rightarrow {}^7F_3$ transitions, respectively. Subsequent emission at 420 nm yields an excitation spectrum with a band around 346 nm. Upon excitation at

346 nm, the corresponding emission spectrum was recorded with a broad band at 420 nm (attributed to the ligand-centred emission) and two weak peaks at 592 and 615 nm (associated to $^5D_4 \rightarrow {}^7F_4$ and $^5D_4 \rightarrow {}^7F_3$ transitions of Tb^{3+} ions, respectively)[15] (Figure 7.48.a). These results indicate that the energy transfer from the ligand to the terbium centre is not complete, being the emission of the ligand the dominating process.

The excitation spectrum of **20** (λ_{em} = 556 nm) exhibits a broad band centred at 367 nm. Upon excitation at 367 nm, the emission spectrum shows a broad band located at 428 nm and a small peak at 617 nm. Subsequent emission at 428 nm, yields an excitation spectrum with a maximum at 356 nm and a second peak at 259 nm. The final emission spectrum was recorded with an excitation at 356 nm and it shows a maximum at 428 nm, a second peak at 592 nm and a third signal at 617 nm (Figure 7.48.b). The maximum is clearly ascribed to ligand-centred emission, while the remaining signals are attributed to emission bands for the Tb^{3+} ion due to transitions between $^5D_4 \rightarrow {}^7F_4$ at 592 nm and $^5D_4 \rightarrow {}^7F_3$ at 617 nm. It has to be noted that the $^5D_4 \rightarrow {}^7F_6$ and $^5D_4 \rightarrow {}^7F_5$ transitions, usually observed at 490 and 545 nm, are masked by the broad band associated to ligand-centred emission in both complexes. This fact suggests a partial energy transfer from the ligand to the Tb^{III} ions, being the emission spectrum dominated by the ligand emission and this is consistent with the fact that complexes **14** and **20** do not exhibit the characteristic green emission when irradiating with UV light.

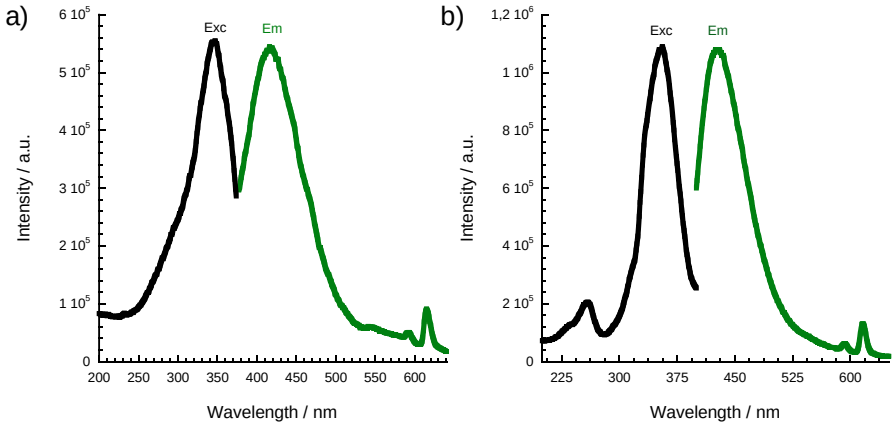

Figure 7.48. a) Excitation and emission spectra of **14**. The excitation spectrum was obtained at 556 nm emission and the emission spectrum was registered under excitation at 277 nm. b) Excitation and emission spectra of **20**. The excitation spectrum was obtained at 428 nm emission and the emission spectrum was registered under excitation at 356 nm.

B. Dysprosium complexes

The excitation spectra of **15** and **21** were obtained by photoexcitation at 575 nm (line of the most intense characteristic $^4F_{9/2} \rightarrow {}^6H_{13/2}$ emission for Dy^{3+} complexes).[15] The excitation spectrum of **15** presents a sharp signal due to light harmonic (287 nm) and two broad bands centred at 260 and 380 nm, being the first one more intense (Figure 7.49.b). Upon excitation at 260 nm, the emission spectrum presents a broad band with a maximum at 419 nm, a sharp peak due to light harmonic and a weak signal at 575 nm (Figure 7.49.a). The first signal is attributed to ligand-centred emission, whereas the latter is ascribed to the most intense and characteristic $^4F_{9/2} \rightarrow {}^6H_{13/2}$ emission for Dy^{3+} complexes. This indicates that energy transfer from the ligand to the Dy^{3+} ions takes place, however, in an inefficient way.

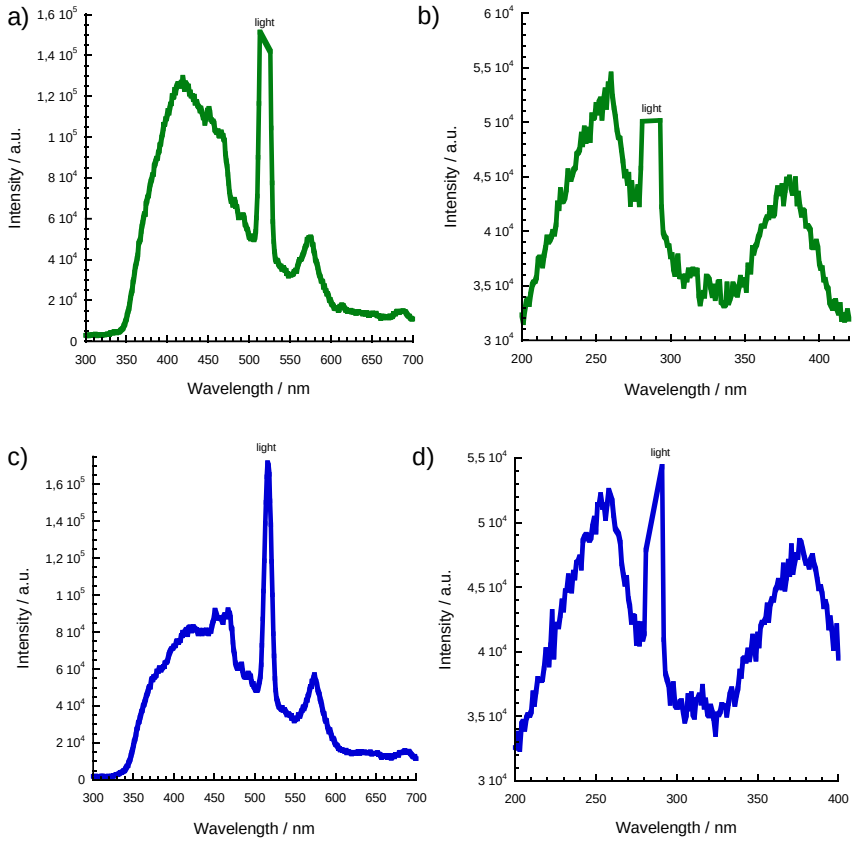

Figure 7.49. a) Emission spectra of **15** registered under excitation at 260 nm. b) Excitation spectrum of **15** obtained at 575 nm emission. c) Emission spectra of **21** registered under excitation at 258 nm. d) Excitation spectrum of **21** obtained at 575 nm emission.

For **21**, the excitation spectrum (λ_{em}= 575 nm) contains a sharp signal due to light harmonic (287 nm) and two broad peaks located at 258 and 376 nm (Figure 7.49.d). As the first signal is more intense, excitation at 258 nm was carried out and the emission spectrum shows a broad band with a maximum at 451 nm, together with a sharp peak associated to harmonic light and a weak signal at 574 nm (Figure 7.49.c). The most intense signal is associated to ligand-centred emission, while the weakest is ascribed to the characteristic $^4F_{9/2} \rightarrow {}^6H_{13/2}$ emission for Dy^{3+} compounds. This clearly indicates that energy transfer from **L2** ligand to the Dy^{3+} ions has been slightly accomplished. These results are in agreement with the fact that both compounds do not show the characteristic blue emission when irradiating with UV light.

7.7. References

[1] B. Yan , *Acc*. *Chem*. *Res*. **2017**, 50, 2789-2798

[2] a) Y. Shi, M.-M. Song, D.-L. Tao, Q.-B. Bo, ACS Omega. 2018, 3, 12122-12131. b) X. Feng, Y. Shang, H. Zhang, R. Li, W. Wang, D. Zhang, L. Wang, Z. Li, *RSC Adv*. **2019**, 9, 16328-16338

[3] J. Zhao, G.-H. Zhu, L.-Q. Xie, Y.-S. Wu, H.-L. Wu, A.-J. Zhou, Z.-Y. Wu, J. Wang, Y.-C. Chen, M.-L. Tong, *Dalton Trans*. **2015**, 44, 14424-14435

[4] Z.-Y. Li, B. Zhai, S.-Z. Li, G. –X. Cao, F.-Q. Zhang, X.-F. Zhang, F.-L. Zhang, C. Zhang, *Cryst*. *Growth Des*. **2016**, 16, 4574-4581

[5] L.-X. You, B.-B. Zhao, H.-J. Liu, S.-J. Wang, G. Xiong, Y.-K. He, F. Ding, J. J. Joos, P. F. Smet, Y.-G. Sun, *CrystEngComm*. **2018**, 20, 615-623

[6] A. B. Ruiz-Muelle, A. García- García, A. A. García-Valdivia, I. Oyarzabal, J. Cepeda, J. M. Seco, E. Colacio, A. Rodríguez-Diéguez, I. Fernández, *Dalton Trans*. **2018**, 47, 12783-12794

[7] a) J.-H. Liu, R.-T. Zhang, J. Zhang, D. Zhao, X.-X. Li, Y.-Q. Sun, S.-T. Zheng, *Inorg*. *Chem*. **2019**, 58, 14734-14740. b) S. Zhang, W. Shi, L. Li, E. Duan, P. Cheng, *Inorg*. *Chem*. **2014**, 53, 10340-10346

[8] W.-J. Chu, X.-W. Hou, Q.-H. Zhao, Y.-T. Fan, H.-W. Hou, *Inorg*. *Chem*. *Comm*. **2010**, 13, 22-25

[9] B. Mu, F. Li, Y. Huang, K. S. Walton, *J*. *Mater*. *Chem*. **2012**, 22, 10172-10178

[10] S. Su, W. Chen, C. Qin, S. Song, Z. Guo, G. Li, X. Song, M. Zhu, S. Wang, Z. Hao, H. Zhang, *Cryst*. *Growth Des*. **2012**, 12, 1808-1815

[11] G. G. Skvortsov, A. S. Shavyrin, T. A. Kovylina, A. V. Cherkasov, A. A. Trifonov, *Eur*. *J*. *Inorg*. *Chem*. **2019**, 5008-5017

[12] Z. Cui, X. Zhang, S. Liu, L. Zhou, W. Li, J. Zhang, *Inorg*. *Chem*. **2018**, 57, 11463-11473

[13] C. Pagis, M. Ferbinteanu, G. Rothenberg, S. Tanase, *ACS Catal*. **2016**, 6, 6063-6072

[14] J.-Z. Gu, Z.-Q. Gao, *J*. *Chem*. *Crystallogr*. **2012**, 42, 283-289

[15] L.-X. You, Z.-G. Li, F. Ding, S.-J. Wang, B.-Y. Ren, Y.-G. Sun, *Inorg*. *Chem*. *Comm*. **2014**, 46, 340-343

[16] Y.-P. Wu, G.-W. Xu, W.-W. Dong, J. Zhao, D.-S. Li, J. Zhang, X. Bu, *Inorg*. *Chem*. **2017**, 56, 1402-1411

[17] M.-L. Han, G.-W. Xu, D.-S. Li, L. M. Azofra, J. Zhao, B. Chen, C. Sun, *ChemistrySelect*. **2016**, 1, 3555-3561

[18] G.-W. Xu, Y.-P. Wu, W.-W. Dong, J. Zhao, X.-Q. Wu, D.-S. Li, Q. Zhang, *Small*. **2017**, 13, 1602996

[19] V. Martins, J. A. L. C. Resende, C. M. Ronconi, *CrystEngComm*. **2017**, 19, 3103-3116

[20] a) B. T. N. Pham, L. M. Lund, D. Song, *Inorg*. *Chem*. **2008**, 47, 6329-6335. b) A. D. Burrows, L. C. Fisher, D. Hodgson, M. F. Mahon, N. F. Cessford, T. Düren, C. Richardson, S. P. Rigby, *CrystEngComm*. **2012**, 14, 188192. c) J. Bai, H.-L. Zhou, P.-Q. Liao, W.-X. Zhang, X.-M. Chen, *CrystEngComm*. **2015**, 17, 4462-4468. d) T. Gadzikwa, B.-S. Zeng, J. T. Hupp, S. T. Nguyen, *Chem*. *Commun*. **2008**, 3672-3674. e) D. J. Tranchemontagne, K. S. Park, H. Furukawa, J. Eckert, C. B. Knobler, O. M. Yaghi, *J*. *Phys*. *Chem*. *C*. **2012**, 116, 13143-13151. f) R. J. Marshall, S. L. Griffin, C. Wilson, R. S. Forgan, *J*. *Am*. *Chem*. *Soc*. **2015**, 137, 9527-9530. g) X.-L. Lv, M. Tong, H. Huang, B. Wang, L. Gan, Q. Yang, C. Zhong, J.-R. Li, *J. Solid State Chem*. **2015**, 223, 104-108. h) A. Dutta, A. G. Wong-Foy, A. J. Matzger, *Chem*. *Sci*. **2014**, 5, 3729-3734

[21] A. Karmakar, A. V. Desai, S. K. Ghosh, *Coord*. *Chem*. *Rev*. **2016**, 313-341

[22] P. Wang, J.-P. Ma, Y.-B. Dong, R.-Q. Huang, *J*. *Am*. *Chem*. *Soc*. **2007**, 129, 10620-10621

[23] A. C. Sudik, A. R. Millward, N. W. Ockwig, A. P. Côté, J. Kim, O. M. Yaghi, J. Am. *Chem*. *Soc*. **2005**, 127, 7110-7118

[24] a) D. Casanova, P. Alemany, J. M. Bofill, S. Alvarez, *Chem.–Eur. J.* **2003**,9, 1281–1285. b) S. Alvarez, P. Alemany, D. Casanova, J. Cirera, M. Llunell, D. Avnir, *Coord. Chem. Rev.* **2005**, 249, 1693–1708. c) M. Llunell, D. Casanova, J. Cirera, J. M. Bofill, P. Alemany. S. Alvarez, SHAPE (Version 2.1), Barcelona, **2013**

[25] S. Alvarez, D. Avnir, M. Llunell, M. Pinsky, *New. J. Chem.* **2002**, 26, 996-1009

[26] a) Spek, A. L, *J. Appl. Crystallogr.* **2003**, 36, 7. b) A. L. Spek, *Acta Crystallogr.* **2009**, 65, 148-155

[27] K. Akhbari, A. Morsali, *Dalton Trans.* **2013**, 42, 4786-4789

[28] M. Mon, E. Tiburcio, J. Ferrando-Soria, R. G. S. Millán, J. A. R. Navarro, D. Armentano, E. Pardo, *Chem. Commun.* **2018**, 54, 9063-9066

[29] J. Xia, B. Zhao, H.-S. Wang, W. Shi, Y. Ma, H.-B. Song, P. Cheng, D.-Z. Liao, S.-P. Yan, *Inorg. Chem.* **2007**, 46, 3450-3458

[30] H. D. Flack, *Acta Cryst.* **1983**, A39, 876-881

[31] a) L. Jia, Y.-C. Hui, Z. Li, H.-L. Sun, Z. Wang, *CrystEngComm.* **2014**, 16, 6483-6490. b) X. Feng, B. Liu, L.-Y. Wang, J.-S. Zhao, J. G. Wang, N. S. Weng, X.-G. Shi, *Dalton Trans.* **2010**, 39, 8038-8049. c) C.-H. Zhan, F. Wang, Y. Kang, J. Zhang, *Inorg. Chem.* **2012**, 51, 523-530. d) X. Feng, R. Li, N. Guo, Y. Sun, S. W. Ng, X. Liu, L. Wang, *Inorg. Chim. Acta.* **2017**, 459, 87-94

[32] L. Sorace, D. Gatteschi, *Lanthanide and Actinides in Molecular Magnetism*. **2015**, Wiley-VCH

[33] M. A. AlDamen, S. Cardona-Serra, J. M. Clemente-Juan, E. Coronado, A. Gaita-Ariño, C. Martí-Gastaldo, F. Luis, O. Montero, *Inorg. Chem.* **2009**, 48, 3467-3479

[34] P. Kalita, A. Malakar, J. Goura, S. Nayak, J. M. Herrera, E. Colacio, V. Chandrasekhar, *Dalton Trans.* **2019**, 48, 4857

[35] Z.-R. Jhu, C.-I. Yang, G.-H Lee, *CrystEngComm.* **2013**, 15, 2456-2465

[36] Q. Tang, Y. L. Yang, N. Zhang, Z. Liu, S. H. Zhang, F. S. Tang, J. Y. Hu, Y. Z. Zheng, F. P. Liang, *Inorg. Chem.* **2018**, 57, 9020-9027

[37] L.-L. Zhu, P. Hu, J.-F. Cao, Y.-H. Zhao, Y.-N. Wu, Y.-X. Zhu, Y. Su, C. Wang, *Polyhedron.* **2018**, 155, 375-381

[38] K. H. J. Buschow, F. R. De Boer, *Physics of magnetism and magnetic materials*. **2003**, Kluwer Academic Publishers

[39] a) S. Shintoyo, T. Fujinami, N. Matsumoto, M. Tsuchimoto, M. Weselski, A. Bienko, J. Mrozinski, *Polyhedron.* **2015**, 91, 28-34. b) N. Roques, S. Perruchas, D.

Maspoch, A. Datcu, K. Wurst, J.-P. Sutter, C. Rovira, J. Veciana, *Inorg. Chim. Acta*. **2007**, 360, 3861-3869

[40] J. Tang, P. Zhang, *Lanthanide Single Molecule Magnets*. **2015**, Springer

[41] a) D. N. Woodruff, R. E. P. Winpenny, R. A. Layfield, *Chem*. *Rev*. **2013**, 113, 5110-5148. b) M. Feng, M.-L. Tong, *Chem*. *Eur*. *J*. **2018**, 24, 7574-7594. c) I. Oyarzabal, A. Rodríguez-Diéguez, M. Barquín, J. M. Seco, E. Colacio, *Dalton Trans*. **2017**, 46, 4278-4286

[42] a) J. Bartolomé, G. Filoti, V. Kuncser, G. Schinteie, V. Mereacre, C. E. Anson, A. K. Powell, D. Prodius, C. Turta, *Phys. Rev. B*. **2009**, 80, 014430. b) I. Mylonas-Margaritis, D. Maniaki, J. Mayans, L. Ciammaruchi, V. Bekiari, C. P. Raptopoulou, V. Psycharis, S. Christodoulou, A. Escuer, S. P. Perlepes, *Magnetochemistry*. **2018**, 4, 45

[43] J.-C. G. Bünzli, C. Piguet, *Chem*. *Soc*. *Rev*. **2005**, 34, 1048-1077

[44] G. Vicentini, L. B. Zinner, J. Zukerman-Schpector, K. Zinner, *Coord*. *Chem*. *Rev*. **2000**, 196, 353-382

[45] A. N. Gusev, M. Hasegawa, G. A. Nishchymenko, V. F. Shul'gin, S. B. Meshkova, P. Doga, W. Linert, *Dalton Trans*. **2013**, 42, 6936-6943

[46] P. Li, Z. Wang, Z. Yang, Q. Guo, *Opt*. *Commun*. **2014**, 332, 83-88

[47] M. Latva, H. Takalo, V.-M. Mukkala, C. Matachescu, J. C. Rodríguez-Ubis, J. Kankare, *J*. *Lumin*. **1997**, 75, 149-169

[48] F. Faschinger, M. Ertl, M. Zimmermann, A. Horner, M. Himmelsbach, W. Schöfberger, G. Knör, H. J. Gruber, *ChemistryOpen*. **2017**, 6, 721-732

[49] M. Shi, C. Ding, J. Dong, H. Wang, Y. Tian, Z. Hu, *Phys*. *Chem*. *Chem*. *Phys*. **2009**, 11, 5119-5123

[50] S. Dasari, A. K. Patra, *Dalton Trans*. **2015**, 44, 19844-19855

[51] S. Biju, D. B. A. Raj, M. L. P. Reddy, B. M. Kariuki, *Inorg*. *Chem*. **2006**, 45, 10651-10660

[52] D. Wang, C. Zheng, L. Fan, J. Zheng, X. Wei, *Synthetic Met*. **2012**, 162, 2063-2068

[53] a) S. Khullar, S. Singh, P. Das, S. K. Mandal, *ACS Omega*. **2019**, 4, 5283-5292. b) G. F. de Sá, O. L. Malta, C. de Mello Donegá, A. M. Simas, R. L. Longo, P. A. Santa-Cruz, E. F. da Silva Jr, *Coord. Chem. Rev*. **2000**, 196, 165-195

[54] K. Zheng, Z. Liu, Y. Jiang, P. Guo, H. Li, C. Zeng, S. W. Ng, S. Zhong, *Dalton Trans*. **2018**, 47, 17432-17440

[55] a) M. Yao, W. Chen, *Anal*. *Chem*. **2011**, 83, 1879-1882. b) T. L. Yang, W. W. Qin, *Indian J. Chem*. **2006**, 45A, 2035-2039

[56] a) M.-L. Gao, X.-M. Cao, Y.-Y. Zhang, M.-H. Qi, S.-M. Wang, L. Liu, Z.-B. Han, *RSC Adv*. **2017**, 7, 45029-45033. b) S.-N. Zhao, X.-Z. Song, M. Zhu, X. Meng, L.-L. Wu, S.-Y. Song, C. Wang, H.-J. Zhang, *RSC Adv*. **2015**, 5, 93-98

[57] Y. Xiao, Y. Cui, Q. Zheng, S. Xiang, G. Qian, B. Chen, *Chem*. *Commun*. **2010**, 46, 5503-5505.

[58] C. Cano-Raya, M. D. F. Ramos, L. F. C. Vallvey, O. S. Wolfbeis, M. Schäferling, *Appl*. *Spectrosc*. **2005**, 59, 1209-121

Final conclusions

Chapter 8: General conclusions

The first part of this thesis has been focused on the preparation of new mononuclear Fe(II) spin crossover materials and study of their thermal, structural and (photo)magnetic properties with the final aim of synthesising multifunctional materials with abrupt spin transitions. Although specific conclusions are included at the end of each chapter, the most significant results will be summarised hereafter:

- The comparative analysis of $[Fe(bpp)_2]^{2+}$ salts with adipate and terephthalate dianions shows that *the rigidity of the building blocks plays a vital role in defining the magnetic properties*. Flexible linkers are presumably able to accommodate the structural rearrangements arising from the spin transition by adjusting their conformation, then, offering a better match with the positive charges of the cationic subnetwork in the high-spin material. Likewise, discontinuous spin transitions are obtained for rigid systems in which the typical *terpyridine embrace* motif is present.

- The comparison of the different magnetic behaviour and crystallinity of anhydrous $[Fe(bpp)_2]^{2+}$ salts combined with adipate dianions provides another example of the *relevance of the thermal treatment used in the desolvation step*. Even though original and rehydrated samples are isostructural, an important remark has been noticed: the desolvation process is easier for the latter material, probably because of the smaller size of the crystallites and/or different arrangement of the crystals that facilitates the loss of water molecules. Contrary to the pristine material, a complete dehydration could be achieved for the rehydrated compound by heating *in situ* in the SQUID with the corresponding footprint in magnetic properties.

- The use of *mononegative linkers* instead of dianions has allowed the *optimisation of the hydrogen-bond connectivity* in $[Fe(bpp)_2]^{2+}$ systems (each cation is surrounded by four anions and each anion by two cations). Although the adventitious presence of solvent molecules in the second iron coordination sphere hinders the prediction of the *hydrogen-bond connectivity*, in some cases it has been achieved and gave rise to crystal networks with a *high degree of cooperativity* and improved magnetic properties.

- Following a basic principle of crystal engineering, the replacement of the rigid terephthalate dianion by the isonicotinate anion has allowed the construction of an *acentric diamond-like crystal lattice*. The anhydrous phase of this material undergoes a phase transition between two ferroelectric structures in the same temperature range in which the spin crossover behaviour is observed. Although the impact of this phase transition in the magnetic properties is small, this is the first time in which a *simultaneous switching of the electric polarisation and magnetic moment of the material* has been accomplished, being a first step towards the construction of electric and magnetic bistable devices for data storage applications. The comparison of this compound with the crystal network containing the nicotinate anion shows that the position of the pyridinic nitrogen atom has a great influence on the connectivity of hydrogen bonds. Thus, leading to materials with different symmetries and properties.

- The replacement of the isonicotinate linker by the isonicotinate N-oxide (isonicNO) anion has yielded two new salts (**5**·2.4H_2O and **6**·5H_2O) in which a deviation from the expected diamondoid-like topology is observed, probably due to the weaker hydrogen-bonding acceptor character of the latter linker compared to the former. Nevertheless, novel and reversible structural rearrangements have been observed to take place in association with abrupt spin transition phenomena in these systems. Specifically, those more important concern a *hydrogen bond isomerisation* and a *proton displacement* between two anions that form a short strong hydrogen bond (SSHB). The first transformation implies a *change in the connectivity between the Fe(II) entities and the anionic sublattice*, indicating that spin transitions are able to trigger transformations that can be difficult to achieve by other means. Instead, the second one opens the way to the possible design of *SCO hydrogen-bonded complexes with ferroelectric properties*.

- Isotopic experiments conducted from the salts containing isonicNO anions show that *hydrogen-bonding influences the spin crossover properties*. In fact, neutron diffraction experiments have allowed the precise location of the nuclei of hydrogen atoms and unambiguously verify that *hydrogen bonds found in the second iron coordination sphere are stronger for the low-spin species in comparison to those in the high-spin state*, a statement previously noticed for some SCO Fe(II) compounds that can be explained by a simple electrostatic model.

Therefore, there is a clear correlation between hydrogen-bonding strength and iron(II) spin state. Furthermore, it has been possible to *trace the interaction path between the iron centres in the HS/LS phase* of **6**·5H_2O *based on the hydrogen bond cooperativity*. The photoinduced high-spin (PIHS) phase and the metastable phase obtained after partial relaxation of the PIHS phase have been characterised, being the analysis of the *atomic displacement parameters* of the atoms present in the latter structure consistent with this interaction path (with higher values for those atoms that are involved in the H-bonding cooperative pathway and undergo relevant displacement upon SCO).

- The widely known dependence of the SCO on the degree of hydration is also observed in all the salts synthesised during this part of the thesis, which can be used in *humidity sensing applications*.

The second part of this thesis is based on the coordination chemistry of a new family of chelating ethynyl-bridged picolinate ligands designed with the aim of increasing the stability of current coordination complexes in water at extreme pH values. The most relevant results can be summarised as follows:

- *Sonogashira-type cross-coupling reactions* have been successfully employed in the synthesis of *polytopic ligands* that consist of a rigid central arylene platform, ethynylene spacers and terminal *chelating picolinate subunits*. In some cases, a second non-chelating pyridine or benzoate unit is also included.

- Copper(II) coordination polymers in which the metal centres are bridged by double *syn*, *anti*- out-of-plane picolinate groups have been obtained. This connectivity provides very *weak overlap between magnetic orbitals*, resulting in almost *insignificant exchange interactions* between the Cu(II) ions. This highlights that higher overlap between the magnetic orbitals is required in order to increase the interaction between the copper centres.

- Luminescent monometallic coordination complexes based on Zn(II) and Eu(III) ions have been prepared using these chelating anionic ligands. Some of them exhibit striking emission properties under irradiation with an appropriate light source, as a consequence of the different planar nature of the ligands involved when ligand-based emission is

involved. Sensing experiments reveal that they can be selectively used as *luminescent probes in aqueous medium towards Fe^{3+} and nitrobenzene detection*. The selective detection performance is based on *luminescence quenching* attributed to resonance energy transfer between the ligands and the quenchers, together with a competitive excitation absorption process between them. These compounds also show a *high stability* in aqueous medium in a wide pH range, which allows their practical use in harsh conditions.

- Finally, a 1D iron(II) complex with high thermal and aqueous stability (in pH solutions ranging from 1 to 12) has been prepared from a novel bisbidentate ethynyl-bridged picolinate ligand. Preliminary results show that it is a promising *catalyst* for the *oxidation of cyclohexane* at ambient pressure and temperature, with *high selectivity for cyclohexanone.*

Resum de la Tesi Doctoral

Introducció

La immensa varietat de blocs de construcció que la química molecular posa al nostre abast ens permet dissenyar una gran quantitat de sistemes útils per a la fabricació de dispositius amb aplicacions tecnològiques basades en processos de reconeixement i commutació molecular. Concretament, els interruptors moleculars binaris són un destacat exemple de sistemes biestables que poden ser revertits entre dos estats estables diferents (ON/OFF) gràcies a l'aplicació d'un estímul extern com pot ser un canvi de temperatura, pH, pressió o llum. Dins d'aquest camp, destaquen els compostos de transició d'espín que poden ser revertits entre dos estats caracteritzats per diferents configuracions electròniques de manera reversible i detectable gràcies al canvi en les seues propietats físico-químiques. Concretament, la transició d'espín pot ser considerada com una transferència electrònica entre els orbitals $e_g \leftrightarrow t_{2g}$ que ocasiona un canvi en les distàncies metall-lligand i angles d'enllaç de l'octaedre de coordinació. Tanmateix, aquesta conversió d'espín comporta la transformació entre un estat diamagnètic (S = 0, baix espín) i una configuració paramagnètica (S = 2, alt espín) amb la corresponent repercussió en les propietats magnètiques i òptiques del material (l'estat de baix espín normalment presenta una coloració intensa com violeta o roig obscur, mentre que l'estat d'alt espín exhibeix una tonalitat més clara com blanc o groc). Aquest fenomen pot ocórrer tant en dissolució com en l'estat sòlid, encara que en el primer cas el procés és merament molecular degut a l'aïllament de les molècules (transició gradual). Contràriament, en l'estat sòlid les variacions estructurals ocasionades com a conseqüència d'aquesta transició electrònica poden ser propagades mitjançant interaccions elàstiques d'un centre metàl·lic als veïns i així successivament al llarg del si del material. En aquesta situació, la transició s'anomena cooperativa (abrupta) i ve acompanyada de discontinuïtats en les propietats òptiques i magnètiques del compost. A més a més, algunes transicions cooperatives tenen lloc amb histèresi tèrmica, la qual cosa permet que aquests sistemes puguen emmagatzemar informació a nivell molecular i justifica el interès focalitzat en l'estudi de les transicions d'espín.

En termes generals, per tal d'augmentar la cooperativitat dels sistemes i, per tant, el seu potencial ús com interruptors moleculars, tres estratègies han sigut desenvolupades. La primera aproximació es basa en connectar els centres metàl·lics mitjançant enllaços de coordinació. La segona estratègia se centra en afavorir la formació d'enllaços d'hidrogen forts gràcies a l'adequada elecció dels lligands i dels acceptors d'enllaç d'hidrogen. Finalment, l'establiment d'interaccions d'apilament de tipus π-π entre els anells aromàtics també ha

demostrat ser una eficient ferramenta per a l'obtenció de sistemes amb un elevat grau de cooperativitat. En aquesta tesi, nous complexos de transició d'espín de ferro(II) han sigut sintetitzats emprant les dos últimes aproximacions que fan ús de l'augment de les interaccions intermoleculars entre els centres metàl·lics. En particular, ens hem centrat en els sistemes $[Fe(bpp)_2]X_n$ (bpp = 2,6-(bis-pirazol-3-il-piridina), n = 1 si X és un anió divalent i n = 2 si X és un anió monopositiu) ja que la major part dels complexos de transició d'espín basats en l'ió metàl·lic Fe^{2+} presenten una esfera de coordinació FeN_6 i el lligand bpp ha generat un gran nombre de sistemes amb una àmplia gamma de comportaments. En general, els materials solvatats són diamagnètics a temperatura ambient i la conversió a l'estat d'alt espín té lloc a majors temperatures. En la majoria dels casos, la desolvatació de les mostres ocorre mentre les transicions tenen lloc, el que comporta una conversió ràpida a l'estat paramagnètic. Les fases anhidres normalment exhibeixen transicions abruptes amb histèresi tèrmica gràcies a l'establiment d'enllaços d'hidrogen entre els fragments –NH dels lligands bpp i els anions presents en l'estructura cristal·lina. Conseqüentment, és ben sabut que les propietats magnètiques d'aquestes sals depenen de la segona esfera de coordinació del ferro (molècules de dissolvent i anions que actuen com acceptors d'enllaç d'hidrogen) i del seu grau de solvatació (que afecta a la propagació de les interaccions intermoleculars).

Un canvi de temperatura és l'estímul extern més freqüentment emprat per a desencadenar una transició d'espín. Tanmateix, també s'ha aconseguit modificar l'estat d'espín d'alguns sistemes amb un alt grau de cooperativitat a baixes temperatures mitjançant irradiació amb un làser de llum adequada. Aquest és l'anomenat efecte *LIESST* (de l'anglès *Light Induced Excited Spin State Trapping effect*) que solen presentar les sals $[Fe(bpp)_2]^{2+}$ amb un temps de vida mitjana dels estats metastables fotoexcitats superior als d'altres sistemes reportats. No obstant això, per damunt dels 50 K la relaxació a l'estat de baix espín és molt ràpida i la informació magnètica es perd. Per tant, encara s'han de desenvolupar sistemes amb temps de vida mitjana dels estats d'alt espín fotoinduïts grans en un interval de temperatures que permeta la seua aplicació real. Recentment, s'han sintetitzat complexos que presenten millores en les seues propietats fotomagnètiques, suposadament gràcies a l'existència d'una geometria altament distorsionada en la fase d'alt espín que estabilitzaria l'estat metastable fotoinduït. Així doncs, una comprensió exhaustiva dels canvis estructurals induïts per la llum podria ser la clau per obtindre finalment un complex molecular operatiu en aquest sentit. Cal mencionar també que encara que el nombre de complexos de transició d'espín que presenten efecte LIESST és prou elevat, els estudis estructurals de totes les fases involucrades són bastant

escassos. Altra manera d'atrapar un sistema en un estat d'alt espín metastable a baixes temperatures és mitjançant l'anomenat efecte TIESST (de l'anglès *Thermally Induced Excited Spin State Trapping effect*). Aquest consisteix en gelar ràpidament (en qüestió de segons) el compost des d'una temperatura en la qual la fase d'alt espín és l'estat estable. En alguns exemples, les fases metastables obtingudes per *quenching* tèrmic o fotoinduïdes són idèntiques i tan sols presenten xicotetes diferències respecte a la cinètica de relaxació. Per contra, en altres sistemes s'han observat diferències estructurals considerables entre les dos fases metastables.

Encara més important és el fet que s'han arribat a sintetitzar materials multifuncionals que combinen la transició d'espín amb una altra propietat d'interès (ordenament magnètic, conductivitat elèctrica, fluorescència, porositat i/o reconeixement molecular), on la conversió d'espín pot modular, inhibir, millorar o no tindre cap influència sobre la segona funcionalitat. En particular, els compostos de transició d'espín poden generar anomalies dielèctriques degut a la diferent distribució de les càrregues positives i negatives del material en les fases d'alt i de baix espín, i constituir així candidats adequats per a la coexistència d'ambdues propietats d'una manera sincronitzada. Açò permetria la fabricació de materials capaços de detectar un canvi de l'estat magnètic mitjançant una senzilla mesura capacitiva, la qual cosa és útil per al processament de les noves tecnologies. De fet, les transicions de fase estructurals associades a les conversions d'espín poden implicar desplaçaments de les molècules que generen canvis en els dipols elèctrics i l'aparició de polarització elèctrica en l'estructura. Aquesta polarització elèctrica espontània pot ser revertida per un camp elèctric i és una característica dels materials ferroelèctrics, que són un subgrup dels materials dielèctrics. El progrés obtingut en aquest context ha sigut limitat fins ara a pesar que moltes transicions d'espín estan associades a transicions de fase estructurals. Probablement açò és degut al fet que els grups espacials en els quals pot cristal·litzar la fase ferroelèctrica són reduïts i tan sols unes poques transformacions estructurals satisfan els requeriments cristal·logràfics perquè una transició ferroelèctrica tinga lloc (transició entre una fase paraelèctrica a alta temperatura i una fase ferroelèctrica a baixa temperatura que ha de cristal·litzar en un dels deu grups puntuals polars, a banda de pertànyer el grup espacial corresponent a un subgrup del de la fase paraelèctrica).

En la segona part d'aquesta tesi doctoral, pel que fa al reconeixement molecular, una gran quantitat de sistemes luminescents han sigut elaborats amb la finalitat de detectar compostos nitroaromàtics i ions metàl·lics com Fe^{3+}. En

ambdós casos, es tracta de residus contaminants que s'acumulen de forma alarmant en les aigües i en el sòl, per tant, es tracta d'un tema urgent que requereix poder detectar la presència d'aquestes espècies a nivell traça. Els sistemes luminescents són especialment prometedors en aquest context, ja que presenten temps de resposta menors i major selectivitat i sensitivitat en comparació amb altres tècniques de reconeixement molecular. A més a més, les interaccions supramoleculars entre els complexos de coordinació i els analits poden augmentar o minvar la resposta luminescent i generar així un dispositiu amb un estat ON i altre OFF, respectivament, que facilita la detecció a simple vista gràcies als canvis en l'emissió del material.

Dins d'aquest camp, els ions lantànids representen una bona alternativa gràcies a les seues propietats luminescents úniques (bandes d'emissió molt estretes i temps de vida mitjana dels estats excitats molt grans). Tanmateix, els complexos metàl·lics que contenen ions d^{10} com ara Zn^{2+} són altres candidats que han demostrat ser extremadament eficients en aquesta tasca. Malgrat això, la majoria dels compostos de coordinació que s'han desenvolupat en aquest context estan construïts a partir de lligands politòpics basats en carboxilats que són fàcilment hidrolitzables en medi aquós i/o en condicions de pH extremes. Conseqüentment, els polímers de coordinació resultants presenten un elevat grau de labilitat que limita les seues aplicacions. Una de les estratègies més comunament utilitzades per tal d'augmentar l'estabilitat d'aquests sistemes se centra en l'ús d'ions metàl·lics d'elevada valència com ara Ti^{4+}, Zr^{4+}, Al^{3+}, Fe^{3+} i Cr^{3+}, la qual cosa ha generat noves famílies de compostos robustos. D'altra banda, també s'han emprat lligands aniònics quelants com catecolats i dicarboxilats dioxidobenzènics per tal de dissenyar nous materials amb elevada estabilitat. Es tracta d'una alternativa escassament investigada en comparació a la mencionada anteriorment i és on s'emmarca aquesta segona part. Concretament, hem seleccionat lligands segmentats per triples enllaços que contenen com a grup funcional quelant l'anió picolinat, ja que aquest és capaç de coordinar pràcticament a qualsevol tipus de metall. Paral·lelament, els triples enllaços proporcionen connectivitat lineal, rigidesa i deslocalització electrònica que afavoreixen les propietats luminescents dels sistemes resultants, alhora que faciliten la predictibilitat en la seua estructura cristal·lina.

Els polímers de coordinació també presenten potencials aplicacions en el camp de la catàlisi, on són emprats com a catalitzadors tant en fase homogènia com heterogènia. Els catalitzadors heterogenis presenten millores pel que fa a la seua separació i reciclatge, a banda de presentar una millor selectivitat que els catalitzadors homogenis corresponents en algunes ocasions. L'oxidació

selectiva d'enllaços C–H d'alcans és una àrea prometedora per a la indústria química degut a la gran quantitat de matèries primeres fòssils existents i, en particular, destaca l'oxidació de ciclohexà a ciclohexanol i ciclohexanona. Açò es deu al fet que aquesta mescla de productes es pot utilitzar en la química industrial del petroli, així com per generar àcid adípic i ε-caprolactama que són dos materials essencials en la preparació de Nylon-6,6 i Nylon-6, respectivament. Actualment, la majoria dels processos industrials estan basats en l'ús de catalitzadors solubles de metalls de transició que requereixen una etapa addicional de separació i altes temperatures i pressions de treball. Tanmateix, s'obté una elevada selectivitat per a la mescla ciclohexanol/ciclohexanona però amb una conversió molt baixa. Conseqüentment, és necessari desenvolupar nous catalitzadors que milloren les conversions actuals i els polímers de coordinació han demostrat ser útils en aquest context. En particular, els polímers més estudiats són els de ferro gràcies a la seua disponibilitat, baixa toxicitat i al fet que aquest ió es troba present en encimes de diferents sistemes biològics que catalitzen transformacions oxidatives d'enllaços C–H. A més a més, l'àcid picolínic ha sigut afegit com a lligand a un catalitzador de ferro i ha donat lloc a un augment en la velocitat d'oxidació de ciclohexà mentre que es manté la mateixa selectivitat i concentració de productes oxidats que en el procés industrial.

Objectius

La primera part d'aquesta tesi (capítols 1-3) versa sobre els compostos de transició d'espín que han sigut objecte d'estudi des del seu descobriment degut al seu potencial per a la fabricació de dispositius optoelectrònics i a la possibilitat de dissenyar diversos materials multifuncionals. El principal objectiu d'aquest treball és fer ús de l'elevada direccionalitat dels enllaços d'hidrogen per a la preparació de noves xarxes supramoleculars de ferro(II) on la transició d'espín es combina amb una segona propietat física o amb alguna transformació estructural d'interés mitjançant l'adequada selecció de la xarxa aniònica. Açò implica estudiar en detall totes les redistribucions estructurals que acompanyen la transició d'espín tèrmica i fotoinduïda. Els objectius específics per tal d'assolir aquest propòsit, així com altres addicionals, es detallen a continuació:

I. Anàlisi de la influència de la rigidesa dels contraanions i del grau d'hidratació en sals de cations $[Fe(bpp)_2]^{2+}$ sobre la transició d'espín. Per dur a terme aquest estudi, dos anions dicarboxilats, un flexible i l'altre rígid, que presenten una connectivitat i longitud anàlogues han sigut seleccionats.

II. Demostració de la importància del tractament tèrmic emprat en el procés de deshidratació d'aquests materials i anàlisi de la seua repercussió sobre les propietats magnètiques i la cristal·linitat del producte final.

III. Comparació de les propietats magnètiques i de l'estructura cristal·lina de les sals construïdes amb anions mononegatius i amb dianions per tal de verificar que la optimització dels enllaços d'hidrogen entre els donadors i els acceptors d'aquestes interaccions és de vital importància per a propagar els canvis estructurals associats a la conversió d'espín.

IV. Combinació de la sal de transició d'espín $[Fe(bpp)_2]^{2+}$ amb anions acèntrics piridinacarboxilat per tal de donar lloc a xarxes cristal·lines de tipus diamant no centrosimètriques que puguen exhibir propietats ferroelèctriques seguint un principi bàsic de l'enginyeria cristal·lina. Tanmateix, se seleccionen dos anions isomèrics piridinacarboxilat que difereixen en la posició del nitrogen piridínic i es pretén determinar quina és la seua influència sobre les propietats estructurals i magnètiques del material.

V. Investigació de l'habilitat dels sistemes $[Fe(bpp)_2]^{2+}$ per a generar estructures no centrosimètriques basades en topologies semblants a la del diamant mitjançant la modulació de la llargària del connector aniònic i estudi de les seues propietats. Concretament, s'ha seleccionat un anió piridinacarboxilat que presenta un àtom d'oxigen addicional respecte als anteriors.

VI. Preparació d'un complex supramolecular de Fe(II) que combina la sal catiònica $[Fe(bpp)_2]^{2+}$ de transició d'espín amb un cocristall que conté un àcid piridinacarboxílic en les seues formes lliure i desprotonada com a possible font de ferroelectricitat. Així mateix, es pretén estudiar el desplaçament protònic entre els dos acceptors d'enllaç d'hidrogen i determinar quina és la influència d'aquesta migració sobre la ruptura de simetria i la transició d'espín del material.

VII. Dur a terme experiments isotòpics per tal de determinar si el canvi en la força dels enllaços d'hidrogen afecta a les propietats de transició d'espín dels materials.

VIII. Comparació dels paràmetres d'enllaç d'hidrogen en la segona esfera de coordinació del ferro obtinguts a partir de dades de difracció de neutrons i de difracció de raigs-X.

L'objectiu principal de la segona part d'aquesta tesi (capítols 4-7) és millorar l'estabilitat en medi aquós dels compostos de coordinació emprats

actualment per al reconeixement molecular de compostos nitroaromàtics i ions Fe^{3+}, així com millorar l'activitat catalítica en l'oxidació del ciclohexà. Per tal d'aconseguir aquests propòsits, els següents objectius particulars han sigut establerts:

IX. Síntesi i caracterització d'una nova família de lligands politòpics segmentats per triples enllaços que contenen com a grups funcionals quelants l'anió picolinat. Complementàriament, alguns d'aquests lligands presenten un segon grup funcional piridina o àcid carboxílic.

X. Estudi de la química de coordinació d'aquests nous lligands amb ions Zn(II) (gràcies al seu extens ús en aplicacions de fluorescència modular), Fe(II) (pel seu paper fonamental en la preparació de catalitzadors útils en reaccions d'oxidació d'alcans) i Cu(II) (degut a les seues propietats magnètiques). Així mateix, també és objecte d'aquesta tesi dur a terme la caracterització estructural i l'anàlisi de l'estabilitat tèrmica i a diferents valors de pH de les sals obtingudes.

XI. Investigació de la química de coordinació d'aquesta nova família de lligands amb ions trivalents lantànids degut a les seus extraordinàries propietats luminescents, així com abordar la seua caracterització estructural, magnètica i l'anàlisi de la seua estabilitat.

Metodologia

En aquesta tesi s'han utilitzat diferents mètodes sintètics i tècniques de caracterització que es detallen a continuació:

Pel que fa als compostos de transició d'espín (primera part de la tesi), tots han sigut construïts a partir del lligand bpp. La síntesi d'aquest lligand té lloc en dos etapes segons el procediment descrit per Lin i Lang. La primera etapa és una reacció de condensació de Claisen-Schmidt en la qual es genera un intermedi carbonílic α,β-insaturat. Posteriorment, dos reaccions consecutives d'atac nucleofílic tenen lloc, la qual cosa genera l'anell pirazol després de la pèrdua de dimetilamina i la corresponent ciclació. Aquest lligand ha sigut caracteritzat per tècniques d'espectroscòpia infraroja, anàlisi elemental, ressonància magnètica nuclear de protó i de carboni i espectrometria de masses.

A partir del lligand bpp, la complexació amb el sulfat o el clorur de Fe(II) s'ha realitzat en recipients tipus Schlenk i en una atmosfera d'argó per tal d'evitar l'oxidació de Fe(II) a Fe(III) en medi $MeOH/H_2O$. D'altra banda, les diferents sals precursores de plata o bari han sigut preparades a partir de la

reacció directa de les sals metàl·liques corresponents i els anions d'interés en les seues formes àcides. En alguna ocasió ha sigut necessari afegir hidròxid de potassi com a base i calfar per tal d'afavorir la formació dels productes desitjats. Totes aquestes sals precursores han sigut caracteritzades per tècniques d'espectroscòpia infraroja, anàlisi elemental i termogravimetria. Finalment, aquestes sals han sigut combinades amb el sulfat o amb el clorur de $[Fe(bpp)_2]^{2+}$ a temperatura ambient o a temperatures lleugerament superiors. En aquestes reaccions de metàtesi, es forma clorur de plata o sulfat de bari que precipiten immediatament i poden ser separats per filtració. D'aquesta manera no queden en el medi de reacció espècies que puguen interferir en la formació de les xarxes supramoleculars d'interés i aquestes cristal·litzen mitjançant evaporació lenta de la dissolució resultant. Aquests materials han sigut caracteritzats per tècniques d'espectroscòpia infraroja, anàlisi elemental, termogravimetria, calorimetria diferencial d'escombratge, difracció de raigs-X de monocristall i difracció de raigs-X en pols. Les seues propietats magnètiques s'han estudiat amb un magnetòmetre SQUID (de l'anglés *Superconducting Quantum Interference Device*) equipat amb un làser que permet la irradiació de les mostres amb diferents longituds d'ona. Ocasionalment, s'han emprat tècniques de difracció de neutrons, experiments de fotocristal·lografia a molt baixes temperatures, espectroscòpia Mössbauer, microscòpia PFM (de l'anglès *Piezoresponse Force Microscopy*), experiments SHG (de l'anglès *Second Harmonic Generation*) i de permitivitat dielèctrica.

Respecte a la segona part de la tesi, la família de lligands politòpics basats en grups funcionals picolinat han sigut sintetitzats aplicant reaccions d'acoblament tipus Sonogashira que ens han permés obtindre els èsters corresponents. En totes les reaccions hem emprat un catalitzador de pal·ladi(0) ($Pd(PPh_3)_4$, on PPh_3 és la trifenilfosfina), trimetilamina com a base i tetrahidrofuran anhidre (THF) com a solvent. En algun cas ha sigut necessari dur a terme una primera reacció addicional d'acoblament on hem emprat una sal de Pd(II) com a catal·litzador ($PdCl_2$) i iodur de coure(I) com a co-catalitzador per tal de preparar un precursor adient. La manipulació dels reactius i del solvent sempre ha tingut lloc dins d'una caixa seca. Tècniques de cromatografia en columna han sigut aplicades en la majoria dels casos per tal de purificar els èsters obtinguts. A continuació, els àcids corresponents han sigut aïllats mitjançant hidròlisi bàsica amb hidròxid de liti en medi THF/H_2O seguida per protonació amb àcid clorhídric. Els èsters i els productes en les seues formes àcides han sigut caracteritzats per tècniques d'espectroscòpia infraroja, anàlisi elemental, ressonància magnètica nuclear de protó i de carboni i espectrometria de masses.

D'altra banda, tots els polímers de coordinació descrits en aquest treball han sigut preparats a partir de mètodes solvotermals que han permés la seua obtenció en forma de monocristalls. Açò implica la barreja directa del lligand orgànic politòpic i de la sal del metall en qüestió en un vial tancat que s'introdueix en un forn a temperatures superiors a la temperatura d'ebullició del solvent. La mescla de solvents més comunament emprada en aquest treball ha sigut dimetilformamida (DMF)/H_2O. En algunes ocasions, ha sigut necessari afegir un modulador àcid (àcid nítric o àcid acètic) o bàsic (piridina) per tal d'aconseguir un adequat grau de cristal·linitat en el compost de coordinació i evitar la formació de fases addicionals. Aquests materials han sigut caracteritzats per tècniques d'espectroscòpia infraroja, anàlisi elemental, termogravimetria, difracció de raigs-X de monocristall i difracció de raigs-X en pols. Les propietats magnètiques d'alguns d'aquests compostos s'han estudiat amb un magnetòmetre SQUID i amb un espectròmetre de ressonància paramagnètica electrònica (EPR). Les propietats luminescents dels complexos que exhibeixen aquestes característiques han sigut estudiades mitjançant mètodes espectroscòpics d'absorció i d'emissió, amb un espectrofotòmetre UV/VIS i un fluorímetre.

Resultats i Conclusions

Durant el desenvolupament de la primera part d'aquesta tesi, s'han obtingut sis xarxes supramoleculars de $[Fe(bpp)_2]^{2+}$ amb transició d'espín basades en l'enllaç d'hidrogen i el seu estudi permet concloure que aquestes interaccions són eficients per propagar els canvis estructurals entre els centres metàl·lics i donar lloc a transicions d'espín amb un alt grau de cooperativitat quan s'optimitza la xarxa d'interaccions entre els cations i els anions. A més a més, aquests complexos de ferro(II) han demostrat ser bons candidats per a la construcció de materials multifuncionals i, concretament, s'han obtingut compostos que combinen la transició d'espín amb la ferroelectricitat o amb una migració de protó. Així mateix, també s'han observat importants canvis estructurals com la isomerització d'un enllaç d'hidrogen o la formació i ruptura d'enllaços d'hidrogen associats a la conversió d'espín. Les conclusions extretes d'aquest treball es detallen a continuació d'acord als seus corresponents objectius:

I. El capítol 2 mostra els resultats de l'anàlisi comparatiu de dos sals que combinen el catió $[Fe(bpp)_2]^{2+}$ amb dos anions dicarboxilat que actuen com acceptors d'enllaç d'hidrogen: l'adipat ($C_6H_8O_4$) que és flexible i el tereftalat ($C_8H_4O_4$) que és rígid ($[Fe(bpp)_2](C_6H_8O_4)\cdot 4H_2O$ (**1**·$4H_2O$) i

$[Fe(bpp)_2](C_8H_4O_4)\cdot 5H_2O$ (**2**$\cdot 5H_2O$), respectivament). Aquest estudi mostra que *per tal d'observar una conversió d'espín, és necessari deshidratar* ambdós materials, fet que està d'acord amb resultats previs. A més a més, aquest estudi revela clarament que *la rigidesa dels anions té un paper fonamental en les propietats magnètiques i en la cristal·linitat del material.* Concretament, s'ha observat que la sal que conté anions adipat es converteix en un material amorf després del procés de desolvatació i que no presenta transició d'espín. Contràriament, la sal construïda amb anions tereftalat manté la cristal·linitat, exhibeix una transició d'espín en dos etapes i amb relativa cooperativitat en les mateixes condicions i efecte LIESST amb una *T*(LIESST) de 63 K. La pèrdua de cristal·linitat és deguda al fet que l'anió adipat pot presentar nombroses conformacions en la fase d'alt espín, ja que la seua flexibilitat li permet acomodar els canvis estructurals associats a la transició d'espín. Tanmateix, aquest és un exemple més de que transicions d'espín abruptes són obtingudes en sistemes construïts a partir d'anions rígids, com l'anió tereftalat, que presenten el motiu estructural *terpyridine embrace*.

II. Tot seguit, s'han obtingut dos fases anhidres diferents de la sal que combina cations $[Fe(bpp)_2]^{2+}$ amb anions adipat (**1**$\cdot 4H_2O$) en funció del tractament tèrmic emprat. Aquestes dos fases difereixen en les seues propietats magnètiques i presenten diferents graus de cristal·linitat (la fase desolvatada a major temperatura és amorfa i roman en l'estat d'alt espín durant tot l'interval de temperatura d'estudi, mentre que la fase deshidratada a menor temperatura conserva la cristal·linitat i presenta una transició d'espín gradual), la qual cosa posa de manifest *que les condicions tèrmiques utilitzades en la desolvatació d'aquests compostos influeixen notablement en les seues propietats.*

III. En el capítol 3 s'utilitzen *anions mononegatius* de tipus piridinacarboxilat com acceptors d'enllaç d'hidrogen enlloc d'anions dicarboxilat. Aquest canvi fa possible l'*optimització de la connectivitat dels enllaços d'hidrogen* (cada centre metàl·lic s'envolta de quatre anions i cada anió es rodeja de dos centres de ferro) entre els cations i els anions, la qual cosa facilita la propagació de les modificacions estructurals associades a la conversió d'espín entre els centres metàl·lics i, d'aquesta manera, *augmenta la seua cooperativitat*.

IV. Particularment, l'ús de l'anió acèntric isonicotinat (isonic) ha donat lloc a la formació d'una estructura cristal·lina no centrosimètrica de tipus diamant ($[Fe(bpp)_2](isonic)_2\cdot 2H_2O$ (**3**$\cdot 2H_2O$)). La fase anhidra d'aquest material presenta una t*ransició de fase entre dos estructures ferroelèctriques en el mateix*

interval de temperatura en el qual s'observa la transició d'espín. Encara que la repercussió d'aquesta transició de fase en les propietats magnètiques del material és menuda (es tracta d'una transició d'espín incompleta i gradual), aquest és *el primer compost* en el qual s'ha observat un canvi simultani de polarització elèctrica i d'estat d'espín, la qual cosa representa un avanç considerable cap a la fabricació de dispositius biestables que combinen funcionalitats elèctriques i magnètiques. També s'ha emprat l'anió nicotinat (nic) amb la finalitat de construir un material amb aquesta doble funcionalitat i determinar la influència de la posició de l'àtom de nitrogen piridínic sobre les propietats del material. No obstant això, la impossibilitat de predir la participació de les molècules de solvent en les interaccions per enllaç d'hidrogen i la menor basicitat d'aquest connector respecte a l'anió isonicotinat ha donat lloc a una modificació considerable de la xarxa d'enllaços d'hidrogen i una estructura diferent a la del diamant ha sigut formada ($[Fe(bpp)_2](nic)_2 \cdot 4H_2O$ (**4**·$4H_2O$)). Aquest material presenta el típic motiu estructural *terpyridine embrace*, una transició d'espín amb relativa cooperativitat i histèresi tèrmica i efecte LIESST parcial amb un valor de *T*(LIESST) de 56 K. Per tant, es pot concloure que la posició de l'àtom de nitrogen afecta dramàticament *la connectivitat dels enllaços d'hidrogen que defineixen la simetria i les propietats del material resultant.*

V. El reemplaçament de l'anió isonicotinat per l'anió N-òxid isonicotinat (isonicNO) en el sistema $[Fe(bpp)_2]^{2+}$ dona lloc a la formació d'una estructura cristal·lina que es desvia de la topologia de diamant esperada ($[Fe(bpp)_2](isonicNO)_2 \cdot 2.4H_2O$ (**5**·$2.4H_2O$)), a pesar de ser un conector també lineal. Probablement açò és degut al fet que el grup N-òxid presenta una menor capacitat acceptora d'enllaç d'hidrogen que el grup piridina. A pesar d'això, aquesta sal és molt interessant ja que presenta una transició d'espín completa i extremadament abrupta prop de temperatura ambient, la qual pot ser induïda tèrmicament i també mitjançant irradiació amb llum roja (amb un valor *T*(LIESST) de 68 K). A més a més, determinacions estructurals a diferents temperatures mostren clarament que una *isomerització d'un enllaç d'hidrogen* té lloc *com a conseqüència de la transició d'espín*. Es tracta de la primera vegada en la que s'observa una transformació estructural d'aquest tipus que implica un reordenament dràstic de la connectivitat entre les xarxes aniòniques i catiòniques, la qual cosa indica que la transició d'espín és capaç de desencadenar transformacions que poden ser difícils d'assolir per altres vies. Tanmateix, s'ha pogut determinar l'estructura cristal·lina de la fase d'alt espín fotoinduïda i és isostructural amb la fase d'alt espín estable a alta temperatura i consistent amb la reisomerització d'aquest enllaç d'hidrogen.

VI. La sal de transició d'espín que combina el catió $[Fe(bpp)_2]^{2+}$ amb l'anió N-òxid isonicotinat en les seues formes desprotonada i lliure ($[Fe(bpp)_2](isonicNO)_2 \cdot HisonicNO \cdot 5H_2O$ (**6**$\cdot 5H_2O$)) cristal·litza en un grup espacial centrosimètric a totes les temperatures d'estudi, la qual cosa evita que puga presentar propietats ferroelèctriques. No obstant això, aquest compost presenta una transició d'espín completa en dos etapes que comporta una *transició de fase cristal·logràfica amb trencament de simetria i formació d'una fase mixta 50% alt espín i 50% baix espín*. Aquesta fase mixta és estable en un rang determinat de temperatures i esdevé metastable a menors temperatures on la fase 100% baix espín és l'estable, amb restabliment de la simetria original. Estudis de difracció de neutrons mostren que en aquesta sal hi ha un protó que es troba enmig de dos anions que estableixen un enllaç d'hidrogen fort i aquest ocupa una posició central en la fase d'alt espín. Al refredar, el compost transita a la fase mixta on el contingut de la cel·la unitat es dobla i existeixen dos subxarxes equivalents a l'observada a alta temperatura, una associada al centre de ferro de baix espín i l'altra al centre de ferro d'alt espín. *El protó que pertany a la subxarxa de baix espín s'ha desplaçat al llarg de l'enllaç d'hidrogen fort, mentre que l'altre roman en una posició central.* Així mateix, en la fase 100% baix espín la simetria es restableix i el protó en qüestió es troba encara desplaçat en el mateix sentit que en la subxarxa de baix espín de la fase mixta. Per tant, *la transició d'espín desencadena la migració d'aquest protó.* Aquest exemple mostra que els canvis estructurals associats a la transició d'espín poden tindre una repercussió important en zones ben allunyades dels centres metàl·lics i il·lustra la possibilitat de dissenyar compostos de transició d'espín ferroelèctrics basats en enllaços d'hidrogen. A més a més, aquest complex exhibeix efecte LIESST amb una relaxació en dos etapes fins assolir la fase completament baix espín (valors de *T*(LIESST) de 68 K i 76 K), i s'han pogut caracteritzar estructuralment les fases d'alt espín fotoinduïda (isostructural a la fase d'alt espín estable a alta temperatura) i mixta després de relaxació parcial. També s'ha observat la formació d'una barrera energètica d'activació fotoinduïda per a la migració del protó.

VII. Els *experiments isotòpics* realitzats amb les sals construïdes a partir de l'anió N-òxid isonicotinat (**5**$\cdot 2.4H_2O$ i **6**$\cdot 5H_2O$) revelen que *les propietats magnètiques d'aquests materials depenen de les interaccions per enllaç d'hidrogen* i s'observa l'estabilització de la fase d'alt espín en deuterar les mostres. De fet, l'estudi per difracció de neutrons de la sal **6**$\cdot 5H_2O$ (on tenim dos centres de ferro(II) amb idèntica composició de la segona esfera de coordinació i a la mateixa temperatura) mostra indubtablement que *els enllaços d'hidrogen presents en la segona esfera de coordinació del ferro són més forts per a les espècies*

que es troben en la subxarxa de baix espín en comparació amb aquelles interaccions anàlogues que s'estableixen en la subxarxa d'alt espín. Conseqüentment, hi ha una *clara correlació entre la força dels enllaços d'hidrogen i l'estat d'espín dels ions Fe(II).* Tanmateix, ha sigut possible traçar el camí d'interacció entre els centres de ferro en la fase mixta en base a la cooperativitat dels enllaços d'hidrogen. L'anàlisi dels paràmetres de desplaçament dels àtoms presents en la fase metastable obtinguda després de relaxació parcial de la fase d'alt espín fotoinduïda és coherent amb aquest (amb valors més alts per als àtoms involucrats en el camí definit per la cooperativitat dels enllaços d'hidrogen i que, per tant, sofreixen un desplaçament major després de la transició d'espín).

VIII. L'anàlisi realitzat a partir de les dades de difracció de neutrons i de raigs-X per al complex **6**·5H_2O revela que no hi ha cap diferència significativa pel que fa a les coordenades de tots els àtoms que no són hidrògens. *Les distàncies N–H obtingudes a partir de les dades de raigs-X són 0.1-0.2 Å menors que aquelles determinades mitjançant les dades de neutrons*. Complementàriament, *les distàncies H···O estan sobrevalorades amb el mateix valor.* A més a més, en augmentar la distància entre els heteroàtoms, també ho fa la divergència entre les dades de difracció de raigs-X i de neutrons.

Respecte a la segona part d'aquesta tesi, s'han preparat satisfactòriament huit lligands polipicolinat segmentats per triples enllaços. S'ha explorat la química de coordinació d'alguns d'aquests lligands i s'ha aconseguit preparar un complex de Zn(II) i dos compostos de coordinació basats en Eu(III) que poden detectar ions Fe^{3+} i nitrobenzè en medi aquós de forma selectiva. Encara que els límits de detecció obtinguts en aquest context no representen cap avanç respecte a les sondes luminescents reportades fins al moment, aquests resultats demostren que és possible preparar materials amb propietats luminescents d'interés en base a aquesta família nova de lligands. També s'ha aconseguit aïllar un complex de Fe(II) amb elevada estabilitat que pot ser un potencial candidat per a futures aplicacions catalítiques. Els resultats més rellevants es detallen a continuació en base als seus corresponents objectius:

IX. El capítol 5 mostra la síntesi i caracterització d'una nova família de lligands politòpics que contenen un anell rígid benzènic central, espaiadors etilínics i subunitats terminals quelants de tipus picolinat que han sigut preparats mitjançant reaccions d'acoblament de Sonogashira. Aquests es poden agrupar en lligands homopolitòpics i en lligands heteroditòpics que presenten

un segon grup funcional no quelant com piridina o benzoat en una de les posicions terminals.

X. El capítol 6 descriu la síntesi i caracterització de complexos divalents construïts a partir d'alguns dels lligands anteriors. Es dona especial èmfasi a la preparació de complexos de Zn(II) i a la seua posterior aplicació per tal de detectar compostos nitroaromàtics i ions Fe^{3+}. Resultats preliminars mostren que un dels compostos de coordinació preparats és capaç de *detectar selectivament ions Fe^{3+} i nitrobenzè* gràcies a un *descens dramàtic en la seua senyal fluorescent* (en anglès anomenat *quenching*) després d'interaccionar amb aquests analits. Açò és degut a un procés de ressonància que implica la transferència energètica entre els lligands i els analits, així com a un procés competitiu d'absorció de l'energia d'excitació entre ambdós. Addicionalment, dos polímers de coordinació de Cu(II) on els centres metàl·lics estan connectats per grups picolinat amb un mode de coordinació *sin*, *anti*- fora-del-pla han sigut obtinguts. Aquesta connectivitat dóna lloc a un solapament molt feble entre els orbitals magnètics, de tal manera que és necessari augmentar aquest solapament per tal d'observar interaccions d'intercanvi apreciables entre els centres de coure(II). Finalment, un compost de coordinació de Fe(II) ha sigut preparat i caracteritzat estructuralment i magnèticament. Resultats preliminars mostren que aquest material pot ser emprat com a catalitzador en la reacció d'oxidació de ciclohexà a temperatura i pressió ambients amb una elevada selectivitat per la formació de ciclohexanona. Tots els complexos obtinguts exhibeixen una elevada estabilitat en medi aquós i en un interval ampli de pH, la qual cosa permet el seu ús en condicions extremes.

XI. El capítol 7 descriu la síntesi i caracterització de polímers de coordinació construïts a partir d'alguns dels lligands anteriors i ions lantànids trivalents. D'entre els ions lantànids explorats que han donat lloc a l'obtenció dels materials en forma cristal·lina, tan sols els derivats d'europi(III) presenten emissió característica de l'ió corresponent (en els derivats de Tb(III) i Dy(III) l'efecte antena no és eficient i l'emissió registrada és deguda bàsicament als lligands). Experiments realitzats amb diferents metalls i molècules de solvent mostren que aquests materials poden ser emprats com sondes luminescents per detectar *selectivament ions Fe^{3+} i nitrobenzè*. D'igual manera que en el cas del complex de Zn(II) anterior, un important descens de la senyal fluorescent és detectat com a conseqüència d'una transferència ressonant d'energia entre els lligands i els analits, així com al fet que ambdós espècies competeixen per absorbir l'energia d'excitació. Aquests materials també poden ser aplicats en condicions extremes, ja que són estables en un rang de pH gran en medi aquós.

Appendix section

Characterisation techniques

A. Elemental analysis

C, H and N elemental analyses were performed in a CE INSTRUMENTS 1110 EA elemental analyser (SCSIE, Universitat de València).

B. Infrared spectroscopy

IR transmission measurements of ligands 1,1'-(2,6-pyridinediyl)-bis-3-(dimethylamino)-2-propen-1-one, bpp, **Me_2L1**-**Me_2L8**, **H_2L1**-**H_2L8**, barium salts ($Ba(C_6H_8O_4)\cdot 0.1C_6H_{10}O_4$, $Ba(C_8H_4O_4)$ and $Ba(C_6H_4NO_3)_2\cdot 4H_2O$), silver salts ($Ag(C_6H_4NO_2)$) and complexes **1**·$4H_2O$, **1**, **2**·$5H_2O$, **3**·$2H_2O$, **4**·$4H_2O$, **5**·$2.4H_2O$, **5**·$1.8H_2O\cdot 0.6D_2O$, **6**·$5H_2O$, **6**·$2.75H_2O\cdot 2.25D_2O$ and **7**-**11** were performed at room temperature on pressed KBr pellets in a fourier transformation-infrared spectrometer NICOLET 5700 (Thermo Electron Corporation) IR in the range 400-4000 cm^{-1}. Transmission measurements of complexes **12**-**22** were performed directly from the powdered samples at room temperature in a fourier transformation-infrared spectrometer (Bruker, alpha II) equipped with an attenuated total reflection (ATR) accessory in the range 400-4000 cm^{-1}.

C. Nuclear magnetic resonance spectroscopy

^1H and ^{13}C-NMR spectra of ligands **Me_2L1**-**Me_2L8** and **H_2L2, H_2L3, HL6**-**H_2L8** were recorded on a Bruker DPX 300 MHz spectrometer (SCSIE, Universitat de València). For the ester derivatives, $CDCl_3$ or CD_2Cl_2 deuterated solvents were used, as indicated in the synthetic part. Some acid ligands were insoluble in common solvents and their NMR spectra could not be recorded (**H_2L1**, **H_3L4** and **H_2L5**). For those that were successfully solubilised, addition of a base was necessary (KOH in D_2O or TBAOH in CD_3CN).

D. Mass spectrometry

ESI-MS mass spectra of esters **Me_2L1**-**Me_2L8** and ligands **H_2L1**-**H_2L3**, **H_2L5**-**H_2L8** were obtained using a Esquire 3000 plus ion trap mass spectrometer or a TripleTOF 5600 SCIEX system (SCSIE, Universitat de València). The MALDI-TOF spectrum of ligand **H_3L4** was measured using a 5800 MALDI TOF/TOF (AB SCIEX)[1] mass spectrometer in positive reflectron mode (3000 shots every position, proteomics facility of SCSIE, Universitat de València). The mass range for all the measurements was 150-900 Da.

E. Thermogravimetric analysis

TG analyses of barium salts ($Ba(C_6H_8O_4)\cdot 0.1C_6H_{10}O_4$ and $Ba(C_8H_4O_4)$), silver salts $Ag(C_6H_4NO_2)$ and complexes **1**·$4H_2O$, **2**·$5H_2O$, **6**·$5H_2O$, **7**, **8**, **10** and **11** were performed on a Setaram Setsys TGA-ATD16/18 apparatus at a scan rate of 10 K·min^{-1}. TG analyses were undertaken under a nitrogen atmosphere for compounds **7**, **10**, **1**·$4H_2O$, **2**·$5H_2O$ and barium salts; whereas for the silver salts $Ag(C_6H_4NO_2)$, complexes **8** and **11** an oxygen atmosphere was used. TG analyses of the barium salt $Ba(C_6H_4NO_3)_2\cdot 4H_2O$ and complexes **3**·$2H_2O$, **4**·$4H_2O$, **5**·$2.4H_2O$, **9** and **12**-**22** were performed on a Mettler-Toledo TGA/SDTA/851e apparatus under N_2 atmosphere at a scan rate of 10 K·min^{-1} or 20 K·min^{-1}.

F. Differential scanning calorimetry measurements

DSC measurements under N_2 atmosphere were performed for complexes **1**·$4H_2O$ and **2**·$5H_2O$ in a Mettler Toledo DSC821e apparatus with warming and cooling rates equal to 4 K·min^{-1}. DSC measurements for **3**·$2H_2O$, **4**·$4H_2O$, **5**·$2.4H_2O$ and **6**·$5H_2O$ were carried out in the same apparatus in the presence of N_2 but at 10 K·min^{-1}.

G. Magnetic properties measurements

Variable-temperature (2-300 K) magnetic susceptibility direct current (dc) measurements were performed on polycristalline samples using a magnetometer (Quantum Design MPMS-XL-5) eqquiped with a SQUID sensor for compounds **7**-**9** and **12**-**22**. Measurements were carried out in a magnetic field of 1000 Oe. Alternate current (ac) data were collected in the range 2-12 K, 2-10 K or 2-14 K for compounds **14**-**17** and **20**-**22** with an applied alternating field of 3.95 Oe at different frequencies in the range 1-997 Hz. Direct current fields between 1000-5000 Oe were applied in order to supress the fast quantum tunnelling of the magnetisation.

For spin crossover complexes (**1**·$4H_2O$-**6**·$5H_2O$), variable-temperature magnetic susceptibility measurements were performed on polycrystalline samples using a magnetometer (Quantum Design MPMS-XL-5) equipped with a SQUID sensor and under a magnetic field of 0.1 T. First, a dehydrated sample of **1** for magnetic measurements was obtained by heating the compound at 460 K in a glass tube under vacuum. The temperature sweeping rate for this compound was as follows: 0.5 K·min^{-1} (2-10 K), 1 K·min^{-1} (10-50 K), 5 K·min^{-1} (50-200K), 2 K·min^{-1} (200-400 K). Secondly, another dehydrated sample of **1** for magnetic

measurements was obtained by heating the compound at 400 K in a glass tube under vacuum. In this case, the temperature sweeping rate was as follows: 2.5 K·min^{-1} (300-400 K), 2.5 K·min^{-1} (400-9 K), 0.4 K·min^{-1} (9-2 K). Dehydrated samples of **2** were obtained *in situ* by maintaining the sample in the SQUID at 400 K for 2 h (until a constant magnetic signal was obtained). The temperature sweeping rate sequence for **2** was: 0.5 K·min^{-1} (2-10 K), 2.5 K·min^{-1} (10-400 K). **3**·2H_2O was desolvated in a sealed tube at 453 K under vacuum, transferred to the SQUID apparatus and its magnetic properties measured in the temperature range comprised between 400 K and 2 K using sweeping rates of 2.15 K·min^{-1} (400-10 K) and 0.5 K·min^{-1} (10-2 K). A dehydrated sample of **4** was obtained *in situ* by maintaining the sample in the SQUID at 400K for 1 h (until a constant magnetic signal was obtained). The temperature sweeping rate was as follows: 1 K·min^{-1} (2-20 K), 2.25 K·min^{-1} (20-200 K), 1.25 K·min^{-1} (200-400 K). Compounds **5**·2.4H_2O, **5**·1.8H_2O·0.6D_2O and anhydrous **5** were measured in settle mode. Two complete cycles of cooling/warming were acquired for the dehydrated material, instead for the remaining samples only one complete cycle was registered. The settle attainment setting consisted on waiting at each temperature until χ has stabilised within the 5% of tolerance before taking the measurement. For the original compound, the sequence of temperature step set was the following: 2 K (300-290 K), 1 K (290-280 K), 0.20-0.25 K (280-265 K), 1 K (265-260 K) and 2 K (260-250 K). The actual average scan rates in the 280-265 K range were 0.054 and 0.073 K·min^{-1} for the cooling and heating modes, respectively. For the deuterated material, 0.2 and 1 K steps were set in the ranges of 280-265 K and 265-250 K, respectively. This resulted in an average scan rate of 0.08 K·min^{-1} in the hysteresis region (280-265 K). The anhydrous sample was obtained by dehydration of the original compound *in situ* in the SQUID equipment. First, it was heated from 300 K to 400 K at 10 K·min^{-1} (sweep) and kept for 2 h at this temperature. Then, the following sequence was applied: 400-300 K (sweep, at 2 K·min^{-1}), 300-175 K (settle mode, with 0.5 K steps), 175-20 K (sweep, at 2 K·min^{-1}) and 20-2 K (sweep, at 0.20 K·min^{-1}). The averaged cooling/warming rate of the temperature range measured using the settle mode was 0.19 K·min^{-1}. The pristine and anhydrous materials were also measured in sweep mode. The warming and cooling rates for the original compound were 0.5 K·min^{-1} between 2 and 20 K and 1.0 K·min^{-1} between 20 and 300 K. An additional experiment around the transition temperature (250-280 K) was performed with warming and cooling rates of 0.5 K·min^{-1}. Again, the anhydrous material was obtained by dehydration of the original compound *in situ* in the SQUID equipment at 400 K for 2 h. Then, its magnetic susceptibility was registered at two different sweeping rates (2 K·min^{-1} and 10 K·min^{-1}) in the 400-2 K temperature range (collecting two complete cycles). Compounds **6**·5H_2O and

6·2.75H_2O·2.25D_2O were measured in the temperature range 2-300 K with warming and cooling rates of 0.2 K·min^{-1} between 2 and 20 K and 2.0 K·min^{-1} between 20 and 300 K. A desolvated sample of **6** was obtained *in situ* by maintaining the sample in the SQUID at 400 K for 2 h and measured at a temperature sweeping rate of 2 K·min^{-1} (100-20 K) and 0.20 K·min^{-1} (20-2 K). Plastic capsules perforated in order to favour solvent loss were employed when dehydration of the samples were performed inside the SQUID.

For photomagnetic measurements of **2**, **4**, **5**·2.4H_2O and **6**·5H_2O the samples were prepared in thin layers to promote full light penetration. Samples **2**·5H_2O and **4**·4H_2O were first dehydrated *in situ* in the SQUID device at 400 K. After slow cooling to 10 K, the samples were irradiated with green or red light (λ = 532 nm for **2** and **4**; λ = 630 nm for **5**·2.4H_2O and **6**·5H_2O, respectively) and the magnetisation was measured. When the saturation point was reached, the laser was switched off and the temperature increased at a rate of 0.3 K·min^{-1} to determine the T(LIESST) value given by the minimum of the $\delta(\chi T)/\delta T$ versus T curve for the relaxation process. For **5**·2.4H_2O and **6**·5H_2O, the relaxation kinetics of the metastable high-spin state have been investigated from 54 K to 59 K and from 72 K to 60 K, respectively. First, the sample was irradiated at 10 K with a red laser in order to reach the photoinduced high-spin phase. Once saturation of the signal was observed, the sample was warmed while irradiating until the chosen temperature. Then, the laser was switched off and the magnetic susceptibility recorded in the dark as a function of time. Furthermore, the relaxation curves of the thermally quenched **6**·5H_2O were obtained between 75 K and 105 K.

H. EPR spectroscopy

EPR spectra (X- and Q-bands) were recorded on polycrystalline powder samples at room temperature in a Bruker ELEXYS E580 spectrometer equipped with a helium continuous-flow cryostat. The samples (compounds **7** and **8**) were measured in quartz tubes and the frequencies used were 3.4082·1010 Hz (Q-band) and 9.472232·109Hz (X-band), with a power of 0.2 mW.

I. Mössbauer spectroscopy

Mössbauer spectra of **1**·4H_2O, **1**, **2**·5H_2O and **2** were collected in transmission mode using a conventional constant-acceleration spectrometer and a 25 mCi ^{57}Co source in a Rh matrix. The velocity scale was calibrated using α-Fe foil. The absorbers were obtained by packing the powdered samples into perspex holders. Isomer shifts are given relative to

metallic α-Fe at room temperature. The low temperature spectra were collected using a bath cryostat with the sample immersed in liquid He or He gas for measurements at 4.1 K and above, respectively. The spectra were fitted to Lorentzian lines using a non-linear least-squares method.[2]

J. Powder X-ray diffraction

Powder X-ray diffraction measurements of compounds **1**-**22** were collected using Cu Kα radiation (λ = 1.54056 Å) at room temperature and in a 2θ range from 2 to 40°. Polycrystalline samples were lightly ground in an agate mortar and filled into a 0.5 mm borosilicate capillary prior to being mounted and aligned on an Empyrean PANalytical powder diffractometer. Simulated diffractograms were obtained from single crystal X-ray data using the *CrystalDiffract* software. Variable-temperature powder X-ray diffraction measurements of **1**, **3**, **4** and **5** were recorded using the same diffractometer equipped with an Oxford Cryostream in the temperature range between 400 K and 142 K.

K. Piezoelectric force microscopy, SHG and dielectric measurements

Nanoscale polarization imaging and local switching spectroscopy were carried out using a resonant-enhanced piezoresponse force microscopy (MFP-3D, Asylum Research). Conductive Pt/Ir-coated silicon probes (EFM-50, Nanoworld) were used for domain imaging and polarisation switching studies. The system is additionally equipped with a prototype high voltage module (power supply, amplifier, tip holder, and sample holder) that allows application of dc voltages up to ± 220 V and imaging at ac voltages up to 110 Vpp (in the single frequency mode) at frequencies of 300-400 kHz. Static domain structure has been studied by applying an ac voltage of 10 Vpp in the original (**3**·2H_2O at 298 K), dehydrated (**3** after heating at 453 K for 20 min, at 385 K and 298 K) and rehydrated samples (**3**·2H_2O at 298 K) of complex **3**. PFM hysteresis loops were obtained at fixed locations of the sample as a function of switching pulse amplitude (pulse duration was 25 ms) superimposed on ac modulation bias with amplitude of 10 Vpp at 335 kHz for the high-temperature and room-temperature measurements of compound **3**. Finally, we carried out the domain switching process in compound **3** at 385 K applying a dc tip bias of +200 V for 2 s and after an opposite bias of −200 V for 2 s. For second-harmonic generation (SHG) experiments of **3**·2H_2O and **3** (obtained *in situ* by heating at 453 K for 2 h), an unexpanded laser beam with low divergence (pulsed Nd:YAG at a wavelength of 1064 nm, 5 ns pulse duration, 1.6 MW peak power, 10 Hz repetition rate) was

used. The instrument model was FLS 920, INSTEC Instruments. The numerical values of the nonlinear optical coefficients for SHG were determined by comparison with a potassium dihydrogen phosphate (KDP) reference. Complex dielectric permittivity of anhydrous **3** was measured with an Agilent 4284A impedance analyser over the frequency range from 500 Hz to 1 MHz with an applied electric field of 0.5 V.

L. Electron microscopy

Energy-dispersive X-ray (EDX) microanalyses were carried out on a scanning electron microscopy (Philips XL30 ESEM, SCSIE, Universitat de València) in order to verify the presence of the corresponding metal in all the synthesised complexes.

M. UV-Vis and photoluminescent properties

UV absorption spectra in solution and in the solid state were recorded at room temperature on a JASCO V-670 absorption spectrometer. Photoluminescent data of complexes **10**, **11**, **12**, **14**, **15**, **18**, **20** and **21** in aqueous suspensions were obtained with a Varian Cary Eclipse spectrometer, in quartz cuvettes (1 cm path-length). For fluorescence emission titrations, 25 mM or 50 mM $Fe(NO_3)_3$ solution in water or 0.1 M nitrobenzene in EtOH were titrated until almost complete quenching of fluorescence. The photoluminescence characteristics were studied using a Xe lamp coupled to a monochromator as the excitation source and an integrated sphere coupled to a spectrometer (Hamamatsu C9920-02 with a Hamamatsu PMA-11 optical detector) in order to quantitatively determine the quantum yield for complexes **10**, **11**, **12** and **18**. Luminescence decay measurements were measured using a Compact fluorescence lifetime spectrometer C11367, Quantaurus- Tau, with LED light source. Fluorescence lifetime measurement software U11487 was used to register the data.

N. Neutron crystallography

6·$5H_2O$ was placed on a close-circuit displex device on the monochromatic four-circle diffractometer D19 at ILL (Grenoble, France). The wavelengths used were 1.455 Å and 0.950 Å, provided by a flat Cu monochromator using the 220 and 331 reflections, respectively, at $2\theta_M = 69.91°$ take-off angle. Similar results were obtained with both wavelengths and, accordingly, only the 1.455 Å-data are discussed in the thesis. The sample was

cooled up to 240 K, 120 K, 95 K and 50 K with 2K/min cooling rate and data collection carried out at the selected temperatures. Additionally, two measurements were undertaken at 95 K and 50 K after complete relaxation of the compound. For both cases, temperature was kept at 95 K for 4 hours in order to achieve complete relaxation prior to data collection at the working temperature. The measurement strategy consisted on 25 omega (ω) scans with steps of 0.07° at different χ and φ positions. These omega scans cover either 79° or 64° depending on the χ angle, in order to avoid collisions with the sample environment. The NOMAD software from ILL was used for data collection. Unit cell determination was done by using PFIND and DIRAX programs, and processing of the raw data was applied using RETREAT and RAFD19 programs.[3] Absorption correction was applied using D19ABS program.[4] All atoms were refined anisotropically without geometrical restraints.
Variable temperature neutron diffraction experiments for **6**·5H_2O were performed on the Cylindrical CCD Laue Octogonal Photo Scintillator (CYCLOPS), a Laue single-crystal diffractometer at the ILL, Grenoble. Data were collected between room temperature and 10 K, both in the cooling and heating modes. The transition from the HS phase to the mixed-spin phase was reproduced at $T_{\downarrow}$ = 166 K on cooling. Relaxation measurements at 95 K indicated complete conversion to the LS phase after 4 h. Further cooling to 10 K shows the absence of any structural transformation at low temperatures. Upon warming back to room temperature, two crystal phase transitions were observed at approximately 117 K and 166 K, defining the range of stability of the mixed-spin phase.

0. Single crystal X-ray diffraction

- Compounds **1**·4H_2O, **1**, **2**·2MeOH·H_2O and **2**·5H_2O

Suitable crystals of **1**·4H_2O, **2**·2MeOH·H_2O and **2**·5H_2O were coated with Paratone N oil, suspended on small fiber loops, and placed in a stream of cold nitrogen on an Oxford Diffraction Supernova diffractometer equipped with a graphite-monochromated Enhance (Mo) X-ray Source (λ = 0.71073 A). Some rehydrated crystals of **1**·4H_2O were dehydrated at 400 K in an oil bath under vacuum. Then, one of them was quickly coated with paratone N oil, suspended on a small fiber loop and placed in a stream of cold nitrogen (120 K) on an Oxford Diffraction Supernova diffractometer equipped with a graphite-monochromated Enhance Mo X-Ray Source (λ = 0.71073 Å). Another identical single crystal was treated in the same way and placed in a stream of hot nitrogen at 298 K. The data collection routines, unit cell refinements, and data processing were carried out

using the CrysAlis software package.[5] The structures were solved using SIR97[6] *via* the WinGX graphical interface,[7] and refined using SHELX-97.[8] The adipate anion present in the dehydrated sample **1** is disordered between two positions with occupancies of 0.5591/0.4409 at 120 K and 0.5481/0.4519 at 298 K. The anisotropic refinement of this disordered anion required the use of DELU, SIMU and DFIX restraints. H atoms on carbon atoms were included at calculated positions and refined with a riding model. H atoms of bpp amino groups were all found in difference maps and refined positionally with the geometrical restraint N–H = 0.89 Å. In **2**·2MeOH·H_2O, all H atoms on water molecules were found in difference maps and refined with geometrical restraints (O–H = 0.82 Å and H···H = 1.30 Å) and with *U*iso(H) = 1.2*U*eq(O). The H atoms of hydroxyl groups of methanol molecules were refined with the riding model available in SHEXL-97 (AFIX 147) and with *U*iso(H) = 1.5*U*eq(O). In **1**·4H_2O, only some H atoms on water molecules could be found in difference maps, which were refined with geometrical restraints as before. In **2**·5H_2O, the water molecules were found to be disordered in several positions with partial multiplicities, and their H atoms were not located. In **1**, **1**·4H_2O and **2**·2MeOH·H_2O all non-hydrogen atoms were refined anisotropically. In **2**·5H_2O, oxygen atoms of disordered water molecules were refined isotropically. Unit cell parameters of **1** were measured in the 280-120 K temperature range (with intervals of 20 K) using the same single-crystal specimen used for the data collection at 298 K.

- Compounds **3**·2H_2O and **3**

One single crystal of **3**·2H_2O was taken from the solution, quickly coated with Paratone N oil, suspended on a small fiber loop, and placed in a stream of cooled nitrogen (120 K) on an Oxford Diffraction Supernova diffractometer. For the structure determination of **3**, some crystals of **3**·2H_2O were first dehydrated at $T \approx 450$ K under vacuum and, then, one of them was quickly coated with Paratone N oil, suspended on a small fiber loop, and placed in a stream of hot nitrogen (338 K) on an Oxford Diffraction Supernova diffractometer. Another identical single crystal was treated in the same way and placed in a stream of nitrogen at 120 K. The data collection routines, unit cell refinements, and data processing were carried out using the CrysAlis software package.[5] The structure solutions and refinements were carried out using SHELXS-97[9] and SHELXL-2014.[10] The structures of **3** are twinned by inversion and were refined using the TWIN and BASF instructions included in SHELXL-2014. All non-hydrogen atoms were refined anisotropically in both crystal structures (DELU restraints were applied to some atoms of **3** to allow their anisotropic refinement). All hydrogen atoms in **3**·2H_2O were found in Fourier difference

maps and refined without restraints. In **3**, the H atoms bonded to carbon atoms were placed in geometrically calculated positions and refined using a riding model. The hydrogen atoms bonded to nitrogen atoms were found in Fourier difference maps and refined without restraints. Unit cell parameters of **3** were measured in the 338-303 K temperature range with intervals of 5 K.

- Compound **4**·4H_2O

A suitable crystal of **4**·4H_2O was coated with Paratone N oil, suspended on a small fiber loop and placed in a stream of cold nitrogen (120 K) on an Oxford Diffraction Supernova diffractometer equipped with a graphite-monochromated Enhance Mo X-Ray Source (λ = 0.71073 A). The data collection routines, unit cell refinements and data processing were carried out using the CrysAlis software package.[5] The structure was solved using SHELXS-97[9] and refined using SHELXL-2017.[10] H atoms bonded to carbon atoms were included at calculated positions and refined with a riding model. H atoms of bpp amino groups were all found in Fourier difference maps and refined positionally with the geometrical restraint N–H = 0.89 Å. Moreover, all H atoms on water molecules were found in difference maps and refined with geometrical restraints (O–H = 0.82 A and H···H = 1.30 Å). All non-hydrogen atoms were refined anisotropically.

- Compounds **5**·2.4H_2O and **5**

For **5**·2.4H_2O, crystal data were collected on different single-crystals (*a*, *b*, *c*, *d* and *e*) and temperatures: data on samples *a* (296 K), *b* (270, 260 and 250 K) and *c* (80 and 30 K) were collected on a Bruker APEX diffractometer, while data on samples *d* (200 K) and *e* (120 K) were collected on an Oxford Diffraction Supernova diffractometer. Between 296 and 120 K the crystals were cooled in a flow of chilled nitrogen gas by using an Oxford Cryosystems Cryostream.[11] Below 120 K, cooling was carried out in a flow of chilled helium with an Oxford Cryosystems HELIX.[12] Sample *c* was measured first at 30 K after being irradiated during 2 h 30 min with a red laser (λ = 630 nm, optical power of 5 mW·cm^{-2}), whilst on the diffractometer (this data corresponds to the photoinduced high-spin (PIHS) phase at 30 K). After full relaxation, the same sample was measured at 80 K. For the structure determination of **5**, a new single-crystal was dehydrated *in situ* at 400 K during 2 h using a stream of hot nitrogen on an Oxford Diffraction Supernova diffractometer prior to data collection at 310 K and at 150 K. The CrysAlis software package[5] was used for the data collection routines, unit cell refinements and data processing of the data acquired in the Oxford Diffraction Supernova diffractometer (equipped with a graphite-

monochromated Enhance Mo X-Ray Source, λ = 0.71073 Å). Empirical absorption corrections were performed using the SCALE3 ABSPACK scaling algorithm. On the other hand, the APEX3 software suite[13] was used for data collection, unit cell determination, data reduction, absorption correction, scaling and space group determination of the data collected on a Bruker APEX diffractometer (equipped with a sealed microfocus tube with monochromated Mo Kα radiation, λ = 0.71073 Å). In all cases, the structures were solved with the SHELXT structure solution program[14] and refined on F^2 using full matrix least-squares methods with the SHELXL-2018[10] software, using Olex2.[15] The structures of **5** are non-merohedrally twinned. The peaks were indexed by using two identical cells with different orientations related by rotation of 180° around the reciprocal b^* axis. The fractional contribution of the minor twinned component refined to 0.483 and 0.499 at 310 K and 150 K, respectively, using the BASF parameter and the HKLF5 instruction in the SHELXL program integrated in the WINGX program suite. All non-hydrogen atoms were refined anisotropically, except the atoms of one disordered isonicNO anion in **5**, which are disordered in two positions related by an inversion center at 310 K. At 150 K, two isonicNO anions are disordered and corresponding non-hydrogen atoms could not be refined anisotropically. H atoms bonded to carbon atoms were included at calculated positions and refined as riding atoms with relative isotropic displacement parameters. Instead, H atoms of bpp amino groups and H atoms of water molecules were found in Fourier difference maps, except for the H-atoms of O6W (which were found only in the structures collected at 200 K, 120 K, 80 K and 30 K) and O3WB (the minor component of a disordered water molecule). Unit cell parameters of **5**·2.4H_2O were measured with intervals of 20 K between 120 K and 260 K and with intervals of 10 K in the 260-300 K temperature range.

- Compound **6**·5H_2O

Crystal data were collected on an Oxford Diffraction Supernova diffractometer equipped with a graphite-monochromated Enhance Mo X-Ray Source (λ = 0.71073 Å). Four different single crystals of **6**·5H_2O were coated with Paratone N oil, suspended on a small fiber loop, and cooled in a flow of chilled nitrogen gas at 240 K, 210 K, 120 K and 95 K, respectively. In the last case, the crystal was kept at 95 K during 4 h prior to data collection. Data collection routines, unit cell refinements and data processing were carried out using the CrysAlis software package.[5] Structures were solved using SHELXS-97[9] and refined using SHELXL-2017.[10] Photocrystallographic measurements were carried out using a Bruker APEX diffractometer equipped with a graphite-

monochromated MoKa radiation (λ = 0.71073 Å). The same single crystal was used for the measurement of the crystal structure of the photoinduced high-spin (PIHS) phase, the structure after partial relaxation of the PIHS phase and the structure obtained from full relaxation of the PIHS state. Compound **6**·5H_2O was cooled until 50 K in a flow of chilled helium with an Oxford Cryosystems HELIX[12] and, then, was irradiated for 60-90 minutes with a red laser (λ = 630 nm, 5 mW/cm^2) whilst on the diffractometer. After this time, laser irradiation was switched off and data collection started. For the second measurement, after reaching the PIHS state, the sample was warmed to 69 K at 18 K/h and then quenched at 50 K in order to acquire crystal data of the mixed phase. Finally, the sample was further heated until 95 K and the fully LS phase could be measured. The APEX3 software suite[13] was used for data collection, unit cell determination, data reduction, absorption correction, scaling and space group determination of the collected data. The structures were solved with the SHELXT structure solution program[14] and refined on F^2 using full matrix least-squares methods with the SHELXL-2018[10] software, using Olex2.[15] All non-hydrogen atoms were refined anisotropically. H atoms bonded to carbon atoms were included at calculated positions and refined with a riding model. Instead, H atoms of bpp amino groups, all H atoms on water molecules and the hydrogen atom that displays the proton migration (H1O) were found in Fourier difference maps and refined without geometrical restraints. Unit cell parameters of **6**·5H_2O were measured with intervals of 10 K in the 120-240 K temperature range.

Difference Fourier maps (F_o-F_c) were calculated for each temperature on a plane through atoms C29, O1 and O5. All Fourier maps were based on a model produced by removing the hydrogen atom in the short strong hydrogen bond (H1O). The contour level used was 0.1 e·$Å^{-3}$, the resolution 0.1 Å and the summation limits (2x2) $Å^2$. On finalising the structure, a LIST 3 command was used and the output FCF structure factors were used as the input to MAPVIEW that is used to visualise the electron-density maps written by the Fourier calculation program of the WiNGX package.[7]

- Compounds **7**-**11**

Suitable crystals of **7**-**11** were coated with paratone N oil, suspended on small fiber loops and placed in a stream of cold nitrogen (120 K) on an Oxford Diffraction Supernova diffractometer equipped with a graphite-monochromated Enhance Mo X-Ray Source (λ = 0.71073 Å). The data collection routines, unit cell refinements and data processing were carried out using the CrysAlis software package for complexes **7**, **8**, **10** and **11**.[5] Compound **9** was measured on a

Bruker APEX diffractometer and the APEX3 software suite[13] was used for data collection, unit cell determination, data reduction, absorption correction, scaling and space group determination. The structures measured on an Oxford Diffraction Supernova diffractometer were solved using SHELXS-97[9] *via* the WinGX graphical interface[7] and refined using SHELXL-2017.[10] The structure of compound **9** was solved with the SHELXT structure solution program[14] and refined on F^2 using full matrix least-squares methods with the SHELXL-2018[10] software, using Olex2.[15] H atoms on carbon atoms were included at calculated positions and refined with a riding model. For compound **9**, H atoms on water molecule O1W were found in difference maps and refined with geometrical restraints (O–H = 0.82 Å and H···H = 1.30 Å) and U_{iso}(H) = 1.2 U_{eq}(O). For compound **10**, O1W water molecule has a partial multiplicity of 0.5 and its H atoms were not located. On the other hand, for compound **11**, H atoms on water molecules were found in difference maps and refined without geometrical restraints. All non-hydrogen atoms were refined anisotropically.

- Compounds **12**-**22**

Suitable crystals of **12**-**22** were coated with paratone N oil, fixed on a small fiber loop and mounted on an Oxford Diffraction Supernova diffractometer equipped with a graphite-monochromated Enhance Mo X-Ray Source (λ = 0.71073 Å) at 120 K. The data collection routines, unit cell refinements and data processing were carried out using the CrysAlis software package.[5] The structures were solved using SHELXT 2018/2 *via* the WinGX graphical interface[7] and refined using SHELXL-2018/3.[10] H atoms on carbon atoms were included at calculated positions and refined with a riding model. For compounds **12**-**17**, H atoms on water molecules and H atoms on ammonium cations were found in difference maps and refined without geometrical restraints. In the case of complexes **18**-**22**, H atoms on water molecules and on acetic acid molecules were not found in Fourier difference maps. All non-hydrogen atoms were refined anisotropically.

References

[1] R. Skelton, F. Dubois, R. Zenobi. *Anal*. *Chem*. **2000**, 72, 1707-1710

[2] J. C. Waerenborgh, P. Salamakha, O. Sologub, A. P. Gonçalves, C. Cardoso, S. Sério, M. Godinho, M. Almeida, *Chem. Mater.* **2000**, 12, 1743-1749

[3] a) A. J. M. Duisenberg, *J. Appl. Cryst.* **1992**, 25, 92-96. b) G. J. McIntyre, R. F. D. Stansfield, *Acta Cryst.* **1988**, A44, 257-262. c) C. Wilkinson, H. W. Khamis, R. F. D. Stansfield, G. J. McIntyre, *J. Appl. Crystallogr.* **1988**, 21, 471-478
[4] J. C. Matthewman, P. Thompson, P. J. Brown, *J. Appl. Crystallogr.* **1982**, 15, 167-173

[5] CrysAlisPro v38.46, Oxford Diffraction Ltd. **2017**

[6] A. Altomare, M. C. Burla, M. Camalli, G. Cascarano, C. Giacovazzo, A. Guagliardi, A. G. G. Moliterni, G. Polidori, R. Spagna, *J. Appl. Cryst.* **1999**, *32*, 115-119

[7] L. J. Farrugia, *J. Appl. Crystallogr.* **1999**,32, 837-838

[8] G. M. Sheldrick, *SHELX-97, an integrated system for solving and refining crystal structures from diffraction data*. **1997**, University of Gottingen, Germany.

[9] G. M. Sheldrick, SHELXS97. *Program for Crystal Structure Solution*. **1997**, University of Gottingen, Germany.

[10] G. M. Sheldrick, *Acta Cryst.* **2015**, C71, 3-8

[11] Cryostream Cooler, Oxford Cryosystems Ltd, Oxford (UK)

[12] A. E. Goeta, L. K. Thompson, C. L. Sheppard, S. S. Tandon, C. W. Lehmann, J. Cosier, C. Webster, J. A. K. Howard, *Acta Cryst.* **1999**, *C55*, 1243-1246

[13] APEX3 Version 2017.3 (Bruker AXS Inc.)

[14] G. M. Sheldrick, *Acta Cryst.* **2015**, *A71*, 3-8

[15] O. V. Dolomanov, L. J. Bourhis, R. J. Gildea, J. A. K. Howard, H. Puschmann, *J. Appl. Cryst.* **2009**, *42*, 339-341

List of publications

[1] Verónica Jornet-Mollá, Carlos Giménez-Saiz, Bruno J. C. Vieira, João C. Waerenborgh and Francisco M. Romero*: Temperature dependence of desolvation effects in hydrogen-bonded spin crossover complexes*. **Dalton Transactions**, 2020. Submitted.

[2] Verónica Jornet-Mollá, Carlos Giménez-Saiz, Laura Cañadillas-Delgado, Dmitry S. Yufit, Judith A. K. Howard and Francisco M. Romero*: Interplay between spin crossover and proton migration along short strong hydrogen bonds*. **Chemical Science**, 2021. DOI: 10.1039/D0SC04918B.

[3] Verónica Jornet-Mollá, Carlos Giménez-Saiz, Dmitry S. Yufit, Judith A. K. Howard and Francisco M. Romero: *A reversible hydrogen-bond isomerization triggered by an abrupt spin crossover near room temperature*. **Chemistry-A European Journal**, 2020, 26. DOI: 10.1002/chem.202003654.

[4] Verónica Jornet-Mollá, Carlos Giménez-Saiz and Francisco M. Romero: *Synthesis, structure, and photomagnetic properties of a hydrogen-bonded lattice of $[Fe(bpp)_2]^{2+}$ spin-crossover complexes and nicotinate anions*. **Crystals**, 2018, 8, 439.

[5] Verónica Jornet-Mollá, Carlos Martín-Mezquita, Yan Duan, Carlos Giménez-Saiz and Francisco M. Romero: *Synthesis, crystal structures and magnetic properties of picolinate-bridged copper(II) chains*. **Journal of Coordination Chemistry,** 2018, 71, 644-656.

[6] Verónica Jornet-Mollá, Yan Duan, Carlos Giménez-Saiz, Yuan-Yuan Tang, Peng-Fei Li, Francisco M. Romero and Ren-Gen Xiong: *A Ferroelectric Iron(II) Spin Crossover Material*. **Angewandte Chemie**, 2017, 56, 14052-14056.

[7] Verónica Jornet-Mollá, Yan Duan, Carlos Giménez-Saiz, João C. Waerenborgh and Francisco M. Romero: *Hydrogen-bonded networks of $[Fe(bpp)_2]^{2+}$ spin crossover complexes and dicarboxylate anions: structural and photomagnetic properties.* ***Dalton Transactions***, 2016, 45, 17918-17928.

[8] Verónica Jornet-Mollá and Francisco M. Romero: *Synthesis of rigid ethynyl-bridged polytopic picolinate ligands for MOF applications*. **Tetrahedron Letters**, 2015, 56, 6120-6122.

List of compounds

List of Ligands

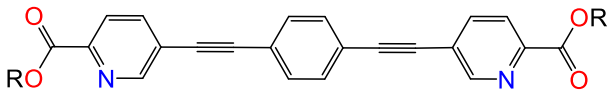

Me_2L1 (R = Me)
H_2L1 (R = H)

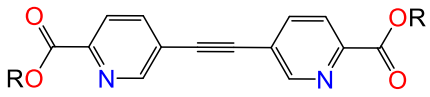

Me_2L2 (R = Me)
H_2L2 (R = H)

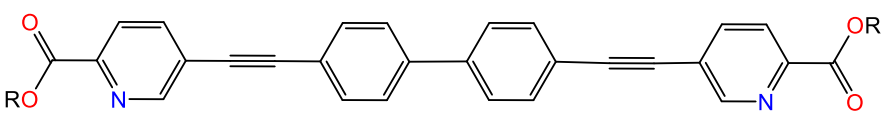

Me_2L5 (R = Me)
H_2L5 (R = H)

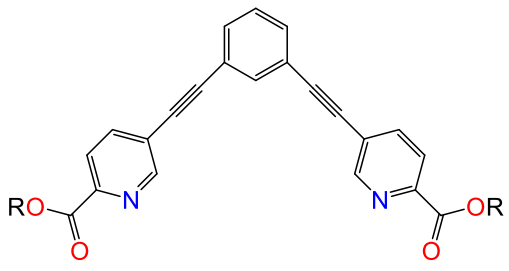

Me_2L3 (R = Me)
H_2L3 (R = H)

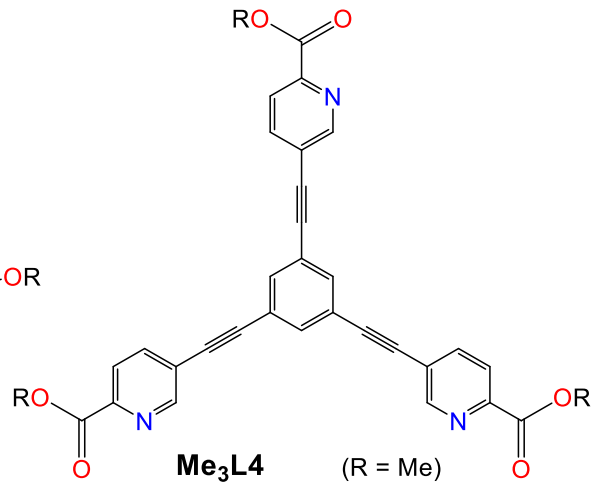

Me_3L4 (R = Me)
H_3L4 (R = H)

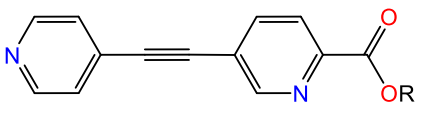

MeL6 (R = Me)
HL6 (R = H)

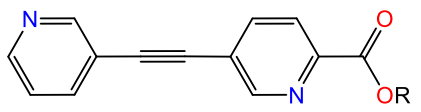

MeL7 (R = Me)
HL7 (R = H)

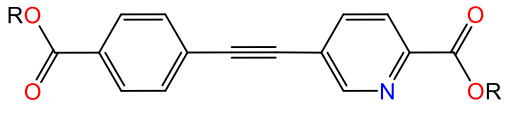

Me_2L8 (R = Me)
H_2L8 (R = H)

List of Complexes

$[Fe(bpp)_2](C_6H_8O_4)\cdot 4H_2O$	**1**·$4H_2O$
$[Fe(bpp)_2](C_8H_4O_4)\cdot 2MeOH\cdot H_2O$	**2**·$2MeOH\cdot H_2O$
$[Fe(bpp)_2](C_8H_4O_4)\cdot 5H_2O$	**2**·$5H_2O$
$[Fe(bpp)_2](isonic)_2\cdot 2H_2O$	**3**·$2H_2O$
$[Fe(bpp)_2](nic)_2\cdot 4H_2O$	**4**·$4H_2O$
$[Fe(bpp)_2](isonicNO)_2\cdot 2.4H_2O$	**5**·$2.4H_2O$
$[Fe(bpp)_2](isonicNO)_2\cdot HisonicNO\cdot 5H_2O$	**6**·$5H_2O$
$[Cu_2(\mathbf{L7})_4]$	**7**
$[Cu_3(\mathbf{MeL8})_6]$	**8**
$[Fe(H_2O)_2(\mathbf{L2})]$	**9**
$[Zn(\mathbf{L7})_2]$	**10**
$[Zn(H_2O)_2(\mathbf{L8})]$	**11**
$[NH_2(CH_3)_2][Ln(H_2O)_2(\mathbf{L8})_2]$	**12-17**

Ln = Eu(**12**), Gd(**13**), Tb(**14**), Dy(**15**), Ho(**16**) and Er(**17**)

$[NH_2(CH_3)_2][Ln(\mathbf{L2})_2]\cdot 1H_2O\cdot 1HAc$	**18-22**

Ln = Eu(**18**), Gd(**19**), Tb(**20**), Dy(**21**) and Ho(**22**)

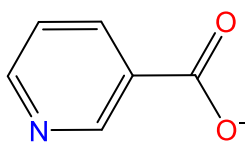

nicotinate

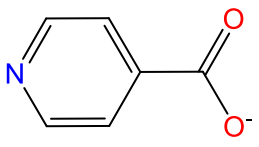

isonicotinate

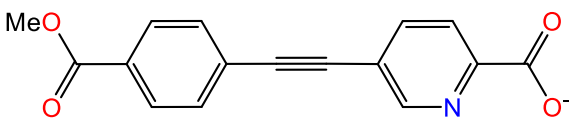

MeL8

Abbreviations

bpp = 2,6-bis(pyrazol-3-yl)pyridine

$C_6H_8O_4^{2-}$ = adipate dianion

$C_8H_4O_4^{2-}$ = terephthalate dianion

isonic = isonicotinate anion

nic = nicotinate anion

isonicNO = isonicotinate N-oxide anion

HisonicNO = isonicotinic acid, N-oxide

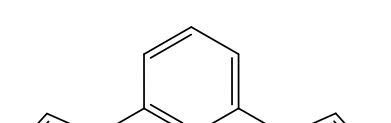

bpp

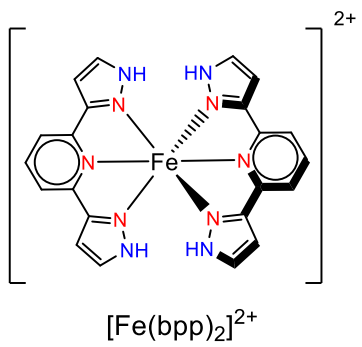

$[Fe(bpp)_2]^{2+}$

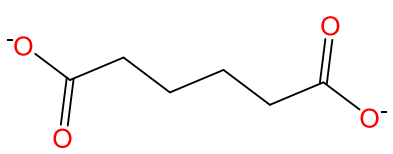

adipate

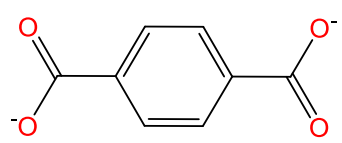

terephthalate

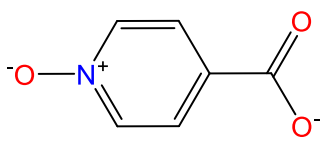

isonicotinate N-oxide

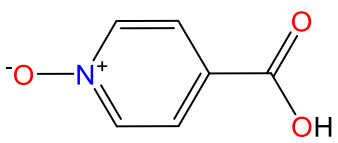

isonicotinic acid, N-oxide